# Snow engineering: recent advances

Philippe Delpech, Thomas K Thiis

**HAL Id: hal-01426073**

**https://cstb.hal.science/hal-01426073v2**

Submitted on 18 Jan 2017

# SNOW ENGINEERING

## Recent advances



**Philippe Delpech, Thomas K. Thiis**

Editors

# ICSE 2016

# 8th International Conference on Snow Engineering

June 14-17, Nantes, France

# Proceedings

Edited by: Philippe Delpech, Thomas K. Thiis

Published by CSTB - Centre scientifique et technique du bâtiment, France

November 2016

# Organizers

Centre scientifique et technique du bâtiment, France          Norwegian University of Life Sciences, Norway

# Conference chair

Philippe Delpech, Thomas K. Thiis

# Scientific committee

Perry Bartlet (Switzerland)
Andrzej Flaga (Poland)
Paolo Formichi (Italy)
Teruyuki Fukuhara (Japan)
Pascal Hagenmuller (France)
Peter Irwin (Canada)
Christian Jaedicke (Norway)
Alan Jones (Canada)
Michael Kasperski (Germany)
Gregorz Kimbar (Poland)

Alex Klein-Paste (Norway)
Holger Koss (Denmark)
Vivian Meylosund (Norway)
Florence Naiim (France)
Michael O'Rourke (U.S.A)
Sergey Pichugin (Russia)
Zoltan Sadowsky (Slovakia)
Toru Takahashi (Japan)
Xuanyi Zhou (China)
Jerzy Zuranski (Poland)

# Preface

Since 1988 seven International Conferences on snow Engineering (ICSE) were held in Santa Barbara, USA (1988, 1992), Sendai, Japan (1996), Trondheim, Norway (2000), Davos, Switzerland (2004), Whistler, Canada (2008), and Fukui, Japan (2012). The ICSE, also known as "SnowEng", is now an established forum for academics, researchers and professional snow engineers, who present, share and interpret the results of their work. Unlike other conferences, ICSE is dedicated to the actual applications of snow sciences to industrial areas, urban planning, road management, building, avalanche engineering and civil engineering.

The 8th edition of the ICSE, was held in Nantes 14-17 June 2016. In response to the call-for-paper we received about 60 abstracts coming from the entire world and illustrating the maintained interest of snow engineering issues in the international community.

The scientific committee selected 43 abstracts for possible oral presentations at the seminar and 10 for posters. In addition, 4 keynote lectures were invited to present overviews on selected topics.
These led to 51 papers published in these proceedings. They were grouped into the following topics:
- Snow drift,
- Structural loading,
- Transportation,
- Buildings / Simulation,
- Avalanche / Snow physics.

These proceedings include papers from 139 authors from 18 countries: Australia, Austria, Canada, China, Denmark, France, Germany, Italy, Japan, Netherland, Norway, Poland, Romania, Russia, Sweden, Switzerland, Ukraine and United States of America.
The papers provide an international state-of-the-art knowledge in the field of snow engineering. They show that the need of expertise in this domain is still high and we feel confident that the ICSE will provide a leading forum for information exchange between researchers and engineers, regulators and other stakeholders in the future.

We would like to thank the members of the scientific committee who did a wonderful work in reviewing the submitted abstracts, the members of the organizing committee, the authors and the sponsoring organizations for their contribution to the success of the conference.

Philippe Delpech, Thomas K. Thiis

*Co-chairman*

# Table of contents

## Session 1: Snow drift I

*Keynote Lecture*

Yoshihide Tominaga

Niigata Institute of Technology, Department of Architecture and Building Engineering, Japan

Ziad Boutanios [1,2] Hrvoje Jasak [2]

[1] Binkz Incorporated, Canada
[2] CFD Lab, FSB, University of Zagreb, Croatia

Tsubasa Okaze [1], Saeka Kato [2], Yoshihide Tominaga [3], Akashi Mochida [4]

[1] Tokyo Institute of Technology, Japan
[2] Takenaka Corporation, Japan
[3] Niigata Institute of Technology, Japan
[4] Tohoku University, Japan

Mengmeng Liu [1, 2], Qingwen Zhang [1, 2], Feng Fan [1, 2]

[1] School of Civil Engineering, Harbin Institute of Technology, China
[2] Key Lab of Structures Dynamic Behavior and Control of China Ministry of Education, Harbin Institute of Technology, China

Sun Xiaoying, He Rijin, Wu Yue

Key Lab of Structure Dynamic Behaviour and Control of the Ministry of Education, Harbin Institute of Technology, China

Jennifer Fiebig, Hans Holger Hundborg Koss

Technical University of Denmark (DTU), Dep. of Civil Engineering, Denmark

Thomas K. Thiis [1, 2]

[1] Norwegian University of Life Sciences, Norway
[2] Multiconsult ASA, Norway

## Session 2 : Structural Loading I

*Keynote Lecture*

Michael Kasperski

Ruhr-Universität Bochum, Research Team EKIB, Germany

Pietro Croce, Paolo Formichi, Filippo Landi, Francesca Marsili

University of Pisa, Department of Civil and Industrial Engineering-Structural Division, Italy

Jerzy Antoni Żurański, Grzegorz Kimbar

Instytut Techniki Budowlanej, ul. Filtrowa 1, 00-611 Warszawa, Poland

Feng Fan [1, 2] Huamei Mo [1], Qingwen Zhang [1, 2], Guolong Zhang [1], Mengmeng Liu [1]

[1] School of Civil Engineering, Harbin Institute of Technology, Harbin, 150090, China
[2] Key Lab of Structures Dynamics Behavior and Control of the Ministry of Education (Harbin Inst. of Tech.), Harbin, 150090, China

Benjamin Czwikla, Michael Kasperski

Ruhr-Universität Bochum, Research Team EKIB, Germany

Shengguan Qiang, Xuanyi Zhou, Ming Gu

State Key Laboratory of Disaster Reduction in Civil Engineering, Tongji University, China

## Session 3 : Avalanche / Snow physics

*Keynote Lecture*

Florence Naaïm

Institut national de recherche en sciences et technologies pour l'environnement et l'agriculture, France

Bruce Jamieson [1,2,] Alan S.T. Jones [3]

[1] Snowline Associates Ltd., Canada
[2] Dept. of Civil Engineering, University of Calgary, Canada
[3] Dynamic Avalanche Consulting Ltd., Canada

## Session 4 : Snow Physics / Snow drift II

## Session 5 : Structural loading II

## Session 6 : Building / Simulation

## Session 7 : Transport

## Poster session

# Session 1

# Snow drift I

# Numerical simulation of snowdrift around buildings: past achievements and future perspectives

Yoshihide Tominaga[1,a]

[1]Niigata Institute of Technology, Department of Architecture and Building Engineering, 1719 Fujihashi, Kashiwazaki, Japan

**Abstract.** This paper reviews the current status of computational fluid dynamics (CFD) modeling of snowdrift around buildings and discusses the review findings to give insight into future applications. First, an overview of past achievements in CFD simulations of snowdrift around buildings is provided by reviewing previous research to clarify their applicability and limitations. Next, recent application examples are presented with respect to several topics. Finally, the remaining development issues and new challenges are presented from an engineering viewpoint. Clearly, CFD has considerable potential, as established in this review. However, to use it appropriately, sufficient attention should be paid to modeling theory and implementation. Because snowdrift is a highly complex phenomenon, we should not excessively rely on numerical simulation. It is important to use data from actual phenomena for all aspects of study.

## 1 Introduction

Under specific conditions of snowfall and wind, a large amount of snowdrift forms on and around buildings. This often leads to the collapse or cracking of buildings because of unbalanced snow loads and overhanging snow on roofs. Moreover, snowdrift on and around buildings not only is very troublesome to remove but also causes difficulties for inhabitants, pedestrians, and vehicular traffic. Therefore, to develop suitable measures for handling difficulties and hazards due to snow in built-up environments, it is necessary to predict the spatial distributions of snow coverage around buildings with high accuracy.

For predicting snowdrift around buildings, considerable experimental research has been carried out over the years using wind or water tunnels. The advantage of such methods is that conditions such as the wind speed, wind direction, and characteristics of snow particles (often modelled by artificial particles) are very controllable. Therefore, these methods have been recognized as useful tools for the practical design for snowdrift around buildings (e.g., [1-5]). However, wind/water tunnels are not always available and are usually expensive and time consuming to use. Furthermore, they have serious limitations with regard to the similarity law. On the other hand, in recent decades, dramatic increases in computational power together with advances in computer software have allowed engineers/researchers to more accurately simulate many types of problems across various engineering realms. Especially, the computational fluid dynamics (CFD) technique has become a strong tool for solving fluid-related engineering problems. CFD simulation has some particular advantages over experimental (full-scale and reduced-scale) testing; it can provide detailed information on the relevant flow variables in the entire calculation domain under well-controlled conditions and without similarity constraints [6]. As a result, the CFD-based numerical simulation technique is expected to be a powerful design tool for addressing the problem of snowdrift around buildings in snowy regions. Hereafter in this paper, "numerical simulation" is used to mean "CFD simulation" only.

This paper reviews the current status of CFD modeling of snowdrift around buildings and discusses the review findings to give insight into future applications. First, in section 2, an overview of past achievements in CFD simulations of snowdrift around buildings is provided by reviewing previous research to clarify their applicability and limitations. Next, in section 3, recent application examples are presented with respect to several topics. Finally, in Section 4, the remaining development issues and new challenges are presented from an engineering viewpoint.

Readers are forewarned that the papers were chosen for this review based on relevance and familiarity to the author, and it is likely that additional and perhaps better examples are available. The author apologizes to all researchers whose valuable contributions are not included in this paper.

## 2 Overview of past achievements

Figure 1 shows the year-wise chart of the number of papers returned by Google Scholar for searches using the keywords "Numerical simulation" and "Snowdrift". It is clearly seen that the number of relevant papers that include these words has increased markedly in recent years.
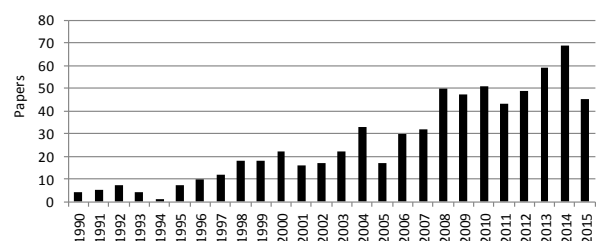


**Figure 1.** Search results for "Numerical simulation" and "Snowdrift" on Google Scholar in March 2016.

[a] Corresponding author: tominaga@abe.niit.ac.jp

**Table 1.** Overview of CFD studies on snowdrift published previously in archival journals.

| Authors (year) | Configuration | Turbulence modeling | Suspension | Saltation | Validation |
|---|---|---|---|---|---|
| Uematsu et al. (1991) [7] | 3D | RANS (0-eq) | EA[a] | MT [21] | Y (FO) |
| Liston et al. (1993) [8] | 2D/fence | RANS (SKE) | NA | MT [22] | N |
| Bang et al. (1994) [9] | 3D/buildings | RANS (SKE) | EA[b] | NA | Y (FO) |
| Sundsbø (1998) [10] | 2D/building step | RANS (1-eq) | EA[c] | TE | N |
| Naaim et al.(1998) [11] | 2D/fence | RANS (MKE) | EA[d] | EF [23] | Y (WT) |
| Sekine et al. (1999) [12] | 2D/building | NA | LA | MT [21] | Y (WT) |
| Tominaga and Mochida (1999) [13] | 3D/actual building | RANS (MKE) | EA[a] | NA | N |
| Thiis (2000) [14] | 3D/model buildings | RANS (SKE) | EA[b] | NM | Y (FO [24]) |
| Beyers et al. (2004) [15] | 3D/isolated cube | RANS (SKE) | EA | TE | Y (FO [25]) |
| Beyers et al. (2008) [16] | 3D/buildings | RANS (SKE) | EA | MT [22] | Y (FO) |
| Tominaga et al. (2011) [17] | 3D/isolated model building | RANS (MKE) | EA[a] | EF [23] | Y (FO [26]) |
| Tominaga et al. (2011) [18] | 3D/isolated model building | RANS (MKE) | EA[a] | EF [23] | Y (FO) |
| Thiis and Ferreira (2015) [19] | 3D/array of pillars | RANS (MKE) | EA[b] | NM | N |
| Okaze et al. (2015) [20] | 2D/drifting snow boundary layer | RANS (MKE) | EA[a] | EF [23] | Y (WT [27]) |

RANS: Reynold-averaged Navier–Stokes; 0-eq =zero-equation (constant eddy viscosity) model; 1-eq = one-equation ($k$) model; SKE = Standard $k$-$\varepsilon$ model; MKE = Modified $k$-$\varepsilon$ models; EA = Eulerian approach; LA = Lagrangian approach; MT = Mass transport rate model; EF = Erosion-flux model; TE = Transport equation for saltation region; Y = yes; N = no; WT = Wind tunnel experiment; FO = Field observation; NA = Not applicable; NM = Not mentioned

[a] Transport equation of drifting snow density
[b] Drift-flux model
[c] Transport equation of snow volume fraction
[d] Transport equation of particle concentration

## 2.1 Papers published in scientific journals

Table 1 lists previous CFD studies on snowdrift around obstacles published in archival journals. Several meteorological studies in regional scales that do not solve the flowfield directly were excluded based on an engineering point of view (e.g., [28-30]). Papers that do not provide enough information about the snowdrift calculation are also excluded from the list.

In the 1990s, applications of CFD to wind engineering problems increased (e.g., [6, 31]), and this technique was being applied to various environmental problems including snowdrift. A pioneering study on numerical simulations of snowdrift around structures by CFD was conducted by Uematsu et al. [7]. In this paper, they proposed an approach in which the velocity field was predicted by a turbulence model, the suspension was modeled by the transport equation of drift density, and the saltation was modelled as a function of friction velocity. This approach has also been employed as a basic model in many other studies. An example of the result obtained using this approach is shown in Figure 2. Shortly thereafter, Liston et al. [8] analyzed the snowdrift around a two-dimensional fence using the standard $k$-$\varepsilon$ model. Here, only the saltation was analyzed and the suspension was not. Bang et al. [9] proposed a snowdrift model of two-phase flow called "a generalized drift-flux model" and applied it to three-dimensional snow deposition around a group of houses. They did not consider the influence of saltation. Sundsbø [10] employed the volume-of-fluid method to create a transient development model of snowdrift and conducted a numerical study on two-dimensional snowdrift around a porous fence in flat terrain

using a one-way coupled model, where the air flow controlled the snowdrift within an Eulerian frame of air
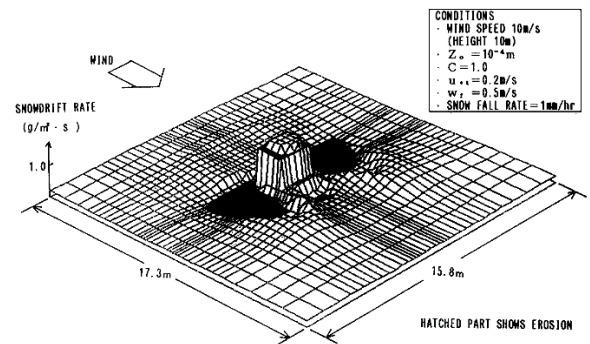


**Figure 2.** Computed wind scoop around a hut [7].
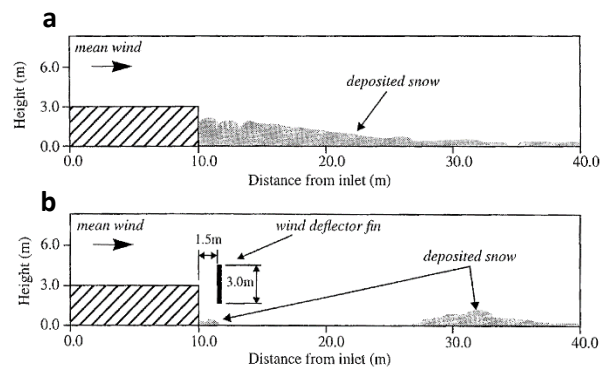


**Figure 3**. Snow accumulation in a building step obtained by numerical simulation (a) without and (b) with a wind deflection fin [10].

**Table 2.** Papers pertaining to CFD studies on snowdrift presented previously at the ICSE.

| Number | Year | Location | Contributions (Target: Authors) |
|--------|------|----------|--------------------------------|
| 3 | 1996 | Sendai, Japan | *Buildings*: Kawakami et al. [32], Waechter et al. [33]<br>*Step*: Sato et al. [34]<br>*Fence*: Sundsbø and Hansen [35] |
| 4 | 2000 | Trondheim, Norway | *Building group*: Thiis and Jaedicke [36]<br>*Two cubical obstacles*: Thiis and Jaedicke [37]<br>*Complex terrain*: Jaedicke et al. [38], Sundsbø and Bang [39]<br>*Slope and road*: Thordarson and Norem [40, 41] |
| 5 | 2004 | Davos, Switzerland | *Mountain hut*: Schaelin et al. [42]<br>*Elevated structures*: Beyers et al. [43] |
| 6 | 2008 | Whistler, Canada | *In-cloud icing on tall buildings*: Beyers et al. [44]<br>*Building with curved roof*: Thiis and Ramberg [45]<br>*Cubical obstacle*: Tominaga et al. [46]<br>*Boundary layer*: Okaze et al. [47] |
| 7 | 2012 | Fukui, Japan | *Fences*: Potac [48]<br>*Boundary layer*: Zhou et al. [49], Okaze et al. [50]<br>*Four buildings*: Ito et al. [51]<br>*Model building*: Tominaga et al. [52] |

velocities. Figure 3 shows the numerical prediction results for snow accumulation on a building step with and without a wind deflection fin. The effect of the deflection fin was clearly demonstrated. Naaim et al. [11] developed an erosion–deposition model in which mass exchange was defined in relation to the flow turbulence, threshold-friction velocity, and snow concentration. They introduced additional terms into the transport equations of $k$ and $\varepsilon$ to take into account the effect of snow particles on turbulence. This model has often been used in subsequent studies. Other different approaches have also been proposed. For example, Sekine et al. [12] applied Lagrangian analysis of a snow particle to snowdrift around a two-dimensional building. Tominaga et al. [13] analyzed the snowdrift around an actual apartment building using the revised $k$-$\varepsilon$ model. In this study, because snow blowing into an elevator hall of the building was the point of interest, the transport equation of drift density was solved only for snow particles suspended in the air. The computational results for the trajectory of snow particles are shown in Figure 4.

In the 2000s, more precise studies on the prediction of snowdrift around buildings were performed based on the accumulated knowledge of engineering CFD and snowdrift modeling. Thiis [14] applied the drift-flux model proposed by Bang et al. [9] to snowdrift around a simple building model and examined its performance by comparing the numerical results with full-scale measurements [24]. In this study, the snow depth was not computed directly but the computational results for the friction velocity of mixed fluid were extrapolated to the area where snowdrifts were expected. Beyers et al. [15] predicted transient snowdrift around a cubic structure using the standard $k$-$\varepsilon$ model and compared the numerical results with experimental data obtained in Antarctica [25]. They concluded that the snowdrift predictions matched well with the measured values in terms of both the location and magnitude, but the simulated results for the accumulation near the cube walls were not generally in accordance with observations. Subsequently, Beyers and Waechter [16] obtained application results for snowdrift around more complex structures, as shown in Figure 5, and
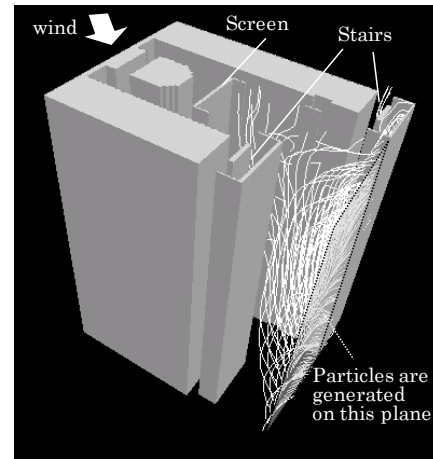


**Figure 4.** Trajectories of snow particles near a building predicted by CFD [13].
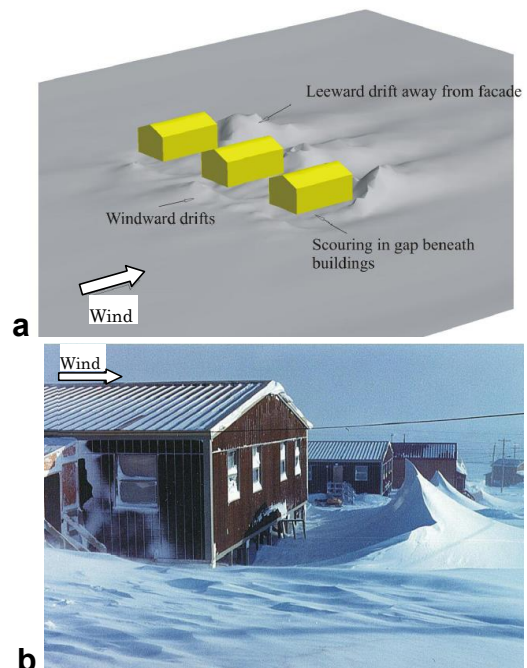


**Figure 5.** Snowdrift simulation around adjacent elevated buildings: (a) CFD simulation and (b) field observation [16].

reported that the prediction results corresponded qualitatively with the actual snowdrift pattern. Tominaga et al. [17] presented the first review of CFD simulations applied to the prediction of snowdrift around buildings. They also presented the CFD prediction results for snowdrift around a cubic building model using a new approach involving a snowdrift model based on experimental and numerical studies. The numerical results were compared with data obtained from detailed field measurements [26] to confirm the accuracy of the new model. More recent studies [18-20] are mentioned in the later sections.

## 2.2 Papers presented at International Conference on Snow Engineering

Important papers on the numerical simulation of snowdrift around buildings have also been presented at previous editions of the International Conference on Snow Engineering (ICSE). The papers from the proceedings that the author felt were relevant are listed in Table 2. The details of the results cannot be explained because of space limitations. Please refer to the original references for further information.

## 3 Recent progress

In this section, noteworthy research topics from recent snowdrift simulation studies are chosen and briefly introduced.

### 3.1 Prediction of roof snow

In the prediction of roof snow loads on buildings, unbalanced snow accumulation due to wind flow is a difficult problem because it involves a complex interaction between snow particle motions and fluid flow affected by the building geometry. So far, only a few attempts have been made to apply CFD to roof snow issues. Thiis et al. [45, 53] predicted the snow distribution on the curved roof of a sports hall located in Oslo and compared the results with measurement results. Figure 6a shows the simulated results for the overall snowdrift pattern on the roof. The location of the end effects can be seen close to the side edge of the roof. Generally, the simulated shape fits the measured shape (Figure 6b) well. This study mainly focused on the reproduction of snow distributions on an actual building under specific weather conditions. There are a few examples in literature wherein the applicability of CFD to snowdrift is examined for a generic configuration. The author recently studied the CFD prediction of snowdrift on a gable-roof building with different roof pitches [54]. In this study, the prediction accuracy of the velocity field around the buildings was validated by comparing the results with wind tunnel experimental data in detail [55]. It should be noted that the correct prediction of the flowfield around roofs with complicated shapes is necessary for the accurate prediction of snowdrift formed on the roof.
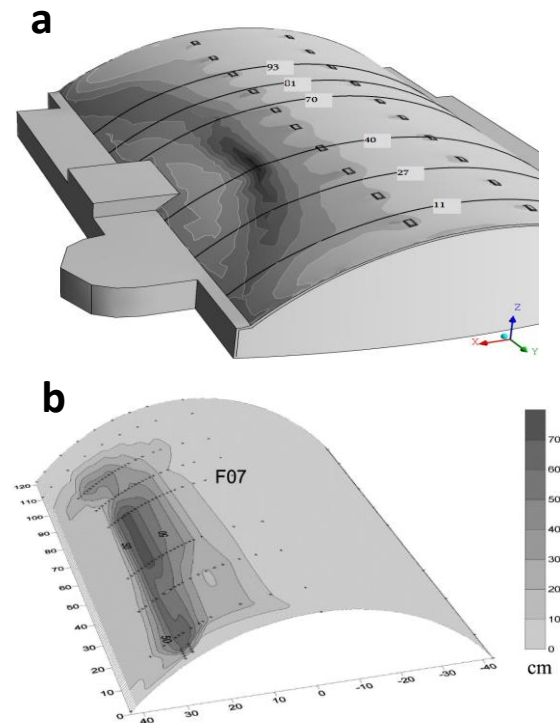


**Figure 6.** Snow deposition on a curved roof: (a) simulated snowdrift pattern and (b) measured snow depth contours [45, 53].
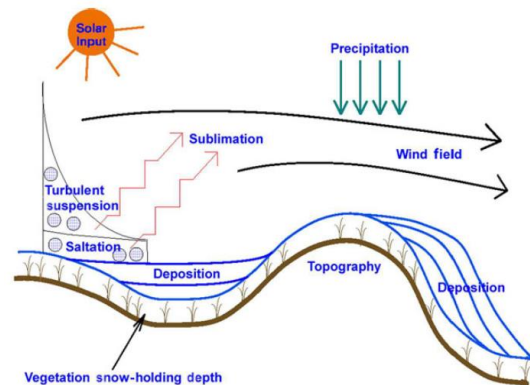


**Figure 7.** Various factors influencing snowdrift formation [28].
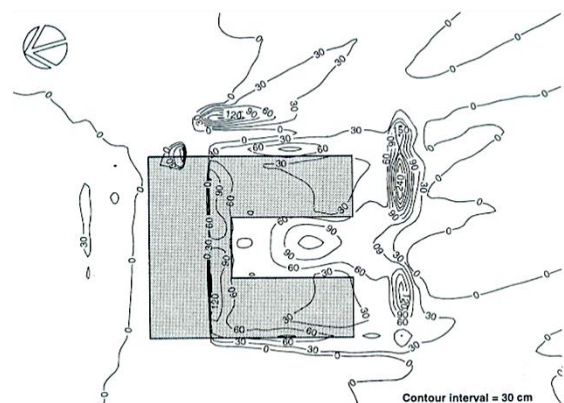


**Figure 8.** Snow deposition pattern predicted by CFD and an FAE computer snow model [35].

## 3.2. Consideration of meteorological influences

As reviewed in the foregoing sections, most previous studies were basically concerned with only the snowdrift formation due to wind during one drifting snow event. However, snow distributions in built-up environments are affected not only by wind but also by many other factors such as temperature, solar radiation, and artificial heat from buildings. These meteorological effects on snow cover have been investigated for predicting an avalanche (e.g., [56]), but very few studies have considered these effects in the civil and architectural fields. In addition, numerical simulations are expected to be used for predicting more multilateral snow accumulation phenomena, as illustrated in Figure 7, because different conditions can be freely considered. That is, the influence of temporal change in the weather conditions and the heat budget of the snow surface on snow accumulation can be studied.

Waechter et al. [35] predicted the snow distributions around a planned building in Antarctica by CFD and a method called the finite area element (FAE). The FAE is a calculation method in which computational domains are divided into finite elements and the temporal variation in the snow depth at each element is computed according to the weather condition. An example of the result is shown in Figure 8. Furthermore, the effects of the terrain, surroundings, and temporal variations in boundary conditions are very important in precisely predicting snow distribution. For example, the prediction of complicated snowdrift formations such as snow flumes as seasonal characteristics by numerical methods has been very difficult. This is because temporal variations in boundary conditions play an important role in such phenomena. That is, snowdrift simulations driven and updated by hourly meteorological data can be a very useful and important contribution to this field. Therefore, a simulation system is required that can predict and evaluate snow coverage distribution with high accuracy while taking into account the above effects. Later, Beyers et al. [44] proposed a methodology for the prediction and simulation of potential in-cloud icing on buildings. In their method, first, an advanced meteorological analysis of the North American Regional Reanalysis meteorological datasets is performed to predict the supercooled droplet availability, temperature, and prevailing wind direction and speed at multiple elevations above the sea level for a particular site. Then, the in-cloud supercooled droplet collection efficiency is determined through the analysis of the flowfield around a building obstacle by CFD. For this type of analyses, research and development results in the meteorological field are very useful. In addition, obtaining reliable experimental data is also important.

The above prediction methods were not examined by comparing their results with observational results. Tominaga et al. [18] developed a system combining a mesoscale meteorological model that predicted precipitation, including snowfall in an area, and a CFD model that predicted snow phenomena on a building scale. The performance of the system was examined by comparing its results with measured data. Figure 9a outlines the prediction system. It consists of a mesoscale



**Figure 9.** Outline of the system used for predicting snow distribution in built-up environments combining a mesoscale meteorological model and a CFD model: (a) schematic structure of the prediction system and (b) analysis procedure of building scale analysis [18].
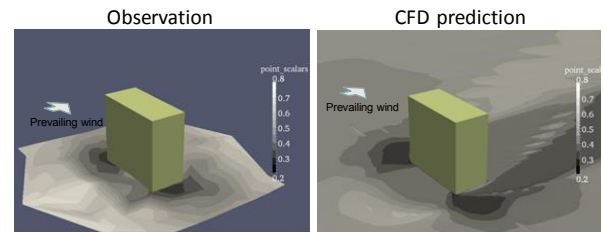


**Figure 10.** Distribution of snow depth: (a) observation and (b) prediction result [18].

meteorological model, snowdrift model, and snowmelt model. Because the models operate independently, each of them can be selected arbitrarily and treated as a module. The analysis procedure of the building scale analysis is illustrated in Figure 9b. In the snowdrift part, the distribution of drifting snow around buildings is simulated by snowdrift analysis based on CFD under snowy weather conditions. In this part, only a transport equation for the drifting snow density is solved under fixed velocity distributions, which are obtained by scaling precomputed wind velocities using the ratio of a reference velocity to the weather conditions. Then, the change in the snow depth attributable to snowmelt is computed by snowmelt analysis based on heat balance analysis on the snow surface under weather conditions including thermal

components such as temperature. The final snow depth distributions can be obtained by summing the two snow depth changes obtained from the two analyses. The snowdrift patterns, i.e., erosion around the upwind corners and deposition in front of and behind a building, obtained by the model show good correspondence with those obtained from field observations, as shown in Figure 10. Later, Ito et al. [50] presented a more advanced system for predicting the spatial distribution of snow depth in urban areas by combining snowdrift and snowmelt models. Although the snowdrift model is the same as that in the previous system, the snowmelt model predicts the snowmelt rate by solving the heat balance equation for the snow surface. The heat balance calculation adopts a coupled approach of convection, conduction, and radiation, including multi-reflections of shortwave and longwave radiation, to accurately predict the heat balance on urban surfaces within the complex wind and thermal environments around buildings.

## 3.3 Application of CFD results to practical design

As described earlier, CFD can provide detailed information on relevant flow variables in the entire calculation domain under well-controlled conditions and without similarity constraints. Therefore, CFD is suitable for considering countermeasures and counterproposals to design problems. Okaze et al. [57] studied the contribution ratios of the snow particles falling from the sky and those from the ground surface to the total snowdrift. These ratios were calculated by solving two transport equations of the two types of snow drifting densities with different settling velocities. Figure 11 shows the normalized snow depth (Figure 11a) and the contribution ratio of snow from the ground surface to the snowdrift (Figure 11b) predicted by CFD around a cubic building. Although the values of the contribution ratio are large at locations laterally away from the building sides, the values are small near the building. This means that the snowdrift near the building is mainly caused by the snow falling from the sky, but that at the laterally distant regions are mainly caused by the snow blown from the ground surface. Such information is quite useful for providing an effective countermeasure to the snowdrift problem around buildings. As a different example, Thiis and Ferreira [19] studied the efficiency of windbreaks comprising three-dimensional arrays of pillars, which were used for snow deposition. The air flow and snow deposition around three different geometrical configurations of pillars were analyzed by CFD. As an example of the result, a predicted snow deposition pattern around windbreaks is shown in Figure 12. Based on the results, an arrangement can be proposed, which can be regarded as an alternative for landscape architects aiming to shelter a specific area. Based on the reliability of CFD simulations, it is important to utilize the extensive information provided by CFD in practical design.
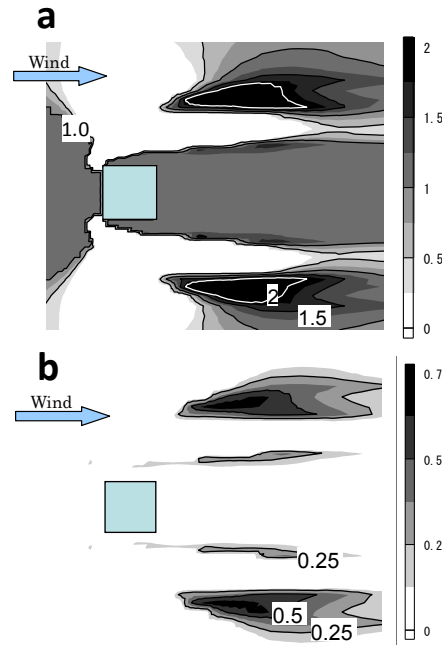


**Figure 11.** Horizontal distribution of (a) normalized snow depth and (b) contribution ratio of snow from the ground surface to the total snowdrift predicted by CFD around a cubic building [57].
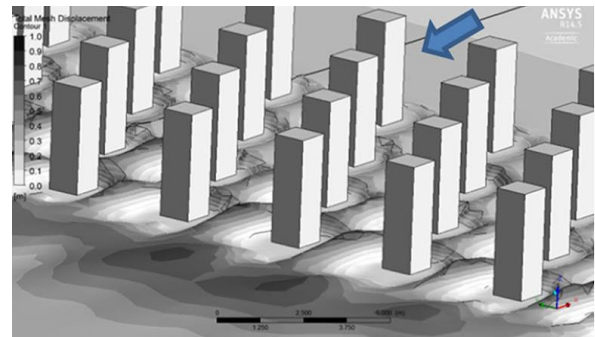


**Figure 12.** Snow deposition pattern around windbreaks predicted by CFD [19].
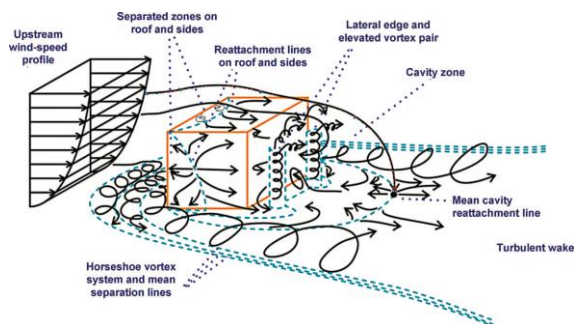


**Figure 13.** Schematic representation of the flow around an isolated low-rise building ([58]; modified from [59]).

## 4 Future perspectives

### 4.1. Model development

The concepts and parameters used in snowdrift modeling have been mostly derived empirically from observations and experiments. Many of the observations and experiments were based on a simple drifting boundary layer developed on a flat plane. However, the flowfield around buildings includes accelerations and decelerations due to separation and recirculation flows, as shown in Figure 13. For example, an estimation model for the transport rate of drifting snow attributable to saltation $Q_{sal}$ proposed by Pomeroy and Gray [22] has often been used in many previous studies. The constant in the model was determined by observation in a drifting boundary layer. However, it should be noted that the proposed relation gives the saturated transport rate of drifting snow based on the assumption that drifting snow in the saltation layer has reached its equilibrium state, where neither wind velocity distribution nor $Q_{sal}$ changes in the streamwise direction. Okaze et al. [27, 47] investigated the change in the spatial distribution of $Q_{sal}$ for non-equilibrium flow in a developing saltation layer and its relationship with wind velocity by performing a wind tunnel experiment using actual snow particles [60]. This experiment was performed on a "loose" snow surface, which was covered with soft snow such as fresh snow (with almost no cohesion between particles); here, snow particles jumped out from the surface because of wind, and a saltation layer developed. Figure 14 provides an outline of the experiment. There were two experimental conditions under which the reference wind velocity $U_0$ was changed. The relationship between the fetch distance and $Q_{sal}$ is shown in Figure 15. The two solid lines parallel to the horizontal axis in the figure show the predicted value of $Q_{sal}$, which was obtained by substituting the presumed $U^*$ (based on the downstream velocity profile where the boundary layer was fully developed) into Pomeroy's relation. The values obtained from Pomeroy's relation are greatly overestimated in almost the entire region with $U_0 = 5.0$ m/s and in the windward region with $U_0 = 7.0$ m/s. Thus, it is problematic to apply Pomeroy's relation (which is based on the equilibrium condition) to a flow around a building in which drifting snow is in non-equilibrium because of acceleration and deceleration. This suggests that the empirical equation of the snowdrift rate used in previous studies does not work appropriately for snowdrift accompanied by rapid acceleration and deceleration of flow such as the flow around buildings. It is necessary to further consider the applicability and validity of the modeling of sub-processes in a saltation layer at the developing stage (non-equilibrium state).

Furthermore, it should be mentioned that the CFD modeling of snowdrift applied previously is based on a Reynolds-averaged Navier–Stokes (RANS) equation model approach. This is expected to be useful for the practical application of CFD to snowdrift around a building. However, in actual situations, the deposition and erosion of snow are closely related to the real downburst and splash effects present in the surface boundary layer.
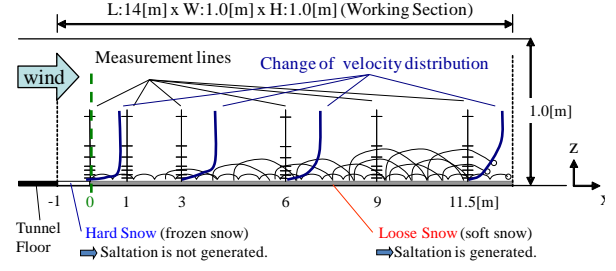


**Figure 14.** Outline of the experiment [27, 47].
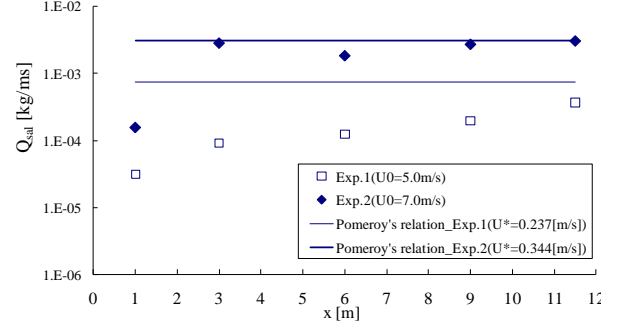


**Figure 15.** Relationship between the fetch distance obtained from experimental results and $Q_{sal}$ [27, 47].

That is, it is important to take the instantaneous turbulent flow structures that generate sweep and ejection events into account in snowdrift modeling. This may mean that RANS approaches are not suitable and large eddy simulation (LES) is required to extract non-isotropic three-dimensional velocity fluctuations. Further investigation should consider such effects on snowdrift modeling.

### 4.2. Validation database

The accuracy and reliability of CFD simulations are points of concern, and solution verification and validation studies are imperative. Verification is defined as the process of assessing numerical uncertainty and estimating the sign and magnitude of the numerical error itself and the uncertainty in that error estimate. On the other hand, validation is defined as the process of assessing modeling uncertainty by using benchmark experimental data and estimating the sign and magnitude of the modeling error itself. In the validation process, reliable measurement data, wherein the boundary conditions are clearly defined, are indispensable for examining prediction results. Unfortunately, only a few studies have provided such reliable measurement data [26, 61]. Field measurements and observations are important because they are based on actual phenomena. However, their results are affected by numerous parameters and the conditions are not controllable. Therefore, advanced experimental facilities, in which various influencing factors such as the wind velocity, temperature, and snow fall rate are fully controllable, have been developed (e.g., [60, 62, 63]). The extensive utilization of such facilities is expected to provide important information for snowdrift modeling. Furthermore, in the near future, it is expected that a validation database will be opened for researchers worldwide and will be available online. In addition,

numerical simulations have certain inherent limitations. The experimental results should be not only used as a validation database but also considered to be complementary to simulation results. Therefore, a "hybrid" approach, in which both methods are complementarily used, is very important to elucidate complex phenomena such as snowdrift.

### 4.3. Best practice guidelines

In CFD simulations, a large number of choices need to be made by the user. It is well known that these choices can have a very large impact on the results. It is of course apparent that the existing practical guidelines for wind engineering [64-67] and general CFD application [68-70] are important and useful for snowdrift modeling. The correct prediction of velocity fields is necessary for obtaining accurate snowdrift calculation results. However, because only few examples of snowdrift around buildings are available currently, the influence of parameters in a snowdrift model on the results is not clear. It is suggested that best practice guidelines for snowdrift calculations by CFD should be provided by accumulating comprehensive sensitive analysis results in the future.

## 5 Conclusions

This article reviewed previous CFD studies on snowdrift around buildings conducted with different research purposes, configurations, boundary conditions, and modeling approaches to provide a perspective on CFD modeling and give some insights into future directions for practical applications. This review provided an overview of CFD applications to snowdrift around buildings in recent years. Clearly, CFD has considerable potential, as established in this review. However, to use it appropriately, sufficient attention should be paid to modeling theory and implementation. Because snowdrift is a highly complex phenomenon, we should not excessively rely on numerical simulation. It is important to use data from actual phenomena for all aspects of study. Furthermore, it is also important to respect traditional approaches such as field observations and physical experiments and to seek a complimentary approach that combines the advantages of experimental and simulation techniques.

## Acknowledgements

## References

1. J.D. Iversen, Comparison of wind-tunnel model and full-scale snow fence drifts, J. Wind Eng. Ind. Aerodyn. **8**(3), 231-249 (1981)
2. F.D.M. Sant'Anna, D.A. Taylor, Snow drifts on flat roofs: wind tunnel tests and field measurements, J. Wind Eng. Ind. Aerodyn. **34**(3), 223-250 (1990)
3. N. Isyumov, M. Mikitiuk, Wind tunnel model tests of snow drifting on a two level flat roof, J. Wind Eng. Ind. Aerodyn. **36**(2), 893-904 (1990)
4. D.J. Smedley, K.C.S. Kwok, D.H. Kim, Snowdrifting simulation around Davis Station workshop, Antarctica, J. Wind Eng. Ind. Aerodyn. **50**, 153-162 (1993)
5. M. O'Rourke, A. DeGaetano, J.D. Tokarczyk, Snow drifting transport rates from water flume simulation, J. Wind Eng. Ind. Aerodyn. **92**(14-15), 1245-1264 (2004)
6. B. Blocken, 50 years of Computational Wind Engineering: Past, present and future, J. Wind Eng. Ind. Aerodyn. **129**, 69-102 (2014)
7. T. Uematsu, T. Nakata, K. Takeuchi, Y. Arisawa, Y. Kaneda, Three-dimensional numerical simulation of snowdrift, Cold Reg. Sci. Technol. **20**, 65-73 (1991)
8. G.E. Liston, R.L. Brown, J.D. Dent, A two-dimensional computational model of turbulent atmospheric surface flows with drifting snow, Ann. Glaciol. **18**, 281-286 (1993)
9. B. Bang, A. Nielsen, P.A. Sundsbø, T. Wiik. Computer simulation of wind speed, wind pressure and snow accumulation around buildings (SNOW-SIM), Energ. Buildings **21**, 235-243 (1994).
10. P.A. Sundsbø, Numerical simulations of wind deflection fins to control snow accumulation in building steps, J. Wind Eng. Ind. Aerodyn. **74-76**, 543-552 (1998)
11. M. Naaim, F. Naaim-Bouvet, H. Martinez, Numerical simulation of drifting snow: erosion and deposition models, Ann. Glaciol. **26**, 191-196 (1998)
12. A. Sekine, M. Shimura, A. Maruoka, H. Hirano, The numerical simulation of snowdrift around a building. Int. J. Comput. Fluid D. **12**, 249-255 (1999).
13. Y. Tominaga, A. Mochida, CFD prediction of flowfield and snowdrift around a building complex in a snowy region, J. Wind Eng. Ind. Aerodyn. **81**, 273-282 (1999)
14. K.T. Thiis, A comparison of numerical simulations and full-scale measurements of snowdrifts around buildings, Wind Struct. **3**(2), 73-81 (2000)
15. J.H.M. Beyers, P.A. Sundsbø, T.M. Harms, Numerical simulation of three-dimensional transient snow drifting around a cube, J. Wind Eng. Ind. Aerodyn. **92**, 725-747 (2004)
16. M. Beyers, B. Waechter, Modeling transient snowdrift development around complex three-dimensional structures, J. Wind Eng. Ind. Aerodyn. **96**, 1603-1615 (2008)
17. Y. Tominaga, T. Okaze, A. Mochida, CFD modeling of snowdrift around a building: An overview of models and evaluation of a new approach, Build. Environ. **46**(4), 899-910 (2011)

18. Y. Tominaga, A. Mochida, T. Okaze, T. Sato, M. Nemoto, H. Motoyoshi, S. Nakai, T. Tsutsumi, M. Otsuki, T. Uamatsu, H. Yoshino, Developm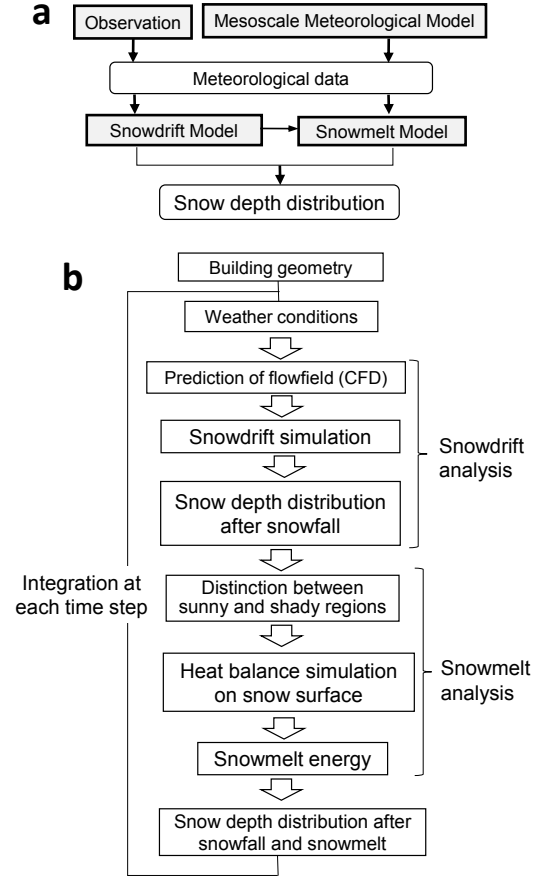ent of a system for predicting snow distribution in built-up environments: Combining a mesoscale meteorological model and a CFD model, J. Wind Eng. Ind. Aerodyn. **99**, 460-468 (2011)

19. T. Thiis, A.D. Ferreira, Sheltering effect and snow deposition in arrays of vertical pillars, Environ. Fluid Mech. **15**, 27-39 (2015)

20. T. Okaze, Y. Takano, A. Mochida, Y. Tominaga, Development of a new k–ε model to reproduce the aerodynamic effects of snow particles on a flow field, J. Wind Eng. Ind. Aerodyn. **144**, 118-124 (2015)

21. J.D. Iversen, R. Greeley, B.R. White, J.B. Pollack, Eolian erosion of the Martian surface, Part 1; Erosion rate similitude. Icarus **26**(3), 321-331 (1980)

22. J.W. Pomeroy, D.M. Gray, Saltation of snow, Water Resour. Res. **26**(7), 1583-1594 (1990)

23. R.S. Anderson, P.K. Haff, Simulation of Eolian Saltation, Science **241**, 820-823 (1988)

24. T.K. Thiis, Y. Gjessing, Large-scale measurements of snowdrifts around flat-roofed and single-pitch-roofed buildings, Cold Reg. Sci. Technol. **30**(1–3), 175-181 (1999)

25. J.H.M. Beyers, T.M. Harms, Outdoors modelling of snowdrift at SANAE IV Research Station, Antarctica, J. Wind Eng. Ind. Aerodyn. **91**(4), 551-569 (2003)

26. S. Oikawa, T. Tomabechi, Daily observation of snowdrifts around a model cube, *Snow Engineering, Hjorth-Hansen, Holand, Loset & Norem (eds)*, 369-375 (2000)

27. T. Okaze, A. Mochida, Y. Tominaga, M. Nemoto, T. Sato, Y. Sasaki, K. Ichinohe, Wind tunnel investigation of drifting snow development in a boundary layer, J. Wind Eng. Ind. Aerodyn. **104-106**, 532-539 (2012)

28. G.E. Liston, M. Sturm, A snow-transport model for complex terrain, J. Glaciol. **44**(148), 498-516 (1998)

29. E.M. Greene, G.E. Liston, R.A. Pielke Sr., Simulation of above treeline snowdrift formation using a numerical snow-transport model, Cold Reg. Sci. Technol. **30**(1-3), 135-144 (1999)

30. G.E. Liston, R.B. Haehnel, M. Sturm, C.A. Hiemstra, S. Berezovskaya, R.D. Tabler, Simulating complex snow distributions in windy environments using SnowTran-3D, J. Glaciol. **53**(181), 241-256 (2007)

31. S. Murakami, Computational wind engineering, J. Wind Eng. Ind. Aerodyn. **36**(1), 517-538 (1990)

32. S. Kawakami, T. Uematsu, T. Kobayashi, Y. Kaneda, Numerical study of a snow wind scoop, *Snow Engineering: Recent Advances, Izumi, Nakamura & Sack (eds)*, 55-62 (1997)

33. P.-A. Sundsbo, E.W.M. Hansen, Modelling and numerical simulation of snow drift around snow fences, *Snow Engineering: Recent Advances, Izumi, Nakamura & Sack (eds)*, 353-359 (1997)

34. T. Sato, T. Uematsu, Y. Kaneda,. Application of random walk model to blowing snow, *Snow Engineering: Recent Advances, Izumi, Nakamura & Sack (eds)*, 133-138 (1997)

35. B.F. Waechter, R.J. Cinclair, G.D. Schuyler, C.J. Williams, Snowdrift control design: Application of CFD simulation techniques, *Snow Engineering: Recent Advances, Izumi, Nakamura & Sack (eds)*, 511-516 (1997)

36. C. Jaedicke, T.K. Thiis, B. Bang, The snowdrift pattern around a small hill in the High Arctic, *Snow Engineering: Recent Advances, Izumi, Nakamura & Sack (eds)*, 75-80 (2000)

37. T.K. Thiis, C. Jaedicke, Changes in the snow drift pattern caused by building extension - Investigations through scale modelling and numerical simulations, *Snow Engineering, Hjorth-Hansen, Holand, Loset & Norem (eds)*, 363-368 (2000)

38. T.K., Thiis, C. Jaedicke, The snowdrift pattern around two cubical obstacles with varying distance - Measurements and numerical simulations, *Snow Engineering, Hjorth-Hansen, Holand, Loset & Norem (eds)*, 369-375 (2000)

39. P.A. Sundsbo, B.Bang, Snow drift control in residential areas - Field measurements and numerical simulations, *Snow Engineering, Hjorth-Hansen, Holand, Loset & Norem (eds)*, 377-382. (2000)

40. S. Thordarson, H. Norem, Simulation of two-dimensional wind flow and snow drifting application for roads: Part1, *Snow Engineering, Hjorth-Hansen, Holand, Loset & Norem (eds)*, 437-443 (2000)

41. S. Thordarson, H. Norem, Simulation of two-dimensional wind flow and snow drifting application for roads: Part2, *Snow Engineering, Hjorth-Hansen, Holand, Loset & Norem (eds)*, 445-452 (2000)

42. A. Schaelin, L. Ilg, M. Benesch, Snow deposition around mountain hut - design optimization by CFD and scaled water channel model and realization of solutions, *Snow Engineering V, Bartelt, Adams, Christen, Sack & Sato (eds)*, 147-155 (2004)

43. J.H.M. Beyers, T.M. Harms, P.A. Sundsbø, Numerical simulation of snow drift around an elevated structure, *Snow Engineering V, Bartelt, Adams, Christen, Sack & Sato (eds)*, 185-191 (2004)

44. J.H.M. Beyers, X. Qiu, R. Hakimi, Meteorological prediction and CFD simulation of in-cloud icing on tall buildings, *In: Proceedings of Snow Engineering VI*, Whistler, Canada (2008)

45. T.K. Thiis, J.F. Ramberg, Measurements and numerical simulations of development of snow drifts of curved roofs, *In: Proceedings of Snow Engineering VI*, Whistler, Canada (2008)

46. Y. Tominaga, T. Okaze, A. Mochida, T. Shida, H. Yoshino, CFD prediction of snowdrift around a cubic building model, *In: Proceedings of Snow Engineering VI*, Whistler, Canada (2008)

47. T. Okaze, A. Mochida, Y. Tominaga, M. Nemoto, Y. Ito, T. Shida, T. Sato, H. Yoshino, Modeling of drifting snow development in a boundary layer and its effects on wind field, *In: Proceedings of Snow Engineering VI, Whistler*, Canada (2008)

48. J. Potac, A 2D numerical modeling of snowdrift development, *In: Proceedings of the 7th International Conference on Snow Engineering (Snow Engineering VII)*, Fukui, Japan (2012)

49. X. Zhou, X. Li, M. Gu, Y. Zhang, P. Huang, A new two-equation model for numerical simulation on snow drifting, *In: Proceedings of the 7th International Conference on Snow Engineering (Snow Engineering VII)*, Fukui, Japan (2012)

50. Y. Ito, A. Mochida, T. Okaze, Y. Sasaki, Y. Tominaga, Development of a prediction method for snow-depth distribution in urban areas based on the coupling of snowdrift and snowmelt models, *In: Proceedings of the 7th International Conference on Snow Engineering (Snow Engineering VII)*, Fukui, Japan (2012)

51. Y. Tominaga, T. Okaze, A. Mochida, M. Nemoto, T. Sato, T. Tsutsumi, Y. Sasaki, Seasonal change of snow distribution around a building: comparison between numerical simulation and filed measurements, *In: Proceedings of the 7th International Conference on Snow Engineering (Snow Engineering VII)*, Fukui, Japan (2012)

52. T. Okaze, A. Mochida, Y. Tominaga, Y. Takano, Numerical modeling of snow particles on turbulent flowfield based on canopy model, *In: Proceedings of the 7th International Conference on Snow Engineering (Snow Engineering VII)*, Fukui, Japan (2012)

53. T. K. Thiis, J. Potac, J.F. Ramberg, 3D numerical simulations and full scale measurements of snow depositions on a curved roof, *In 5th European & African Conference on Wind Engineering*, Florence (2009)

54. Y. Tominaga, T. Okaze, A. Mochida, CFD simulation of drift snow loads for an isolated gable-roof building, *8th International Conference on Snow Engineering*, Nantes, France (2016) (to be submitted)

55. Y. Tominaga, S. Akabayashi, T. Kitahara, Y. Arinami, Air flow around isolated gable-roof buildings with different roof pitches: Wind tunnel experiments and CFD simulations, Build. Environ. **84**, 204-213 (2015)

56. P.B. Bartelt, M. Lehning, A physical SNOWPACK model for avalanche warning services. Part I: numerical model, Cold Reg. Sci. Technol. **35**, 123-145 (2002)

57. T. Okaze, A. Mochida, Y. Tominaga, Y. Ito, H. Yoshino, CFD prediction of snowdrift around a cube using two transport equations for drifting snow density, *In 5th International Symposium on Computational Wind Engineering (CWE2010)*, Chapel Hill, North Carolina, USA (2010)

58. B. Blocken, T. Stathopoulos, J. Carmeliet, J.L.M. Hensen, Application of computational fluid dynamics in building performance simulation for the outdoor environment: an overview, J. of Build. Perform. Simu. **4**(2), 157-184 (2011)

59. R.P. Hosker, Flow and diffusion near obstacles. In:D. Randerson, ed. *Atmospheric Science and Power Production*. (Office of Scientific and Technical Information, United States Department of Energy 1984)

60. T. Sato, K. Kosugi, A. Sato, Saltation-layer structure of drifting snow observed in wind tunnel, Ann. Glaciol. **32**, 203-208 (2001)

61. T. Tutsumi, T. Chiba, T. Tomabechi, Snowdrifts on and around buildings based on field measurement, *In: Proceedings of the 7th International Conference on Snow Engineering (Snow Engineering VII)*, Fukui, Japan (2012)

62. P. Delpech, P. Palier, J. Gandemer, Snowdrifting simulation around Antarctic buildings, J. Wind Eng. Ind. Aerodyn. **74-76**, 567-576 (1998)

63. P. Delpech, T. Thiis, Applications of "snowind" engineering – climatic wind tunnel methods, Technical Transactions iss. 12. Civil Engineering iss. **2-B**, 381-403 (2015)

64. J. Franke, C. Hirsch, A.G. Jensen, H.W. Krüs, M. Schatzmann, P.S. Westbury, S.D. Miles, J.A. Wisse, N.G. Wright, Recommendations on the use of CFD in wind engineering, *In: van Beeck,J.P.A.J.(Ed.), Proceedings of the International Conference on Urban Wind Engineering and Building Aerodynamics. COST ActionC14, Impact of Wind and Storm on City Life Built Environment.* Von Karman Institute, Sint-Genesius-Rode, Belgium (2004)

65. J. Franke, A. Hellsten, H. Schlünzen, B. Carissimo, (Eds.), *Best practice guideline for the CFD simulation of flows in the urban environment* (COST Office, Brussels, 3-00-018312-4, 2007)

66. Y. Tominaga, A. Mochida, R. Yoshie, H. Kataoka, T. Nozu, M. Yoshikawa, T. Shirasawa, AIJ guidelines for practical applications of CFD to pedestrian wind environment around buildings, J. Wind Eng. Ind. Aerodyn. **96**(10-11), 1749-1761 (2008)

67. B. Blocken, Computational Fluid Dynamics for urban physics: Importance, scales, possibilities, limitations and ten tips and tricks towards accurate and reliable simulations, Build. Environ. **91**, 219-245 (2015)

68. M. Casey, T. Wintergerste, *ERCOFTAC Special Interest Group on Quality and Trust in Industrial CFD, Best Practice Guidelines* (ERCOFTAC, Brussels, 2000)

69. W.L. Oberkampf, T.G. Trucano, C. Hirsch, Verification, validation, and predictive capability in computational engineering and physics. Appl. Mech. Rev. **57**(5), 345-384 (2004)

70. C. Hirsch, The Development of a Framework for CFD Validation and Best Practice: The QNET-CFD Knowledge Base, Chinese J. Aeronaut. 19(2), 105-113 (2006)

# Improvements of the viscous treatment of the snow phase in two-way coupled Eulerian-Eulerian simulations of drifting snow

Ziad Boutanios[1,2,a] and Hrvoje Jasak[2]

[1]*Binkz Incorporated, Laval, Quebec, Canada*
[2]*CFD Lab, FSB, University of Zagreb, Zagreb, Croatia*

**Abstract.** This paper presents an extension to a viscous model of the snow phase developed by the authors. The original model is developed from first principles, based on analogy between Lagrangian and Eulerian representations of the snow phase in the creeping layer. Here, the original model is extended to the snowbed, the saltation and the suspension layers, and both original and new viscous models are compared and discussed. The original formulation consists of a two-way coupled four-equation Navier-Stokes system with all drifting snow layers resolved, for a single snow particle size. Validations of the original viscous model against controlled wind tunnel drifting snow experiments showed good agreement in the snow fluxes in the saltation layer, provided the separately computed contributions of several snow particle size classes are combined in a two-parameter Gamma particle size distribution. The extended viscosity model is seen to greatly improve the predictions of snow fluxes in the suspension layer, providing a good match to experimental measurements. No improvements are seen in the airflow velocity and turbulent kinetic energy profiles since the momentum coupling term between phases is not affected by the improvements. Recommendations are made for future work.

## 1 Introduction

Several drifting snow models are available in the literature, most of which are based on Reynolds Averaged Navier-Stokes (RANS) formulations in the Eulerian-Eulerian and Eulerian-Lagrangian frames regarding the air and snow phases. Both approaches can yield reasonable results compared to experiments but the Eulerian-Eulerian approach requires a lower computational effort since Lagrangian particle tracking requires a great deal of particles to yield statistically meaningful results [1].

Presently, Eulerian-Eulerian modelling of drifting snow is based on two main approaches: the transport of snowdrift density approach and the Volume of Fluid (VOF) approach. The snow density transport approach solves a scalar transport equation of the snow density in the suspension layer where the motion of the snow phase does not affect the airflow (one-way coupling), in addition to the one-way coupled airflow continuity and momentum equations. Instead of solving the snow momentum equation, the snow particle fall velocity is either assumed constant [2, 3], or calculated using a buoyancy-based formula derived from the equations of motion of spherical particle in steady-state airflow [4]. Another variation on the snow density approach solves the mixture continuity and momentum equations in two-way coupled form [3]. Different treatments of turbulence are used such as a Prandtl mixing layer [2], a standard k-epsilon model with a particle effect correction [3], and a Launder-Kato k-epsilon model with particle effect correction as well [4]. All these methods represent the saltation layer as a boundary condition on the snowbed surface obtained from an equilibrium empirical formulation of the transport rate of drifting snow in the saltation layer [5]. This empirical formulation was shown to overpredict the transport rate of snow in non-

equilibrium situations [6]. An exception is the approach of Tominaga et al. [4] that resolves the saltation layer with the same equations as the suspension layer. Another notable exception is a two-way coupled formulation which fully resolves both saltation and suspension layers without equilibrium empirical boundary conditions [7]. However, the snow saltation layer transport equations are based on self-similarity equilibrium relationships between both phases.

The VOF approach is similar to the snow density approach in that it solves another one-way coupled system of equations consisting of the mixture continuity and momentum equations, in addition to a scalar transport equation of the volume fraction of one of the phases. The latter equation is equivalent to a continuity equation and the drift velocity between the phases is set to different constant values in the different snow transport layers [8] or calculated with a drift flux term [9]. The drift flux term [10] is strictly valid for negligible particle inertia which applies only to the smallest particles transported by turbulence into the suspension layer, and not the larger ones in the saltation layer. All the approaches previously described calculate the snow depth by explicitly accounting for the contributions of saltation and suspension fluxes based on experimental equilibrium relationships.

A two-way coupled approach is taken by Boutanios and Jasak [11] where separate Navier-Stokes systems are solved for each phase and coupling between the phases is accounted for through drag and lift. The Navier-Stokes system solved is:

$$\frac{\partial \alpha_k \rho_k}{\partial t} + \nabla \cdot \alpha_k \rho_k \mathbf{u}_k = 0 \qquad (1)$$

$$\frac{\partial \alpha_k \rho_k \mathbf{u}_k}{\partial t} + \nabla \cdot \alpha_k \rho_k \mathbf{u}_k \mathbf{u}_k = -\alpha_k \nabla p + \nabla \cdot \alpha_k \boldsymbol{\tau}_k + \alpha_k \rho_k \mathbf{g} + \mathbf{M}_k \quad (2)$$

Here, k=1,2 is the index of either phase, $\alpha_k$ is the phase volume fraction, $\rho_k$ is the phase density, $\boldsymbol{\tau}_k$ is the phase stress tensor, $\mathbf{u}_k$ is the phase velocity vector, $p$ is the

---

static pressure field, and **g** is the gravitational acceleration vector. $\mathbf{M}_k$ is the momentum exchange term between the phases which consists of the drag and lift forces, found by scale analysis to be the dominant forces for drifting snow [7]. Turbulence is accounted for with the standard k-ε model, without particle effects. The snow phase shear stress term in the momentum equation above requires a snow viscosity parameter, so one was developed from first principles based on an analogy between a Lagrangian rolling particle on the snowbed and a corresponding Eulerian flowing fluid. This analogy is shown in Figure 1. The two-way coupled viscous approach showed good agreement with experimentally measured snow fluxes in a controlled wind tunnel experiment [12], provided the distribution of particle sizes is accounted for by statistically combining the results of several single diameter simulations. Boutanios and Jasak [11] do not need to specifically compute the change in snow depth since convection and diffusion fluxes are already part of the Navier-Stokes system of equations.
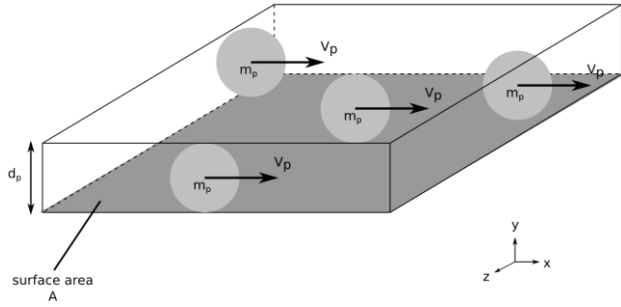


**Figure 1.** Lagrangian particles in Eulerian control volume.

In this paper, the derivation of the viscosity model is extended to the snowbed, and the upper saltation layer and the suspension layer. Comparisons of the numerical results of the extended viscosity model to the numerical results the original viscosity model, and to the experimental measurements are provided and discussed.

# 2 Extended viscosity model

The extended viscosity model consists of Equations (3), (4) and (5), applying to the snowbed, the creeping/saltation layer, and the suspension layer respectively.

$$
v_s = \begin{cases}
\dfrac{\tau_t}{2\rho_s \varepsilon_s} & \text{in snowbed} & (3) \\[3mm]
-\dfrac{F_{d,v} d_p}{6\alpha_a \varepsilon_s} + \dfrac{\tau_t}{2\rho_s \varepsilon_s} & \text{in creeping/saltation layer} & (4) \\[3mm]
C_t^2 v_t & \text{in suspension layer} & (5)
\end{cases}
$$

Here, $v_s$ is the snow phase kinematic viscosity, $\rho_s$ is the snow density, $\tau_t$ is the drifting threshold shear stress, $\varepsilon_s$ is the snow rate of strain, $F_{d,v}$ is the drag force per unit

volume, $d_p$ is the snow particle diameter, $\alpha_a$ is the air volume fraction, $v_t$ is the air turbulent viscosity, and $C_t$ is the turbulent viscosity multiplier as determined by Gosman et al. [13] for dilute particle-laden flows. Since the flow in the suspension layer is one-way coupled, we use here a constant $C_t=1$. The original viscosity model consists of Equation (4) which is strictly applicable in the creeping and saltation layers. However, tests have shown that it can be used in the snowbed as well by retaining only the threshold shear stress contribution to the viscosity as shown in Equation (3). In the suspension layer the flow is extremely dilute and one-way coupled, with transport of the snow provided by turbulent lift. There, the snow phase flow is essentially inviscid, but turbulent transport is accounted for in a Boussinesq fashion through $C_t$ the turbulent viscosity multiplier, as shown in Equation (5). Validation results are presented in the next section.

# 3 Validation against experimental data

## 3.1 Experimental setup

Validation of the extended viscosity model is done against the same experimental data used to validate the original model, as well as the original model itself. The experimental data was measured in a controlled wind tunnel drifting snow experiment carried out by the Tohoku university group [14] in Japan. In the Tohoku experiments, the profiles of mass flux of drifting snow, wind velocity, and turbulence statistics were measured under several different wind speed conditions, and at four different measurement stations in the wind tunnel working section shown in Figure 2. The measurement stations were located at X=3, 6, 9, and 11.5 m. Loose snow is deposited in a 2 cm deep gutter along the length of the tunnel floor which is preceded by a 1 m fetch of frozen non-drifting hard snow, in order to generate a non-equilibrium saltation layer. The measured airflow velocity and turbulence kinetic energy at station X=0m were used as boundary conditions for the numerical simulations. These profiles are shown in Figure 3 where $Z_r=0.2$ m and $U_r\approx 7.0$ m/s are the reference height and airflow velocity.
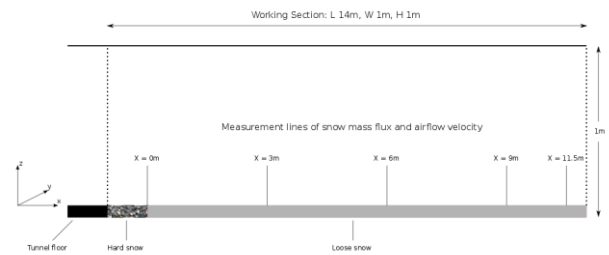


**Figure 2.** Side view of the mid-section of the wind tunnel working section (flow direction from left to right).
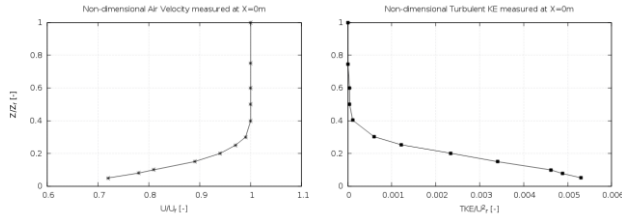
**Figure 3.** Numerical inlet boundary conditions, as measured in the wind tunnel at X=0 m.

Samples of the snow particles used in the experiment are shown in Figure 4. These are quite irregular and bulky, rarely smaller than 0.50 mm in either length or width, which implies a particle distribution with an average diameter larger than 0.50 mm. It should be noted that particle sizes occurring in natural snow and mechanical breakage phenomena are best described with a two-parameter Gamma Probability Distribution Function (PDF), be it as aggregate on the ground [15] or drifting above it [16].
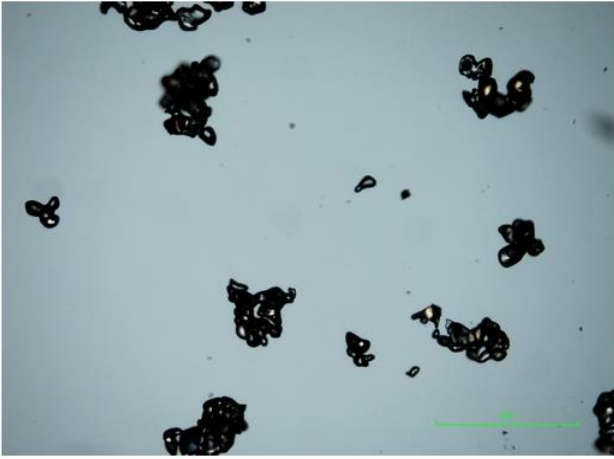


**Figure 4.** Sample of the experiment snow particles.

### 3.2 Numerical setup

The 2D computational mesh used for the simulations is shown in Figure 5. The top part of the figure is a close-up of the mesh at the inlet of the computational domain of the wind tunnel at X=0m, with the loose snow layer in the gutter shown in white. The mesh is fully structured hexahedral with a transverse element size of 4 mm in the gutter and at the top of the tunnel. The longitudinal element size in the flow direction along the X-axis is about 6 cm. Tests were carried out with a mesh twice finer in both directions and the results varied by less than 15% so results obtained from the present mesh can be reasonably considered mesh-independent. Simulations were carried out at a threshold shear stress of 0.052 Kg/(m.s2) which is the minimum experimentally observed value for drifting.
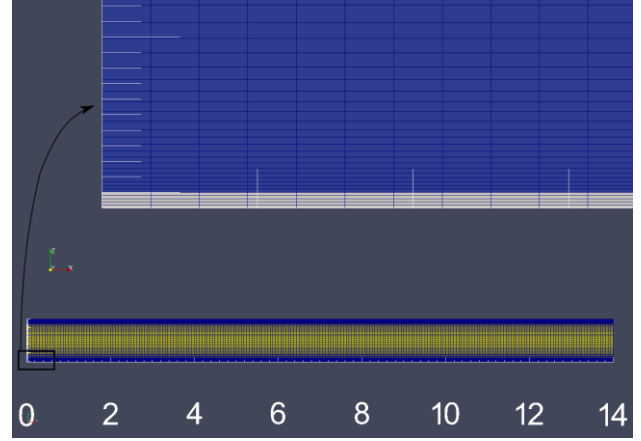


**Figure 5.** Close-up of the numerical mesh near the tunnel inlet showing the snowbed in the gutter (above), and an overall view of the mesh (below).

Seven transient simulations were carried out for constant particle diameters ranging from 0.1–1.3 mm. Boutanios and Jasak [11] show that a statistical combination of the individual solutions is required to account for the natural particle size segregation occurring normal to the snowbed in drifting snow [16]. Here, the individual simulations are accordingly combined into one average diameter solution, according to the particle class weights of a two-parameter Gamma distribution with an average diameter of 0.7 mm, shown in Figure 6 below.
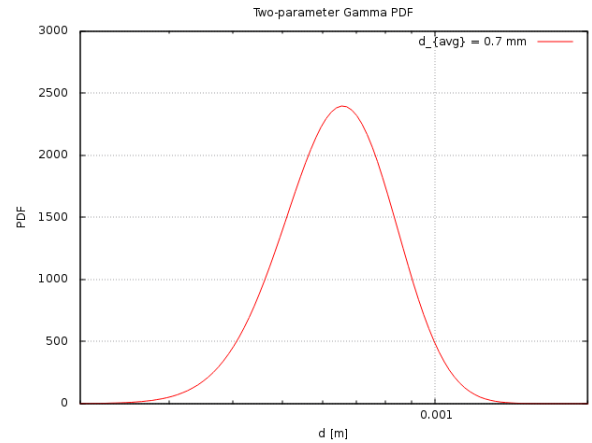


**Figure 6.** Two-parameter Gamma distribution with average diameter of 0.7 mm.

The average diameter solution was then compared to the experimentally measured profiles for both original and extended viscosity models. It should be pointed out that the experimental profiles were measured within a 30s window at all four measurement stations, under negligible bed erosion conditions. The same approach was adopted in extracting the numerical profiles from the simulation data for the comparisons to be valid.

### 3.2 Snow flux profiles

The snow flux profiles for the 0.7mm average diameter solutions of the original viscosity model at X=11.5m is shown in Figure 7 below.
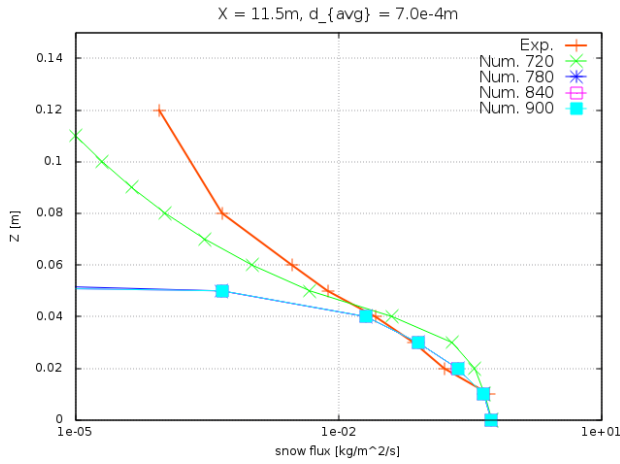
**Figure 7.** Numerical snow flux profile vs. experimental measurements, for $d_{avg}$=0.7mm at X=11.5m; original viscosity model.

The numerical results indicate that the original viscosity model does a good job in matching the experimental measurements in the saltation layer, which extends up to about Z=4cm. The simulation snow fluxes are also seen to be stable enough to provide a 30s measurement window during which a stable snowbed can be observed, thus satisfying the comparison requirements to the experimental measurements. The results also imply that the particle average size at X=11.5m in the experiments could be around 0.7mm. This makes sense given the snow particle sample shown in Figure 4. The agreement between experiment and simulations is not good in the suspension layer, above Z=4cm, since transport by suspension is due to turbulent lift and that effect is not included in the original viscosity model.

The same snow flux profiles for the 0.7mm average diameter solution for the extended viscosity model at X=11.5m is shown in Figure 8. The extended viscosity treatment into the suspension layer, based on the Gosman Ct model, is seen to produce substantial amounts of turbulent lift across both saltation and suspension layers. The 0.7mm average size solution is much closer to the experimental measurements and exhibits the stable conditions required to match the experimental measurement window.
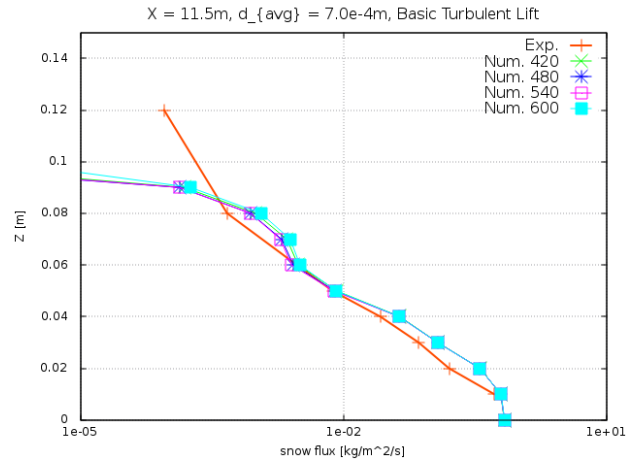


**Figure 8.** Numerical snow flux profile vs. experimental measurements for $d_{avg}$=0.7mm at X=11.5m, extended viscosity model.

## 3.2 Non-dimensional airflow velocity profiles

The non-dimensional airflow velocity profiles for the 0.7mm average diameter solutions of the original viscosity model at X=11.5m is shown in Figure 9 below.
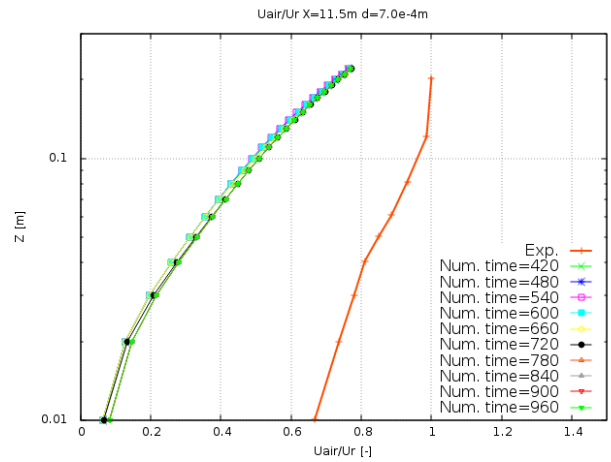


**Figure 9.** Numerical non-dimensional airflow velocity profiles vs. experimental measurements, for $d_{avg}$=0.7mm at X=11.5m; original viscosity model.

The simulation results exhibit the required stability for taking the experimental measurements and the shapes of the curves are very similar to the experimental curve shape. However, there is a large quantitative difference between simulations and experiment.

The non-dimensional airflow velocity profiles for the 0.7mm average diameter solutions of the extended viscosity model at X=11.5m are shown in Figure 10 below. The results of the extended viscosity model are very close to those of the original viscosity model, and no improvement is noticed as with the snow flux profiles. This discrepancy is due to a known deficiency of the k-ε turbulence model which is used here. The turbulent kinetic energy is overestimated by k-ε, and this excess turbulent kinetic energy can only come from a velocity deficit based on the model's formulation. The excess

23

turbulent kinetic energy production can be assessed in Figure 11 and Figure 12 below.
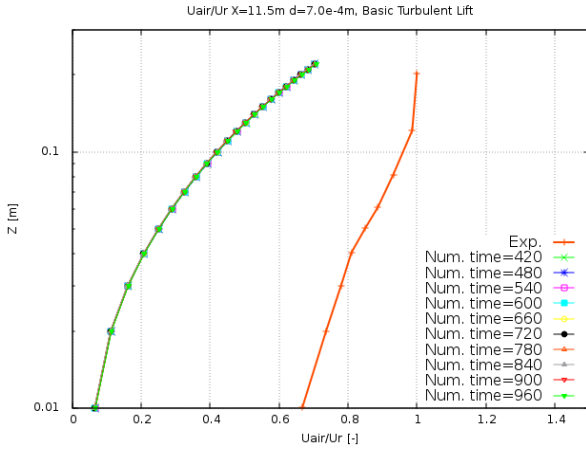


**Figure 10.** Numerical non-dimensional airflow velocity profile vs. experimental measurements for davg=0.7mm at X=11.5m, extended viscosity model.
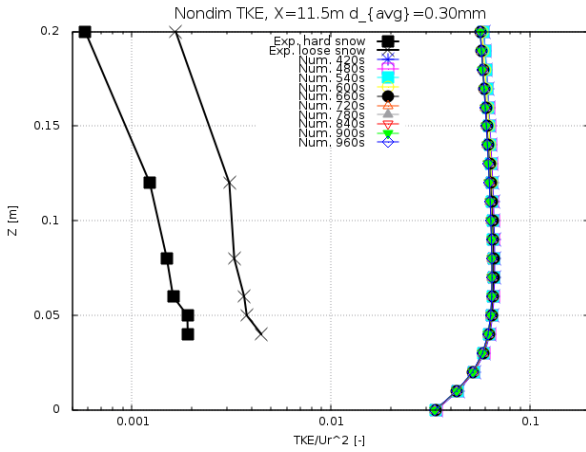


**Figure 11.** Numerical non-dimensional TKE profile vs. experimental measurements for $d_{avg}$=0.7mm at X=11.5m, original viscosity model.
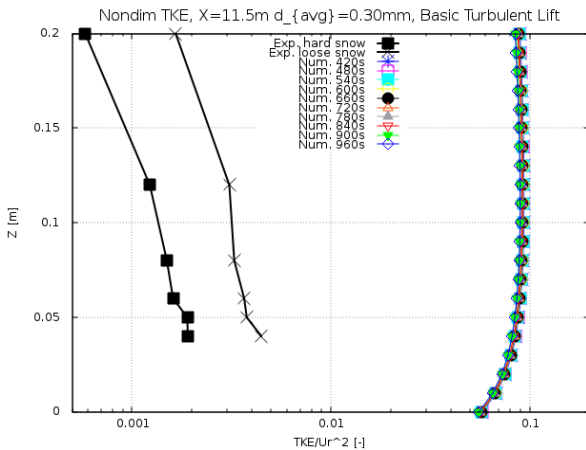


**Figure 12.** Numerical non-dimensional TKE profile vs. experimental measurements for davg=0.7mm at X=11.5m, extended viscosity model.

The black line with solid squares is the turbulent kinetic energy profile measured at X=11.5m for a layer of hard snow that does not drift. This was done in the experiment to assess the drifting particles effect on turbulent kinetic energy. The black line with x symbols is a measurement of the turbulent kinetic energy profile for drifting snow. Clearly there is production of turbulent kinetic energy by the drifting particles. Moreover, the experiment authors report that their ultra-sonic anemometer could not measure small-scale fluctuations at frequencies higher than 20Hz. It is then expected that the actual turbulent kinetic energy would be even higher than measured. However, the simulation results for both viscosity models are more than an order of magnitude larger than the experimental measurements so it is not likely that the small-scale component would make up the large differences seen in Figure 11 and Figure 12. The extended viscosity model has no effect on the airflow velocity and the turbulent kinetic energy profiles because the viscosity is part of the viscous stress tensor only in Equation (2) and does not affect the momentum coupling term which would impact the air momentum equation and the airflow velocity as a consequence.

## 4 Conclusions and future work

The extended viscosity model was found to provide a notable improvement in the suspension layer on the original one. This improvement provided a good match in the snow flux profiles across the saltation layer, and well into the suspension layer. The improvement is due to the modelling of the turbulent lift through the Gosman $C_t$ turbulent multiplier in a Boussinesq fashion.

There was no improvement in the airflow velocity profiles since the viscosity only affects the viscous stress tensor and not the momentum coupling term. The airflow velocity deficit is due to an excess production of the turbulent kinetic energy by the k-ε turbulence model, and there are different ways to remedy this deficiency in the k-ε formulation [17][18]. Other options include switching to the k-ω SST model which does a better job at predicting turbulent kinetic energy, or even the higher order DES and LES turbulence models. Work is already underway to this effect.

Another area of improvement is modifying the code to be able to handle several particle diameters simultaneously. This would eliminate the significant computational overhead required in computing several individual particle diameter simulations, and combining them in a post-processing exercise to get the particle size distribution effect. Handling several particle classes simultaneously can be done by solving a Probability Density Function transport equation, or solving the continuity and momentum balance equations of several diameter classes directly. The latter approach is being implemented and tested presently with three particle classes.

## Ackowledgments

## References

1. B. Lee, J. Tu, C. Fletcher. On numerical modeling of particle-wall impaction in relation to erosion prediction: Eulerian versus Lagrangian method. Wear **252**.
2. T. Uematsu, T. Nakata, K. Takeuchi, Y. Arisawa, Y. Kaneda. Three-dimensional numerical simulation of snowdrift. Cold Regions Science and Technology **20**.
3. M. Naaim, F. Naaim-Bouvet, H. Martinez. Numerical simulation of drifting snow: erosion and deposition model. Annals of Glaciology **26**.
4. Y. Tominaga, T. Okaze, A. Mochida. CFD prediction of flowfield and snowdrift around a building complex in a snowy region. Building and Environment **46**.
5. J. Pomeroy, D. Gray. Saltation of snow. Water Resources Research **26**.
6. T. Okaze, A. Mochida, Y. Tominaga, M. Nemoto, Y. Ito, T. Shida. Modeling of drifting snow development in a boundary layer and its effect on windfield. The Sixth Snow Engineering Conference, Whistler, B.C., Canada.
7. P. Gauer. Blowing and drifting snow in Alpine terrain: a physically-based numerical model and related field measurements. PhD dissertation, ETH Zurich.
8. P. Sundsbø. Numerical simulations of wind deflection fins to control snow accumulation in building steps. Journal of Wind Engineering and Industrial Aerodynamics **74-76**.
9. J.H.M. Beyers. Numerical modeling of the snowdrift characteristics surrounding the SANAE IV research station. PhD dissertation, University of Stellenbosch.
10. B. Bang, A. Nielsen, P. Sundsbo, T. Wiik. Computer simulation of wind speed, wind pressure and snow accumulation around buildings (SNOW-SIM). Energy and Buildings **21**.
11. Z. Boutanios, H. Jasak. Two-way coupled Eulerian-Eulerian simulations of drifting snow with viscous treatment of the snow phase. Journal of Wind Engineering and Industrial Aerodynamics (submitted for publication).
12. T. Okaze, A. Mochida, Y. Tominaga, M. Nemoto, T. Sato, Y. Sasaki, K. Ichinohe. Wind tunnel investigation of drifting snow development in a boundary layer. Journal of Wind Engineering and Industrial Aerodynamics **104-106**.
13. A.D. Gosman, R.I. Issa, C. Lekakou, M.K. Looney, S. Politis. Multidimensional modelling of turbulent two-phase flows in stirred vessels. AIChE J., **38(12)**.
14. T. Okaze, A. Mochida, Y. Tominaga, M. Nemoto, T. Sato, Y.Sasaki, K. Ichinohe. Wind tunnel investigation of drifting snow development in a boundary layer. J. Wind Eng. Ind. Aerodyn., **104-106**.
15. F. Budd. The drifting of nonuniform snow particles. Stud. Antarctic Meteorol., Am. Geophys. Union, Antarctic Res. Ser., **9**.
16. R.A. Schmidt. Vertical profiles of wind speed, snow concentration, and humidity in blowing snow. Boundary Layer Meteorology, **23**.
17. P.A. Durbin. On the k-3 stagnation point anomaly. Int. J. Heat and Fluid Flow, **17**.
18. V. Guimet, D. Laurence. A linearised turbulent production in the k-epsilon model for engineering applications. In Engineering Turbulence Modelling and Experiments, **5**.

# CFD prediction of snowdrift in a building array

Tsubasa Okaze[1,a], Saeka Kato[2], Yoshihide Tominaga[3], Akashi Mochida[4]

[1] Tokyo Institute of Technology, 4259 Nagatsuta-cho, Midori-ku, Yokohama, Japan
[2] Takenaka Corporation, 4-1-13 Hommachi, Chuo-ku, Osaka, Japan
[3] Niigata Institute of Technology, 1719 Fujihashi, Kashiwazaki, Japan
[4] Tohoku University, 6-6-11 Aoba, Aramaki Aza, Aoba-ku, Sendai, Japan

**Abstract.** This study aimed to investigate the performance of CFD prediction of snowdrift in and around a building array. The studied building array was located in Sapporo, Japan, and consisted of 12 one-story buildings built in three rows and four columns. The snowdrift model was based on two transport equations for two drifting snow densities corresponding to snow particles falling from the sky and those lifted up from the surface by strong wind. The predicted results were compared with field measurement results. The predicted snow depth distribution showed good agreement with measurement results, except for the region in front of windward buildings and the open space that allows flow in the prevailing wind direction.

## 1 Introduction

Approximately 60% of Japan consists of snowy regions; in such regions, snowdrift formation around buildings can considerably affect human activities. Computational fluid dynamics (CFD) is expected to be a useful tool for simulating snowdrift around buildings in such snowy regions.

Recently, Okaze et al. [1] proposed a new snowdrift model based on two transport equations of drifting snow densities for two different types of settling velocities corresponding to snow particles falling from the sky and those lifted up from the snow surface by strong winds. The proposed model was validated with detailed field measurements around a cubic building model in Sapporo, Japan by Oikawa et al. [2]. In almost all the previous studies, including those of the authors, the performance of the model was quantitatively validated only for snowdrift around an isolated building.

Snowdrift formation is more complicated for multiple buildings. Bang et al. [3] predicted snowdrift patterns (e.g., deposition/erosion) around three houses located in northern Norway by using a drifting flux model with two-phase flow equations. Thiis [4] predicted snowdrift around two adjacent cubical buildings by using the model proposed by Bang et al. [3]. Beyers and Weacher [5] demonstrated the results of the application of snowdrift predictions for three elevated-houses. However, very few studies have dealt with the performance of the model for predicting snowdrift in and around multiple buildings because of the lack of detailed full-scale field measurements needed for validation. To take effective preventive measures against snowdrift in an actual urban environment, snowdrifts need to be predicted quantitatively around buildings under a complicated flow field. Recently, Tsutsumi et al. [6] conducted a detailed field measurement around twelve buildings by using a 3D laser scanner with a resolution of 0.5 m. This measurement data is useful for the validation of CFD models.

This study aims to investigate the performance of the snowdrift model by comparing CFD model results with field measurements obtained by Tsutsumi et al. for snowdrift formation around a building array [6].

## 2 Outline of the snowdrift model

In this study, a CFD model based on two transport equations for two drifting snow densities [1] was applied to predict snowdrift formation around buildings. The drifting snow density was divided into two parts: the density of complex-shaped snow particles falling from the sky $\langle \Phi_{sky} \rangle$ and that of snow particles lifted up from the snow surface by strong winds $\langle \Phi_{surf} \rangle$, which are often broken apart by repeated collision with the snow surface. Thereafter, two transport equations for the two drifting snow densities, i.e., eqs.(1) and (2), were solved to predict the spatial distributions of both types of drifting snow densities with two different settling velocities.

$$\frac{\partial \langle \Phi_{sky} \rangle}{\partial t} + \frac{\partial \langle \Phi_{sky} \rangle \langle u_i \rangle}{\partial x_i} + \frac{\partial \langle \Phi_{sky} \rangle \langle wf_{sky} \rangle}{\partial x_3} = \frac{\partial}{\partial x_i} \left[ \frac{\nu_t}{\sigma_s} \left( \frac{\partial \langle \Phi_{sky} \rangle}{\partial x_i} \right) \right] \quad (1)$$

$$\frac{\partial \langle \Phi_{surf} \rangle}{\partial t} + \frac{\partial \langle \Phi_{surf} \rangle \langle u_i \rangle}{\partial x_i} + \frac{\partial \langle \Phi_{surf} \rangle \langle wf_{surf} \rangle}{\partial x_3} = \frac{\partial}{\partial x_i} \left[ \frac{\nu_t}{\sigma_s} \left( \frac{\partial \langle \Phi_{surf} \rangle}{\partial x_i} \right) \right] \quad (2)$$

To define the boundary conditions of the transport equations for $\langle \Phi_{sky} \rangle$ and $\langle \Phi_{surf} \rangle$ on the snow surface, the following assumptions were made: the snow particles falling from the sky break apart immediately upon collision with the snow surface, and no snow particles with their original complex shapes re-entrain from the surface. Based on these assumptions, the turbulent flux of $\langle \Phi_{sky} \rangle$ at the snow surface was set to zero.

$$\frac{\nu_t}{\sigma_s} \left( \frac{\partial \langle \Phi_{sky} \rangle}{\partial x_3} \right) \bigg|_{surface} = 0 \quad (3)$$

On the other hand, as mentioned earlier, all snow particles lifted up from the surface are assumed to immediately change to an approximately spherical shape owing to repeated collisions with the snow surface. The boundary condition for $\langle \Phi_{surf} \rangle$ is given by eq.(4) by using the erosion flux on surface $E_{surf}$ kg/(m$^2$·s). Here, erosion occurs when the friction velocity on the surface $\langle u^* \rangle$ is larger than the threshold friction velocity ($\langle u^* \rangle > \langle u^*_t \rangle$).

[a] Corresponding author: okaze.t.aa@m.titech.ac.jp

The relationship between friction velocity and erosion flux for blowing sand as proposed by Shao and Li [7] was used to model the erosion flux on the snow surface attributed to the shear stress exerted by wind.

$$E_{surf} = -\frac{\pi\zeta}{6}\rho_i\langle u*\rangle\left(1-\frac{\langle u*_t\rangle^2}{\langle u*\rangle^2}\right)\Delta x\Delta y \quad for \quad \langle u*\rangle > \langle u*_t\rangle \quad (4)$$

The model coefficient $\zeta$ is set to $1.0 \times 10^{-5}$. When erosion does not occur ($\langle u*\rangle \leq \langle u*_t\rangle$), a zero gradient condition is adopted for $\langle\Phi_{surf}\rangle$ because $E_{surf} = 0$ in such a situation. Snow deposition per unit time and per unit area is expressed as $\langle\Phi\rangle_p\langle wf\rangle$. Here, the subscript "$p$" represents the value at the first grid point. The deposition fluxes $D_{sky}$ and $D_{surf}$ kg/(m$^2$·s) corresponding to $\langle\Phi_{sky}\rangle$ and $\langle\Phi_{surf}\rangle$ are given as follows:

$$D_{sky} = -\langle\Phi_{sky}\rangle_p\langle wf_{sky}\rangle\Delta x \quad (5)$$

$$D_{surf} = -\langle\Phi_{surf}\rangle_p\langle wf_{surf}\rangle\Delta x \quad (6)$$

Finally, the net deposition rate $M_{total}$ kg/(m$^2$·s) is given as shown below:

$$M_{total} = D_{sky} + D_{surf} + E_{surf} \quad (7)$$

The change in snow depth per unit time $\Delta z_S$ m/s is obtained from $M_{total}$ divided by the accumulated snow density $\rho_S$ kg/m$^3$:

$$\Delta z_S = \frac{M_{total}}{\rho_S} \quad (8)$$

Then, the change in snow depth during snowfall period was calculated by multiplying the variation of snow depth per unit time by the time during snowfall period. The period was set to an hour in each simulation as mentioned later in chapter 3. In this study, the influence of surface change on the flow field was not considered.

# 3 Prediction of snowdrift around buildings

## 3.1 Computational conditions

A field measurement was conducted on the campus of Hokkaido University of Science in Sapporo, Japan, from December 2009 to February 2010 by Tsutsumi et al. [6]. The building array consisted of 12 one-story prefabricated buildings built in three rows and four columns with intervals of 2.7 m. The dimensions of each building were 2.4 m (D) × 5.4 m (W) × 2.7 m (H) as shown in Figure 1. The depth of snow around the buildings was measured using a 3D laser scanner with a resolution of 0.5 m. Although the snow depths were measured on January 7 and February 8, 2010, we selected the snowdrift event that occurred from December 12, 2009 to January 7, 2010 as the first test case to investigate the performance of the prediction model. The meteorological data used as boundary conditions were obtained from the observational data of Yamaguchi meteorological station, which is the station nearest to the measurement site. Figure 2 shows a wind rose diagram obtained from Yamaguchi meteorological station during the measurement period. The prevailing wind was west-northwest. Figure 3 shows time histories of the measured

hourly averaged data at Yamaguchi station during the measurement period (Dec. 12, 2009–Jan. 7, 2010). The wind velocity was measured at a height of 10 m. It was assumed that snowfall occurred when precipitation was observed and the temperature did not exceed 2.0°C. The steady-state change of snow depth per unit time given by eq.(8) was computed with the hourly averaged meteorological data when snowfall was considered to occur. Then, the hourly change in snow depth was calculated by multiplying the variation in snow depth per unit time by 3600 s (= 1 h). Finally, the total change in snow depth was estimated by summing the hourly change in snow depth during snowdrift events. Inflow and top boundary conditions of $\langle\Phi_{sky}\rangle$ were given by using eq.(9):

$$\langle\Phi_{sky}\rangle = \frac{\rho_s h*}{\langle wf_{sky}\rangle\Delta t_s} \quad (9)$$

Here, $h*$ m is the reference snow depth defined as a snow depth at each snowfall for a period $\Delta t_s$[s] (= 3600 s) in regions unaffected by buildings. The reference snow depth was estimated by the following relation:

$$h* = \frac{P\rho_W}{\rho_S} \quad (10)$$

where, $P$, $\rho_W$ and $\rho_S$ mean hourly measured precipitation



(1) Birds-eye view



(2) Arrangement plan
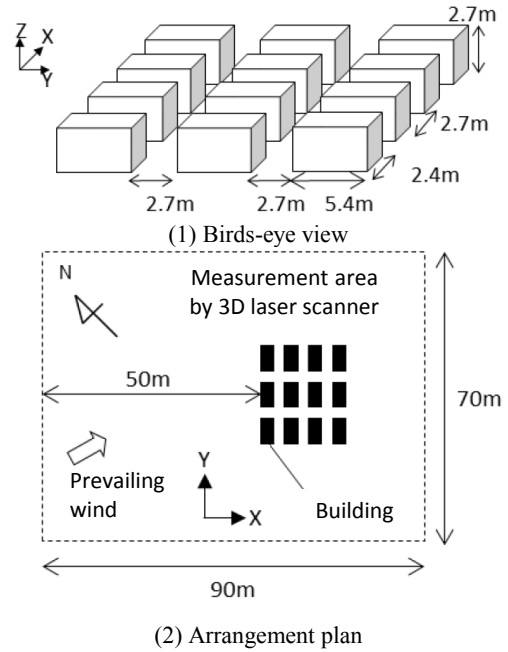
**Figure 1.** Schematic view of field measurement [6]
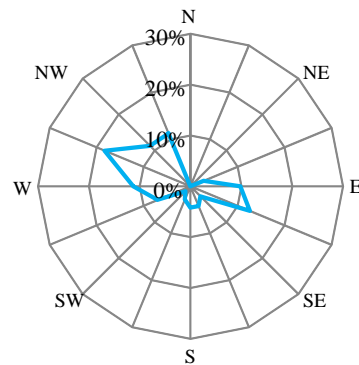


**Figure 2.** Wind rose at Yamaguchi station
(Dec. 12, 2009–Jan. 7, 2010)

(1) Wind velocity



(2) Precipitation and temperature
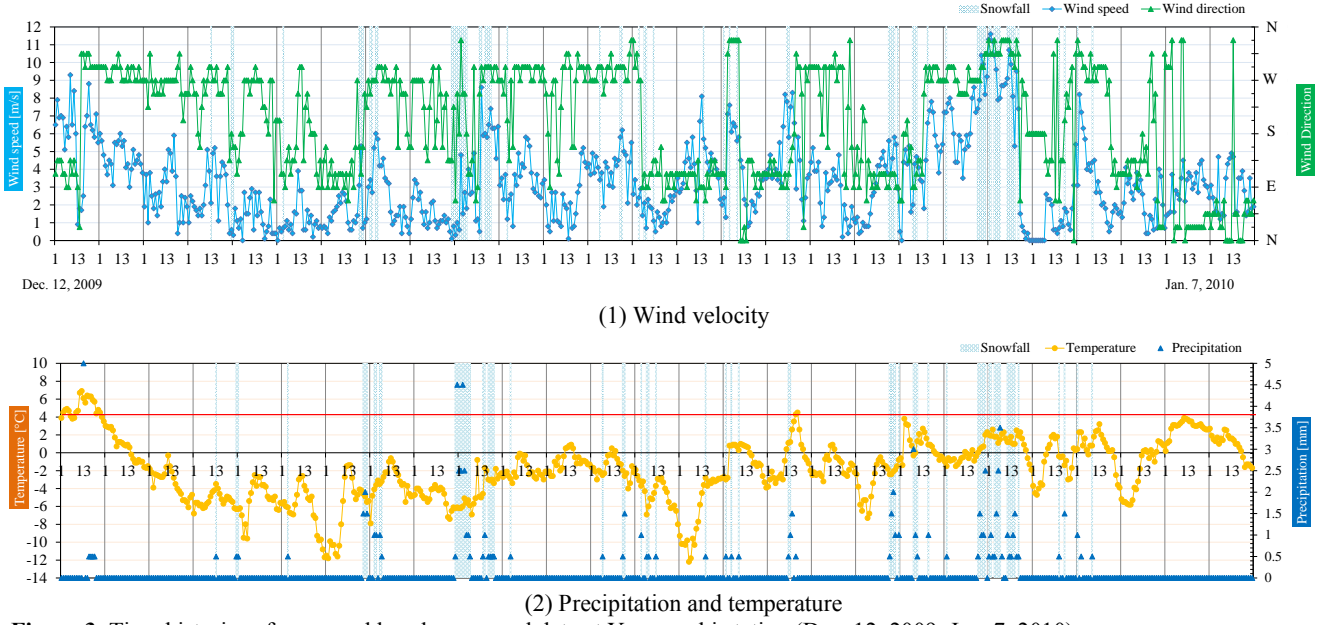
**Figure 3.** Time histories of measured hourly averaged data at Yamaguchi station (Dec. 12, 2009–Jan. 7, 2010)

<table>
<tr><td colspan="2" align="center">**Table 1.** Computational conditions</td></tr>
<tr><td>Grid discretization</td><td>$50(x_1) \times 42(x_2) \times 21(x_3)$</td></tr>
<tr><td rowspan="4">Inlet boundary</td><td>$\langle u_1 \rangle$, $\langle u_2 \rangle$: $z_0$-type logarithmic law ($z_0 = 0.41$ m which corresponds to the roughness length surrounding low-rise houses)</td></tr>
<tr><td>$\langle u_3 \rangle = 0$</td></tr>
<tr><td>$k = \langle u* \rangle^2 / C_\mu^{0.5}$</td></tr>
<tr><td>$\varepsilon$: assuming the local equilibrium of production of $k$ and energy dissipation rate ($P_k = \varepsilon$)</td></tr>
<tr><td>Outlet boundary</td><td>Zero gradient condition</td></tr>
<tr><td>Ground boundary</td><td>$z_0$-type logarithmic law ($z_0 = 1.0 \times 10^{-3}$ m: roughness length on snow surface)</td></tr>
<tr><td>Building wall boundary</td><td>Generalized logarithmic law</td></tr>
<tr><td>Lateral and upper boundaries</td><td>Slip wall condition</td></tr>
<tr><td>Spatial derivatives for convection term</td><td>QUICK scheme</td></tr>
<tr><td>Turbulence model</td><td>Revised $k$-$\varepsilon$ model proposed by Durbin [8]</td></tr>
</table>

<table>
<tr><td colspan="2" align="center">**Table 2.** Parameters of snow</td></tr>
<tr><td>Snowfall velocity corresponds to $\langle \Phi_{sky} \rangle$: $\langle wf_{sky} \rangle$</td><td>$-1.0$ m/s</td></tr>
<tr><td>Snowfall velocity corresponds to $\langle \Phi_{surf} \rangle$: $\langle wf_{surf} \rangle$</td><td>$-0.2$ m/s</td></tr>
<tr><td>Threshold friction velocity: $\langle u*_t \rangle$</td><td>0.20 m/s</td></tr>
<tr><td>Density of accumulated snow: $\rho_S$</td><td>100 kg/m³</td></tr>
</table>

proposed by Durbin [8] was employed as the base model to calculate eddy viscosity. Parameters related to the property of snow are summarized in Table 2. For the purpose of this study, it was assumed that other factors related to changes in snow depth, such as snowmelt, were negligible.

**3.2 Results and discussion**

The snow depth was normalized by the reference snow depth $h*$ that was not affected by buildings.

Figure 4 shows the distribution of the measured and predicted snow depths on January 7. The eroded regions between the longer sides of the buildings as observed in the CFD results correspond to the regions as determined from the measurement. However, the large snow depth measured in front of the windward building was not reproduced by CFD. One reason for this disagreement can be that an hourly averaged wind velocity was applied to the computation. Hence, although large erosion usually occurs when the instantaneous wind velocity is greater than the threshold velocity in real situations, this effect is not included in this CFD model.

Figure 5 compares the longitudinal distributions of snow depths along sections A-A' and B-B' shown in Figure 1. In section A-A', which represents the space obstructed by buildings, the distribution of snow depth obtained by CFD shows good agreement with that obtained from the measurement, except for the region in front of windward buildings. The observed erosion between buildings and the accumulation of snow near the

at Yamaguchi meteorological station, a density of water and a density of accumulated snow, respectively. The density of accumulated snow was assumed to 100 kg/m³ as that of fresh snow. The vertical profile of mean wind velocity at inflow boundary obeys the $z_0$-type logarithmic law. The roughness length $z_0$ was set to 0.41 m corresponding to surrounding low-rise houses around the measurement site. Other computational conditions for CFD are listed in Table 1. These conditions basically follow guidelines for practical applications of CFD to pedestrian wind environment proposed by the Architectural Institute of Japan [9]. The revised $k$-$\varepsilon$ model

building wall are well reproduced. In section B-B', which represents the open space allowing flow in the prevailing wind direction, the CFD generally underestimated snow depth, and peak values observed in the measurement results were not well reproduced by CFD.

This underestimation is also attributed to the fact that this simulation did not consider the temporal high wind speed velocity, as mentioned earlier. Therefore, the amount of snow directly transported from the windward side of buildings to the region between buildings was underestimated.

## 4 Conclusions

Snowdrift in and around building arrays was predicted using CFD. The predicted distribution of snow depth agreed well with the measured snow depth values, except for the regions in front of windward buildings and the open space allowing flow in the prevailing wind direction. The effect of temporal change in wind velocity on the accuracy of steady-state simulation will be examined in future studies.

## References

1. Okaze T., Mochida A., Tominaga Y., Ito Y., Yoshino H., CFD prediction of snowdrift around a cube using two transport equations for drifting snow density, Proceedings of the 5th International Symposium on Computational Wind Engineering (2010)
2. Oikawa S., Tomabechi T., Daily observation of snowdrifts around a model building. Proceedings of the 4th International Conference on Snow Engineering, 149-156 (2000)
3. Bang B., Nielsen A., Sundsbø P. A., Wilk T., Computer simulation of wind speed, wind pressure and snow accumulation around buildings (SNOW-SIM). Energy and Buildings, 21, 235-243 (1994)
4. Thiis K. T., Large scale studies of development of snowdrifts around buildings. Journal of Wind Engineering and Industrial Aerodynamics, 91, 829-839 (2003)
5. Beyers M., Waechter B., Modeling transient snowdrift development around complex three-dimensional structures. Journal of Wind Engineering and Industrial Aerodynamics, 96, 1603-1615 (2008)
6. Tsutsumi T., Chiba T., Tomabechi T., Snowdrefts on and around buildings based on field measurement, Proceedings of the 7th International Conference on Snow Engineering, 9-17 (2012)
7. Shao Y., Li. A., Numerical modeling of saltation in the atmospheric surface layer, Boundary-Layer Meteorology, 91, 199-225 (1999)
8. Durbin, P.A., On the k-3 stagnation point anomaly. Int. J. Heat and Fluid Flow, 17, 89-90 (1996)
9. Tominaga, Y., Mochida, A., Yoshie, R., Kataoka, H., Nozu, T., Yoshikawa, M., Shirasawa T., AIJ guidelines for practical applications of CFD to pedestrian wind environment around buildings. Journal of Wind Engineering and Industrial Aerodynamics, 96(10-11), 1749-1761 (2008)
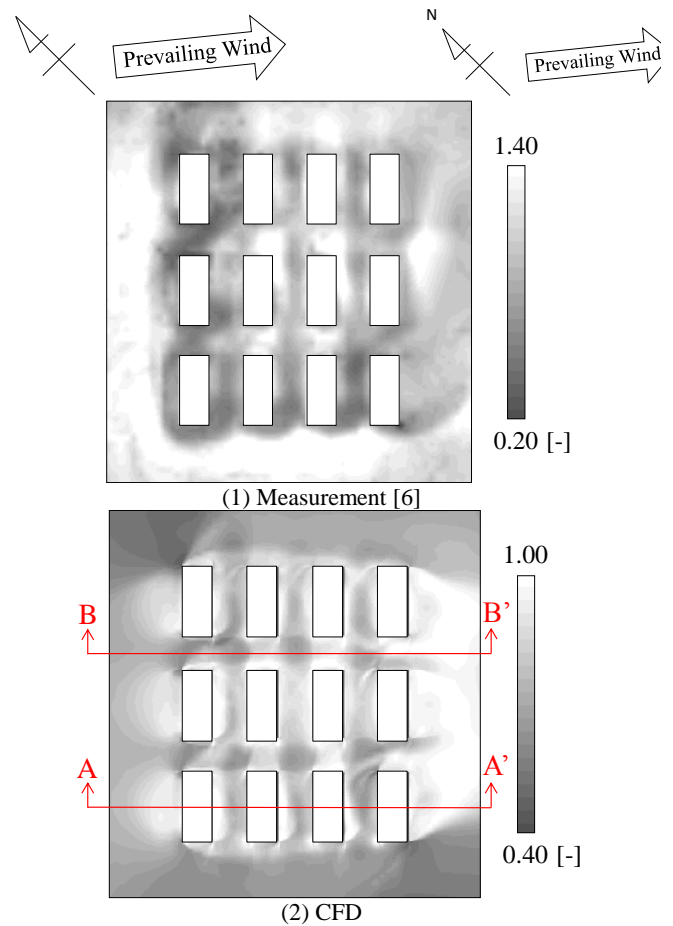
**Figure 4.** Horizontal distribution of snow depth on January 7, 2010
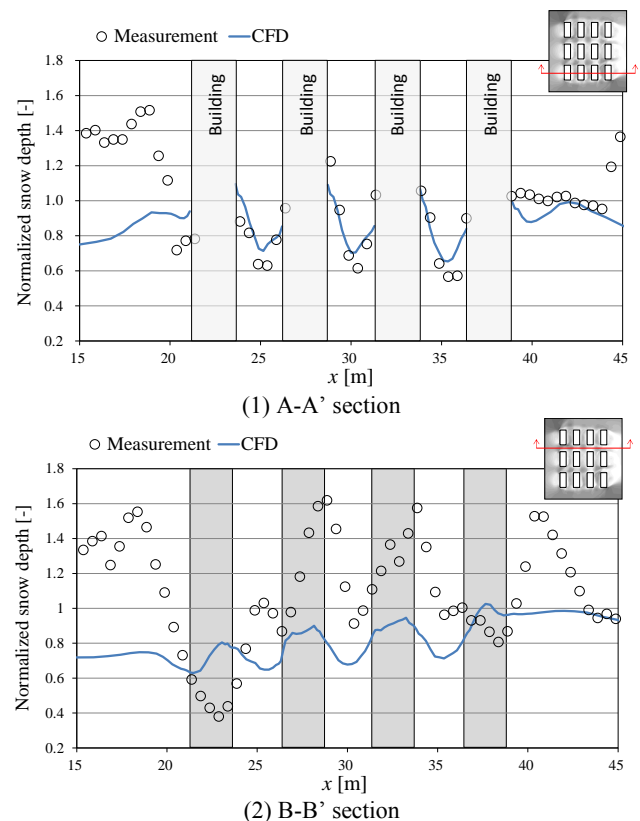


**Figure 5.** Longitudinal distribution of snow depth on January 7, 2010

# Outdoors experiments of snowdrift on typical cubes based on axial flow fan matrix in Harbin

Mengmeng Liu[1, 2], Qingwen Zhang[1, 2], and Feng Fan[1, 2]

[1]*School of Civil Engineering, Harbin Institute of Technology, Harbin 150090, China*
[2]*Key Lab of Structures Dynamic Behavior and Control of China Ministry of Education, Harbin Institute of Technology, Harbin 150090, China*

**Abstract.** Snowdrifts around different model buildings were investigated in wind tunnel and outdoor environment, considering the serious problems caused by snowdrifts around buildings when formed on undesirable places. The formation of snowdrifts is highly connected to the wind speed around the buildings. Some experiments have been carried out to find the relationship between the snow deposition around the building and wind speed. The experiments were conducted with the same model, $1000\times1000\times1000$ mm$^3$ but under three different wind speeds. All of the experiments were based on a new type of laboratory equipment - axial flow fan matrix, which was placed outdoor. The laboratory equipment can produce stable wind field within a certain range and a speed range of 1~10.5 m/s. The laboratory equipment was placed in a narrow strip between two buildings in Harbin China. The temperature around was measured during the experiments. The snowdrift height around the model was surveyed in approximately 1000 points and contour maps produced. The results proved that different wind speeds had a significant influence on the pattern of the snowdrifts produced.

## 1 Introduction

Snowdrift formation around buildings should be considered areas prone to be snowy and windy to ensure proper accessibility and safety of buildings. Most of the researchers use numerical simulation to model snow accumulation around buildings, while this tool needs to be carefully validated before it can be used for planning purposes. Important understanding for use in such validation is gathered in outdoor full-scale experiments and wind tunnels experiment. Full-scale experiment is sparsely reported. As an appropriate profiler to simulate snowdrift problems around buildings, wind tunnel experiment methods have been explored for many years. Related research has been undertaken in several studies.

Naaim et al. [1] reviewed the conditions for a correct simulation of snowdrifts in wind tunnels, or outdoor environment, by comparing requirements proposed by four scientists (i.e., Kind, 1975, 1985; Iversen, 1979, 1980, 1981, 1982, 1984; Anno, 1984; Tabler, 1980). Delpech [2] overviewed the snowdrift mechanisms, discussed the experimental procedures based on similarity parameters proposed in the scientific literature. The simulation of wind induced snow drifting around buildings by using artificial snow, in the Jules Verne climatic wind tunnel, was carried out later, based on the proposed criteria. Okaze el at. [3] carried out a series of wind tunnel measurements over a loose snow surface to investigate the characteristics of drifting snow phenomenon in a non-equilibrium boundary layer and to obtain data for examining the numerical model of snow transport coupled with computational fluid dynamics (CFD). Furthermore, as above, wind tunnel experiments on snowdrifts usually used artificial snow as a substitute of natural snow, which cannot fully reflect the motion of natural snow particles. LÜ XiaoHui [4] conducted a series of experiments in wind tunnel to investigate the motion of natural snow. The results indicated that the mass flux rates of snow exponentially decreased with height whereas the snow transport rate increased exponentially with wind velocity.

Although various studies dealing with snowdrift simulation have been carried out in recent years, due to the limitation of the experimental instrumentation and funds, such experiments suffer a lot from scaling problems and artificial snow [5, 6]. Compromises must be made based on the objective of the experiment.

To solve the problems, Harbin Institute of Technology（HIT）proposed a new kind of experimental equipment, axial flow fan matrix, which aimed at the experiments of snow drifting. The experimental equipment was composed of a 2×2 fan matrix, wind rectifier, and a snow simulator. Considering the device is sited outdoors, the experimental equipment was placed in a narrow strip between two buildings to reduce the interference of the external environment. In order to meet the experimental requirements, the laboratory equipment could produce stable wind field within a certain range and a speed range of 1~11.5 m/s.

Treating the building as a cube with flat roof, several experiments were conducted to find the relationship between wind speeds and the pattern of the snow accumulation around buildings.

## 2 Outdoors experiments of snowdrifts around cube model

### 2.1 Experiment condition and method

The experiment was performed within the campus of Harbin Institute of Technology (HIT), China (Figure 1). It was a part of a large snow engineering program. The natural wind speed in this area has been previously found to be very small during winter. This condition makes the area ideal for snowdrift measurements.

**Figure 1.** Locations of experiments

To find the relationship between wind speeds and the pattern of the snow accumulation around buildings, three experiments using the same model but under three different wind speeds-2.5m/s, 3.5m/s, 4.5m/s, were conducted. The model was of cube shape with dimensions of 1000 ╳ 1000 ╳ 1000 mm3.

The experiments were conducted on February 1st, 2016, based on the axial flow fan matrix (Figure 2). The snow used during the experiments comes from real snow. During the experimental process, snow density and natural temperature were measured. Natural wind speed and direction were measured at 1.8m on a PC-4 automatic weather station (Figure 3), and the sampling interval was 1 minute.



**Figure 2.** Experiment equipment



**Figure 3.** PC-4 automatic weather station

## 2.2 Results

Figure 5 shows the snowdrift geometry measured at afternoon on February 1st, 2016. The natural temperature is about -13℃.

During the experiments, the natural wind in the experiment site was measured (Figure 4).
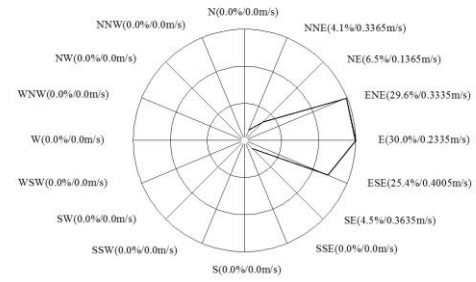


**Figure 4.** Wind frequency diagram in the winter of 2015-2016



**Figure 5(a).** Photos of snowdrift with 2.5m/s wind speed



**Figure 5(b).** Photos of snowdrift with 3.5m/s wind speed



**Figure 5(c).** Photos of snowdrift with 4.5m/s wind speed

The incidence angle of the wind was 0° on the windward wall. During the experiments, the model was fixed on the experimental platform with a uniform flat bottom. The distance between the model and the outlet surface of wind was 2m.

Every experiment would last for 10min. At the end of the experiment, the height of the snowdrifts was measured with a straight edge tool in approximately 1000

points around each building. Because the data were measured manually, the measurement accuracy was down to millimeter level. The points were chosen for optimal description of the curvature of the snowdrifts. The Kriging method was used to interpolate a surface between the measured points. Figure 6 showed the contour map of snowdrift.
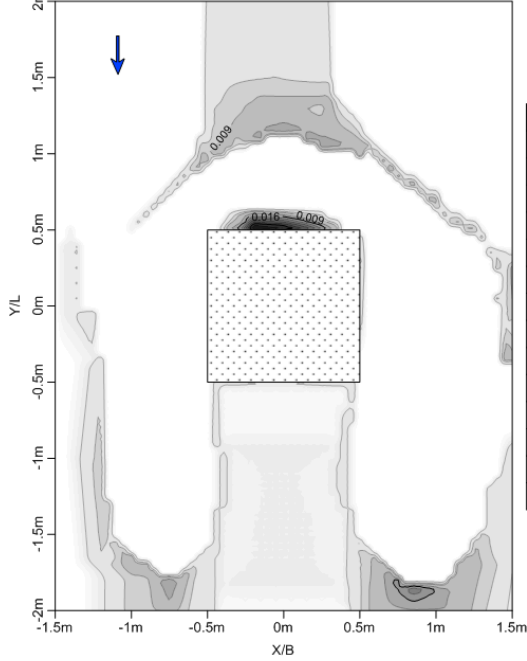


**Figure 6 (a).** Contour map of snowdrift with 2.5m/s wind speed
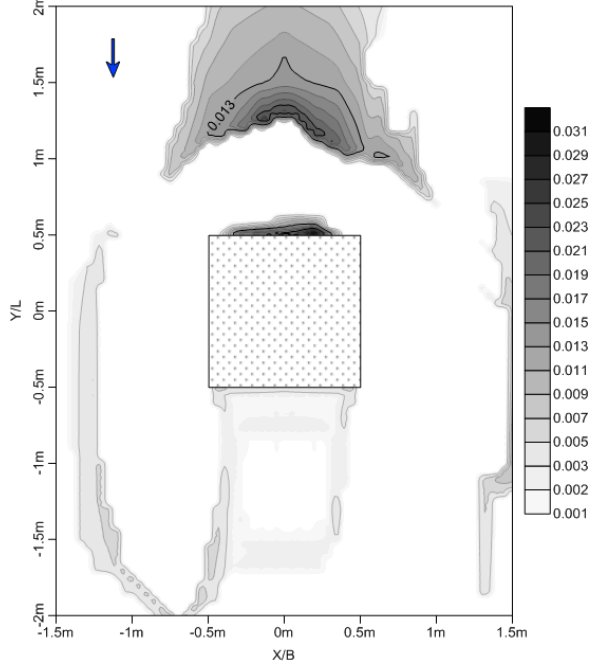


**Figure 6 (b).** Contour map of snowdrift with 3.5m/s wind speed
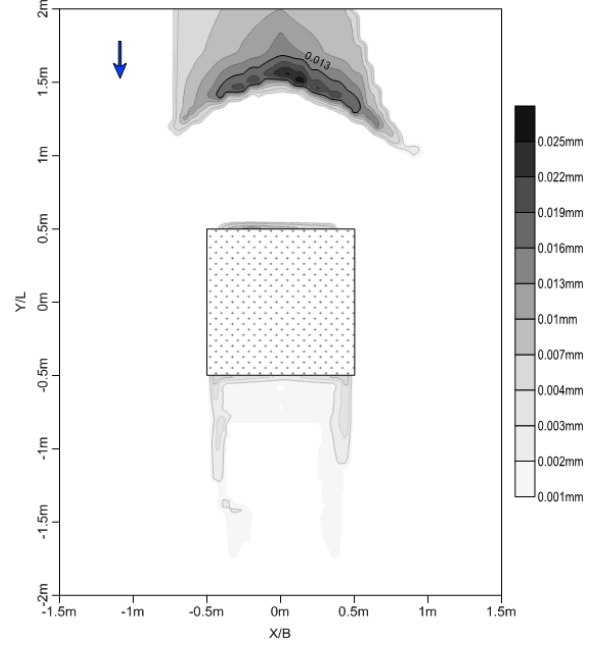


**Figure 6 (c).** Contour map of snowdrift with 4.5m/s wind speed

## 3 Comparison and analysis

The temperature during the experiment ranged between -10℃ and -13℃. The 1 min average natural wind speed in the period was ranging from 2.5 to 4.5 m/s.

The snowdrifts around the same model building, presented in Fig. 6, showed more or less the same basic characteristics. The accumulation pattern proved the close relationship between wind speed and snowdrift around buildings.

The results of the three experiments show some identical characteristics. The snowdrifts showed a symmetrical distribution, similar to the wind-induced vortices. Just close to the upwind, there was a short steep inclining snowdrift, but the range of the snowdrift was short. There was a sharp increasing of snowdrift in an area, which was from a certain distance to the upwind surface. With the distance away from the upwind surface becoming larger, the accumulation effect weakened. In the leeward side of the model, there was less but uniformed snow accumulation.

However, because the simulated wind speed was different, each experiment result showed unique characteristics. Comparing the three snow distribution contour maps we could conclude that:

Figure 6 (a) shows the results of the experiment under the wind speed 2.5 m/s. The height of snowdrift close to the upwind surface was the highest and the range of snowdrift was the largest. At about 0.6m away from the upwind surface, there came an area of obvious snow deposition and a maximum height of snowdrift. With the increase of distance away from upwind surface, the height of snowdrift decreased. Although there was no snowdrift near the model on both sides, at about 0.6m away from the upwind surface, there was some small snowdrift. At about 1.2 m away from downwind, there were two obvious snow depositions on both sides. The whole snowdrifts showed a typical horseshoe pattern.

Figure 6 (b) shows the results of the experiment under the wind speed 3.5 m/s. The height of snowdrift close to the upwind surface was slightly lower and the range of snowdrift was slightly smaller. At about 0.75m away from the upwind surface, there was a steep inclining snowdrift ending in a sharp edge and a maximum height of snowdrift, indicating the extension of the upwind recirculation zone. With the increase of distance away from upwind surface, the height of snowdrift decreased. At about 0.8m away from the upwind surface, there was some small snowdrift. There appeared an area with no snowdrift in the range of 0.5m~1m away from the downwind surface and no obvious area of snow deposition appeared on both sides.

Figure 6 (c) shows the results of the experiment under the wind speed 4.5 m/s. The height of snowdrift close to the upwind surface was the lowest and the range of snowdrift was smallest. At about 1.0m away from the upwind surface, there was a most obvious steep inclining snowdrift ending in a sharp edge and a maximum height of snowdrift, indicating the extension of the upwind recirculation zone. In the measuring range, there was no snowdrift on both sides of the model. A typical horseshoe pattern of snowdrift appeared at the area close to the downwind surface.

## 4 Conclusions

This paper has investigated the characteristics of snowdrift in outdoor experiments based on axial flow fan matrix. The results proved that different wind speeds had significant influences on the pattern of the snowdrifts produced. As the wind speed increased, the snowdrift just close to the upwind surface decreased rapidly, the snowdrift away from the upwind surface became stronger and steeper and the distance between the sharp snowdrift and the upwind surface became larger. Although the sphere of influence was not measured, we could predict that the range of wind influence on snowdrift became larger as the wind speed increased.

## References

1. N. bouvet. J. Surv. Geophys. 5-6, 711 (1995)
2. Delpech Ph, Palier P, Gandemer J. Snowdrifting Simulation around Antarctic Buildings[J]. Journal of Wind Engineering and Industrial Aerodynamics, 74-76, 567-576 (1998)
3. Tsubasa Okaze, Akashi Mochida, Yoshihide Tominaga. Wind tunnel investigation of drifting snow development in a boundary layer[J]. Journal of Wind Engineering and Industrial Aerodynamics, 104-106, 532-539(2012)
4. LüXiaoHui, Huang N, Tong D. Wind tunnel experiments on natural snow drift[J]. Science China Technology Science, 55, 927-938 (2012)
5. Thomas K. Thiis, Yngvar Gjessing. Large-scale measurements of snowdrifts around flat-roofed and single-pitch-roofed buildings[J]. Cold Regions Science and Technology 30. 175-181(1999)
6. J.H.M. Beyers, T.M. Harms. Outdoors modelling of snowdrift at SANAE IV Research Station, Antarctica[J]. Journal of Wind Engineering and Industrial Aerodynamics, 2002, 91 : 51-569. (2004)
7. A. Mecke, I. Lee, J.R. Baker jr., M.M. Banaszak Holl, B.G. Orr, Eur. Phys. J. E **14**, 7 (2004)
8. M. Ben Rabha, M.F. Boujmil, M. Saadoun, B. Bessaïs, Eur. Phys. J. Appl. Phys. (to be published)
9. Luigi T.De Luca, *Propulsion physics* (EDP Sciences, Les Ulis, 2009)
10. F. De Lillo, F. Cecconi, G. Lacorata, A. Vulpiani, EPL, **84** (2008)

# Numerical simulation of snowdrift on a membrane roof and wind-induced response analysis under coupled wind and snow loads

SUN Xiaoying[1], HE Rijin[1], WU Yue[1]

[1]*Key Lab of Structure Dynamic Behaviour and Control of the Ministry of Education, Harbin Institute of Technology, 150090 Harbin, China*

**Abstract.** Long-span structures are quite sensitive to uneven distributed snow loads, therefore it is vital to estimate the wind-induced redistribution snow loads accurately. This paper presents the results of numerical simulation of snowdrift on a long-span membrane roof at first. Based on Euler-Euler method in multi-phase flow theory, the numerical simulation adopt Mixture model by employing commercial CFD software FLUENT. Assuming the snow is evenly distributed at the initial time in simulation, and the initial snow depth is calculated by the referenced snow pressure in Chinese Load Code, combined with the snow deposition and erosion model, the result is given as the counter map of snow distribution coefficient under different wind velocities and directions, and we give the most unfavourable form of snow distribution. Next, the uneven distributed snow is set as static load on the membrane roof, and the unsteady aerodynamic force is obtained by numerical simulation either, then the wind-induced response under coupled wind and snow load is analysed, the results show that uneven distributed snow is a disadvantage mechanical condition to this structure. Finally, under the condition of laying air-blowing pipelines on the roof, the snow sweeping process is simulated by employing transient solver in FLUENT, the result is given as the time dependent residual snow mass fraction and snow mass flux which provide some useful suggestions on practical application.

## 1 Introduction

Wind causes substantial snow accumulation and unevenly redistributed on and around buildings which often leads to structural damage or even collapse. Long-span structures are quite sensitive to unevenly distributed snow loads, therefore it is vital to estimate the wind-induced redistribution snow loads accurately.

Transportations of snow particles can be classified into three process i.e. creep, saltation and suspension ([1]). Creep is a process in which snow particles moves by rolling or creeping on the snow surface under low wind speed, the height of creep is usually below $0.01m$. Saltation is a process in which snow particles move with repeat leaping up or jumping on the snow surface under relatively high wind speed, the height of saltation is usually below $0.1m$. If wind speed continues to increase, the snow particles are transported upwards by turbulent eddies and moved far downwind, this process is called suspension, the floating height of snow particles in suspension is about $0.1{\sim}100m$. The snow transport rate in creep is so small that can be neglected, as well as previous research, the snow movement in creep is not considered.

Currently, there are mainly three methods to estimate snowdrift namely field observation, wind tunnel test and numerical simulation. Field observation is the most realistic approach to obtain the uneven snow distribution, but this approach requires precise measurements for snow scale and meteorology conditions and relies heavily on the meteorology conditions. Wind tunnel test constrained greatly by the similarity criterion and cost a lot. Numerical simulation was firstly adapted to analysis snowdrift by Uematsu at 1991 ([2]) and now widely used by researchers.

## 2 Numerical modelling

Based on one way coupled assumption, the snow particle effects on the turbulence are not considered, the simulated turbulence is influenced directly by the snow phase through the wall function.

Based on Euler-Euler approach in multiphase flow theory, there are three multiphase models supported by FLUENT, i.e. the VOF model, the Mixture model and the Eulerian model. Compared these three models, Mixture model allowing better stability and smaller computation labour, while sharing nearly the same precision with Euler model. For this reason, this paper adopt Mixture model to simulate snowdrift.

### 2.1 Governing Equations ([3])

In Mixture Model, the air and snow shares the same mass continuity equation and momentum conservation equation as following formulas.

#### 2.1.1 Mass continuity equation

$$\frac{\partial \rho_m}{\partial t} + \nabla \left( \rho_m \vec{v}_m \right) = 0 \qquad (1)$$

Where $\rho_m = \sum\limits_{k=1}^{2} f_k \rho_k$ is the mixture density of air and snow，$f_k$ is the volume fraction of the air ($k$=1) and snow ($k$=2), $\vec{v}_m = \sum\limits_{k=1}^{2} (f_k \rho_k \vec{v}_k) / \rho_m$ is velocity of the mixture phase.

Corresponding author: sxy_hit@163.com

### 2.1.2 Momentum Conservation Equation

$$\frac{\partial(\rho_m \vec{v}_m)}{\partial t} + \nabla \cdot (\rho_m \vec{v}_m \vec{v}_m) = -\nabla p + \nabla \cdot \left[ \mu_m (\nabla \cdot \vec{v}_m + \nabla \cdot \vec{v}_m^T) \right]$$
$$+ \rho_m \vec{g} + \vec{F} + \nabla \cdot (\sum_{k=1}^{2} f_k \rho_k \vec{v}_{dr,k} \vec{v}_{dr,k}) \quad (2)$$

Where $\mu_m = \sum_{k=1}^{2} f_k \rho_k$ is the mixture dynamic viscosity, $\vec{F}$ is the body force, $\vec{v}_{dr,k} = \vec{v}_k - \vec{v}_m$ is the drift velocity for phase $k$.

### 2.1.3 Snow Volume Fraction Equation

$$\frac{\partial(\rho_s f)}{\partial t} + \nabla \cdot (\rho_s f \vec{v}_m) = -\nabla \cdot \left( f \rho_s \vec{v}_{dr,s} \right) + \sum (m_{sa} - m_{as}) \quad (3)$$

Where $\rho_s$ and $f$ are the snow density and volume fraction respectively, $m_{sa}$ and $m_{as}$ are the mass converted between air and snow, in this paper $m_{sa}$ and $m_{as}$ refers to 0.

## 2.2 Deposition and erosion model

Wall shear stress is a very important parameter in snowdrift, the snow particle begins to move when the wall shear stress $\tau$ on the snow surface exceed the threshold wall shear stress $\tau_t$, otherwise the snow particle remains stationary. The threshold wall shear stress $\tau_t$ is usually determined through field observation and the wall shear stress can be derived from the logarithmic law. Here and after, we use friction velocity $u_*$ to replace the wall shear stress $\tau$ and obeys the following relation:

$$u_* = \sqrt{\tau/\rho} = \frac{\kappa u(z)}{\ln(z/z_s)} \quad (4)$$

Where $\kappa$ refers to Von Karman constant which equal to 0.4, $z_s$ is the aerodynamic roughness height over a snow surface which is optimized to $3.0 \times 10^{-5} m$.

The snow mass flux of erosion $q_{ero}$ is simplified as a function of the excess friction velocity available above the threshold friction velocity. The deposition flux $q_{dep}$ is calculated to be proportional to snow concentration $f$ and the snow fall velocity $w_f$.

$$q_s = \begin{cases} q_{ero} = A_{ero} \left( u_*^2 - u_{*t}^2 \right) & u_* > u_{*t} \\ q_{dep} = \rho_s f w_f \dfrac{u_{*t}^2 - u_*^2}{u_{*t}^2} & u_* \leq u_{*t} \end{cases} \quad (5)$$

Where $A_{ero}$ is a proportionality coefficient representing the snow pack bounding strength which is chosen to be $7.0 \times 10^{-4}$ ([4]), $u_{*t}$ is the threshold friction velocity which is chosen to be 0.2 m/s ([1]), $w_f$ is the snowfall velocity of snow particles which is chosen to be 0.2 m/s.

If the initial snow depth is assumed to be $h_0$ and the time of wind acting on snow surface is $\Delta t$, then the depth of snow can be represented as:

$$h = h_0 + \frac{q_s}{\rho_s} \Delta t \quad (6)$$

## 2.3 Turbulence Model

The turbulence model employed in numerical simulation of snowdrift varies from scholars. Uematsu ([2]) adopt the mixing length theory in his pioneering works on CFD prediction of snowdrift, Beyers (2004, [5]) adopt the standard $k - \varepsilon$ model and points out that it is necessary to critically examine the influence of inaccuracies isotropic turbulence assumption on the snow accumulation and erosion, ZHOU and LI ([6]) adopt the modified RSM model which take account of the snow particle's effect on turbulence. HONG ([7]) compared the results of different turbulence models with field observation and optimized $k d k l d \omega$ model for snowdrift simulation.

In this paper, the $k d k l d \omega$ model is adopted. The $k d k l d \omega$ model is considered to be a three-equation eddy-viscosity type, which includes transport equations for turbulent kinetic energy ($k_T$), laminar kinetic energy ($k_L$), and the inverse turbulent time scale ($\omega$).

$$\frac{Dk_T}{Dt} = P_{K_T} + R + R_{NAT} - w k_T - D_T + \frac{\partial}{\partial x_j} \left[ \left( v + \frac{\alpha_T}{\alpha_K} \right) \frac{\partial k_T}{\partial x_j} \right] \quad (7)$$

$$\frac{Dk_L}{Dt} = P_{KL} - R - R_{NAT} - D_L + \frac{\partial}{\partial x_j} \left[ \left( v \frac{\partial k_L}{\partial x_j} \right) \right] \quad (8)$$

$$\frac{D\omega}{Dt} = C_{\omega 1} \frac{\omega}{k_T} P_{K_T} + \left( \frac{C_\omega R}{f_\omega} - 1 \right) (R + R_{NAT}) \frac{\omega}{k_T} - C_{\omega 2} \omega^2$$
$$+ C_{\omega 3} f_\omega \alpha_T f_W^2 \frac{\sqrt{k_T}}{d^3} + \frac{\partial}{\partial x_j} \left[ \left( v + \frac{\alpha_T}{\alpha_k} \right) \frac{\partial k_T}{\partial x_j} \right] \quad (9)$$

## 2.4 Boundary conditions

### 2.4.1 Wind profile

The fully developed inlet wind velocity profile is determined from the power law profile:

$$\bar{u}(z) = u_0 \left( \frac{z}{z_0} \right)^\alpha \quad (10)$$

The reference velocity $u_0$ and the height above the surface $z_0$ are 10 m/s and 10 m respectively. Note that the friction velocity $u_*$ at inflow boundary should exceed the threshold friction velocity $u_{*t}$ so that the snowdrift could initiate.

## 2.4.2 Snow particle concentration profile

The inlet snow particle concentration profile is given by an empirical formula proposed by Pomeroy, Gray &Male ([8], [9]), in which the inflow snow concentration is set as constant within saltation layer ($z \leq h_{sal}$) and decreases exponentially with the increase of height within suspension layer ($z > h_{sal}$).

$$f = \begin{cases} \dfrac{0.68}{u_p u_* h_{sal} g} u_{*_t} \left( u_*^2 - u_{*_t}^2 \right) & z \leq h_{sal} \\ 0.8 \exp\left[ -1.55 \left( 4.78 u_*^{-0.544} - z^{-0.544} \right) \right] & z > h_{sal} \end{cases} \quad (11)$$

Where $u_p$ is the average velocity of the snow particle in saltation layer which is chosen to be $2.8 u_{*_t}$ suggested by Pomeroy ([8]), $h_{sal}$ is the height of the saltation layer which is determined by the following formula ([8]):

$$h_{sal} = 1.6 \frac{u_*^2}{2g} \quad (12)$$

# 3 Numerical simulation of snowdrift

## 3.1. Geometrical modelling

The membrane structure (Figure 1) is located in Changchun, northeast China, a famous heavy-snowfall region. This mast supported tension structure spans about 188$m$, the highest point of the membrane part is about 18$m$ and the height of masts is about 48$m$. For simplicity, the masts and surrounding landscape are neglected in CFD modelling. Due to its Hyperbolic Paraboloids building shape, snow stacks easily in the central concave region, therefore the snow load is one of the control loads in structural design.



**Figure 1.**Long-span membrane structure.

Based the symmetry properties of this structure, four wind directions (i.e. 0°, 30°, 60°, 90°) are considered to estimate the effect of wind direction on snow distribution. The dimension of the computational region was selected as X×Y×Z=10L×21B×7H which is large enough to neglect the influence of the computational region boundary on interior flow field, where L, B, H refers to the across-wind dimension, along-wind dimension and the height of the structure respectively.
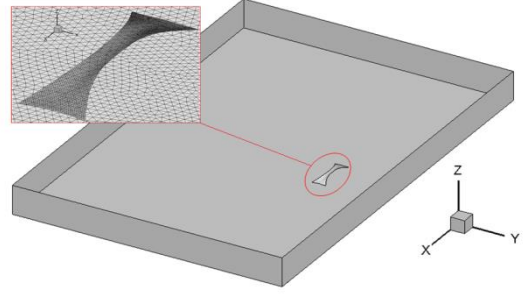


**Figure 2.**Sketch of model and computational region.

## 3.2 Results

The following results are given as counters of the Snow distribution factor $\mu_r$ which is defined as:

$$\mu_r = \frac{S_k}{S_0} \quad (13)$$

Where $S_k$ refers to standard value of snow loads which can be calculated as $S_k = \gamma_{snow} h_{snow}$, $\gamma_{snow}$ is the snow density which is chosen as 1500 $N/m^3$ by measured data, $h_{snow}$ is calculated by Eq. (6). $S_0$ is the reference snow pressure which is 0.45 $kN/m^3$ according to Chinese load code for the design of building structures (GB 5009-2012, [10]).
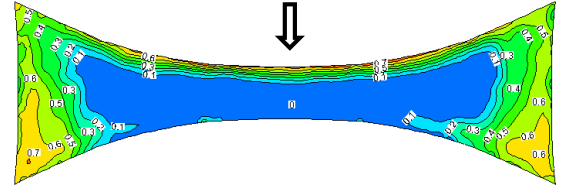


**Figure 3.**Snow distribution factor under **0°** wind direction
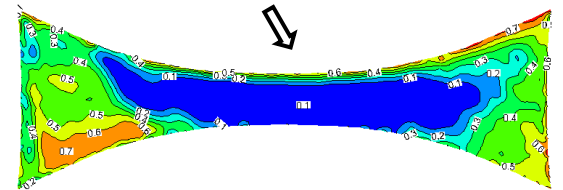


**Figure 4.**Snow distribution factor under **30°** wind direction
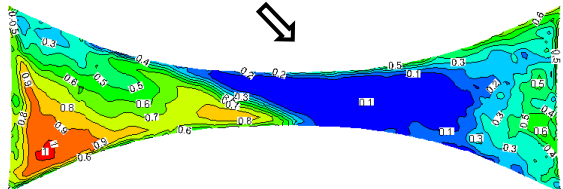


**Figure 5.**Snow distribution factor under **60°** wind direction
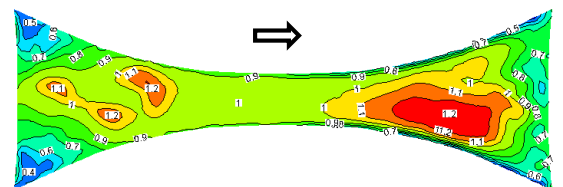


**Figure 6.**Snow distribution factor under **90°** wind direction

Under 0° wind direction, the whole membrane roof is represented as erosion region. In the middle part of the membrane roof, there is nearly no snow exists ( $\mu_r$ =0) because of high wind velocity, but there is a strip area in the windward side where snow accumulates ( $\mu_r$ =0.1~0.7) because of the flow separation. In both sides of the membrane roof, snow accumulates due to low wind speed, and snow accumulates heavier in leeward side of the membrane roof than that in windward side, this may attributes to the snow particles in windward side were blown away and deposits in leeward side of the roof.

Under 30° and 60° wind direction, the whole membrane roof is represented as erosion region too, and their snow distribution patterns are very similar with each other. Snow mainly accumulates in the left part of the membrane roof and the 60° case accumulates much more snow than that of 30° case, this non-symmetrical load may bring about disadvantage effect on the membrane structure.

Under 90° wind direction，the whole membrane roof is mainly represented as deposition region which is very different from other three cases. Most part of the roof has a snow distribution factor $\mu_r$ > 1 and the maximum snow distribution factor occurs in in the leeward part excess 1.2. There are two major reasons: one is the profile of the membrane roof is very close to streamline in 90° case, this results in week flow separation and relatively low wall shear stress on the snow surface, so most part of the roof has a snow distribution factor $\mu_r$ > 1. The other reason is that the structure has a dimension of 188$m$ along windward direction, it is long enough that the snow particles blown away in the windward part deposits substantially in the leeward part.

Comprehensively analysing these four cases, the membrane roof is divided into 64 zones (Figure 7) to give the most disadvantageous snow distribution factor of each partition for design use, the partition scheme is in accordance with the PTFE and ETFE zone. Due to the symmetry, only 16 zones were presented to give the most disadvantageous snow distribution factor.
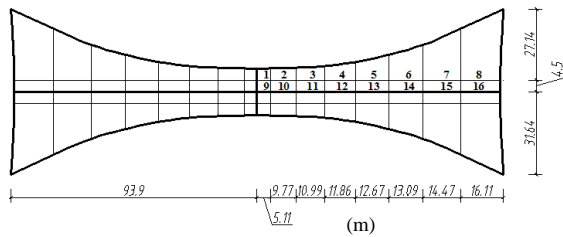


**Figure 7.**Sketch of partition schemes of the membrane roof

Table 1 presents the most disadvantageous snow distribution factors, it is the maximum value of snow distribution factor in each zone among these four wind direction cases. From table 1 we can find that the most disadvantageous snow distribution factors in concave area (zone 10~15) excess 1.0 entirely, the maximum value come up to 1.23. Note that the results in this paper is obtained under the condition of the wind velocity at 10$m$ height is 10$m/s$, the more disadvantage situation may

occur at lower wind speed but longer acting time.

**Table 1.**Most disadvantageous Snow distribution factors

| Zone Number | 1 | 2 | 3 | 4 | 5 | 6 | 7 | 8 |
|---|---|---|---|---|---|---|---|---|
| $\mu_r$ | 0.95 | 0.94 | 0.94 | 1.01 | 1.05 | 1.07 | 0.93 | 0.77 |
| Zone Number | 9 | 10 | 11 | 12 | 13 | 14 | 15 | 16 |
| $\mu_r$ | 0.99 | 1.01 | 1.09 | 1.19 | 1.23 | 1.22 | 1.10 | 0.95 |

# 4 Numerical simulation of snow-sweeping

In northeast China, the long winter causes durable snow load. What's more, the snow melts due to indoor heating and then frozen if the temperature goes down, this melt-frozen process causes the snow density increases with time which increases the roof load. For this reason, it is necessary to sweep the snow away especially for long-span roofs.

## 4.1. Geometrical modelling and parameters

In order to sweep away snow on the membrane roof, we designed an air blowing pipeline system see Figure 8. The pipelines are installed along with the boundary of the PTFE and ETFE membrane zones, each pipeline has several air-outlets. The pipeline has a circular cross section with a diameter of 10$cm$; the air-outlet has a rectangle cross section with a dimension of 12$cm$×6$cm$.



(a)



(b)
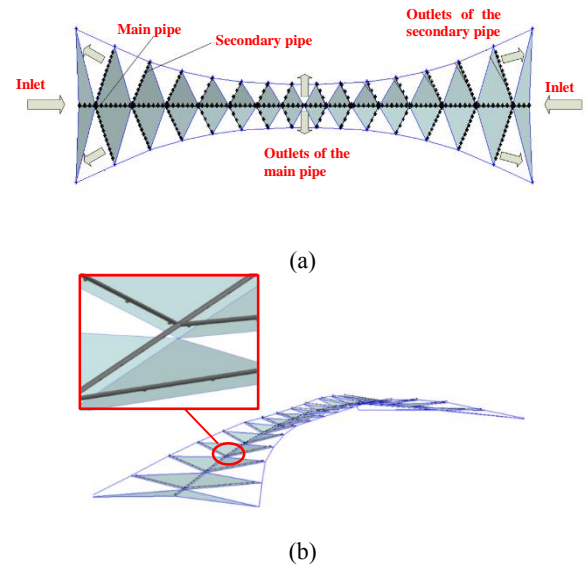
**Figure 8.** Sketch of air blowing pipeline system (a) layout plan, (b) three-dimensional effect graph

The initial snow depth is set as 40$cm$ which is about 1.23$h_0$, the air blowing velocity is selected as 2$m/s$, 3$m/s$, 4$m/s$, 5$m/s$ respectively to estimate the effect of air blowing velocity on snow sweeping results.

The flow field changes rapidly and usually the snow

sweeping process finished in a short time, this process cannot be simulated by steady solver. So the transient solver is adopted which can obtain the residual snow mass concentration. The multiphase model is selected as Mixture model either, and time step in transient simulation is select as small as $10^{-3}s$ for convergence requirement.

## 4.2. Results

The results are given as residual snow mass fraction and dimensionless snow mass flux defined blew.

The residual snow mass fraction is defined as (14), where $m$ refers to the residual snow mass at time $T$, and $m_0$ refers to the snow mass at the initial moment.

$$f = \frac{m}{m_0} \tag{14}$$

In order to make a comparison of snow sweeping efficiency in different cases, the dimensionless snow mass flux is defined as (15), where $Q$ is the summation flux on all the outlets of the computational region, and the $Q_{max}$ is the maximum snow mass flux in all these 4 cases which occurs in the initial moment of the $5m/s$ case, $Q_{max}=16870$ kg·s$^{-1}$.

$$q = \frac{Q}{Q_{max}} \tag{15}$$

Figure 9 compared the residual snow mass fraction varying pattern under four air blowing velocity cases, it is clear that the higher air blowing velocity is, the faster snow sweeping process is, thus the snow sweeping efficiency is positively related to the air blowing velocity which verifies our ordinary experience. Through further analysis we can see that the snow sweeping efficiency decreases rapidly with time, about 70% of snow is blew away during the first 4s.

If the residual snow mass fraction equals to 5% can be set as the competition criterion of the snow sweeping process, the completion time of $2m/s$, $3m/s$, $4m/s$, $5m/s$ case is 14s, 12s, 10s, 8.5s respectively, which is approximately linearly related to the air blowing velocity. Figure 10 gives the snow volume fraction contour map at some key point in time of the $5m/s$ case.



**Figure 9.** Residual snow mass fraction



|  |  |  |
|---|---|---|
| (a) t=2s | (b) t=4s | (c) t=6s |
| (d) t=8s | (e) t=10s | (f) t=12s |
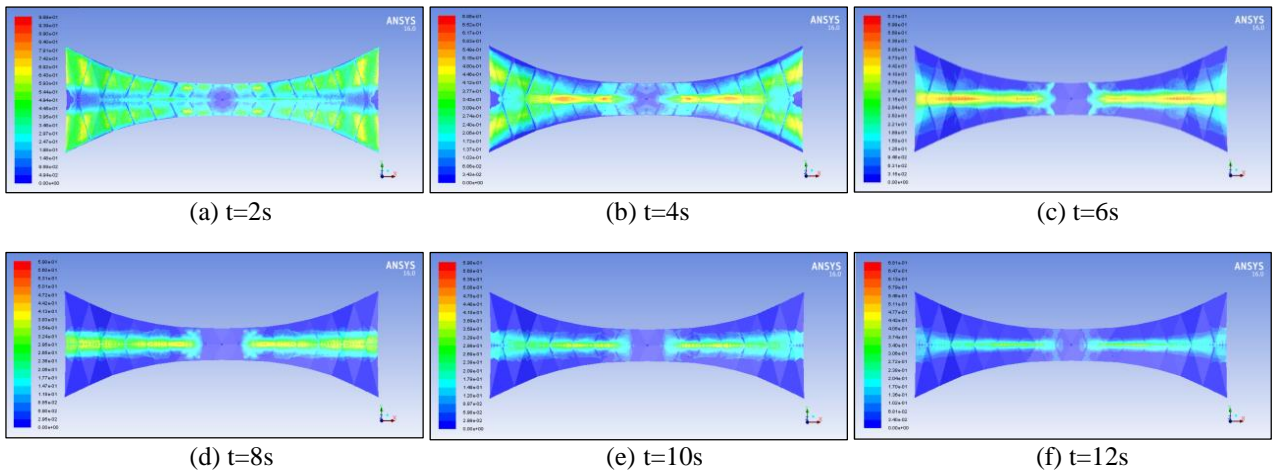
**Figure 10.** Snow volume fraction contour map of the $5m/s$ case
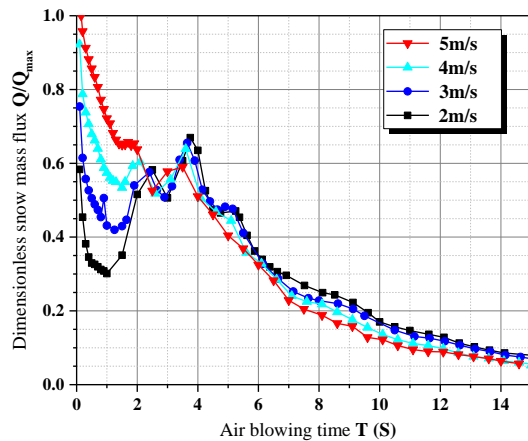
**Figure 11.** Dimensionless snow mass flux

Figure 11 gives the dimensionless snow mass flux. During t=0~2s, the dimensionless snow mass flux is positively related to the air blowing velocity too. But the varying tendency show some difference from the residual snow mass fraction after 4s, the curve show a negative correlation between the dimensionless snow mass flux and the air blowing velocity, this is because most the snow is blew away during the initial stage in the high air blowing velocity case, so the snow mass flux decreases rapidly and the higher air blowing velocity have a lower snow mass flux, but the difference is so small that doesn't affect the final completion order.

## 5 Conclusions

Based on the Mixture multiphase model, a three dimensional numerical simulation of snowdrift and snow sweeping were presented, the simulation obtained the most disadvantageous snow distribution factors of the membrane roof which indicates concave area (zone 10~15, see Figure 7) accumulates the largest snow loads, with the maximum snow distribution factor come up to 1.23. The snow sweeping simulation indicates 70% of snow were swept away during the first few seconds and the total time of the sweeping process is within 14s. In our practice operation, we can use a high velocity in the initial stage which has a high efficiency, after the majority of the snow were swept away, we can use a relatively low velocity to save energy.

## References

1. Tominaga Y, Okaze T, Mochida A. CFD modeling of snowdrift around a building: An overview of models and evaluation of a new approach. *BUILD ENVIRON*, 46(4), 899-910 (2011).
2. Uematsu T, Nakata T, Takeuchi K. Three dimensional numerical simulation of snowdrift. *COLD REG SCI TECHNOL*, 1(20), 65-73 (1991).
3. Inc. A. ANSYS FLUENT Theory Guide. (Ed.2011)
4. Beyers M, Waechter B. Modeling transient snowdrift development around complex three-dimensional structures. *J WIND ENG IND AEROD*, 96(10-11), 1603-1615 (2008).
5. Beyers JHM, Sundsbø PA, Harms TM. Numerical simulation of three-dimensional, transient snow drifting around a cube. *J WIND ENG IND AEROD*, 92(9), 725-747 (2004).
6. Li X.F, Zhou X.Y, Gu M. Modified RSM turbulence model in snowdrift simulation. *14th National Wind Engineering Symposium* .Beijing, China. (2009)
7. Hong C.B. Numerical simulation of snowdrifting on typical form of long-span roofs. MSc thesis. Harbin Institute of Technology, (2012)
8. Pomeroy JW. Saltation of Snow. *Water resource research*, (1990).
9. Pomeroy JW. Steady-state suspension of snow. *J HYDROL*, (1992).
10. Chinese load code for the design of building structures (*GB 50009*). (Ed.2012)

# Developing experimental method for investigating snow deposition around buildings using snow substitutes

Jennifer Fiebig[1,a], Hans Holger Hundborg Koss[1]

[1]Technical University of Denmark (DTU), Dep. of Civil Engineering, Building 118, 2800 Kgs. Lyngby, Denmark

**Abstract.** The phenomenon of wind-driven snow in the arctic and other snow-prone regions has been a significant problem for the built environment for centuries, but the integration of snow deposition in structural design and urban planning is still insufficient and challenging. A traditional way of studying snow deposition on and around buildings is wind-tunnel testing on a reduced scale using a substitute material for snow. This paper gives an overview of experimental approaches from the literature and presents the development of a test set-up in which the emphasis is on the physical properties and aerodynamic performance of the substitute material. The assessment of its fluid mechanical similarity is based on phenomenological comparison with Benchmark observations in the nature. The experimental study was carried out in the small boundary-layer wind tunnel at DTU Civil Engineering and full-scale observations are conducted on research sites in Greenland. The fall velocity of the substitution in comparison to the prototype snow could not determine a velocity scale for the experiment. On the other hand, the phenomenological effect of snowdrift is sufficiently accurate to replicate the deposition characteristic and the ground-area distribution.

## 1 Introduction

Adaption to extreme climatic conditions has been a challenge since the first human settlements in arctic and other snow prone regions. The evolution of traditional buildings and shelters was based on experience and led to optimised designs with respect to construction resources and environmental impact. However, the transition from settlements to cities with higher development density has led to modern building designs that deviate significantly from the traditional housing concepts and fail to take into account many aspects of environmental impact. One important aspect is the accumulation of wind-driven snow on and around buildings. The observed climatic trend of increasing temperature adds to the severity of this problem. Higher temperatures cause higher snow densities and an increasing tendency for combined snow and rain events resulting in wet and heavy snow. As a consequence, the loads from massive snow accumulation frequently exceed the carrying capacity of roof structures leading to local damages or to the total collapse of the supporting structure. Melt water penetrates the building causing deterioration of both the material structure and the indoor climate. Snow depositions around and between buildings block roads and building entrances and require frequent clearing.

Distribution and magnitude of these phenomena depend to a large extend on the air motion around buildings. Wind tunnel testing is a proven method for simulating the airflow interaction of building structures and provides a suitable platform for investigating snow transportation and deposition. However, experimental simulations of snowdrift in a boundary-layer wind tunnel struggle with scaling issues. A review of research on modelling snowdrift showed a parametric variability problem when to satisfy a large number of requirements [1]. A considerable amount of authors proposed accurate parameters for snowdrift in wind tunnel testing without agreeing on the most important parameters to fulfil when simulating snow drift [2,3].

Additionally, the model of snowdrift differs from nature due to thermodynamic effects in the multiphase flow [4]. The mass is transported by the turbulent fluxes and because of the rate of phase change, ice to water vapour occurs. Additional simulation difficulties derive from the behaviour of snow consisting of different modes: a surface creep layer, a saltation layer, and suspension layer. [5,6] An observation in-situ shows the effect of the 2-phase flow like accumulation formation on facades, indicated in Figure 1 and the snow trace phenomenon in Figure 2. The simulation methods are still under development to fulfil the similitude laws within these layers and recent studies focus on particle density of the substitute in association with time duration of snow events and wind velocity hence large scale observation showed a correlation [2], [7–9].



**Figure 1** Snow deposition phenomenon, Hospital in Nuuk, Jennifer Fiebig 2015.

General observation in snowdrift testing is the relevance of the accuracy in flow scale, geometric scale, particle saltation length, snowdrift rate and time scale to obtain representative results of the physical snowdrift

---

[a] Corresponding author: jenfi@byg.dtu.dk

modelling [1, 2, 3, 4, 7, 8, 14, 15, 16]. The aim of the study is to establish a well-documented experimental setup suitable for an extensive parametric study of snow deposition and accumulation and sufficiently accurate to conclude not only on the ground-area distribution but also on the accumulation height. The setup will be used as main tool in a research project investigating the interaction between architectural designs, snow loading and ground-level accumulation between buildings. Furthermore, the documentation of the used material shall allow for benchmarking with numerical methods of snow drift simulation.



**Figure 2** The tracing effect of snowdrift on a roof structure, Jennifer Fiebig 2015.

# 2 Full-scale and experiment

## 2.1 Observation in situ
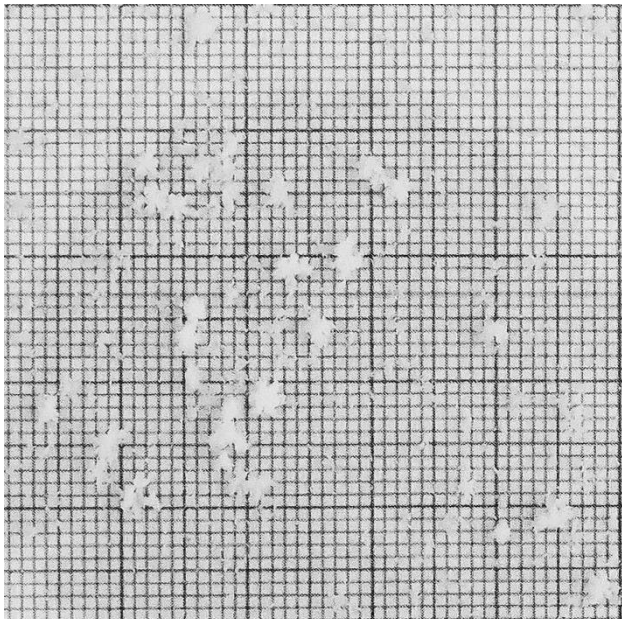


**Figure 3** Snowflakes on millimetre paper with division 1 x 1mm Nuuk 2015.

First in-situ observations of snow drift and accumulation were conducted on DTU premises in Sisimiut, Greenland, operated by the Center of Arctic Technology and Sustainable Solutions (ARTEK). Paralleling to the photometric documentation of snow accumulation on and around buildings weather data was recorded using a medium level compact wireless weather station. The recoded data together with the in-situ observation provided information about the phenomenon in comparison to a model in the wind tunnel simulation. Based on the limited prototype data in-situ of snow deposition on a building over certain duration, an additional comparison from literature was needed. The density $\rho_p$ of prototype snow in the Antarctic has been measured by Mitsuhashi in 1982 with values from 500-900 kg/m³. The particle diameter for prototype snow in the Antarctic had a range of 100-150 μm[14]. On both sides in Greenland, Nuuk and Sisimiut, a millimetre paper method was selected in order to identify the size of snowflakes. Figure 3 illustrates the fallen snowflakes in Nuuk on a millimetre paper with 1x1mm division. Weather data was recorded on 15/12/2015 with an air temperature of -7°C, a humidity of 76 %, atmospheric pressure of 995.5 hPa and a wind direction from north. The classification of prototype snow in comparison to model snow validated the findings in the experimental development in respect to the similarity law for scaling.

## 2.2 Wind tunnel preparation

The study was carried out in the wind tunnel laboratory at the Technical University of Denmark (DTU), Department of Civil Engineering. The wind tunnel has a closed air circulation (Göttinger type) with a test section that can be operated in a fully closed, open and in blockage-tolerant configuration.
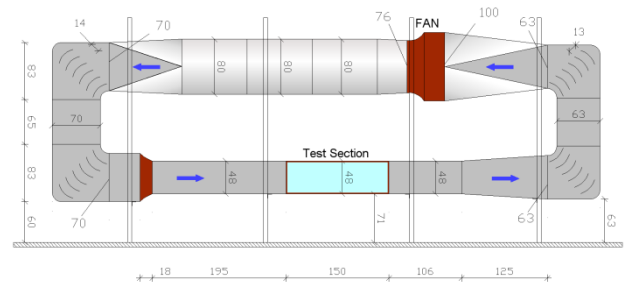


**Figure 4.** Overall layout of the small boundary-layer wind tunnel at DTU Civil Engineering.

Figure 4 shows the overall layout and dimension of the wind tunnel. The test section has a cross-flow dimension of 0.48m in width and 0.48m in height and a length of 1.5m. The turbulent flow reflecting the main properties of the atmospheric boundary-layer (ABL) is generated in the flow processing unit upstream the test section. Generally the boundary-layer wind profile is defined by the logarithmic equation:

$$u(z) = \frac{u_*}{k} ln\left(\frac{z}{z_0}\right) \qquad (1)$$

Deviations from the logarithmic profile can occur if complex terrain or katabatic winds and see-breeze define the conditions[10], [11]. The roughness height $z_0$ for snow covered surfaces is varying with friction velocity and is to define as following:

$$z_0 = c \frac{u_*^2}{g} \qquad (2)$$

The value $c$ is the constant for the different snow types with values of 0.015 found by Joffre (1982) and 0.018 by Schmidt (1982) for fresh cold snow[11]. Literature provides different measured roughness heights from a flat snow surface with $z_0 = 0.0001$ to a snow covered surface $z_0 = 0.002$ [10–12]. Additionally, the snow flux influences the wind profile shape and the wind velocity which was found by Föhn [13]. For the experimental set-up the mean wind velocity was measured without model snow (Figure 5). Eventually some airborne particles would fly into the sensitive openings of the measurement advice. Alternatively the simulation with model snow was measured with an Anemometer. The flow properties of the simulated atmospheric boundary-layer (ABL) have been measured analogically with a pitot tube and digitally with the cobra probe. In this experiment the exponent model (Eq.3) from the Eurocode for the normalization of the measured wind profile was applied:

$$\frac{u(z)}{u(z_{ref})} = \left(\frac{z - d_0}{z_{ref}}\right)^\alpha \qquad (3)$$

The factor $\alpha = 0.17$ fitted a category between II and III for suburban and villages. This category matched with findings in literature for snowdrift simulation and also describes the rocky landscape and small villages in Greenland [14]. As earlier mentioned by Föhn the wind profile changes when snow particles fall into the flow. The effect was also considered in a snowdrift simulation by D.H. Kim, K.C.S. Kwok, and H.F. Rohde. The authors measured the generated wind profile without and with model snow and measured that the curve of the wind profile changed from category II to I and reflected thereby the Antarctic characteristic [14], [15]. In this experiment we assumed that the generated category between III and II did not have major changes and defined a snow covered surface in category II.

The wind tunnel simulation shall be capable of reflecting the ground-near transportation but also the accumulation on roof areas. Especially for the latter process the substitution material need to be airborne at higher levels to enter the flow field around roof tops and has to be able to accumulate on flat and on inclined surfaces. For this purpose a special seeding mechanism was installed to have control over the snow rate and simultaneously be able to test both, the suspension layer and the surface near saltation process.

At the beginning of the test section a set-up for the seeding technique with snow substitute was mounted on top of the wind tunnel (Figure 6). The seeding process is generated by a motor witch sets a wooden box with a mesh at the bottom, in motion. Through this technique the supplied particles of the substitute fall into the generated ABL flow and start drifting within the test section. For the snowdrift simulation a blockage-tolerant configuration was installed within the test section.
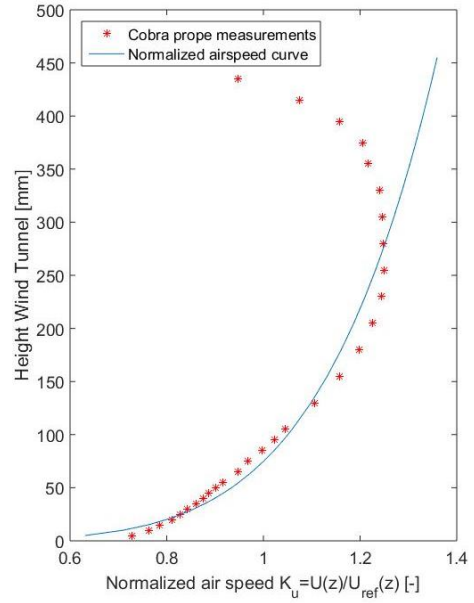


**Figure 5** generated atmospheric boundary-layer (ABL)
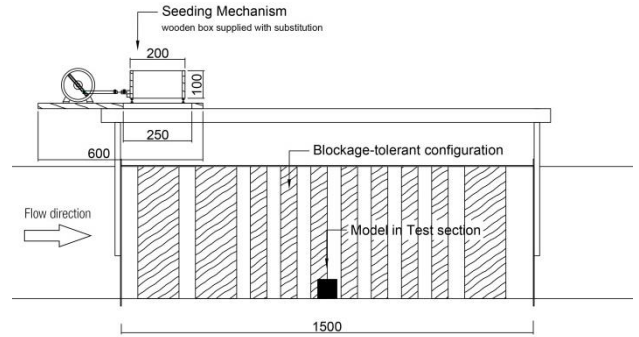


**Figure 6** Sketch of snowdrift configuration.

## 2.3 Model and prototype snow Materials

Modelling snow with substitution material implies inevitably a simplification of the physical process regarding thermodynamics, wind-driven transportation and compacting. As a consequence, the ambition of the simulation does not aim on establishing a full physical similarity but rather a phenomenological similarity to observations in nature (chapter 2.1). Furthermore, it is not the author's intention to develop a simulation method from scratch but to draw from experience of earlier studies reported in literature. Here, all considerations take their origin in the understanding and/or description of the process in nature.

Snow is constantly in a sublimation process meaning that it melts and re-freezes again or even vaporises. Prototype snow is deforming into a round shape like grains undergoing a metamorphism process when it deposits on the surface [11]. This behaviour can be simulated by erosion/ saltation tests (e.g. Bagnold's sand erosion tests) using granular substitute materials suitable

for modelling of the phenomenon. The granular material is less than ideal to accumulate e.g. on a test steep roof model or other specific constructions. Further studies have been initiated to test the performance with powdery materials [14] in order to improve the representation of snow drift and snow deposition.

Following granular-type (saltation layer) materials have been specified so far: 1. Two types of Semolina (hard grains of flour), and 2. wheat bran and saw wood ash. As for the powdery substitute (suspension layer) the following materials have been looked at: baking powder, wheat flour and potato flour. The characterisation of the substitution material focused on following aspects:
−   Geometric shape and size of the material particles
−   Particle density
−   Aerodynamic specification of fall velocity

Under a scanning electron microscope (SEM) different samples of grains and powder materials were investigated. Through this method, we were able to determine the average size of the particles and describe the structure and surface. With a SEM analysis (scanning electron microscope), zoomed images of the substitute samples are displayed by scanning it with a focused beam of electrons. Following samples have been scanned and analysed regard their size and shape:

Substitute as powders
−   Baking powder
−   Potato powder
−   Wheat flour

The powders are fine particles and have been zoomed into 100, 500 and 1000 times. For the determination of the particle sizes the scans of 500 times zoom were chosen for a suitable estimation of the structure and size.

Substitute as grains
−   Wheat bran
−   Semolina
−   Fine Semolina / Groats
−   Saw dust

Grains are coarse and larger than the powdery materials, therefore the scans were zoomed in with 100 and 500 times. A photometric analysis determined the length and the radios of the particles. For the powders in 500 zoom, the division of the reference lineal was 100 μm, which is equal to 400px. The grains in 100 times zoomed had a reference lineal of 500 μm and equal to 400px. The pixel displays the optical reference of the different sizes in the picture. Figure 7 and 8 illustrate the general method of the measurement, both the grains and the powder materials.
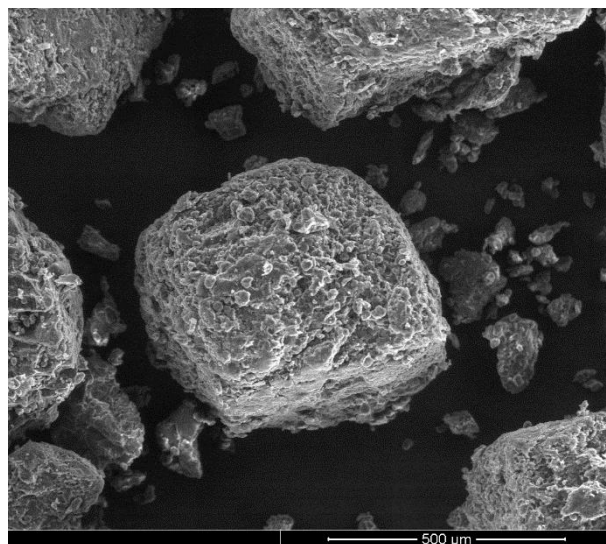


**Figure 7** Semolina under the microscope. Division of the reference lineal is 500 μm.

After specifying structure and size of the particles a pycnometer method was accomplished to determine also the density of the substitute in g/m$^3$:

$$\rho = \frac{m}{v} \tag{4}$$

For the determination the DS standard DS/CEN ISO/TS 17892-3:2004 was applied. For each substitute material 4g was supplied to the pycnometer. Eventually powder material would dissolve in water therefore ethanol was used to calculate the density of the substitutes.
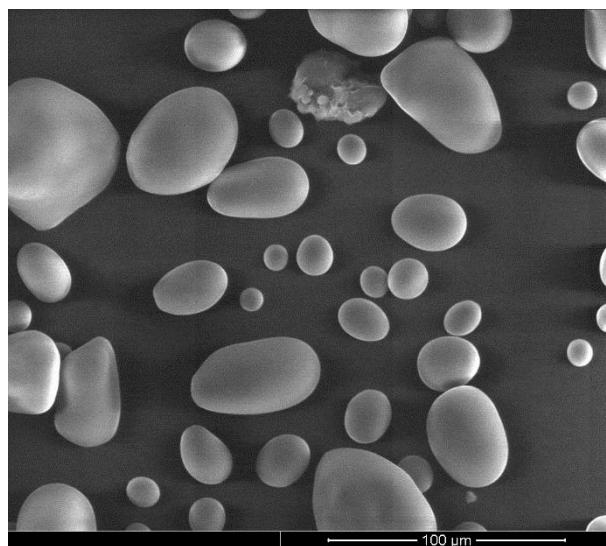


**Figure 8** Potato powder under the microscope. Division of the reference lineal is 100 μm.

An aerodynamic specification of the fall velocity was determined as a third classification for the substitutes. The particle fall velocity was measured photometric and visualised with a laser beam. Following configurations with the Camera (Canon EOS 700D) have been adjusted: ISO 1600; Exposure 1/20 sec (0.05sec); f/9. In numerus pictures the mean fall velocity has been read from a reference lineal in the layer of the laser beam. The fall

velocity shall give an estimation of the velocity scale for the simulation:

$$L_v = \frac{v_m}{v_p} \qquad (5)$$

Particles have been supplied through the seeding mechanism and have been photographed while falling through a laser beam. Particles which fall into the laser beam layer got visible. The reference lineal indicates how long the particle falls within the exposure time of the camera. Figure 9 shows the length of falling potato powder particles in an exposure time of 0.05sec.
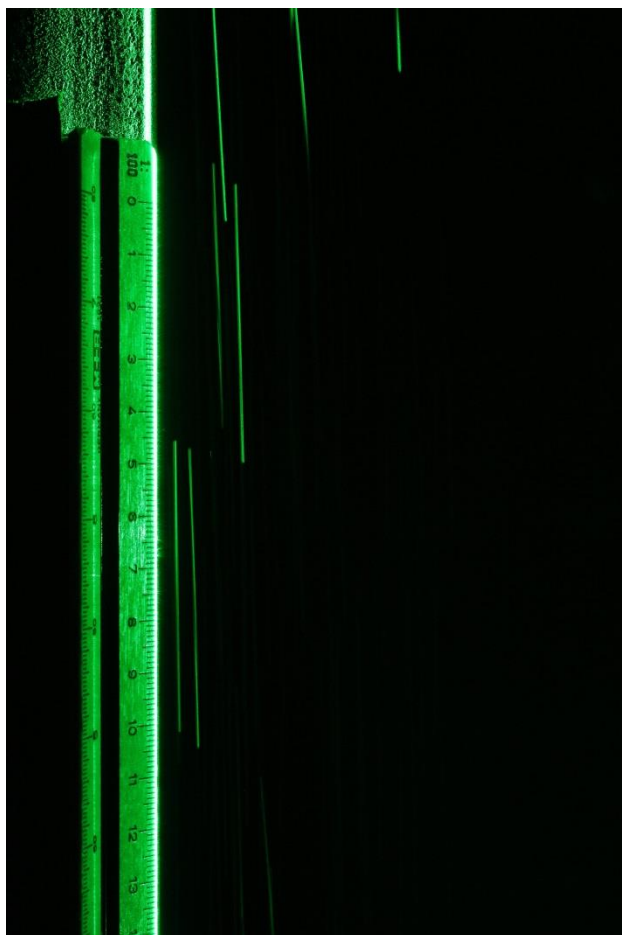


**Figure 9** Determination of fall velocity m/s of Potato powder in 0.05sec.

### 2.4 Test performance with snowdrift

After the specification of the substitution material and the preparation of the wind tunnel a test performance with substitution was simulated. Earlier researcher (Kind [6] and D.H. Kim et al. [15]) found the best agreement of similarity with high density materials. Sodium Bicarbonate with 1000 kg/m³ and a size of 50 μm was found to reproduce the most similar snow accumulation shape compared to the nature, while nine other different materials have been tested [15].

Based on the findings in literature that the particle size has to be considered to not be smaller than 30 μm, rather bigger we selected potato powder for the simulation [15]. The test model was a black concrete rectangular of 7 x 7 cm for a better contrast between the

white substitution and the model. The model was placed in the middle of the test section. A tachometer controlled the rotation speed of the seeding mechanism which was filled with the substitute. The supplied material of potato powder was 2,28kg in the seeding mechanism. With velocities from 1,3m/s to 3m/s snow accumulation in the middle of the wind tunnel section occurred. In order to control at which wind-speed accumulation in the middle of the section starts to build up and at the same time being able to measure while particles drift in the section, an anemometer was used. After the duration of 8:20 minutes a mass of 2,28kg fell rough the seeding process.

## 3 Results

As mentioned previously, the aim of the simulation is to develop an experimental method which can reproduce the phenomenological similarity of snow effects observed in the nature. In this section, we evaluated the specification methods before the test performance with substitution was carried out and compare it with data from literature.

The photographic measurement with millimetre paper in Nuuk shows an average diameter of snowflakes from 1000-3000 μm (Figure 3). Similar results were found in Sisimiut from 500-3000μm (data not shown). This result is significantly different from the measurements found in literature in the Antarctic, shown earlier in section 2.1. Because of the phase change, the snowflakes in-situ formed into a bigger formation. Nevertheless, the results do not show a correlation to the actual wind-driven snow events in Greenland and deposition of snow on and around structures. But they are parameters for similarity laws and define the scale in simulating the nature phenomenon. Therefore the investigation of different substitutes in size, density and the terminal fall velocity are specified. The results are summarised in Table 1.

**Table 1** Specification of substitute size $r$ or $l$, density $\rho_m$, fall velocity $v_m$

| Substitute | d [μm] | ρ [g/cm3] | v [m/s] |
|---|---|---|---|
| Baking powder | 2.25-37.25 | 2.0717 | 0.98 |
| Flour (Wheat) | 15.0-75.0 | 1.4564 | 0.72 |
| Fine semolina (mannagryn) | 71.0-500 | 1.4199 | 1.28 |
| Potato powder | 10.0-62,5 | 1.4934 | 0.76 |
| Saw dust | 88-500 | 1.3517 | 0.33 |
| Semolina | 675 | 1.3128 | 0.95 |
| Wheat bran | 152.5-562.5 | 1.3176 | 0.75 |

**Table 2** Overview of specification of snow

| | d [μm] | ρ [g/cm3] | v [m/s] |
|---|---|---|---|
| Prototype snow | 500-3000 | 0.500-0.900[14] | 0.3-2.0[15] |

As a comparison, the determination of the terminal fall velocity of snow with 0.3-2.0m/s depending on the snow type measured by Mellor 1965[15] is shown in Table 2. The results in Table 1 show that the sizes of the substitution are smaller compared to the prototype, but the density is higher and the terminal fall velocity is similar. That means a length $L_v$ for the velocity scale can´t be defined by the aerodynamic specification of fall velocity and the particle size for model and prototype. In fact the significance and relevance of similarity has been discussed by other authors while reproducing the snow accumulation characteristic without fulfilling the physical requirements correctly, but experiments have shown similar snow formations which have been observed in the nature[1, 2, 3, 4,7, 8, 14, 15, 16]
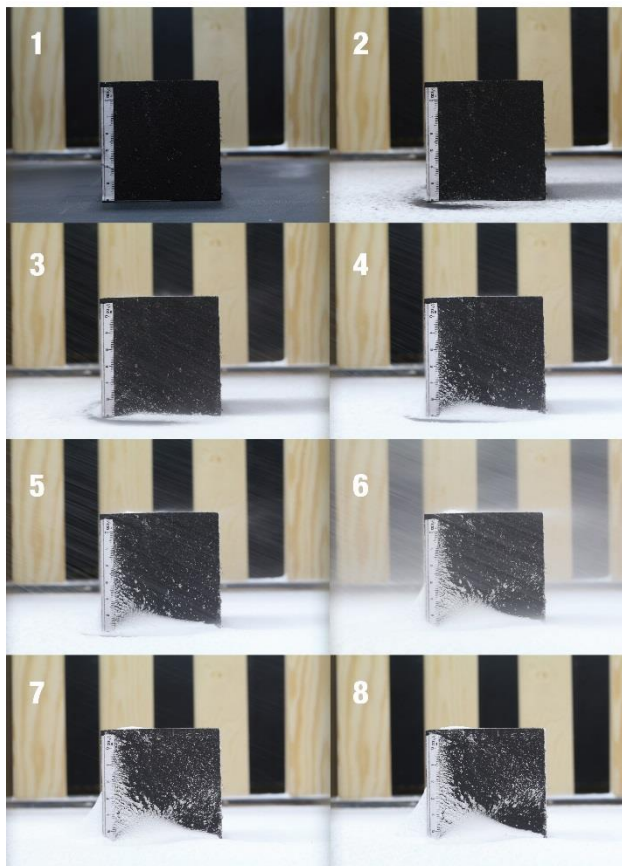


Figure 10 Snowdrift with potato powder every 60sec with 3 m/s.

From this starting point the snowdrift simulation was carried out without fulfilling the similarity law between model and prototype particle. Mainly the snow effects in suspension and saltation shall be reflected on a simple model shape like a cube. In agreement with the literature the wind profile should be generated correctly to transport the particles in their aerodynamic physical nature. The accumulation and deposition on the model in the test performance over the duration of 8.20 minutes is presented in Figure 11. First particles start to accumulate on the sides walls of the rectangular and shape pattern in a circle upwards. The edges of the rectangular show an aerodynamic flow pattern as in erosion tests (e.g. Bagnold's sand erosion tests). Deposition on the front

side accumulates and the side walls show a snow-flow pattern on the rectangular. The particles attach to each other and start to build a formation on the walls.
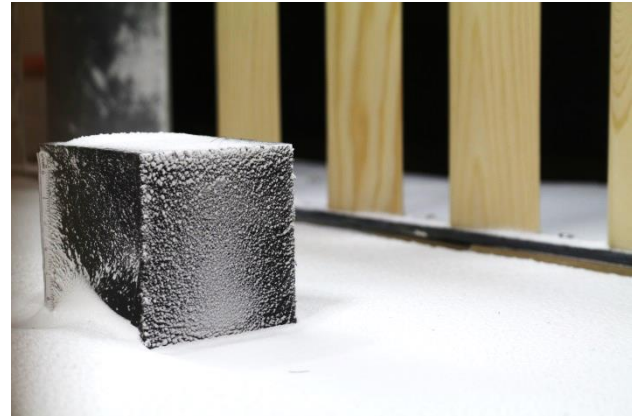


Figure 11 Snow drift pattern after 8.20 minutes on a rectangular model.

In general, aerodynamic snow-effects illustrated in Figure 11 are reproduced with the experimental method. Picture 6 in Figure 10in the time lapse shows the trace of saltation process behind the rooftop. Likewise, the phenomenon of deposition of particles in front of the model is displayed. After the duration of 8:20 minutes the accumulation shape in the front is 4cm high and the side shape 2cm. On the backside of the rectangular the aerodynamic flow pattern is clearly printed.

# 3 Discussion

The integration of snow deposition in structural design and urban planning through an experimental method has been investigated mainly in the theoretical improvement of the similarity requirements. Furthermore, it is still insufficient and challenging to fulfil the physical laws of a 2-phase with snowdrift.

Literature and the research so far could not agree on a methodology to establish a correct physical similarity, as reported in the previous sections. So far the aspect of the phenomenological improvement have been largely ignored or wasn't in focus. The development of the documented experimental setup is suitable for an extensive parametric study of snow deposition and accumulation and sufficiently accurate to conclude not only on the ground-area suspension but also on roof structures in the suspension layer. The set-up will be the main tool for parametric simulations to investigate the interaction between architectural designs, snow loading and ground-level accumulation between buildings. The length $L_v$ was not found therefore the simulation was a dimensionless study with aspect on the characteristic of snow deposition on a structure. Here the significance of the relevance of snowdrift similitude parameters occurs, as other researcher discussed before [16]. The development of the experimental set-up allows a flexibility of reproducing not only the saltation process and the accumulation on the near surface ground.

Furthermore, the documentation of the used material and the parametric possibility allows benchmark, with numerical methods of snow drift simulation, to collect a wide range of data.

Architectural case studies with a parametric investigation in snow deposition, accumulation or even the effect of a trace line behind a roof structure can be simulated for data collection and optimizing the structural design of buildings. A similar tracing effect in literature [16], here called the reverse riming formation has been found and simulated from a reference case. Unlike this experiment, the snow particles started to shape a formation based on the long duration. The research in this paper and the comparison to literature shows that not all similarity laws are needed when simulating the phenomenon of snow accumulation and deposition on structural design.

## 4 Conclusions

Main significance in the future is the phenomenological accuracy of different shape formation which has to be studied in a parametric study with regular verification to the nature. An accurate generated atmospheric boundary-layer for simulating snowdrift is needed for modelling the nature phenomenon of wind-driven snow. Main focus is the phenomenological similarity of the snow deposition / formation without fulfilling all similarity laws for the substitution in regard to the prototype. This will forward the experimental development and the design process of urban planning in cold regions.

## 5 Acknowledgements

## References

1. F. Naaim-Bouvet and M. Naaim, Ann. Glaciol., **26**, 212–216 (1998)
2. W. Wang, H. Liao, M. Li, and H. Huang, Open J. Civ. Eng., **3**, 13–17 (2013)
3. F. Naaim-Bouvet, Surv. Geophys, **16**, 711–727 (1995)
4. R. A. Schmidt, Rev. Geophys. Sp. Phys., 20, 39–44 (1982)
5. R. J. Kind, J. Wind Eng. Ind. Aerodyn., 36, 855–866, (1990)
6. R. J. Kind, Cold Reg. Sci. Technol., 12, 217–228 (1986)
7. C.-E. Teleman, Constr. Arhit., **60**, 147–163 (2014)
8. X. Zhou, J. Hu, and M. Gu, *Nat. Hazards*, **74**, 1629–1648 (2014)
9. T. K. Thiis, J. Wind Eng. Ind. Aerodyn., **91**, 829–839 (2003)
10. S. Thordarson, PhD thesis*, Norwegian University of Science and Technology NTNU*, (2002)
11. C. Jaedicke, PhD thesis, *University of Bergen*, (2001)
12. J. W. Pomeroy and D. H. Male, *Seasonal Snowcovers: Physics, Chemistry, Hydrology*, Springer Netherlands (1987)
13. P. M. B. Föhn, J. Glaciol., **26**, 469–480 (1980)
14. Smedley, D. J., Kwok, K. C S, Kim, D. H., J.Wind Eng. Ind. Aerodyn., **50**, 153-162, 1993
15. D.H. Kim, K.C.S. Kwok, H.F. Rohde, Report, *Similitude Requirements of Snowdrift Modelling for Antarctic Environment, University of Sydney,* (1991)
16. K.C.S. Kwok, D.H. Kim, D. J. Smedley, H.F. Rohde, J.Wind Eng. Ind. Aerodyn., **41-44**, 2797-2808, (1992)

# Use of numerical simulations of snow drift in planning of infrastructure – A case study from Northern Norway

Thomas K. Thiis[1, 2]

[1]*Norwegian University of Life Sciences, Ås, Norway*
[2]*Multiconsult ASA, Tromsø, Norway*

**Abstract.** A large industrial development is planned in Honningsvåg in Northern Norway. The area is characterized by subarctic climate with long cold winters. The vegetation on the site is sparse, and the wind exposure gives problems with snow drifting. This paper is a study of the snow drifting at the site and around some of the planned buildings. Based on numerical simulations and meteorological observations, snow depth maps of the site are produced for four different meteorological conditions.

## 1 Introduction

Generally, an assessment of snow drifts around buildings and in terrain should be performed in "scale levels". The first important level is to determine which zones in the terrain that are naturally subjected to snow accumulation and large snow depth. When the most critical zones are identified and avoided, the second level would be an assessment of the position and orientation of the buildings on the site. The last level would be to identify any possible small scale problems including position of doors, sunshade and ventilation openings. This report mainly deals with the first level, snow distribution in the terrain.

## 2 Field site

The project in Honningsvåg involves a large development of the surrounding terrain as well as introduction of several new buildings of different sizes. The planning of the Veidnes project has not yet reached the detail phase, and the study is therefore concentrated on how the terrain influences the snow accumulation. In addition, the effect of some of the larger buildings has been included. Figure 1 shows a model of the planned project together with a wind rose showing wind statistics during the winter months. Figure 2 shows a panorama of the site taken the 2. March 2014 from the hill in the south-east part of the area. This is before the snow melting season has started.

The snow depth maps were made for four different meteorological conditions. These are the maximum short

2013/2014 in which there was a field inspection, the year representing the mean yearly cold precipitation and the extreme year, represented by the year with largest sum of winter precipitation since 1957 at the closest meteorological station. The wind conditions used in the simulations are the same for all the meteorological years and is explained later. Table 1 shows the meteorological conditions from the three selected years and the short-term maximum. Table 2 shows the distribution of joint precipitation and wind in the area since 1957. Most of the precipitation incidents occur with a precipitation intensity of less than 5 mm/24h and a wind speed between 5-10 m/s. The climate at the site is mild enough to prevent ice-covering of the fiord. This limits the fetch at the site to the open water body.
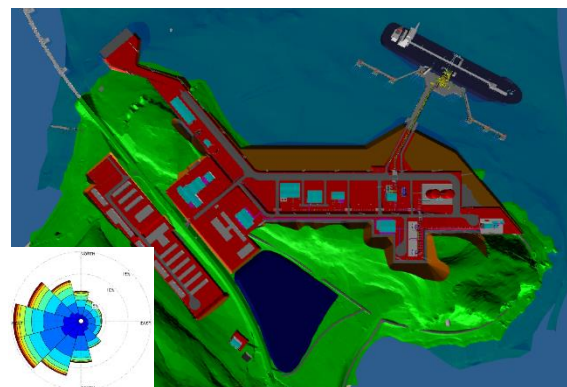


**Figure 1.** 3D model of study site. Terrain cutting in red.



**Figure 2.** Panorama view of site, seen from south-east.

term continuous snowfall, which will be the design criterion for the snow clearing utility service, the year

---

[a] Corresponding author: thomas.thiis@nmbu.no

**Table 1.** Cold precipitation at Repvåg, close to Veidnes.

| Period | mm cold precipitation (-1 C) | Hour of precipitation at 5mm/12h |
|---|---|---|
| Max. short term snowfall | 36 | 86.4 |
| 2013/14 | 121 | 290.4 |
| Mean | 176 | 422.4 |
| Extreme | 382 | 916.8 |

Using Tabler's [1] guideline for determining yearly snow transport, the yearly mean snow transport is calculated to 24 tons/meter. The same guidelines classifies the snow transport to be controlled by the snowfall. Tabler describes 24 tons/meter as "light-to-moderate" snow drifting. To simplify the simulations, only the meteorological situation with cold precipitation are considered. In addition, the wind conditions during precipitation are divided in three speed classes and six directional classes, given in table 3.

**Table 2.** Joint distribution of cold precipitation (Air temperature<-1°C) and average wind speed during precipitation time and 12 hours after, from Slettnes and Repvåg (1957-2012), cold precipitation 31% of the time

| Joint distribution of cold precipitation and average wind speed [ % of cold precipitation time] | | | | | | | |
|---|---|---|---|---|---|---|---|
| | Sum of cold precipitation last 24 hours [mm water equivalent] | | | | | | |
| | 0-5 | 5-10 | 10-15 | 15-20 | 20-25 | >25 | All amounts |
| Average 10 min wind speed during and 12 hours after precipitation [m/s] — 0-5 | 23.10 | 2.26 | 0.64 | 0.35 | 0.13 | 0.19 | 26.67 |
| 5-10 | 52.61 | 8.22 | 2.45 | 0.83 | 0.22 | 0.38 | 64.72 |
| 10-15 | 3.98 | 2.36 | 0.99 | 0.13 | 0.10 | 0.00 | 7.55 |
| >15 | 0.25 | 0.48 | 0.22 | 0.03 | 0.06 | 0.00 | 1.05 |
| All speeds | 79.96 | 13.32 | 4.30 | 1.34 | 0.51 | 0.57 | 100.00 |

**Table 3.** Wind climate at Veidnes during precipitation at Repvåg.

| Direction[deg] | 0m/s | 5m/s | 10m/s | SUM |
|---|---|---|---|---|
| 15 | 2.2 % | 16.9 % | 2.6 % | 21.6 % |
| 75 | 2.6 % | 7.4 % | 0.8 % | 10.7 % |
| 135 | 1.4 % | 1.7 % | 0.2 % | 3.2 % |
| 195 | 4.6 % | 5.5 % | 2.1 % | 12.2 % |
| 255 | 4.4 % | 14.6 % | 5.3 % | 24.3 % |
| 315 | 2.0 % | 19.0 % | 7.1 % | 28.0 % |
| SUM | 17.1 % | 65.0 % | 17.9 % | 100.0 % |

# 3 Method

To simulate the spatial wind field and snow accumulation in the terrain, the general purpose finite volume CFD code ANSYS CFX 14 was applied. Twelve different characteristic weather situations were simulated in addition to the snow accumulation during calm weather. The simulations results in accumulation flux maps were snow accumulation [kg/m²s] is simulated for each grid cell

near the surface. The thirteen characteristic situations, (twelve situations of joint wind and precipitation and one with precipitation in calm weather) were then weighted according to the measured climate at the site (table 3) and combined to form maps showing the snow depth distribution at the end of years with different weather.

The CFD code solves the incompressible, time averaged Navier-Stokes equations, using the $k$-$\varepsilon$ RNG turbulence model to close the set of equations. It is widely used in simulations of wind around buildings and it is capable of producing realistic results. The two phase fluid flow is solved with the Euler-Euler approach. Both the air and the snow phase possess its own flow field and the fluids interact via the drag force calculated using the Schiller-Naumann drag model. The simulation boundary conditions are assumed to be blowing snow with a precipitation intensity of 5 [mm/12h] which is equivalent to 1.157E-04 [mm/s] or a flux of 1.157E-04 [kg/m²s]. With an estimated terminal fall velocity of 0.5 [m/s] (Mason, 1962), the snow mass concentration in the air becomes 2.3E-4 [kg/m³]. In the present analysis, the density of snow particles when suspended in the air is set to 150 kg/m³ and the density of the snowpack is set to 300 kg/m³. The radius of the snow particles is set to 0.15 mm, a parameter that is mainly important for the determination of the particle/air interaction. The vertical wind velocity distribution, at the inlet boundary, follows the logarithmic expression in Eq. (1).

$$u(z) = \frac{u_*}{\kappa} \ln\left( \frac{z}{z_0} \right) \qquad (1)$$

where $u(z)$ is the wind speed at a given height $z$, $z_0$ is the aerodynamically height of the roughness elements, set to 0.0001m, $K$ is the von Karman's constant (equal to 0.41), and $u_*$ is the friction velocity set according to Table 4. Two wind speeds are simulated for each wind direction; these are 5 m/s and 10 m/s.

**Table 4.** Inlet velocity coefficients of the two simulation cases, according to Eq. (1)

| | $u_*$ | $u_{(10m)}$ |
|---|---|---|
| $U_5$ | 0.18 | 5 |
| $U_{10}$ | 0.37 | 10 |

## 3.1 Simulation of snow erosion and accumulation

To simulate the snow depth distribution, thirteen characteristic situations are considered. For the twelve characteristic situations where wind is a participating mechanism, the erosion ($q_{ero}$) and deposition ($q_{dep}$) fluxes are calculated according to Naaim et al. [2]:

$$q_{ero} = B\rho(u_*^2 - u_{*_t}^2) \quad \text{if} \qquad u_* \geq u_{*_t} \qquad (2)$$

$$q_{dep} = Cw_f \frac{u_{*_t}^2 - u_*^2}{u_{*_t}^2} \quad \text{if} \qquad u_* < u_{*_t} \qquad (3)$$

where $B$ is a coefficient representing the intergranular bonding in the surface layer, $\rho$ is the density of the air and

$u_*$ is the air friction velocity. By definition, $u_{*t}$ is the threshold friction velocity of the snow below which aeolian snow transport ceases; it ranges from 0.07 to 0.25 m/s for fresh and dry snow and from 0.25 to 1 m/s for old, wind hardened snow, and is here set to 0.3 m/s. This value, which is marginally higher than "fresh and dry snow", allows for slightly higher deposition fluxes in areas of

$u_* < u_{*t}$ and is meant to compensate for the exclusion of episodes of wind without precipitation. $C$ is the snow concentration in the air with units [kg/m$^3$] and $w_f$ is the terminal fall velocity of a snow particle. In the present simulation the value of $B\rho$ is set to $7*10^{-4}$ and $w_f$ is set equal to 0.5 m/s. The resulting net flux is then determined by

$$q_{erodep} = q_{dep} - q_{ero} \qquad (4)$$

In this form, the effect of impinging particles on the erosion of the surface is ignored. Also the effect of the change of geometric shape of the snow surface is ignored. Naaim et al. [2] produced realistic simulations of snowdrifts around snow fences with this model. However, they state that, in leeward accumulation zones, the model is very sensitive to the ratio $u_* / u_{*t}$, implying that the quality of the air flow simulation near the surface is important. The method has previously been used to calculate snow drift on roofs [3]

## 4 Results and discussion

Based on numerical simulations and meteorological observations, snow depth maps of the site are prepared for four different meteorological periods. An example of the characteristic snow flux deposition map for 5 m/s and wind direction 315$^0$ is shown in figure 3.
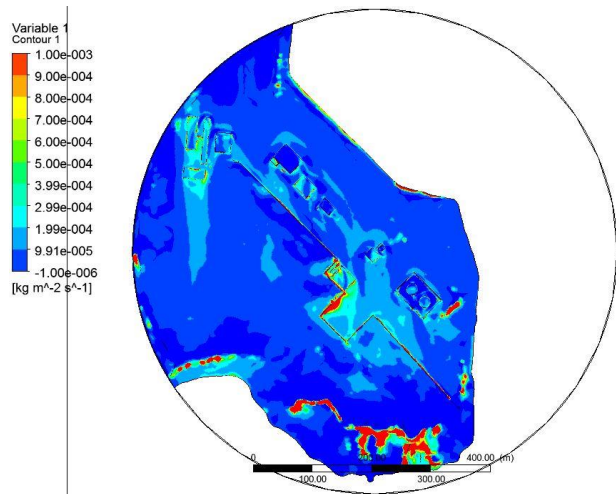


**Figure 3.** Snow accumulation flux at Veidnes, wind direction 315°, wind speed 5 m/s.

Figure 4 shows snow depths in 25 points measured with a snow sonde in March 2014, before the snow cover has started to melt. The simulations representing the winter of 2013/14 shows a variation of snow depth from close to zero to deeper than 2.5 meters, figure 5. This is confirmed by in-situ measurements from the same winter given in figure 4.



**Figure 4.** Snow depth measurements [cm] at some point of interest 2. March 2014.
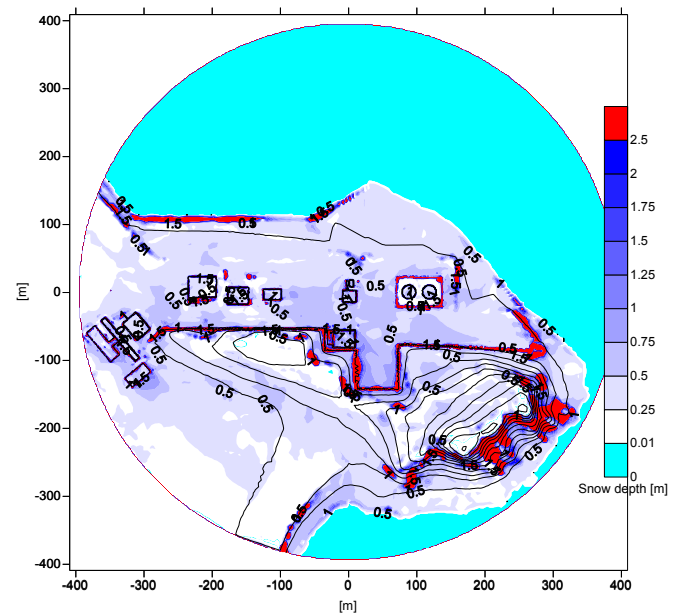


**Figure 5.** Simulated snow depth distribution at the site, winter 2013/14

The snow depth distribution at the site in a year with mean cold precipitation is shown in figure 6. The differences from the 2013/14 winter is small in the areas exposed to wind. However, in the terrain cutting close to the center of the site will experience considerably more snow. This is because the terrain cutting creates a sheltered area where blowing snow particles will accumulate. This is even more pronounced in the year of extreme cold precipitation, shown in figure 7.
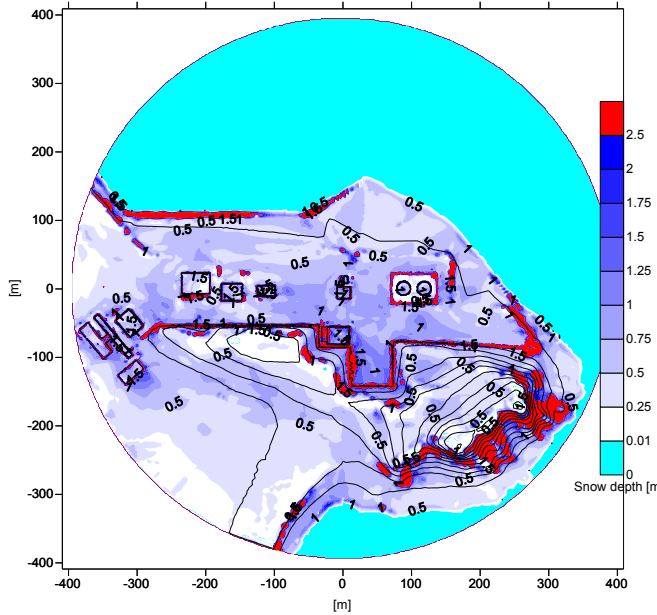
**Figure 6.** Simulated snow depth distribution at the site, year with mean precipitation.



**Figure 7.** Simulated snow depth distribution at the site, year with extreme precipitation.

The extreme conditions indicate that large parts of the planned terrain cuts will be covered in snowdrifts deeper than 2.5 meters. In such conditions, also the buildings at the site, located in the western part of the site, will be largely affected by the snow. The snowdrifts surrounding the buildings will exceed 2.5 m height. However, due to the large size of the numerical grid cells compared to the building structure in this area, the results are indicative. More accurate could be obtained with grid refinement in this area. The simulated snow depth in the area situated leeward of the hill, south-east in the simulation domain, is relatively deep compared to the rest of the domain. The terrain slope in this area is steep, some places more than $45^0$, and snow sliding is to be expected. The simulations do not account for snow sliding, thus the simulated snow depth in this area is presumably too deep. However, the accumulation potential indicates that this area might be subjected to avalanche hazard.

The last simulation concerns the snow accumulation during a short-term extreme snowstorm. This will serve as an estimate of the on-site capacity for snow clearing during operation. The meteorological measurements shows that the most severe snowing event since 1957 was 36 mm water equivalents in 24 hours. The wind direction of extreme precipitation events is usually north-west, thus $315^0$ is chosen as the wind direction for this case. The wind speed distribution of the case is based on the mean wind climate during precipitation given in table 3, ie. 17% of the time 0 m/s, 65% of the time with wind speed 5 m/s and 18% of the time with wind speed 10 m/s. Note that the snow density of the accumulated snow is set to 200 kg/m$^3$ in this case, which will influence the calculated snow depths. Figure 8 shows the snow depth distribution after such snowstorm. The results show that also a short-term extreme event will create snowdrifts which are more than 2.5 meter deep in some areas. Figure 9 shows a close up of the snowdrifts around the buildings in the west part of the site. The simulations indicate the position and size of the small-scale snow drifts around the buildings.
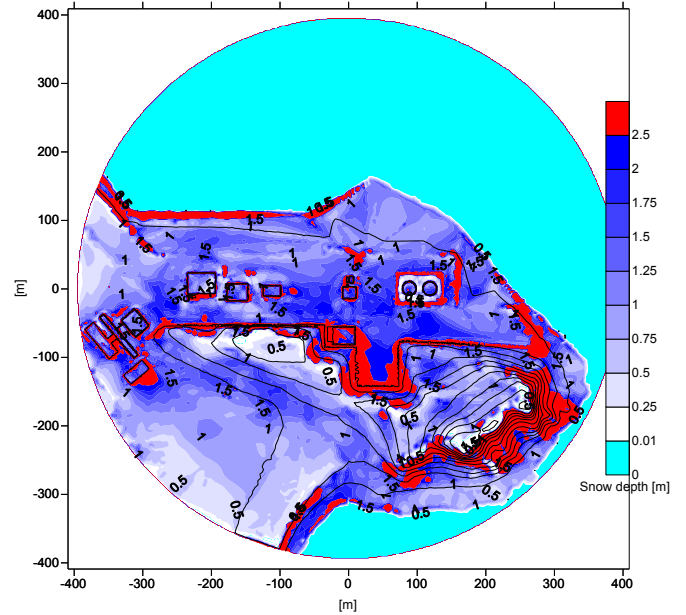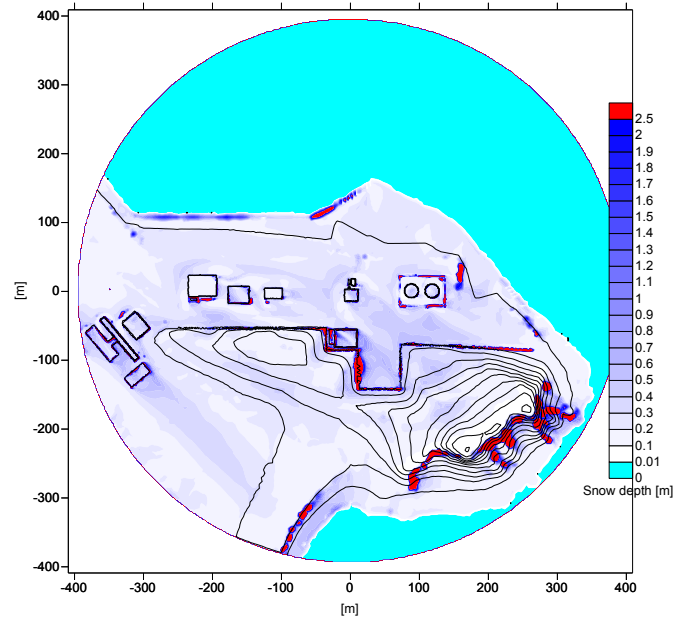


**Figure 8.** Simulated snow depth distribution at the site, short-term snowstorm.
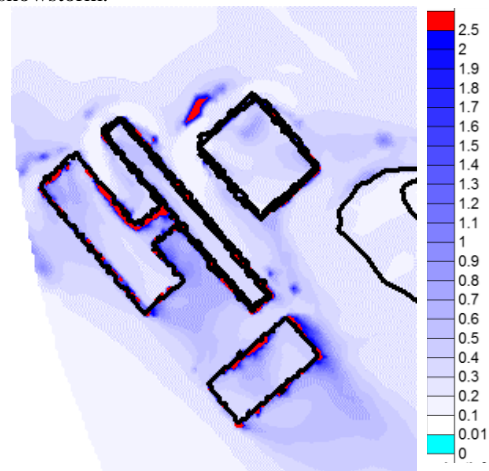


**Figure 9.** Simulated snow depth distribution around buildings in the western part of the site after short-term snowstorm.

50

## 5 Conclusions

Based on numerical simulations and meteorological observations, snow depth maps of Veidnes are produced for four different meteorological conditions. The snow drifting severity at Veidnes is classified as "light to moderate" according to literature. The simulations demonstrate how numerical simulations can be used as a planning tool in larger industrial sites where snow drifting is expected. Even if the in-situ measurements does not allow for direct comparison due to the low number of observations, the numerical method reproduces the main characteristics of the observed snow cover of the winter of 2013/14. This gives credibility to the use of the results for planning of the site.

The simulations representing the winter of 2013/14 shows a variation of snow depth from close to zero to deeper than 2.5 meters. The extreme conditions indicate that large parts of the planned terrain cuts will be covered in snowdrifts deeper than 2.5 meters. In such conditions, buildings at Veidnes will be affected by the snow.

It is recommended to avoid placing buildings and infrastructure close to terrain cuts. It is further recommended to install sufficient snow fencing to reduce snow accumulation around buildings and in the terrain.

## Acknowledgement

## References

1. Tabler R.D. (2003) Controlling blowing and drifting snow with snow fences and road design, NCHRP project 20-7 (147)
2. Naaim, M., Naaim-Bouvet, F., Martinez, H. (1998) Numerical simulation of drifting snow: erosion and deposition models, Annals of Glaciology 26: 191-196.
3. Thiis, T.K., Potac, J, Ramberg, J. F. 3D numerical simulations and full scale measurements of snow depositions on a curved roof.: *Proceedings from 5th European & African Conference on Wind Engineering.* : Firenze University Press 2009 ISBN 9788864530383. s. 371-374

**Session 2**

# Structural loading I

# Probabilistic concepts in snow engineering - from observations to the specification of consistent design values including climate change

Michael Kasperski

*Ruhr-Universität Bochum, Research Team EKIB. 44780 Bochum, Germany*

**Abstract.** Consistent probabilistic concepts are required to specify the design snow loads for structures. The paper presents some basics on probability theory and discusses the fundamental reliability demands. For complex problems simulation techniques can be applied. The paper explains how a bad quality of the generated random numbers can ruin a simulation. For the snow load on the ground, extreme value statistics can be performed based on annual extremes or based on independent peaks over a threshold. The paper points out that both approaches lead to the same probability information. In Europe, exceptional snow loads have been considered as design scenario. The respective events have been identified as outliers in the ensembles. The paper reveals that the strategy used in the scope of the European snow research project fails and may lead to considerable underestimations of the design snow loads. A consistent strategy is presented how to deal with outliers. The snow loads on roofs are influenced by the wind, thus making the shape factor a random variable. A probabilistic model is available for gable roofs. The paper presents corresponding results for the design values. Furthermore, the combination of wind and snow is discussed. Finally, the question of possible long term trends in the snow climate is studied.

## 1 Introduction

Probability theory is a branch of mathematics which is required in structural engineering as soon as it comes to the specification of design values for action effects or the resistance. The long way from observations or experimental results to the final design values requires a lot of choices which are difficult to evaluate in their consequences since humans have no natural understanding of the concept of probability.

This unfortunate shortcoming in the evolution of human thinking can be illustrated by the following example which refers to a famous TV-show in the USA and is known as the Monty-Hall dilemma. After several challenges the final candidate finds him- or herself in front of three doors. Behind one of the doors, there is the fantastic first price; the room behind the two other doors is empty. The candidate is asked by the hosting show-master Monty Hall to choose a door. Then the show-master – knowing where the first price is hiding - opens one of the remaining doors which with no surprise gives view to an empty room. Finally, the show-master asks the candidate if he or she remains with the initial choice or if the candidate wants to change the door. The puzzling question arises which is the best strategy to optimize or maximize the probability of winning the first price: Staying faithfully with the initial choice or fickly make a new choice? Most people have difficulties to find the answer for this problem of conditional probabilities; and it is easy to convince a layman by simply claiming that it doesn't matter which door is chosen since when two doors are still closed, the probability is 50:50 for getting the first price anyway.

The second section of this paper therefore briefly summarizes some basics in probability theory and presents the fundamental reliability demands which are applied in structural design.

When mathematical skills are missing or when problems become too complex for an analytical approach, researchers and engineers today can apply the modern tool of simulation. The core of simulation techniques is an efficient and reliable pseudorandom number generator. Basic demands will be discussed in section 3.

Section 4 presents the probabilistic models for the snow loads on the ground. Two approaches are discussed: the extreme value statistics based on annual extremes and the so-called peaks-over-threshold approach. The latter introduces as further variable the number of events per year. If this variable is modelled by the Poisson distribution both approaches are identical.

In the European snow load codification, exceptional snow loads have been included. These loads have been identified as statistical outliers. Section 5 discusses the statistical stability of identifying outliers in a confined ensemble and shows that with the wrong strategy estimated design snow loads become too small.

Snow and wind belong together like wind and waves. The accumulation and distribution of snow is influenced by the wind. Furthermore, in the design, combinations of these two climatological actions have to be considered. Section 6 presents the influence of wind on the design values of snow on gable roofs and discusses the derivation of combination factors. A consistent approach is presented which specifies a single combined wind-snow load case.

Over the recent decades, winters in Germany have been different to what they used to be in the past. Missing snow falls torture the tourist industry, and in many tourist areas snow canons are used to obtain at least small stripes of snow to allow for skiing. The question arises, if it is possible to identify long term trends in the snow climate which justify reducing the design snow loads. Section 7 presents a probabilistic approach to this problem.

---

[a] Corresponding author: michael.kasperski@rub.de

## 2 Basics in probability theory and fundamental reliability demands

The classical definition of probability is based on a chance experiment which can result in N mutually exclusive and equally likely outcomes. If $N_A$ of these outcomes result in the occurrence of the event A, then the probability of A is simply obtained as the ratio of the number of successful outcomes to the number of all possible outcomes:

$$p(A) = \frac{N_A}{N} \qquad (1)$$

A simple example is given with the chance experiment of throwing a die. The set of all possible outcomes, called the sample space, is obtained as the integer numbers from 1 to 6. If the event A is defined, for instance, as getting a result larger than 4, two of the six outcomes are successful. So, the probability of A becomes 2/6 = 1/3.

The generalized definition of probability which can be applied to any random process is obtained as the relative frequency of the event A which is the ratio of $n_A$ occurrences in N observations for N going to infinity:

$$\lim_{N \to \infty} p(A) = \frac{n_A}{N} \qquad (2)$$

$n_A$ - occurrences of event A

For a discrete process, the event A can be defined as a set of specific outcomes; for a continuous process, the event A has to be specified as a set of specific ranges of outcomes. Basically, the probability lies in the range from 0 to 1. The probability 0 is obtained for the impossible event; the probability 1 corresponds to the certain event.

The complement of an event 'A' is the event 'not A'. The event A and its complement are mutually exclusive. The probability of the complementary event is obtained as:

$$p \,(\text{not } A) = 1 - p(A) \qquad (3)$$

The distribution of the probability for a random process x over the range of all possible outcomes is called the probability density function f(x). For a continuous process, the probability is obtained as the area under the probability density in the ranges of the specified outcomes. The integral over the probability function from $-\infty$ to x is called the cumulative probability distribution or often simply the probability distribution F(x):

$$F(x) = \int_{-\infty}^{x} f(u)\, du \qquad (4)$$

The basic relation between the probability density and the cumulative probability distribution is shown in figure 1. The area under the probability density function f(x) from $-\infty$ to a specific value x occurs as the amplitude of the cumulative probability distribution F(x). The cumulative probability distribution F(x) therefore describes the non-exceedance probability of a specific value x. Basically, the probability density has no negative values, and F(x) is monotonically increasing from 0 to 1.

If a chance experiment, having the probability $p_1$ for a specific event A, is repeated several times, the probability that the event A is occurring increases with each further trial. From everyday experience, it is obvious that the corresponding accumulation of probability has to be non-linear. The number of trials until event A finally occurs is smaller than infinity; however, it may by a large number.

For L repetitions the accumulated probability $p_L$ for the event A occurring at least once in the L trials is obtained as:

$$p_L(A) = 1 - \left(1 - p_1(A)\right)^L \qquad (5)$$

Figure 2 shows the basic accumulation behaviour on the example of a perfect coin, a perfect die and the once-in-fifty-years event. The respective events are: occurrence of head, occurrence of six and exceedance of the once-in-fifty-years event.
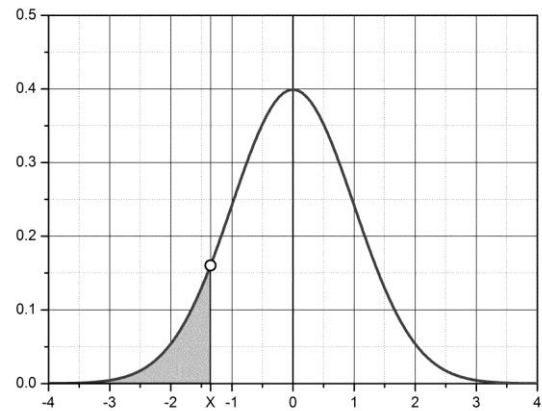


probability density function f(x)
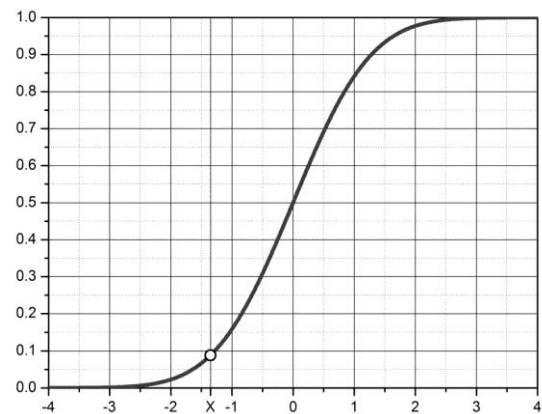


cumulative probability distribution F(x)

**Figure 1**: Relation between the probability density function f(x) and the cumulative probability distribution F(x)
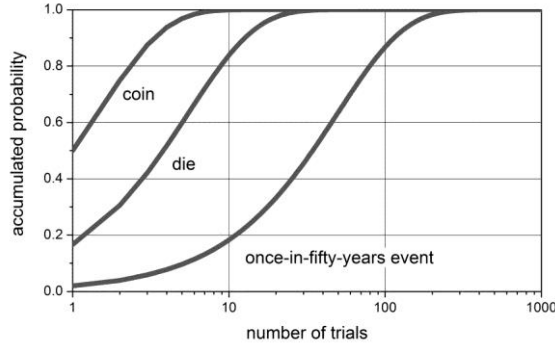
**Figure 2:** Accumulation of the probability of event A occurring at least once in L trials

Equation (5) specifies the average probability of event A occurring at least once in L trials. The number of occurrences of event A in L trials forms a random sequence. The corresponding probability density is given with the Bernoulli distribution:

$$f(N) = \binom{N}{L} \cdot p^N \cdot q^{L-N} \qquad (6)$$

L - number of trials
N - number of successful trials
p - probability of success
q - probability of failure = 1 - p

For the event of getting no head for throwing the coin twice, the sample space is no head, one head and two heads. The corresponding probabilities are 0.25, 0.50 and 0.25. For the die-experiment the sample space and the corresponding probabilities are summarized in table 1 assuming a series of six throws.

**Table 1:** Probabilities of the random number of successful trials in 6 throws for the event getting a six for a perfect die

| $N_6$ | 0 | 1 | 2 | 3 | 4 | 5 | 6 |
|---|---|---|---|---|---|---|---|
| p | 0.34 | 0.40 | 0.20 | 0.054 | 0.0080 | 0.00064 | $1/6^6$ |

$N_6$ - number of successful trials in 6 throws

The number of trials k needed to get one success follows the geometric distribution:

$$f(k) = (1-p)^{k-1} \cdot p \qquad (7)$$

For experiments with a small probability of success p, i.e. for rare events, and a great number of repetitions L, the Bernoulli distribution can be simplified and becomes in the limit for p $\rightarrow$ 0 and N $\rightarrow$ $\infty$ the Poisson distribution:

$$f(N) = \frac{\lambda^N}{N!} \cdot \exp(-\lambda) \qquad (8)$$

$\lambda$ - average number of occurrence during the given time interval

For the once-in-50-years event, $N_{av}$ becomes 1 for 50 years observation. The probability of getting no exceedance of the once-in-50-years event in 50 years observation is 0.368. This approximated value differs slightly from the true value of $0.98^{50} = 0.364$. One single exceedance in 50 years is obtained with the probability of 0.368, two exceedances occur with a probability of 0.184, three exceedances with 0.061, four with 0.015, five with 0.003 and so on.

The inter-arrival times of a Poisson process follow the exponential distribution which is given as follows:

$$f(T) = \frac{1}{\lambda} \cdot \exp\left( -\frac{T}{\lambda} \right)$$
$$F(T) = 1 - \exp\left( -\frac{T}{\lambda} \right) \qquad (9)$$

with 1/$\lambda$ - average arrival rate

The average arrival rate is 1/50 for the once-in-50-years event. The corresponding probability density and cumulative probability distribution are shown in figure 3.
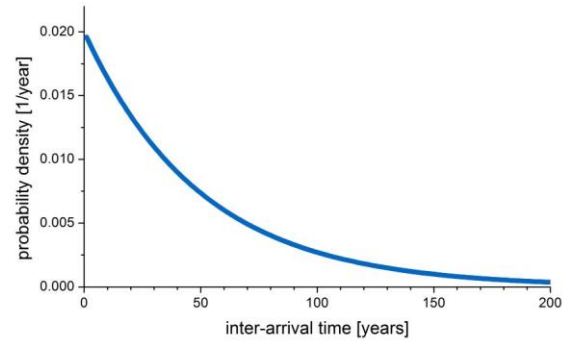


probability density f(T)
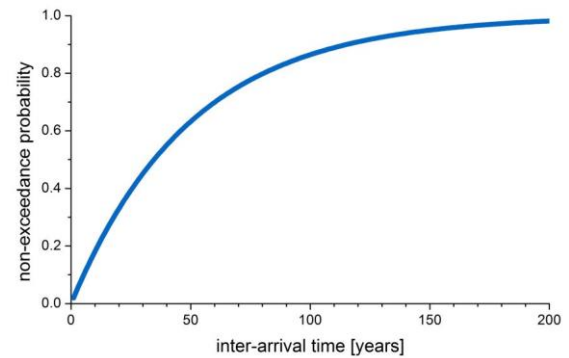


cumulative probability distribution F(T)

**Figure 3**: Inter-arrival time of exceedance of the once-in-50-years event

The annual exceedance probability of the once-in-M years event is 1/M. Thereby, M often is referred to as the return period. It is important to note that this term may lead to the impression that there is a regular basis for the occurrence of this event. As can be seen on the example of table 2, which summarizes some probabilities for different ranges of inter-arrival times for the once-in-fifty years event, the inter-arrival times show a large random scatter. As consequence, calibration of structural design rules against existing successful design practice is a kind of self-deception.

Figure 4 shows a typical time series of the random exceedances of the once-in-fifty-years event for 40 consecutive 50 year periods. The largest observed inter-arrival interval in this example is 215 years.

**Table 2**: Examples of inter-arrival times for exceedance of the once-in-fifty years event

| T | < 10 | < 20 | > 50 | > 100 | > 200 |
|------|-------|-------|-------|-------|-------|
| f(T) | 0.181 | 0.330 | 0.368 | 0.135 | 0.018 |
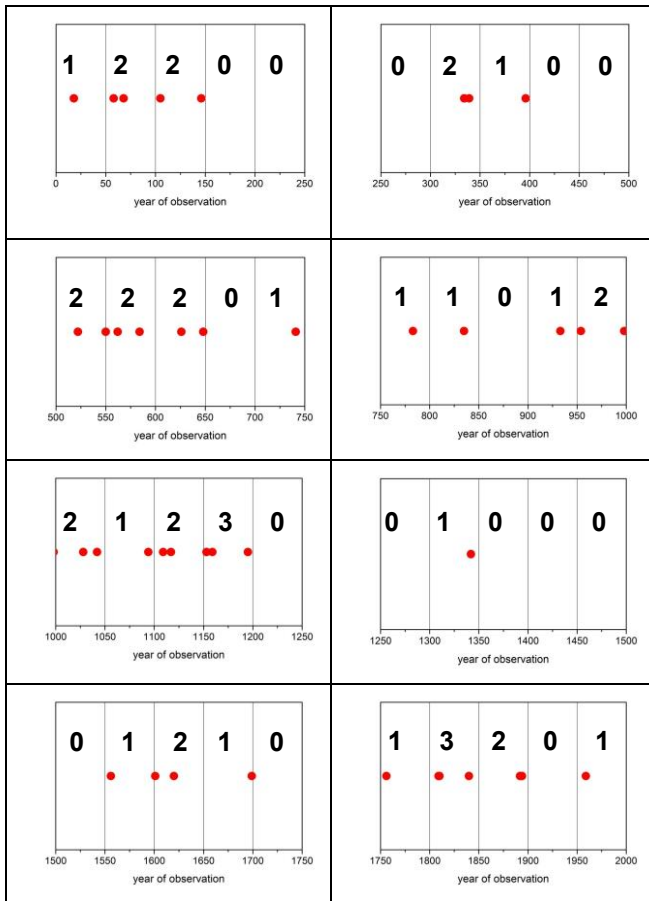


**Figure 4**: Typical time series of the random exceedance of the once-in-fifty-years event for 40 consecutive 50 years periods

In a general way reliability is defined as the probability that a system or component performs its required functions under stated conditions for a specified period of time. In structural engineering, system or component mean the structure or structural elements. The required functions are structural safety, serviceability, durability and robustness. The stated conditions are the actions which are occurring during the construction and anticipated use. Finally, the specified period is the design or projected working life.

Structural safety is the ability of a system or component to withstand all actions as planned. Serviceability is the ability of a system or component to remain fit for the use it is required. These two demands are considered with the Ultimate Limit State (ULS) and the Serviceability Limit State (SLS). Durability is the ability of a system or component to guarantee the structural safety and serviceability during the specified lifetime. Robustness is the ability of a system or component to withstand accidental events like fire, explosions, impact or consequences of human error, with damages which are not disproportional to the triggering event.

The complementary to reliability is the failure probability. For R being the capacity or the resistance of a system and E being the stress or action effect, the failure probability can be obtained from the convolution of the two contributing probability densities. Failure occurs if E becomes larger than R, i.e. the limit state function for a linear system is simply R-E = 0. The failure probability $p_f$ then is obtained by the so-called failure integral as:

$$p_f = \int_{R=0}^{\infty} f_R(R) \cdot \int_{E=R}^{\infty} f_E(E) \, dE \, dR \tag{10}$$

with $f_R$ and $f_E$ - probability densities of the resistance and the action effect

The second integration in equation (10) can be replaced by a term including the cumulative probability distribution of E:

$$p_f = \int_{R=0}^{\infty} f_R(R) \cdot \left[1 - F_E(R)\right] dR \tag{11}$$

with $F_E$ - cumulative probability distribution of E

It is important to note that the failure integral leads to the average failure probability. The probability distribution of the failure rate usually shows large positive skewness.

Not all of today's Standards do allow considering the projected working life as an explicit design variable; instead, they often consider implicitly a general value of 50 years. Typical values for the projected working life are 1 - 5 years for temporary structures, 10 - 40 years for industrial structures and buildings, 60 - 80 years for residential buildings and 100 - 150 years for bridges.

Action effects are internal forces like bending moments or normal forces, or stresses from a combination of internal forces, or deflections or any other structural response which has to be considered in the design process. In the general case, several actions with different origin will occur simultaneously and will test the designed structure in regard to a sufficient resistance. Beside snow actions, usually at least actions induced by dead load and wind have to be considered. It is important to note that a consistent evaluation of the reliability requires knowledge of the static system and basic structural behaviour.

Since the solution of the failure integral is too complex for the every-day engineering practice, Standards have introduced the so-called operative failure probability and the corresponding reliability index. The latter is obtained as the corresponding negative value of the reduced variate of the inverse of the standardized normal distribution $\Phi$, i.e.:

$$p_f = \Phi(-\beta)$$
$$\beta = \Phi^{-1}(1-p_f) \qquad (12)$$

In a simplified approach the design target is met by comparing the design value of the resistance R to the design value of the action effect E in the following inequation:

$$E_{des} \leq R_{des} \qquad (13)$$

If E has no physical upper limit, failure may occur for any given level of R, and the major accumulation of the failure probability extends over a large range of R and/or E, respectively. In other words: failure may occur for events E which are below the design value of the action effects.

The design values $R_{des}$ and $E_{des}$ can be obtained from statistics for the respective random variables if corresponding target values for the exceedance probabilities are specified. Target values of the reliability can be specified in dependence of the consequences of failure. In the Eurocode EN-1990, three consequence classes (CC) are distinguished. The complete set of the European Action Standards EN-1991 basically aims to provide the required information for CC2 which is described with medium consequences for loss of human life; economic, social or environmental consequences are considerable. Typical examples are residential and office buildings and public buildings where consequences of failure are medium. CC3 covers failures with high consequences for loss of human life, or economic, social or environmental consequences are very great. Bridges, stadia and concert halls belong to this class. The lowest consequence class CC1 is characterized by low consequences for loss of human life, and economic, social or environmental consequences which are small or negligible. A typical example is given with commercial greenhouses where normally no person enters.

The target values for the reliability associated with the ULS are specified in EN 1990 as minimum values of the

reliability index $\beta$ with reference to 50 years and 1 year. They are summarized in table 3. Additionally in table 4, the corresponding approximate target failure probabilities are given.

**Table 3**: Target reliability values in EN 1990

| Reliability Class | 1 year | 50 years |
|---|---|---|
| RC3 | 5.2 | 4.3 |
| RC2 | 4.7 | 3.8 |
| RC1 | 4.2 | 3.3 |

**Table 4**: Approximate target failure probabilities in EN 1990

| Reliability Class | 1 year | 50 years |
|---|---|---|
| RC3 | 1/10,000,000 | 1/100,000 |
| RC2 | 1/1,000,000 | 1/10,000 |
| RC1 | 1/75,000 | 1/2,000 |

In a simplified approach, EN-1990 specifies the design values for the resistance and the action effects based on a unique pair of coordinates which are

$$R_{des} = -0.8 \cdot \beta; \ E_{des} = 0.7 \cdot \beta \qquad (14)$$

For CC2, the design value of the resistance corresponds to the 0.1%-fractile value, i.e:

$$p(R \leq R_{des}) = 0.001 \qquad (15)$$

With reference to a single year, the design value for the action effect has an exceedance probability of 1/2000:

$$p(E \leq E_{des}) = 0.0005 \ / \ year \qquad (16)$$

Instead of specifying this design values directly, most Standards still use the concept of partial factors, i.e. the target value $R_{des}$ will be replaced by the ratio of a characteristic value $R_k$ and a corresponding partial factor $\gamma_M$, i.e. the design value is obtained as:

$$R_{des} = \frac{R_k}{\gamma_M} \qquad (17)$$

Different materials have different partial factors, thus reflecting the different levels of scatter on the resistance side. Basically, the larger the scatter, the large must be the partial factor.

For the design value of the action effects the corresponding equation is:

$$E_{des} = \gamma_E \cdot E_k \qquad (18)$$

with $\gamma_E$ – partial factor for the action effect

The choice of the characteristic value is free, since for every value of e.g. $E_k$ there is a corresponding value $\gamma_E$ which leads to the target value $E_{des}$. In recent years, most Standards, however, prefer to choose an annual exceedance probability of 1/50, thus suggesting that the return period is coupled with the implicitly assumed design working life of 50 years. In the German annex to EN-1990, the partial factor for unfavourable variable loads is uniformly set to 1.5, thus suggesting that the wind and the snow climate show the same scatter all over Germany and furthermore equal the scatter of imposed loads.

A more transparent and consistent approach specifies explicitly the target probabilities for the design values of the actions considering different structural classes, e.g. ISO 22111 (2007) Bases of design of structures – General requirements [1] or ISO 4354 (2009) Wind actions on structures [2].

A refined classification of the consequence classes and the importance level of buildings and structures is given in table 5. The corresponding tentative target values for the exceedance probabilities of the design wind and snow loads are given in table 6 with reference to the projected working life and in terms of an annual exceedance probability for the example of L = 50 years. Basically, the required annual exceedance probabilities for any other projected working life can be obtained from the inverse of equation (5) as:

$$p_{year} = 1 - \left(1 - p_{lifetime}\right)^{1/L} \quad (19)$$

with L – projected working life in years

**Table 5**: Refined classification of consequence classes

| Class | Building or structure type |
|---|---|
| 0 | Buildings or structures presenting no hazard to life and other property in the case of failure, e.g. free field solar parks |
| 1 | Buildings or structures presenting a low degree of hazard to life and other property in the case of failure, e.g. agricultural buildings without regular human occupancy, greenhouses without public access |
| 2 | Buildings or structures not included in class 0, 1, 3 and 4, 5, e.g. office buildings, commercial buildings, factories, residential buildings |
| 3 | Buildings or structures that are designed to contain a large number of people, e.g. high-rise buildings, stadia and concert halls |
| 4 | Buildings or structures that are essential to post-disaster recovery or associated with hazardous facilities, e.g. hospitals, bridges |
| 5 | Buildings or structures that are essential to safe the lives of people in case of extreme natural hazards, or have inestimable cultural value, e.g. shelter buildings, monuments |

Table 6: Tentative values for the exceedance probabilities of the design wind and snow loads

| Class | $p_{lifetime}$ | $p_{year}$ (L=50 years) |
|---|---|---|
| 0 | 0.40 | 1:100 |
| 1 | 0.20 | 1:200 |
| 2 | 0.10 | 1:500 |
| 3 | 0.05 | 1:1000 |
| 4 | 0.025 | 1:2000 |
| 5 | 0.01 | 1:5000 |

## 3. Simulation as design tool

The core module of any simulation is the random number generator. In 1970, Robert Coveyou created the famous words that *the generation of random numbers is too important to be left to chance*. Strictly speaking the numerically generated results have to be called pseudorandom numbers since they are generated by deterministic algorithms. If the starting or seed value for the procedure remains the same, a once produced sequence can be generated again and again. This is the basic difference to a true sequence of random numbers.

The basic demand to the random numbers is that they are uniformly distributed in the range from 0 to 1. Then, the random numbers can be interpreted as probabilities, and can be translated to any target probability distribution e.g. by the inverse transformation method as illustrated in figure 5.
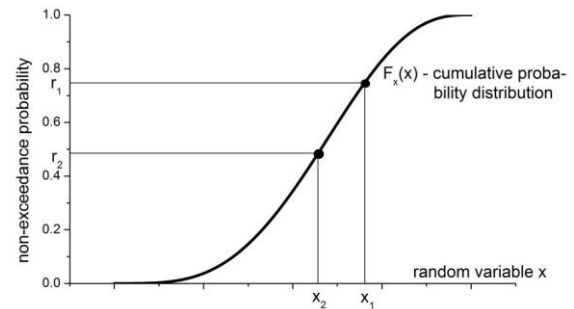


**Figure 5**: Example of using random numbers $r_i$ to generate random values $x_i = F^{-1}(r_i)$

The basic demands for the generated random numbers are:
- The period length of the sequence should be large enough to avoid any repetition of the sequence in the actual simulation problem.
- There should be no internal correlation in the sequence.
- The demand to a uniform distribution is met for n dimensions, e.g. for two dimensions it is required that $x_{i-1}$ is uniformly distributed for whatever small range is specified for $x_i$.

A bad random number generator can ruin a simulation. An illustrative example is shown in figure 6, applying the routine ran1 from Numerical Recipes [3]. In the version of 1992, the authors state that *in fact we do not know of any statistical test that ran1 fails to pass, except when the number of calls starts to become on the order of the period, say $10^8$*. The example generates for a complete year $365.25 \cdot 24 = 8766$ hourly mean wind speeds following a Weibull distribution which is given as:

$$F_v(v) = 1 - \exp\left(-\left(\frac{v}{v_0}\right)^k\right) \qquad (20)$$

with $v_0 = 4.36$ m/s and $k = 1.78$
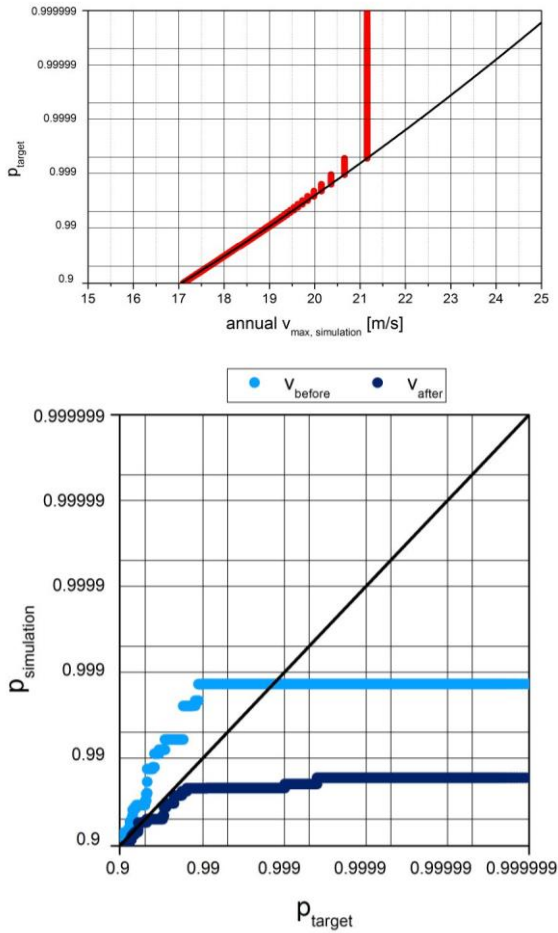




**Figure 6**: Example of a applying a bad random number generator

From each set, the maximum wind speed is sampled together with the hourly mean value before and after the extreme. Altogether, $10^7$ runs are performed. The first feature to notice is that the largest generated value is fixed with a value of 21.157 m/s thus indicating that the largest value being smaller than 1 is $1-1/2^{24}$. Since the demand of uniform distribution for more than one dimension is not met, the wind speeds in the hour before and after the maximum show strange probability distributions. Basically, the neighbouring hours should have the same probability distribution. Since the values are limited by the actual maximum value, the distribution

should show an under-linear characteristic; however, they should increase in a strict monotonic way. The bad ran1-generator leads to fixed values for the neighbouring hours, thus ruining the simulation completely.

Much better results are obtained with the class of Mersenne Twister random number generators. Their names derive from the length of the period which is given by a Mersenne prime. The first version has been published in 1997 by Matsumoto and Nishimura [4] and provides the unbelievable period of $2^{19937}-1$. The demand to uniform distribution is met for 623 dimensions. The code is available for free in the internet. The largest number smaller than 1 is $1 - 1/(2^{32}-1)$. The improved version SFMT [5] is faster than the original version, the dimension of uniform distributions is better and the period is pushed even further to $2^{216091}-1$. The largest number below 1 is $1 - 1/(2^{35}-1)$. Another high-quality random number generator [6] has been introduced as KISS (Keep It Simple Stupid). The 64 bit version has a period of $2^{121} + 2^{63} - 1$. The largest number below 1 is $1 - 1/(2^{32}-1)$.

Basically, the largest number below 1 becomes important and may cause problems when the target probability distribution extends to infinity and when the ensembles become large. Then, all the simulations end up with the same largest number. A typical example is obtained for traffic-induced loads for bridges which often are assumed to follow a normal distribution. Today's design scenarios [7] consider 10,000 trucks per day and 200 busy days per year. Each truck has 5 axles. With a projected working life of 100 years, the required number of random weights is $5 \cdot 10,000 \cdot 200 \cdot 100 = 10^9$. The simulation with the KISS-algorithm leads to only $2^{32} = 4.295 \cdot 10^9$ different random numbers, i.e. repeated runs over the projected working life produce on average in 1 of 4.295 runs the same largest number, which in terms of the reduced variate of the standardized normal distribution is 6.2303.

A refined approach fills each gap between the original integer numbers between $-2^{31}$ and $2^{31}-1$ with $2^{21}$ uniformly distributed values, thus ending up with $2^{53}$ random numbers which matches a double precision floating point number. The final random number is obtained from two calls of the KISS-random number generator:

$$r = (r_{1,KISS} + 2^{31} + \frac{r_{2,KISS}/2^{11} + 2^{20}}{2^{21}-1})/(2^{32}-1) \qquad (21)$$

with r uniformly distributed in [0, 1]

The largest value smaller 1 then becomes $1 - 1/(2^{53}-1)$, which for a normal distribution corresponds to a reduced variate of 8.2095. If the gaps are filled with the complete available range of $2^{32}$ numbers, a quadruple precision format is required thus extending the range of numbers smaller than 1 to $1-1/(2^{64}-1)$. The corresponding reduced variate of the standard normal distribution becomes 9.080.

Finally, a simulation is only as good as are the assumed models to describe the contributing processes. An inconsistent model may ruin the simulation results as may a bad random number generator.

## 4. Probability models for the snow load on the ground

There are two options to analyse the extreme values of the observed snow loads. The straight forward method is based on annual extremes; the corresponding theoretical probability distribution is the generalized extreme value distribution (GEVD) which is given as:

$$F(x) = \exp\left[-\left(f_1 - sign(\tau)\cdot f_2 \cdot \frac{x\text{-}m}{\sigma}\right)^{1/\tau}\right] \qquad (22)$$

m - mean value,
$\sigma$ - standard deviation,
$\tau$ - shape parameter

The coefficients $f_1$ and $f_2$ depend on the actual shape parameter $\tau$ and are given as follows:

$$f_1 = \Gamma(1+\tau), \; f_2 = \sqrt{\Gamma(1+2\cdot\tau) - f_1^2} \qquad (23)$$

$\Gamma$ - Gamma function

For positive shape parameters, type III distributions are obtained. This family of distributions has a finite upper tail, which cannot be exceeded with a probability of 1. The maximum value is given as:

$$x_{max} = m + \sigma\cdot\frac{f_1}{f_2} \qquad (24)$$

Negative shape parameters lead to the family of the type II distributions. These distributions have a finite lower tail. For $\tau = 0$, the extreme distribution type I is obtained, i.e. in the limit equation (22) becomes:

$$F(x) = \exp\left[-\exp\left(-\left[\gamma + \frac{\pi}{\sqrt{6}}\frac{x\text{-}m}{\sigma}\right]\right)\right] \qquad (25)$$

$\gamma$ - Euler constant = 0.577216

The distributions of type II and III each form a family of curves with specific characters. Compared to the type I distribution, they show as special feature a certain curvature when plotted in Gumbel probability paper (figure 7). Generally, a probability paper is a graph paper with one axis specially ruled to transform the distribution function of a specified theoretical expression to a straight line when it is plotted against the variate as the abscissa. While the curves for the type II distribution bend in a concave shape in respect to the axis of the reduced variate, the curves corresponding to type III show a distinct convex character. These two types are separated by the type I distribution which appears in the plot as a straight line.

Some studies use the normal or log-normal distribution to describe the trace of the non-exceedance probability of annual extremes. In figure 8, the respective traces are shown. Obviously, these approaches can be covered with corresponding type III or type II distributions.

The alternative approach is based on extremes over a threshold value. This strategy makes sense in snow climates which do not lead to a continuous snow cover through the whole winter period, and/or do not have snow in each winter. As additional parameter, the number of independent events per twelve-month cycle has to be considered. The appropriate theoretical expression for the non-exceedance probability per event is given with the generalized Pareto distribution (GPD) as:

$$F(x) = 1 - \left[1 - \frac{x - x_s}{s}\cdot k\right]^{1/k} \qquad (26)$$

$x_s$ - threshold value
s - scale parameter
k - shape parameter

In case of a positive shape factor, the distribution has a finite upper tail which cannot be exceeded. The corresponding largest value is given as:

$$x_{max} = x_s + s / k \qquad (27)$$

For k = 0, the exponential distribution is obtained:

$$F(x) = 1 - \exp\left(-\frac{(x - x_s)}{s}\right) \qquad (28)$$

The annual non-exceedance probabilities are obtained from combining the probabilities of the number of events and non-exceedance probabilities as follows:

$$p(x \leq x_{ref} \mid year) = \sum_{N=0}^{\infty} p(N)\cdot p(x \leq x_{ref})^N \qquad (29)$$

If the number of events per twelve month follows the Poisson distribution, the trace from equation (29) can be expressed by the GEVD as given in equation (22). The Poisson distribution is given as:

$$p(K) = \frac{\lambda^K}{K!}\exp(-\lambda) \qquad (30)$$

with $\lambda$ - average number of events per 12 month cycle

For very rare events, i.e. for $p(x \leq x_{ref})$ close to unity, equation (29) can be simplified to:

$$p(x \leq x_{ref} \mid year) = p(x \leq x_{ref})^\lambda \qquad (31)$$

Translating the GPD in combination with the Poisson distribution to the corresponding annual GEVD leads to the same exponents:

$$k = \tau \qquad (32)$$

The basic relation between the scale in the GPD and the standard deviation in the GEVD is given as:

$$\sigma = (c_0 + c_1 \cdot \ln \lambda + c_2 \cdot \ln^2 \lambda) \cdot sc \qquad (33)$$

The coefficients $c_0$, $c_1$ and $c_2$ depend on the actual $\tau$-values. For positive $\tau$-values the following approximations apply:

$$c_0 = 1 - 0.1 \cdot \tau - 0.1 \cdot \exp(1) \cdot \tau^2$$
$$c_1 = 0.02672 - 1.07426 \cdot \tau + 0.25264 \cdot \tau^2 \qquad (34)$$
$$c_2 = -0.05419 \cdot \tau + 0.6 \cdot \tau^2$$

For negative $\tau$-values, the coefficients become:

$$\ln c_0 = 0.25242 - 1.10219 \cdot \tau + 3.3628 \cdot \tau^2$$
$$c_1 = -0.78782 \cdot \tau + 5.15605 \cdot \tau^2 \qquad (35)$$
$$\ln c_2 = -7.9336 - 31.11332 \cdot \tau + 38.14 \cdot \tau^2$$

The corresponding mean value is obtained as:

$$m = x_{th} + \frac{sc}{\tau} - \sigma \cdot \frac{f_1}{f_2} \qquad (36)$$

The limiting case $\tau = 0$ leads to:

$$m = x_{th} + (\gamma + \ln \lambda) \cdot sc$$
$$\sigma = \frac{\pi}{\sqrt{6}} \cdot sc \qquad (37)$$
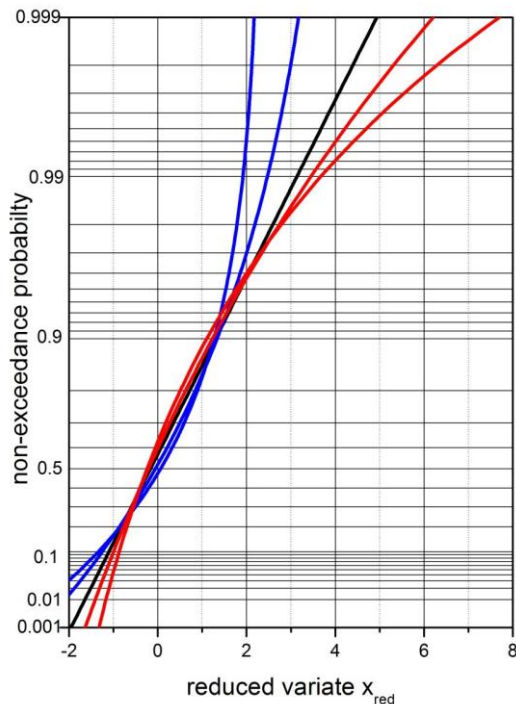


**Figure 7**: Traces of extreme value distributions in Gumbel probability paper
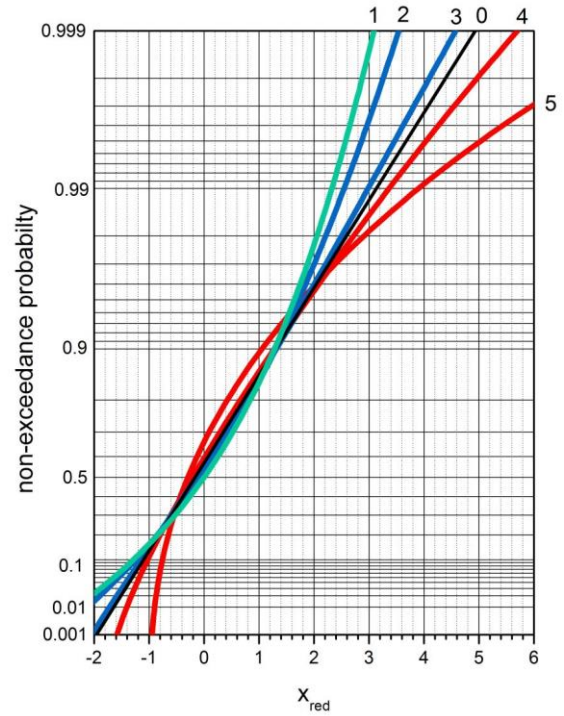


**Figure 8**: Traces of the normal and log-normal distribution in Gumbel probability paper
1 - normal distribution, 2 – 5 log-normal distribution with V = 0.1, 0.3, 0.5 and 1.0, 0 – extreme value distribution type I

For the estimation of the parameter triple (m, $\sigma$, $\tau$) or ($\lambda$, sc, k), different methods can be applied:

- the method of moments,
- the maximum likelihood method,
- the least-square approach
- the method of L-moments
- the Best Unbiased Linear Estimator

For some of the above methods, the plotting position of the individual observations is required which is estimated as:

$$p_i \ (x \le x_l) = \frac{i - \alpha}{N + (1 - 2 \cdot \alpha)} \qquad (38)$$

with i – position of the observation $x_i$ in the ascending sorted list

Typical values for $\alpha$ are in the range from 0 to 0.5. In Gumbel's original concept [8], $\alpha$ is set to zero. Later, Gringorten [9] recommended that for plots in the Gumbel probability paper $\alpha = 0.44$ should be used. Basically, the estimated values for the design snow load will decrease if $\alpha$ increases.

For a confined ensemble, each of the above methods leads to different values of the describing parameters. The statistical stability of the identified parameters remains poor even for large observation periods of several decades. This is shown in the following on the

example of observed snow loads at Dresden, which has been published already in [10].

Figure 9 shows the trace of the observed non-exceedance probabilities for 59 independent events in 28 winter periods at Dresden and the identified theoretical distribution. The corresponding parameters are $s_c$ = 0.2105 kN/m², $k$ = 0.163 and $\lambda$ = 2.107. The identified curve seems to be an quiet convincing fit of the observed trace, i.e. the identified GPD seems to be an appropriate model. The naïve design value for a projected working life of 50 years becomes 0.975 kN/m² for a class 3 structure.
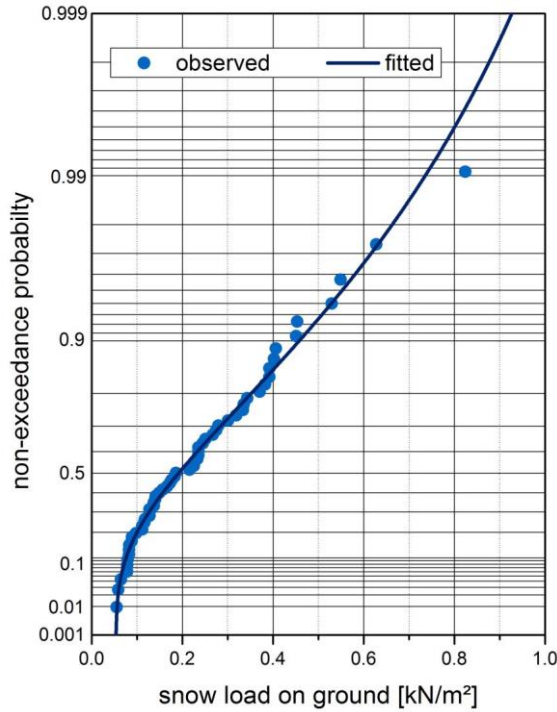


**Figure 9**: Trace of the observed non-exceedance probability of the snow load on the ground and identified theoretical distribution (Dresden 1978/79 - 2005/06)

The analysis of the statistical stability of the identified parameter-triple ($\lambda$, $s_c$, $k$) is based on simulations. In figure 10, the 90%-confidence intervals are shown. The example illustrates that the naïve estimation of the design value purely based on the identified statistical parameters is not recommended. Obviously, an ensemble size of even 100 years is not large enough to specify the design value in a sufficient small two-sided confidence interval. Therefore, EN 1990 recommends applying a one-sided confidence interval to avoid an overestimation of the resistance and an underestimation of the action effects. Since large confidence values lead to over-conservative design, as compromise between safety and economy the 75% confidence is chosen.

The problem of confined ensembles also effects the estimation of the design values for wind and temperature. The question if the extremes follow type I, II or III often can hardly be answered. A pragmatic approach therefore assumes that extremes follow the extreme value distribution type I.

If the applied estimation method does lead to the desired confidence level, an adjusting factor is required. A consistent approach is discussed in [10].
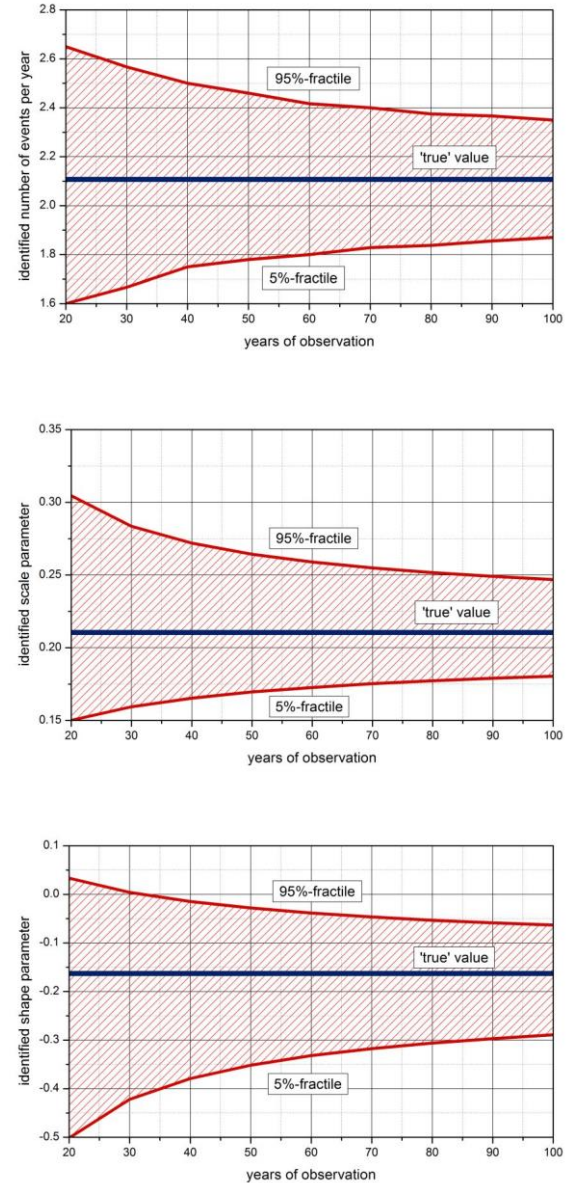


**Figure 10**: Influence of the ensemble size on the statistical stability of the estimated parameter triple ($\lambda$, $s_c$, $k$) [9]

## 5. Outliers

The general definition defines an outlier as an observed value which lies considerably outside the range of the other observations. Outliers may occur by chance or may indicate erroneous observations. The latter can be removed from the ensemble. For the randomly observed outlier, a consistent and generally agreed strategy is still missing. An outlier may influence or distort the estimation of the describing parameters of the assumed probability distribution, thus leading to biased design values. This is illustrated in figure 11 for the extreme value distribution type I varying the ensemble size from 8

to 64 and considering exceedance probabilities 1/R for the randomly observed event from R = 100 to 2000.

The fitting procedure for the (N-1) values leads to a straight line for the identified theoretical distribution, i.e. the true observations can be replaced by equidistant points along the straight line. Then, it is easy to calculate the bias due to the outlier on the estimated design value which here is chosen with p (x ≤ $x_{des}$) = 0.999. The smaller the ensemble and the larger the return period R of the outlier, the larger will be the distorting effect of the outlier.
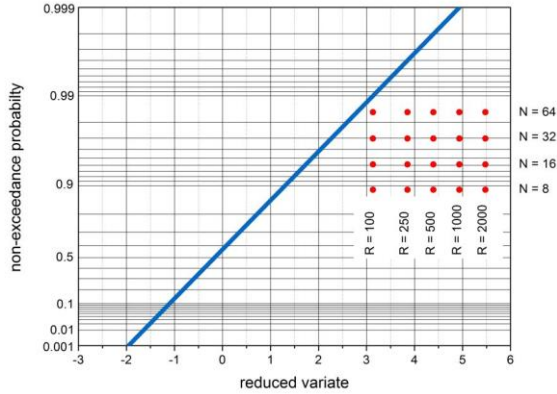


**Figure 11**: Relative position of outliers to the lsq-fitted trace for the reduced sample
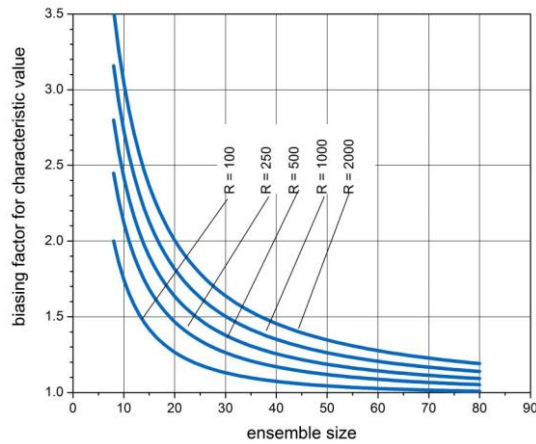


**Figure 12**: Biasing factor for the estimated design value with p(x ≤ $x_{des}$) = 0.999 / per year

Unfortunately, the real world problem is a bit more complex due to the fact that for a confined ensemble the detection of an outlier is not always successful since the true describing parameters may not be correctly identified. Basically, the evaluation of an ensemble in regard to an outlier results in one of four cases:

- true 1: the ensemble contains no outlier and the detection method identifies no outlier

- true 2: the ensemble contains an outlier and the detection method identifies an outlier

- error 1: the ensemble contains no outlier but the detection method identifies the largest observation as outlier

- error 2: the ensemble contains an outlier but the detection method fails to identify the largest observation as outlier

In simulations, it is possible to distinguish these four classes; however, in a real world problem, the results are only sorted in two classes, namely:

- no: the detection method has not identified an outlier

- yes: the detection method has identified an outlier

Based on simulations, for each of the four cases, the corresponding probabilities can be obtained. The final evaluation is based on the probability of case yes which is the sum of true 2 and error 1.

The following example illustrates the uncertainties in the outlier detection based on an ensemble size of N = 32 observations. The return period is chosen as R = 500. Then, on average, an outlier is expected in 32 observations with a probability of (1- $(1-1/500)^{32}$) = 6.2%. The mean value and the standard deviation are obtained from a least-square fit in the probability paper applying the plotting position i/(N+1). It is important to note that this agrees with the strategy of identifying exceptional snow fall events in Europe. The outlier is identified based on the so-called k-method:

$$x_{out} > m_{N-1} + k \cdot \sigma_{N-1} \tag{39}$$

with $m_{N-1}$ and $\sigma_{N-1}$ – statistical parameters for the ensemble without the largest value

The weighting factor k is obtained as the reduced variate of the respective probability distribution for the specified target exceedance probability 1/R of an outlier. For R = 500, the weighting factor k becomes 4.395 for the Gumbel distribution, which is the inverse of equation (25) for F(x) = 0.998.

Since the chosen plotting position overestimates the standard deviation, the detection probability for the case true 2 is only 2.23%, i.e. only about 1 of 3 true outliers is detected. Erroneous outliers are obtained with a probability of 0.74%, i.e. about 1 of 4 detected outliers is not really an outlier. Increasing the return periods R for the definition of an outlier leads to a decreasing detection rate for true outliers and an increasing rate of erroneous outliers.

The main conclusion at this stage has to be that the exceptional snow loads in the Eurocode are not based on scientific sound statistics. Figure 13 shows the probability traces for randomly estimated characteristic values with $p_{annual}$ (x > $x_k$ = 1/50) and design values with $p_{annual}$ (x > $x_d$ = 1/1000) for the four classes true1, true2, error1, error2 and for the resulting combinations no and yes. If erroneously an outlier is removed, the estimated characteristic and design values are far on the unsafe side, as can be seen with the traces for error 1. Failing to identify an outlier on the other hand leads to drastic overestimations (error 2). However, the observed trace does not reveal if or if not the detected outlier is a true outlier. Therefore, the final evaluation has to be based on the traces for the cases that the detection method identifies the largest value to be an outlier (yes) or not

(no). For the case that no outlier is detected, the traces reveal that the characteristic value is under-estimated with a probability of 30.8%. The estimation of the design value leads to an error probability of 29.7%. Both values are not that far from the EN-recommended target-value of 25%.

However, if the detection method identifies the largest value as an outlier, the error probabilities increase drastically to 52.9% for the characteristic value and

51.5% for the design value. These high levels of under-design are not acceptable. For all stations, where exceptional snow loads have occurred, the estimated characteristic values are on the unsafe side with a probability of about 50%. It is strongly recommended to increase the respective snow loads as soon as possible applying an appropriate adjusting factor for the respective ensemble sizes.



$p_{true1} = 93.05\%$

$p_{true2} = 2.23\%$

$p_{error1} = 0.74\%$

$p_{error2} = 3.98\%$

$p_{no} = 97.03\%$

$p_{yes} = 2.97\%$
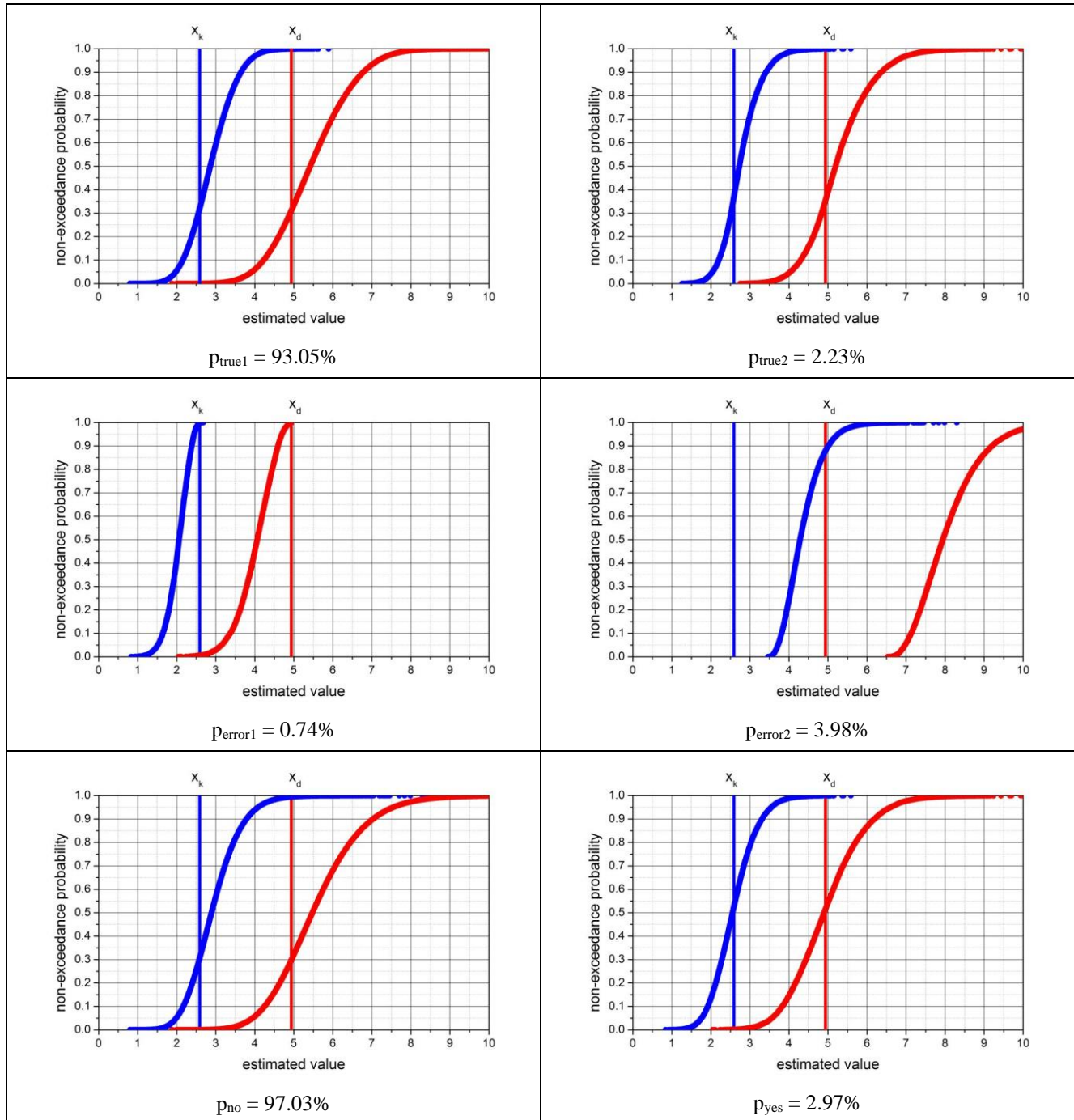
**Figure 13**: Traces of the estimated characteristic and design value for different error-cases and their combinations

The question arise, how the detection strategy can be improved. Changing the plotting position to the recommended value by Gringorten increases the detection rate to about 45%, the rate of false outliers

increases to 33%. The method of moments leads to a detection rate of true outliers of 38.6%; however, the rate of wrong outliers is increased by a factor of about 18 compared to the initial strategy, i.e. for 10% of the

random ensembles, an outlier is identified with about only 1 of 4 being a true outlier.

For the application of BLUE the problem has to be solved how to obtain the weighting coefficients for a censored ensemble. In [13] tables are presented, however only for ensemble size up to 30. In [14] a series approximation is proposed for the calculation of the BLUE-weighting coefficients for larger ensemble sizes. This routine can be re-written to obtain weighting coefficients for censored ensembles as well. The detection rate with BLUE increases to 69%, the rate of false detections is 42%. It is important to note that both cases yes and no require an adjusting factor for the estimation of the design values to meet the 75% confidence level.

# 6. The influence of wind

Basically, the wind speed during a snow fall event will influence the amount of snow on the roof. The stronger the wind blows, the lesser snow will accumulate on the roof. During and after the snow fall event, wind may lead to a re-distribution of the snow masses on the roof. A probabilistic model for the snow on gable roofs is presented in the JCSS probabilistic model code [15], specifying probability distributions for the shape factor $\mu$ and the re-distribution coefficient $c_r$ which depend on the mean wind speed. The roof snow loads for the upwind and downwind part of the roof is specified as follows:

$$s_1 = \left(\eta - c_r\right) \cdot s_{gr}$$
$$s_2 = \left(\eta + c_r\right) \cdot s_{gr}$$

(40)

In [16], a refined proposal for the design values of the shape factor and the re-distribution coefficient is presented. The basic strategy convolves the probability densities of the shape factor, the re-distribution coefficient and the snow loads on the ground. The identified values for the shape factor explicitly depend on the mean wind speed at roof height. Basically, beside the non-uniform snow load distribution it is always advised to check the balanced snow load with $s_1 = s_2 = \mu \cdot s_{gr}$ as well. Figure 14 summarizes the results for the assumption that the snow loads follow an extreme value distribution type I.

The actual EN-document on snow actions recommends a shape-factor of 0.8. It is important to note that this value requires mean wind speeds in the range from 5 to 10 m/s.

For the final design of a structure, the combined action effects have to be considered. Today's standards follow the pragmatic strategy of specifying accompanying load amplitudes, which are modelled by combination factors, i.e. the two design scenarios are full wind load plus a reduced snow load and full snow load plus a reduced wind load. In figure 15, the trace of the non-exceedance probabilities of the largest hourly wind speed in individual storms is plotted for Dresden. The average number of storms per twelve month cycle is 1.19,

the fit of the GPD leads to a threshold value of $v_{th} = 15.1$ m/s, a scale value of $v_{sc} = 2.170$ m/s and a shape parameter of 0.2092.
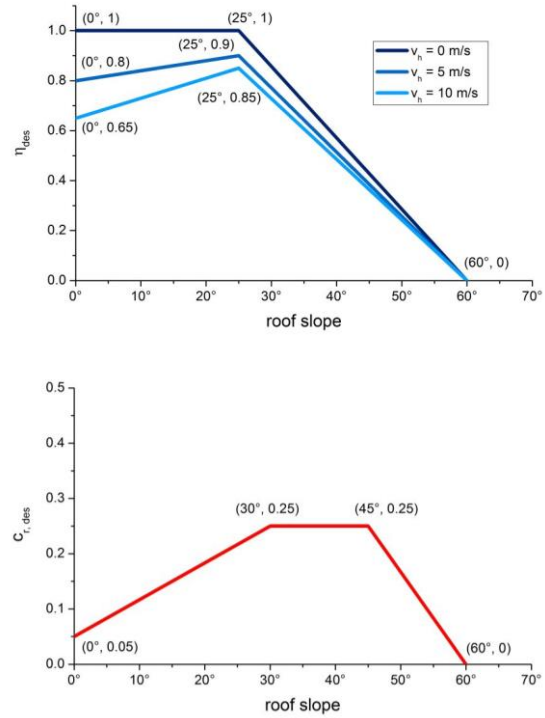


**Figure 14**: Design values for the snow loads on gable roofs [15]
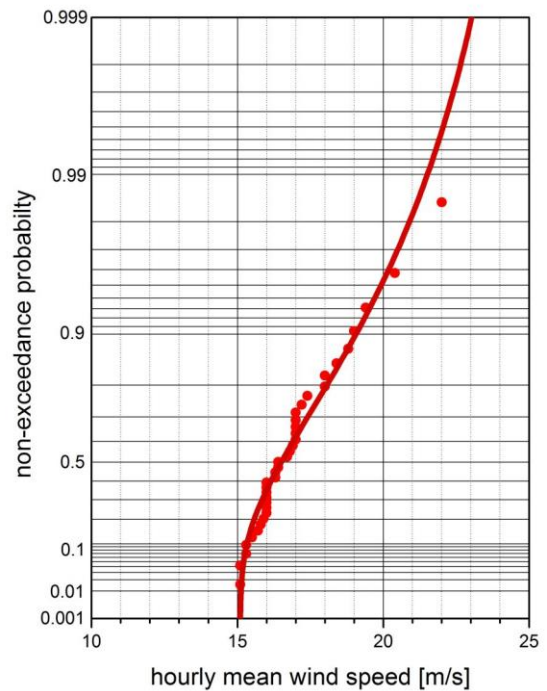


**Figure 15**: Probabilistic model for hourly wind speeds in storms (Dresden: 1973 – 2007)

The analysis of the wind-snow climate has to be based on the observed snow heights which are available with one value per day. The snow loads are only available for

65

three times per week. In a simplified approach, all 24 hourly mean wind speeds are assigned to the height of snow cover of that specific day.

In figure 16, the wind-snow climate is analysed for Dresden. For each level of snow on the ground, the mean value of all observed hourly wind speeds is shown. Additionally, the largest observed value is shown. Obviously, the probability of getting a storm when there is snow reduces with increasing snow height. The mean value of the wind speed decreases for increasing snow height. Fitting a linear trend allows evaluating the expected wind conditions for the level of characteristic and the design snow loads. Therefore, in figure 16 tentative levels are marked for the characteristic and the design snow load. For the design snow level, the mean value of the expected wind speed will be in the range of 2 m/s. The corresponding velocity pressure is 0.0025 kN/m², assuming the air density is 1.25 kg/m³. This wind load is small enough to justify that the design snow load requires no accompanying wind load, i.e. the respective combination factor is 0.
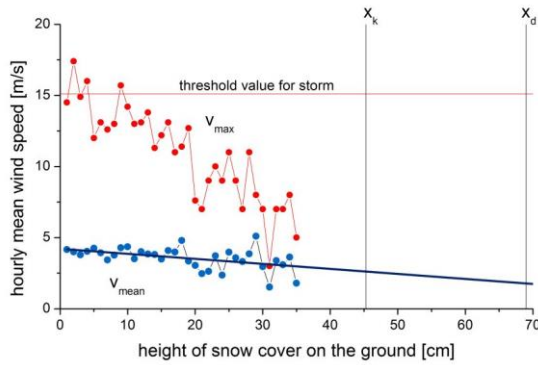


**Figure 16**: Wind conditions for different levels of the snow height on the ground (Dresden 1973-2007)

For the analysis of the joint-probability of storm wind speeds and accompanying snow only 17 observations are available, which does not allow developing a sophisticated model for the joint-probability of snow and wind. The observations however suggest that the larger the wind speed, the smaller will be the snow height. The largest observed wind speed with 2 cm snow on the ground is 17.4 m/s.

A refined approach tries to extrapolate from the basic population of the observed wind speeds for different snow height levels. In figure 17, the histogram of the observed wind speeds is shown for a snow height of 9 cm. Obviously, the histogram can be fitted to a Weibull distribution which is given as:

$$f(v) = \frac{k}{v_0} \cdot \left(\frac{v}{v_0}\right)^{k-1} \cdot \exp\left(-\left(\frac{v}{v_0}\right)^k\right) \qquad (41)$$

with $v_0$ – scale parameter, $k$ – shape parameter

The fitting procedure is based on a least-square fit of the cumulative probability distribution. This gives larger weight to higher values than fitting the density. Figure 18 shows the dependency of the two describing parameters $v_0$ and $k$ on the height of the snow cover for a range up to 25 cm. Beyond this value, the number of observed wind speeds is no longer large enough to obtain stable estimates of the Weibull distribution.
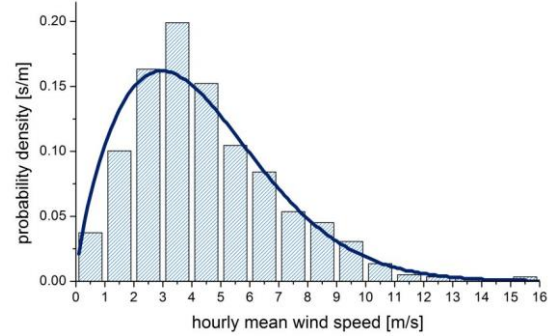


**Figure 17**: Histogram of the observed hourly wind speeds for a snow height of 9 cm and fitted Weibull distribution
(Dresden 1978-2007: v0 = 4.87 m/s, k = 1.73)
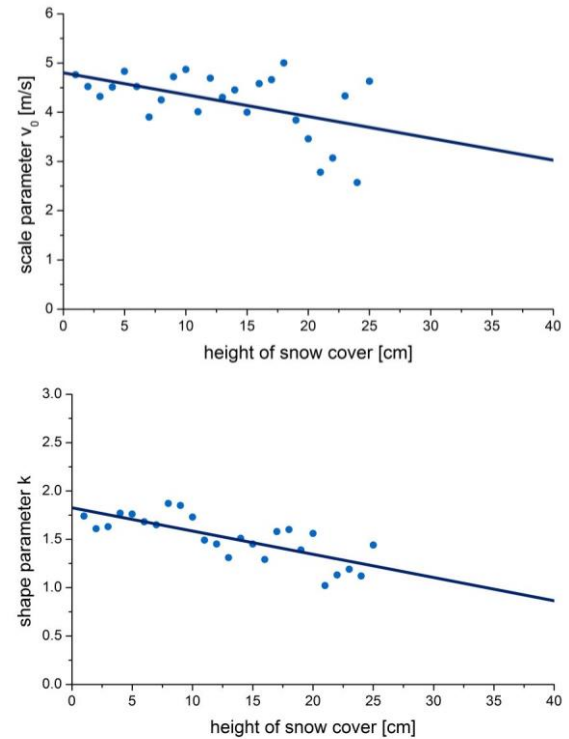


**Figure 18**: Change of the identified scale and shape parameter of the Weibull distribution for wind speeds for different levels of snow height on the ground (Dresden 1978-2007)

Both parameters show a clear decreasing trend with increasing snow height. Hence, it seems to be justified to assume that for a storm at Dresden no snow loads have to be considered. Then, the corresponding combination factor can be assumed as 0. Many stations in the non-mountainous regions of Germany show a similar snow-wind climate, i.e. the DIN-EN-recommended com-

bination factors are far on the safe side with 0.6 for wind and 0.5 for snow for altitudes not above 1000 m.

Figure 19 presents the wind-snow climate for Rostock. The threshold value for storm is 17 m/s; 13 of 61 observed snow events with snow heights above 5 cm occur in storms. Since the amount of snow on the roof depends on the wind conditions, obviously, two scenarios have to be considered. The first scenario includes all snow events with wind speeds below storm level. For this ensemble, the observed wind speeds again show a trend to smaller values for increasing snow height. For the second scenario the interdependence of snow and wind is shown in figure 20.
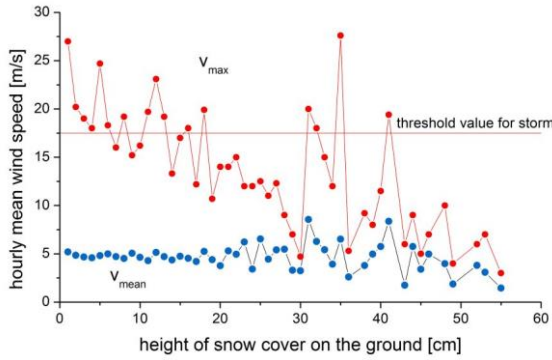


**Figure 19**: Wind conditions for different levels of the snow height on the ground (Rostock 1954-2007)
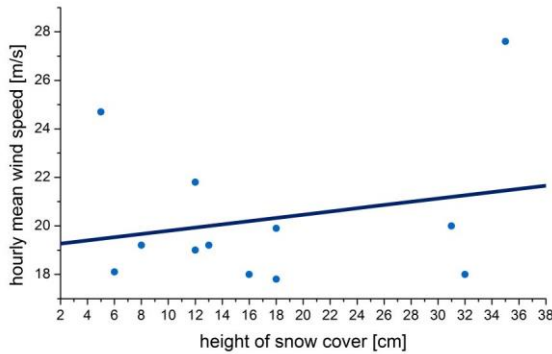


**Figure 20**: Snow heights for largest storm wind speeds (Rostock 1954-2007)

A linear fit identifies an increasing trend, the correlation coefficient is 0.225; however, the statistical stability is poor with a probability of 0.483. Therefore, it seems to be reasonable to consider that storm wind speeds and snow heights are not correlated.

For Rostock, the two scenarios occur with different probabilities: 80% for snow and no storm, and 20% for snow and storm. Then, the exceedance probability of example given a bending moment in a structure becomes:

$$p(M > M_{des}) = 1 - \left(1 - p_1 \cdot p_{ex,1}\right) \cdot \left(1 - p_2 \cdot p_{ex,2}\right) \quad (42)$$

with $p_1$, $p_2$ – probability of scenario 1 and 2
$p_{ex,1}$, $p_{ex,2}$ – probability of $M_1$ or $M_2$ larger $M_{des}$
$M_1$, $M_2$ – bending moment in scenario 1 or 2

Since there is only one conditional equation, which is the target exceedance probability as specified in table 6, there is an infinite number of combinations to distribute the individual probabilities $_{pex,1}$ and $p_{ex,2}$. One reasonable approach is to demand that both individual contributions are the same. Assuming a class 3 structure and 50 years projected working life specifies as target an annual exceedance probability of 1/1000. The individual targets then become:

$$p_{ex,1} = 1 - \frac{1 - p_{target}^{1/2}}{p_1}$$

$$= 1 - \frac{1 - 0.999^{1/2}}{0.2} = 0.9975 = 1 - 1/400 \quad (43)$$

$$p_{ex,2} = 1 - \frac{1 - p_{target}^{1/2}}{p2}$$

$$= 1 - \frac{1 - 0.999^{1/2}}{0.8} = 0.99937 = 1 - 1/1600$$

The final question deals with the combination factors. Strictly speaking, for the specification of the combined loads, the structural behaviour has to be considered. Then, instead of two separate load cases only a single combined load is obtained. This load can be identified based on the LRC-method [17] which is used in wind engineering to specify the effective load distribution. The following input values are required: mean values and standard deviations of the snow and wind actions and their correlation $\rho_{sw}$. Additionally, weighting factors $a_s$ and $a_w$ have to be considered which are the considered structural responses due to unit snow load and unit wind load. Finally, an appropriate target peak factor g is required. The maximum structural response $R_{max}$ then is obtained from the following load combination:

$$R_{max} = a_s \cdot \left(\overline{s} + g \cdot \rho_{Rs} \cdot \sigma_s\right) + a_w \cdot \left(\overline{w} + g \cdot \rho_{Rw} \cdot \sigma_w\right) \quad (44)$$

with $\overline{x}$ - mean value and $\sigma_x$ – standard deviation

The two weighting coefficients are specified as:

$$\rho_{Rs} = \frac{a_s \cdot \overline{s} + a_w \cdot \rho_{sw} \cdot \sigma_w}{\sigma_R}$$

$$\rho_{Rw} = \frac{a_w \cdot \overline{w} + a_s \cdot \rho_{sw} \cdot \sigma_s}{\sigma_R} \quad (45)$$

The standard deviation of the structural response $\sigma_R$ is given with:

$$\sigma_R = \sqrt{a_s \cdot \sigma_s^2 + a_w \cdot \sigma_w^2 + 2 \cdot \rho_{sw} \cdot a_s \cdot a_w \cdot \sigma_s \cdot \sigma_w} \quad (46)$$

The load amplitudes for the two combined loads can be expressed as a reduction factor times the individual design loads for wind and snow. The reduction factors especially depend on the ratio of the structural weighting factors. In the following example, it is assumed that

extremes of snow and wind follow the Gumbel distribution. The peak factor is set to 4.936, corresponding to an annual exceedance probability of 1/1000. The variation coefficient of the wind loads is assumed as 0.3, the corresponding value for snow is 0.45. Figure 21 shows the corresponding reduction factors. The results clearly show that the consistent codification of combined wind and snow actions is not trivial.
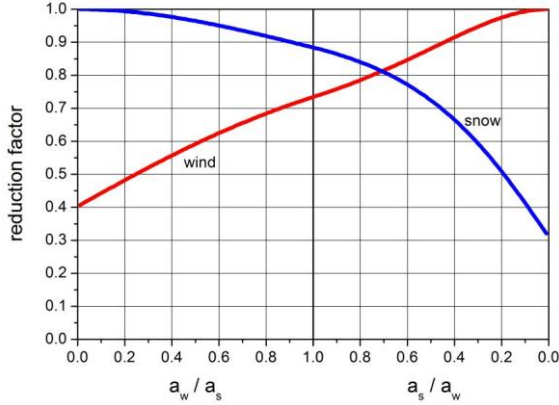


**Figure 21**: Reduction factors for the combined wind and snow actions

For two uncorrelated Gumbel distributions, the accompanying load is given with the mode, which is obtained as follows:

$$x_{mode} = x_{mean} - \frac{\sqrt{6}}{\pi} \cdot x_{sdev} \cdot \gamma \tag{47}$$

Then, the two combination factors are given as:

$$\psi_{sw} = \frac{w_{mode}}{w_{des}}; \ \psi_{ws} = \frac{s_{mode}}{s_{des}} \tag{48}$$

The two load combination then become:

$$\begin{aligned} LF\ 1&: s_{des} \ \otimes \ \psi_{sw} \cdot w_{des} \\ LF\ 2&: w_{des} \ \otimes \ \psi_{ws} \cdot s_{des} \end{aligned} \tag{49}$$

For the example values, the two combination factors become $\psi_{sw} = 0.35$ and $\psi_{ws} = 0.25$. The quality of this approach can be evaluated by the ratio of the maximum structural response based on the EN-approach to the real maximum which is shown in figure 22. Additionally, the obtained exceedance probability in a projected working life of 50 years is shown. The target exceedance probability is met for cases where either the snow or the wind load is of no importance. Unacceptable solutions are obtained if the target exceedance probability of about 5% is exceeded by a factor of 2. Then, in this example, the range for $a_w/a_s$ from 0.65 to 3.50 leads to clear under-design. For the recommended DIN-EN combination factors, which are rather based on tradition than on research, the results are closer to the target. The example

points out that a revision of combination factors should not be based on a pure analysis of the actions.
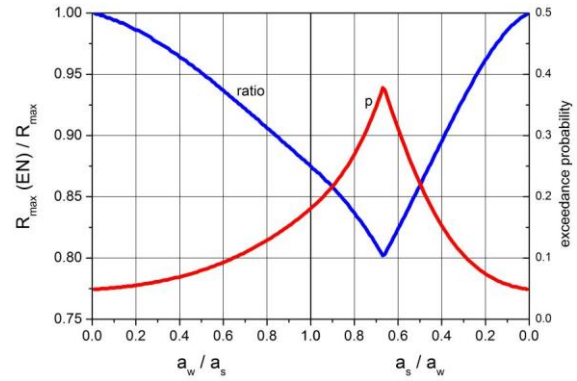


**Figure 22**: Ratio of the structural response based on load combinations using combination factors to the largest response and corresponding exceedance probability of the design value

# 7. Analysis of possible climate change

As has been shown in chapter 4, observation periods of only a few decades of snow loads on the ground do not allow identifying the underlying process. In the worst case, the extreme value statistics for an individual station will even not answer the question, if the extremes follow the type I, II or III extreme value distribution. A consistent approach considering that the true extreme snow climate remains unknown has been presented in [10] for the estimation of the design value considering a one-sided target confidence interval of 75%. The basic idea is to identify in a first step all snow climates which randomly may lead to the observed parameter triple ($\lambda_{obs}$, $sc_{obs}$, $k_{obs}$). Simulations then identify the corresponding relative frequencies for each triple ($\lambda_i$, $sc_i$, $k_i$). The final probabilities that the snow climate j leads to the observed values is given as:

$$p_j = \frac{rel\ f_j}{\sum_i rel\ f_i} \tag{50}$$

Basically, the number of events and the scale and shape parameter can be treated as independent since they do not occur in the same probability distribution. Then, the simulation effort is reduced. Figure 23 shows on the example of Dresden the huge range of possible Poisson distributions randomly leading to the observed 59 events in 28 winter periods. The obtained distribution is slightly skewed, the mean value is 60, the standard deviation is 7.753. The possible range for $\lambda$ extends from 35 to 85. In figure 24, the joint probability distribution for the possible combinations of sc and k randomly leading to the observed values is shown.

For each possible triple ($\lambda_i$, $sc_i$, $k_i$), a design snow load can be calculated. Sorting the possible design values in ascending order and adding simultaneously the corresponding $p_i$ values leads to a trace of the non-

exceedance probabilities of probable design values, assuming a specific value for the projected working life and specifying the target structural class. With the target confidence level of 75% the best estimate of the design snow load is obtained. Table 7 compares some results from the naïve approach (the observed values are used directly to estimate the design values) to the consistent probabilistic approach.
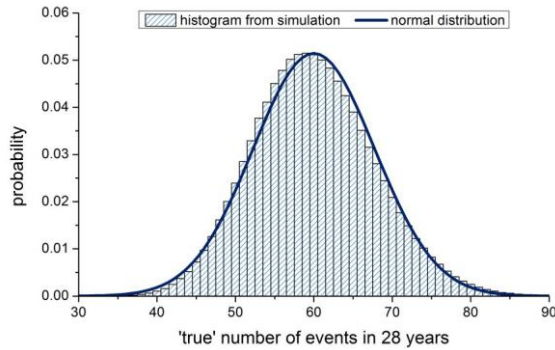


**Figure 23**: Probability density of observing 59 values in 28 winter periods for different $\lambda$-values with $\lambda = N_{true}/28$
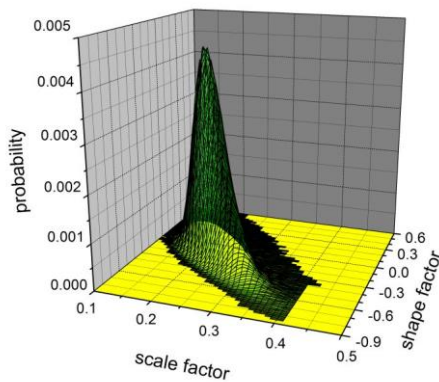


**Figure 24**: Joint-probability density sc-k of observing 59 values leading randomly to sc = 0.2105 kN/m², k = 0.163

**Table 7**: Comparison of design values for the snow load in [kN/m²] on the ground for Dresden (1978-2007), structural class 3

| L | 10 | 20 | 50 | 80 |
|-------|-------|-------|-------|-------|
| best | 0.984 | 1.064 | 1.164 | 1.212 |
| naïve | 0.863 | 0.915 | 0.975 | 1.000 |
| ratio | 1.14 | 1.16 | 1.19 | 1.20 |

Figure 25 shows the number of independent events and the corresponding maximum snow load over the time. Both traces suggest a trend. The number of events increases, while the intensity decreases over time. These findings seem to be plausible with the scenario of milder winters. Former long periods of continuous snow cover now are interrupted by fairly warm weather; the amount of snow decreases. Fitting a linear trend to the number of events leads to 0.03 more events per year. A linear trend fitted to the snow load amplitudes identifies a decrease in the intensity of 0.002 [kN/m²] per event. It is important to note that the classical approach is based on the average value which is appropriate for the centre of the observation period. The extrapolation of the trend for the number of events to the year 2017 leads to an expected number of events of 2.886, instead of the observed average of 2.107. The expected mean value of the snow loads on the ground has to be obtained considering the increasing number of events. The expected value for the year 2017 is 0.111 kN/m². Extending the linear trend further into the future, however, soon leads to snow loads below zero. This scenario obviously is violating the basic features of the process. A physically more reasonable approach fits a linear trend to the logarithms of the observed snow loads. Then, in the limit, snow loads become zero in the future. From a structural engineer's point of view this approach seems fairly bold.
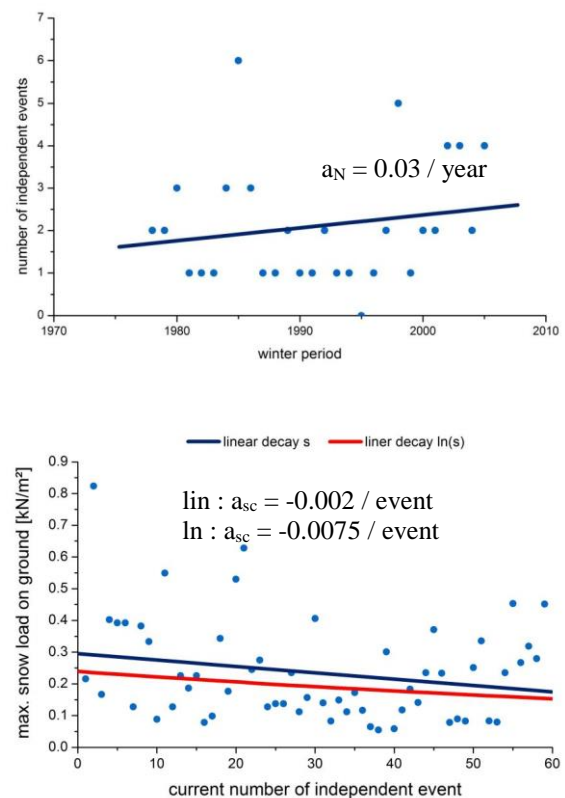




**Figure 25**: Suggested trends in the number of events per year and the amplitude of snow loads (Dresden 1978-2007)

Once all possible combination of the parameter quintuple ($\lambda$, sc, k, $a_N$, $a_{sc}$) have been identified, joint probability distributions can be obtained. This approach has been successfully applied for the specification of the design wind speed in [18]. Figure 26 shows the joint-probability for the linear trend in the number of events per year and the true average number per year. The

random possible trend ranges from -0.05 to 0.11. The average number of observed events per year ranges between 35/28 to 95/28. The joint distribution is slightly skewed for $a_N$ and considerably skewed for $\lambda$. For the trends in the scale the joint probabilities have three dimensions: sc, k and $a_{sc}$. The joint probability of $a_{sc}$-k for a specific sc-value is almost symmetric in regard to the value of the observed trend; in regard to k, the densities are skewed.

Figure 27 shows the joint probability for $a_{sc}$ and sc accumulated over all k-values. This joint-probability is irrelevant for the identification of the best estimated of the design snow load. However, the figure illustrates that for each true scale value sc and true positive trends $a_{sc}$ there is a considerable probability that the observed negative trend is obtained. For these cases, the true design snow load will be larger than the design snow load obtained with the naïve approach.
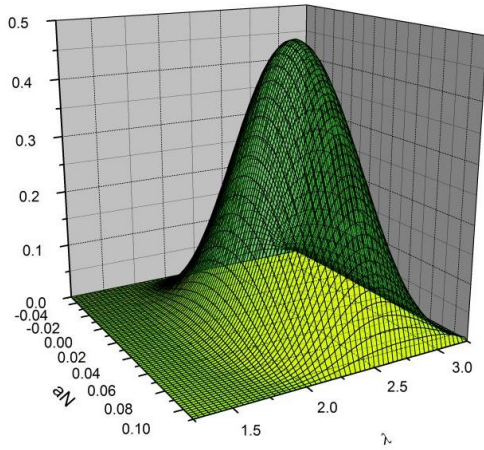


**Figure 26**: Joint probability of $a_N$-$\lambda$ randomly leading to the observed average number of events per year and the observed linear trend (Dresden 1978-2007)
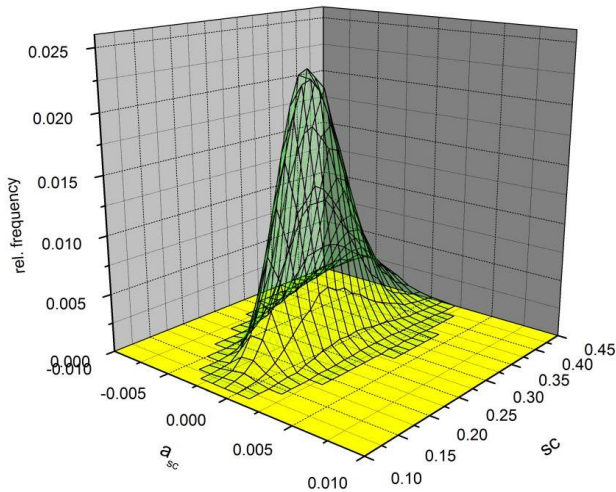


**Figure 27**: Joint probability of $a_{sc}$-sc randomly leading to the observed scale and observed linear trend (Dresden 1978-2007)

Similar to the approach before, for each quintuple ($\lambda$, sc, k, $a_N$, $a_{sc}$) a relative frequency is found based on simulations. For each combination, a design snow load is obtained. It is important to note that the exceedance probability of the design snow load is no longer constant over time, but changes with each year. The exceedance probability in the lifetime then is obtained as 1 minus the product of the non-exceedance probabilities in each individual year over the lifetime:

$$p_L(s > s_{des}) = 1 - \prod_{i=M}^{L+M}\left(1 - p_i(s > s_{des})\right) \qquad (51)$$

with L – lifetime in years
$p_L$ – exceedance probability after L years
$p_i$ – individual exceedance probability in year i
M – starting year of exposure

The design value has to be obtained iteratively. It is important to note that the accumulated exceedance probability in the lifetime depends on the start of the exposure period.

Sorting the design snow loads for each scenario (lifetime in years, starting year of exposure and target structural class) in ascending order and summing the relative frequencies finally again leads to the trace of the non-exceedance probability of the possible design snow loads. The best estimate for each scenario is obtained with the non-exceedance probability 75%, thus meeting the confidence target.

In figure 28, the respective curves are shown for an assumed lifetime of 50 years for a class 3 structure varying the starting years from 1986 to 2026. In this example, the decreasing trend in the snow load amplitudes has more weight than the increasing trend in the number of events, i.e. the later the start of the exposure, the smaller are the design snow loads.

Table 8 summarizes the best estimates of the design snow load for exposures starting from 1986 to 2026. All five values are larger than the value obtained by applying the naïve approach, i.e. if long-term trends are considered then the snow loads increase, although the identified dominant trend is negative.
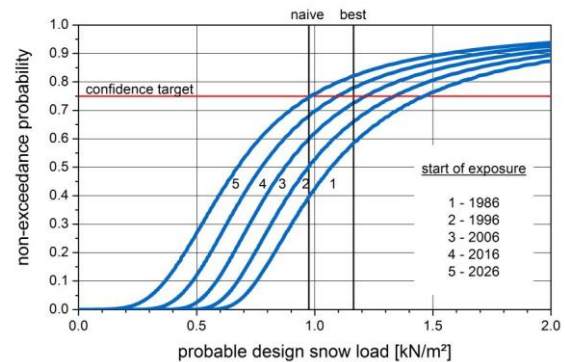


**Figure 28**: Probably design snow loads for L = 50 years and structural class considering long term trends in the snow climate (Dresden 1978-2007)

**Table 8**: Best estimates for the design snow load in kN/m² for Dresden considering long-term trends in the snow climate for different starting years of exposure (L = 50 years, structural class 3)

| year | 1986 | 1996 | 2006 | 2016 | 2026 |
|------|------|------|------|------|------|
| $s_{des}$ | 1.461 | 1.337 | 1.216 | 1.096 | 0.983 |

Compared to the best estimate considering a stationary snow climate, more favourable design snow loads are obtained for exposures starting in 2016 and later. It is worth mentioning that for exposures starting earlier than 2016 the design with the best estimate assuming a stationary snow climate would be on the unsafe side. In other words: The decision to exploit favourable long-term trends leads inevitably to the conclusion that existing structures are under-designed. Considering only the favourable effects and neglecting the consequences of a refined model of the snow climate for the evaluation of the existing structures is double thinking.

# 8. Summary and conclusions

The design of a structure in regard to snow actions can be separated in the following steps:

- Specification of the design target
  With reference to the projected lifetime, an appropriate value of the exceedance probability of the design snow load has to be chosen. It is reasonable to distinguish structural classes, thus considering the different consequences of a failure. Since the estimation of the corresponding design value is based on confined ensembles, additionally a target value for the one-sided confidence interval has to be specified. The basic document EN 1990 recommends a confidence target of 75%.

- Specification of the design value for the snow loads on ground
  The probability distribution of the underlying process can be identified based on annual extremes or on extremes above a specific threshold. An appropriate theoretical model for the annual extremes is given with the Generalized Extreme Value Distribution; the peaks-over-threshold approach uses the Generalized Pareto Distribution. The latter approach requires as additional random variable the number of events per twelve month cycle; this random parameter can be modelled by the Poisson distribution. Then, both approaches theoretically lead to identical traces of annual non-exceedance probabilities. Since usually the observation data are limited, the true distribution can hardly be identified. A fair compromise may be obtained by assuming an extreme value distribution type I for the annual non-exceedance probabilities. The uncertainties in the estimated design values depend on the size of the ensemble and the estimation

method. Generally, an adjusting factor is required to meet the target confidence. A further biasing effect may be obtained if the ensemble contains an outlier. A consistent treatment of outliers requires a high detection rate of true outliers and a small error rate for erroneously identified outliers. The strategy developed in the scope of the European research project is based on a least-square fit in the probability paper of the Gumbel distribution with plotting position of 1/(N+1) for N being the ensemble size. This method has a fairly poor detection rate. The majority of outliers will not be identified. A more consistent approach uses BLUE for the identification of outliers, leading to a considerably increased detection rate. Simply removing an identified outlier from the ensemble may lead to considerable underestimations of the design value. Specific adjusting factors are required to balance this short-coming. It is strongly recommended to revise the European national snow load maps in this regard.

- Specification of the design value of snow loads on the roof
  The snow loads accumulated on a roof are influenced by the wind. It is reasonable to consider the shape factor as a random variable. Additionally, the distribution over the roof can be assumed as random. The design value for these parameters can be obtained from a convolution of the contributing probability densities. Based on the JCSS probabilistic model code, a refined proposal has been worked out. The shape factor explicitly depends on the wind speed during snow fall events. Respective statistics reveal that for many regions in Germany the wind speeds tend to zero for increasing snow loads on the ground. Then, the shape factor for flat roofs tends to unity. It is important to note that the corresponding shape factor specified in the Eurocode is 0.8 and therefore underestimates the design snow loads by 20%.

- Specification of a combined wind-snow action scenario
  The Eurocode like most standards uses for the estimation of action effects under combined actions the strategy of specifying accompanying loads, which are specified based on combination factors. The specified values in Germany for snow and wind are rather based on tradition than on recent scientific analysis. For many regions in Germany, strong storms will not occur when there is snow on the ground. Then, the combination factor for accompanying snow will be zero. If additionally the wind speeds tend to small values for increasing snow load values, the corresponding wind loads become negligible small, i.e. the combination factor for accompanying wind is zero as well. In other regions, storm and snow may occur simultaneously. Then, two scenarios have to be covered: snow without storm and snow together with storm. The joint probability density for the latter scenario can be modelled in a first approach as uncorrelated extreme value distributions type I. Then, the accompanying load amplitude is given with the mode of the respective probability distribution. The

final evaluation of the combined wind and action effects has to be based on structural responses. Basically, the method of accompanying loads tends to underestimate the structural responses. For any refined approach it is therefore strongly recommended to consider the structural behaviour.

- The treatment of a possible climate change or of natural long-term trends in the wind-snow climate will be one of the challenges in future codification work. A consistent approach accepts that the true parameters of the probability distributions of the underlying physical processes cannot be identified since the ensembles of observed data are much too small. The same conclusion is true for the basic shape of trends. A reasonable approach therefore describes the trends by a simple linear law. For larger negative trends, the amplitudes in the future may become smaller than zero, thus leading to physical inconsistencies. For these cases, the snow load simply can be set to zero, and the corresponding non-exceedance probability becomes unity. A refined shape of negative trends is based on a linear model for the logarithms of the respective variable, thus avoiding negative values. Based on simulations, a range of possible true climates and trends can be identified which randomly lead to the observed values. In a next simulation step, the corresponding joint-probability densities for the parameter quintuple ($a_N$, $\lambda$, $a_{sc}$, sc, k) can be obtained. Each possible combination of the parameters leads to a specific design value. Sorting these design values in ascending order together with the corresponding probability and integrating the joint-probability densities finally leads to a trace of random design values. The best estimate of the design value is obtained considering the target confidence. Even with the bold approach of accepting zero snow loads in the future, for the chosen example of Dresden the best-estimates of the design snow load are larger than those values obtained with the naïve approach of assuming that the observed values are the true values and long-term trends do not exist. It is important to note that negative trends may be observed randomly even if the true trend is positive. While for dominant positive trends the design values increase in the future, a dominant negative trend leads to a decrease of future design values. On the other hand, existing structures may turn out to be under-designed.

## Acknowledgement

## References

1. ISO 22111 (2007): Bases of design of structures – General requirements
2. ISO 4354 (2009): Wind actions on structures
3. W.H. Press, S.A. Teukolsky (1992): Numerical Recipes in Fortran 77: The Art of Scientific Computing, Cambridge University Press,
4. M. Matsumoto, T. Nishimura (1998): Mersenne twister. A 623-dimensionally equidistributed uniform pseudo-random number generator, ACM Transactions on Modeling and Computer Simulation, 3-30
5. M. Matsumoto (2010) : Mersenne Twister homepage, A very fast random number generator of period $2^{19937}$-1,
   www.math.sci.hiroshima-u.ac.jp/~m-mat/MT/SFMT
6. G. Marsaglia (2003): Random number generators, Journal of Applied Statistical Methods, 2, 2-13
7. BAST – Bundesanstalt für Straßenwesen (2009) Effects of heavy goods vehicle traffic on the bridges of the federal roads (in German)
8. E.J. Gumbel (1958): Statistics of Extremes, Columbia University Press, New York · London
9. I.I. Gringorten (1963): A plotting rule for extreme probability paper, Journal of Geophysical Research, 68, 813-814
10. M. Kasperski (2012): A consistent approach for estimating the design value of the snow load on the ground from confined ensembles, in Proc. of 7th Int. Conf. on Snow Engineering, Fukui, Japan
11. B. Czwikla, M. Kasperski (2016): Specification of the design value of the ground snow load considering measurements of the snow height – part 1: single stations, ICSE 2016, Nantes
12. L. Sanpaolesi et al. (1998): Phase 1 Final Report to the European Commission, Scientific Support Activity in the Field of Structural Stability of Civil Engineering Works:Snow Loads. Dept of Structural Engineering, University of Pisa
13. N. Balakrishnan, P.S. Chan (1992) Order statistics from extreme value distribution, II: Best linear unbiased estimates and some other uses, Commun. Statist.-Simula., 21(4), 1219-1246
14. A. Childs, N. Balakrishnan (2002) Series approximations for moments of order statistics using MAPLE, Computational Statistics & Data Analysis 38, 331-347
15. JCSS, Probabilistic Model Code Part 2: Load Models, 2.12 Snow Load, 99-CON-DYN/M0097 February 2002 1 JCSS-VROU-07-02-96
16. B. Czwikla, M. Kasperski (2012) Design snow loads for gable roofs, Proc. 7 ICCSM - International Congress of Croatian Society of Mechanics, Zadar, Croatia, May 22 - 25, 2012, Zadar
17. M. Kasperski (1992) Extreme wind load distributions for linear and nonlinear design. Engineering Structures 14, 27-34
18. M. Kasperski (2010) A new approach for the specification of the design wind speed considering long-term trends, Global Environmental Research, Vol. 13 No. 2, 161-168

# Climate Change: impact on snow loads on structures

Pietro Croce[1], Paolo Formichi[1,a], Filippo Landi[1] and Francesca Marsili[1]

[1]University of Pisa, Department of Civil and Industrial Engineering-Structural Division, Largo Lucio Lazzarino - 56126 Pisa, Italy

**Abstract.** A general procedure to evaluate future trends in snow loads on structures is illustrated aiming to study influences of climate change at European scale, to assess its impact on the design of new structures as well as on the reliability levels of existing ones, also in view of the next revision of the Eurocodes. Analysing high quality registered meteorological data of daily temperatures, rain and snow precipitations in nine Italian weather stations, conditional probability functions of occurrence of snow precipitation, accumulation and melting have been preliminarily determined as functions of daily air temperatures. By means of Monte Carlo simulations and based upon daily output of climate models (daily max. and min. temperatures and water precipitation) yearly maxima of snow loads for various time intervals of 40 years in the period 1980-2100 have been simulated, deriving, via the extreme value theory, the characteristic ground snow loads at the sites. Then, the proposed procedure has been implemented in a more general methodology for snow map updating, in such a way that the influence of gridded data of precipitation, predicted by global climate models, on extreme values of snow loads is duly assessed. Preliminary results demonstrate that the outlined procedure is very promising and allows to estimate the evolution of characteristic ground snow loads and to define updated ground snow load maps for different climate models and scenarios.

## 1 Introduction

As structural design is often governed by climatic actions, alterations of climatic actions caused by climate change could significantly impact design of new structures as well as the reliability of existing ones. For this reason some research groups, based in different areas of the world, are investigating the problem, especially aiming to study the possibility to transfer the outputs of climate models which refer to geographical cells of large dimensions on a suitably smaller scale, allowing to derive characteristic values of climatic actions from the above mentioned outputs. In particular, effects of climate change on snow loads have been recently investigate in Germany [1], Norway [2] and Canada [3], focusing on their influence on the reliability of built environment.

A general procedure for the estimation of climate change influence on ground snow loads is presented; such a procedure, combining the outputs of global climate models with measured data, allows to refine the snow load predictions arriving to a geographical resolution adequate to take into account also micro-climate effects, depending on the local orography.

The procedure, which is general enough to permit sound estimation of future trends in snow loading on structures, aims more specifically to address the impact of climate change on the assessment of new and existing structures, also in view of the evolution of the second generation of Eurocodes, and Eurocode EN 1991 - Part 1-3 - Snow loads [4] in particular, as requested by Mandate M/515 of European Commission [5] to CEN [6].

## 2 Snow load on structures: State of Art

### 2.1 Definition of ground snow load

The definition of snow loads on structures in the current version of the structural Eurocodes is largely based upon the results of the European Snow Load Research Project (ESLRP) [6] and, in particular, on the European Ground Snow Load Map elaborated within that research. This map was the first snow load map derived at European scale with a strong scientific basis [7] and its elaboration started from the analysis of the basic snow data collected across 18 European countries, which at that time were members of CEN. By applying extreme value statistics to these observations, the characteristic ground snow loads were derived corresponding to a given probability of exceedance (the 2% upper percentile on yearly base, corresponding to a return period of about 50 years), taking into account both the influence of exceptional snowfalls or no snowy winters. It must be also stressed that in [7], exceptional snow loads were considered for the first time at European scale, on sound scientific bases, giving also appropriate guidance for their identification.

### 2.2 European snow load maps

Beside the characteristic ground snow loads at weather stations, the research allowed to identify ten major European climatic regions, and the corresponding snow maps, elaborated through GIS software: generally, in each climatic region the ground snow load depends on the altitude according to suitably derived law, except in Norway and Iceland, where snow load is practically independent of altitude. Based on the above snow map, each National Standard Body of CEN member states, produced their own national map of ground snow load, published in the National Annex to EN 1991-1-3.

## 3 Problem statement

### 3.1 Climate change impacts

The evidence of climate change is unequivocal [8]: the average global temperature, currently around 0,8°C above pre-industrial level, continues to rise, even more

---

<sup>a</sup> Corresponding author: p.formichi@ing.unipi.it

evidently in Europe [9]. Consequences of climate change, like alteration of natural processes, modifications of precipitation patterns, melting of glaciers, rise of sea levels and so on, are increasingly evident. For this reason, whatever the warming scenarios and the level of success of mitigation policies, in the coming decades the impact of climate change needs to be considered, taking into account possible delay in achieving targets in reduction of greenhouse gas emissions as well as adaptation measures to deal with economic, environmental and social consequences of climate change [10].

A global assessment of climate change science is presented by the recent IPCC (International Panel on Climate change) Report [11]. The assessment considers new evidence of past, present and projected future climate change foresees by several independent scientific studies, based on observations of the climate system, theoretical studies of climate processes and simulations using climate models. Predictions of climate change are based on a set of four Representative Concentration Pathways (RCPs) scenarios, where radiative forcing target level, estimated for the year 2100, are fixed in comparison with pre-industrial values [12]. Globally, these scenarios generally lead to further warming and changes in the water cycle, but trends can be different or even opposite on local scale.

The EU response to climate change is an adaption strategy to enhance the capacity to withstand it and the readiness to respond to its impacts, particularly in most vulnerable key sectors like infrastructures and buildings, characterised by a long life span and high costs [10]. In this respect, a central role is played by technical standards and by their evolution during the lifetime cycle of the infrastructures and buildings [13]; implications of climate change for new and existing structures is then a key aspect in the development of second generation of Eurocodes [6]. In this context, the present study aims to determine the effects of Climate Change on snow loads on structures, implementing suitable numerical procedures to derive characteristic snow loads from available global and regional climate models.

### 3.2 Snow load in a changing climate

One of the trite remarks about global warming is that, as obvious consequence of it, a reduction of snow is generally expected, but it is not said. In fact, although in consequence the global warming frequency of snow events should reduce, the intensity of extreme snow events may increase, since the capacity of the atmosphere to hold moisture (and to form snow particles in case of sudden temperature's drop) increases with temperature. This may lead to the increase of both snow density and occurrence of extreme snowfalls in regions where temperatures still may happen to be below freezing level during precipitation events [1].

The above considerations are confirmed by some spectacular and catastrophic collapses of lightweight roof structures caused by snow, which occurred in the last years all around the Europe [14] and [15] like the roof collapse of the Katowice Exhibition Hall (2006), which caused 65 victims and over 170 injured people (Figure 1). A more wide illustration of some relevant failures can be found in [16], while the reliability level of existing structures designed with the current versions of Eurocodes, especially for those structures more sensitive to an increase of snow loads, like lightweight structures of widespan roofs, is discussed in [16] and [17].



**Figure 1.** Roof collapse of Katowice Exhibition Hall

To assess the evolution of the ground snow load and its impact on new and existing structures, future trends, in terms of intensity and frequency of precipitations in cold areas, should be compared with those adopted to develop current versions of snow load maps for structural design.

A suitable numerical methodology is proposed in order to estimate characteristic ground snow loads from available results of global and regional climate models (GCMs and RCMs) in the mid to long term time, according different scenarios RCPs.

As just said, the interpretation of the outputs of climate models is complicated by their spatial resolution, typically too coarse to study specific sites, which does not allow a direct evaluation of snow load trends. For this reason, the proposed procedure has been calibrated and validated against high quality measured data available for time series of 50 or more years and particular attention has been devoted to identify suitable techniques to check the homogeneity of the available data populations.

Finally, it must be stressed that intrinsic uncertainty affecting climate projections in different climate models reflects on their outcomes, so that conclusions about increase/decrease of actions need careful interpretations.

## 4 Procedure for the estimation of future trends of ground snow loads

The proposed procedure consists of four steps:
- analysis of observed data series in order to derive conditional probability functions, linking snowfall and snow melting conditions with precipitation data and air temperature;
- development of a predictive model to evaluate snow loads from available meteorological data;
- calibration and validation of the model predictions against observed data series;
- implementation of the model on projected data series from global climate change models.

### .4.1 Analysis of observed data series

Relevant meteorological data recorded in the past, daily temperatures and precipitation (water equivalent and snow cover depth), have been collected and analysed with the purpose to seek the conditions of maximum and minimum daily temperature, $T_{max}$ e $T_{min}$, at which snow cover depth increases, in case of precipitation of height $h_r$, or decreases, melting or increasing densities, and rainfalls are likely to occur.

In particular, seven different situations have been identified comparing day $n$ and day $n-1$:

1. total melting of snow cover present at day $n-1$;
2. partial melting of the snow cover present at day $n-1$;
3. constant snow cover depth without precipitation;
4. rainfall in absence of snow cover at day $n-1$;
5. rainfall and total melting of the snow cover present at day $n-1$;
6. precipitation on snow cover with snow depth decreasing;
7. snowfall with increasing of snow cover;

and, following the flowchart shown in figure 2, the daily measured data can be allocated according to them.
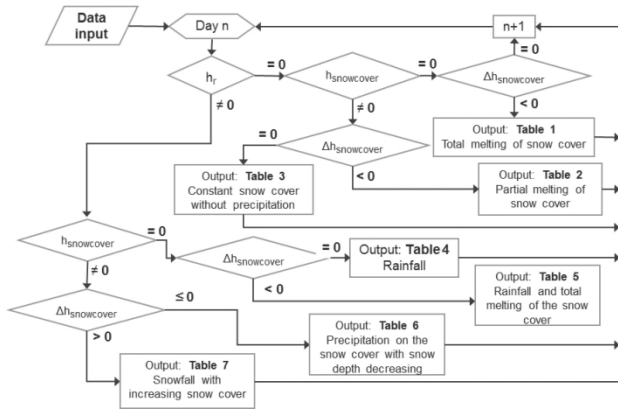


**Figure 2.** Flowchart for allocation of daily measured data

For each relevant situation, the frequency histograms have been then derived according to the conditions

$$Z(\bar{T}_{min}, \bar{T}_{max}) = number\ of\ cases\ of\ each\ situation\ for\ which$$

$$\left(\bar{T}_{max} - \frac{\Delta T}{2}\right) < T_{max,n} < \left(\bar{T}_{max} + \frac{\Delta T}{2}\right)$$

$$\left(\bar{T}_{min} - \frac{\Delta T}{2}\right) < T_{min,n} < \left(\bar{T}_{min} + \frac{\Delta T}{2}\right)$$

$$-20°C < \bar{T}_{min} < 40°C\ ;\ -20°C < \bar{T}_{max} < 40°C\ ;\ \Delta T = 1°C\quad(1)$$

The histogram of frequencies for each of the seven situations are then converted into continuous surfaces $f_j(T_{max}, T_{min})$ by means of up to three two-dimensional Gaussian functions

$$f_j = \sum_i a_i\, e^{-\frac{1}{2}\left\{\left[\frac{(T_{max}\cos\beta_i + T_{min}\sin\beta_i) - (\mu_{max,i}\cos\beta_i + \mu_{min,i}\sin\beta_i)}{\sigma_{max,i}}\right]^2 + \left[\frac{(T_{min}\cos\beta_i - T_{max}\sin\beta_i) - (\mu_{min,i}\cos\beta_i - \mu_{max,i}\sin\beta_i)}{\sigma_{min,i}}\right]^2\right\}}\quad(2)$$

being $i$ the number of the Gaussian functions, which is assumed equal to the number of local maxima of the histogram.

In eq. (2), each Gaussian function is defined by 6 parameters:

- $a_i$ amplitude
- $\beta_i$ angle of rotation with respect to x-axis ($T_{max}$)
- $\mu_{max,i}$ median value with respect to x-axis ($T_{max}$)
- $\mu_{min,i}$ median value with respect to y-axis ($T_{min}$)
- $\sigma_{max,i}$ standard deviation with respect to x-axis ($T_{max}$)
- $\sigma_{min,i}$ standard deviation with respect to y-axis ($T_{min}$).

The parameters $\beta_i, \mu_{max,i}, \mu_{min,i}$ are derived from the peak values of the histograms, while the other parameters, $\sigma_{max,i}, \sigma_{min,i}, a_i$ are estimated by means of least squares method and imposing the condition of unitary volume underlying the surface ($\sum_i a_i = 1$).

Once derived the probability distribution function of the seven conditions $f_j$ for each relevant condition, $j=1,\ldots7$, it is possible to define conditional probability functions of snowfall and snow melting for given values of the daily temperatures, $\bar{T}_{max}$ and $\bar{T}_{min}$. In particular, it results that

- the conditional probability function of snowfall in presence of precipitation is

$$P(snowfall(\bar{T}_{max}\ \bar{T}_{min})\ |\ prec) = \frac{n_7 \cdot f_7}{n_7 \cdot f_7 + n_4 \cdot f_4}\quad(3)$$

where $n_7$ is the number of cases of effective snowfall (condition 7) and $f_7$ is the consistent probability function previously defined; $n_{4-5}$ is the number of cases of rainfall (conditions 4 plus 5) and $f_{4-5}$ is the consistent probability function (an example of such a function for the Italian weather station of Spigno Monferrato is reported in Figure 3);
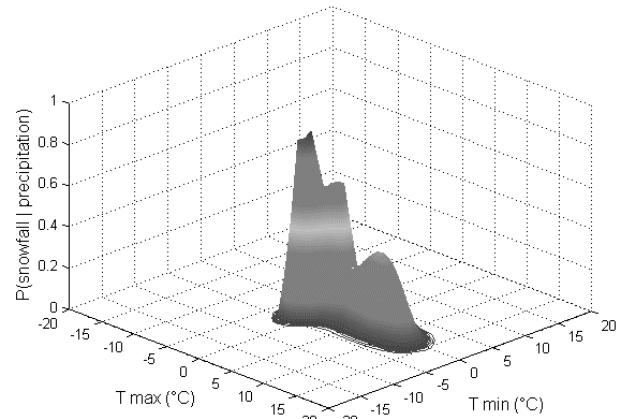


**Figure 3.** Conditional probability function of snowfall in presence of precipitation – (Spigno Monferrato – I)

- the conditional probability function of melting of snow cover in presence of snow cover is

$$P(snowmelt(\bar{T}_{max}\ \bar{T}_{min})\ |\ snowcover) = \frac{n_{1-2} \cdot f_{1-2}}{n_{1-2} \cdot f_{1-2} + n_3 \cdot f_3}\quad(4)$$

where $n_{1-2}$ is the number of cases of snow melting (conditions 1 plus 2) and $f_{1-2}$ is the consistent probability function; $n_3$ is the number of cases of constant snow cover (condition 3) and $f_3$ is the consistent probability function previously defined and, obviously, $\bar{T}_{max} > 0°C$,(an example, for the Italian weather stations is reported in Figure 4)
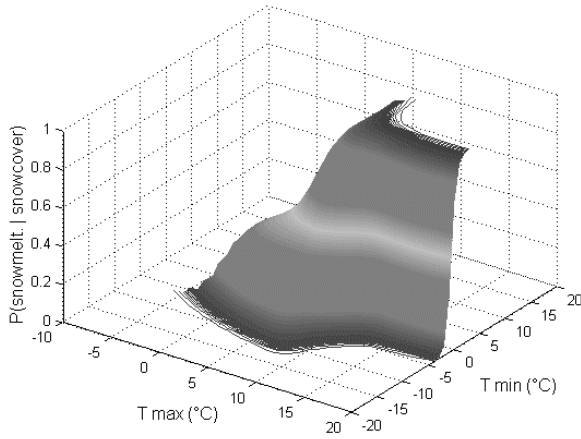
**Figure 4.** Conditional probability function of snow melting in presence of snow cover – Italy

## 4.2 Predictive model

A predictive model to evaluate ground snow loads has been then developed based on the previously determined conditional *pdfs*. In Figure 5, it is presented the flowchart of the algorithm which has been implemented through a suitable Monte Carlo simulation.

The input data of the algorithm are three relevant meteorological daily data: the maximum and minimum air temperatures, $T_{max,n}, T_{min,n}$, and the precipitation in mm of water, $h_{r,n}$, at the *n*-th day.

The probability of snowfall with increasing snow cover depth is estimated by checking the following conditions:

$$T_{min,n} < 5°C \ \wedge \ h_{r,n} \neq 0 \ \wedge \ P\big(snowfall(\bar{T}_{max,n}, \bar{T}_{min,n}) \mid prec\big) > R, \quad (5)$$

where $0 \leq R \leq 1$ is derived from the randomly generated number, modified with the hypercube latin sampling technique.

When conditions (5) are satisfied, the increase of the ground snow load $\Delta q_n$ at the *n*-th day is estimated in terms of water equivalent measured by the rain gauge:

$$\Delta q_n = 0{,}01 \cdot h_{r,n} \ \ kN/m^2 \ \ with \ h_{r,n} \ in \ [mm] \ . \quad (6)$$

At the $(n+1)$-th day, several alternative and mutually exclusive events can happen, with an associated probability of occurrence:

- if snowfall conditions (5) are satisfied again, the ground snow load $q_{n+1}$ is calculated as

$$q_{n+1} = q + 0{,}01 \cdot h_{r,n+1} \ kN/m^2 \quad (7)$$

- if snow melting conditions are satisfied, i.e.

$$P\big(snowmelt(\bar{T}_{max,n+1}, \bar{T}_{min,n+1}) \mid snowcover\big) > R \quad (8)$$

snow melts, partially or totally, being $R$ defined before: the melting is assumed to be proportional to the value of $\bar{T}_{max,n+1}$, so that the updated ground snow load becomes

$$q_{n+1} = q_n \cdot \left(1 - \left(\frac{T_{max,n+1}}{20}\right)\right) \ where \ 0°C \leq \bar{T}_{max,n+1} \leq 20°C \quad (9)$$

but, if $\bar{T}_{max,n+1} > 20°C$ or $q_{n+1} < 0{,}025 \ kN/m^2$ total melting is considered.

- if rainfall precipitation occurs in case of snow cover, the new ground snow load is given by

$$q_{n+1} = q_n + h_{r,n+1} \cdot 0{,}01 \ \ kN/m^2 \leq 1{,}25 \cdot q_n \quad (10)$$

but, if $q_n < 0{,}01 \cdot h_{r,n+1}$ total melting is considered.



**Figure 5.** Flow chart of the algorithm for the estimation of yearly maximum ground snow load

The Monte Carlo simulation has been repeated for all days of the year, in order to estimate the yearly maximum ground snow load, $q_{max}$. For each year, the process has been iterated 10'000 times: the median value of the distribution of each series has been taken as the best estimate of the maximum ground snow load for the examined year. Concerning the number of iterations, calibration exercises proved that $10^4$, $10^5$ or $10^6$ iterations give practically coincident results.

From the set of the $N$ yearly simulated maxima, the characteristic value $q_k$, associated to the probability of 2% to be exceeded in one year, has been finally derived, via extreme values analysis, as sketched in Figure 6.



Gumbel Probability Paper
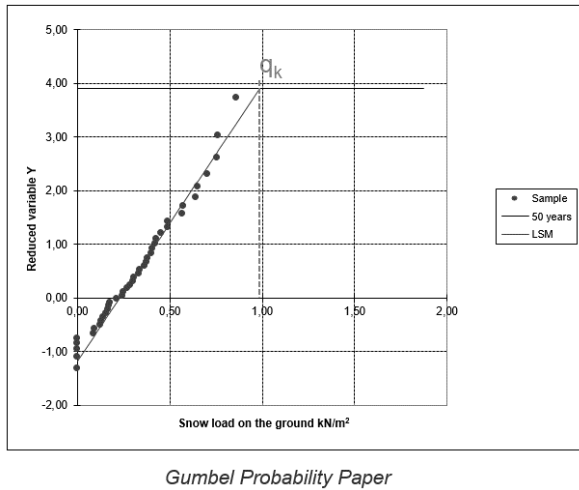
**Figure 6.** Characteristic value of ground snow load

## 4.3 Calibration of the model

The methodology illustrated above has been initially tested against the observed data series of nine Italian weather stations (Figure 7), where high quality daily data are available for long time series (more than 50 years).

These weather stations have been selected between the 125 Italian stations, whose data were collected in the Database of the University of Pisa during the European Snow Load Research Project (ESLRP) [7].

The results compared with those obtained by ESLRP (Table 1) show that the outlined procedure is very promising and allows not only to derive characteristic ground snow loads, but also to assess the effects on solid precipitation measurements of snow transport phenomena caused by wind (Figure 8) [18] through an appropriate parameter, $K_{corr}$.

The parameter $K_{corr}$, which is characteristic of each climatic area, takes into account the systematic errors of snow precipitation measurements at the rain gauge [19] [20] which are mainly due to wind field deformation above the gauge orifice (Figure 9), and depend on the wind speed, the intensity of precipitation and the type of the gauge [19].

## 4.3 Analysis of climate projections

Once performed the calibration of the procedure against registered data series, which allowed to estimate the

correction factor $K_{corr}$, the analysis has been extended to projected data series provided by different climate models (GCMs and RCMs) and different scenarios (RCPs) up to 2100. In particular, they have been used available high resolution data EUR11 (grid resolution of 12.5 km) developed within the EUROCORDEX initiative [21] [22] for the control period 1981-2005 (*Historical Experiment*) where "run" is forced by observed atmospheric composition changes[23] and for the future period 2006-2100 (*RCPs Experiment*) where "run" is forced by scenarios RCPs[23] illustrated in Table 2

The analysis has been carried out for subsequent time windows, each spanning over forty years; the obtained estimates of characteristic ground snow loads ($q_k$) are illustrated in Figure 10 for some of the nine tested Italian weather stations.



| Country | Station | LON [°] | LAT [°] | Altitude [m] | $q_{kESLRP}$ [kN/m²] |
|---|---|---|---|---|---|
| IT | Ascoli Piceno | 13,56 | 42,90 | 136 | 1,12 |
| IT | Bologna | 11,36 | 44,50 | 51 | 1,67 |
| IT | Castelnuovo Garfagnana | 10,43 | 44,12 | 276 | 1,14 |
| IT | Lodi | 9,51 | 45,32 | 80 | 1,19 |
| IT | Massafra | 17,13 | 40,58 | 116 | 0,54 |
| IT | Pesaro | 12,91 | 43,92 | 11 | 1,07 |
| IT | San Giuseppe Jato | 13,19 | 37,97 | 450 | 0,94 |
| IT | Spigno Monferrato | 8,36 | 44,55 | 476 | 2,40 |
| IT | San Severo | 15,39 | 41,68 | 87 | 0,74 |

**Figure 7.** Italian weather station used in the analysis

**Table 1.** Results of the algorithm for ESLRP data.

| Country | Station | Characteristic Ground Snow Load [kN/m²] | | $K_{corr} = q_k/q_{KESLRP}$ |
|---|---|---|---|---|
| | | Tested Procedure $q_k$ | ESLRP [7] $q_{kESLRP}$ | |
| IT | Ascoli Piceno | 0,68 | 1,04 | **1,53** |
| IT | Bologna | 0,99 | 1,66 | **1,68** |
| IT | Castelnuovo Garfagnana | 1,14 | 1,20 | **1,05** |
| IT | Lodi | 0,76 | 1,20 | **1,58** |
| IT | Massafra | 0,16 | 0,54 | **3,38** |
| IT | Pesaro | 0,67 | 1,07 | **1,60** |
| IT | San Giuseppe Jato | 0,50 | 1,21 | **2,42** |
| IT | Spigno Monferrato | 0,88 | 2,55 | **2,90** |
| IT | San Severo | 0,46 | 0,80 | **1,74** |
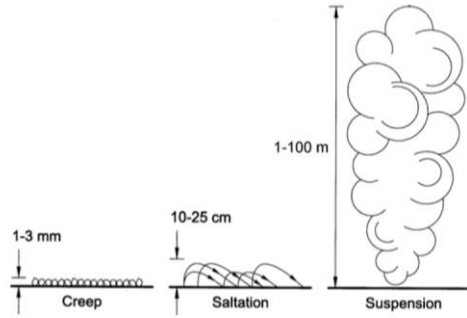
**Figure 8.** Snow transport phenomena [18]
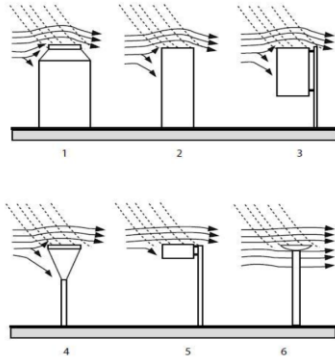


**Figure 9.** Wind field deformation at the rain gauge [14]

**Table 2.** Climate models and scenarios

| RCM | Resolution | Driving GCM | Driving Experiment | Period |
|---|---|---|---|---|
| DMI-HIRHAM5 | EUR11 (0,11°≈12.5km) | EC-EARTH | Historical | 1981-2005 |
| | | | RCP4.5 | 2006-2100 |
| | | | RCP8.5 | 2006-2100 |
| CNRM-ALADIN5.3 | EUR11 (0,11°≈12.5km) | CNRM-CM5 | Historical | 1981-2005 |
| | | | RCP4.5 | 2006-2100 |
| | | | RCP8.5 | 2006-2100 |
| KNMI-RACMO22E | EUR11 (0,11°≈12.5km) | HadGEM2-ES | Historical | 1981-2005 |
| | | | RCP4.5 | 2006-2090 |
| | | | RCP8.5 | 2006-2100 |

Finally, to assess the variability of climate models and scenarios, for the nine investigated stations the characteristic values of ground snow loads associated to different scenarios ($q_{kRCP4.5}$ and $q_{kRCP8.5}$) have been compared, adopting different climate models.

Considering 40 years intervals shifted by 10 years, the ratio between $q_{kRCP8.5}$ and $q_{kRCP4.5}$ has been determined for the period 1981-2100, obtaining the trends shown in Figure 11.

The results show a general decrease of characteristic snow loads for the investigated stations, but the expected decreasing trend of the ratio $q_{kRCP8.5}/q_{kRCP4.5}$, namely a more marked decrease of snow loads linked to increasing emissions, is not confirmed for all of them.
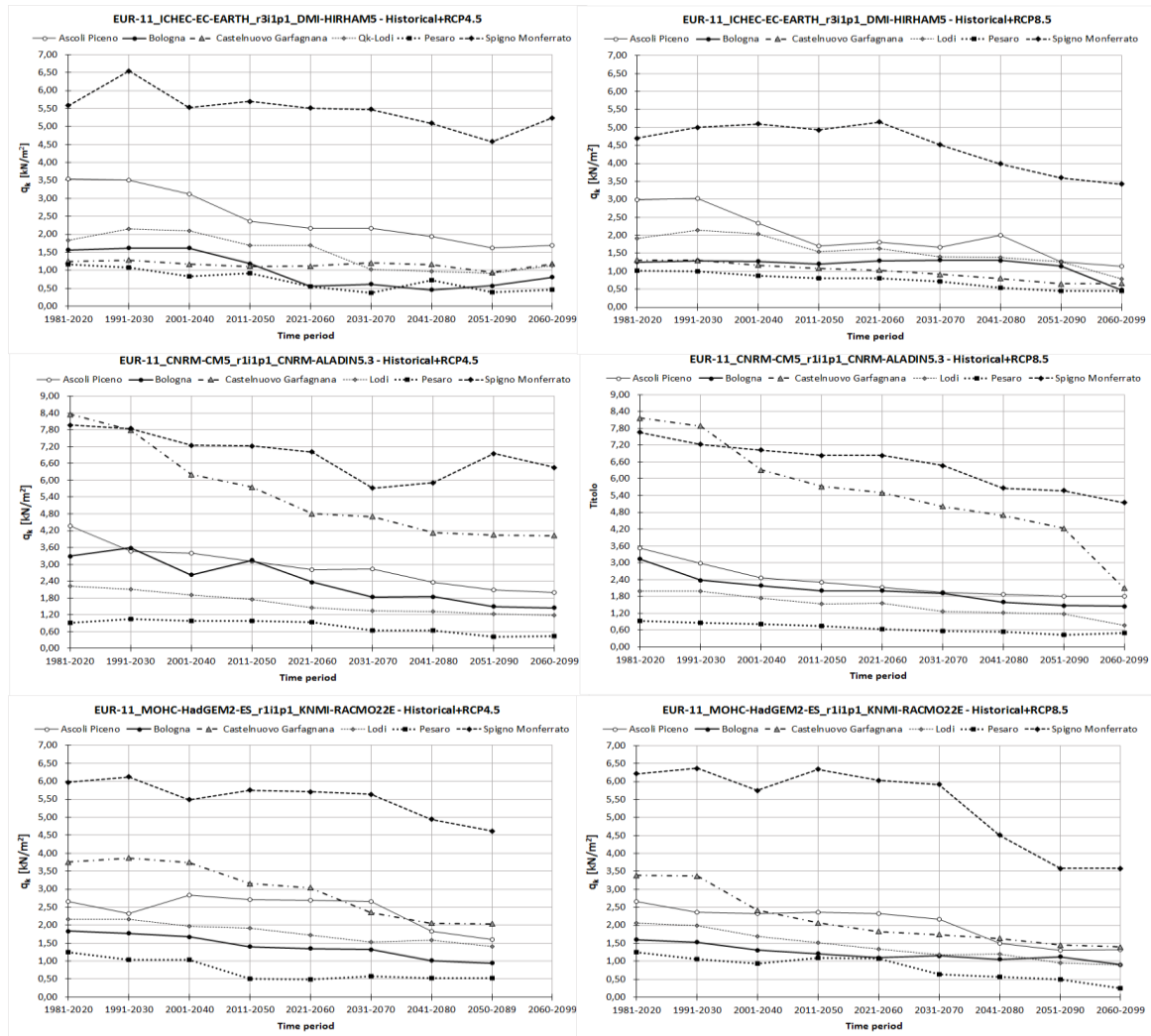


**Figure 10.** Future trends of $q_k$ [kN/m$^2$] for different climate models and scenarios
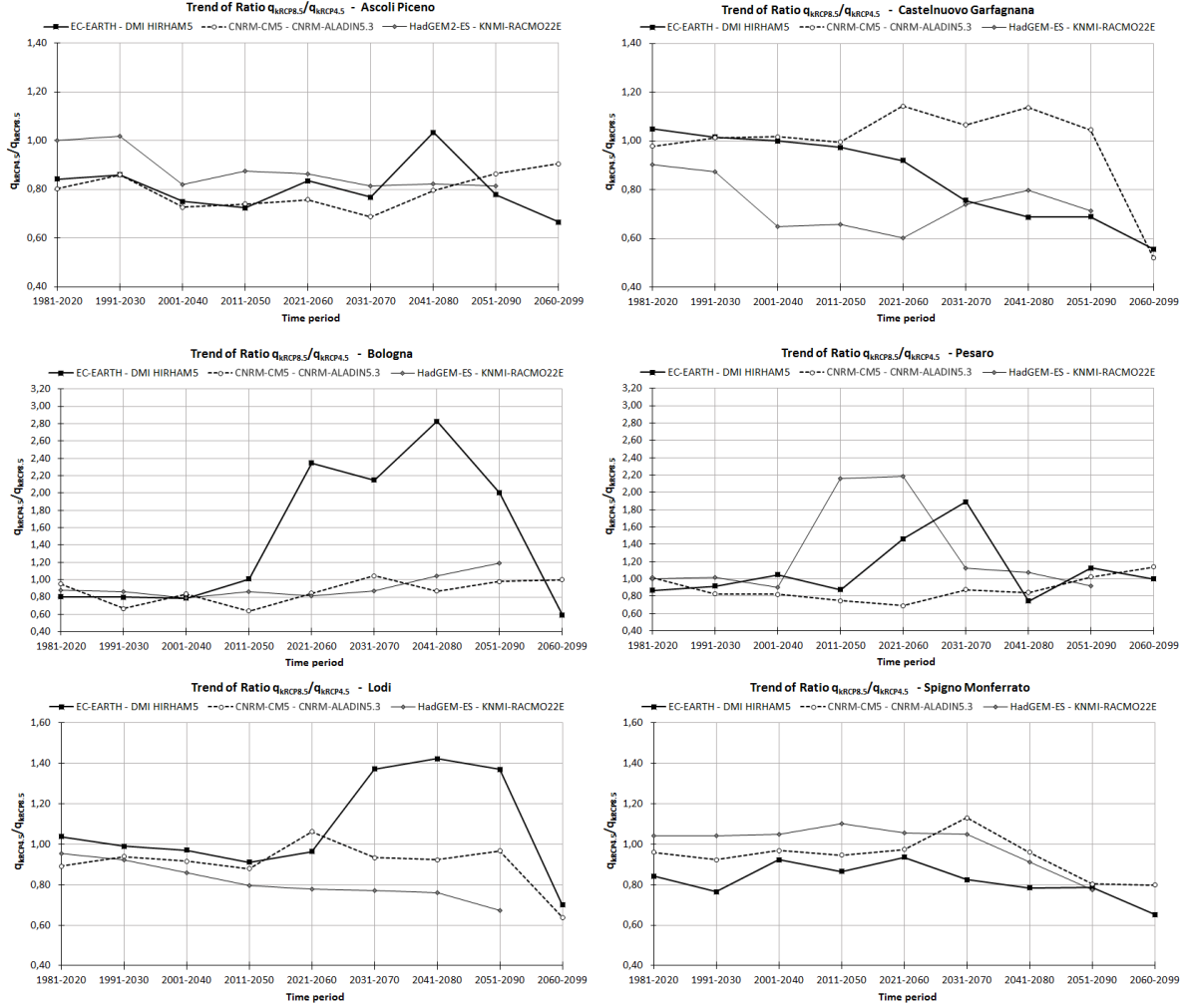
**Figure 11.** Trend of the ratio between $q_{kRCP8.5}$ and $q_{kRCP4.5}$ for different climate models and different stations

# 5 Preliminary results on snow map comparison

The proposed procedure seems very appropriate for creation of snow maps taking into account the effects of climate change, since it allows to estimate characteristic ground snow loads on the basis of daily data for the minimum and maximum temperature and precipitation, which are typically available as outputs of climate change projections for all possible scenarios.

Then, extending the previous analysis to a larger number of weather stations it is possible to obtain enough local information to update snow maps. The updated versions of the maps, critically compared with the current versions, will provide so a comprehensive overview of the impact of climate change, according to various RCPs scenarios [4].

However, before arriving to obtain consistent snow maps, further calibration is needed.

Indeed, climate projections are provided, in the higher resolution models, for cell of about 12,5×12,5 km (EUR11 - 0,11° on a rotated grid) and are generally agreed to represent area averaged data rather than point

process data, especially for precipitation data [24]. Therefore, the analysis of gridded precipitation data can lead to an underestimation of extremes [24] [25].

## 5.1 Comparison of observed gridded data and observed point data

In order to assess a calibration method for the analysis of gridded datasets, able to correct the underestimation of extremes, the above mentioned issue has been especially studied for Italy, comparing characteristic ground snow loads obtained using grid cell data (E-OBS dataset) with those obtained by the European Snow Load Research Project (ESLRP) for the Mediterranean region [7]. In Figure 12, the location of the Italian weather stations considered in ESLRP is reported on the grid cell map of E-OBS.

The results confirm that characteristic values computed by the analysis of gridded data are typically lower than values obtained by point-data and that the difference

$$\Delta q_k = q_{kESLRP} - q_{kEOBS} \tag{11}$$

generally increases with the site altitude (Figure 13).

Starting from these results, a regression analysis has been carried out and a relationship between the difference of characteristic values $\Delta q_k$ and altitude above the sea level $A$ has been estimated as

$$\Delta q_k = a \cdot \left[ 1 + \left( \frac{A}{b} \right)^2 \right] \frac{kN}{m^2} \text{ with A in [m]} \qquad (11)$$

where the parameters $a$ and $b$ have been calculated for each one of the four climatic zones defined by EN1991-1-3 for Mediterranean region in Italy obtaining the curves illustrated in Figure 14, 15 and 16. As in zones 3 and 4 the amount of available data is limited, the zones themselves have been merged.
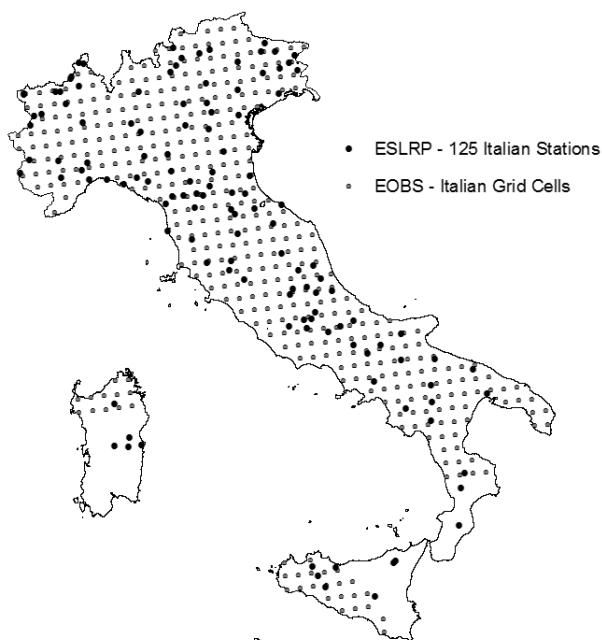


**Figure 12.** EOBS – Grid Cells and ESLRP weather stations for Italy
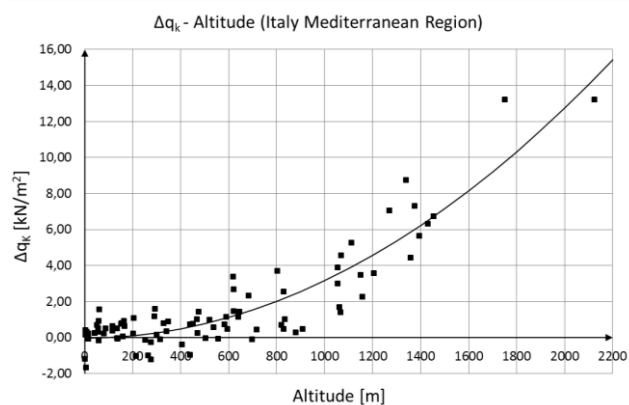


**Figure 13.** $\Delta q_k$– Altitude (Italy - Mediterranean Region)

Once these relationships are available, it is possible to draw, according to the results obtained by the analysis of gridded data, the snow load map on the ground, corrected in such a way that the data are referred to the sea level. This correction is very important because it allows to evaluate also results obtained for characteristic ground

snow loads by the investigation of projected data with respect to the current code's previsions. (Figure 17).

Then, the next step will be the analysis of projected data, provided by different climate models, in order to derive maps of future trends of characteristic ground snow loads.

## 5.2 Actual trend of variation of ground snow load

Before the study of projected data, EOBS gridded data for Italian region have been analysed for subsequent time periods of thirty years in order to estimate both the actual trend of variation of characteristic ground snow loads and its future evolution.

The results are illustrated in Figure 18 and show different trends for Italian regions.
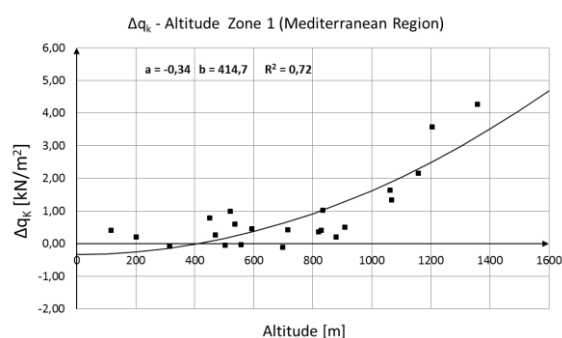


**Figure 14.** $\Delta q_k$ -Altitude (Italy - Mediterranean region - zone 1)
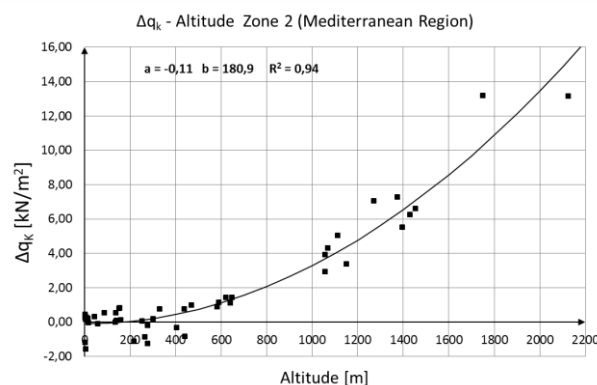


**Figure 15.** $\Delta q_k$– Altitude (Italy Mediterranean region-zone 2)
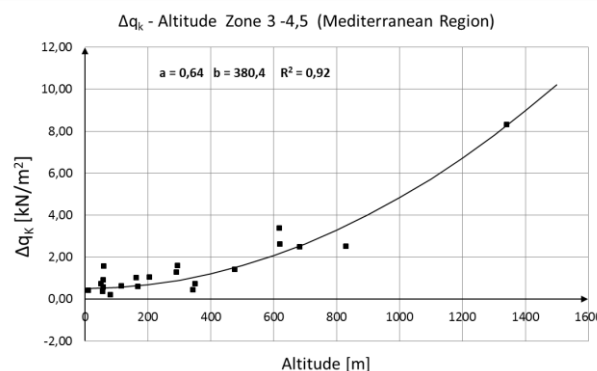


**Figure 16.** $\Delta q_k$–Altitude (Italy Mediterranean region-zones 3-4)
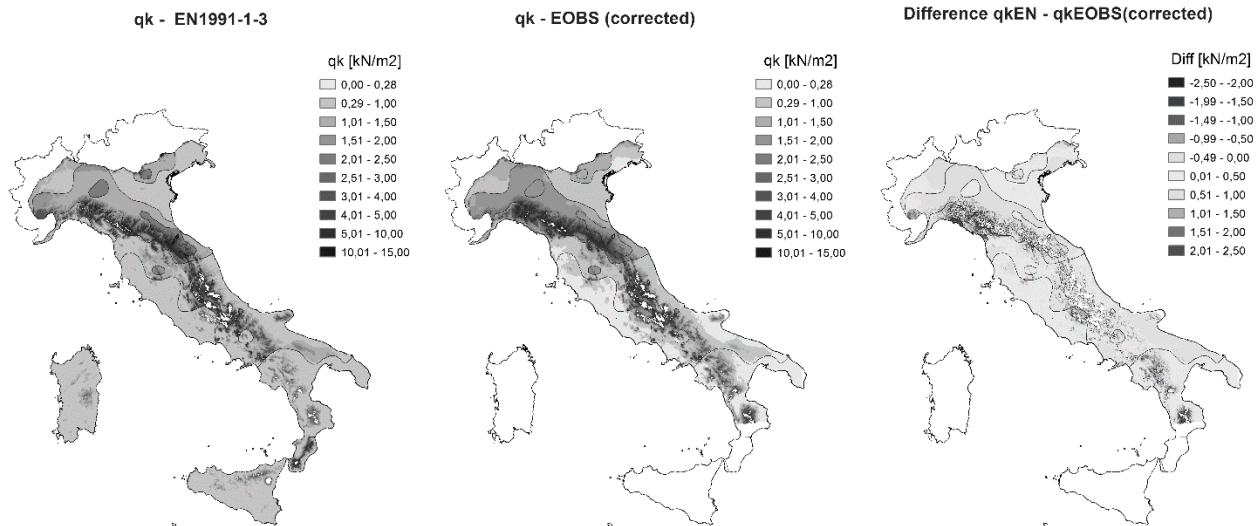
**Figure 17.** Comparison of Snow Load Map of EN1991-1-3 and Snow Load Map obtained using EOBS data corrected with altitude relationship
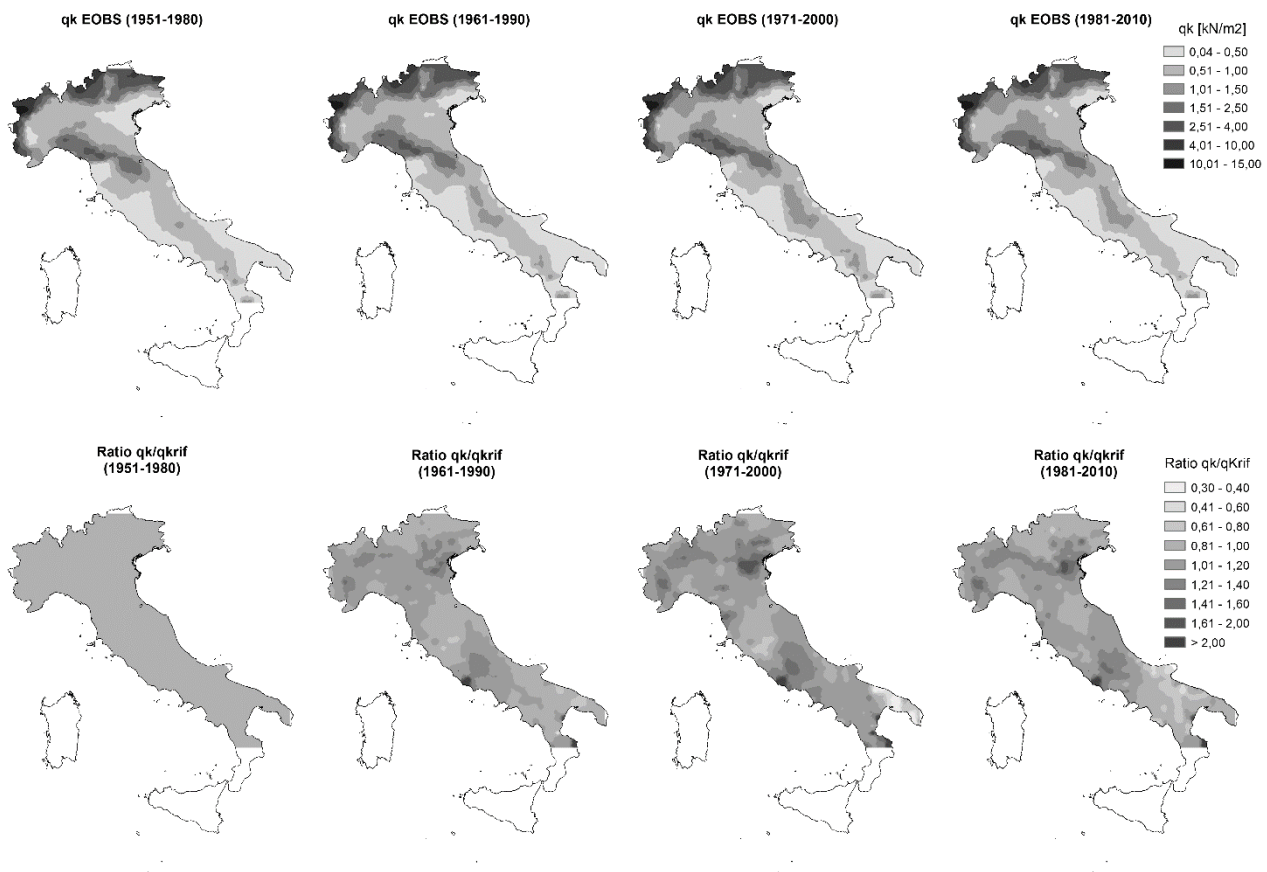


**Figure 18.** Snow load maps obtained using different periods of EOBS data

# 6 Conclusions

Implication of climate change on snow loads could have very high impact on design of structures as well as in assessment of existing ones. The problem is very relevant as it is demonstrated by a high number of structural collapses of lightweight structures due to snow.

For this reason, the setup of a suitable procedure to predict the snow load on ground according to various climate change scenarios could represents a very strong improvement in definition and adaption of snow load maps. This issue is particularly relevant in Europe, also in view of the development of future generation of Eurocodes.

Aiming to tackle this relevant issue, a general procedure to evaluate future trends of ground snow loads

for structural design, taking into account the influence of climate change is proposed, based on Monte Carlo method.

The procedure, starting from the analysis of historical meteorological observations, allows to estimate ground snow loads and their characteristic values, on the basis of daily outputs of climate models, which are typically available (daily temperature extremes $T_{max}$, $T_{min}$ and height of precipitation $h_r$).

The preliminary implementation of the outlined procedure is very promising and shows that there is a concrete possibility to arrive to define a general methodology for the estimate of characteristic snow loads on ground, according to prediction derived from climatological models, also on a local scale. Since the presented methodology seems to be able to appreciate the evolution of the snow load during the time, it should also allow proper refinement and updating of the snow load maps, according the real trends.

Extending the analysis to predicted data series covering a large enough number of weather stations across Europe, it will be possible to compare the future trends of snow loads, for each available emission scenario, with the current European snow load maps, assessing their evolution and their impact on structural design, in line with the requests by the European Commission to CEN in Mandate M515 within the European adaptation to climate change policy, in view of the development of the second generation of Eurocodes.

## References

1. U. Strasser, Natural Hazard and Earth System Science, **8,** p.1-8 (2008)
2. H.T.T. Tayet, H.O. Hygen and T. Kvande., EMS 2013-230, **10** (2013)
3. CAN/CSA - S502-14 - *Managing changing snow load risk for building in Canada's North* (2014)
4. UNI EN 1991-1-3:2004 – Eurocode 1: Actions on structures – Part 1-3: General Actions – Snow Loads
5. M/515 EN - *Mandate for amending existing Eurocodes and extending the scope of Structural Eurocodes* (2012)
6. CEN/TC250 - *Response to Mandate M/515 - Towards a second generation of Eurocodes* (2013)
7. DGII-D3 - Scientific support activity in the field of structural stability of civil engineering works. Snow loads - FINAL REPORT (1996)
8. <http://climate.nasa.gov/evidence/>
9. European Environment Agency, *Climate Change, impacts and vulnerability in Europe* - EEA report n°12 (2012)
10. European Commission, *An EU strategy on adaptation to climate change* -COM 213 Final report (2013)
11. WG1AR5-IPCC, *Climate change 2013 – The physical Science Basis* -
12. D. P. Van Vuuren, J. Edmonds, M. Kainuma et al., Climatic Change, **109,** 5-31 (2011)
13. European Commission, *Adapting infrastructure to climate change* -SWD 137 Final report (2013)
14. J. Geis, K. Strobel and A. Liel, Journal of Performance of Construction Facilites, **26(4)**, 377-388(2012)
15. E. Früwald, E. Serrano, T. Toratti, et al., *Report TVBK-3053,* Lund University, Lund (2007)
16. M. Holicky, Engineering Sciences, **58,** 51-57 (2007)
17. M. Holicky and M. Sykora, Forensic Engineering, 2009:444-453
18. M. Mellor, Cold Regions Science and Egineering Part III, Section A3c (1965)
19. B.E. Goodison, P.Y.T. Louie and D. Yang, WMO/TD N872 (1998)
20. A. Lendvai, R. Ranzi, G. Peretti et al., AINEVA-Neve e Valanghe, **84**, 12-21 (2014)
21. D. Jacob, J. Petersen, B. Eggert et al., Reg Environ Change, **14**, 563-578 (2014)
22. S. Kotlarsky, K. Keuler, O.B. Christensen et al., Geoscentific Model Development, **7**, 1297-1333.
23. K.E. Taylor, R.J. Stouffer and G.A. Meehl, Bulletin of American Meteorological Society, **April 2012**, 485-498.
24. M.R. Haylock, N. Hosfra, A.M.G. Klein Tank et al., Journal of Geophysical Research, **113**,D20119 (2008)
25. E. C. Mannashardt-Shamseldin, R. L. Smith, S. R. Sain et al., The annals of Applied Statistics, **4**, 484-502 (2010)

# European snow load map – past and present

Jerzy Antoni Żurański[,1] and Grzegorz Kimbar[1a]

[1]*Instytut Techniki Budowlanej, ul. Filtrowa 1, 00-611 Warszawa, Poland*

**Abstract.** For few decades there has been a natural trend for harmonization of structural codes in the regional and global scales. An example of this trend is the elaboration of Eurocodes. One of the main items in the Eurocode for snow actions is a common map of the ground snow load in Europe. The paper deals with old values of the ground snow load in the Central Europe as well as the present state and use of maps given in Annex C to the Eurocode 1. It is stated that the present European maps of snow loads have been used in limited range. An attempt is made to explain the reason of such situation and to present possible further works.

## 1 Introduction

The extensive work was done to elaborate European maps of snow loads when preparing the Eurocode for snow loads in the frame of the European Committee of Standardisation (CEN) [6]. On the base of data from 18 countries eight snow load regions were established, crossing the borders of countries. Results of the work in the form of maps and dependence of the snow load on the ground on the altitude above sea level constitute the Annex C to the Eurocode for snow loads [1]. Fifteenth or even more years later it would be useful to review how they have been used in practice. Another purpose of the paper is to summarize the gained experience and to plan further works. They are necessary because during the time which has gone the new countries have joined the European Committee for Standardisation.

## 2 Old values of snow load in Europe

For a long time snow load, which has to be taken into structural calculations, have been established on the base of everyday, winter weather observations. An example of such an approach can be found in the book by Thullie [7]: "*In our countryside snow layer on roofs is usually not higher than 0.6 m. Taking this value and assuming that snow is approximately 8 times lighter than water is, we receive [...] a round value of snow load 80 kg/m²*". It was rounded from 75 kg/m² (0.75 kN/m²) and it is worth to mention that this value has been used in Central Europe for many years, even until II WW. It should be also pointed out that it was the value of snow load on flat roofs. Similar approach was reported by Holzer in his historical article [3].

Probably two turning points of snow load definition in Europe can be seen: the first − just after the II WW and the second one − 50 years later when the Eurocode for snow load was elaborated. These two turning points show three periods in the history of snow load maps in Europe: before IIWW, after it and since the elaboration of Eurocodes.

Above mentioned value, recommended in XIX century, was applied in several countries of Central Europe to the end of II WW. Next a distinct difference was seen: in the Central − East European countries dominated by the former Soviet Union snow load values were established according to the Soviet code. The snow load values in that code were smaller than older ones in subordinated countries. For example in former German Democratic Republic the value of $0.5$ kN/m² [8] was much smaller than $0.75$ kN/m² in Germany, still in force in Federal Republic of Germany in 1976 [1]. In Polish standards snow load for the first zone, the majority of territory, was successively diminished from $0.8$ kN/m² established before II WW to $0.5$ kN/m² in 1960s [11]. By the end of 1970s this value was identified as having only 5 year return period. In other countries were maritime climate occurs, e.g. in France, lower values were usually applied. Two categories were distinguished: normal and exceptional snow loads [6].

In early codes and recommendations, as mentioned above, there was no difference between snow load on flat roofs and on the ground. Probably the first such a difference was introduced in the ISO standard [5] based on the Canadian experience. In 1970s the probabilistic analysis was undertaken, which was influential for snow load values in European countries by the end of XX century.

## 3 Snow load maps in Eurocode

For snow load map to the Eurocode a new approach was applied, proposed by Gränzer [3].[4] As a result the Annex C to the Eurocode 1 was elaborated [2] [8].
On the base of data from 18 countries eight snow load regions were established, crossing the borders of countries. Values of the snow load on the ground were reduced to the sea level and given also as a function of the snow zone number. Results of the work in the form of maps and parabolic dependences of the snow load on the

---

[a] Corresponding author: g.kimbar@itb.pl

ground on the altitude above sea level constitute the Annex C to the Eurocode for snow loads [2].



**Figure 1.** Base snow load values in zones according to combined national anexes in Alpine region.



**Figure 2.** Base snow load values in zones according to Appendix C of [1] in Alpine region.

## 4 Present uses of snow load maps

Eighteen National Annexes to the Eurocode for snow loads and two separate maps are now available from the following countries: Belgium, Czech Republic, Denmark, Finland, France, Germany, Holland, Iceland, Italy, Lithuania, Luxembourg, Poland, Romania, Slovakia, Spain, Sweden, Switzerland and UK (together with a map of Ireland). Among them Czech Republic, Iceland, Lithuania, Poland, Romania and Slovakia were not taken into account when preparing maps of snow regions to the Eurocode.

Maps given in Annex C to the Eurocode for snow action have been conceived as a helpful material for national code-writers. However, the use of these maps is rather limited (Fig. 1 and 2). The snow load zones in National Annexes differ from these given in Eurocode. Only in two countries zone numbers are explicitly introduced into the formula for characteristic value of snow load, in the UK and Ireland.

In three countries (Germany, Italy and Switzerland) the parabolic formula for the dependence of snow loads

on altitude is used, according to recommendations in Annex C. In other countries linear dependence is used.

Almost in all countries the minimum value of altitude is given. Below this altitude the value of snow load is constant. It seems that detailed dependence of snow load on low altitudes is not preferable. These minimum values range from 100 m to 400 m, even to higher altitudes in some places (as in Romania). Differences in approaches to the snow load value become clearly visible at administrative borders. Different base values and altitude formulae can result in step difference on borders even by a factor of two (example on Figure 3).

Hence, it may be stated that the present European maps of snow loads has been accepted in limited range.

The question arises – why? It may be said that probably the main reason is the devotion to the traditional approaches in particular countries. Another question arises: how to improve this situation and to harmonise national maps with neighbours?



**Figure 3.** Characteristic ground snow load on the Germany-France border according to national anexes of [1].
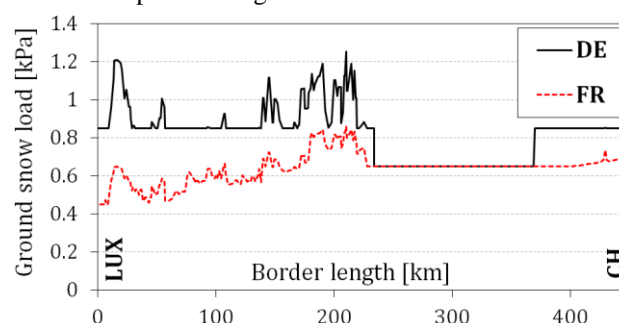
## 5 Harmonisation of European snow loads

The first step may be a short comparison of snow loads at borderline between several countries in Central West and Central East Europe. Results are presented in the Table 1

As it can be seen there are discrepancies between snow loads at borderlines in particular countries. Only in one case there is the same value, 0.65 kN/m$^2$: in French zone C1 and German zone 1, however, for different altitudes, 200 m in France and 400 m in Germany. If altitude is 400 m, the same in both countries, then snow loads are different, 0.85 kN/m$^2$ in France and 0.65 kN/m$^2$ in Germany (Fig. 3). It would be desirable that harmonization would be possible on the base of bilateral agreements between neighbouring countries. As en example of harmonisation of snow load may serve a map of snow loads in Poland and its eastern neibourgs (Figure 4). However, it should be told that snow load zones of Polish eastern neighbours were harmonised with others on their own accord. Finally, it has not be the harmonisation with the same values of snow loads. It would be sufficient if the valuse would differ not much.

**Table 1**. Snow loads along borderlines in Central West and Central East Europe

| Country | $A_{min}$, m | $s_k$ | $s_k$ | $A_{min}$ | Country |
|---|---|---|---|---|---|
| Belgium | 100 | 0.5 | 0.45 | 200 | France |
| Belgium | 100 | 0.5 | 0.65 | 200 | France |
| Belgium | 200 | 0.62 | 0.45 | 200 | France |
| Belgium | 200 | 0.62 | 0.65 | 200 | France |
| Belgium | 100 | 0.50 | 0.85 | 285 | Germany |
| Belgium | 285 | 0.72 | 0.85 | 285 | Germany |
| Belgium | as above | as above | 0.70 | Not given | Holland |
| France A1 | 200 | 0.45 | 0.85 | 285 | Germany z.2 |
| France B1 | 200 | 0.55 | 0.85 | 285 | Germany z.2 |
| France C1 | 200 | 0.65 | 0.85 | 285 | Germany z.2 |
| France C1 | **200** | **0.65** | **0.65** | **400** | Germany z.1 |
| France C1 | **400** | **0.85** | **0.65** | **400** | Germany z.1 |
| Denmark | All | 0.90 | 0.85 | 285 | Germany |
| Germany z.1 | 400 | 0.65 | 0.70 | Not given | Holland |
| Germany z. 2 | 285 | 0.85 | 0.7 | 300 | Poland z.1 |
| Germany z. 2 | 285 | 0.85 | 0.9 | 300 | Poland z.2 |
| Germany z.3 | 255 | 1.10 | 0.7 | 300 | Poland z.1 |
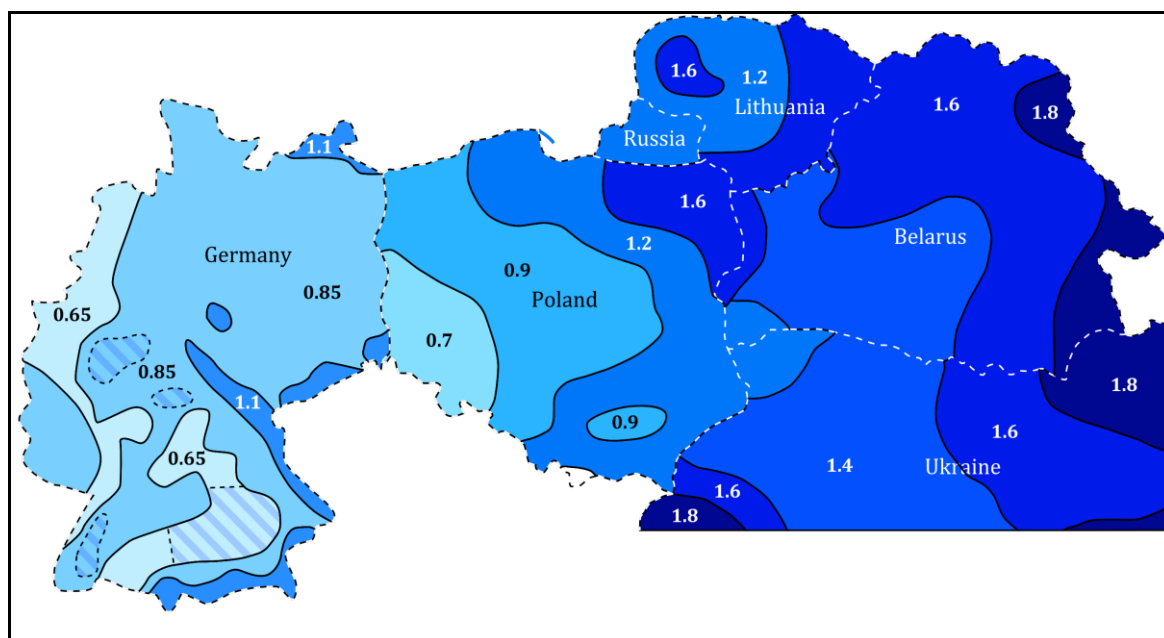


**Figure 4**. Map of the characteristic values of snow load on the ground in Poland and its neighbours

# 6 Climate change and snow load

It may be stated that all predicted values of snow load in Europe have been calculated on the base of data measured during last several decades. These elaborations have been done with silent assumption about constant and the same climatic conditions in the past and in the future. Now a question arises how to take onto account the possible climatic change. A simplest answer would be: to look at the annual run of data. An example is shown in Figure 5. If the data from 1950/51 to 1994/95 are taken into account the decreasing of snow load is obvious.
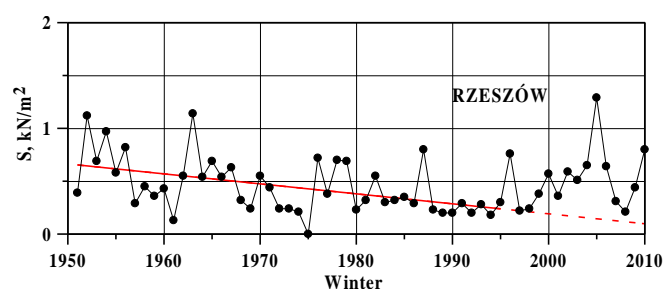


**Figure 5**. Annual run of the yaerly (winter) maxima of the ground snow load at meteorlogical station Rzeszów Jasionka (Poland).

Based on this period of observation one may come to the conclusion that in 2019 there will be no snow in Rzeszów. However, the maximum value from the period 1950 – 2010 was measured in 2005.

This example is unique from Poland. At other meteorological stations there are different trends of annual run of snow, increasing or decreasing of the annual maxima snow load but not so defined as in Rzeszów in 1950 – 1995. The main conclusion which may be drawn is that longer period of observation is necessary for a forecast of the influence of climate change on the structural snow loads.

# 7 Concluding remarks

Initial simplistic European approach to snow load value was substantially enhanced in the course of XX century with a vast body of field measurements and use of statistical methods. This approach found its most recent conclusion in formulation of Annex C to the Eurocode 1. The aim of this document was to provide national regulatory bodies with guidance in the process of preparing local snow load maps, and by this mean to promote harmonisation in the CEN member countries. Nevertheless, the adoption of this document happened to be sparse. This situation yields inconvenient and irrational inconsistencies, especially at borders as well as complicates usage of the Eurocode 1 on an international level. Improvement of this state of affairs is at hand, because apparently there are no fundamental obstacles other than local customs persisting in the engineering community. The question remains if the advantage of harmonisation is worth breaking those already established customs.

# References

1. EN 1991-1-3:2003 Eurocode 1 – Actions on structures. – Part 1-3: General actions – Snow load
2. M. Gränzer, Zur Festlegung der rechnerischen Schneelasten. „Bauingenieur", 58 (1983) 1-5
3. M. Gränzer, New ground snow loads for a European standard. Proc. of the Fourth Int. Conf. on Snow Engineering, Balkema (2000)
4. S. M. Holzer, Kleine Geschite der Schnee- und Windlast im 19.Jahrhundert, Bautechnik 83, no 11, (2006)
5. ISO 4355 :1980 Basis for design of structures – Determination of snow loads on roofs (1980)
6. Régles definissants les effets de la neige et du vent sur les constructions et annexes (Régles NV 65 révisées 1967 et annexes), Paris (1968)
7. L. Sanpaolesi, Scientific support activity in the field of structural stability of civil engineering works. Snow loads. Final Report. University of Pisa, September (1999)
8. TGL 32274/05 Lastannahmen für Bauwerke. Schneelasten. DDR, Berlin 1976
9. M. Thullie, Handbook of building static for engineers, architects and students (in Polish), Lwow (1886)
10. J.A. Żurański, Snow Loads on Roofs in East European Standards and Codes of Practice. - First International Conference on Snow Engineering, Santa Barbara 1988, CRREL Special Report 89-6, 1989
11. J.A. Żurański, A.Sobolewski, Snow loads in Poland (in Polish). Instytut Techniki Budowlanej, Warszawa 2009

# Some ongoing researches to improve codified structural design under snow loads in China

Feng Fan[1, 2, a], Huamei Mo[1], Qingwen Zhang[1, 2], Guolong Zhang[1] and Mengmeng Liu[1]

[1]School of Civil Engineering, Harbin Institute of Technology, Harbin, 150090, China
[2]Key Lab of Structures Dynamics Behavior and Control of the Ministry of Education (Harbin Inst. of Tech.), Harbin, 150090, China

**Abstract.** Roofs in cold regions with heavy snowfalls could experience unbalanced or non-uniform snow loads caused by snow drifting or sliding, this could cause significant damage or collapse to the roof. The unbalanced snow load patterns recommended by the Chinese design code are originally based on that for Union of Soviet Socialist Republics (USSR) and have been calibrated several times, but documents to support such codifications are unclear. Besides, the provisions are mainly specified for regular-sized roofs but not long-span roofs. With the growing of applications of long-span roofs in recent years in China, there are practical demands for investigations of unbalanced snow loads on them since such investigations are rarely available. Therefore, an investigation of the unbalanced snow loads on roofs, especially for long-span roofs, is warranted. This paper summarizes some of the research activities on this subject at Harbin Institute of Technology (HIT), including statistics analysis of meteorological data, at-site measurements of snow depth and snow density on flat roofs, wind tunnel tests of model buildings, as well as numerical simulations of snowdrifting. Some of the works that are to be conducted in the near future are also presented and discussed.

## 1 Introduction

Snow load, which is usually unbalanced under the action of wind, is one of the dominant live loads that should be considered carefully in the structural design for buildings in cold regions with severe winter climate, especially for long-span roofs, which are sensitive to unbalanced loads. Heavy snow loads have caused failures of roof structures for many buildings; a very pathetic example of such failures is the collapse of the Katowice Fair Building in Poland, which caused 65 fatalities and 130 injuries [1].

The unbalanced snow load patterns for regular roofs are specified by the Chinese Load Code for the Design of Building Structures (GB 50009-2012) [2]. However, the provisions in the earliest version of this code (published in 1954) were based on that for Union of Soviet Socialist Republics (USSR). Although the specifications have been calibrated for 5 times since then (in 1958, 1974, 1987, 2001 and 2012, respectively), documents supporting such calibrations are rarely available.

Besides, the specifications for unbalanced snow load patterns in the code are mainly for roofs with regular sizes but not for long-span roofs. As one can imagine, the wind field around the long-span roofs may differ from that for regular-sized roofs, which will result in different patterns of unbalanced snow loads. On the other hand, with the growing of economy and societal needs, many structures with long-span roofs such as airport terminals, railway stations, stadiums and exhibition halls have been constructed in China in recent years. The safety of these structures are of public concern since the buildings' costs are usually high and, more importantly, the number of people accommodated by these buildings is relatively large, many fatalities could be caused in the case of roof collapses.

Consequently, it's of great interests for one to investigate the distribution of snow loads on roofs, especially for long-span roofs, to improve the codified structural design under snow loads in China. Previous studies in recent years have conducted some related investigations on this subject [3-5], but their investigations were mainly focused on specific buildings, which may not be applicable other buildings. Therefore, a more general study is expected.

Techniques for investigations of roof snow loads include at-site measurements, wind tunnel tests (or water flume tests) and numerical simulations. For sloped roofs, however, at-site measurements are usually unrealistic because of the danger of operating on the wet, slippery roof in a freezing and windy environment, and that remote measurements are not always available. When real snow particles are not available, wind tunnel tests can be considered only for flat roofs as well, because model particles, such as silica sands, can hardly stay on sloped roofs, which is not the case for the real non-disturbed snow. Tests carried out in climatic wind tunnel where temperature is controlled, such as those described by [6, 7], is not always available. In this context, numerical simulation techniques become prior to the other two approaches in the investigation, although the validity of the numerical model should firstly be verified based on at-site measurements and/or wind tunnel tests before its application.

In this paper, some of the research activities on the investigations of unbalanced snow loads on roofs at Harbin Institute of Technology (HIT, Harbin, China) are summarized, these include statistics analysis of meteorological data, at-site measurements of snow depth and snow density on flat roofs, wind tunnel tests of snowdrift around model buildings, as well as numerical simulations of snowdrifting. Some of the works that are to be conducted in the near future is also presented and discussed.

---

[a] Corresponding author: fanf@hit.edu.cn

## 2 Ongoing research programs focused on snow loads at HIT

### 2.1 Statistics analysis of meteorological data

Ground snow load is the basis for calculation of roof snow loads in design codes. It's indicated that insufficient code provisions are one of the main observed causes of structural damage [8]. Consequently, accurate estimation of ground snow load is of important significance for the design of roof snow loads.

Basic ground snow load in the Chinese design code [2] is defined as the 50-year return period value of annual maximum ground snow load. As stated by the code, the annual maximum ground snow load is modelled as a Gumbel variate in the analysis of extreme ground snow load in China; and that annual maximum snow depth with a regional average snowpack bulk density is used to estimate the extreme ground snow load when measurements of ground snow load are not available [2]. However, no document is available to detail the estimation process of the recommended basic ground snow load in the code. To possibly improve the specification of basic ground snow load in China, meteorological data including snow depths and ground snow loads are collected from local meteorological agencies. Also assembled are surface wind speeds, precipitation and air temperature. Information for above mentioned meteorological data is summarized in table 1.

**Table 1.** Information of collected meteorological data

| Variable | No. of stations | Time periods | Measurement frequency |
|---|---|---|---|
| Ground snow depth | 734 | 1951-2010 | Daily |
| Ground snow load | 733 | 1999-2008 | 5-daily |
| Wind velocity | 839 | 1951-2013 | Daily |
| Precipitation | 839 | 1951-2013 | Daily |
| Air temperature | 839 | 1951-2013 | Daily |

With these data available, several topics could be discussed. Studies that are being conducted by the authors and being considered to be conducted in the near future include the probabilistic distribution model of annual maximum ground snow depth, estimation of regional average snowpack bulk density, and relation between snow density and environmental variables such as air temperature and precipitation.

### Probability model for annual maximum snow depth

As mentioned above, the annual maximum ground snow load (or snow depth) is modelled as a Gumbel variate in the Chinese design code [2]. This is consistent with the practice in Canada [9, 10], Europe [11, 12], and in Japan [13, 14] (the Gumbel distribution is fitted only to the upper 1/3 of all the data plotted on Gumbel probability paper in Japan). However, Log-normal distribution is adopted to estimate the extreme ground snow water equivalent (SWE) in the US [15, 16]. The inconsistency of adopted probability model for annual maximum snow load (or SWE, or snow depth) is likely due to the different climate conditions in different regions. An analysis of annual maximum ground snow loads for a northeastern province in China showed that, when compared to Gumbel distribution, Log-normal distribution is preferred for most of the stations in that province [17]; this is inconsistent with the recommendation in the Chinese design code. Considering this inconsistency and the availability of up to 60 years of daily ground snow depth data for more than 700 stations nationwide, it is of great interest for one to examine the preferred probability model for annual maximum snow depth in China.

Preliminary investigation shows that among 330 considered stations, Log-normal distribution is preferred by 186 of them, and that Gumbel is preferred by the remaining 144 stations. This could be clear evidence that if a single probability model should be used in the analysis of extreme ground snow load, Log-normal distribution seems to be the better choice. Further investigation is needed to verify this finding and to evaluate the influence of switching the probability model from Gumbel to Log-normal on the estimated 50-year return period value of annual maximum ground snow load.

### Snowpack bulk density

Snowpack bulk density is a random variable with significant variability [15], it's a complex function of snow depth, snow temperature, snow deposition history, and the initial density of the individual snow layers [18]. Attempts had been made by [18] to relate the snowpack bulk density with snow depth, snow age, and snow classes, where snow classes has taken into account the effects of climate (temperature and wind), the relation is written as [18]:

$$\rho_b = (\rho_{max} - \rho_0)[1 - \exp(-k_1 \cdot h - k_2 \cdot DOY)] + \rho_0 \qquad (1)$$

where $\rho_{max}$, $\rho_0$, $k_1$, and $k_2$ vary with snow class, DOY runs from -92 (1 Oct.) to +181 (30 Jun.) with no 0 value. With the data shown in table 1 available, a model similar to Eq. (1) but applicable to China could be developed in the near future, this is one of the objectives of the ongoing programs at HIT.

In the Chinese design code, it's stated that a fixed regional average snow density could be used to convert annual maximum snow depth into ground snow load in the case where direct measurement of ground snow load is not available [2]. The National Building Code of Canada (NBCC) also uses average seasonal snowpack density to convert snow depth into ground snow load [9], while a nonlinear relation between 50-year return period value of ground snow load and 50-year return period value of ground snow depth is adopted in the US [16, 19].

The recommended regional average snow density by the Chinese design code is shown in figure 1. It can be seen from figure 1 that the country is divided into 6 zones for the assignment of regional average snow density. In this manner, there is sharp increase or decrease for the

snow density on the boundaries between the 6 zones, resulting in larger differences in the estimated extreme ground snow loads for locations that are close enough to each other but belong to different zones. Consequently, a more detailed and smooth zoning map for regional average snow density is desired to reduce such effect. Efforts are being made by the authors on this subject.
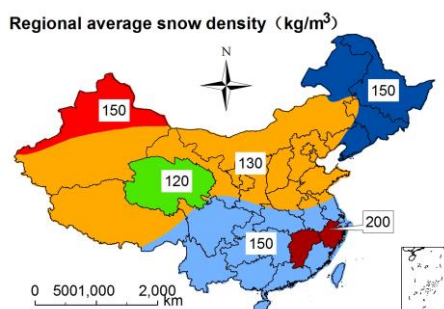


**Figure 1.** Regional average snow density recommended by the Chinese design code

Alternatively, a nonlinear relation between the 50-year return period value of ground snow load and 50-year return period value of ground snow depth, such as the one adopted by ASCE load standard[16], could be considered to aid the conversion between the two extreme variables. However, 10 years of ground snow load data is insufficient to achieve a reliable estimate for the 50-year return period value of ground snow load, thus, development of such nonlinear relation could be considered only when more data is made available for ground snow loads in the future.

## 2.2 At-site measurements for unbalanced snow load profile

Unbalanced roof snow load, caused by snow drifting or snow sliding, is the main contribution to snow-induced structural damage. For this reason, special attention are paid to the unbalanced snow load profile by building codes such as those in China [2], Canada [10], US [16] and in Europe [12].

As indicated by the 1954 version of the Chinese design code, the snow provisions were mainly based on that for USSR. Although it's emphasized that the provisions were made by considering the observations in China, no detailed reports are available to introduce the technical supports for such considerations. For example, it's mentioned by [20] that concurrent measurements of snow depth on roofs and on ground were conducted in Heilongjiang, Liaoning, Inner Mongolia, Xinjiang and Hunan provinces in 1979, but no reports related to this program were found by the authors.

In contrast, there are sufficient case histories in the US and Canada to aid the calibration of snow provisions in building codes there. For example, 28 case histories were developed in [21] to investigate unbalanced snow load on gable roofs in the US, and that snow provisions for stepped roofs in the ASCE load standard were based on more than 350 case histories [22, 23]. Snow

provisions in National Building Code of Canada were also based on sufficient data measured on roofs [24-26].

In this context, to collect data for the distribution of roof snow loads, at-site measurements of snow depth and snow density have been carried out on two flat roofs and on open ground in the campus of HIT since the snow season of 2010-2011 (see figure 2). Figure 3 shows an example of measured snow depth profile for one of the cross sections selected in the measurements. It can be seen from this example that snow tend to deposit in the location where elevation changes on the roof, the deposited snow can reach the top of the parapet while the snow depth in the middle part of the section is very limited. This observation is common among the measurements up to now. Quantitative analysis for the relation between the deposited snow depth, ground snow depth, parapet height and wind speed could be expected when sufficient measurements become available, this will help one to understand the unbalanced roof snow loads on stepped roofs, and behaviour of snow in the wind flow.
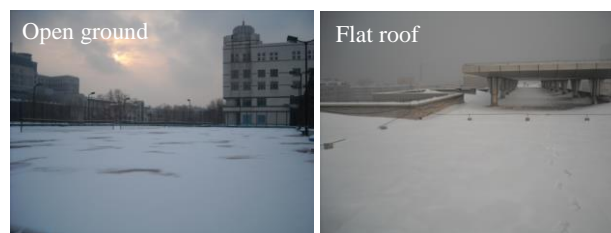


**Figure 2.** Locations where at-site measurements of snow depth and snow density were conducted
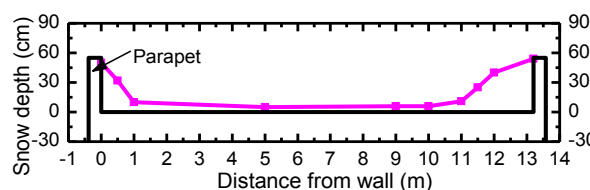


**Figure 3.** Example of measured snow depth profile

While snow depth on flat roofs or on stepped roofs can be measured directly by rulers by hand, those on gable roofs and arched roofs (in general, sloped roofs) cannot be done in the same way because it's unlikely for one to stay on such roofs safely to conduct the measurement. Consequently, sloped roofs are not included in the measurement program mentioned above. Considering the fact that long-span roofs are usually designed to be arched (e.g., cylindrical or spherical), and that snow loads on such roofs is usually of particular interest, it's desired by the authors to include sloped roofs into the measurement program in the future. A possible way to reach this purpose is to employ photogrammetric techniques using Unmanned Aerial Vehicle (UAV). An UAV have been equipped to HIT (see figure 4) and efforts are being made to use this equipment to measure snow depth. However, issues such as influence of low air temperature on the UAV's operation and strong reflection of the snow surface to the camera are still to be solved

before such measurement can be conducted. Once this equipment is made feasible for the measurements, snow depths on sloped roofs, especially on long-span roofs, will be conducted immediately and will last for years.



**Figure 4.** UAV equipped for the purpose of photogrammetric measurement of roof snow depth

Sufficient measurements of roof snow depth for various types of roofs are expected at the end of this program. These data will be used as the basis to examine the validity of snow provisions in the Chinese design code and subsequently possible suggestions for the calibration of the provisions.

## 2.3 Wind tunnel tests

Wind tunnel modelling is one of the most effective ways to investigate the role of wind on snow accumulation. Investigations of snowdrift around/on buildings have been carried out in several previous studies. For example, Iversen [27] conducted a series of experiments on scale models of snow fences in the Iowa State University environmental wind tunnel using glass sphere as model particles. Isyumov and Mikitiuk [28] examined the drifting and redistribution of snow on large-area two-level flat roof by carrying out wind tunnel model test by using bran as model particles, while artificial snow was used by Delpech and Gandemer [6] to simulate snow drifting around buildings for Antarctic Concordia research station. Nevertheless, similarities between prototype and model are still big challenges for wind tunnel tests of snowdrifting today. A reliable modelling depends on similitude criteria, including geometric, dynamic and kinetic criteria [6]. Yet, it's generally accepted that fully correct, reduced scale modelling of snowdrifting is not possible in practice [29], consequently, compromises need to be made in the modelling. It's indicated by Anno [30] that it would be allowable to abandon Froude scaling if the shape of a snowdrift depends on the shape of wakes and the wind speed at the reference height, but this is not the case if the shape of snowdrift depends on the saltation trajectory. Kind [29] recommended to use high density particles in air in the modelling where time scaling and quantitative accuracy are more important than convenience, this is based on the observation that saltation dynamics of high density particles in air are dynamically similar to those of real snow in air.

While snowdrift around buildings or snow fences are relatively widely investigated by wind tunnel tests (e.g.,

[6, 27, 30]), investigation of snowdrift on building roofs is rarely available, especially for sloped roofs, this is due to the restriction of model particles' properties. Model particles such as sand, sawdust, glass spheres do not reproduce all inter-particle forces [6], this would result in the difficulty to model the snow on sloped roofs, even when the angle of repose for the model particle is equal to that for real snow. Considering this limitation, wind tunnel tests are not conducted directly for snowdrift on building roofs, but for snowdrift around standard model: cubic building model. The test results of snowdrift around cubic model will then be used as the benchmark to verify the validity of numerical simulation model that will be presented in the next section, the investigation of snowdrift on roofs will primarily rely on the numerical simulations thereafter.

For the wind tunnel test of snowdrift around cubic building model, a prototype with sizes of $1m \times 1m \times 1m$ was installed on an open ground in the campus of HIT and the snow depth around it was measured after each snowfall event. After conducting the measurement, the snow was cleaned to make sure there is no snow remained around the cube before next snowfall event. Figure 5 shows the distribution of snow around the cube after one of the snowfall events in the 2014-2015 season. The lateral erosion is clearly showed in this figure. However, there is no distinct deposition of snow in the windward or leeward side of the cube, this observation is different from that made by Oikawa et al. [31] in Sapporo, Japan and by Beyers et al. [32] in Antarctica; this is probably caused by the differences of snow properties and wind conditions in different regions. The measurement will keep going to collect as many cases as possible, and those cases with relatively steady wind direction will be selected as the prototype for the wind tunnel tests in the future.
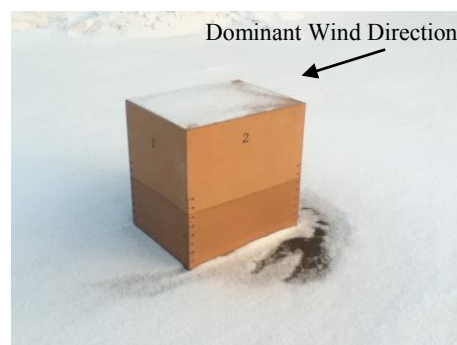


**Figure 5.** Snow accumulation around the cube prototype

Some preliminary investigations have been conducted by the authors in a wind tunnel of open circuit type with a cross section of 50cm $\times$ 50cm. Figure 6 shows the setup for the tests. In these tests, approaching wind is set uniform and the floor of the wind tunnel is covered by a uniform layer of model particles, no feeding or supply of particles is made during the experiments. The scaling of the test's parameters is carried out mainly by considering the criteria given by Eq. (2) and Eq. (20) in [33] and model particles are selected as bicarb soda powder.

Results showed that there are discrepancies between the tested model and its prototype. This is mainly because 1) the wind for the prototype is turbulent and the direction is varying during the snowfall, this cannot be modelled in the wind tunnel tests; and 2) snow particles are in falling movement in the prototype by are settled in the tests. Further improvements are needed to address these issues to reduce the discrepancies.
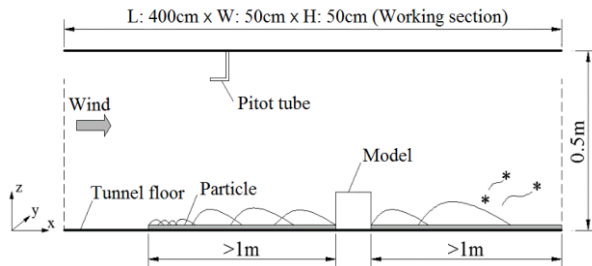


**Figure 6.** Schematic view of the wind tunnel test's setup

Considering the fact that the wind condition is not controlled in the prototype experiment, one may desire to control the wind to reduce the uncertainties involved in the experiment. For this purpose, a $2 \times 2$ fan matrix is being constructed at HIT to pursue a stable wind direction and a desired wind speed for a specific duration in the prototype experiment (see figure 7 for illustration). Facilities such as temporal walls will be used to make sure the snow was uniformly distributed around the cube model during each snowfall event; the temporal walls will then be removed and the fans started. By doing in this way, the authors are expecting to make the prototype much more similarly modelled in the wind tunnel tests than it is in the current stage.
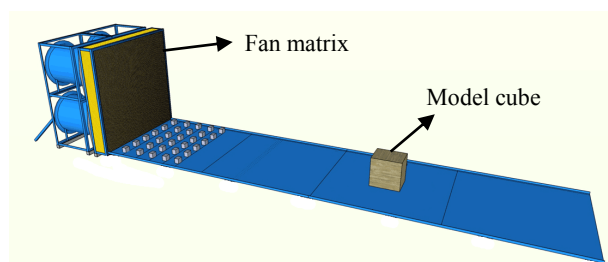


**Figure 7.** Schematic view of the proposed wind-controlled prototype experiment

## 2.4 Numerical simulations

As mentioned above, at-site measurements and wind tunnel tests for snowdrift on sloped roofs is unrealistic due to some technical limitations such as the human safety and the satisfaction of similitude criteria. Consequently, the Computational Fluid Dynamics (CFD) technique may be an appropriate tool for the investigation of snow load on such roofs.

Application of CFD technique on simulation of snowdrift has been investigated for decades and was review by Tominaga et al. [34]. A typical model for simulating snowdrift using CFD technique is the one presented by Beyers et al. [32]. In this model, it's assumed that the air-snow system is highly dilute and that only one-way coupling between the fluid and discrete phase is considered, i.e., the snow particles follow the continuous phase but do not influence it. The air-snow system is treated as turbulent, incompressible, Newtonian two-phase fluid flow and Eulerian approach was adopted. The inlet snow flux for the saltation layer was modelled as the empirical relations obtained by measured data by Pomeroy and Gray [35] and the one for suspension layer is based on Pomeroy and Male [36].

It's found that in most of the previous studies, the investigation is focused on snowdrift around buildings, for example, around snow fences [37, 38], cube models [32, 34], and building complex [39, 40]; those related to snowdrift on building roofs is quite rare. In this program, a model similar to the one presented by Beyers et al. [32] will be developed and to be validated by the wind tunnel tests mentioned earlier in the previous section, snowdrift on building roofs, especially on long-span roofs, will then be simulated by using the validated numerical model. These simulation results, supplemented by the at-site measurements, will help us to interpret the snow provisions in the design code and to possibly improve the provisions.

Besides, once the validity of numerical simulation model is verified, it could be a very useful tool for the design of buildings in snowy regions, especially for those with complicated shape and that shape coefficient is not given by the code. For one aspect, based on the simulation results, enhancements can be made to the structural elements where snowdrift tends to accumulate; second, the shape of the roof can be improve to avoid deposition of snow in the locations where snow accumulation is not expected.

## 3 Closing remarks

The snow load provisions in the Chinese design code are originally based on that for USSR and have been calibrated several times, but documents supporting such codifications are rarely available. Besides, with the growing of applications of long-span roofs in recent years in China, there are practical demands for investigations of unbalanced snow loads on these roofs since such investigations are rarely available. Therefore, an investigation of the unbalanced snow loads on roofs, especially for long-span roofs, is warranted. In this paper, some of the research activities on this subject at HIT, including statistics analysis of meteorological data, at-site measurements of snow depth and snow density on flat roofs, wind tunnel tests of model cube, as well as numerical simulations of snowdrift on building roofs are summarized. The programs are supposed to be finished at the end of 2018 and a detail report related to the interpretation to the snow load provisions in the Chinese design code and suggestions to possible calibration of the provisions is expected at that time. For this objective, several key techniques problems are to be solved or improved in the near future, these include:

1) Development of a more detailed and smooth zoning map for regional average snow density;

2) Photogrammetric measurement of roof snow depth using UAV installed with high-resolution camera;

3) Development of acceptable wind tunnel tests for cube model that are in good agreement with its prototype;

and 4) Development and validation of CFD numerical model for simulating snowdrift around cube model.

## References

1. A. Biegus, K. Rykaluk, Eng. Fail. Anal., **16**, 1643 (2009)
2. GB 50009-2012, *Load code for the design of building structures* (China Architecture & Building Press, Beijing, 2012) (in Chinese)
3. X.Y. Zhou, M. Gu, X.F. Li, J. Build. Struct., **29**, 7 (2008) (in Chinese)
4. X.Y. Sun, C.B. Hong, Y. Wu, J. Vib. Shock, **33**, 36 (2014) (in Chinese)
5. Y. Li, X.F. Yuan, J. Build. Struct., **35**, 130 (2014) (in Chinese)
6. Ph. Delpech, P. Palier, J. Gandemer. J. Wind Eng. Ind. Aerod., **74-76**, 567 (1998)
7. L. Sanpaolesi, Commission of the European Communities DGIII/D-3 Final report phase II. (1999)
8. M. Holicky, M. Sykora. *Proc. Fifth Congress on Forensic Engineering*, ASCE. 444 (2009)
9. M. J. Newark et al. Can. J. Civil. Eng., **16**, 267 (1989)
10. NRC. *National Building Code of Canada*. Ottawa (2010)
11. L. Sanpaolesi, Commission of the European Communities DGIII/D-3 Final report phase I. (1998)
12. BSI. *Eurocode 1 –Actions on structures – part 1-3: General actions – Snow loads*. London (2003)
13. M. Izumi, H. Mihashi, T. Takahashi, *First International Conference on Snow Engineering*, Santa Barbara, California (1988)
14. AIJ. *AIJ recommendations for loads on Buildings*. Tokyo (2004)
15. B. Ellingwood, R. Redfield, J. Struct. Eng., **109**, 950 (1983)
16. ASCE. *Minimum Design Loads for Buildings and Other Structures*. Reston (2010)
17. H. M. Mo, F. Fan, H. P. Hong, Nat. Hazards, **77**, 543 (2015)
18. M. Sturm et al., J. Hydrometeorol., **11**, 1380 (2010)
19. R. L. Sack. J. Struct. Eng. **142** (1) (2015)
20. B.N. Hou, C.A. Wei, Metallurgical Buildings., (2), 61 (1982) (in Chinese)
21. M. O'Rourke, M. Auren, J. Struct. Eng., **123**, 1645 (1997)
22. M. O'Rourke, W. Tobiasson, E. Wood, J. Struct. Eng., **112**, 2080 (1986)
23. M. O'Rourke, C. DeAngelis, J. Struct. Eng., **128**, 1330 (2002)
24. D. A. Taylor, Can. J. Civil Eng., **6**, 85 (1979)
25. D. A. Taylor, Can. J. Civil Eng., **8**, 63 (1981)
26. D. A. Taylor, Can. J. Civil Eng., **19**, 59 (1992)
27. J. D. Iversen, J. Wind Eng. Ind. Aerod., **8**, 231 (1981)
28. N. Isyumov, M. Mikitiuk, J. Wind Eng. Ind. Aerod., **36**, 893 (1990)
29. R. J. Kind, Cold Reg. Sci. Technol., **12**, 217 (1986)
30. Y. Anno, Cold Reg. Sci. Technol., **8**, 241 (1984)
31. S. Oikawa, T. Tomabechi, T. Ishihara, J. Snow Eng. Japan, **15**, 283 (1999)
32. J. H. M. Beyers, P. A. Sunsbo, T. M. Harms, J. Wind Eng. Ind. Aerod., **92**, 725 (2004)
33. R. J. Kind, Atmos. Environ., **10**, 219 (1976)
34. Y. Tominaga, T. Okaze, A. Mochida, Build. Environ., **46**, 899 (2011)
35. J. W. Pomeroy, D. M. Gray, Water Resour. Res., **26**, 1583 (1990)
36. J. W. Pomeroy, D. H. Male, J. Hydrol., **136**, 275 (1992)
37. T. Uematsu et al., Cold Reg. Sci. Technol., **20**, 65 (1991)
38. M. Naaim, F. Naaim-Bouvet, H. Martinez, Ann. Glaciol., **26**, 191 (1998)
39. Y. Tominaga, A. Mochida, J. Wind Eng. Ind. Aerod., **81**, 273 (1999)
40. M. Beyers, B. Waechter, J. Wind Eng. Ind. Aerod., 96, 1603 (2008)

# Specification of the design value of the ground snow load considering measurements of the snow height – part 1: single stations

Benjamin Czwikla, Michael Kasperski[a]

*Ruhr-Universität Bochum, Research Team EKIB. 44780 Bochum, Germany*

**Abstract.** The straight-forward approach to the specification of the design value of the ground snow loads is based on measurements of the water equivalent. In Germany, this parameter however is only available for a few stations and the most recent decades. Based on a snow density model for each individual station, the additional years of observed snow heights can be used to increase the statistical stability of the estimated design value of the snow load on the ground.

## 1 Introduction

The straight-forward approach to the specification of the design value of the ground snow loads is based on measurements of the water equivalent. Since the acquisition of this observation variable is rather time-consuming not all meteorological stations provide this information. For stations which do provide the water equivalent, the observations usually cover only the recent decades, i.e. the majority of observation data provides only the height of snow cover. Using these data for the specification of snow loads requires a consistent model for the snow density $\rho_s$ which translates the snow heights $h_s$ to snow loads s:

$$s = \rho_s \cdot h_s \tag{1}$$

For exploiting the observation years of snow heights of a single station, obviously it is sufficient to develop an individual snow density model for each station. For Germany, this step increases the number of observations on average by a factor of about 2, thus improving the statistical stability of the estimated design values. The individual models require simultaneous measurements of snow heights and water equivalents.

The number of German stations only measuring the snow heights is by a factor of about 14 larger than the number of stations measuring the water equivalent. Exploiting this huge amount of data requires a regional model of the snow density. This paper discusses the available models for the snow density, specifies required features and presents a new approach which is based on extreme value statistics for both the water equivalent and the snow heights.

## 2 Models for the snow density

The basic demand for any model probably deals with the number of parameters to be identified, i.e. the best approach follows the demand to have as few parameters as possible and as many parameters as required. Basically, snow density in the context of translating the height of a snow cover to snow loads means the average density of the snow pack. Then it seems to be reasonable that the model should be monotonic in regard to the height of snow cover and probably should have a limiting value.

The simplest model, used e.g. in [1] is based on a linear approach and uses only two parameters:

$$\rho_s = a \cdot h_s + b \tag{2}$$

In Russia [2], the influence of the height is considered to be smaller by introducing the square root:

$$\rho_s = a \cdot \sqrt{h_s} + b \tag{3}$$

A more general approach introduces as third variable an unknown exponent for the height [1]:

$$\rho_s = a \cdot h_s{}^c + b \tag{4}$$

These models have in common that a limiting value has to be specified for the snow density.

In [3], a three-parameter model has been developed which describes the snow density between two limiting values $\rho_0$ and $\rho_\infty$:

$$\rho_s = \rho_\infty \cdot \frac{h_{ref}}{h_s} \cdot \ln\left[1 + \frac{\rho_0}{\rho_\infty} \cdot \left(\exp\left(\frac{h_s}{h_{ref}}\right) - 1\right)\right] \tag{5}$$

Finally, in [4], a four-parameter model is proposed which uses as additional parameter the age of the snow cover in days DOY:

$$\rho_s = (\rho_\infty - \rho_0) \cdot \left[1 - \left(\exp\left(-k_1 \cdot h_s - k_2 \cdot DOY\right)\right)\right] + \rho_0 \tag{6}$$

Other approaches aim in translating the snow height into snow loads only for a specific annual non-exceedance probability [2], e.g. in USA for a return period of 50 years or in Japan for a return period of 100 years.

## 3 New approach

The new approach extends the above idea of translating the snow height into a corresponding snow load for the complete trace of non-exceedance probabilities. This approach leads to an average probabilistic model of the snow density depending on the snow height.

---

[a] Corresponding author: michael.kasperski@rub.de

In a first step, it is assumed that the traces of the annual non-exceedance probability follow the extreme value distribution type I (Gumbel distribution) which is given as:

$$F(x) = \exp\left[-\exp\left(-\left(\gamma + \frac{\pi}{\sqrt{6}} \cdot \left(\frac{x-m}{\sigma}\right)\right)\right)\right] \qquad (7)$$

with m – mean value, $\sigma$ - standard deviation, $\gamma$ - Euler constant $\approx 0.5772$

In the probability paper, both traces appear as straight lines; dividing the two linear equations leads to the following simple approach:

$$\rho_s = \rho_\infty - \frac{\Delta\rho \cdot h_{ref}}{h_s} \qquad (8)$$

The limiting density $\rho_\infty$ depends on the standard deviations of the snow load and the snow heights:

$$\rho_\infty = \frac{\sigma_s}{\sigma_h \cdot g} \qquad (9)$$

with g – gravitational acceleration $\approx 9.81$ m/s²

The term $\Delta\rho$ is obtained as the weighted difference of the two mean values. For consistency in the dimensions, it is required to introduce a reference height:

$$\Delta\rho = \frac{\rho_\infty \cdot m_h - m_s / g}{h_{ref}} \qquad (10)$$

In this approach, the reference height is an arbitrary value and can be assumed as $h_{ref} = 1$ m.

The individual traces of extreme snow heights and snow loads are based on the maximum observations during independent events with a continuous snow cover, i.e. the observations do not necessarily occur on the same day. The approach can either be based on yearly extremes or on individual events above a specific threshold value. For the latter ensemble, the non-exceedance probability per event is translated to the annual non-exceedance probability by using the following relation:

$$p_{annual}(x \le x_{ref}) = \sum_{K=0}^{\infty} p(K) \cdot p_{event}(x \le x_{ref})^K \qquad (11)$$

with  p(K) – probability of having 0, 1, 2, 3, 4… independent snow events in a 12 month period
$p_{event}$ – non-exceedance probability per event

Basically, the annual probabilities in equation (11) follow the generalized extreme value distribution if the number of events per year follows a Poisson distribution and the non-exceedance probability per event corresponds to the Generalized Pareto distribution. If the annual probabilities follow the Gumbel distribution, then, the consistent model demands that the individual events follow an exponential distribution which is given as:

$$F(x) = 1 - \exp\left(-\frac{(x - x_{th})}{sc}\right) \qquad (12)$$

with sc – scale parameter, $x_{th}$ -  threshold value

The Poisson distribution is given as:

$$p(K) = \frac{\lambda^K}{K!} \exp(-\lambda) \qquad (13)$$

with $\lambda$ - average number of events per 12 month cycle

The translation scheme of the probabilistic event-based model to the probabilistic annual model looks as follows:

$$m = x_{th} + (\gamma + \ln\lambda) \cdot sc$$
$$\sigma = \frac{\pi}{\sqrt{6}} \cdot sc \qquad (14)$$

For the identification of the 'true' model for the snow density, the fitting procedure should aim in unbiased estimates of the four describing parameters which are the mean values and the standard deviations of the extremes of the snow heights and the water equivalents, respectively. This obviously can be achieved by applying BLUE, i.e. the Best Linear Unbiased Estimator. Usually, for the Gumbel distribution, an alternative notation is used:

$$F(x) = \exp\left[-\exp\left(-\left(\frac{x-\mu}{\beta}\right)\right)\right] \qquad (15)$$

The two parameters $\mu$ and $\beta$ are obtained as weighted sums of the observations $x_i$ which have to be sorted in ascending order:

$$\mu = \sum_{i=1}^{N} x_i \cdot A_i$$
$$\beta = \sum_{i=1}^{N} x_i \cdot B_i \qquad (16)$$

with N – ensemble size

The mean value and the standard deviation are obtained as follows:

$$m = \mu + \beta \cdot \gamma$$
$$\sigma = \frac{\pi}{\sqrt{6}} \cdot \beta \qquad (17)$$

Usually, the required weighting coefficients A and B are provided for a set of annual extremes, i.e. the non-exceedance probabilities are assumed to be equidistant. Respective tables for ensembles sizes up to N = 30 can be found in [5]. For larger ensembles sizes, the weighting coefficients can be obtained based on a Taylor series expansion [6].

Equation (11) leads to non-equidistant probability values. The required weighting coefficients can be achieved based on [6] by simply exchanging the individual p-values $p_i = i/(N+1)$ by the corresponding value from equation (11).

Alternatively, a least square fit in the Gumbel probability paper provides unbiased estimates if the appropriate plotting position as recommended by Gringorton [7] is used, i.e. the probability $p_i$ becomes:

$$p_i = \frac{i\text{-}0.44}{N+0.12} \tag{18}$$

The target probability distribution occurs as a straight line. The demand that the sum of the squared differences between observation and theoretical value should be minimal leads to a simple system of two linear equations:

$$\begin{vmatrix} \sum_{i=1}^{N} x_i^2 & \sum_{i=1}^{N} x_i \\ \sum_{i=1}^{N} x_i & N \end{vmatrix} \cdot \begin{bmatrix} c_1 \\ c_2 \end{bmatrix} = \begin{vmatrix} \sum_{i=1}^{N} x_i \cdot y_i \\ \sum_{i=1}^{N} y_i \end{vmatrix} \tag{19}$$

The coordinate y in the probability paper is given as:

$$y_i = \text{-}\ln\left(\text{-}\ln\left(p_{i,\,annual}\right)\right) \tag{20}$$

Finally, the two unknown parameters m and $\sigma$ are obtained from $c_1$ and $c_2$ as follows:

$$m = \frac{\gamma \text{ - } c_2}{c_1},\ \sigma = \frac{\pi}{\sqrt{6}} \cdot \frac{1}{c_1} \tag{21}$$

Once the model for the snow density has been obtained, the next step is to translate the additional observations of $h_s$ to corresponding snow loads s. Then, the design value can be estimated based on an increased ensemble.

Tentative target values of the annual exceedance probability of the design snow load on the ground are specified in [8] for different consequence classes. The design value $s_{des}$ then is obtained as follows:

$$s_{des} = m_s + s_{des,\,red} \cdot \sigma_s \tag{22}$$

The reduced design value depends on the target exceedance probability:

$$s_{des,\,red} = \left(-\ln\left(-\ln\left(p_{target}\right)\right)-\gamma\right) \cdot \frac{\sqrt{6}}{\pi} \tag{23}$$

It is important to note that the increased ensemble size is still far away from infinity, i.e. any estimation of the design value is influenced by statistical uncertainties. In accordance to the demands in the EN 1990 – Basis of Design, the final extreme value statistics aim in a one-sided confidence interval of 75%. Since an estimation

based on BLUE leads on average to the true value, the corresponding one-sided confidence is only in the range of 50%. Therefore, an additional adjusting factor is required to increase the confidence in the final design values to the desired level:

$$s_{des} = m_s + s_{des,\,red} \cdot \sigma_s \cdot c_{ad}\left(p_{target},\,N\right) \tag{24}$$

The adjusting factor depends on the ensemble size and the target exceedance probability. It can be obtained for any estimation method based on simulations.

# 4 Derivation of the adjusting factor

For confined ensembles, the estimations of the mean value and the standard deviation of the extremes contain some uncertainties. Basically, the smaller the ensemble, the larger will be the random scatter in the estimated values. The randomness can be analysed based on simulations. The following results are based on 1,000,000 independent runs, assuming that the basic variable follows the Gumbel distribution with zero mean and a standard deviation of 1. Figure 1 shows the estimated statistical parameters for different ensemble sizes for a set of annual extremes.
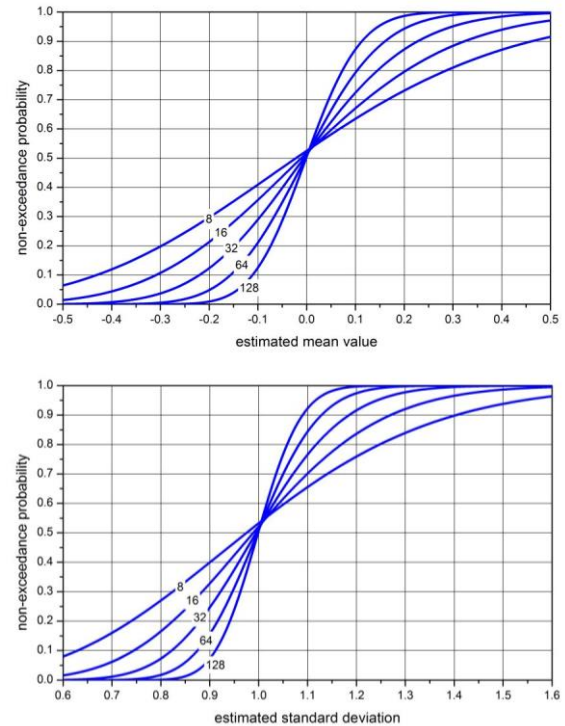


**Figure 1**: Randomness in the estimated mean value and standard deviation for an ensemble of annual extremes following the Gumbel distribution for different ensemble sizes

The design value is estimated introducing a target exceedance probability of 1/1000 per year. Figure 2 shows the probability distribution of the estimated design value for different ensemble sizes of annual extremes. The true target value is obtained from equation (19) as

$s_{des, red} = 4.936$. Additionally, the 90%-confidence interval is shown.

Since a reasonable two-sided confidence interval requires a very large ensemble size, which usually is not available, the basic strategy in design is to avoid underestimations in case of actions and over-estimations in case of the resistance. Then, a one-sided confidence interval is used. Applying the target confidence recommended in the Eurocode requires shifting the traces of the non-exceedance probabilities to the right side with the basic aim that all traces go through the anchor point which is given with the true design value and the chosen error target. The latter is obtained as 1-conf, where conf is the confidence target. This shifting of the traces increases inevitably the probability of overestimating the design value which leads to uneconomic design. The higher the confidence demand, the higher is the probability of an uneconomic design. The 75%-target value is therefore a fair compromise to balance the demands to safety and economy.
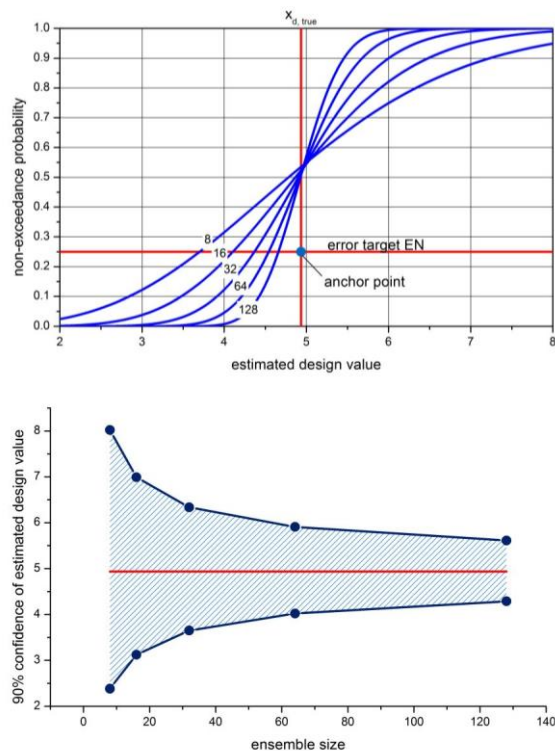




**Figure 2**: Randomness in the estimated design value with $p_{target} = 0.999$ for an ensemble of annual extremes following the Gumbel distribution for different ensemble sizes and two-sided 90%-confidence interval

The required adjusting factor can be obtained iteratively based on simulations. Figure 3 shows the respective results for ensemble sizes from 8 to 128. It is important to note that in this approach all annual extremes have to be larger than zero, i.e. this approach is recommended for snow climates which in each year show a continuous snow cover over the whole winter season.

For snow climates where in some individual years there is no snow at all and / or for snow climates which might have more than one independent period of

continuous snow cover per winter season, the approach based on equation (11) has to be used. Then, beside the actual number of observation years the average number $\lambda$ of independent periods with continuous snow cover has to be considered for the specification of the adjusting factor. The respective results are shown in figure 4.
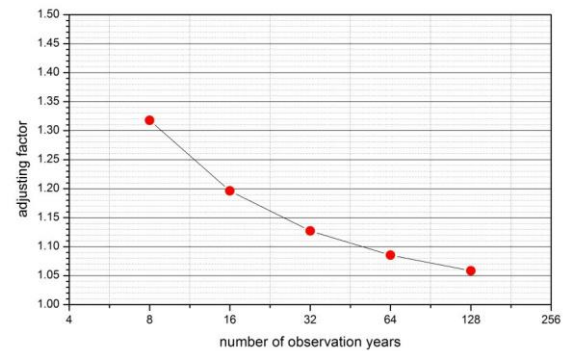


**Figure 3**: Adjusting factor for the estimation of the design value for annual extremes following the Gumbel distribution, $p(s > s_{des}) = 0.001$ / year
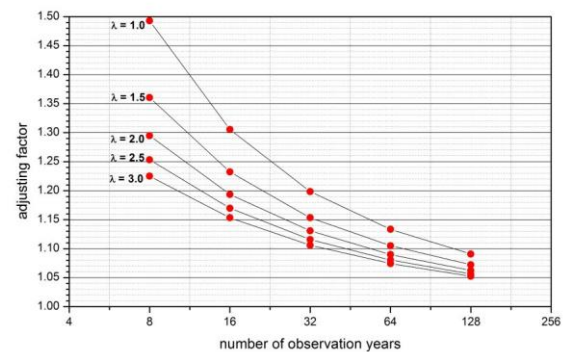


**Figure 4**: Adjusting factor for the estimation of the design value for extremes above a threshold value following the exponential distribution and for the number of events following the Poisson distribution for different average number of independent events $\lambda$, $p(s > s_{des}) = 0.001$ / year

## 4 Example of application

One of the places in Germany with really long weather records is the station at Aachen. Observations for the height of snow cover start already in 1892. However, there are some gaps. The years 1904 and 1915-1929 are missing. Since 1950, water equivalents are sampled if the snow cover is at least 1 cm. The snow climate at Aachen is characterized by eventual mild winters without considerable snow. In the period from 1950 to 2006 there are 17 winters without snow. Altogether, in 56 winter seasons 83 independent events with a continuous snow cover are observed providing both the snow load and the snow height. Figure 5 shows the traces of the non-exceedance probability and the fitted theoretical model for the snow loads. In figure 6, the corresponding trace for the snow heights is shown.

The final model for the snow density for Aachen is then identified as:

$$\rho_s = 161.238 - \frac{3.129 \cdot h_{ref}}{h_s} \ [kg/m^3] \qquad (25)$$
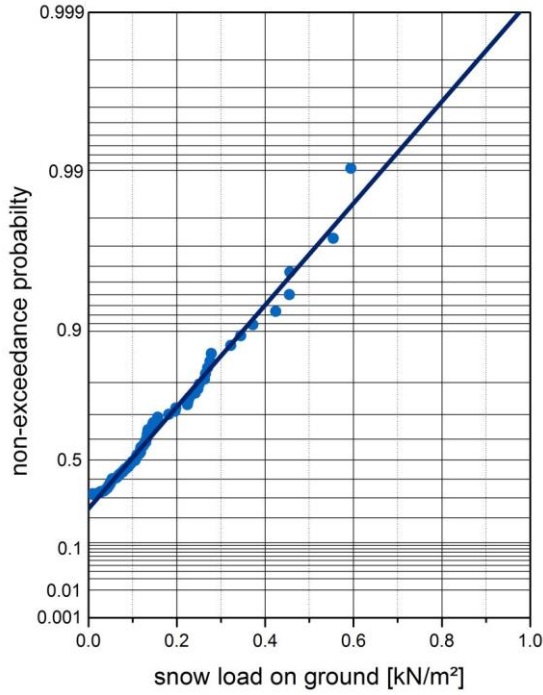


**Figure 5**: Probability plot for the snow loads at Aachen (1950-2006)
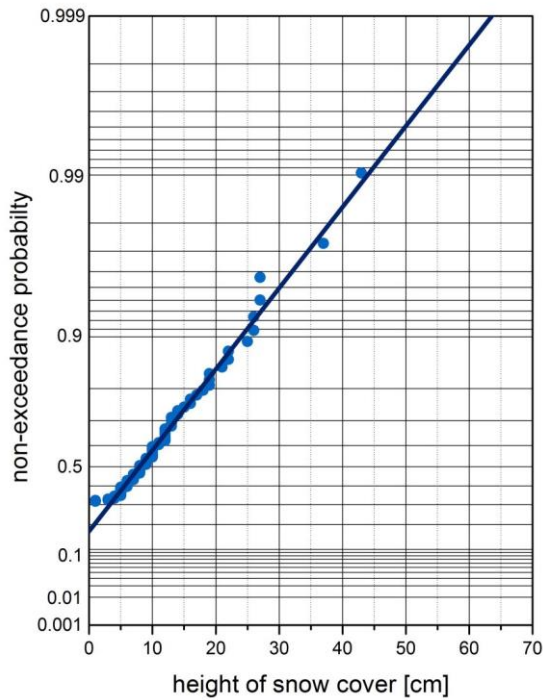


**Figure 6**: Probability plot for the snow heights at Aachen (1950-2006)

Figure 7 compares the identified model of the snow density at Aachen to the observed values for the 83 independent events. It is important to note, that the snow density model has to extend to values which are in the range of the design value of the snow heights.

Based on the identified snow-density model, the observation years from 1892 to 1949 lead to 163 further observations, i.e., the ensemble size is almost three times larger. However, many early observations correspond to snow heights of only a few centimetres. Therefore, it is reasonable to introduce an individual threshold value which for Aachen can be assumed as $s_{lim} = 0.05$ kN/m². Then, the average number of independent events becomes 1.37 per twelve month cycle. The total number of events is increased to 129. Figure 8 shows the extended trace of annual non-exceedance probability for the observation period from 1892 to 2006.
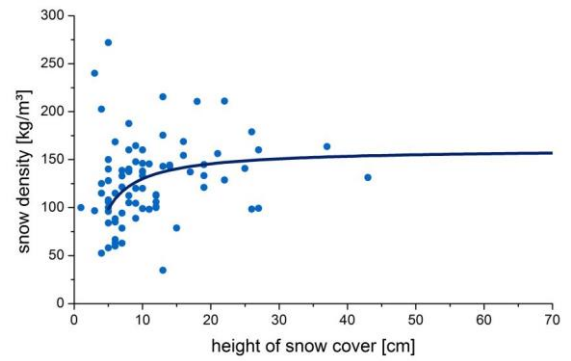


**Figure 7**: Probabilistic model of the snow density (Aachen 1950 – 2006)
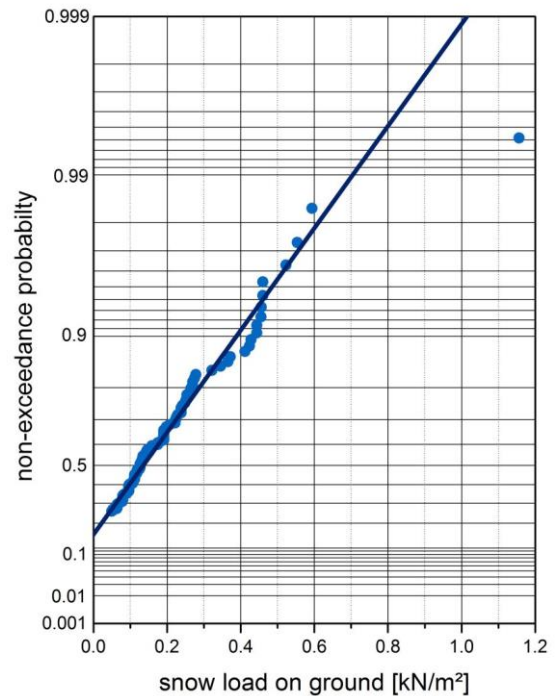


**Figure 8**: Probability plot for the estimated snow loads at Aachen (1892-2006)

The extended ensemble obviously contains an outlier which occurred in the winter of 1908. This value is almost twice as large as the second largest observed snow load in 1987. For the outlier, the corresponding observed snow height is 75 cm, which is 1.75 times larger than the second largest snow height of 43 cm which was observed in 1969.

The least-square fit therefore neglects this outlier. The final estimation of the design value requires an appropriate adjusting factor. For the initial ensemble, the adjusting factor is 1.131, for the increased ensemble it slightly reduces to 1.102. The final design value in accordance to equation (22) then becomes 1.10 kN/m². This value is smaller than the actual DIN-EN value which is 1.5 * 0.85 = 1.275.

For most stations, the records of the water equivalent start in the 1950s. However, a few stations show considerable shorter periods either due to a later starting year or due to gaps in the observation, e.g. Dresden with the starting year 1978 or Jena with missing data from 1980 to 1990. Therefore, the statistical uncertainties in the identified parameters may vary from station to station.

Furthermore, not all traces show similar well-behaved shapes as in the above example for Aachen. Figures 9 and 10 show the respective traces of the observed snow loads and snow heights for Schwerin from 1947 to 2006.
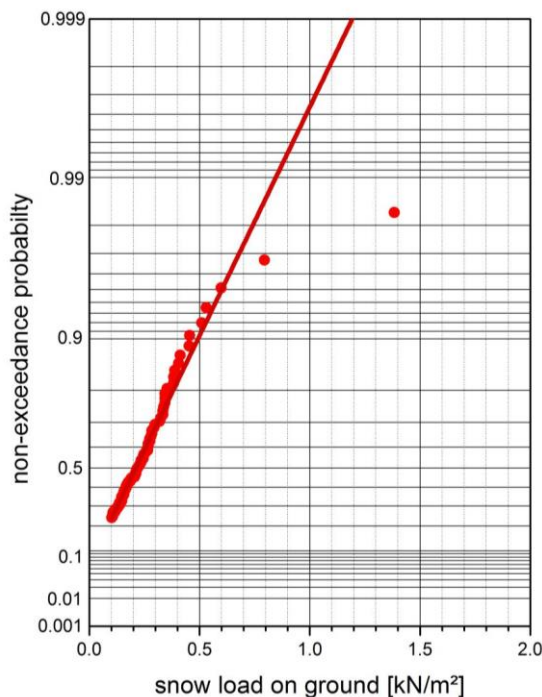


**Figure 9**: Probability plot for the snow loads at Schwerin (observation period 1947-2006)

While the trace of the snow loads suggests a type II extreme value distribution, the trace of the snow heights seems to follow a type III extreme value distribution. The question arises, if the largest observed value in the snow loads really is an outlier.

Nevertheless, for the identification of the snow density model the largest observed snow load is ignored. The identified model for the snow density at Schwerin is shown in figure 11. The supposed outlier occurs with an extremely large density of more than 450 kg/m³ for a snow height of 30 cm.
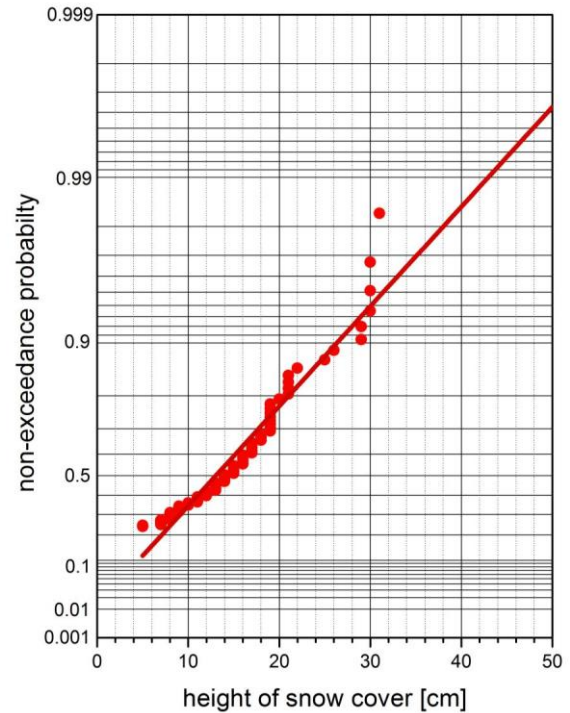


**Figure 10**: Probability plot for the snow heights at Schwerin (observation period 1947-2006)
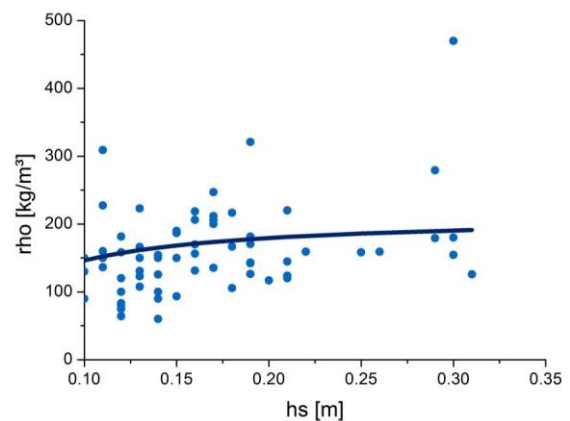


**Figure 11**: Probabilistic model of the snow density for Schwerin (observation period 1947 – 2006)

# 4 Versus a snow density model for Germany

In a first step, the data of 225 stations are analysed. Figure 12 shows the positions of the stations on a map of Germany. The minimum requirement for applying the new approach is 10 years of simultaneous observations of snow load and snow height.

Figure 13 shows the interdependency of the parameters of the snow density model. For the majority

of stations, the model predicts an increase of the snow density with snow height. Only about 4% of the stations show the opposite behaviour, i.e. for small snow heights the snow density is large, and the snow density decreases for increasing snow height. The results so far suggest that there is a non-linear decreasing trend for $\Delta\rho$ if $\rho_\infty$ increases.
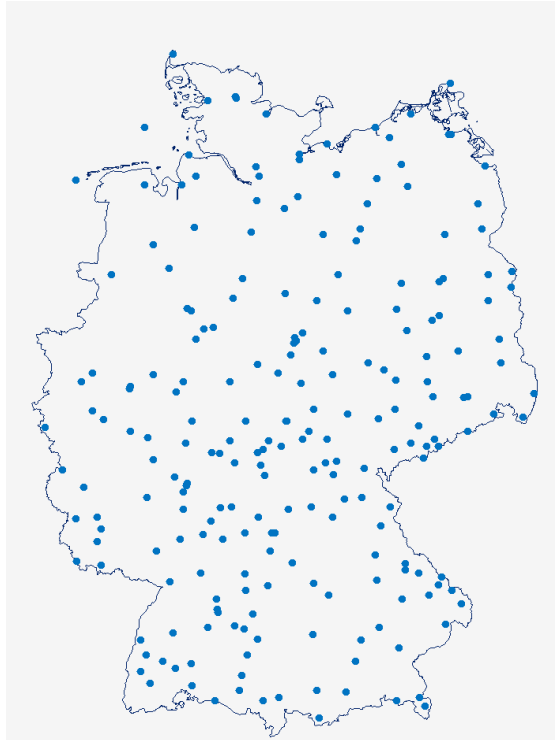


**Figure 12**: Distribution of analysed German stations
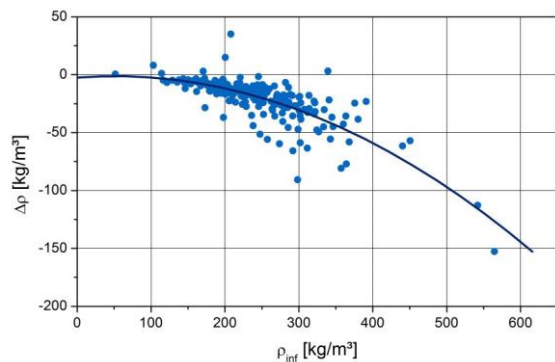


**Figure 13**: Interdependency of the parameters of the snow density model for 225 stations in Germany

The results so far suggest that the snow densities do not depend on the altitude for stations below 250 m. This finding is in agreement with the basic setting of base values of the design snow load in the German snow load standard DIN-EN 1991-1-3/NA:2010-12. For Germany, three basic zones are specified. For zone 1 and 2, additionally regions 1a and 2a are distinguished. The minimum characteristic values are 0.65, 0.85 and 1.1 kN/m² for zone 1, 2 and 3. The appropriate values for the zones 1a and 2a are obtained by multiplying the

corresponding values of zone 1 or 2 with 1.2. For Germany, the partial factor for the snow load is 1.5

In figure 14 the identified design snow loads are plotted versus the altitude for altitudes below 250 m, for sake of simplicity however only for stations in zone 1 and 2. It is important to note that these estimates do not contain the adjusting factor to meet the target confidence, i.e. on average the results correspond to the true design values.

The results suggest that for zone 1 the minimum design value can be further reduced. For zone 2, many stations show a considerable larger design snow load than is specified in the German snow load code although the adjusting factor has not yet been considered. This comparison underlines the need of a consistent analysis of the German snow climate to meet the demands of safety and economy.
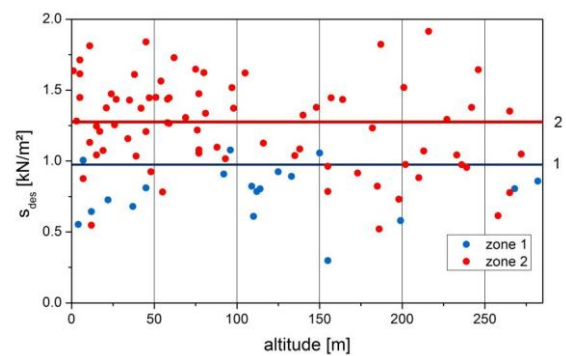


**Figure 14**: Improved design values for German stations with altitudes below 250 m in comparison to the specifications of DIN-EN 1991.1

# 5. Summary and conclusions

The straight-forward approach to the specification of the design value of the ground snow loads is based on measurements of the water equivalent. These observations are available in Germany for about 550 stations, however only for the recent decades. Observations for the snow height on the other hand start for some stations already at the end of the 19th century. On average, the observation period of the snow height is twice the observation period of snow loads. Therefore, the statistical stability of estimated design values of the snow load can be increased by exploiting the additional data for the snow heights. This requires a model for the snow density

The new approach identifies the snow density as a probabilistic optimum, i.e. the approach demands that the traces of the annual non-exceedance probabilities of the observed snow heights and snow loads fall together if the optimum snow density model is applied. Assuming that both traces follow the extreme value distribution type I leads to a two-parametric model for the snow density.

It is important to note that the identification of the snow density model requires an unbiased estimator. For annual extremes, this unbiased estimator is provided with

the Best Linear Unbiased Estimator for the Gumbel distribution. If the model is based on independent events above a threshold value, new sets of BLUE-coefficients are required. Alternatively, the estimation can be based on Gringortons plotting position which also leads to unbiased estimates.

The final estimation of the design value has to meet a once-sided confidence which in the Eurocode is specified as 75%. Since the increased ensemble, which combines truly observed snow loads and estimated snow loads based on observed snow heights, is still far away from having a size close to infinity, adjusting factors are required to push the confidence of the unbiased estimates to the target value. These adjusting factors can be derived based on simulations. The paper presents corresponding figures for annual extremes and independent events.

## Acknowledgement

## References

1. T. Jonas, C. Marty, J. Magnusson: Estimating the snow water equivalent from snow depth measurements in the Swiss Alps, Journal of Hydrology 378 (2009) 161–167
2. ISO 4355 (2013) Determination of snow loads on roofs
3. M. Gränzer, *Angaben von Schneelasten, geographisch nach Zonen gegliedert für den Eurocode "Lasten"*. Landesstelle für Baustatik, Baden-Württemberg. Landesstelle für Baustatik, Baden-Württemberg, Tübingen 1989 (in German)
4. J.L. McCreight, E.E. Small: Modeling bulk density and snow water equivalent using daily snow depth observations, The Cryosphere, 8, 521–536, 2014
5. N. Balakrishnan, P.S. Chan : Order statistics from extreme value distributions, II : Best linear unbiased estimates and some other uses, Communications in Statistics – Simulation and Computation, 1219-1246, 1992
6. A. Child, Balakrishnan, N. (2002) Series approximations for moments of order statistics using MAPLE, Computational Statistics & Data Analysis 38, 331-347
7. I.I. Gringorton : A plotting rule for extreme probability paper, Journal of Geophysical Research, 68, 1963, 813-814
8. ISO 22111 (2007): Bases of design of structures – General requirements

# Research on reliability of roof structures designed by Chinese codes

Shengguan Qiang, Xuanyi Zhou[a], Ming Gu

*State Key Laboratory of Disaster Reduction in Civil Engineering, Tongji University, Shanghai 200092, China*

**Abstract.** In this paper, the annual maximum ground snow loads of three representative cities in China are simulated by a snowmelt model based on available historical meteorological data, and six probabilistic models are chosen for describing them and are evaluated by K-S test, AIC and Q-Q plots. Additionally, basing on the six different probabilistic models for annual maximum ground snow loads, the reliability indices of steel roof members in the three cities are assessed. The results indicate that the fit of a probabilistic model to annual maximum ground snow loads, especially to the high quantiles, has great influence on reliability assessment of roof structures.

## 1 Introduction

Load and resistance factor design (LRFD) method has been widely used to building design. In LRFD method, structural safety is expected to achieve a targeted level by using different partial factors for resistance and different loads. However, the reliability of roof structures whose design is governed by snow loads is actually of much uncertainty. For instance, Takahashi and Ellingwood (2005) investigated reliability of roofs subjected to extreme snow load in Japan, they presented that steel roof members designed by the *Japanese Building Code* (JBC) appear to have a lower reliability against snow load compared to roof members designed by codes in the United States, Canada, or Western Europe, because that the partial factor for snow load and the snow density in JBC are not conservative [1]. Kozak and Liel (2015) studied the reliability of two types of steel roofs under snow loads designed according to ASCE 7-10, they found that the reliability of studied roof types is highly dependent on the location and seasonal snowfall patterns at the building location and the inclusion of serviceability deflection limits in design [2]. However, the influence on reliability assessment of the uncertainty of the probabilistic model for the annual maximum ground snow loads of a city has not been considered in their researches. In fact, there are maybe multiple underlying probabilistic models for annual maximum ground snow loads of a city, and different results of reliability assessment will be got if different probabilistic models are used to characterize annual maximum ground snow loads for assessing structural reliability.

In this paper, the annual maximum ground snow loads of three representative cities in China, which include Beijing, Nanjing and Hohhot, are simulated by a snowmelt model presented by Zhou et al. (2013) [3]. Then, three underlying probability distributions and three types of parameter estimation methods are combined into six different probabilistic models to fit the annual maximum ground snow loads, and K-S test, Akaike information criterion (AIC) and Q-Q plots are adopted as tools to evaluate the quality of these models. Finally, the reliability indices of steel roof members designed by Chinese load code GB50009-2012 [4] in the three cities are investigated on the basis of the six probabilistic models for snow loads, and the influence on reliability

[a] Corresponding author: zhouxytj@tongji.edu.cn

assessment of different probabilistic models for snow loads is discussed.

## 2 Samples of annual maximum ground snow loads

Most weather stations in China give information on ground snow accumulation simply in terms of the depth of snow without simultaneous measurements of snow density [4]. Hence, a mean snowpack density has to be used to estimate ground snow load in Chinese load code GB 50009-2012. Thus, uncertainty of snowpack density which is an important source of the variability of ground snow loads has been ignored.

Zhou et al. (2013) presented a snowmelt model based on the mass-and-energy balance models, which can be used to simulate ground snow loads with available historical meteorological data, including daily average wind speed, temperature, relative humidity, and amount of snowfall or rainfall. With the help of the snowmelt model, the annual maximum ground snow loads of Beijing, Nanjing and Hohhot during 60 winters from November 1, 1951 to March 31, 2011 are simulated. Fig.1 shows the sample of simulated snow loads of Beijing, and Tab.1 lists the mean value and coefficient of variation (COV) of the annual maximum ground snow loads of the three cities. The coefficient of variation (COV) is defined by the ratio of standard deviation to mean value.
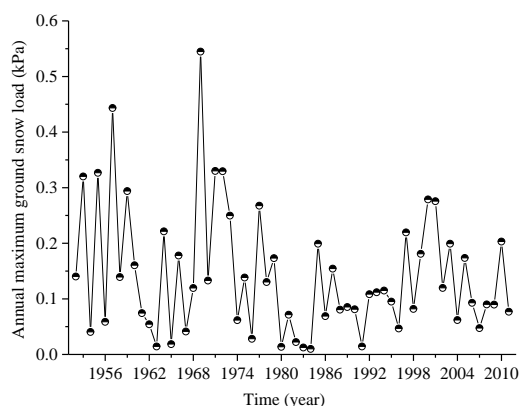


**Fig. 1.** Sample of annual maximum ground snow loads in Beijing

**Tab.1.** Mean value and coefficient of variation

|  | **Beijing** | **Nanjing** | **Hohhot** |
|---|---|---|---|
| mean (kPa) | 0.14 | 0.23 | 0.30 |
| COV | 0.79 | 1.02 | 0.30 |

## 3. Structural design

In accordance with GB 50009-2012, LRFD method should be used to design a building structure. For the ultimate limit states, considering the combination of dead and snow loads on a roof, the design value of load effect $S_d$ is determined by formula (1), meanwhile structural resistance must meet formula (2).

$$S_d = \max\{1.2S_{Dk} + 1.4\gamma_L S_{Srk},\ 1.35S_{Dk} + 1.4\gamma_L \varphi_c S_{Srk}\} \quad (1)$$

$$\gamma_0 S_d \le R_k / \gamma_R \quad (2)$$

where 1.2 and 1.35 are partial factors for dead load when design is governed by variable load and dead load, respectively. 1.4 is partial factor for variable loads. $\varphi_c$ is the coefficient of combination value of variable loads which is 0.7 for snow load. $S_{Dk}$ and $S_{Srk}$ are the effects of characteristic dead load and characteristic snow load, respectively. $\gamma_L$ is the adjustment coefficient which should be considered if the design working life of a building is different from design reference period which is 50 years defined by GB 50009-2012. $\gamma_0$ is the importance factor of structures which is related to the category of structural safety. $R_k$ is the characteristic value of structural resistance, and $\gamma_R$ is partial factor for resistance which varies with the type and material of structural components and a value of 1.1 is used herein.

The characteristic value of snow load on a building roof is defined by the product of characteristic ground snow load and ground-to-roof conversion factor as follows,

$$S_{rk} = \mu_k S_{gk} \quad (3)$$

in which $\mu_k$ is the characteristic value of ground-to-roof conversion factor, which is also termed as the shape coefficient. $S_{gk}$ is the characteristic value of ground snow load $S_g$ and is specified as the 0.98 quantile of the probability distribution of $S_g$. Only uniform distribution of snow load is taken into consideration for the design of a flat roof in GB 5009-2012, and a conservative value 1.0 of $\mu_k$ is specified for the design of flat roofs. The values of $S_{gk}$ for different locations are tabulated in GB50009-2012.

Since the characteristic value of dead load depends on various factors, a ratio of characteristic snow-to-dead load, which is assumed at the range of [0.25, 2.0] in this paper, is used to determine it.

## 3 Assessment of structural reliability

Structural reliability index depends on the variability of structural resistance and loads, and corresponds to the

design working life of a building which is 50 years specified by *Unified standard for reliability design of engineering structures* (GB 50153-2008) for common buildings [5]. According to the severity of possible consequences caused by structure failure, buildings are classified into three safety categories in GB 50153-2008. The safety category of the studied roof structures in this paper is assumed to be II, therefore the importance factor $\gamma_0$ is 1.0 and the target reliability index is 3.2 which means the probability of structural failure in 50 years is not more than $6.9 \times 10^{-4}$ if the failure of structural members is ductile. The reliability indices of steel roof members in the three cities which include Beijing, Nanjing and Hohhot are assessed through Monte-Carlo simulation in this paper, and the influences on reliability assessment of different probabilistic models for ground snow loads is also investigated.

### 3.1 Limit state function

Reliability of roof structures can be defined by the limit state function as follows:

$$g(R,D,S) = R - (C_D D + C_S S) \quad (4)$$

where $C_D$ and $C_S$ are the conversion coefficients of load to effect for dead load and snow load, respectively. Reliability assessment would not be influenced by assumption $C_D = C_S = 1$ when snow load and dead load are all uniformly distributed on the roof surface, which means that the spatial variability of dead and snow load are ignored. R, D, and S are dealt as random variables, and Monte-Carlo simulation is adopted to calculate structural reliability indices. Probability of structural failure equals to the probability of $g(R,D,S) < 0$.

### 3.2 Structural resistance

The suggestion of Ellingwood (1982) is taken herein that resistance of a steel roof member can be defined by a lognormal distribution, with a mean 1.07 times its characteristic value and coefficient of variation 0.15 [6]. Characteristic value of resistance is determined by formula (2) and (3) according to Chinese load code GB 50009-2012.

### 3.3 Dead load

Dead load of a roof structure mainly refers to its self-weight, which hardly changes with working time in general. Thereby, dead load is also treated as a random variable that does not vary with time. Normal distribution was suggested by Ellingwood (1982) to describe it [6], the mean value is 1.05 times its characteristic value, and coefficient of variation is 0.10.

### 3.4 Snow load

Snow load on a roof is generally defined by the product of the ground-to-roof conversion factor $\mu$ and the ground snow load $S_g$. Conversion factor $\mu$ can be

modelled as a lognormal random variable referring to O'Rourke (1983) [7]. Thiis and O'Rourke (2015) statistically analysed the database containing simultaneous measurements of roof and ground snow loads in southern Norway [8]. They obtained the shape coefficient $\mu$ for low-slope roofs (0-5°) with mean 0.73 and standard deviation 0.12. It is assumed herein that the ground-to-roof conversion factor $\mu$ for flat roofs in the three cities of China has the same parameters.

JCSS proposes that Ferry Borges-Castanheta process can be used to describe variable loads. Thus, the maximum value of snow load in the design working life T of a building is given by,

$$F_T(x) = [F(x)]^T \tag{5}$$

where $F(x)$ is the cumulative distribution function of the annual maximum ground snow load, $F_T(x)$ is the cumulative distribution function of the maximum ground snow load in the design working life of a building.

GB 50009-2012 proposes that Gumbel distribution should be used to characterize the annual maximum ground snow depth, and method of moments (MOM) should be used to estimate the parameters of Gumbel distribution. Nonetheless, Gumbel distribution, generalized extreme value (GEV) distribution, and lognormal distribution are considered for the simulated annual maximum ground snow loads. Method of moments (MOM), maximum-likelihood estimation (MLE), and least square method (LSM) are employed to estimate the parameters of Gumbel distribution. MOM and MLE are applied to lognormal distribution. MLE is adopted for GEV distribution. The Kolmogorov-Smirnov (K-S) test is adopted to examine the applicability of above mentioned probabilistic models, and Akaike information criterion (AIC) defined by formula (6) is used to measure the relative quality of above probabilistic models for annual maximum ground snow loads.

$$AIC = 2k + n \ln (RSS) \tag{6}$$

where n denotes the sample size of simulated snow loads and k denotes the number of parameters of distribution. RSS is the residual sum of squares. The preferred model is the one with the minimum AIC value.

The results of Kolmogorov-Smirnov test indicate that all of the above mentioned distributions and corresponding parameter estimation methods are applicable to the annual maximum ground snow loads. The relative quality of different models according to AIC are compared in Tab. 2. The '1st' means the minimum AIC value, and the '6th' implies the worst model.

**Tab.2** AIC of different models

| Models | Beijing | Nanjing | Hohhot |
|---|---|---|---|
| Gumbel(MOM) | 5th | 4th | 2nd |
| Gumbel(MLE) | 2nd | 6th | 5th |
| Gumbel(LSM) | 1st | 5th | 1st |
| Lognormal(MOM) | 6th | 3rd | 4th |
| Lognormal(MLE) | 4th | 2nd | 3rd |
| GEV(MLE) | 3rd | 1st | 6th |

Furthermore, Q–Q plots are used to graphically compare the simulated data sets to the underlying theoretical models, as showed in Fig.2 (a)~1(c). The x

coordinate of a point on the plot corresponds to one of the quantiles of the simulated snow load data set, and the y coordinate of the point is the same quantile of an underlying theoretical distribution. If a distribution characterize the data set well, the points in the Q-Q plot will approximately lie on the line y=x. It can be found that the model with the minimum AIC value fit the overall data best on the Q-Q plots of the three cities, but many outliers appear at low quantiles and high quantiles. Notably, the goodness of fit to high quantiles is more important for reliability assessment, compared to low quantiles, because that the maximum value of ground snow load in the design working life which is usually 50 years is directly related to structural failure. However, the high quantiles are too scattered to fit well. In order to clarify the influence of the models for annual maximum ground snow loads on structural reliability assessment, all the underlying distributions for annual maximum ground snow loads mentioned above are considered.
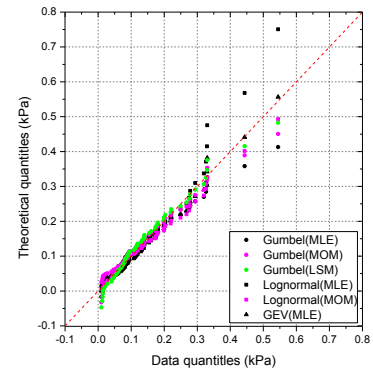


(a) Beijing
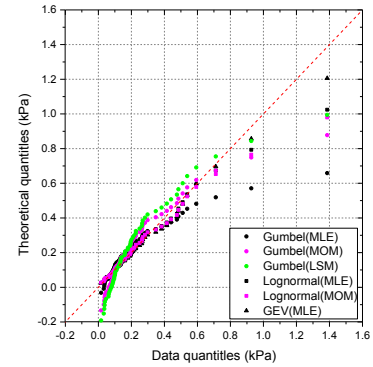


(b) Nanjing
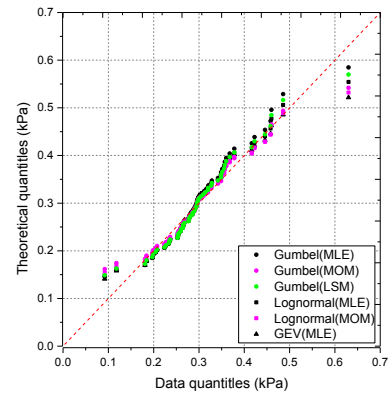


(c) Hohhot

**Fig.2** Q-Q plots for comparison of different probability models to annual maximum ground snow loads

103

Basing on the distribution of annual maximum values, Monte-Carlo method is used to simulate the maximum ground snow loads in the design working life of a building, which is 50 years in general. A procedure of generating the maximum ground snow loads in 50 years on the basis of the distributions of annual maximum ground snow loads is explained as follows:

(1) Firstly, 1,000,000 sets of annual maximum ground snow load samples are generated by Monte-Carlo simulation, each set contains 50 data.

(2) Then, the maximum values in every set of annual maximum ground snow loads are picked out to act as the maximum ground snow loads in 50 years. Thus, the sample of maximum ground snow loads in the design working life of a building is assembled.

## 4 Results and discussion

As showed in Tab. 1 and discussed in section 3.4, the annual maximum ground snow loads in Beijing, Nanjing, and Hohhot have different variability. K-S test indicate that all of the 6 probabilistic models considered in this paper can be used for the annual maximum ground snow loads of the three cities, whereas different distributions and parameter estimation methods lead to great difference in estimating high quantiles. In order to explore the influences on structural reliability assessment of this difference, all of the 6 models are adopted as the basis of the distribution of the maximum ground snow loads in 50 years, and Monte-Carlo simulation is employed to calculate structural reliability indices. The results are displayed as Fig. 3.



(a) Beijing



(b) Nanjing
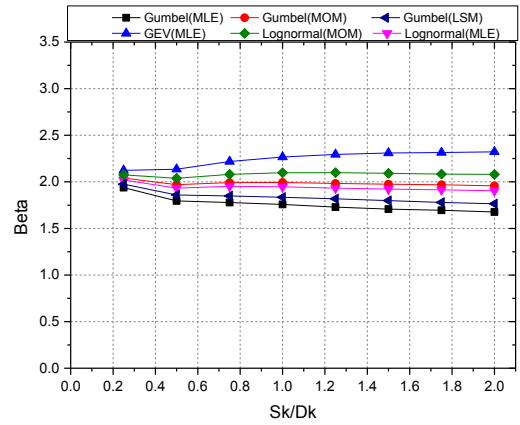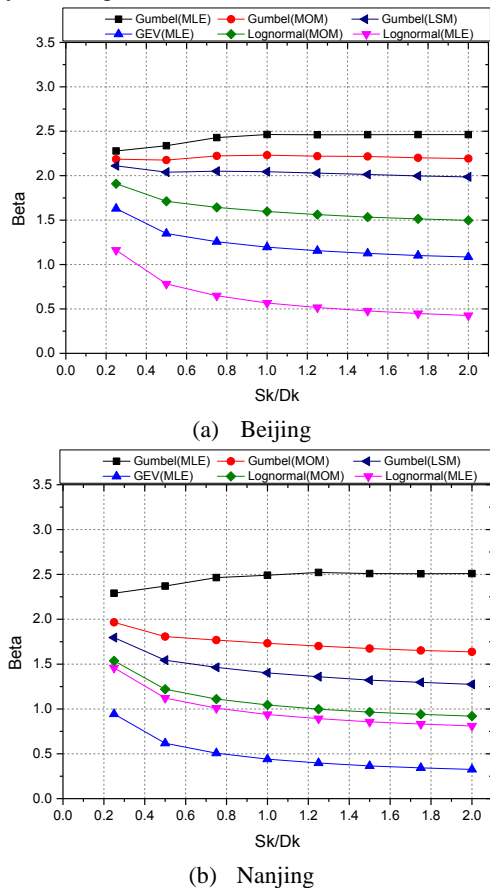


(c) Hohhot

**Fig. 3.** Reliability indices for steel roof members designed by Chinese codes in different cities.

Fig.3 (a) shows that different distributions and parameter estimation methods lead to great difference in results of structural reliability assessment for Beijing, which is consistent with the influence on high quantile estimation. Combining Fig.3 (a) with Fig.2 (a)，one can find that the model which is a combination of Gumbel distribution and MLE gets the minimum estimation of high quantiles in Q-Q plots of Beijing, but lead to the maximum estimation of structural reliability indices. Conversely, the model that is composed of lognormal distribution and MLE gets the maximum estimation of high quantiles in Q-Q plots of Beijing, but lead to the minimum structural reliability indices. It also can be found from Fig.2 (a) that the model consisted by GEV distribution and MLE fit well to the high quantiles of Beijing's annual maximum ground snow loads, therefor the reliability assessment results basing on it is the most believable and other results are overestimated or underestimated.

From Fig.3 (b), one can find the similar results of Nanjing compared to Beijing that if a model underestimate the high quantiles, it will lead to an overestimated structural reliability assessment. Fig.2 (b) shows that the six models all underestimate the high quantiles of Nanjing, therefor the reliability indices of steel roof members in Nanjing are overestimated.

Fig.3 (c) shows that the reliability indices of steel roof members in Hohhot approximately lies at the range [1.7, 2.3], which are influenced less by the models for annual maximum ground snow loads compared to Beijing and Nanjing. The reason is that the 6 models have almost the same goodness of fit to the high quantiles of Hohhot.

Comparing the results of the three cities, one can find that the difference of high quantile estimation by the six models tends to become more and more obvious as the COV increases, and the same trend of the influence on reliability assessment can be found.

Furthermore, it can be found that the influence on structural reliability assessment of probabilistic models for snow loads become larger slightly with the increase of the ratio of characteristic snow-to-dead load. The reason for this is that the total load effect will have greater

variability if the ratio is larger on the condition that the variability of snow load is greater than that of dead load.

## 5 Conclusions

GB 50009-2012 proposes Gumbel distribution for annual maximum ground snow loads, and method of moments (MOM) for estimating parameters. Nonetheless, six different models which are the combination of three distributions and three parameter estimation methods are considered for annual maximum ground snow loads in this paper to investigate structural reliability indices of steel roof members in three representative cities of China. The results indicate that an appropriate probabilistic model for annual maximum ground snow loads is very important to structural reliability assessment. The main conclusions of this paper are the following:

(1) If a model overestimate the high quantiles of annual maximum ground snow loads, it will lead to conservative assessment of structural reliability. Whereas structural reliability will be overestimated if the model used for annual maximum ground snow loads underestimate the high quantiles.

(2) The larger the COV of annual maximum ground snow loads is, the more difficult it is to fit the high quantiles well, and more uncertainties in structural reliability assessment will be found.

(3) The influence on structural reliability assessment of probabilistic models for snow loads tends to be a little greater with the increase of the ratio of characteristic snow-to-dead load.

## References

1. T. Takahashi, and B. R. Ellingwood, Reliability-based assessment of roofs in Japan subjected to extreme snows: incorporation of site-specific data, Eng. Struct. ,**27**:89-95 (2005)
2. D. L. Kozak, and A. B. Liel, Reliability of steel roof structures under snow loads, Struct. Saf., **54**: 46-56 (2015)
3. X. Y. Zhou, Y. Q. Zhang, M. Gu, et al, Simulation method of sliding snow load on roofs and its application in some representative regions of China ,Nat. Hazards,**67**: 295-320 (2013)
4. Ministry of Construction of the People's Republic of China, General Administration of Quality Supervision, Inspection and Quarantine of the People's Republic of China, *Load code for the design of building structures* (GB 50009-2012), China Building Industry Press, Beijing (2012)
5. Ministry of Construction of the People's Republic of China, General Administration of Quality Supervision, Inspection and Quarantine of the People's Republic of China, *Unified standard for reliability design of engineering structures* (GB 50153-2008), China Building Industry Press, Beijing (2008)
6. B. Ellingwood, T. V. Galambos, Probability-based criteria for structural design, Struct. Saf., **1**(1): 15-26 (1982)
7. M. O'Rourke, U. Stiefel, Roof snow loads for structural design, J. Struct. Eng., **109**(7): 1527-1537 (1983)
8. T. K. Thiis, M. O'Rourke, Model for Snow Loading on Gable Roofs, J. Struct. Eng., 04015051 (2015)

# Session 3

# Avalanche / Snow physics

# The importance of field measurements and observation systems in snow engineering: examples in the fields of avalanche dynamics and drifting snow

Florence Naaim-Bouvet

*Univ. Grenoble Alpes, IRSTEA, UR ETNA, Saint Martin d'Hères, France*

**Abstract.** At a time when public finances are low and the cost of setting up, operating, maintaining and managing observation systems high, it is essential to understand the importance of field data in snow engineering. This paper will explain and demonstrate this importance using practical examples in the fields of avalanche dynamics and drifting snow. For snow avalanche dynamics, a huge effort has been made to carry out and manage field measurements and observations and to disseminate data at the European or even global level. This has led to significant progress in related snow engineering applications. For drifting snow, however, much still needs to be done. Ongoing work and propositions aimed at enhancing the data base and improving the management of field observations will be presented.

## 1 Introduction

Observation systems capable of providing data for snow engineering purposes are costly to set up, operate, maintain and manage. At a time when public funding is increasingly hard to come by, it is important to understand the essential nature of field data in snow engineering. This paper presents a number of examples in the field of snow avalanche dynamics and drifting snow that clearly illustrate this point. They are based on my professional experience acquired in these fields as an engineer and researcher.

In snow science and more generally in geophysics, observation lies at the heart of research (Figure 1). The first process in the scientific method [1] involves the observation of a phenomenon, event or "problem." Observation leads to a question that needs to be answered to satisfy human curiosity or solve a given problem. To answer the question, a hypothesis is formed. Once the hypothesis has been established, an experiment must be designed to prove or disprove the hypothesis.

In Earth sciences, including snow science, application of the scientific method can sometimes be complicated by the fact that the Earth is not a controlled laboratory. Many variables are involved. Scientists must design controlled and repeatable experiments to develop and validate theories. Note that there is a permanent exchange and mutual enrichment between theory, observation, numerical experiments and laboratory experiments.

Working at very different spatial scales represents an additional complexity. For example, for drifting snow, the scale of interest extends from that of the particle (if we focus on the splash function) to the continent (if we are interested in surface mass balance in Antarctica).

Snow engineers have various tools at their disposal to solve problems and design various works. These tools are mainly based on research results. As in snow science, observation is important and provides the necessary background (Figure 2). The choice of final design values requires statistical methods based on observations. Moreover, the analysis of experts relies on personal observations compiled in their minds over the years to form "living" data bases. Physical and numerical simulations are often used to solve a given problem but

field experiments first provide the benchmarks for the development and calibration of such models.

Snow research contributes to snow engineering and snow engineering in turn provides feedback, questions to investigate and practical problems to solve.
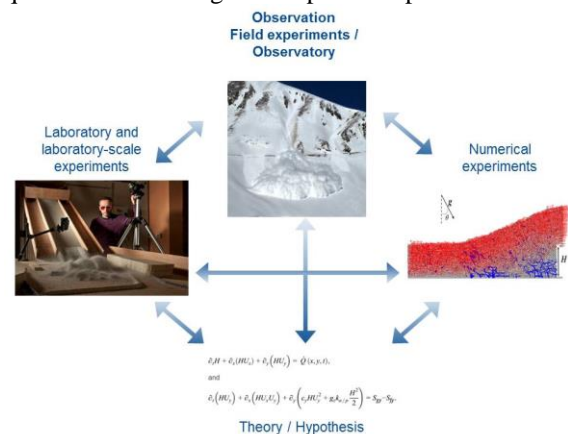


**Figure 1.** The role of observation in snow science
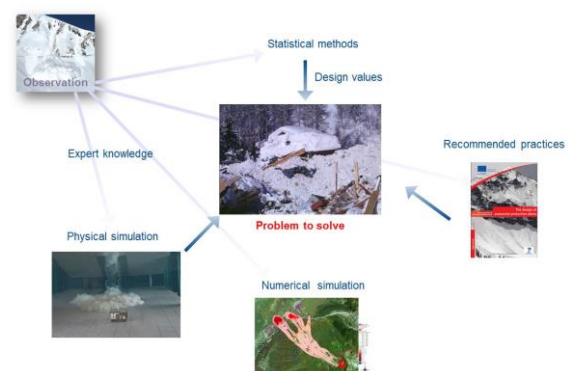


**Figure 2.** The role of observation in snow engineering

In an attempt to be more practical than theoretical, the importance of field measurements and observation systems in snow engineering will be illustrated in this paper with specific examples. For snow avalanche dynamics, a huge effort has been made to carry out and manage field measurements and observations and to disseminate data at European and even global levels.

Significant results have been transferred to snow engineering. For drifting snow, much work remains to be done and many questions have not yet been answered.

The paper is organized as follows: Section 2 discusses the importance of field measurements from avalanche test sites, presents data from avalanche surveys and deals with the combined use of avalanche surveys and numerical models. Section 3 focuses on the lack of data for drifting snow and briefly introduces ongoing attempts to improve and better manage observations in this field.

## 2 Avalanche dynamics

Snow avalanches represent a serious problem in our society. In the United States and Canada, most avalanche accidents involve recreational users, but in other part of the world houses and businesses are also at risk (01-02/1992: 261 deaths in Turkey – 05/1998: 250 deaths in India – 01/1993: 239 deaths in Russia – 03/1997: 100 deaths in Afghanistan – 01/1954: 200 deaths in Austria – 1950/1951: 98 deaths in Switzerland – 02/1970: 39 deaths in France – 02/1999: 17 deaths in Switzerland and 12 deaths in France).

As we can see, there are many areas in Europe that have a long and tragic history of avalanche accidents. This is probably the reason that research on this topic is very active in Europe, as can be seen from an analysis of search results in the Scopus data base presented for different countries (Figure 3).
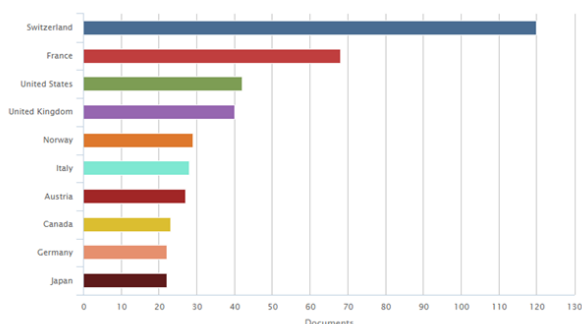


**Figure 3.** Scopus data base search results presented for different countries (search keywords: "Avalanche" + "Flow" / date: May 2016)

### 2.1 Field measurements on avalanche test sites

All European research centres dealing with avalanche dynamics are aware of the importance of field measurements and perform full-scale avalanche experiments even though they are costly, time-consuming and dangerous. Such experiments provide data that is essential to the understanding and modelling of avalanche motion, even if it can take several years to obtain reliable results. Many different configurations of avalanche types and paths need to be studied. A number of European countries have jointly planned and conducted such experiments through three successive European FP projects (SAME, CADZIE and SATSIE) [2]) and two bilateral INTERREG ALCOTRA projects (DYNAVAL

and MAP[3]) [3]. A dozen full-scale test sites have been involved, though at present only five are still operative (Table 1).

Rather than describe the sites and their instrumentation and configuration in detail, we will focus on their complementarities in terms of configuration and range of pressure, velocity, path length and drop height, as can be seen clearly in Table 1. The smallest site is in Italy, with a path length of 400 m and a maximal pressure of 0.5 tonnes/m². The biggest site is in France, with a path length of 7000 m and a maximal pressure of 100 tonnes/m². Note that all these sites are open to collaborations and can accommodate sensors provided by other sites or teams.

The Taconnaz avalanche path (Chamonix, France) (Figure 5) [4] is extremely long. An international road and several buildings are located in the area at risk, leading to the design of an avalanche protection system. Avalanches mainly consist of dry snow with ice blocks breaking from the glacier and cannot be artificially released.

The Vallée de la Sionne (Switzerland) avalanche path (Figure 4) [5] ends with an inverse slope on which a bunker houses staff during the experiments. The site is probably the best equipped with a unique collection of field-hardened sensors to measure avalanche velocity, impact pressure, flow depth and density.

The Ryggfonn (Norway) (Figure 6) [6] runout ends at a catching dam which was built to test the effectiveness of such a mitigation measure.

As opposed to others full-scale avalanche test sites in Europe, the runout at Lautaret (Figure 7) [7] is a natural open slope. Flow height, vertical profiles of pressure and velocity are measured along a mast which was destroyed in 1995 and subsequently rebuilt. Note that measurement equipment has been destroyed at least once on all the experimental sites.



**Figure 4.** Vallée de la Sionne avalanche test site (photo courtesy of SLF)
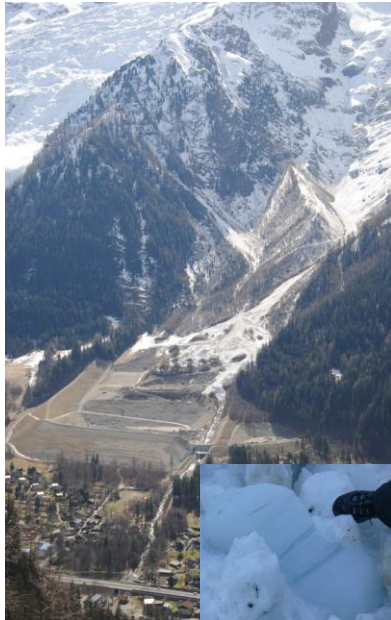
**Figure 5.** Taconnaz avalanche test site (inset: ice blocks in snow avalanche deposit)



**Figure 6.** Ryggfonn (avalanche test site (photo courtesy of NGI)



**Figure 7.** Lautaret avalanche test site

Seehore peak (Figure 8) [8] in Italy is the latest test site to have been set up and is used to study artificially released small and medium avalanches, while the majority of the existing sites study large avalanches.



**Figure 8**. Seehore peak avalanche test site (photo courtesy of E. Bovet)

Much has been learned over the last 10-15 years from this well-organized network of avalanche test sites. Recorded data helps us understand the physical processes of a flowing avalanche or an avalanche impacting on catching dams or others obstructions. Such data is also used to calibrate avalanche-dynamics models. In this paper, we will focus on two main results now used in snow engineering.

### 2.1.1 Erosion and deposition processes

The analytical and numerical models used in practical calculations of snow avalanche dynamics contain a questionable simplification: they assume that avalanche mass is constant meaning that no snow cover entrainment or mass deposition takes place along the avalanche path.

In order to establish the mass balance of an avalanche, he distribution of the snow before and after avalanche release (Figure 9) has been measured first by photogrammetry and then by laser scanning [9]. These measurements have shown that the avalanche mass can be 6-7 times higher than the released mass [10]. This has led to the development of advanced erosion and deposition models used in numerical models. The validation of such advanced models requires in turn more detailed measurements of the processes within the avalanche and therefore more sophisticated field measurements.
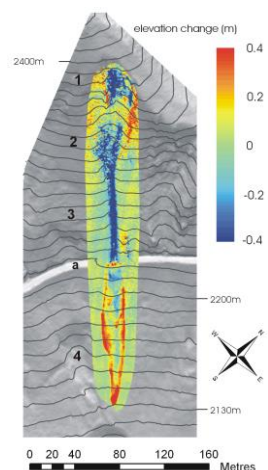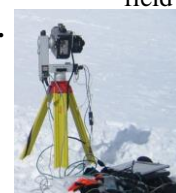


**Figure 9**. Map of the elevation difference as measured by laser scanning for the avalanche released on the Col du Lautaret path on 13 February 2013. [7]

**Table 1.** Key features of avalanche test sites (updated from [2])

| | Seehore Italy 2009 Small size | Lautaret France 1973 Small to medium size | Ryggfonn Norway 1980 Medium size | Vallée de La Sionne Switzerland 1999 Large size | Taconnaz France 2010 Large size |
|---|---|---|---|---|---|
| **Release** | Artificial | Artificial | Artificial | Artificial/natural | Natural |
| **Path length** | 400- 500 m | 800 m | 2100 m | 2700 m | Up to 7000 m |
| **Drop height** | | 450 m | 975 m | 1300 m | 3000 m |
| **Mean slope** | 38° | 36° | 31° | 29° | 25° |
| **Deposit volume** | 200-400 m$^3$ | 500-10,000 m$^3$ | 10,000 m$^3$ - 100,000 m$^3$ | 300,000 m$^3$ | 1, 600,000 m$^3$ |
| **Pressure** | 0.5 t/m$^2$ | 3-5 t/m$^2$ | 60 t/m$^2$ | Up to 100 t/m$^2$ | Up to 100 t/m$^2$ |
| **Velocity** | Up to 30-40 m/s | Up to 30-40 m/s | Up to 60 m/s | Up to 50-70 m/s | Up to 70 m/s |

## 2.1.2 Impact pressure

The impact pressure P can be expressed as a function of the dynamic pressure where $C_D$ is the effective drag coefficient (eq. 1).

$$P = \frac{C_D \rho U^2}{2} \qquad [1]$$

where $\rho$ the flow density and U the flow velocity upstream of the obstacle.

$C_D$ is generally taken as 1. It has been shown that the drag coefficient increases as the Reynolds number decreases (Figure 10) so that high pressures can still be exerted at low velocities in the runout zone, as observed in MontRoc (Figure 11) near Chamonix during the 1999 avalanche disaster in France. Avalanche hazard maps are used as regulation for land use planning. It shows the maximum between the centennial and maximal observed run-outs. The hazard levels are colour-coded red, blue and white according to the impact pressure. Using a constant value of 1 for the drag coefficient leads to an underestimation of the avalanche hazard in the locations where the velocities are low such as run-out zones.
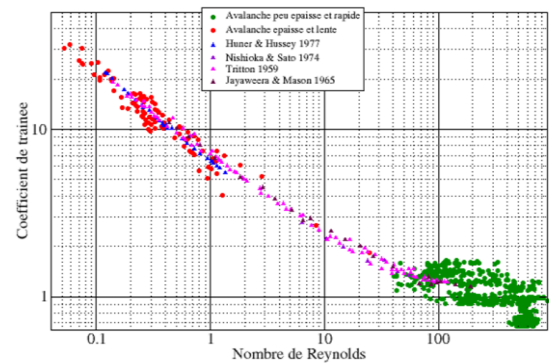


**Figure 10**. $C_D$ as function of the Reynolds number [11]

**Figure 11**. High pressure exerted at low velocities in the runout zone of Péclerey avalanche that hit MontRoc village (9 February 1999) – F. Rapin/IRSTEA.

## 2.2 Observatories: permanent avalanche surveys

Observatories generally measure fewer variables but offer greater data availability over time compared to specific field measurement campaigns that are more often dedicated to particular research topics and practical questions.

In France, an extensive avalanche data base is available. The Enquête Permanente sur les Avalanches (E.P.A.) is a descriptive report including quantitative (runout altitudes, deposit volumes,…) and qualitative (flow regime, release cause,…) information for selected avalanche paths. This chronicle is characterized by its long duration. Furthermore, it was set up by a forest engineer and not by a scientist. The first avalanches were recorded in the Savoie region in 1899. 3936 paths are monitored each winter, involving 465 towns and 260 observers. In all, 85,000 events are available over the last century (www.avalanches.fr).

The data series in this unique data base are unusually long, even if some of them are incomplete and suffer from quality problems. This data base was initially devoted to the evaluation of forest damage but is now highly valuable for other applications. For instance, it provides an accurate view of the spatio-temporal fluctuations of avalanche activity over the last century in the context of climate change.

At the scale of the entire French Alps, a major turning point can be noted around 1978 [13]: between 1946 and 1978 we observe an increase of 0.1 avalanche occurrences per winter and per path and a roughly 55 m lower runout altitude. And between 1978 and 2010, the reverse occurs: we notice a decrease of 0.1 avalanche occurrences per winter and per path and the runout altitude rose 55 m.

The same trend is observed if we consider the runout altitude corresponding to a return period of 10 years. Considering the clearly non-stationary nature of this phenomenon, the issue that must be addressed is: How can we evaluate long term avalanche hazards?

There has also been a general decrease of around 12% in the proportion of powder snow avalanches since 1973.

This decrease appears to be consistent with increasing winter temperatures over the same period.

## 2.3 Combined use of permanent avalanche surveys and numerical models

### 2.3.1 Local predetermination using statistical-dynamical approaches

Even if we consider stationary conditions, determination of a 100-year event in the framework of protection design is not so obvious.

Legal regulations for land use planning are based on return periods that vary depending on the country. For example, it is a 100-year return period in France. The 100-year volume and runout distance can be directly calculated from the EPA data base. However, protection dam design requires estimates of impact pressure. The example of the Taconnaz avalanche provides greater insight into how the problem has been solved by combining an avalanche-dynamics model and the EPA data base.

The Taconnaz avalanche path (Figure 5) is located in the Chamonix valley close to Mont Blanc. It is the largest European avalanche path with roads and buildings located within the zone of risk. The Taconnaz path is 7 km long with a vertical drop of 2 km and a mean slope of 25°. A total of 75 events have been recorded in the data base. Each recorded event was back-calculated using a numerical model of dense flow to define parameters (the volume and the Froude number, F defined as the square root of the ratio between the kinetic and potential energies corresponding to the maximum discharge) at the entry of the runout zone upstream of the defence structures. Then, a statistical analysis of these parameters allowed characterization of 100-year return period events. The 100-year values were 3.58 for the Froude number and 1.6 Mm$^3$ for the volume. Finally, physical (Figure 12) and numerical (Figure 13) models of dense avalanches interacting with defence structures were combined in order to design the most effective passive structure to contain the reference scenarios.



**Figure 12**. Small-scale physical model of the runout zone fed with granular flows from a channel of adjustable slope and equipped with a reservoir at the top to release granular material
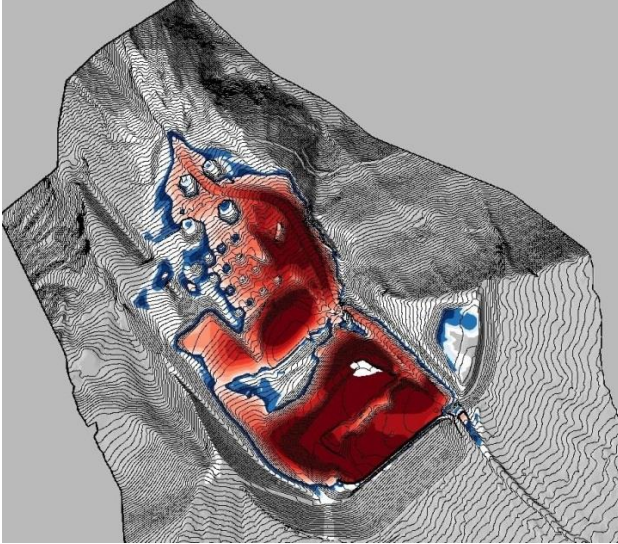
Figure 13. Final deposits determined by numerical simulation

## 2.3.2 Correlation between friction coefficients and the physical properties of snow

Even rough data can be used to gain an in-depth understanding of avalanche flow dynamics.

Naaim et al. [15] have combined the EPA data base with avalanche-dynamics models and snowpack models to link avalanche friction coefficients and the physical properties of snow.

A total of 735 historical avalanches released on 26 paths and recorded in the EPA chronicle since 1958 have been back-analyzed using a depth-averaged model with a high-resolution digital model acquired by laser scanning. The initial snow depth and snow cohesion were computed using the detailed CROCUS snowpack model fed with data from a SAFRAN meteorological analysis. More than 940,000 simulations were performed.

The results show that the static friction coefficient increases quasi-linearly with temperature (Figure 14), meaning that the runout distance should decrease with temperature. This is consistent with previous results which suggested that the decrease in runout distance was due to atmospheric warming that modified the average characteristics of snow. Focusing on liquid water content (Figure 15), it can be shown that the static friction coefficient decreases strongly for high values, typically those higher than 35 kg m$^{-3}$
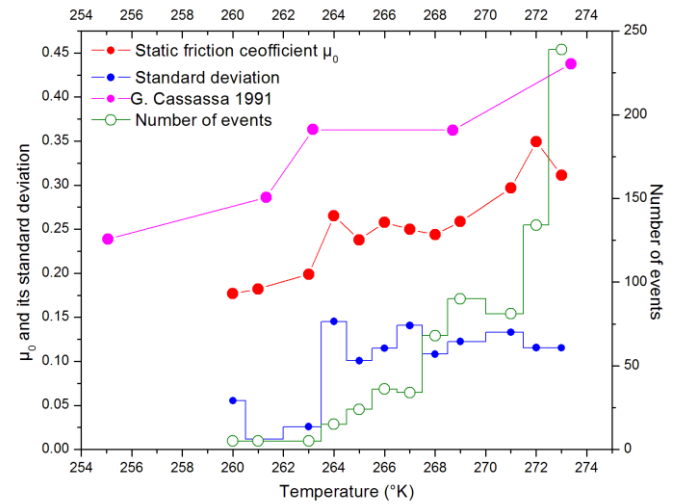


Figure 14. Back-analyzed static friction coefficients $\mu_0$ as function of average snow temperature T [15]
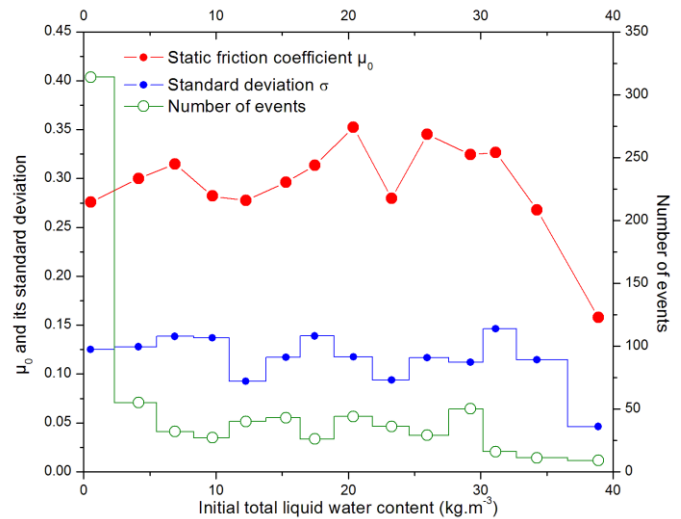


Figure 15. Back-analyzed static friction coefficients $\mu_0$ as versus liquid water content [15]

This section has provided a brief overview of practical lessons learned from avalanche dynamics field measurements and observations, which are not dedicated only to the validation of numerical models, as some may think. A huge effort has clearly been made to carry out and manage field measurements and observations and to disseminate data. The progress achieved in the field of avalanche dynamics is the result of many years of data acquisition and human and financial investments. In the field of drifting snow, much remains to be done, as will be discussed in the next section. Neither numerical and physical models nor expert knowledge can answer all practical questions, as shown by numerous examples. For this reason, efforts must be continued to set up and manage observations in the field.

# 3 Drifting snow

## 3.1 Estimation of drifting snow fluxes

The estimation of drifting snow fluxes remains an open question. Consider for example the case of Gouter refuge [16].

The new Gouter refuge was constructed in 2012 at a height of 3835 m on the normal route to Mont-Blanc, 200 meters from the old refuge. Drifting snow was a problem at the old refuge (Figure 16). For the new refuge, the architects wanted to design a building with main and backup exits free of snow and a drinking water supply fed by melting snow (Figure 17). Small scale experiments were carried out in a wind tunnel (Figure 18) and led to several recommendations for the building.

- Shape: aerodynamic (ovoid)
- Orientation: major axis of the ellipse parallel to the prevailing wind direction
- Layout: entrance in the front of the building and the melting container in the back
- Overhang: as much as possible.



**Figure 16**. Snowdrift around the former buildings. The red arrow indicates the prevailing wind direction



**Figure 17.** Melting container in the back of the building



**Figure 18.** Small-scale model in the wind tunnel (H. Raguet)

However one question remains unanswered. It concerns the amount of snow that can be expected to cover the melter for a given duration. This is an important question given that the melter container must supply water for 120 people. Unfortunately, it cannot be answered for several reasons. First of all, there is no consensus on similitude requirements for storm duration [17]. However, the main problem concerns data. In fact there are not enough data to quantify a reference snow storm for the project (annual snow storm, for example). Furthermore even if wind data were available, drifting snow quantities could not be estimated accurately. Empirical formulae available in the literature produce divergent results [18].

## 3.2 Projected trends in the context of climate change

The formation of snowdrifts on roads causes disturbances to communication and transportation systems.

This was the case during the winter of 2005 when the A75 motorway linking Belgium and Spain was closed for 6 days due to the formation of snowdrifts (Figure 19) at La Fageolle pass, one of the highest motorway passes in Europe [19].



**Figure 19.** A75 closed to traffic: snow-removal operations

In France, drifting snow is generally controlled by artificial snow fences. However, forested strips are being

used increasingly because they are better adapted to multidirectional wind. Unfortunately, such a solution takes time to become effective, as illustrated by the photos in Figure 20 and Figure 21, taken 26 years apart.



**Figure 20.** Forested strips planted in 1991 to control snowdrifts at La Fageolle pass



**Figure 21.** The same forested strips in 2007

Decision makers voiced strong doubts when it was suggested to extend the existing forested strip to strengthen snowdrift control. They wanted assurance that drifting snow storms would still exist at this location 30 years from now, when the proposed solution would become effective.

Unfortunately, we lack the necessary data to assess the effects of climate change on blowing snow storms.

## 3.3 Field measurements and observations for drifting snow

Even if drifting snow represents a serious problem, it is less important in our society than avalanches. Research on drifting snow is not mainly conducted in the countries of the Alps (Figure 22) and the research network is less organized. Even if there is a need, the strategy differs from that adopted for avalanches.
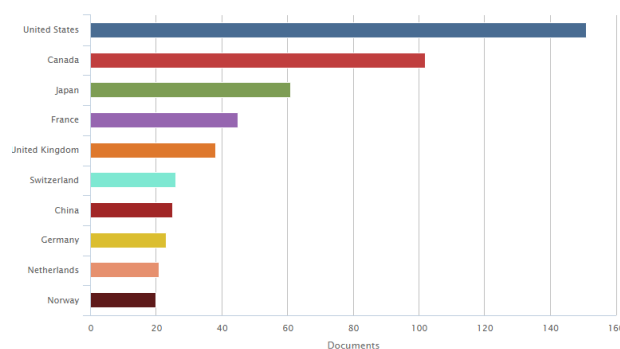


**Figure 22.** Scopus data base search results presented for different countries (search keywords: "Drifting snow" + "Blowing snow" / date: May 2016)

For France there are two experimental test sites dedicated to drifting snow within the framework of the CRYOBS-CLIM observatory: Lac Blanc Pass and Adélie Land.

CRYOBS-CLIM (the CRYosphere, an OBServatory for the CLIMate) is aimed at gathering monitoring results and long-term observations performed by French research institutes on mountain glaciers, polar ice-sheets, seasonal snow cover and mountain permafrost and to provide relevant tools and observational data to a wide community so that they can address major societal issues such as water resources, ice-related hazards, atmospheric processes, avalanches, sea level rise and global climate change. The long-term observation strategy is based on in-situ (automated and manual) and remote (photogrammetry, LiDAR, satellite) monitoring of snow- and ice-related variables. Observations will be disseminated to the entire scientific community through a data base (http://www.cryobsclim.osug.fr/) that will be released in 2017.

### 3.3.1 Lac Blanc Pass

Lac Blanc Pass (2720 m a.s.l.), in the French Alps, is a part of the CRYOBS-CLIM network. It has been operated by IRSTEA and Météo France since 1990 and is dedicated to the observation of a typical high altitude snowpack strongly affected by drifting and blowing snow.

The aim is to study the physical processes involved in a mountainous context, create a data base for numerical modelling and create a 25-year long climatological reference at 2720 m a.s.l.

Due to the surrounding topography, winds are 80% from the north-east or the south. Moreover snow transport is observed 10.5% of the time in winter [21]. Initially, the site was mainly equipped with conventional meteorological stations and a network of snow stakes (Figure 23). Then new sensors (Figure 24) and technologies (ultrasonic anemometers, drifting snow sensors including snow particle counters and laser scanners [22]) (Figure 25) were installed, making it possible to develop new knowledge dealing with the relationships between threshold velocities and

morphological features of snow grains and snow flux profiles including parameters such as fall velocity and Schmidt number, histograms of particle widths, aerodynamic roughness, sastrugi and gust factors.

The physical processes involved in drifting snow have thus been studied more deeply, making it possible to better take them into account in models. At the same time, the instrumentation has made it possible to estimate the output parameters (snow depth) with a higher spatial resolution.

Note that data from 28 Flowcapt acoustic snowdrift flux sensors, operated in mountainous environments (France, Spain, Italy, Switzerland, Chili), are available on line (http://www.iav-portal.com/).

FlowCapt acoustic sensors, designed to measure the fluxes of snow transported by wind, have been compared to optical snow particle counters, considered herein as the reference at the Lac Blanc Pass, where a bench test for the wind transport of snow was set up. The two existing generations of FlowCapt have been compared. Both seem to be good detectors for the transport of snow by wind, but refinements still need to be made to accurately estimate drifting snow fluxes [23]. The third generation is currently being tested.



**Figure 23.** Conventional meteorological station and a network of snow stakes



**Figure 24.** Ultrasonic anemometer, wind anemometer profile, acoustic and optical snow transport sensors



**Figure 25.** Terrestrial laser scanner and general view of the experimental site.

### 3.3.2 Adélie Land

More recently a similar experimental test site has been set up in Antarctica (Figure 26). Measurements are less intensive due to logistical constraints [24]. The site is managed by LGGE (Laboratory of Glaciology and Environmental Geophysics, CNRS, Grenoble) with the logistical support of the French Polar Institute.

Net erosion of snow by the wind may contribute significantly to the surface mass balance of the Antarctica coastal zone. However, there are very few field observations to confirm this hypothesis and to evaluate numerical models developed for this purpose [25]. Adélie Land is characterized by strong and frequent katabatic winds which are the strongest in the world in terms of mean wind speed at sea level. They are often associated with wind transport of snow. A field campaign was therefore launched in 2009. The observation system consisting in three automatic weather stations was deployed with Flowcapt acoustic drifting snow sensors close to the coast. The stations were set up at different locations, ranging from 1 to 100 km inland. One of them has a 7-m mast with six levels of anemometers and thermohygrometers (Figure 27).



**Figure 26.** Work environment in Antarctica (photo courtesy of LGGE – Grenoble)
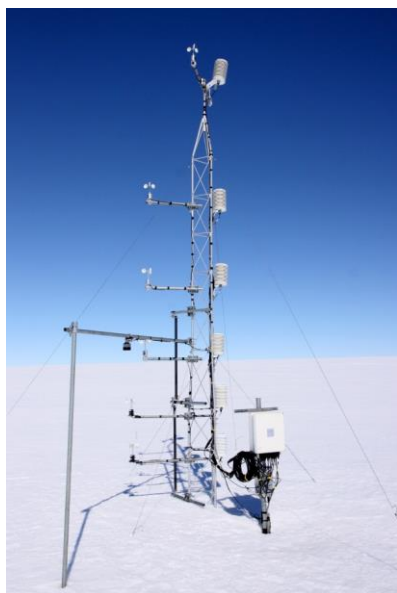
**Figure 27.** Flowcapt sensor (foreground) with a 7-m mast with six levels of anemometers and thermohygrometers (photo courtesy of LGGE – Grenoble)

Drifting snow is a complex phenomenon at different spatial scales and is representative of the mutual interaction between the atmosphere and snow cover. Accurate field measurements covering long periods of time are extremely difficult to acquire. As is the case with avalanches dynamics, addressing this problem therefore requires a combination of resources, teams, sites, specialties and expertise.

Such a measurement programme is underway at Lac Blanc Pass and Adélie Land, two French experimental sites managed by three different institutes (IRSTEA, Météo France and LGGE). It will make it possible to observe and model drifting snow and validate and refine new and existing models. Further progress could be achieved by sharing this information at a global level.

## Conclusions

The importance of field data in snow engineering has been demonstrated thorough the paper using specific examples dealing with avalanche dynamics and drifting snow.

It is true that operating and maintaining experimental sites and observatory systems requires tremendous effort.

Nevertheless, given the importance of such measurements in snow research and risk management, research institutes should be encouraged to secure funds and human resources to maintain the level of these data series.

The importance of sharing data to cover a large spatial and temporal scale is well recognized and we must enhance and take full advantage of the complementary nature of the different sites.

Data exchange is of course a sensitive topic. Nevertheless several initiatives to this end have already been taken at a global level concerning different aspects of the cryosphere including snow. The objectives include facilitating:

- the standardisation of measurements and data collection
- the analysis, archiving and publication of such data
- the interaction and collaboration between scientific and operational communities.

Some examples we can cite include GCW (Global Cryosphere Watch from World Meteorological Organization), IACS (International Association of Cryospheric Science) and GEWEX-INARCH (International Network for Alpine Research Catchment Hydrology). However, effective use of the different networks can be confusing. All aspects related to snow engineering may not be taken into account and the cryosphere includes components other than snow such as lake, river and sea ice, glaciers, ice caps and ice sheets, frozen ground and permafrost.

In conclusion, much work remains to be done and observation systems and field measurements relevant to snow engineering still need to be organized at a global level.

## References

1. C.V. McLelland, The Nature of Science and the Scientific Method, The Geological Society of America, (2006).
2. Barbolini, M., Issler, D., Avalanche Test Sites and Research Equipment in Europe: An Updated Overview. SATSIE Avalanche Studies and Model Validation in Europe, (2006).
3. Manuel pour l'étude de l'intéraction de l'écoulement d'une avalanche avec un obstacle, projet n°48 DYNAVAL, (2012).
4. H. Bellot, F. Naaim-Bouvet, M. Naaim, P. Caccamo, T. Faug, F. Ousset, Taconnaz avalanche path: pressure and velocity measurements on breaking mounds, *Proceedings of International Snow Science Workshop Grenoble – Chamonix Mont-Blanc,* 1378-1382, (2013).
5. B. Sovilla, J. McElwaine, W. Steinkogler, M. Hiller, F. Dufour, E. Surinach, C Perre Guilen, J-T Fisher, E. Thibert, D. Baroudi, The full-scale avalanche dynamics test site Vallée de la Sionne, *Proceedings of International Snow Science Workshop Grenoble – Chamonix Mont-Blanc,* 1372-1377, (2013).
6. P. Gauer, K. Kristensen, Four decades of observations from NGI's full-scale avalanche test site Ryggfonn – Summary of experimental results, Cold Regions Science and Technology, **125,** 161-176 (2016).
7. E. Thibert, H. Bellot, X. Ravanat, F. Ousset, G. Pulfer, M. Naaim, P. Hagenmuller, F. Naaim-Bouvet, T. Faug, K. Nishimura, Y. Ito, D. Baroudi, A. Prokop, P. Schon, A. Soruco, C. Vincent, A. Limam, R. Hero, The full-scale avalanche test-site at Lautaret Pass (French Alps), Cold Regions Science and Technology, **115***,* 30-41, (2015).
8. M. Maggioni, M. Freppaz, E. Ceaglio, D. Godone, D. Viglietti, E. Zanini, M. Barbero, F. Barpi, M. Borri Brunetto, E. Bovet, B. Chiaia, V. De Biagi, B. Frigo, O. Pallara, A new experimental snow avalanche test site at Seehore peak in Aosta Valley (NW Italien Alps) – part I: Conception and logistics, Cold

Regions Science and technology, **85**, 175-182, (2013).

9. A. Prokop, P. Schon, F. Singer, G. Pulfer, M. Naaim, E. Thibert, A. Soruco, Merging terrestrial laser scanning technology with photogrammetric and total station data for the determination of avalanche modeling parameters, Cold Regions Science and Technology, **110**, 223-230, (2015).

10. Sovilla, B., and Bartelt, P., 2002. Observations and modelling of snow avalanche entrainment, Natural Hazards and Earth System Sciences, **2**, 169–179, (2002)

11. M. Naaim, N. Eckert, G. Giraud, T. Faug, G. Chambon, F. Naaim-Bouvet, D. Richard, Impact du réchauffement climatique sur l'activité avalancheuse et multiplication des avalanches humides dans les Alpes Françaises, La Houille Blanche, (2016).

12 E. Bourova, E. Maldonado, J-B Leroy, R. Alouani, N. Eckert, M. Bonnefoy-Demongeot, M. Deschatres, A new web-based system to improve the monitoring of snow avalanche hazard in France, Nat. Hazards Earth Syst. Sci., **16**, 1205-1216, (2016).

13. N. Eckert, C.J Keylock, H. Castebrunet, A. Lavigne, M. Naaim, Temporal trends in avalanche activity in the French Alps and subregions : from occurrences and runout altitudes to unsteady, Journal of Glaciology, **59(213),** 93-114, (2013).

14. M. Naaim, T. Faug, F. Naaim-Bouvet, N. Eckert, Return period calculation and passive structure design at the Taconnaz avalanche path, France, Annals of Glaciology, **51(54),** 89-97, (2010).

15. M. Naaim, Y. Durand, N. Eckert, C. Chambon, Dense avalanche friction coefficients: influence of physical properties of snow, Journal of Glaciology, **59(216)**, 771-782 (2013).

16. F. Naaim-Bouvet, J. Pietu, Building's design in a blowing snow context: case of mountain retreat « Gouter » (Mont-Blanc Massif), *12th congress Interpraevent, Grenoble, France*, (2013).

17. F. Naaim-Bouvet, Comparison of requirements for modeling snowdrift in the case of outdoor and wind tunnel experiments, Surveys in Geophysics, **16**, Number 5-6, 711-727, (1995).

18. J.J Doorschot and M. Lehning, Equilibrium saltation: mass fluxes, aerodynamic entrainment, and dependence on grain properties, Boundary layer Meteorology, **104**, 111-130 (2002).

19. F. Naaim-Bouvet, S. Monier, V. Mauduit, M. Boulet, France's A75 Motorway: protection from snowdrifts at the Fageole summit, *14th International Winter Road Congress, Andorra,* (2014).

20. F. Naaim-Bouvet, G. Guyomarc'h, H. Bellot, Y. Durand, M. Naaim, V. Vionnet, C. Genthon, K. Nishimura, Y. Ito and A. Prokop, Lac Blanc Pass: a natural wind-tunnel for studying drifting snow at 2700ma.s.l., *International Snow Science Workshop Grenoble Chamonix-Mont-Blanc, France,* October 7-11, 1332-1339, (2013).

21. V. Vionnet, G. Guyomarc'h, F. Naaim Bouvet, E. Martin, Y. Durand, C. Bel, H. Bellot, P. Puglièse, Occurrence of blowing snow events at an alpine site over a 10-year period: observations and modeling, Adv. Water Res., **55**, 53-63, (2013).

22. P. Schön, A. Prokop, V. Vionnet, G. Guyomarc'h, F. Naaim-Bouvet, M. Heiser, Improving a terrain-based parameter for the assessment of snow depths with TLS data in the Col du lac Blanc area, Cold regions Science and Technology, **114**, 15-26, (2015).

23. A. Trouvilliez, F. Naaim-Bouvet, H. Bellot, C. Genthon, and H. Gallee, Evaluation of the Flowcapt acoustic sensor for the aeolian transport of snow, Journal of Atmospheric and Oceanic Technology, **32(9),** 1630–1641, (2015).

24. A. Trouvilliez, F. Naaim-Bouvet, C. Genthon, V. Favier, L. Piard, H. Bellot, C. Agosta, C. Palerme, C. Amory and H. Gallée, A novel experimental study of aeolian snow transport in Adelie Land (Antarctica), Cold regions Science and Technology, **108**, 125-138 (2014).

25. H. Gallee, A. Trouvilliez, C. Agosta, C. Genthon, V. Favier, F. Naaim-Bouvet, Transport of snow by the wind: a comparison between observations in Adélie Land, Antarctica, and simulations made with the Regional Climate Model MAR. Boundary-Layer Meteorology, **146**, Issue 1, 133-147 (2013).

# Effect of reporting rate on vulnerability with an example for snow avalanche risk to backcountry recreationists in Canada

Bruce Jamieson[1,2,a] and Alan S.T. Jones[3]

[1] *Snowline Associates Ltd., Calgary, Canada*
[2] *Dept. of Civil Engineering, University of Calgary, Canada*
[3] *Dynamic Avalanche Consulting Ltd., Revelstoke, BC, Canada*

**Abstract.** The vulnerability component in risk assessments or risk-based design may be based on damage models, expert judgement or records of damage. When based on records of damage, we show the calculated vulnerability is sensitive to the reporting rate for events that did not cause the specified level of damage, and derive an adjustment to the vulnerability. Using recreationists caught in snow avalanches in Canada – for which non-fatal involvements are poorly reported – we apply the adjustment and discuss the resulting vulnerability.

## 1 Introduction

In assessments for snow and other hazards, risk includes three components: probability of the event (typically for each scenario of specified magnitude), exposure of elements of value, and vulnerability. This third component, vulnerability V, is the expected fraction of loss, $0 \leq V \leq 1$, given that the elements of value are impacted. Vulnerability can be based on damage models, records of damage, or expert judgement. When vulnerability V is based on records, the reporting rate for events that caused a specified level of damage, $N_D$, and events that did not, $N_N$, should be similar, otherwise the vulnerability will be biased towards the better recorded event.

## 2 Adjusting vulnerability for the reporting rate

When based on records of damage, vulnerability V can be expressed

$$V = \frac{N_D}{N_{Impacted}} = \frac{N_D}{N_D + N_N} \qquad (1)$$

While events that cause damage tend to be well recorded, in some situations events that do not cause damage are not as well recorded. If the reporting rate for events that do not cause the specified level of damage is R < 1, then the corrected vulnerability $V_R$ is

$$V_R = \frac{N_D}{N_D + N_N/R} \qquad (2)$$

which assumes that all events that cause the specified level of damage, $N_D$, are recorded.

From Eq. 1,

$$N_N = N_D(1/V - 1) \qquad (3)$$

Substituting Eq. 3 in Eq. 2 yields

$$V_R = \frac{V}{V + (1-V)/R} \qquad (4)$$

Figure 1 shows the adjusted vulnerability $V_R$ for R = 0.1, 0.4 and 0.9. For most risk assessment applications, R $\geq$ 0.9 likely yields sufficient accuracy; however, lower values of the reporting rate could compromise the accuracy of vulnerability and hence risk calculations.

[a] Corresponding author: bruce.jamieson@snowline.ca
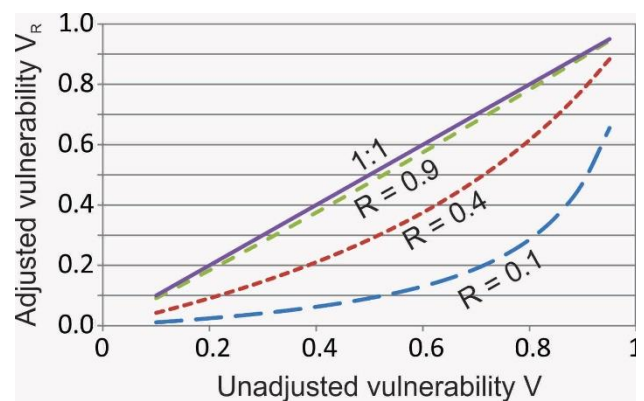
**Figure 1**. Sensitivity graph for the effect of the reporting rate R on vulnerability.

Equation 3 is not specific to risk due to snow hazards. It can be applied to any hazard for which vulnerability is based on records of damage. It may be relevant to risk to structures such as masts, snowpack support structures and buildings due to snow creep, snow glide or snow avalanches. However, we recognize that vulnerability may — alternatively — be based on damage models [1] or expert judgement. Also, many structures threatened by natural hazards are designed based on safety factors applied to expected loads [2] rather than on risk.

## 3 Example for the vulnerability of recreationists caught in potentially fatal snow avalanches

Most studies of vulnerability for people caught in snow avalanches assume that all non-fatal involvements are reported. However, in a recent Canadian study Jamieson and Jones [3] used the results of a survey to argue that only about 10 % of persons caught in, but not killed by, an avalanche during recreation in Canada are reported.

In Canada, avalanche size is reported based on a five level scale for destructive potential from 1 (relatively harmless) to 5 (largest known) [4] (Table 1). Half-sizes are often used. The size classes are sometimes prefixed by a D

to distinguish the classes from other international classifications.

**Table 1**. Classes of avalanche size by destructive potential [4]

| Size[a] | Destructive potential | Typical mass (t) | Typical path length (m) |
|---|---|---|---|
| D1 | Relatively harmless to people. | <10 | 10 |
| D2 | Could bury, injure or kill a person. | $10^2$ | 100 |
| D3 | Could bury a car, destroy a small building, or break a few trees. | $10^3$ | 1000 |
| D4 | Could destroy a railway car, large truck, several buildings, or a forest with an area up to 4 ha. | $10^4$ | 2000 |
| D5 | Largest snow avalanches known; could destroy a village or a forest of 40 ha. | $10^5$ | 3000 |
| [a] the D prefixing the number is a recent addition to distinguish the classes from another numerical avalanche size classification also used in North America. | | | |

Based on Canadian data for recreationists caught in potentially fatal avalanches (Size D2 and larger), the unadjusted vulnerability V is 0.19 [5]. The vulnerability adjusted for R = 0.10 is $V_R$ = 0.03 (Eq. 4) as shown in Table 2.

Jamieson and Jones [3] identified three factors that contribute to this surprisingly low vulnerability:

- The recreationists are typically caught when on skis or a snowmobile high in an avalanche path (Figure 2).
- They have some skill to escape a moving avalanche.
- They wear avalanche transceivers, and are accompanied by other recreationists capable of companion rescue with transceivers, shovels and probes.

In the absence of these factors, vulnerability would be higher [3].

We recognize that the definition of "potentially fatal" based on the Canadian size classification [4] may contribute to the low vulnerability. This adjusted vulnerability does not apply to non-recreationists (Figure 3) and will not apply to countries with a different definition of a potentially fatal avalanche.

The vulnerability adjusted for non-reporting is difficult to validate. In a study of the efficacy of balloon packs, Haegeli et al. [6] reasonably assumed that most non-fatal involvements would be reported in fatal avalanches. However, the selection criteria included deployed balloon packs, excluding many of the smaller potentially fatal avalanches in which recreationists are often caught. Further, Haegeli et al. did not partition their results by avalanche size [4], which is required for comparison with the adjusted vulnerability in Table 2. We sought individual well documented avalanches with numerous people caught

and at least one fatality, and found one such avalanche. The Size D3 avalanche on 2013-03-13 about 18 km west of Revelstoke, BC caught 50 to 100 people in the runout zone, injured 32 and killed 2 [7], making it suitable for comparison with the adjusted vulnerability $V_R$. In this single avalanche with many involvements, 0.02 to 0.04 of those caught were killed. While vulnerability from a single avalanche cannot be used to validate the vulnerability, the fatality rate is not inconsistent with vulnerability $V_R$ = 0.07 for a Size 3 avalanches based on R = 0.10 (Table 2).

**Table 2**. Avalanche vulnerability for recreationists in Canada by avalanche size, 1984-2011 [5]

| Avalanche size [4] | Relative frequency of recreationists caught (n = 1343) | Probability of death if caught, $V_R$ | |
|---|---|---|---|
| | | R = 1 | R = 0.10 |
| D2 | 0.55 | 0.07 | 0.007 |
| D2.5 | 0.22 | 0.20 | 0.02 |
| D3 | 0.17 | 0.43 | 0.07 |
| D3.5 | 0.06 | 0.63 | 0.15 |
| Frequency-weighted vulnerability | | 0.19 | 0.03 |



**Figure 2**. When caught, recreationists are typically caught near the top of an avalanche such as this whereas non-recreations are typically caught in the runout of the avalanche. B. Jamieson photo.

**Figure 3.** This person standing at the toe of a stopped avalanche illustrates two common characteristics of a non-recreationist caught in an avalanche, e.g. caught low in path, and not on skis or snowmobile. B. Jamieson photo.

In a 2012 study [8], Jamieson et al. assumed a reporting rate for non-fatal involvements of R = 0.05 to 0.10 and used the adjusted vulnerability to calculate the risk to backcountry skiers for various levels of avalanche danger. While this required simplifying assumptions for exposure and terrain, it illustrates an application of adjusting vulnerability for reporting rate in risk calculations.

## 4 Summary

For risk-based design or risk assessments, vulnerability can be based on records of damage, expert judgement, or damage models. When based on records of damage, incomplete recording of events that did not cause specified levels of damage can lead to overestimation of vulnerability. We are unsure how many vulnerability calculations, including those relevant to snow hazards, are based on records of damage. This paper derives an equation to adjust vulnerability for incomplete recording of specified levels of damage.

We demonstrate the vulnerability adjustment using recreationists caught in snow avalanches, for which underreporting of non-fatal involvements is common in Canada. The adjusted vulnerability is lower than most previously published values. This is attributed to underreporting of non-fatal involvements as well as factors relating to recreational exposure to avalanches, the skill of victims to sometimes escape a moving avalanche, and rescue capability by suitably equipped companions. The definition of "potentially fatal" varies between countries and may also affect the adjusted vulnerability. The vulnerability to snow avalanches of people outside buildings or on roads will be higher.

For avalanche vulnerability calculations, we propose that recreational activity be analyzed separately from non-recreational activity. Avalanche involvements during recreation or avalanche mitigation work are characterized by

1. the victim or another person in the group of recreationists triggers the avalanche

2. the victim is usually caught high in the path (Figure 2)
3. the victim is usually on skis, snowboard or snowmobile
4. the victim has some training and skill to escape the moving avalanche
5. the victim is usually wearing an avalanche transceiver and surviving members of the group have transceivers, avalanche probes, shovels and skill in companion rescue.

None of these five characteristics are common for non-recreational exposure to avalanches (Figure 3). While the contribution of the individual factors to vulnerability has received little attention, this would be worthwhile research.

## References

1. D. Bertrand, M. Naaim and M. Brun. Nat. Hazards Earth Syst. Sci., **10**, 1531-1545 (2010)
2. European Commission. *The Design of Avalanche Protection Dams. Practical and theoretical developments and results*. Ed. by T. Jóhannesson, D. Issler, P. Gauer and K. Lied, European Commission, EUR 23339 (2009)
3. B. Jamieson and A.S.T. Jones. The effect of under-reporting of non-fatal involvements in snow avalanches on vulnerability, *12th International Conference on Applications of Statistics and Probability in Civil Engineering*, June 2015, Vancouver, BC, Canada (2015)
4. D.M. McClung and P.A. Schaerer. Snow avalanche size classification. Canadian Avalanche Committee. Avalanche Workshop, 3-5 Nov. 1980. Associate Committee on Geotechnical Research. Technical Memorandum 133, National Research Council of Canada, 12-27 (1981)
5. B. Jamieson and A.S.T. Jones. Vulnerability: Caught in an avalanche - then what are the odds? *Proceedings of the 2012 International Snow Science Workshop in Anchorage, Alaska*, 1-8 (2012)
6. P. Haegeli, M. Falk, E. Proctor, B. Zweifel, F. Jarry, S. Logan, K. Kronholm, M. Biskupic and H. Brugger. Resuscitation 85, 1197-1203 (2014)
7. J. Kelly. Avalanche.ca – The Journal of Canada's Avalanche Community **93**, 20-21 (2010)
8. B. Jamieson, J. Schweizer, J., and C. Shea. Simple calculations of avalanche risk for backcountry skiing, *International Snow Science Workshop*. Swiss Federal Institute for Forest, Snow and Landscape Research WSL, Davos, Switzerland, pp. 336-340 (2009)

# Seismic responses of snowpack on a slope in a vibration experiment

Yusuke Harada[1,a], Wataru Takahashi[1], Satoshi Omiya[1], Hiroki Matsushita[2], Takahiro Chiba[3] and Masaru Matsuzawa[1]

[1]*PWRI, Civil Engineering Research Institute for Cold Region, 1-3-1-34 Hiragishi, Toyohira-ku, Sapporo, 062-8602, Japan*
[2]*PWRI, Snow Avalanche and Land Slide Research Center, 2-6-8 Nishiki, Myoko, Niigata, 944-0051, Japan*
[3]*Hokkaido University of Science, 7-15-4-1 Maeda, Teine-ku, Sapporo, 006-8585, Japan*

**Abstract.** A vibration experiment was conducted to understand the seismic response of the snowpack on a slope. The following were found. 1) The dynamic magnification factor of a snowpack on a slope increases linearly with increase in the height of the snowpack when the input seismic motion has a short period. 2) Regardless of the snow grain shape, the natural mode of a snowpack on a slope is the primary mode. 3) The dynamic magnification factor is greater for melt forms than for rounded grains, and is greater for wet snow than for dry snow.

## 1 Introduction

When a large-scale earthquake occurs, it is necessary to know the conditions of damage and to quickly start rescue and evacuation operations. During the snowy season, avalanches caused by earthquakes have the potential to obstruct information-gathering activities and rescue operations. Recently in Japan, roads were closed at many locations by earthquake-induced avalanches in the northern area of Nagano Prefecture in March 2011 [1] and in the northern area of Tochigi Prefecture in February 2013 [2]. It is very important to prepare for such situations under the assumption that earthquakes can cause avalanches. The local disaster prevention plans of some Japanese municipalities clearly recognize the potential for avalanches to occur during and after an earthquake in the snowy season. However, the snowpack and seismic motion conditions that assess the risk of earthquake-induced avalanche have not been clarified. To enhance disaster prevention and damage mitigation with respect to earthquake-induced avalanches, clarification of the occurrence mechanism of earthquake-induced avalanches and proposals for a risk assessment method for such avalanches are thought to be useful.

There have been many reports of avalanche damage following earthquakes in the U.S.A., Russia, the western Himalaya mountains, Switzerland, Japan and elsewhere [1-7]. To clarify the conditions under which earthquake-induced avalanches occur, Podolskiy et al. (2010) [3] investigated the relationship between the location of earthquake-induced avalanches and the scale and distance from the epicenter of the earthquake by using the previous cases. For the earthquake-induced avalanche that occurred during the March 12, 2011, earthquake (M. 6.7) in northern Nagano Prefecture, Kamiishi et al. (2012) [1] conducted a snow-profile observation in the starting zone of the avalanche, and based on the observations, examined the stability of the snowpack on slopes at the time of earthquakes. Matsushita et al. (2013) [2] conducted observations and examinations similar to those of Kamiishi et al. for an earthquake-induced avalanche that occurred after the February 25, 2013 earthquake in northern Tochigi Prefecture. Matushita et al. (2014) [8] examined cases of earthquake-induced avalanches for which the observation data of the snowpack around the avalanche occurrences were reported [1, 2, 5, 6] and investigated the conditions under which earthquake-induced avalanches tend to occur based on the concept of the stability of the snowpack on the slope. As for the stability of the snowpack on a slope, Chernouss et al. (2002) [9], Matsuzawa et al. (2007) [10] and Pérez-Guillén et al. (2014) [7] conducted theoretical examinations in which seismic motions were considered. Chiba et al. (2015) [11] conducted a seismic response analysis in which the snowpack on the slope was modeled by a particle system shear model.

There have been reports on analyses based on vibration experiments using snow blocks that reproduced the snowpack on a slope during an earthquake. Podolskiy et al. (2010) [12] demonstrated that snowpack failure resulting from seismic motion is initiated when tensile failure occurs in a weak layer. Kamiishi et al. (2012) [13] examined the failure of a snowpack that included a weak layer and showed that it is possible for the horizontal vibration to affect the snowpack more than the vertical vibration does. Matsushita et al. (2013) [14] demonstrated that the acceleration in the direction in which the snow layers are subjected to tensile force was greater than the acceleration in the direction in which the snow layers are subjected to compressive force.

The above-stated assessment methods for the stability of the snowpack on the slope, which consider the seismic motion, assume that an earthquake-induced avalanche occurs when the ground surface acceleration generated by the seismic motion is the same as the acceleration of the snowpack on the slope. However, depending on the magnitude and frequency of the seismic motion, the snowpack may undergo greater acceleration than the ground surface does. In addition, the transfer of seismic acceleration in the snowpack may differ with differences in grain shape. It is thought to be necessary to clarify the basic relationship between the state of snowpack and the seismic motion. In this study, the authors conducted vibration experiments to investigate the characteristics of the seismic response of the snowpack on a slope. Based on the experimental findings, we proposed a method for estimating the risk of earthquake-induced avalanches in which snowpack stability is considered in static analysis. Our current study addresses only the lateral vibration, and

[a] Corresponding author: harada-y@ceri.go.jp

the avalanches are assumed to start as a result of shear fracture.

# 2 Experimental methods

The experiment was conducted at the Ishikari Test Field, Japan (N43°12'55'', E141°23'23'') from January 2014 to March 2015. The measured items were the acceleration of the snowpack specimen (hereinafter: "the specimen"), the acceleration of the shaking table, and certain physical properties of the specimen (snowpack height, and snow layer structure, grain size, density, hardness and temperature).

First, snow blocks were cut from natural snowpack to make the specimens. Each snow block was reshaped into a parallelogram specimen (angles: 60° and 120°) 40 cm wide by 55 cm long by 40 to 70 cm high. A slope model (50 cm wide by 55 cm long) with an angle of 30° was anchored to a shaking table (200 cm wide by 200 cm long: SPTDU-20K-85L-50T) installed inside a building. The specimen was placed on the slope such that the snow layer structure would parallel the slope (Figure 1). To prevent the underside of the snowpack from sliding, 5-cm nails were installed on the slope at 6-cm intervals in the downslope and cross-slope directions. In addition, the L-steel member on the acceleration (positive) side was fixed with a clear acrylic board and vises.

Next, 3 to 6 accelerometers (18 × 18 × 24 mm, 40g: ASW-5A) were inserted into the snowpack with a vertical spacing of 10 to 20 cm. For some experiments, we used specimens weighted with a 15-kg lattice weight (30 cm wide by 45 cm long by 5.3 cm high) fixed to the snowpack with 32 U-shaped fixtures each weighing 0.075 kg (8 cm wide by 15 cm long).

After the accelerometers were installed, the specimen was accelerated in the horizontal direction for 3 min (Figure 1). By means of sweep acceleration where the acceleration of the shaking table was fixed and the frequency was varied between 1 and 10Hz. The range of input acceleration to the shaking table was varied between 0.1G and 0.9G (1G = 9.81 m/s²). The accelerations of the specimen and the shaking table were measured every 0.04 sec.

# 3 Experimental results

## 3.1 Response characteristics of the specimens

The vibration experiment was conducted 194 times,
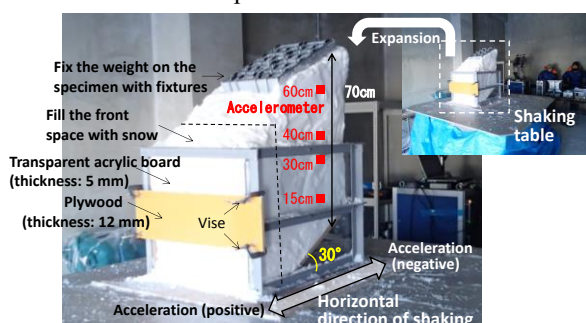


**Figure 1.** The shaking table and specimen.

with combinations of specimen conditions and accelerations varied. In this experiment, the maximum value of the rate of acceleration of the snowpack on the shaking table (hereinafter: "the dynamic magnification factor" (DMF)) of snowpack on the slope was found to be about 10Hz (period: 0.10s) for all specimens. The DMF was higher for greater input accelerations and greater weights, and for higher locations in the snowpack varied from 1 to 10Hz. Figure 2 shows the relationship between frequency and DMF.

## 3.2 The DMF by grain shape and height

Using the results of this experiment, we compiled the following data on each specimen: snow grain shape, mean snow density (kg/m³), mean snow hardness (kN/m²), specimen weight (kg), snowpack depth (m), "weight converted snowpack depth" for the weighted specimen (the total of the specimen's weight and the weight is converted to snow depth), input acceleration (G) and the max. value of DMF (hereinafter: "max. DMF") measured by the accelerometers. We measured the max. DMF at various input accelerations and created 800 data profiles. In this study, we classified the snow type as "dry rounded grains", "wet rounded grains", "dry melt forms" or "wet melt forms", based on the 50% higher grain shape and dry or wet of the specimen (Fig.
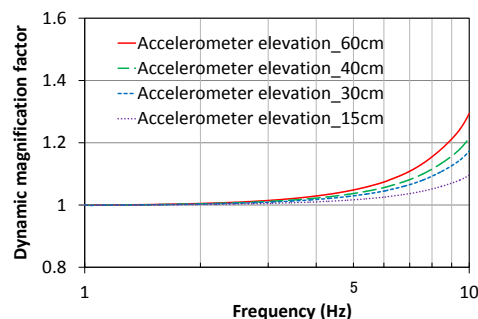


**Figure 2.** DMF vs. frequency (example).
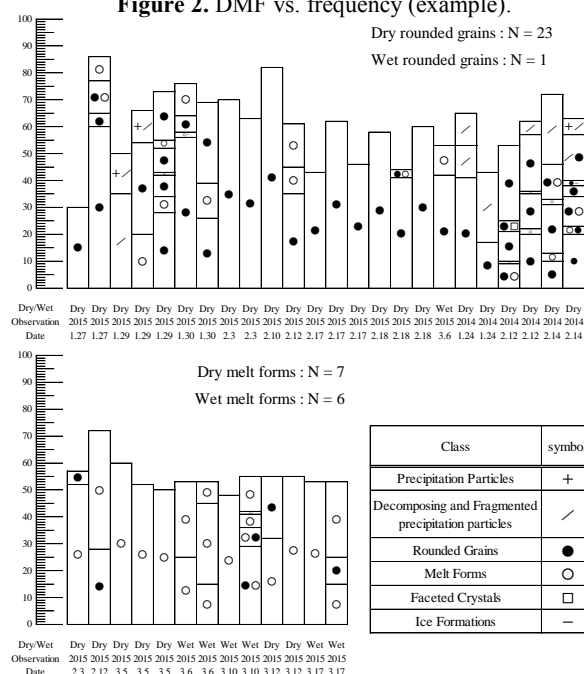


**Figure 3.** The layered structure of the specimens, with dry or wet snow, and the date of the experiment.

3). The accelerometers were installed at four height ranges: 10 - 20cm, 30 - 39cm, 40 - 49cm, and 50 - 60cm.

We performed single regression analyses to obtain correlation coefficients. The objective variable was the max. DMF for an input acceleration whose explanatory variable was one of following: mean snow density, mean snowpack hardness, specimen weight, snowpack depth, weight converted snowpack depth, if the specimen is a weighted one, or input acceleration (Figure 4). The analyses found a positive correlation between the heights of the accelerometers and the input acceleration (G), between the heights of the accelerometers and weight (kg), and between the heights of the accelerometers and the weight converted snowpack depth (m) in all types of specimens and for all levels of accelerometer height. For the correlations between accelerometer heights and snow depth (m), between accelerometer heights and mean density ($kg/m^3$), and between accelerometer heights and mean hardness ($kN/m^2$), some of the data points plot with positive correlations, others with negative correlations, and yet others with near zero correlations. We made multiple regression equations for each group of accelerometers grouped in accordance with the range of installed elevation from the underside of the snowpack (i.e., 10 -20cm, 30-39cm, 40-49cm, and 50-60cm) for each snow type (hereinafter: "accelerometer elevation") (Table 1). Where, $y$ is the max. DMF, $x_1$ is the input acceleration (G) and $x_2$ is the weight (kg). The weight converted snow depth was treated as being included in the weight, because the snow depth was determined based on the weight. Wet rounded grains was excluded from this analysis because too few cases with such snow quality were found.

When the DMF at the frequency of 10Hz is 100%, the average value of the increase ratio in the DMF was calculated by using the data for each grain shape at the 30 - 39cm accelerometer height and at 0.5Hz intervals (Table 2). For each grain shape, the acceleration at 1 Hz (period: 1.0 S) was 0%; in other words, the acceleration was about the same as that of the shaking table. However, when the frequency increased gradually and approached 10 Hz (period: 0.10 S), the acceleration gradually increased. The DMFs increased about 80 percentage points from 5 Hz (period: 0.20 S) to 10 Hz (period: 0.10 S), and about 25 percentage points between 9 Hz (period: 0.11 S) and 10 Hz. No marked differences in the tendency of increase based on the grain shape were found. The standard deviation in the rate of increase in DMF for melt forms was greater than the standard deviation in the rate of increase in DMF for rounded

**Table 1.** Relationship between the max. value of DMF ($y$), and input acceleration ($x_1$) and weight ($x_2$).

| Snow type | Accelerometer elevation | Mean elevation | N | Multiple regression equation | $R^2$ |
|---|---|---|---|---|---|
| Dry rounded grains | 10～20cm | 15.7cm | 140 | $y=0.116x_1+0.003x_2+0.944$ | 0.452 |
| | 30～39cm | 30.3cm | 97 | $y=0.190x_1+0.005x_2+0.919$ | 0.449 |
| | 40～49cm | 40.7cm | 91 | $y=0.257x_1+0.007x_2+0.868$ | 0.487 |
| | 50～60cm | 54.4cm | 77 | $y=0.399x_1+0.007x_2+0.844$ | 0.407 |
| Dry melt forms | 10～20cm | 15.0cm | 51 | $y=0.261x_1+0.005x_2+0.808$ | 0.513 |
| | 30～39cm | 30.0cm | 44 | $y=0.513x_1+0.008x_2+0.676$ | 0.778 |
| | 40～49cm | 40.8cm | 49 | $y=0.546x_1+0.009x_2+0.639$ | 0.523 |
| | 50～60cm | 50.4cm | 39 | $y=0.677x_1+0.011x_2+0.524$ | 0.539 |
| Wet melt forms | 10～20cm | 15.0cm | 55 | $y=0.357x_1+0.006x_2+0.761$ | 0.582 |
| | 30～39cm | 30.0cm | 48 | $y=0.577x_1+0.009x_2+0.630$ | 0.554 |
| | 40～49cm | 40.0cm | 48 | $y=0.725x_1+0.011x_2+0.543$ | 0.607 |
| | 50～60cm | 50.0cm | 41 | $y=1.043x_1+0.012x_2+0.442$ | 0.629 |

Note: Wet rounded grains was excluded from this analysis due to the small number of such samples.
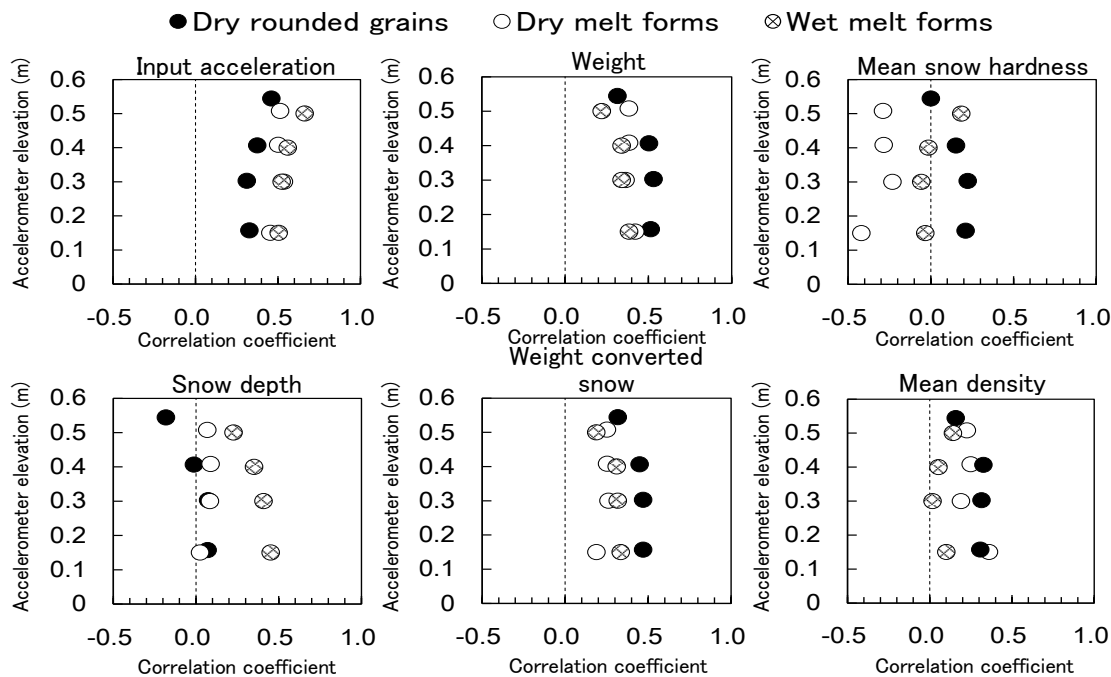


**Figure 4.** The average elevations of the accelerometers and the relationship between the maximum DMF and the correlation coefficient of each measured items.
See Table 1 for the average elevation of accelerometer and N for each snow type.

grains. The relationship between grain shape and increase in the DMF relative to the frequency increase was determined as shown in Table 3.

## 3.3 Trial calculation for DMF of snowpack on a slope

We calculated the max. DMF, $y$, by substituting an arbitrary input acceleration for $x_1$ and by substituting the mean snowpack weight for each snow type for $x_2$. The snowpack weight was calculated as the product of volume and density. The volume of snow for each snow type was obtained by multiplying the mean cross-sectional area of the specimen at the time of the experiment ($0.176 m^2$) by the mean value of converted snowpack depth, which was 0.689 m for the dry rounded grains, 0.658 m for the dry melt forms and 0.624 m for the wet melt forms. Density was set in accordance with the *Japanese Dictionary of Snow and Ice* as follows [15]: 325 kg/$m^3$ for dry rounded grains, 400 kg/$m^3$ for dry melt forms and 500 kg/$m^3$ for wet melt forms. Consequently, the values calculated for normal snowpack weight were as follows: 39.4 kg for dry rounded grains, 46.3 kg for dry melt forms and 54.9 kg for wet melt forms.

From the normal snowpack weights and the multiple-regression equation for arbitrary acceleration (Table 1), the DMFs were obtained. Figure 5 plots the DMF for each accelerometer elevation. A linear approximation was made for the DMF plotted for each input acceleration. The results show that the DMF increases proportionally to the accelerometer elevation. The acceleration is higher for the accelerometers at higher elevations. Consequently, regardless of the type of snow, the natural mode of specimens that assumed snowpack on slope is the primary mode. At the acceleration of 0.2G, the distribution of DMFs for melt forms has roughly the same shape as that for rounded grains. At accelerations of 0.4G or greater, the DMF is greater for melt forms than for rounded grains, and the DMF is greater for wet snow than for dry snow.

## 3.4 Difference in DMF by grain shape

Fig. 6 shows the DMF by weight of specimen at the input acceleration of 0.5 G at the height of 30 - 39cm, and the relationship between the DMF and the mean snow hardness and between the DMF and the mean density. In this result it is found that, for the dry rounded grains, the DMFs are high for high mean density, hardness, and weight. In the dry melt forms and wet melt forms, the above relationship is not found. Many of the data points for the dry melt forms and wet melt forms are high in density and DMFs than those for rounded grains. We estimated the cause of the differences in the DMFs between dry and wet snow in the results discussed in Section 3.3. A snowpack behaves as an elastic body when

**Table 2.** Increase ratio for DMF when the DMF at 10 Hz is normalized to 100 %.

| Period (S) | Freque ncy (Hz) | Dry rounded grains N = 97 | | Dry melt forms N = 44 | | Wet melt forms N = 48 | |
|---|---|---|---|---|---|---|---|
| | | Avg. | Std Dev. | Avg. | Std Dev. | Avg. | Std Dev. |
| 1.000 | 1 | 0.0% | 0.0% | 0.0% | 0.0% | 0.0% | 0.0% |
| 0.667 | 1.5 | 0.7% | 0.7% | 0.8% | 0.5% | 0.8% | 0.6% |
| 0.500 | 2 | 2.4% | 1.6% | 2.7% | 1.4% | 2.3% | 1.2% |
| 0.400 | 2.5 | 4.4% | 2.0% | 4.6% | 1.8% | 4.1% | 1.6% |
| 0.333 | 3 | 6.7% | 2.5% | 6.7% | 2.3% | 6.2% | 2.1% |
| 0.286 | 3.5 | 9.6% | 2.9% | 9.3% | 2.7% | 8.7% | 2.7% |
| 0.250 | 4 | 12.9% | 3.2% | 12.3% | 3.3% | 11.6% | 3.2% |
| 0.222 | 4.5 | 16.8% | 3.3% | 15.7% | 3.8% | 15.0% | 3.9% |
| 0.200 | 5 | 21.1% | 3.6% | 19.7% | 4.5% | 18.8% | 4.6% |
| 0.182 | 5.5 | 26.0% | 3.9% | 24.1% | 5.1% | 23.1% | 5.4% |
| 0.167 | 6 | 31.3% | 4.3% | 29.2% | 5.8% | 27.9% | 6.1% |
| 0.154 | 6.5 | 37.4% | 4.5% | 34.8% | 6.4% | 33.4% | 6.8% |
| 0.143 | 7 | 44.1% | 4.8% | 41.1% | 6.8% | 39.5% | 7.4% |
| 0.133 | 7.5 | 51.4% | 4.9% | 48.2% | 7.2% | 46.4% | 7.8% |
| 0.125 | 8 | 59.5% | 4.8% | 56.4% | 7.3% | 54.3% | 8.1% |
| 0.118 | 8.5 | 68.2% | 4.3% | 65.4% | 7.2% | 63.3% | 7.9% |
| 0.111 | 9 | 77.7% | 3.8% | 75.3% | 6.1% | 73.6% | 6.9% |
| 0.105 | 9.5 | 88.1% | 2.7% | 86.5% | 4.1% | 85.6% | 4.7% |
| 0.100 | 10 | 100.0% | 0.0% | 100.0% | 0.0% | 100.0% | 0.0% |

Note: The data for the accelerometer elevation of 30 - 39 cm
Avg.: Average, Std Dev.: Standard deviation

**Table 3.** Relationship between the increase ratio of DMF ($y$ (%)) and the frequency ($x$), when the DMF at 10 Hz is 100 %.

| Snow type | N | Relational equation | $R^2$ |
|---|---|---|---|
| Dry rounded grains | 97 | $y = 0.041x^{2.41}$ | 0.989 |
| Dry melt forms | 44 | $y = 0.045x^{2.34}$ | 0.992 |
| Wet melt forms | 48 | $y = 0.041x^{2.37}$ | 0.994 |



**Figure 5.** Relationship between accelerometer elevation and DMF based on experiment (10Hz).

the magnitude and duration of forces acting on it are small [16]. In this experiment, the snowpack was given shear force by vibration in the horizontal direction. Elasticity (or stiffness) against such input acceleration can be considered to behave as follows. Yamanoi and Endo (2002) [17] expressed the shear strength of precipitation particles, decomposing and fragmented precipitation particles, rounded grains, and dry melt forms in terms of a power function of density, and showed that the sheer strength of dry melt forms was smaller than those of other types of snow, and that the sheer strength of wet snow was smaller than that of dry snow. Kinoshita (1960) [18] expressed the hardness of dry snow in terms of a power function of density. For the increase in snow density, the dry rounded grains increases in hardness and shear strength. The rigidity against horizontal force increases when hardness and shear strength increase. Therefore, it is suggested that the DMF decreases. However, the weight also increases with the increase in hardness and shear strength, which is the reason for the great DMFs for rounded grains shown Fig. 6. In contrast, the dry melt forms has lower shear strength than dry rounded grains, so the shear strain of the dry melt forms against horizontal input acceleration is greater than that of dry rounded grains. Weight also effects shear strength. Therefore, the greater is the input acceleration, the greater is difference in DMF between dry melt forms and dry rounded grains. This trend is much more obvious for wet snow than for dry snow (Figure 5).

## Rounded Grains



## Melt Forms
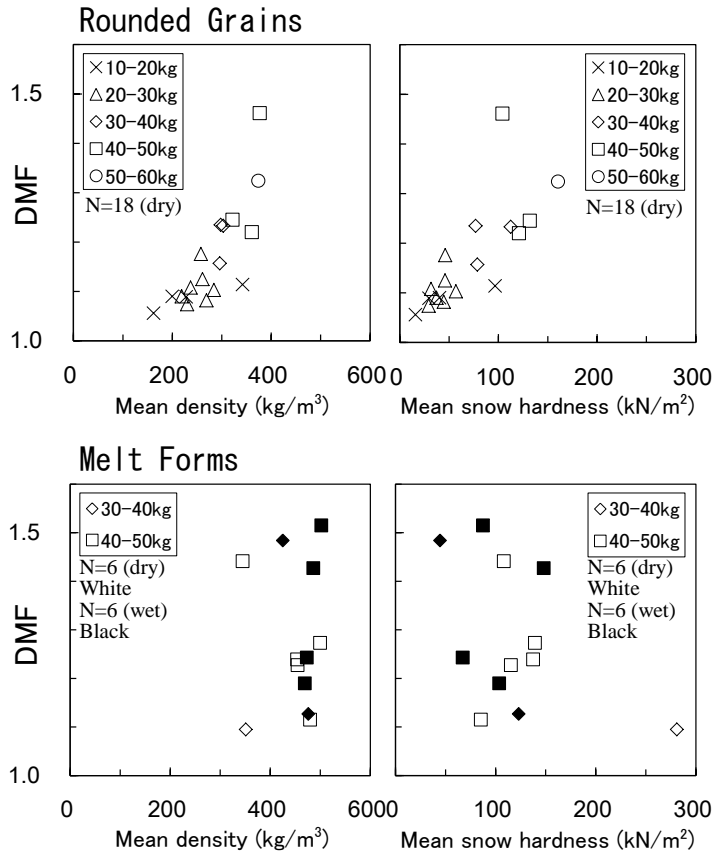


Note: This is data for the accelerometer elevation of 30 - 39 cm and the input acceleration 0.5 G, without weighting.

**Figure 6.** Relationship between DMF and the mean density, and between DMF and the hardness.

# 4. Estimation of the likelihood of earthquake-induced avalanches

First, the snowpack stability on the slope (*SI*: stability index) was assessed. Then, the risk of avalanche occurrence was estimated by using the results of the vibration experiment in Chapter 3 and the snowpack data measured at the time of previous avalanches.

## 4. 1. Stability of the snowpack on the slope

The stability of the snowpack on the slope in nature *SI* is expressed as a ratio of the shear strength $\Sigma_s$ of the subject snow layer to the shear stress $\sigma_n \sin\psi$ acting on the snow layer (Equation (1) and Fig. 7 (a)). The smaller is the *SI* value, the less stable is the snowpack on the slope. The *SI* value is used for assessing the stability of the snowpack on the slope and for indicating the occurrence of avalanches [19], [20].

$$ SI = \frac{\Sigma_s}{\sigma_n \sin\psi} = \frac{C + \sigma_n \cos\psi \tan\phi}{\sigma_n \sin\psi} \qquad (1) $$

Where, $\Sigma_s$ is the shear strength (N/m²) of the subject snow layer, such as a weak layer; and $\sigma_n$ is the snowpack load (N/m²) per unit volume above the weak layer as determined from the thickness $D$ (m), density $\rho$ (kg/m³), and gravitational acceleration $g$ (m/s²) of the layers above the weak layer ($\sigma_n = g\rho D$). $\psi$ is the slope gradient (°). The right-hand side of Equation (1) is the shear strength $\Sigma_s$ expressed in terms of the Mohr-Coulomb yield criterion. Maeno and Kuroda (1986) [16] maintained that when the density of snow is low or the vertical load $\sigma_n$ is great, application of this criterion does not produce accurate results because of the compressibility of snow. However, Nakamura et al. (2010) [21] demonstrated that the criterion held well even for low-density snow. Therefore, the authors of this study assume that the Mohr-Coulomb yield criterion holds for all types of snow. *C* is the cohesive force (N/m²) of snow particles. In this study, a measured value of shear frame index *SFI* is used. tan$\varphi$ is the internal friction coefficient of the snow particles.

For actual snowpack on a slope, the critical value for avalanche occurrence is not necessarily 1 at the stability expressed in Equation (1), because other factors such as lateral connection between the sides of the snowpack and the sides of the surrounding snow cover influence the stability of the snowpack on the slope *SI* [19]. To clarify the critical value for avalanche occurrence, examinations for critical stability index *SI* have been done using actual cases of avalanches. For example, in Canada, a value of about 1.5 was presented as the threshold value of stability indicator *SI* for avalanche occurrence [22]. A study on avalanche occurrences at roadside slopes in Hokkaido, northern part of Japan, in which a snowpack model was used to investigate the snowpack stability index *SI* at the time of avalanche occurrence [20], found that avalanches tend to occur when the snowpack stability index *SI* is 2.5 or lower and that the number of avalanches markedly increases when *SI* falls to 2.0 or lower. Based on the

above, a stability index of 2.0 or lower is considered to be the threshold for avalanche occurrence in this study, and an *SI* of 1.5 - 2.0 is classified as "small risk", 1.0 - 1.5 is classified as "middle risk", and 1.0 or lower is classified as "great risk".

## 4. 2 Stability of the snowpack on the slope considering seismic motion

The stability of the snowpack on the slope at the time of an earthquake $SI_E$ is expressed by Equation (2), which is obtained by adding the horizontal seismic coefficient $a$ (Fig. 7 (b)), as an external force, to Equation (1) [1], [2], [3], [10].

$$SI_E = \frac{C + \sigma_n(\cos\psi - a\sin\psi)\tan\varphi}{\sigma_n(\sin\psi + a\cos\psi)} \quad (2)$$

The horizontal seismic coefficient $a$ of Equation (2) is a ratio of the horizontal acceleration of seismic motion (gal) to the gravitational acceleration (gal), which is a horizontal acceleration (G). The horizontal seismic coefficient $a$ is used for assessing the stability of the embankment at the time of earthquake [24] and for examining the aseismic performance of road facilities [25]. Therefore, we used the horizontal seismic coefficient $a$ in examining the conditions for avalanche occurrence at the time of earthquake.

When we assume that the natural mode of snowpack on the slope, which was determined in Chapter 3, holds true even for snow depths greater than those in our vibration experiment, the horizontal seismic coefficient $a'$ of an arbitrary snow depth $H'$ and frequency $f$ is expressed by Equation (3).

$$a' = a\{(SR_{10Hz} - 1)IR + 1\} \quad (3)$$

Where, $SR_{10Hz}$ is the DMF (Table 1, Fig. 5) at the height $H'$ of the snowpack on the slope at 10 Hz, and $IR$ is the rate of increase in DMF for a given frequency when the DMF for 10 Hz is regarded as 100 % (Table 3).

In addition to proposing Equation (2), Matsuzawa et al. (2007) [10] proposed the stability index of the snowpack

on the slope as $SI_E'$. In their proposal, the seismic motion and the tensile force (tensile fracture strength) that is generated by the bonding between snow particles and that acts in the slab on the slope were considered. The index was proposed based on the safety factor assessment of embankment slopes at the time of earthquake. In this study, we propose Equation (4), in which the above-mentioned horizontal seismic coefficient $a'$ is considered in the equation of Matsuzawa et al.

$$SI_E' = \frac{CL + \sigma_n L(\cos\psi - a'\sin\psi)\tan\varphi + \Sigma_t D}{\sigma_n L(\sin\psi + a'\cos\psi)} \quad (4)$$

Where, $L$ is the length of snowpack on the slope (m), $\Sigma_t$ is the tensile fracture strength of the snow (N/m²), and $D$ is the thickness of the snow layer above the weak layer (m).

## 4. 3 Stability of the snowpack on the slope at avalanche occurrence

To investigate the occurrence conditions of earthquake-induced avalanches, Matsushita et al. (2014) examined earthquake-induced avalanches for which snow cover observation data, including avalanche type and snowpack data were available [8]. In the current study, we use four cases of surface avalanches from the report of Matsushita et al. whose peak ground acceleration (gal) and frequency (Hz) were measured by the Strong Motion Seismograph Networks (K-net, KiK-net) of Japan's National Institute for Earth Science and Disaster Prevention, and we perform a trial calculation for the stability of snowpack on the slope. (See Introduction and Table 4.) The snow layers above the sliding surface in the earthquake-



**Figure 7.** Forces acting on the snowpack on the slope.
(a) Load and strength of the snowpack on the slope (b) Horizontal seismic coefficient of seismic motion.

**Table 4.** Conditions of the earthquake-induced avalanches.

| Cases | Earthquakes | | | | Distance between the Strong Motion Observatory and the avalanche (km) | Avalanche type | Slope Angle $\psi$ (°) | Bed surface | | | Snowpack above the bed surface | | | | | Snowpack below the bed surface | | | Snow-profile observation station |
|---|---|---|---|---|---|---|---|---|---|---|---|---|---|---|---|---|---|---|---|
| | Date | Magnitude (M) | Horizontal seismic coefficient $a$ ※1 | Frequency $f$ ※1 (Hz) | | | | Length $L$ (m) | Grain type | Cohesive force $C$ (N/m²) | Load $\sigma_n$ (N/m²) | Thickness $D$ (m) | Depth $H$ (m) | Density $\rho$ (kg/m³) | Main snow type | Depth $H'$ (m) | Density $\rho'$ (kg/m³) | Main snow type | |
| 2011 northern Nagano Prefecture #1 | 2011/3/12 | 6.7 | 0.72 | 11.2 | 15 | Surface Slab | 35 | 10※2 | Melt Forms | 1580 | 1178 | 0.61 | 0.75 | 197※2 | Melt Forms | 1.62 | 197※3 | Wet melt forms | Mochi, Tokamachi, Niigata Prefecture |
| 2011 northern Nagano Prefecture #2 | | | | | 6 | Surface Slab | 25 | 10※2 | Melt Forms | 780 | 1813 | 0.56 | 0.62 | 330※2 | Melt Forms | 2.04 | 330※3 | Wet melt forms | Nonaka, Tokamachi, Niigata Prefecture |
| 2013 northern Tochigi Prefecture #1 | 2013/2/25 | 6.3 | 1.25 | 4.3 | 4 | Surface Slab | 42 | 9.5 | Faceted Crystals | 1510 | 744 | 0.41 | 0.55 | 185 | Rounded Grains | 0.99 | 316 | Dry melt forms | Okukinu, Nikko, Tochigi Prefecture |
| 2014 northern Tochigi Prefecture #2 | | | | | | Surface Slab | 42 | 9.5 | Faceted Crystals | 2890 | 1626 | 0.74 | 1.00 | 224 | Rounded Grains | 0.66 | 224 | Dry melt forms | Okukinu, Nikko, Tochigi Prefecture |

Note 1: The horizontal seismic coefficient $a$ is the maximum value, and the frequency $f$ is that for the max.
Note 2: The value is from the figure in the reference [1].
Note 3: The density of the snow in the upper section of the snowpack was used as a substitute, because we did not have the data for this [1].

induced avalanche in northern Nagano Prefecture were melt forms [1], and those in northern Tochigi Prefecture were mainly rounded grains [2]. Therefore, we use a relational equation of tensile fracture strength (Eqs. (5a), (5b)) for each snow type developed by Watanabe (1977) [25].

$$\Sigma_t = 7.78 \times 10^{-3} \rho^{2.60} \text{ (Melt Forms)} \qquad (5a)$$

$$\Sigma_t = 3.40 \times 10^{-4} \rho^{3.24} \text{ (Rounded Grains)} \qquad (5b)$$

The stability of snowpack on the slope for each of the earthquake-induced avalanches was calculated based on the above. The left graph in Fig. 8 compares the stability $SI_E$' in which the horizontal seismic coefficient $a$' is used to consider the DMF (Equation (4)) and the stability $SI$ in which the $a$' is not considered (Equation (1)). There were cases with $SI$ (shown as the horizontal axis) of 1.5 or lower (i.e., the mid to high degree of avalanche occurrence risk). It was thought that, in these cases, the snowpack on the slope was in an unstable condition before the earthquake [1]. For cases with $SI$ of 1.5 or higher, the $SI_E$' is 1.5 or lower. It is thought that, in these cases, the snowpack had been relatively stable before the earthquake, and when the external force of the earthquake motion was exerted on the snowpack, it became unstable and avalanches occurred. The right graph in Fig. 8 compares the $SI_E$' determined by using Equation (4) and the $SI_E$' determined by substituting the horizontal seismic coefficient $a$ of the seismic motion into Equation (4) (i.e., the equation of Matsuzawa et al. [10]). The difference between the two is shown as the difference between the calculated $SI_E$' values. In the earthquake in northern Nagano Prefecture (frequency: 11.2 Hz), the decrease in #1 was 0.95 and the decrease in #2 was 0.99. In the earthquake in northern Tochigi Prefecture (frequency: 4.3 Hz), the decrease in #1 was 0.15 and the decrease in #2 was 0.11. The above demonstrates that, for seismic motion with short periods and for snowpack whose snow depth $H$' below the weak layer is great (Table 4), the decrease in stability is great.

## 4. 4 Trial calculation of the risk of avalanche occurrence based on snow depth and horizontal seismic coefficient

When expressing avalanche occurrence likelihood, the use of the stability of snowpack on the slope as an index is not practical, because it is necessary to estimate the stability of snowpack on the slope based on the snowpack observation data each time. We had assumed that the risk of avalanche occurrence increases in stages when the snowpack stability of the slope $SI_E$' is 2.0 or lower, and we conducted a case study to show the avalanche occurrence risk at the time of earthquake. In our study, which is based on Equation (4) and considers snow type, the depth of snowpack on the slope $Hs$ (m) (Fig. 7 (a)) is used as an index. Here, we assume a dry surface slab avalanche. The model slope shown in Fig. 7 (a) is used, and the conditions are as follows: A layer of faceted crystals that can become a weak layer exists in the rounded grains layer, and the rounded grains layer above the weak layer starts to flow when seismic motion (horizontal motion) with a frequency of 10 Hz causes a shear fracture in the weak layer. The density of 325 kg/m³ is set for rounded grains (Sec. 3.3), and the density of 200 kg/m³ is set for faceted crystals by selecting the smallest value for the density range of 200 - 400kg/m³ [15]. For the slope gradient $\psi$, 40° is selected, because many dry surface slab avalanches occur on slopes with gradients of 30° - 45°, and the frequency peak of the occurrence distribution is near 40° [26]. In addition to the above settings, the variables for Equation (4) are set as follows.

The cohesive force of snow particles in the weak layer $C$ (N/m²) is determined by using the relational equation for shear strength $\Sigma_s$ which was measured by Watanabe [25] in the condition without snow load above the weak layer (Equation (6)). In this case, it is possible to regard $\Sigma_s = C$, because Equation (1) gives 0 for the snow load $\sigma_n$.

$$C = 3.56 \times 10^{-5} \rho^{3.36} \text{ (Faceted Crystals)} \qquad (6)$$

$C$ = 1918 N/m² is obtained by substituting a density of
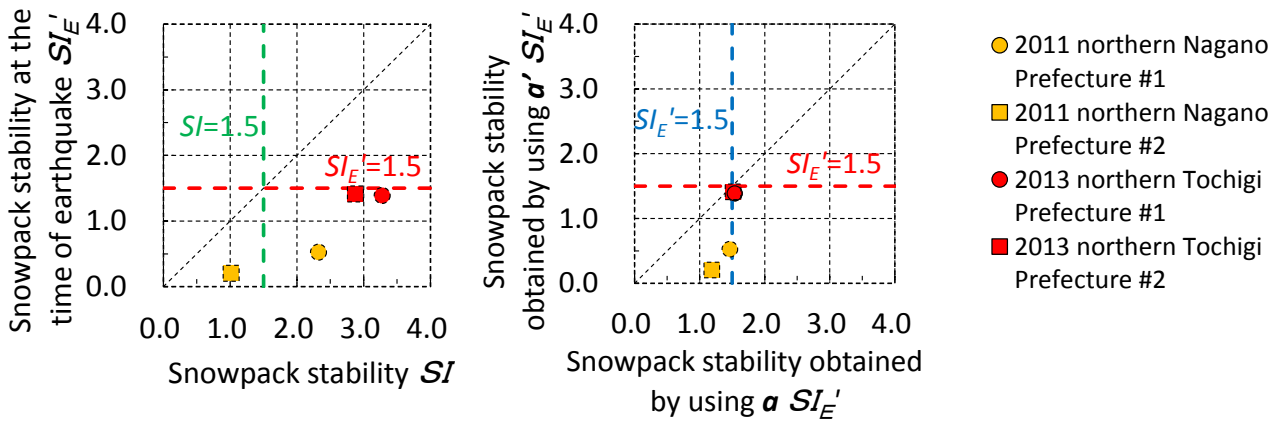


**Figure 8.** The calculation results for the stability of the snowpack on the slope.
Left: Comparison between the stability index $SI_E$' determined by using horizontal seismic coefficient $a$', for which DMF was considered (Eq. (4)), and the stability index $SI$ determined by not considering the $a$' (Eq. (1)).
Right: Comparison between the $SI_E$' obtained by using Eq. (4) into which $a$' was substituted and the $SI_E$' obtained by using Eq. (4) into which $a$ was substituted.

200 kg/m³ for faceted crystals into Equation (6).

The internal friction coefficient tan$\varphi$ is considered in the cases for precipitation particles, decomposing and fragmented precipitation particles, and faceted crystals, but is negligible for the other types of snow [17], [27]. In a previous study, the internal friction coefficient for precipitation particles tan$\varphi$ = 0.46 - 2.0 [10], [28], that for decomposing and fragmented precipitation particles tan$\varphi$ = 0.23 [11], and that for faceted crystals tan$\varphi$ = 0.21 [29]. In our current study, to assume faceted crystals as the weak layer, 0.21 was set as the internal friction coefficient.

For the thickness of the snow layer above the weak layer $D$ (m), we used 0.60 m, which was roughly the average value of the occurrence frequency distribution of slab thicknesses (i.e., the thickness above the weak layer) obtained from 200 dry snow slab avalanches examined by McClung and Schaerer [26].

For the snow load above the weak layer per unit volume $\sigma_n$ (N/m²), $\sigma_n$ = 1911 N/m² was obtained by multiplying 325 kg/m³, which is the density of the rounded grains layer, by the thickness of the snow layer above the weak layer $D$ = 0.6 m and the gravitational acceleration $g$. The tensile fracture strength $\Sigma_t$ (N/m²) for the snow above the weak layer was obtained as $\Sigma_t$ = 46771 N/m², based on Equation (5b), which is an equation for the tensile fracture strength of rounded grains.

For the length of the snowpack on the slope $L$ (m), 10 m and 20 m were used. The arbitrary snow depth $H'$ and the horizontal seismic coefficient $a'$ at frequency $f$ were obtained by using Equation (3), Table 1 and Fig. 5. The arbitrary snow depth $H'$ can also be determined by using Equation (7).

$$H' = Hs - \frac{D}{\cos \psi} \quad (7)$$

Fig. 9 and Fig.10 show the relationships between the snow depth $Hs$ and the horizontal seismic coefficient of seismic motion $a$ when the stability of snowpack on the slope $SI_E'$ is 1.0, 1.5 and 2.0. The length of the snowpack on the slope in Fig. 9 is 10 m, and that in Fig. 10 is 20 m.
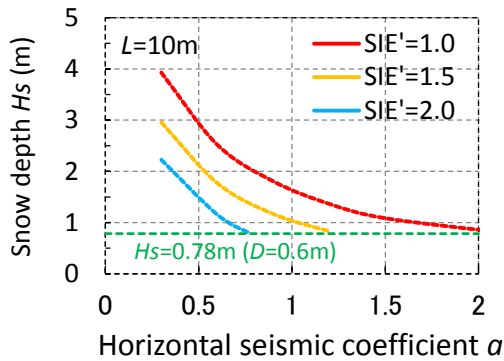
The regions above the blue curves in the figures indicate the regions where the stability of snowpack on the slope $SI_E'$ is 2.0 or lower. The curves in the graphs show that the snow depth and the likelihood of avalanche occurrence are proportional, and that when $SI_E'$ becomes 1.0 or lower (red curves and the regions above them), the avalanche likelihood becomes very high. With increases in the horizontal seismic coefficient and the length of the snowpack on the slope, the snow depth that has to be considered in the risk assessment of avalanche occurrence became smaller.

From the above, it is thought that the risk of earthquake-induced avalanche occurrence can be indicated by using snow depth $Hs$ and horizontal seismic coefficient $a$ as indexes and by using Equation (4), for which variables are set based on the concept of stability of snowpack on the slope. When the weak layer is assumed to be near the bottom of the snowpack, it is also thought that risk assessment of the occurrence of full-depth avalanches is possible by giving an appropriate friction coefficient to the equation.

## 5. Summary and future issues

In this study, a vibration experiment was conducted that focused on the seismic response of the snowpack on the slope. The experiment found that the seismic response to short-period vibration increases proportionally to the increase in the snowpack height, that the DMF of melt forms is greater than that of rounded grains, and that the DMF of wet snow is greater than that of dry snow. We propose a method for estimating the risk of avalanche occurrence in which the snow depth at the time of earthquake $Hs$ and the horizontal seismic coefficient $a$ are used as indexes.

The conditions of the snowpack on the slope at the time of earthquake in winter vary depending by location and period in winter. When the snowpack on the slope is dry new snow due to snowstorm, it tends to be unstable and it may slide even when the snow depth and the horizontal seismic coefficient are smaller than the estimated index values. In the future, we will further investigate the risk of avalanche occurrences for various



**Figure 9.** Relationship between snow depth $Hs$ and horizontal seismic coefficient $a$ of seismic motion.
(Calculation conditions: frequency: 10 Hz; slope gradient: 40°; The snowpack: rounded grains; weak layer: faceted crystals; internal friction coefficient of the weak layer: tan$\varphi$ = 0.21; length of the slope: 10 m.)
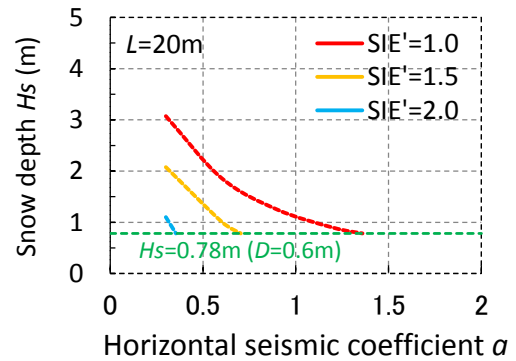
**Figure 10.** Relationship between snow depth $Hs$ and horizontal seismic coefficient $a$ of seismic motion.
(Calculation conditions: frequency: 10 Hz; slope gradient: 40°; The snowpack: rounded grains; weak layer: faceted crystals; internal friction coefficient of the weak layer: tan$\varphi$ = 0.21; length of the slope: 20 m.)

snow types and vibration frequencies, and further our studies on the risk of earthquake-induced avalanches in winter.

## Acknowledgments

## References

1. Kamiishi, I., et al., *J. Jpn. Soc. Snow Ice* (Seppyo), **74**, 159-169(2012). [In Japanese with English abstract]
2. Matsushita, H., et al., *Proceedings of International Snow Science workshop Grenoble*, 1122-1129 (2013)
3. Podolskiy, E. A. et al., *Journal of Glaciology*, **56**, 431-446 (2010).
4. Kazakov, N. A., et al., *Mater. Glyatsiol. Issled.* (Data of Glaciological Studies), **88**, 102–106 (2000). [In Russian with English abstract]
5. Higashiura, M. et al., *Rep. Nat. Res. Cent. Disaster Prev.*, **21**, 103-112 (1979). [In Japanese with English abstract]
6. Ogura, Y., et al., *Ann. Rep. Saigai-ken, Niigata Univ.*, **23**, 9-15 (2001). [In Japanese with English abstract]
7. Pérez-Guillén, C., et al., *Cold Regions Science and Technology*, **108**, 149-162 (2014).
8. Matsushita, H., et al., *Monthly Report of Civil Engineering Research Institute for Cold Region*, **733**, 39-44, (2014). [In Japanese]
9. Chernouss, P., E., et al., *Proceedings of the International Snow Science Workshop Penticton, BC, Canada*, 25-30, (2002).
10. Matsuzawa, M., et al., *Proceedings of Snow Ice Hokkaido* (Hokkaido no Seppyo), **26**, 95-98 (2007). [In Japanese]
11. Chiba, T., et al., *Proceedings of Snow Ice Hokkaido* (Hokkaido no Seppyo), **34**, 91-94 (2015). [In Japanese]
12. Podolskiy, E. A. et al., *Journal of Glaciology*, **56**, 447-458 (2010).
13. Kamiishi, I., et al., *Proceedings of 2012 cold region technology conference*, **28**, 49-52 (2012). [In Japanese]
14. Matsushita, H., et al., *Proc. JSSI & JSSE Joint Conference 2013 in Kitami*, 222 (2013). [In Japanese]
15. Japanese Society of Snow and Ice (Eds.), *Japanese Dictionary of Snow and Ice, 2nd edition*, 246 (2014). [In Japanese]
16. Maeno, N. and Kuroda, T., *Structure and physical properties of snow and ice*, 162-164 (1986). [In Japanese]
17. Yamanoi, K. and Endo, Y., *J. Jpn. Soc. Snow Ice* (Seppyo), **64**, 443-451 (2002). [In Japanese with English abstract]
18. Kinoshita S., Low Temperature Science, Ser., **A19**, 135-146 (1960). [In Japanese with English abstract]
19. Japanese Society of Snow and Ice (Eds.), Guidebook of snow observations, 31-53, 79-96 (2010). [In Japanese]
20. Nishimura K., et al., *Proceedings of 2005 cold region technology conference*, **21**, 244-248 (2005).
21. Nakamura, T., et al., *J. Glaciol.*, **56(196)**, 333-338 (2010).
22. Perla, R., *Canadian Geotechnical Journal*, **14-2**, 206-213 (1977).
23. Japan Road Association: *Verification of Embankment Stability against the Action of Seismic Motion, The Guideline for Road Earthwork: Embankment works*, 2010 Edition, 119 – 127 (2010). [In Japanese]
24. Japan Road Association: *Using Static Verification to Verify Aseismic Capacity, Specifications for Highway Bridges and in "Chapter V. Aseismic Design" of the Associated Instruction Manual*, 57 – 108 (2010). [In Japanese]
25. Watanabe, Z., *Sci. Rep. Fukushima Univ.*, **27**, 27-35 (1977).
26. McClung, D.M. and P. Schaerer, *The avalanche handbook, 3rd Edition* (2006).
27. Jamieson, J. B., and Johnston C. D., *Ann. Glaciol.*, **26**, 296-302 (1998).
28. Seki, S., et al., Preprints of the 1998 conference Japanese Society of Snow and Ice, 183 (1998).
29. Zeidler,A. and B.Jamieson, *Cold Regions Science and Technology*, **44**, 194-205 (2006)

# Friction along a slider on snow

Werner Nachbauer[1,a], Sebastian Rohm[1], Christoph Knoflach[1], Joost van Putten[2], Michael Hasler[2]

[1]Department of Sports Science, University of Innsbruck, Austria
[2]Centre of Technology of Ski and Alpine Sports, University of Innsbruck, 6020 Innsbruck, Austria

**Abstract.** The purpose of this study was to analyse friction along a slider on snow. The experimental approach consisted of friction measurements of four identical sliders of different lengths of 10, 25, 75 and 100 cm at 5 different velocities. The measurement took place on a linear tribometer located inside a cold laboratory. The normal force was adapted to assure the same contact pressure for the 4 sliders. The local friction force along the theoretical 100 cm slider model was calculated by subtracting the friction force of the next shorter slider from the slider and assigning this difference to the slider segment by which they differed. The local coefficient of friction along the slider revealed high friction in the front part (0-10 cm), considerably lower one in the second segment (10-20 cm), constant or slightly increased one in the middle part (25-75 cm), and towards the end increased friction (75-100 cm). This may be attributed to dry friction in the front part, subsequently smaller friction due to lubrication by meltwater and finally increased capillary drag towards the end.

## 1 Introduction

Based on [1] it is known that a liquid water film between ski and snow accounts for the low friction of skis on snow. [2] proposed different friction mechanisms that are caused by different thicknesses of the melt water layer. Without a water film, or even with a very thin one, dry friction dominates. With increasing water film thickness, mixed friction (dry/wet) comes up and finally with even thicker water films, wet friction dominates. [3] described friction along a ski, where the water film builds up as the ski slides and hence different friction mechanisms dominate along the ski. Later findings about a quasi-liquid layer on ice crystals [4] suggest that additional mechanisms may be involved. No experimental results are available to support models of different friction regimes on a sliding ski. The purpose of this study was to develop a method to measure the local coefficients of friction (CoF) of different sections along a ski.

## 2 Method

The study was carried out on the linear tribometer of the Department of Sport Science of the University of Innsbruck (Fig. 1). It is a friction test device which allows the measurement of the friction force of whole skis [5]. The tribometer is located in a cooling chamber. Air and snow temperature were set to -8°C. Fresh artificial snow was filled into the tribometer trough, compressed and evened. The snow had an average grain size of 0.2 mm and a density of 450 kgm-3.

To determine the CoF along a ski, wooden sliders of 10, 25, 75 and 100 cm running lengths with a width of 4.9 cm were produced. Tips and tails were 7 cm long with a radius of 20 cm. The sliders were flat without camber. Ultra-high molecular weight polyethylene ski bases were attached to the sliders by double-sided tape. All bases were grinded and waxed with liquid paraffin in the same way. The normal force was adapted for the different sliders to assure a homogeneous contact

pressure of 5.7 kPa. Each slider was tested at speeds of 0.5, 1, 2, 5 and 10 ms-1. For each test, series of 15 consecutive runs were measured, with each series starting on a fresh snow track. The friction force was averaged over the third through the fifteenth run. The local friction force for the 100 cm slider model was calculated by subtracting the friction force of the next shorter slider from the slider and assigning this difference to the slider segment by which they differed. The local CoF values along the slider model were calculated as quotient of friction force and normal force on the segments.



**Figure 1.** The linear tribometer of the Department of Sport Science of the University of Innsbruck

## 3 Results

Figure 2 shows the friction forces of the 4 sliders of different lengths at the velocities 0.5, 1, 2, 5 and 10 ms-1. Friction stayed nearly constant at velocities from 0.5 – 2 ms-1 and increased at higher velocities for all slider lengths.
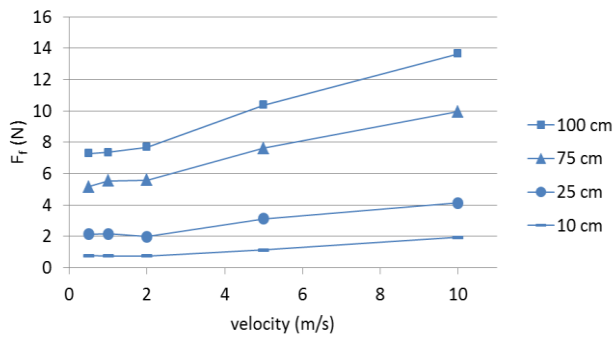
ᵃ Corresponding author: werner.nachbauer@uibk.ac.at

**Figure 2.** Friction force $F_f$ vs. velocity for the 4 sliders of different lengths

In Figure 3 the CoF for the 4 different slider lengths are presented. A considerable decrease of the CoF was measured by increasing the slider length from 10 to 25 cm. For the 75 cm slider no further reduction of the CoF and for the 100 cm slider a slight increase was detected. These observations were more pronounced for the higher velocities of 5 and 10 ms$^{-1}$.
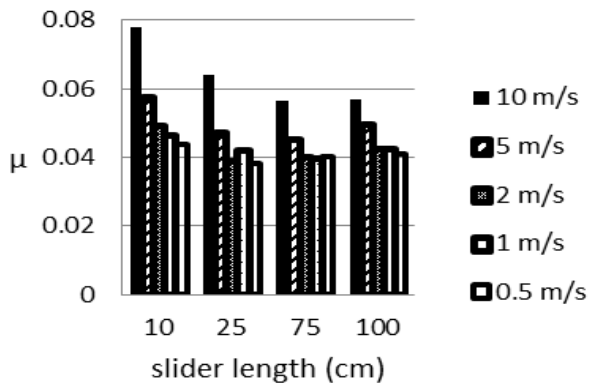


**Figure 3.** Friction coefficient $\mu$ vs. slider length for different velocities

In Figure 4 the local CoF along the theoretical slider model are shown for the five tested velocities. The CoF was high in the first segment (0-10 cm), decreased strongly in the second segment (10-20 cm) and then stayed about constant or increased slightly in the third segment (25-75 cm), and increased in the end segment (75-100 cm).

The overall CoF of the 100 cm slider calculated by integrating the local CoF over the slider length increased with increasing speed: 0.041 (0.5 ms$^{-1}$), 0.042 (1 ms$^{-1}$), 0.043 (2 ms$^{-1}$), 0.050 (5 ms$^{-1}$), and 0.058 (10 ms$^{-1}$).

## 4 Discussion

To our knowledge the only study on the influence of the runner length on friction is from the year 1955 [6]. In accordance with our results a clear reduction of the CoF with increasing length from about 10 to 40 cm was found. The author suggested that it is likely that a smaller runner has more contact per unit than a larger one. Another explanation may lie in the melting of snow by frictional heating. Since the dry friction portion in front of the slider does not depend on the slider length the impact of

dry friction on the total friction increases with decreasing slider length.
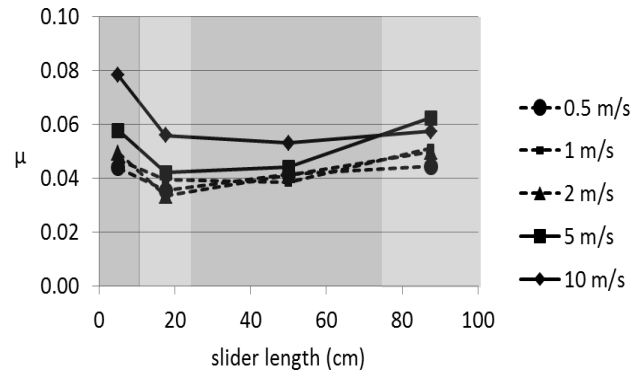


**Figure 4.** Local friction coefficients $\mu$ along the theoretical slider model at different velocities. Slider tip is at 0 cm and endpoint at 100 cm.

Interestingly, the local CoF along the slider revealed a similar pattern as suggested by the ideas and theoretical considerations described in [3]. High friction in a small portion of the front of the slider due to dry friction, subsequently smaller friction due to lubrication by meltwater and higher friction towards the end due to the increase of capillary drag may cause the measured friction distribution. It has to be noted that contrary to a real ski the measured slider had a uniform longitudinal load distribution.

## References

1. F.P. Bowden, T.P. Hughes, The Mechanism of Sliding on Ice and Snow. Proceedings of the Royal Society of London Seriea A, Mathematical and Physical Sciences 172:280-298 (1939).
2. S.C. Colbeck, The kinetic friction of snow. Journal of Glaciology 34:78-86 (1988).
3. S.C. Colbeck, A review of the processes that control snow friction. US Army Cold Regions Research and Engineering Laboratory Monograph 92-2 (1992).
4. J.G. Dash, H.Y. Fu, J.S. Wettlaufer, The premelting of ice and its environmental consequences. Reports on Progress in Physics 58:115-167 (1995).
5. W. Nachbauer, P. Kaps, M. Hasler, M. Mössner, Friction Between Ski and Snow. In: Braghin F, Cheli F, Maldifassi S, Melzi S, Sabbioni E (eds.) The Engineering Approach to Winter Sports, pp. 17-32. Springer New York, Place Springer New York (2016).
6. R. Ericksson, Friction of Runners on Snow and Ice. US Army Cold Regions Research and Engineering Laboratory Report (1995).

# Gliding friction of back country climbing skins

Michael Hasler[1,a], Sebastian Rohm[1], Christoph Knoflach[1], Joost van Putten[2] and Werner Nachbauer[1,2]

[1]Centre of Technology of Ski and Alpine Sports, University of Innsbruck, Austria
[2]Department of Sports Science, University of Innsbruck, Austria

**Abstract.** The purpose of this study was to analyse the gliding friction behaviour of climbing skins for back country skiing. On a linear tribometer positioned inside a low temperature laboratory, 2 different skins were tested over a wide range of normal forces at two velocities. The friction test showed that the type of skin has a major influence on the gliding performance. The coefficient of friction decreased with increasing normal load and was not affected by the velocity.

## 1 Introduction

Climbing skins are called skins because the first back country skiers in Norway used marine seals' skin and fur attached to their ski bases to prevent sliding backwards while walking uphill. Nowadays they consist of a textile construction of synthetic and/or mohair material. The outer surface of the climbing skin has hairs or scales that grab the snow, preventing backward movement of the skis. When the skis are moved forward, these surfaces flatten out to allow some glide. There is a huge variety of skins on the market. Beside geometric cut and mechanical fixation mechanism to the ski, they vary in material (nylon, mohair and combinations), fibre length, mechanical binding of the fibres to the supporting textile (v- or w-shape) and additional (hydrophobic) surface treatment. Little scientific evidence exists on the quantitative differences of friction under realistic conditions. [1] measured the friction of small samples under laboratory conditions and performed gliding tests in the field. The coefficients of friction (CoF) were between 0.1 and 0.2 and the correlation of the skin rankings between field and lab tests was good, but not for all specimens. The performance of the different materials and construction techniques is commonly only assessed by experts of the field.

During the gliding phase of a step, normal force on and velocity of the ski vary strongly. According to Coulombs law the friction force is assumed to be linear proportional to the normal force and thus the proportional factor $\mu$ is constant. However, from prior studies it is known that CoF can depend on velocity (e.g. polyethylene [2]) and normal force (e.g. textiles [3]). Hence, in the present study, the gliding friction of skins was measured at different normal forces and different velocities.

## 2 Method

The study was carried out on the linear tribometer of the Department of Sport Science of the University of Innsbruck (Fig. 1). It is a friction test device which allows the measurement of the friction force of whole skis over a length of up to 24 m [2]. The tribometer is located in a cooling chamber. Air and snow temperature was set to -5°C. Fresh artificial snow was filled into the tribometer trough, compressed and evened. The snow had an average grain size of 0.2 mm and a density of 470 kgm$^{-3}$.



**Figure 1.** The linear tribometer of the Department of Sport Science of the University of Innsbruck.

Two different skins were tested. One was designed for regular ski tourers with a 70% mohair and 30% nylon structure (Climb, Pomoca Sa, Suisse) and the other for competitors and experienced ski tourers (Race, Pomoca Sa, Suisse). The skins were attached to a wooden slider with a running length of 100 cm and a width of 5 cm. Tips and tails were 7 cm long with a radius of 20 cm. The sliders were flat without camber. The skins were tested in gliding direction at two speeds (2.5 ms$^{-1}$ and 5 ms$^{-1}$) at normal forces of 8, 17, 58, 145, and 266 N.

For each test, series of 5 consecutive runs were measured, with each series starting on a fresh snow track. The friction force was averaged over the second through the fifth run. For further analysis, the measurements from 2 to 5 were used to calculate a mean value. The CoF were calculated as quotient of friction force $F_f$ and normal force $F_n$.

---

[a] Corresponding author: michael.hasler@uibk.ac.at

## 3 Results

Figure 1 shows the friction force $F_f$ versus the normal force $F_n$. The progressions showed a clearly non-linear behaviour for both skins. $F_f$ of the Race-skin was always lower than $F_f$ of the Climb-skin, whereat the difference increased with increasing normal load.
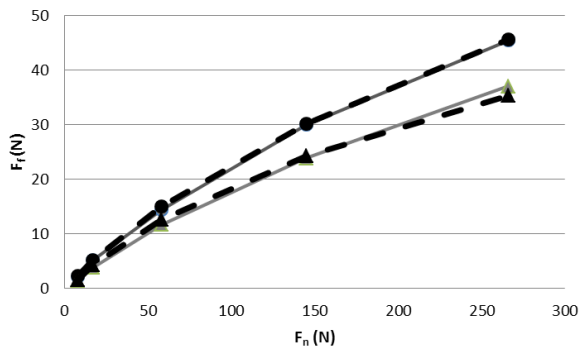


**Figure 2.** Friction force $F_f$ vs. normal load $F_n$ of two skins (Climb-skin: circle; Race-skin: triangle) at the velocities of 2.5 ms-1 (full line) and 5 ms$^{-1}$ (dashed line).

Figure 2 shows the effect of the normal load on CoF for the Climb- and Race-skin for the two measured velocities. The gliding friction of the Race-skin was clearly superior to the Climb-skin at all velocities and normal forces. Except for the lowest loads, CoF decreased with increasing normal load at both velocities. Regarding the different velocities, no differences in CoF were observed.
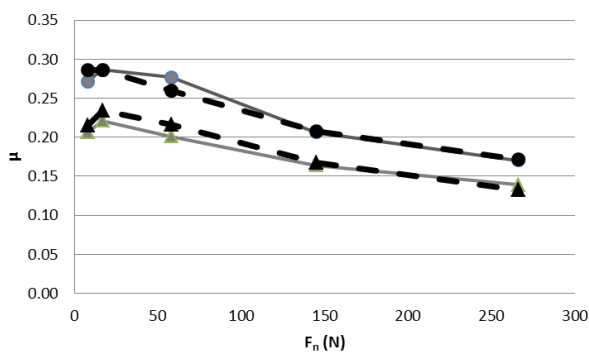


**Figure 3.** Coefficient of friction $\mu$ vs. the normal load $F_n$ (Climb-skin: Circle; Race-skin: Triangle) for the velocities of 2.5 ms$^{-1}$ (full line) and 5 ms$^{-1}$ (dashed line).

## 4 Discussion

There is a clear difference of the CoF between the two tested skins. The climb skin is designed for regular ski tourers with a mixture of comparatively long mohair and nylon fibres, whereas the race skin uses exclusively short mohair fibres. The length of the fibre is empirically known to affect the friction of skins on snow. With

decreasing fibre length, the friction is thought to be reduced [1] which is in accordance with our measurements. However, the underlying mechanism needs to be investigated.

Except for very low loads, the CoF for both skins decreases with increasing normal load. The initial lower values of the CoF at a normal load of 8 N may be attributed to an incomplete contact of the fibres with the snow. With further increasing load, the fibres might align better to the motion direction due to the pressure and the motion relative to the snow and hence CoF decreases.

The velocity showed no effect on the CoF of the tested climbing skins. Velocity effects were studied for other materials like polyethylene and PTFE [4,5] or steel [6] and revealed different results at similar snow temperatures as we studied. Usually an increase of CoF with velocity is explained by an increase of a melt water film. The velocity independence and the high CoF may be an indication that in the friction of back country skins on snow dry friction is dominating.

## Acknowledgement

## References

1. M. Auer, *Die Alpen*, **12**, 27 (2006)
2. W. Nachbauer, P. Kaps, M. Hasler, M. Mössner, *The Engineering Approach to Winter Sports,* (Springer New York) 17 (2016)
3. M. Hasler, K. Schindelwig, W. Nachbauer, *Book of Abstracts of the 21st International Congress on Ski Trauma and Skiing Safety 8.-13.3.2015* 68 (2015)
4. M. Shimbo, Friction on snow of ski soles, unwaxed and waxed. Scientific study of skiing in Japan, 99 (1971)
5. E. Spring, Valtion teknillinen tutkimuskeskus. Metallilaboratorio (1988)
6. S. Rohm, M. Hasler, C. Knoflach, J. van Putten, S. Unterberger, K. Schindelwig, R. Lackner, W. Nachbauer, Tribology Letters **59**:1 (2015).

# Snow physics / Snow drift II

# Characterizing the snowpack stratigraphy and its mechanical stability with hardness profiles measured by the Avatech SP1

Pascal Hagenmuller[1,a], Thibault Pilloix[1]

[1]Météo-France/CNRS, CNRM-GAME/CEN, 1441 rue de la piscine, 38400 St Martin d'Hères, France

**Abstract.** Hardness has long been recognized as a good predictor of snow mechanical properties and thus as an indicator of snowpack stability. However, the usual measurement of hardness with a ramsonde lacks in resolution and misses snowpack features which are critical to assess its stability. The new snow penetrometer Avatech SP1 appears as a promising alternative by combining handy manipulation and millimetric vertical resolution. In this paper, we evaluate the SP1 accuracy in terms of penetration resistance and depth by comparing the SP1 profile with the profiles measured by the ramsonde and a reference penetrometer, the SMP. The capacity of the SP1 to detect unstable snowpack configurations is further assessed by modelling the snow pack stability directly from the measured hardness profile, which is then compared to stability tests. A method to aggregate numerous hardness profiles of similar snowpack configurations is also presented and provides a practical tool to extract synthetic information for the avalanche forecaster out of the large potential amount of data provided by the SP1.
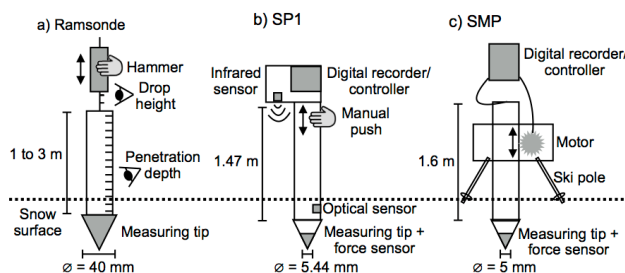
## 1 Introduction



**Figure 1 :** Different snow penetrometers: (a) ramsonde, (b) Avatech SP1 and (c) Snow MicroPenetrometer (SMP).

The ramsonde (Fig. 1a) is used since the 1930's by avalanche forecasting services worldwide to provide quantitative information about snow stratigraphy. It measures hardness, defined as the resistance to penetration of an object into snow. However, due to the limited resolution of the instrument, a ramsonde profile does not include information about very thin snowpack features such as weak layers, which are critical to assess the snowpack stability. A ramsonde profile has thus to be complemented by time-consuming and possibly subjective stability tests and manual stratigraphy.

Recently, new portable high-resolution digital penetrometers such as the Snow MicroPenetrometer (SMP)[1] and the Avatech SP1 (www.avatech.com) were developed (Figs. 1b, 1c). They benefit from very sensitive force sensors and are expected to capture thin snowpack features invisible for the ramsonde (Fig. 2). On the contrary to the SMP whose price and fragility limit its usage to research, the SP1 is particularly easy to use and to transport in the field. It has the potential to become a common tool among snow professionals such as ski patrollers, mountain guides and avalanche forecasters.

The goal of this study is to assess the pros and cons of the SP1 in the framework of avalanche risk forecasting and to present methods to exploit the data provided by this new instrument. The presented work is based on preliminary measurements conducted in the French Alps

a Corresponding author: pascal.hagenmuller@meteo.fr

during winter 2014-2015. It will be complemented by measurements with the latest version of the SP1 (SP2) and feedbacks of regional forecasting centres of Météo-France during winter 2015-2016.

## 2 Methods and results

### 2.1 Evaluation of SP1 in terms of penetration resistance and depth
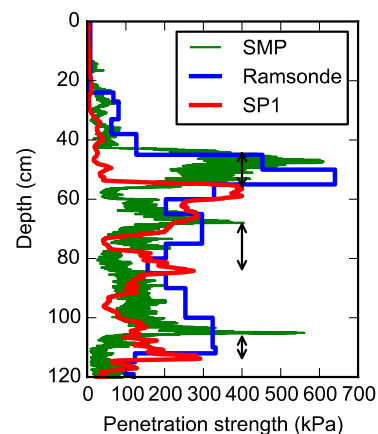


**Figure 2:** Example of hardness vertical profiles measured by the SMP, the ramsonde and the SP1. The arrows indicate some depth lags.

In order to evaluate the accuracy and resolution of the SP1 in terms of penetration resistance and depth, co-located SP1, SMP and ramsonde profiles were measured and compared. The layers detected by the SP1 appear to be translated with a variable depth lag in comparison to the layers detected by the SMP (Fig. 2). The SMP depth accuracy is better than 1 cm. These depth lags are thus due to errors of the SP1 depth sensor. The alternating soft and hard layers are correctly reported by the SP1. The higher vertical resolution of the SP1 enables to capture detailed features that are not visible in the ramsonde profile.

The difference between two hardness profiles can be decomposed into depth lags and residual hardness differences. To allow quantitative comparison between hardness profiles, we used an algorithm that matches two profiles by adjusting the layer thicknesses that maximize the hardness correlation [2]. Applied to 14 co-located SMP/SP1 profiles, the algorithm estimates the SP1 depth error in the range [-20, 20] cm with a standard deviation of 7.8 cm and a mean relative hardness error of 30%. Further tests will be conducted to evaluate the impact of the snow stratigraphy on the SP1 accuracy.

## 2.2 Evaluation of SP1 in terms of modelled failure initiation and propagation indices
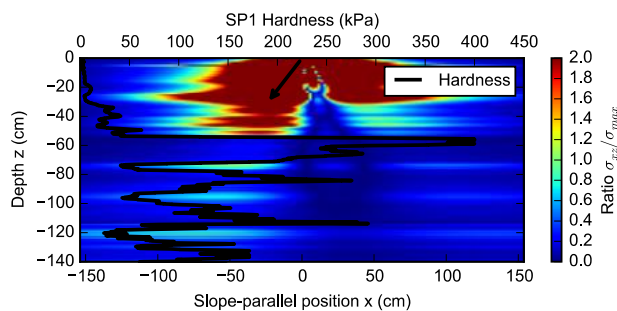


**Figure 3:** Modelled distribution of the ratio between shear stress due to a skier point load (arrow) and shear strength, in a heterogeneous 38°-inclined slab. This ratio represents the likelihood of failure initiation.

In the framework of avalanche forecasting, the SP1 capability of detecting unstable snowpack configurations cannot be directly derived from the evaluation of the SP1 in terms of penetration resistance and depth. It must be specifically evaluated. Moreover, it is necessary to develop an automatic method to assess the stability of a given hardness profile in order to point out the most critical situations among numerous profiles to the avalanche forecaster [3].

To this end, we adapted the method developed by [4] to SP1 data. The main idea of this method is to derive the mechanical properties of each layer from the hardness and to feed a finite element slab model with these layer properties (e.g. Fig. 3). This model then computes the likelihood of failure initiation and propagation.

On going combined stability tests and hardness profiles measured with the SP1 and SMP will help to evaluate the capability of the SP1 to detect avalanche-prone stratigraphy and the benefit of the very high resolution of the SMP. Indeed, force fluctuations measured with the SMP can be linked to microstructural parameters and are not accessible with the SP1.

## 2.3 Spatial variability

For the purpose of real time analysis of the snowpack stability, the important amount of data collected by digital penetrometers, such as the SP1, must be quickly synthesized into a characterization representative of the test site of given altitude and aspect ranges.

At decameter scale, most snow layers are continuously present in the snowpack and the observed variability mainly originates from the varying thickness of each layer [5]. Assuming that depth deviations explain most of the observed variability and do not affect intensive layer properties, the algorithm used for the SP1/SMP comparison (see 2.1) is adapted to match multiple SP1 profiles by minimizing their intra-set hardness variability [2].

We successfully applied this algorithm on SP1 profiles and tracked centimetric layers over 20 m with little hardness variability (Fig. 4). The apparent spatial variability due either to real spatial variability or depth measurement errors must thus not hinder the development of high vertical resolution point snow measurements, which can provide information relevant at larger scale. Moreover, the method provides a practical way to synthetize numerous hardness profiles into one representative profile and estimates of the spatial variability of the snowpack in terms of layer depth and hardness.

# References

1. M. Schneebeli. Cold Reg. Sci. Technol. 30, 101–114 (1999).
2. P. Hagenmuller, T. Pilloix. A new method to compare snow hardness profiles. Submitted.
3. G. Giraud. In ISSW 97–104 (1992).
4. B. Reuter, J. Schweizer, A. van Herwijnen. The Cryosphere 9, 837–847 (2015).
5. Sturm, M., Benson, C. Ann. Glaciol. 38, 253–260 (2004).
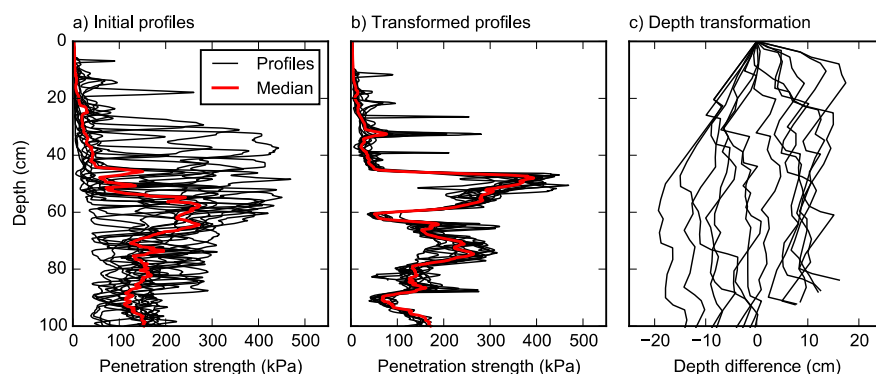
**Figure 4:** The intra-set variability of the initial profiles (a) is minimized by adjusting the layer thicknesses on each (b). The transformations to go from the transformed profiles (b) to the initial profiles (a) are shown on subfigure (c).

# Improvement of requirements for modeling snowdrifts in wind tunnels based on the measurements at Harbin

Qingwen Zhang[1, 2], Guolong Zhang[1, 2] and Feng Fan[1, 2]

[1]*School of Civil Engineering, Harbin Institute of Technology, Harbin 150090, China*
[2]*Key Lab of Structures Dynamic Behavior and Control of China Ministry of Education, Harbin Institute of Technology, Harbin 150090, China*

**Abstract.** Snowdrifts around cuboid models were investigated in wind tunnel and outdoors, considering the serious problems caused by snowdrifts around buildings when formed on undesirable places. Outdoor measurements were carried out to investigate the characteristics of drifting snow and to obtain data for comparison with wind tunnel results. The outdoor measurements were conducted at Harbin China, with model dimensions $750 \times 600 \times 750$mm. Wind direction and speed were measured every 1 minute. Snowdrift heights around models were surveyed in approximately 400 points and contour maps produced. Then, a simulation of wind induced snowdrifts around reduced scale models, by using sodium bicarbonate in a direct wind tunnel, was described. The measurement at Harbin was selected as the prototype. Experimental procedure was proposed based on Kind's similarity parameters. With the results comparison between models and prototypes, the required length of upstream fetch was discussed.

## 1 Introduction

As an appropriate profiler to simulate snowdrift problems around buildings, wind-tunnel experimental methods have been explored for many years. However, due the limitation of the experimental instrumentation and the complexity of the two-phase flow, similarity criteria cannot all be satisfied simultaneously. Compromises must be made based on the objective of the experiment. Related research has been undertaken in several studies (e.g., Kind; Anno; Iversen; Delpech).

Kind [1, 2] identified the important similarity criteria by analyzing the saltation process and discussed the compromises in modelling procedures. Naaim et al. [3] reviewed the conditions for a correct simulation of snowdrifts in wind tunnels, or outdoor, by comparing requirements proposed by four scientists (i.e., Kind, 1975, 1985; Iversen, 1979, 1980, 1981, 1982, 1984; Anno, 1984; Tabler, 1980). Delpech [4] overviewed the snowdrift mechanisms, discussed the experimental procedures based on similarity parameters proposed in the scientific literature. The simulation of wind induced snow drifting around buildings by using artificial snow, in the Jules Verne climatic wind tunnel, was carried out later, based on the proposed criteria. Okaze el at. [5] carried out a series of wind tunnel measurements over a loose snow surface to investigate the characteristics of drifting snow phenomena in a non-equilibrium boundary layer and to obtain data for examining the numerical model of snow transport coupled with computational fluid dynamics (CFD). Furthermore, as the previous wind tunnel experiments on snowdrifts usually used artificial snow as a substitute of natural snow, which cannot fully reflect the motion of natural snow particles. LÜ XiaoHui [6] conducted a series of experiments in wind tunnel to investigate the motion of natural snow (fresh snow and old snow). The results indicated that the threshold velocity of fresh snow is less than that of old snow, and that the mass flux rates of the two kinds of snow

exponentially decrease with height whereas the snow transport rate increases exponentially with wind velocity.

Although various studies dealing with snowdrift simulation have been carried out in past years, more details need determination, e.g. the right length of correctly modelled terrain, complete with particles, upstream of the region of interest. It is set to be roughly one or more meters by experience.

## 2 Outdoor experiments of snowdrifts around cuboid models

### 2.1 Study site and setup

The outdoor experiments were undertaken on an open flat base within the campus of Harbin Institute of Technology (HIT), China (Figure 1). It was part of a large snow engineering program. The wind pattern in this area has been previously found to be constant during the winter (Figure 2). The uniform wind direction makes the area ideal for snowdrift measurements.
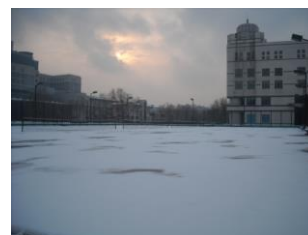


**Figure 1.** Locations where outdoor measurements were conducted
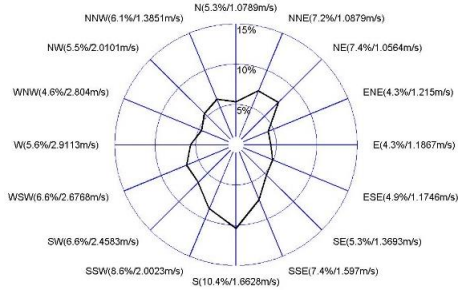
**Figure 2.** Wind frequency diagram in the winter of 2012-2013

The models were of rectangular shape with dimensions 750╳600╳750mm, which were set in the north direction.

The models were installed on December 15 on flat bare ground (Figure 3). In the following 3 months, Snow density and height were measured. Wind speed and direction were measured at 1.8m on a PC-4 automatic weather station, and the sampling interval was 1 minute.



**Figure 3.** Model setup

## 2.2 Results

The results on 2014/12/29 have been selected for this investigation. Figure 4 shows the snowdrift geometry measured on 29th December, 2014. The incidence angle of the wind was 22.5° on the windward wall. The mean wind speed in the dominant direction was approximately 0.7m/s (at 1.8m) and the maximum speed was 1.6m/s, as indicated in Figure 5.



**Figure 4.** Photo of snowdrift geometry on 2014/12/29
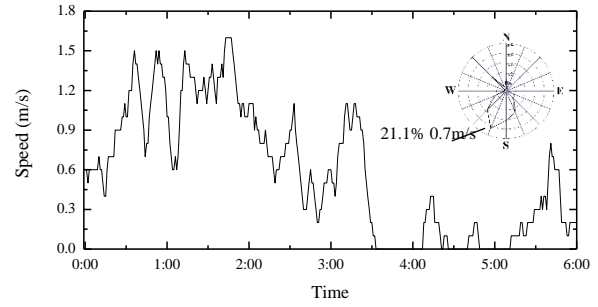


**Figure 5.** Wind speed and rose map for the whole period on 2014/12/29 at Harbin

The mean snow thickness on the flat ground was 30mm. Approximately 400 points of snow heights around models were used to interpolate a surface, as indicated in Figure 6.
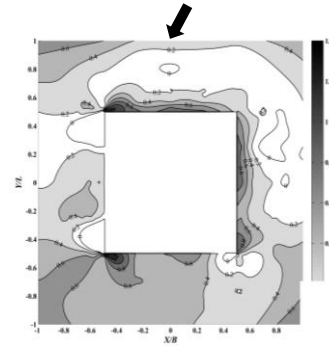


**Figure 6.** Contour map on 2014/12/29 at Harbin

# 3 Experimental reduced scale snowdrift simulations

Considering the uncertain details in wind tunnel experiments, a series of experiments were conducted for comparison with the field measurements.

## 3.1 Kind's simulation requirements

Kind's approach [1] is an essential theory in wind tunnel experiments. It consists of topography modeling, flow modeling, saltation modeling, drifting pattern modeling and time scales.

### 3.1.1 Geometric similarity

The model and prototype length scale should be determined first, according to the cross area of wind tunnel. The traditional limit is 5%.

$$\frac{L_{\mathrm{M}}}{L_{\mathrm{P}}} = \mathrm{constant}$$

Here, $L_{\mathrm{M}}$ is the reference length of the model and $L_{\mathrm{P}}$ is the reference length of the prototype. Unlike model scale, the length scale ratio of the model and prototype

snow particle size can be ignored, according to Kind's analysis [1].

### 3.1.2 Similarity of surface particle motion

If it is assumed that drag is the only aerodynamic force acting on a free-flying particle. The requirements for dynamic similarity of two-phase flow involving free-flying particles are thus shown to be:

$$\left(u_{th}^*/V\right)_M = \left(u_{th}^*/V\right)_P$$
$$\left(V_{TER}/V\right)_M = \left(V_{TER}/V\right)_P$$
$$\left(V^2/Lg\right)_M = \left(V^2/Lg\right)_P$$

Here, $u_{th}^*$ is the threshold shear velocity, $V$ is the reference velocity of the flow, $V_{TER}$ is the terminal velocity of the particles, $L$ is the reference length, $g$ is the gravitational acceleration, subscript M denotes models and subscript P denotes prototypes.

### 3.1.3 Reynolds number limits

$u_{th}^*/2g\nu$ should be greater than 30 for both model and prototype, or the Reynolds number should be matched in the model and prototype cases.

### 3.1.4 Time scale

Time scaling of the snowdrift is an important similarity requirement in relating experimental results to prototype conditions. For mass accumulations the ratio of model to prototype time scales is given by the usual relationship, namely

$$\left(\frac{t_M^*}{t_P^*}\right)_{\substack{mass \\ accumulation}} = \frac{L_M/V_M}{L_P/V_P}$$

But for volume accumulation the ratio is given by the modified relationship

$$\left(\frac{t_M^*}{t_P^*}\right)_{\substack{volume \\ accumulation}} = \frac{\rho_P/\sigma_P}{\rho_M/\sigma_M} \cdot \frac{L_M/V_M}{L_P/V_P}$$

Here, $\rho$ is the density of fluid and $\sigma$ is the density of particles.

Also, the model and prototype flow fields must be kinematically similar. The particles used for simulation of snow drifting should lie within a fairly narrow size range. If possible, the angle of repose of the model and prototype materials should be equal.

## 3.2 Experimental parameters

A direct type wind tunnel, with a test section that was 400cm long, 50cm wide, and 50cm high, was used in this experiment. Figure 7 shows a schematic view of the wind tunnel and model location.
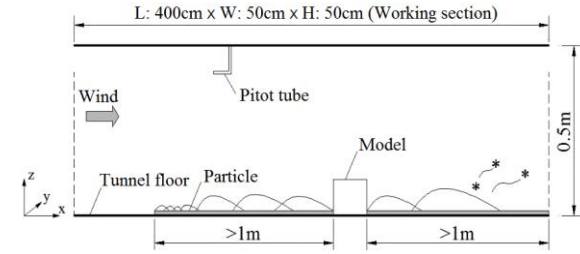


**Figure 7.** Schematic view of the wind tunnel measurements

Since little guidance can at present be offered as to the required length of the upstream fetch, the length was set to be more than one meter as Kind suggested.
The outdoor measurements, conducted by authors at Harbin China, was selected as the prototype data.

The experimental parameters were determined based on the prototype parameters discussed above, according to Kind's similarity criteria.
Table 1 shows the experimental modeling parameters based on the prototypes at Harbin.

**Table 1.** Experimental parameters based on the prototypes at Harbin

| NO. | Prototype | Particle | Scale | Length of upstream (m) | Thickness (mm) | Speed (m/s) | Duration |
|-----|-----------|----------|-------|------------------------|----------------|-------------|----------|
| 1-1 | Harbin | NaHCO$_3$ | 1/8 | 1 | 5 | 5.5 | 15min |
| 1-1.5 | Harbin | NaHCO$_3$ | 1/8 | 1.5 | 5 | 5.5 | 15min |
| 1-2 | Harbin | NaHCO$_3$ | 1/8 | 2 | 5 | 5.5 | 15min |

### 3.3 Comparison of model and prototype snowdrifts

Figure. 8 compares the snow depth distributions obtained from the experimental model and the Harbin prototype. The darkest part in the figure indicates deep snow coverage. Snow depth is normalized by the mean snow thickness on flat ground. The coordinates of distribution on the X and Y axes are also normalized by the size of the model for the same axis.

Although the observed snow accumulation shows some differences to the predicted particle build-up, it does seem that the model satisfactorily predicts the accumulation location and scale. The first zone is the windward deposition before the cuboid, the second zone is the deposition in the leeward recirculation zone behind the cuboid and the third zone is erosion windward at a distance from the cuboid.

Compared with the upstream fetch lengths of 1.0 and 2.0m, the results for 1.5m correspond in greater detail with the prototype, i.e. the deposition in zone 1 and the deposition pattern in zone 2. Besides, the partial distribution is predicted at corners lateral to the cuboid. Therefore, this suggests that a reasonable length of upstream fetch is close to 1.5m.
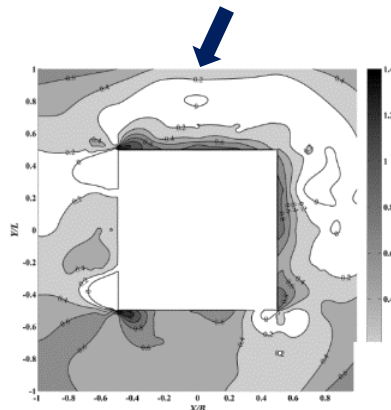


**a)** Contour map of Harbin prototype
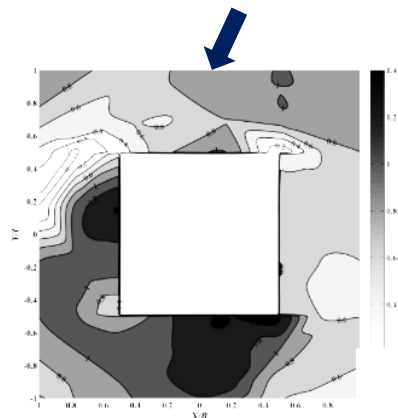


**b)** Models with 1.0m lengths of upstream fetch
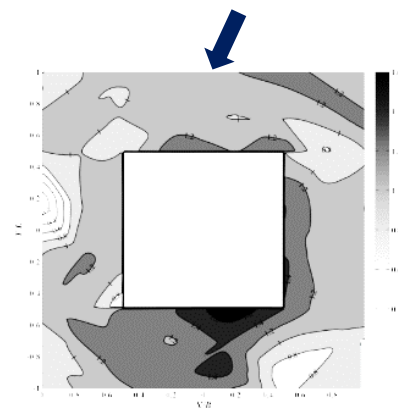


**c)** Models with 1.5m lengths of upstream fetch
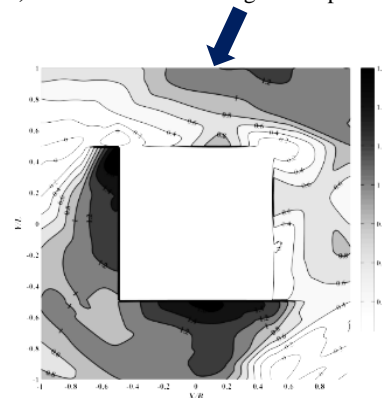


**d)** Models with 2.0m lengths of upstream fetch

**Figure 8.** Contour map of Harbin prototype and models with 1.0, 1.5 and 2.0m lengths of upstream fetch

## 4 Conclusions

This study has investigated the characteristics of drifting snow in outdoor measurements and wind tunnel tests. The following results were obtained. If upstream fetch is used to supply particles, it is suggested that the required length of the upstream fetch is 1.5m and a slight change is needed according to the specific snowdrift pattern. If the main pattern is deposition, this length needs to be increased. If the main type is erosion, reasonably short upstream fetches will probably suffice in all cases.

## References

1. R.J. Kind. J. Atmos. Environ. **10**, 219 (1976)
2. R.J. Kind. J. Cold Reg. Sci. **12**, 217 (1986)
3. N. bouvet. J. Surv. Geophys. **5-6**, 711 (1995)
4. P. Delpech, P. Palier, J. Gandemer. J. J. Wind Eng. Ind. **74-76**, 567 (1998)
5. T. Okaze, A. Mochida, Y. Tominaga, M. Nemoto, T. Sato, Y. Sasaki, K. Ichinohe. J. Wind. Eng. Ind. Aerodyn. **104-106**, 532 (2012)
6. X. LÜ, H. Ning, T. Ding. J. Technol. Sc. **55(4)**, 927 (2012)

# A new method for predicting snowdrift on flat roofs

Luyang Kang[1], Xuanyi Zhou[1,a] and Ming Gu[1]

[1]*State Key Lab of Disaster Reduction in Civil Engineering, Tongji University, Shanghai, China*

**Abstract.** Currently Eulerian method is employed by most scholars for the research on snow drifting around a building or on building roofs through CFD techniques. However, there is no scholar taking account of angle of repose of snow on the numerical simulation of snow drifting on roofs. In this paper, a new method for numerical simulation of snow drifting on flat roofs is employed, in which repose angle of snow is taken into account. The one-way coupling assumption is made for the interaction of wind and snow. The erosion or accumulation on snow surface is obtained by the calculation of snow flux on snow surface. The results of snow transports rates on flat roofs obtained by numerical simulation are analyzed in detail. Fitting equations are given to reflect the influence of roof span and wind velocity on transport rates of flat roofs.

## 1 Introduction

In recent years, with the development of computer technology, more and more scholars begin to study snowdrift through numerical simulation method [1, 2]. Based on the difference for treating snow phase, numerical simulation of snowdrift can be divided into two categories: Lagrangian method and Eulerian method. The difference lies in that the former directly simulate the trajectory of snow particles, while the latter studies the movement of snow particles based on space. Through Lagrangian method, the movement mechanism of snow particles can be studied more intuitively from the micro perspective. However, due to the requirement to track a large number of snow particles, it is difficult to promote this method in engineering applications. Currently, Eulerian method is employed by most scholars for the research on snow drifting around a building or on building roofs through CFD techniques.

Different from snowdrift around buildings, when snow accumulates on roofs, it will hold a certain repose angle at the edge of roofs, which will affect the wind-snow motion on roofs. However, there is no scholar accounting for this factor on the numerical simulation of snow drifting on roofs. To solve this problem, a new method for numerical simulation of snow drifting on flat roofs is applied in this paper. During numerical simulation, repose angle of snow is taken into account in the initial pattern of snow cover and one-way coupling steady method is applied.

Due to the fact that there is few field data about the mechanism of snow drifting on building roofs, when determining drift snow loads on building roofs, empirical relations for snow transport rate on building roofs, which are referred to field measurement on the ground, are usually used [3]. This method cannot take account into the influence of complex flow field of wind around the roof on the snow transport. Whereas, numerical simulation could study snow transport on roofs in detail. Hence, the new numerical method is used herein to simulate snow transport on flat roofs. The results of snow transport rates obtained by numerical simulation are analyzed in detail. Fitting equations are given to reflect the influence of roof span and wind velocity on transport

rates of flat roofs. The simulated results are compared with field measurement data on the ground.

## 2 Method of numerical simulation

### 2.1 Numerical method

The turbulent air field is modelled by employing the Reynolds averaged Navier-Stokes (RANS) equations of motion, in which the realizable k-ε model is adopted. For simulation of snow phase, Eulerian method is applied. The one-way coupling assumption is made for the interaction of wind and snow, namely snow drifting occurs under the action of wind whereas the migration of snow does not affect the movement of air. The erosion or accumulation on snow surface is obtained by the calculation of snow flux on snow surface.

The equations that govern the snow phase and adopted in the paper were referenced from Tominaga [2],

$$\frac{\partial(\rho_s f)}{\partial t} + \frac{\partial(\rho_s f u_j)}{\partial x_j} = \frac{\partial}{\partial x_j}\left(\nu_t \frac{\partial \rho_s f}{\partial x_j}\right) + \frac{\partial}{\partial x_3}\left(-w_f \rho_s f\right) \qquad (1)$$

where $u_j$ is the wind velocity which is calculated through the equations governing the air phase, $\nu_t$ is the turbulent kinematic viscosity, $\rho_s$ is the density of snow, $f$ is the snow volume fraction, $\rho_s f$ is the drifting snow concentration, and $w_f$ is the settling velocity of snow particles.

The erosive or accumulative snow fluxes on the snow surface of boundary condition are calculated using the formulas [1, 4] below,

$$q_{dep} = \phi w_f \frac{u_{*_t}^2 - u_*^2}{u_{*_t}^2}, \quad u_* < u_{*_t}$$

$$q_{ero} = -A_{ero}(u_*^2 - u_{*_t}^2), \quad u_* > u_{*_t} \qquad (2)$$

where $\Phi$ is the snow concentration, which can be obtained from the numerical results of snow field. $A_{ero}$ is a coefficient that represents the snow pack bonding

a Corresponding author:zhouxytj@tongji.edu.cn

strength. A value of $A_{ero} = 7 \times 10^{-4}$ was employed for the present analysis [1, 4].

The total snow mass flux $q_{total}$ on the snow surface is expressed as,

$$q_{total} = q_{ero} + q_{dep} \qquad (3)$$

## 2.2 Numerical model

For in most current load codes and standards snow load on a flat roof is one of important content about calculating snow loads, this paper choose flat roof as the research object. The span of the flat roof studied is 12 m - 108 m (L) and the height is 6 m (H). Fig.1 demonstrates the dimensions of the flat roof studied.
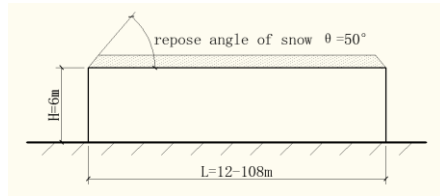


**Figure 1.** Dimensions of the flat roof

The two-dimensional snow transport on the prototype flat roof is modelled in the study. The model for numerical simulation is full scale and the calculation domain is 16L×30H. Structured progressive mesh was employed as grid scheme, growth factor of grid was 1.1 and the total number of quadrilateral grid cell was 60-455 thousands. The snow was supposed to be paved on the roof initially, which means only snow drifting without snowfall has been simulated.

Physical properties of snow particles used in numerical simulation are shown in Table 1. This study does not measure the physical properties of natural snow particles, and their values are determined with related literature [2, 5].

**Table 1.** Physical properties of snow particles

| Property | Value |
|---|---|
| Diameter $d$ | 0.15 mm |
| Density $\rho$ | 150 kg m$^{-3}$ |
| Threshold friction velocity $u_{*t}$ | 0.15 m s$^{-1}$ |
| Angle of repose $\theta$ | 50° |
| Setting velocity $w_f$ | 0.20 m s$^{-1}$ |

Table 2 shows the some key simulation parameters for the calculation conditions. Five different wind velocities are studied, and the total simulated conditions are 25. The initial snow depth is supposed to be 100 mm. The settings of boundary conditions and wind profiles refer to Zhou [6]. Thus, they are not given here in detail.

**Table 2.** Calculation conditions

| Parameter | Value |
|---|---|
| Roof height $H$ | 6 m |
| Roof span $L$ | 12 m, 24 m, 48 m, 72 m, 108 m |
| Wind velocity at the roof height $U_H$ | 4 m/s, 6 m/s, 8 m/s, 10 m/s, 12 m/s |
| Snow depth | 100 mm |

## 2.3 Validation of the Numerical Method
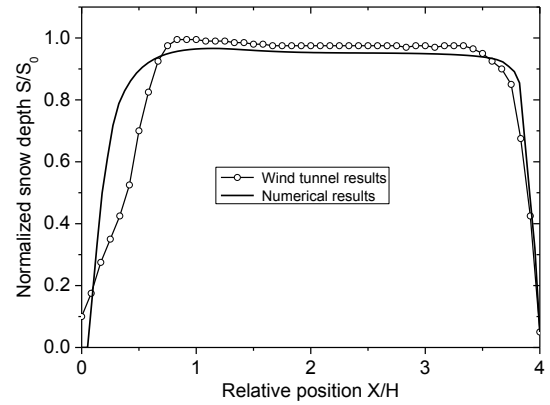


**Figure 2.** Snow distribution on roof surface [6]

Scaled model test was conducted by Hu [7] at TJ-1 wind tunnel of Tongji University for the snow drifting on flat roofs, in which high-density silica sand was used and the geometric scale ratio of the test was 1:25. Zhou [6] made a full comparison of the numerical results using this method with those from wind tunnel test and field measurement. For in this paper, only initial snow transport rate on flat roofs are studied, the comparison of redistribution of snow in phase I are demonstrated in Fig. 2. In the figure, dimensionless snow depth is the ratio of the end-time snow depth of each phase on roof surface to initial snow depth $S_0$ (prototype 50 cm; model 20 mm). The snow distribution on the roof surface obtained from the numerical simulation was similar to that of the wind tunnel test in Phase I. Snow on the entire roof surface was eroded, and the erosion in the middle region was relatively uniform. The erosion amount obtained from the numerical simulation was slightly larger than that from the wind tunnel test in the middle roof. Whereas, in the front and rear regions the erosion amount of numerical simulation was slightly smaller than that from the wind tunnel test.

# 3 Results of numerical simulation

Field measurement of snow transport rate is usually conducted on the ground. There is few data about the snow transport rate on roofs. Due to the complex flow field around the roof, snow drifting on a roof could be significantly different from that on the ground. Whereas numerical method is a good way to obtain these prototype

data. In this section, snow transport rates from numerical simulation are discussed in detail.

## 3.1 Flow field of wind velocity

Fig. 3 shows the streamline of wind velocity around a flat roof, which is representative for the streamline of wind is almost the same for different roof spans. Before the wind begins blowing, the snow deposited on the roof is supposed to be paved uniformly on the roof with a repose angle. Due to this repose angle of snow at the roof edge, significant flow separation cannot be observed around the roof. The separation strength has been weakened significantly. The direction of wind velocity near snow surface is approximately parallel to the snow surface. From Fig. 3, we could deduce that snow particles are blown off the roof along the snow surface under the action of wind. Test results of Hu [7] proved this phenomenon.
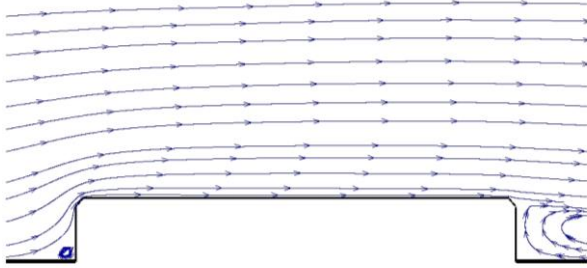


**Figure 3.** Flow field around the flat roof (L = 48 m)

## 3.2 Snow transport rate on flat roofs

In current load standards and codes, exposure coefficient, which is the ratio of roof snow loads to ground snow loads, is commonly used to reflect the effects of wind or other environment factors. Combined with meteorological data, transport rate could be used to determine snow loads on flat roofs. Hence, transport rate is analyzed here in detail.
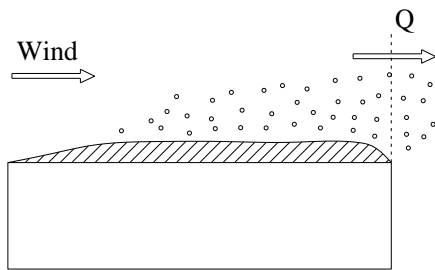


**Figure 4.** Transport rate of snow on a flat roof

Snow transport rate for a flat roof is defined here as the total snow mass blown off the roof per unit time and unit width, as shown in Fig. 4. Specifically, snow transport rate on roof surface is the product of bulk particle density and the integration of snow depth change

per unit width per unit time along the entire roof span. The calculation formula is as follows,

$$Q = \rho_b \int_L \Delta h(x)dx \tag{4}$$

Fig. 5 shows the influence of roof span on the snow transport rate for flat roofs. As one might expect, snow transport rate $Q$ increases with the increasing roof span. The increasing amplitude is large for small span roof, and the amplitude decreases as roof span becomes larger. Logarithmic law is the most suitable for the relation between snow transport rate $Q$ and roof span $L$. Fitting equations using logarithmic relation at different wind velocities are also given in Fig. 5.
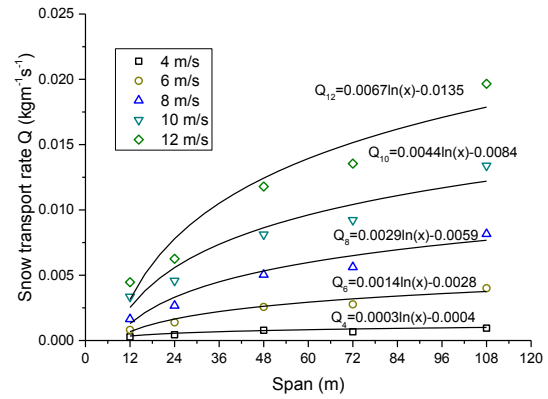


**Figure 5.** $Q$ as a function of $L$

We could find from Fig. 5 that without snowfall snow transport on flat roofs are limited to the upwind fetch distance. Different from the relation given in Fig. 5, the reduction factor for snow transport rate on the ground given by Takeuchi [8] appears to be proportional to the square root of the fetch distance $\sqrt{F/210}$. Whereas based on field measurement, Tabler [9] gave this reduction factor as $(1-0.14^{F/T})$, where $T$ is the minimum distance for fully developed snow transport.
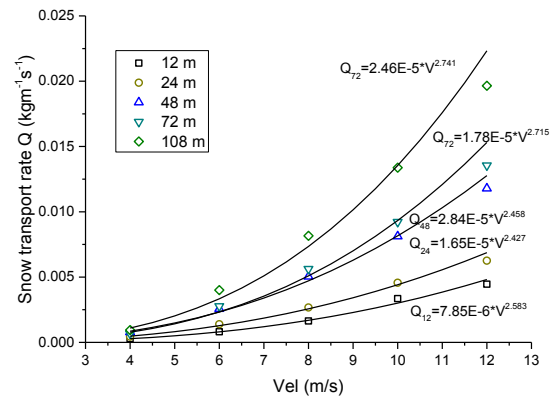


**Figure 6.** $Q$ as a function of $V_H$

Fig. 6 shows the influence of wind velocity at the roof height $V_H$ on snow transport rate $Q$. Similar to the empirical formulae obtained from field measurement on the ground (Table 3), the relation between $Q$ and $V_H$

meets the power law. In addition, transport rates are increasing functions of wind velocity at the roof height.

Fitting functions of power law are given in Fig. 6. For the roof profile affects the wind flow around the roof, the growth rate of $Q$ for flat roofs is lower than that on the ground. The power of the fitting functions is between 2.4 and 2.7 for flat roofs. Whereas, the power of the empirical formulae obtained by ground field measurement, which are shown in Table. 3, is between 3 and 4. The order of $Q$ from numerical simulation is the same as the field data, which could be seen in Fig. 7.

**Table 3.** Empirical formulae for snow transport rate $Q$ ($gm^{-1}s^{-1}$), [8, 9]

| Investigator | Formula |
|---|---|
| Khrgian | $Q = -5.8 + 0.267U_1 + 0.123U_1^2$ |
| Inanov | $Q = 0.0295U_1^3$ |
| Mel'nik | $Q = 0.092U_1^3$ |
| Dyunin | $Q = 0.0334(1 - (4/U_1))U_1^3$ |
| Komarov | $Q = 0.011U_1^{3.5} - 0.67$ |
| Budd et al. | $\log Q = 1.22 + 0.0859U_1$ |
| Kobayashi et al. | $Q = 0.03U_1^3$ |
| Takeuchi | $Q = 0.0029U_1^{4.16}$ (dry snow) |
| Tabler | $Q = 0.00427U_{10}^{3.8}$ |

According to the square-root relationship used by O'Rourke [3], when roof span is larger than 210 m, the reduction factor would be larger than 1.0. Whereas, Tabler [9] used a better model to reflect the increase of transport rate with fetch distance, where the upper limit for the reduction factor is 1.0. Thus, the following equation used by Tabler is applied to compare the simulated results.

$$Q(U_{10}) = 4.27 \times 10^{-6}U_{10}^{3.8}(1 - 0.14^{L/210}) \qquad (5)$$

Here, the unit of $Q$ is $kgm^{-1}s^{-1}$. For fresh snow, the minimum fetch distance for fully developed snow transport is set as 210 m, which was also used by O'Rourke [3]. Wind velocity at 10 m height is supposed to be the same as that at the roof height $V_H$.

The comparison of calculated results is shown in Fig. 7. To make it clear, only results of three different spans are shown. Comparison results for the other two spans have the same trend. At the lower wind velocity, the snow transport rate $Q$ on the ground is lower than that for roof. At a certain wind velocity, snow transport rate achieves the same value between that on the roof and that on the ground. This wind velocity is approximately 8 m/s for L = 108 m, 9 m/s for L = 48 m, and 10.5 m/s for L = 12m. Here, we call this velocity as equilibrium velocity. When $V_H$ is larger than the equilibrium velocity, due to a larger power of the empirical formula, snow transport

rate on the ground is larger than that on the roof. At 12 m/s, compared with $Q$ on the roof, snow transport rate on the ground is 18.7%, 52.3%, 53.8% respectively larger for the roof span 12 m, 48 m and 108m. This means that when the empirical formula on the ground is used to predict snow loads on flat roofs, a lower wind exposure coefficient would be obtained, which is unfavourable for roof structures.
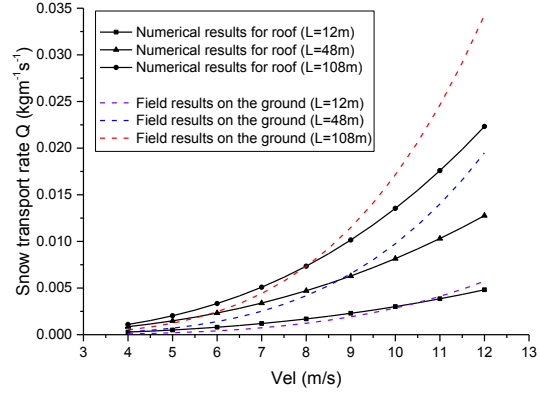


**Figure 7.** Comparison of snow transport rate $Q$

# 4 Conclusions

In this paper, a new simulation method of snow drifting on flat roofs, where repose angle of snow is taken into account, is applied to calculate snow transport rates on flat roofs. The simulated results are compared with field measurement data on the ground. The main conclusions are as follows:

(1) The initial pattern of snow cover on roof surface has great influence on the wind-snow motion on roof surface. The existence of angle of repose of snow will alter the position of flow separation at the roof edge and weaken the strength of flow separation thus the snow redistribution on the roof is greatly affected. The direction of wind velocity near snow surface is approximately parallel to the snow surface.

(2) Snow transport rate $Q$ increases with the increasing roof span. Logarithmic law is the most suitable for the relation between snow transport rate $Q$ on the roof and roof span $L$. Whereas the relation between $Q$ and $V_H$ meets the power law.

(3) Compared with empirical formulae obtained on the ground, the power of the fitting equations for $Q$ on the roof is lower. At lower wind velocity, the snow transport rate $Q$ on the ground is lower than that for roof. When $V_H$ is larger than the equilibrium velocity, due to a larger power of the empirical formula, snow transport rate on the ground is larger than that on the roof.

## References

1. J.H.M. Beyers, P.A. Sundsbø, T.M. Harms, Numerical simulation of three-dimensional, transient snow drifting around a cube, J. Wind Eng. Ind. Aerodyn., **92**(9): 725-747, (2004).
2. Y. Tominaga, T. Okaze, A. Mochida, CFD modeling of snowdrift around a building: An overview of models and evaluation of a new approach, J. Bui. Env., **4**:899-910, (2011).
3. O'Rourke, M., DeGaetano, A., Tokarczyk, J.D., Analytical Simulation of Snow Drift Loading. J. Struct. Eng. **131**, 660–667, (2005).
4. Naaim, M., Naaim-bouvet, F., Martinez, H., Numerical simulation of drifting snow: erosion and deposition rn.odels. Ann. Glaciol. **26**, 191–196, (1998).
5. D. Kuroiwa, Y. Mizuno, M. Takeuchi, Micromeritical properties of snow, *Proc. of Intl. Con. on Low Temp. Sci.*: *Phys. of Snow and Ice*, **1**(2): 751-772, (1967).
6. Zhou, X., Kang, L., Gu, M., Qiu, L., Hu, J., Numerical simulation and wind tunnel test for redistribution of snow on a flat roof. J. Wind Eng. Ind. Aerodyn. **153**, 92–105, (2016).
7. J. Hu. *Experimental study on wind-induced snow motion on building roof surface*, Master Thesis, Tongji University, (2013).
8. Takeuchi, M., Vertical profile and horizontal increase of drift-snow transport. J. Glaciol. **26**, 481–492, (1980).
9. Tabler R D., *Controlling blowing and drifting snow with snow fences and road design.* National Cooperative Highway Research Program Project, NCHRP Project 20-7(147), (2003)

# Improved design relations for roof snow drifts

Michael O'Rourke[1] and John Cocca[2]

[1]Rensselaer Polytechnic Institute, New York, USA
[2]Wiss, Janney, Elstner Associates, Inc., Connecticut, USA

**Abstract.** The paper will present new relations for roof snow drifts which include a measure of winter windiness. The relation was developed by determining the annual maximum drift loads at 42 locations across the US through physics based numerical simulation using 19 years of weather records for both snowfall and wind speed at each location. Annual maximum were then used to determine the 50 year MRI drift for various upwind fetch distances. The new building code suitable design drift relation involving a map-able wind parameter, 50 year ground snow load and upwind fetch was then developed using multiple regression analysis.

## 1. Introduction

Structural loads due to drifted snow continue to be one of the key considerations for roof design in North America. As an example, a FEMA building collapse investigation team surveyed damage to school roofs in the Greater Boston region resulting from record snow in February 2015. For all four schools visited, collapse was due to localized roof snow drifts.

In North American building codes, snow drift loads were originally taken to be a multiple of the ground snow load. Current relations for the height of the roof snow drift are based upon an analysis of insurance company case histories, in which the height is presented as a function of the ground snow load and the fetch (i.e. length) of the upwind snow source area. Absent from the current relations is any measure of the local wind speed during the winter.

## 2. Current U.S. roof step drift relations

Current U.S. building codes utilize a roof snow drift relation based upon a statistical analysis and multiple regression analysis of empirical case history information. The location, ground snow load and roof geometry were the typical available case history parameters. However wind speed and direction for the case history drifts was generally not available. Hence the current U.S. empirical relation bases drift size on ground snow load (50 year MRI value in ASCE 7) and upwind fetch.
Specifically for a roof step in Figure 1 with wind from left to right, the height of the nominally triangular roof snow drift above the balanced snow, $h_d$, is given by:

$$h_d = 0.43(L_u)^{\frac{1}{3}}(P_g + 10)^{\frac{1}{4}} - 1.5 \qquad (1)$$

where $h_d$ is in feet, the upwind fetch, $L_u$, is in feet and the 50 year ground snow load, $P_g$, is in lbs/ft². As one might expect, the drift height is an increasing function of the upwind snow source region characterized by the fetch and ground snow load. However the increase is not linear. If the upwind fetch or the ground snow load were to double, the drift height would increase but not double.
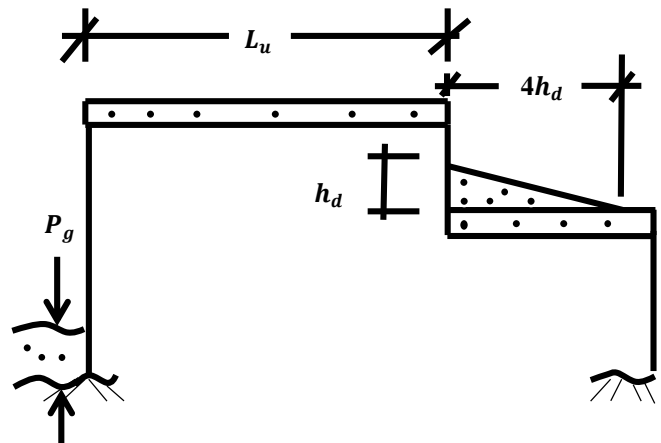


**Figure 1.** Roof Snowdrift at Leeward Roof Step

The horizontal extent of the roof step drift is taken as four times its height. The 1:4 rise to run is thought to be related to the angle of repose for drifted snow. Finally the snow density $\gamma$ (lbs/ft³) needed to convert drift height into drift load is given

$$\gamma = 0.13p_g + 14 \qquad (2)$$

The snow density increase with ground snow load is due to compaction (densification) near the bottom of the snow pack, due to the weight of the snow near the top.

The relations in equation (1) and (2) have been in use in the U.S. for the past 20 years or more. Although intuitively appealing, they do not include wind which theoretically should influence roof snow drift size.

It can be argued that improvements in drift load estimation procedures in building codes and load standards require an ability to numerically simulate roof snow drifts.

## 3. Simulation of roof snow drifts

Fortunately Tabler (1994) provides guidance in his pioneering work related to snow fences at highway cuts. Tabler considered a two-step physics based process wherein the snow flux or transport rate of snow is first established and then a trapping efficiency is applied to estimate drift size. As one might expect, Tabler's transport rate for an unlimited fetch $T_r(V)$ (lbs/foot width perpendicular to the wind direction/hr) for ground snow is a function of wind speed

$$T_r(V) = (4.8 * 10^{-4})V^{3.8} \qquad (3)$$

where V is the wind speed in miles/hr at a height of 32.8 ft (10 m). Based upon full scale measurements by Takeuchi (1980), an upwind fetch of roughly 750 ft (225 m) is needed for full (unlimited fetch) transport. For shorter fetch distances, a correction factor is utilized

$$T_r(V) * (L/750)^{0.5} \qquad (4)$$

where L is the upwind fetch in feet.

The wind flow patterns and trapping efficiency for a snow fence upwind of a highway cut are much different than those for a roof step in Figure 1. Based upon water flume tests, O'Rourke et al. (2005) have shown that the trapping efficiencies at a leeward roof step ranged between 47 and 58%, and a 50% trapping efficiency is used herein. That is, for a leeward roof step the initial growth rate (prior to complete filling of the aerodynamic shade region) is half the transport rate in equation (2) for unlimited fetch distances or equation (3) for fetch distances less than 750 ft.

Cocca (2006) used these procedures to determine the maximum annual leeward roof step drift for the years 1977 through 1996 (19 years) at 46 locations across the U.S. The 19 samples of the maximum annual drift load were fit with a Gumbel Distribution to determine the 50-year MRI drift load again at 46 locations across the U.S. The drift load was characterized by a dimensionless quantity, the drift ratio, DR. DR was defined as the 50 year drift load (half the drift height times drift length times snow density) divided by the product of the 50-year ground snow load, $P_g$ and the roof upwind fetch, $L_u$. Since the trapping efficiency is taken as 50%, the maximum possible value for DR is 0.5. This would correspond to a winter with a 50-year ground snow load and enough wind to blow all the snow on the upper level roof towards the roof step.

As one might expect, the 50 year drift ratio is a decreasing function of the upwind fetch and the 50-year ground snow load. For given amounts of ground snow and winter wind, one obtains smaller drift ratios for increasing upwind fetch distances. Similarly, for given upwind fetch and winter winds, one obtains smaller drift

ratios for increasing ground snow loads. In both cases, if the snow source area (proportional to product of fetch and ground snow load) is increasing, a fixed amount of winter wind will be able to transport only a smaller percentage of the upwind snow source.

Somewhat surprisingly, the DR also varied significantly with location. Figure 2 shows the 50-year drift ratios for an upwind fetch of 250 feet. Notice that areas with particularly large drift ratios are the upper Midwest (the Dakotas and Nebraska) and leeward of Lake Erie (Erie PA and Buffalo NY). Areas with particularly small drift ratios are located in the Pacific Northwest (Helena MT, Landers WY, Spokane WA and Yakima WA). For the five locations in the U.S. with a 50 year ground snow load in the 30 to 25 psf range, the drift ratios, again for a 250 foot upwind fetch, varied from 0.014 to 0.205, more than an order of magnitude difference. Clearly there is significant variation of winter windiness across the U.S. Note that the current ASCE 7 (ASCE, 2010) drift relations in equations (1) and (2) are functions of the upwind fetch and ground snow load, but not local winter windiness. As such they underestimate the snow drift hazard for some locations (upper Midwest) while overestimating it for other locations (Pacific Northwest).
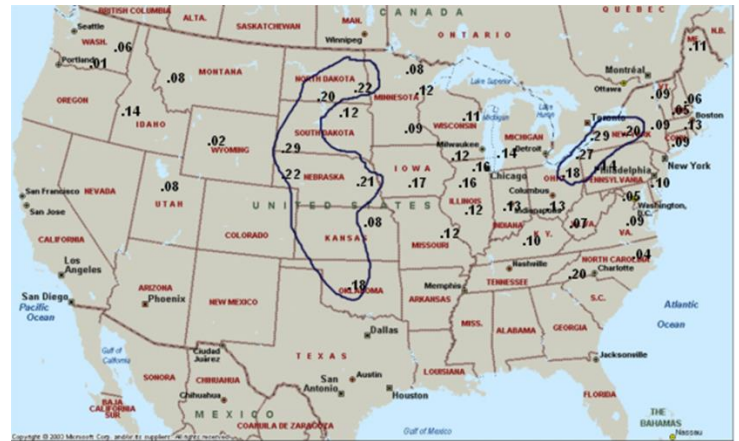


**Figure 2.** Simulated 50-year drift ratios for upwind fetch $L_u = 250$ ft.

As shown above, the site location in general and the local winter windiness in particular, have a significant influence on the magnitude of roof snow drifts. In order to incorporate this influence into a relationship suitable for use in building codes and load standards, a number of parameters were tested to determine a mapable value to characterize "Winter Windiness". Specifically three parameters were considered. The first, W1, was the mean wind speed over the winter months. The second was W2, the percent time when the wind speed was greater than the snow transport threshold of 10 MPH. The third, W3, was the mean value of the wind speed to the 3.8 power when the wind speed was greater than 10 MPH. It turned out that W2 provided the best fit to the physics based simulated 50-year drift ratio values. Figure 3 is a plot of the winter windiness parameter W2 for various regions in the U.S. For the 46 locations across the U.S., W2 ranged

from 0.167 to 0.725 with a mean of .484 and a standard deviation of 0.119. As one might expect, W2 was high for the Upper Midwest (.498 to .659) and lee of Lake Erie (0.626 to 0.659), while W2 was low for the Pacific Northwest (0.152 to 0.353).
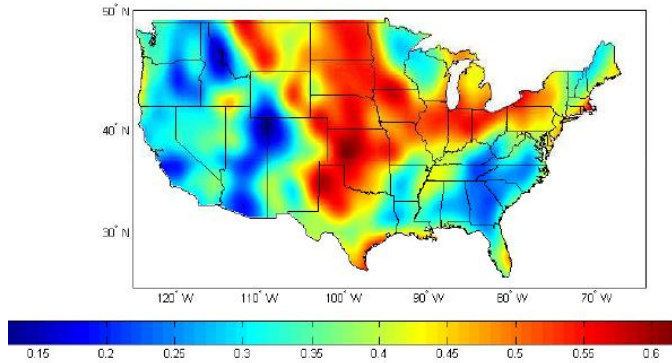


**Figure 3.** U.S. map of Winter Windiness Parameter W2

Multiple regression analysis resulted in the following building code suitable predictive formula for the 50-year drift ratio.

$$DR = \frac{4.89\, W_2^{1.81}}{P_g^{.254} L_u^{.296}} \qquad (5)$$

Note that the 50-year ground snowload, $P_g$ (psf) and the upwind fetch, $L_u$ (ft.) are both in the denominator, that is DR is a decreasing function of both $P_g$ and $L_u$. However since the drift size (lbs/ft) is the product of DR, $P_g$ and $L_u$, drift size is an increasing function of $L_u$ and $P_g$ which is generally consistent with Equation (1) for the drift height, $h_d$.

## 4. Comparison between physics based and code suitable relations

Figure 4 shows a comparison of DR from the physics based numerical simulation and the code suitable value from Equation (5). The origin constrained best fit straight line thru the data points has a slope of 1.05: 1.0 and a correction coefficient $R^2$ of 0.43.



**Figure 4.** DR Simulated vs. DR Predicted Using W2

Tables 1 thru 3 present the minimum, maximum, mean and standard deviation for the 50 year drift ratio from the physics based numerical simulation $DR_{sim}$, drift ratio from the code suitable predictive equati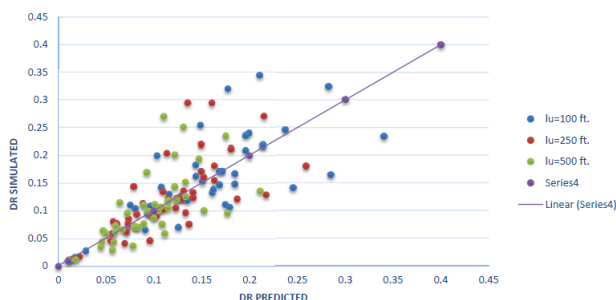on $DR_{pred}$, and from the current ASCE 7 procedure $DR_{ASCE}$, for upwind fetch distances of 100, 250 and 500 feet. Also presented are the ratios of Pred/Sim and ASCE/Sim.

Note that Figure 4 and Tables 1 thru 3 suggest that "on average" the code suitable predictive equation (Equation 5) provides a reasonable match to the expected physics based 50 year drift ratio. In Figure 4, the best fit straight line has a slope of 1.05:1.0. This is consistent with the mean values in Tables 1 thru 3 for the ratio Pred/Sim for upwind fetch distances of 100, 250, and 500 feet (1.04, 1.04, and 1.06 respectively). Also the range mean and standard deviation for $DR_{pred}$ (minimum value of 0.013, maximum value of 0.259 mean of 0.118 and standard deviation of 0.051 for $L_u$ = 250 feet) are similar to those for $DR_{sim}$ (0.013, 0.294, 0.125, and 0.066 again for $L_u$ = 250 feet).

However although "on average" $DR_{pred}$ nominally match $DR_{sim}$, Figure 4 shows significant differences in $DR_{pred}$ and $DR_{sim}$ values. As shown in Tables 1 thru 3, the ratio $DR_{pred}/DR_{sim}$ can be as low as roughly 0.5 and as high as roughly 2.0. That is, W2 is not the perfect parameter to characterize winter windiness. First of all, it is not the typical wind speed, simply the percentage of time the speed is above the threshold. Similarly, it does not provide a direct measure of the wind speed during and immediately after significant snowfalls. Rather it includes periods well before and after significant snowfall events. These "well before" and "well after" periods would have minimal impact on drift formation. Finally, drift size would be longer if the winter wind was typically out of the same direction, as opposed to out of multiple directions over the course of a given winter. Note in this regard that consistency of direction is not measured by W2.

For all its drawbacks, W2 is an easy to evaluate parameter and correlates reasonably well with ASCE 7 maps for the 3-second gust speed concurrent with freezing rain, which one uses to determine atmospheric icing loads in ASCE 7.

**Table 1.** 50 year Drift Ratios for $L_u$ = 100 ft.

|  | $DR_{Sim}$ | $DR_{Pred}$ | $DR_{ASCE}$ | $\dfrac{Pred}{Sim}$ | $\dfrac{ASCE}{Sim}$ |
|---|---|---|---|---|---|
| Min. | 0.016 | 0.017 | 0.133 | 0.516 | 0.406 |
| Max. | 0.344 | 0.34 | 0.256 | 1.78 | 9.01 |
| Mean | 0.158 | 0.155 | 0.164 | 1.04 | 1.46 |
| St. Dev. | 0.075 | 0.068 | 0.03 | 0.316 | 1.47 |

**Table 2.** 50 year Drift Ratios for Lu = 250 ft.

| | $DR_{Sim}$ | $DR_{Pred}$ | $DR_{ASCE}$ | $\dfrac{Pred}{Sim}$ | $\dfrac{ASCE}{Sim}$ |
|---|---|---|---|---|---|
| Min. | 0.013 | 0.013 | 0.114 | 0.460 | 0.427 |
| Max. | 0.294 | 0.259 | 0.250 | 2.06 | 10.576 |
| Mean | 0.125 | 0.118 | 0.151 | 1.04 | 1.82 |
| St. Dev. | 0.066 | 0.051 | 0.033 | 0.341 | 1.895 |

**Table 3.** 50 year Drift Ratios for $L_u$ = 500 ft.

| | $DR_{Sim}$ | $DR_{Pred}$ | $DR_{ASCE}$ | $\dfrac{Pred}{Sim}$ | $\dfrac{ASCE}{Sim}$ |
|---|---|---|---|---|---|
| Min. | 0.012 | 0.011 | 0.099 | 0.409 | 0.442 |
| Max. | 0.270 | 0.211 | 0.230 | 2.12 | 10.37 |
| Mean | 0.103 | 0.096 | 0.136 | 1.06 | 2.05 |
| St. Dev. | 0.06 | 0.042 | 0.031 | 0.388 | 2.089 |



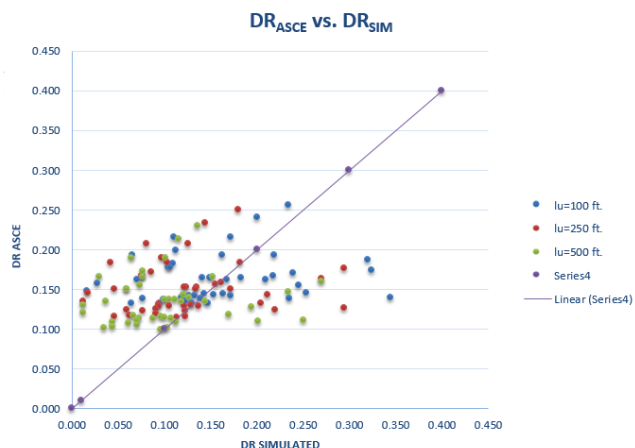**Figure 5**: DR ASCE vs. DR Simulated

## 5. Comparison between simulated and ASCE

Figure 5 shows a comparison of DR from the physics based numerical simulations and the corresponding drift ratios from the current ASCE 7 relations in Equation (1) and (2). For each of the 46 locations, drift ratios are determined for the three values of $L_u$; 100, 250 and 500 feet.

The most striking characteristic of Figure 5 is the relatively wide range of physics based $DR_{sim}$ values in comparison to the relatively narrow range for $DR_{ASCE}$. The $DR_{sim}$ values range from roughly 0.015 to roughly 0.30 while the $DR_{ASCE}$ values only range from roughly 0.10 to roughly 0.25. Hence for many sites the expected physics based DR is much lower than the DR from the current ASCE 7 provisions. Specifically for three fetch distances considered, $DR_{ASCE}$ was larger than the expected value (i.e. $DR_{sim}$), for about 75% of the sites (68% for $L_u$ = 100 ft, 78% for $L_u$ = 250 ft, and 83% for $L_u$ = 500 ft).

The apparent overestimation associated with current ASCE drift relations is also evident by the ratios in Tables 1 thru 3. On average for the three fetch distances considered, the mean of the $DR_{ASCE}/DR_{sim}$ ratio was about 1.78 (1.46 for $L_u$ = 100 ft, 1.82 for $L_u$ = 250 ft, and 2.05 for $L_u$ = 500 ft), with the overestimation increasing with increasing fetch distance.

Hence although W2 is an imperfect wind parameter, the drift size from the code suitable predictive equation utilizing W2 provides a much better estimation of the expected drift size from the physics based numerical simulation than the current ASCE relations which include no winter wind parameter.

## 6. Comparison between code suitable and ASCE

Based upon the proceeding discussion, one could argue that drift relations based upon the code suitable predictive equation utilizing the winter wind parameter W2 (equation 5) are an improvement over the current ASCE 7 drift relations. The effects of this change would vary from site to site.

For example W2 for Lexington KY happens to be the mean value of 0.484, while Boston MA has the highest W2 (0.725) and Yakima WA has the lowest (0.167). For an upwind fetch of 250 feet, the 50 year drift ratios predicted by Equation (5) are 0.133, 0.217, and 0.013 for Lexington, Boston, and Yakima respectively. The 50 year drift ratios predicted by the ASCE procedure in Equation (1) and (2) for the same three cities are 0.190, 0.130 and 0.135 respectively. Hence if the current drift relations (equations 1 and 2) were replaced by the predictive relation (equation 5) the mean 50-year drift (lbs/ft) would decrease by roughly 30% (.133/.190 = .7). For particularly windy places such as Boston the 50-year drift (lbs/ft) would increase by about 70% (.217/.130 = 1.67), while for particularly calm locations such as Yakima, the 50 year drift ratio decreases by as much as 90% (.013/.135 = .096). That is, if the predictive relation in Equation 5 were used, drift loads for some locations would increase but for most locations they would decrease. Note that these values are based upon site specific values for both $P_g$ and W2. Due to the "rounding up" that typically occurs when parameters are mapped, the net effect for typical locations would be a decrease of something less than 30%.

## 7. Conclusions

Herein current roof step drifts from the ASCE 7 provisions are compared with physics based simulated and code suitable predicted roof step drifts. The ASCE 7 drift provisions were based upon an analysis of drift load case histories from insurance company files in which wind speed information was not available. The simulated drifts were based upon the physics of drift formation

(snow transport from the snow source area, and trapping at the aerodynamic shade region), utilizing 19 years of snowfall and wind speed information at 46 sites across the US. Finally various easily mapped winter wind parameters were investigated in order to determine a predictive relation suitable for use in building codes and load standards.

The code suitable predictive relationship was found to provide a reasonable estimate to the expected drift size based upon the physics of drift formation (i.e., simulated drift). Comparison of the ASCE drifts to the simulated drift suggest that the inclusion of a winter windiness parameter is quite important. That is, expected drift from numerical simulation showed much more variability (both larger and smaller drift loads) that those from the current ASCE 7 provisions.

Finally if the building code suitable predictive relation were to replace the current ASCE 7 relations, one would expect that on average design drift sizes (lbs/ft) would be reduced by roughly 30%. For some locations the reduction would be about 90%. At location which experience much stronger than average winter wind the design drift would increase by about 70%.

## References

1. ASCE (American Society of Civil Engineers), 2010, Minimum design loads for building and other structures ASCE/SEI 7-10, ASCE, Reston VA, USA.
2. Cocca, J. (2006) Mathematical Simulation of 50-Year Snow Drift Ratios. MS Thesis, Rensselaer Polytechnic Institute.
3. M. O'Rourke, A. DeGaetano and J. D. Tokarczyk, 2005: Analytical Simulation of Snow Drift Loading, *Journal of Structural Engineering.* ASCE, Vol. 121. No. 4, April.
4. R. D. Tabler, 1994: Design Guidelines for the Control of Blowing and Drifting Snow, *Strategic Highway Research Program SHRP-H-381, National Research Council,* pp. 364.
5. M. Takeuchi 1980: *Vertical Profile and Horizontal Increase of Snow – Drift Transport,* J. Glaciology Vol. 26 pp. 481 – 492.

# Session 5

# Structural loading II

# Specification of the design value of the ground snow load considering measurements of the snow height – part 2: regional approach

Michael Kasperski, Benjamin Czwikla [a]

*Ruhr-Universität Bochum, Research Team EKIB. 44780 Bochum, Germany*

**Abstract.** A regional model for the snow density is required to exploit the large number of stations which only monitor the snow height. Starting point are simultaneous observations of the water equivalents and the snow heights. Since the ensembles are confined, the station-wise input data have an inherent uncertainty. Furthermore, the observation period may vary. The shorter the observation period, the larger will be the uncertainties. The paper explains how to study the uncertainties based on simulations and presents a new strategy for considering the uncertainties in the identification of the model parameters. As example of application, the correlation of snow loads is studied for 14 stations in Mecklenburg-Vorpommern, Germany.

## 1 Introduction

The straight-forward approach to the specification of the design value of the ground snow loads is based on measurements of the water equivalent. Since the acquisition of this observation variable is rather time-consuming not all meteorological stations provide this information. For stations which do provide the water equivalent, the observations usually cover only the recent decades, i.e. the majority of observation data provides only the height of snow cover. Using these data for the specification of snow loads requires a consistent model for the snow density $\rho_s$ which translates the snow heights $h_s$ to snow loads s:

$$s = \rho_s \cdot g \cdot h_s \tag{1}$$

For exploiting the observation years of snow heights of a single station, obviously it is sufficient to develop an individual snow density model for each station. For Germany, this step increases the number of observations on average by a factor of about 2, thus improving the statistical stability of the estimated design values. The individual models require simultaneous measurements of snow heights and water equivalents.

The number of German stations only measuring the snow heights is by a factor of 10 larger than the number of stations measuring the water equivalent (fig.1). Thus, interpolation between stations becomes easier, especially if additional parameters are to be considered as e.g. the altitude. Exploiting this huge amount of data requires a regional model of the snow density. This paper discusses the strategies to develop a regional model. Starting point is the approach for single stations as described in [1].

A naïve approach simply uses the identified parameters of the single stations as input for the geostatistics. Then, only data sets of the same length and quality should be used, thus avoiding biasing effects from different statistical stability of the input data. However, for the snow data in a specific region, the length of the observation periods might vary considerably. Then, it is required to consider the different level of uncertainties in the input data.

This paper develops a basic strategy for a refined approach. Chapter 2 explains how uncertainties can be studied based on simulations. Basic tool is the NORTA-approach which allows generating correlated data for any combination of probability distributions. In chapter 3, the refined approach is illustrated based on a simple example of a linear law. Chapter 4 presents results for a spatial correlation model of the snow loads.
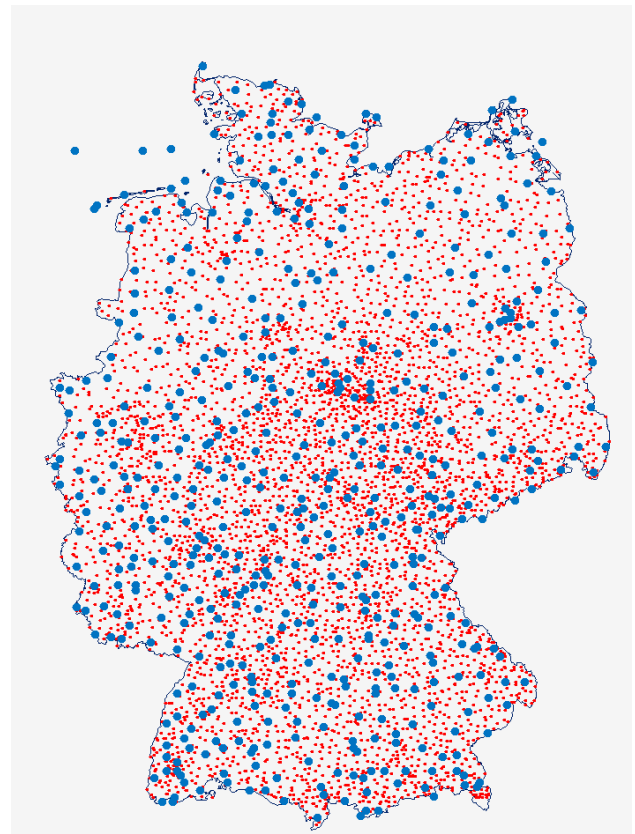


**Figure 1**: Distributions of stations measuring the water equivalent and stations measuring only the snow height. (Germany, 2006)

---

[a] Corresponding author: benjamin.czwikla@rub.de

## 2 Stastical stability of the identified parameters of the snow density model

The developed snow density model [1] assumes that both the water equivalents and the snow heights follow an extreme value distribution type I. The snow density is described by a two parameter model as follows [1]:

$$\rho_s = \rho_\infty - \frac{\Delta\rho \cdot h_{ref}}{h_s} \tag{2}$$

The limiting density $\rho_\infty$ is obtained as the ratio of the standard deviations of the snow load and the snow heights:

$$\rho_\infty = \frac{\sigma_s}{\sigma_h \cdot g} \tag{3}$$

with g – gravitational acceleration $\approx$ 9.81 m/s²

The term $\Delta\rho$ is obtained as the weighted difference of the two mean values:

$$\Delta\rho = \frac{\rho_\infty \cdot m_h - m_s / g}{h_{ref}} \tag{4}$$

The reference height, which is required for consistency in the dimension, is an arbitrary value and can be assumed as $h_{ref} = 1$ m.

For confined ensembles, the statistical uncertainties in the estimated mean value and standard deviation are discussed in [1]. As main conclusion it is stated that even for observation periods beyond 100 years, the estimated parameters might deviate from the true parameters. Since the parameters of the snow density model are obtained as combinations of uncertain input values, the uncertainties in the final results will be larger than in the input values.

A consistent analysis of the uncertainties can be based on simulations. Since the snow loads and the snow heights are correlated, the simulations have to be based on the NORTA-strategy [2], which

- first generates correlated variables $x_n$ and $y_n$ following the standardized normal distribution,
- then transfers these values to correlated uniformly distributed variables u and v with u = $\Phi(x_n)$ and v = $\Phi(y_n)$, where $\Phi$ is the cumulative probability distribution for the standardized normal distribution, using e.g. the error function
- and finally transfers u and v into two correlated variables $t_1$ and $t_2$ which may follow any target probability distributions (NORTA = Normal To Anything)

The generation of correlated variables $x_n$ and $y_n$ is based on two uncorrelated standardized normally distributed variables $x_n$ and $z_n$ using the following transformation:

$$y_n = r \cdot x_n + \sqrt{1-r^2} \cdot z_n \tag{5}$$

with r – target correlation between $x_n$ and $y_n$

The transformation into two correlated uniformly distributed variables u and v leads to a distortion in the correlation, i.e. the obtained correlation between u and v differs from the input correlation of $x_n$ and $y_n$ [3]:

$$r_{uv} = \frac{6}{\pi}\arcsin\left(\frac{r_{xy}}{2}\right) \tag{6}$$

While in the first transformation step from normally distributed variables to uniformly distributed variables the whole solution space is kept with values for the correlation $r_{uv}$ from -1 to + 1, the further transformation to the final target distributions may lead to a limited solution space.

The final joint probability density of $t_1$ and $t_2$ is obtained from the joint normal probability density $f_{xy}$ as follows:

$$f_{t_1t_2}(t_1,t_2) = \frac{f_{xy}\left(x_n(u), y_n(v), r_{in}\right)}{f_x\left(x_n(u)\right) \cdot f_y\left(y_n(v)\right)} \cdot \frac{\partial u}{\partial t_1} \cdot \frac{\partial v}{\partial t_2} \tag{7}$$

where the joint normal probability density is given as:

$$f_{xy}(x_n,y_n) = \frac{\exp\left(-\frac{x_n^2+2\cdot x_n \cdot y_n+y_n^2}{2\cdot\left(1-\rho_{in}^2\right)}\right)}{2\cdot\pi\cdot\sqrt{1-\rho_{in}^2}} \tag{8}$$

The probability densities $f_x$ and $f_y$ correspond to the normal probability density:

$$f_x(x_n) = \frac{1}{\sqrt{2\cdot\pi}} \cdot \exp\left(-\frac{x_n^2}{2}\right) \tag{9}$$

The terms $\partial u/\partial t_1$ and the $\partial v/\partial t_2$ are the partial derivatives of the respective target cumulative probability distributions. Finally, the correlation $r_{out}$ results from a double integration over $t_1$ and $t_2$ supposing that the two integration variables are used in normalized form, i.e. have a zero mean and a standard deviation of 1:

$$r_{out} = \iint_{t_1,t_2} f_{t_1t_2}(t_1,t_2)\, dt_1\, dt_2 \tag{10}$$

For $t_1$ and $t_2$ following the extreme value distribution type I, the range of possible correlations is limited on the negative side with $r_{min}$ = -0.8858. The required input correlation $r_{in}$ for the generation of correlated normally distributed variables in equation (5) can be approximated by a polynomial of 3rd order as follows:

$$r_{in} = \frac{r_{out}^3}{209.6} - \frac{r_{out}^2}{14.55} + \frac{r_{out}}{0.9397} \tag{11}$$

with $r_{out}$ – target correlation between $t_1$ and $t_2$

Figure 2 presents examples of joint-probability densities for varying correlations of two variables following the type I extreme value distribution. The contour lines are oriented at the major diagonal and clearly show the skewness to the right tails.
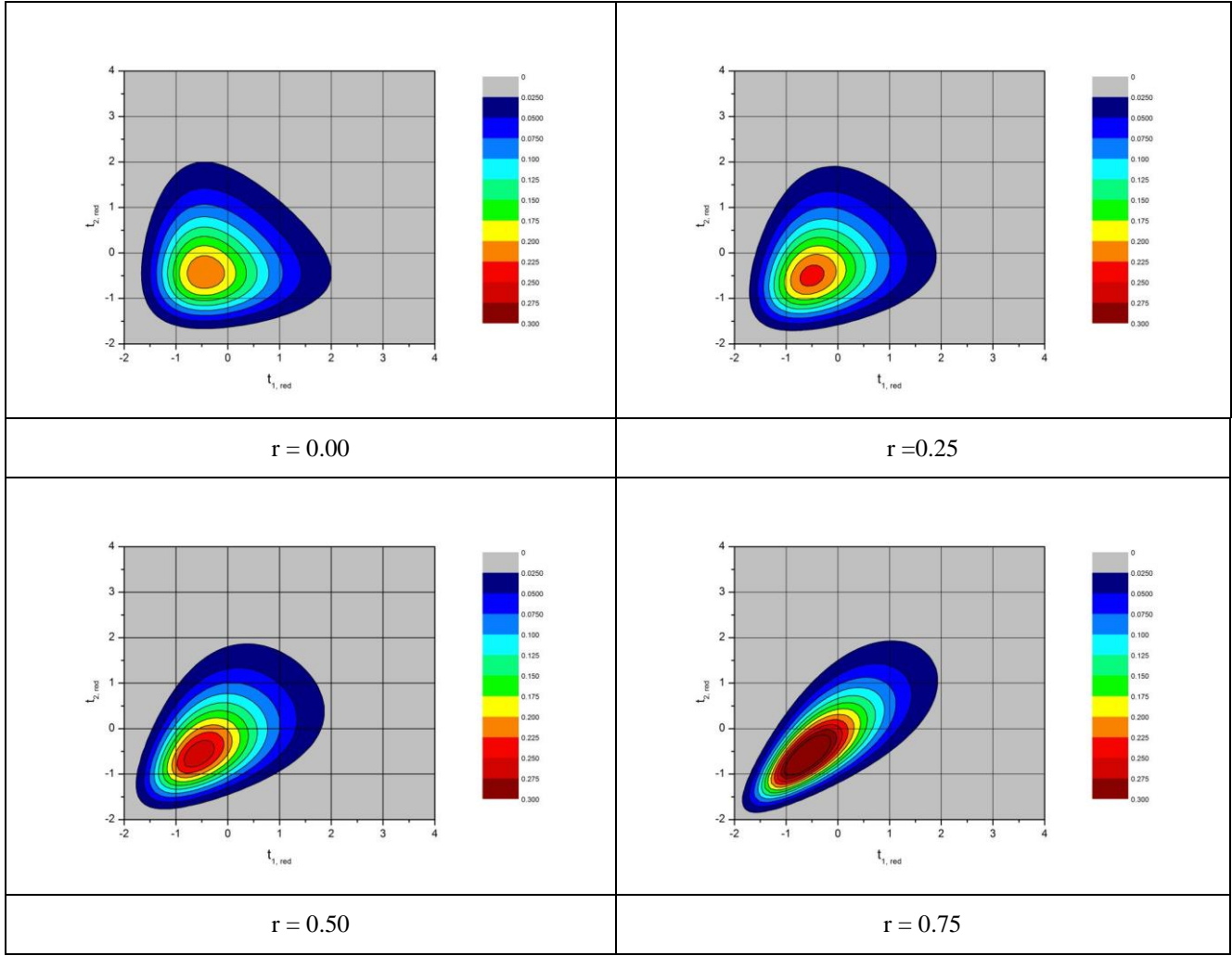
**Figure 2**: Examples of the joint-probability density of two correlated random variables for different correlations

For confined ensembles, the observed correlation may deviate from the true correlation. This is shown in figure 3 for two correlated variables following the extreme value distribution type I varying the ensemble size K and the true correlation r.

For the 225 analysed stations, the range of observed correlations is shown in figure 4. The majority of stations show large positive correlations; the average observed correlation is 0.82. It is reasonable to assume that the larger the correlation the higher will be the statistical stability of the density model.

The analysis of the statistical stability of the snow density model is more or less based on the results for Aachen. The correlation is set to 0.95, the threshold value for the snow loads is 0.05 kN/m², the scale is 0.15 kN/m2. The corresponding values for the snow heights are 0.01 m for the threshold value and 0.1 m for the scale. The average number of events is set to 1.5, the observation period is 56 years. The snow density model then becomes:

$$\rho_s = 152.91 - \frac{3.568 \cdot h_{ref}}{h_s} \ [kg/m^3] \qquad (12)$$

with $h_{ref} = 1$ m

Figure 5 shows the scatter in the identified parameters of the snow density model. The two parameters show a strong negative correlation, i.e. for larger values of $\rho_\infty$ the parameter $\Delta\rho$ decreases. Figure 6 presents the cumulative probability distributions of the estimated snow density parameters. For both parameters, the randomly estimated values follow approximately a normal distribution.

The parameter $\rho_\infty$ has a variation coefficient of about 7%, the 90% confidence interval leads to values from 137.4 kg/m³ to 164 kg/m³, which correspond to a relative range from 0.9 to 1.07 around the true value of 1. The variation coefficient of the randomly estimated parameter $\Delta\rho$ is about 25%. The 90% confidence interval ranges from 2.42 kg/m³ to 4.67 kg/m³. Normalisation with the true value of 3.57 kg/m³ leads to a relative range of 0.68 to 1.31. The statistical stability of $\Delta\rho$ is considerably smaller than the statistical stability of $\rho_\infty$.

**Figure 5**: Random scatter in the identified parameters of the snow density model assuming that the annual non-exceedance probabilities of the snow height and the snow load follow the extreme value distribution type I input values:

snow loads: $x_{th}$ = 0.05 kN/m², sc = 0.15 kN/m²; snow heights: $x_{th}$ = 0.01 m, sc = 0.1 m; correlation 0.95, average number of events 1.5 per year, 56 years observation period





**Figure 6**: Cumulative probability distributions of the randomly estimated parameters of the snow density model

**Figure 3**: Range of randomly estimated correlations for two variables following the extreme value distribution type I, r – true correlation value, K – number of observations
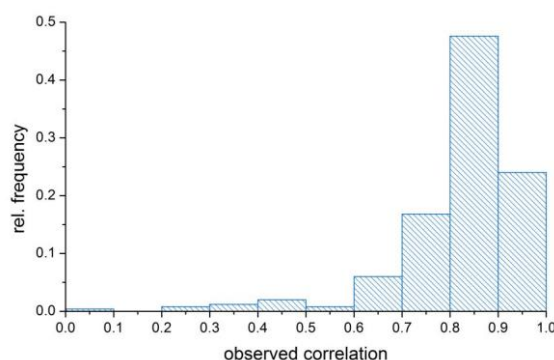


**Figure 4**: Range of observed correlations for snow load and snow height for 225 German stations

Although in the above example the correlation between the snow height and the snow load has been assumed to be very large, the statistical stability of the estimated parameters of the snow density model is not convincing. Therefore, the station-wise identified parameters do not form a sound basis for the development of a regional model if the uncertainties are not considered.

## 3. Consideration of statistical uncertainties in the input data

A more reasonable approach uses for each individual station the probability density of the randomness in the uncertain parameters as a weighting factor. This strategy is illustrated in figure 7 for a sample of four points which are assumed to follow a linear law. The typical least square fit minimizes the sum of the squared differences between the theoretical model $y = a \cdot x + b$ and the observed values. Within the new strategy, for each support point a different statistical uncertainty is assumed, here represented by normal distributions with different standard deviations. The optimum fit is obtained as the straight line leading to the maximum sum of the probability densities for the four entries:

$$\sum_i f_y(y_i) \overset{!}{=} \max \qquad (13)$$

In case of a linear approach and normal distributions for the uncertainties, the final equation becomes:

$$\sum_i \frac{1}{\sigma_i \cdot \sqrt{2\pi}} \exp\left(-0.5 \cdot \left(\frac{a \times x_i + b - m_i}{\sigma_i}\right)^2\right) \overset{!}{=} \max \qquad (14)$$

with $m_i$ and $\sigma_i$ - mean value and standard deviation for point i

Table 1 summarizes the chosen input values for the example. These input values and the classical least square fit solution are shown in figure 7. The probabilistic optimum considering the demand from equation (14) leads to $y = 0.8951 \cdot x + 0.2246$.

**Table 1**: Uncertainties of the example input values

| x | 1 | 2 | 3 | 4 |
|---|---|---|---|---|
| ymean | 1.1 | 2.1 | 2.9 | 3.8 |
| ysdev | 0.1 | 0.15 | 0.12 | 0.09 |
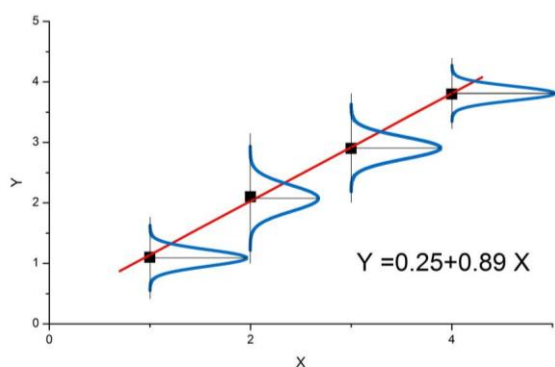


**Figure 7**: Illustrating example of considering uncertainties for the identification of the theoretical model

It is important to note, that the distribution of the uncertainties may differ from the normal distribution, e.g. the uncertainties may be skewed or limited. If no theoretical density is available, the uncertainties may be modelled based on simulations.

## 4. Example of application

For the development of a spatial model of the snow density it is vital to analyse the spatial correlation of the basic observation data for the snow heights and the snow loads. As example of application, the correlation structure of the snow loads in Mecklenburg-Vorpommern is studied. There are 14 stations with simultaneous observations of the water equivalent and the snow height, however with considerable different observation periods as shown in figure 8. The longest period covers 60 years, the shortest only 17 years. Therefore, uncertainties will vary considerably.

Basically, 14 stations lead to $(14^2-14)/2 = 91$ correlation coefficients. A minimum of 10 simultaneous observations is introduced for estimating the correlation for any pair of stations. Only observations are considered which occur at both stations in a time window of three days. These restrictions reduce the number of observed correlations to 64. As a first approach, the estimated correlations are plotted versus the distance between stations in figure 9.
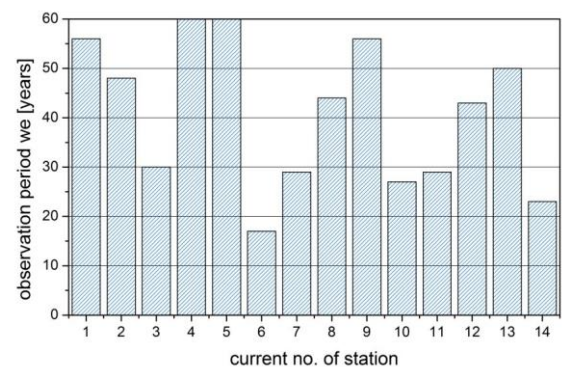


**Figure 8**: Variation of the observation period in years for 14 stations in Mecklenburg-Vorpommern
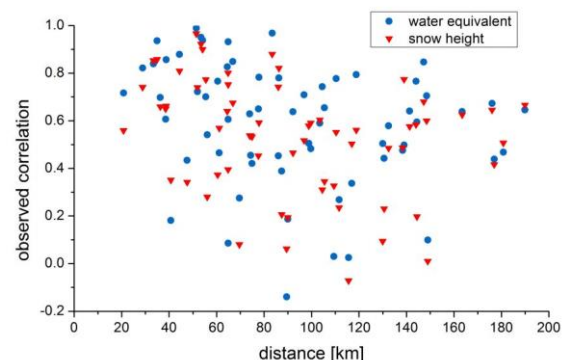


**Figure 9**: Observed correlations for 14 stations in Mecklenburg-Vorpommern for the water equivalent and the corresponding snow height

The latter strategy is also best if the uncertainties are to be considered. Figure 10 presents some examples of the probability densities of the uncertainties of the observed correlations for ensemble sizes of 10 and 40. The respective densities are obtained from simulations as follows:

- generate 10,000 runs of N pairs of correlated variables following the target distribution for a sufficient grid of different $r_{true}$ values and calculate the random correlation

- count for classes of observed correlations [$r_{obs} - \Delta r/2$, $r_{obs} + \Delta r/2$] the number of random correlations for each assumed $r_{true}$ value

- estimate the histogram of the uncertain correlation as the relative frequency which is the number of random correlations for each assumed $r_{true}$ value over the total sum of all random correlations for the specific class of observed correlations
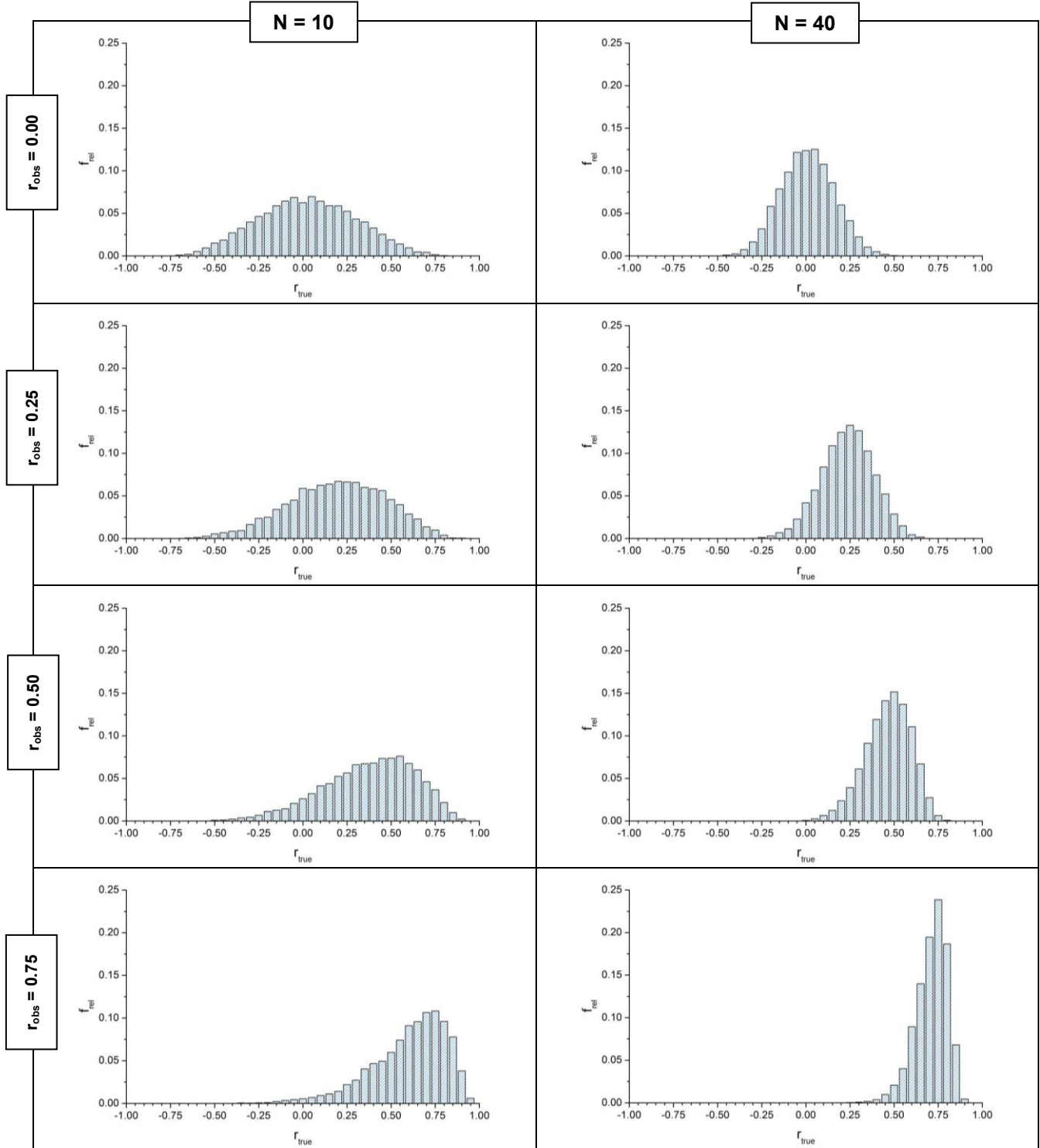


**Figure 10** : Probability densities of the true correlation for different observed random correlations for N = 10 and N = 40 observations, both random variables follow the extreme value distribution type I

Since the correlation is independent from the mean value and the standard deviation of the two variables, the simulation only needs to vary N and $r_{true}$.

Basically, the uncertainties become smaller for increasing ensemble size. For an observed correlation of zero, the uncertain correlation is symmetric. If the absolute value of the observed correlation increases, the probability density of the uncertain input correlation becomes skewed and the scatter reduces.

The observed correlations in figure 9 suggest as basic simple law an exponential decay depending only on the distance between two stations:

$$r(\Delta x) = \exp\left( -\frac{\Delta x}{L_{ref}} \right) \tag{15}$$

with $\Delta x$ – distance between two station
$L_{ref}$ – reference value

There are two options for the classical approach of a least-square fit. The first step is to take the logarithm of both sides leading to:

$$\ln\left(r(\Delta x)\right) = A \cdot \Delta x \tag{20}$$

The straight-forward approach uses the following sum:

$$A = \frac{\sum_i \Delta x_i^2}{\sum_i \ln\left(r(\Delta x_i)\right) \cdot \Delta x_i} \tag{21}$$

This approach gives larger weight to small observation values. Equal weight for all observations is obtained if the summands in equation (21) are weighted with the observation values:

$$A = \frac{\sum_i r(\Delta x_i) \cdot \Delta x_i^2}{\sum_i r(\Delta x_i) \cdot \ln\left(r(\Delta x_i)\right) \cdot \Delta x_i} \tag{22}$$

This approach, however, only works if all observed correlations are larger or equal zero. Some of the observed correlations in figure 9 do not meet this demand. If the number of negative correlation entries remains small, a less strict approach simply ignores these values. A consistent approach is obtained if the sum of the squared differences is minimized directly by varying the reference value $L_{ref}$:

$$\sum_i \left( r(\Delta x_i) - \exp\left( -\frac{\Delta x_i}{L_{ref}} \right) \right)^2 \overset{!}{=} \min \tag{23}$$

Negative correlations randomly occur even for clearly positive $r_{true}$ values if the ensemble is small. These observations do not violate the assumed model which only leads to positive values.

Figure 11 presents the final results in terms of the identified correlation model for the snow loads in Mecklenburg-Vorpommern. The best estimate of the reference length is 213.6 km. This result is obtained iteratively by solving equation (13) for 44 input values of $\Delta x$ and 44 corresponding probability distributions of random correlations.
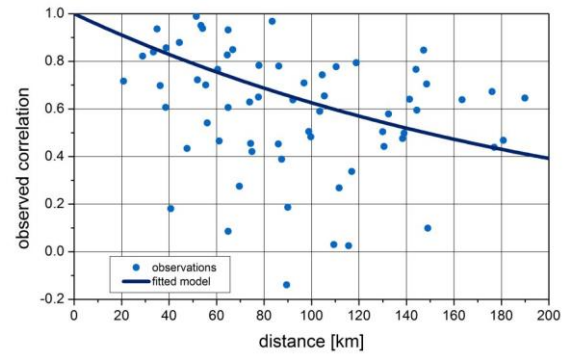


**Figure 11**: Identified model for the spatial correlation of the snow loads in Mecklenburg-Vorpommern considering uncertainties in the observed correlations

## 5. Summary and conclusions

The straight-forward approach to the specification of the design value of the ground snow loads is based on measurements of the water equivalent. These observations are available in Germany for about 550 stations. About 5500 stations measure only the snow height. For codification of the design snow load, usually maps are developed, i.e. a spatial model is required which interpolates the obtained station-wise values. Geostatistical tools allow interpolations considering further influence parameters as e.g. the altitude. The interpolation in a specific region obviously can be improved if a snow density model is available. Then, also the stations measuring only the snow height can be used for the interpolation as well, i.e. the density of the input grid is increased considerably.

A naïve approach simply uses the obtained station-wise data. This strategy does not allow considering different uncertainties in the input values from station to station. A new strategy is developed which considers the uncertainties by using the station-wise probability densities as weighting coefficient for the fitting of the theoretical model. The uncertainties can be analysed based on simulations.

## Acknowledgement

# References

1. B. Czwikla, M. Kasperski: Specification of the design value of the ground snow load considering measurements of the snow height – part 1: single stations, ICSE 2016, Nantes
2. M.C. Cario, B.L. Nelson: Modelling and Generating Random Vectors with Arbitrary Marginal Distributions and Correlation Matrix, 1997, http://citeseerx.ist.psu.edu/viewdoc/summary?doi=10.1.1.48.281
3. S.T. Lee, J.L. Hammond: Generation of pseudo-random numbers with specified univariate distributions and correlation coefficients. IEEE Transactions on Systems, Man and Cybernetics, 557-561, 1975

# Collapse process of pipe-framed greenhouses under snow loading

Kazuya Takahashi[1], Yasushi Uematsu[1,a]

[1]Department of Architecture and Building Science, Tohoku University, Sendai 980-8579, Japan

**Abstract.** The present paper investigates the collapse process of pipe-framed greenhouses under snow loading based on a non-linear finite element anaysis, in which not only geometrical but also material non-linearity are taken into account. Both even and uneven distributions of snow load are considered. The non-linear behavior of the frame up to the collapse is numerically analysed. Buckling analysis of the frame is also carried out. The objective of the present paper is to establish more reasonable snow resistant design of pipe-framed greenhouses commonly used in the agricultural and horticultural industries in Japan. First, two-dimensional analysis is carried out with a basic model without reinforcement in order to understand the fundamental behavior of the frame up to the collapse, when a part of the frame touches the ground. Then, some measures of reinforcement to improve the snow resistance of the frame are discussed. The effect of reinforcement on the maximum load capacity is made clear. It is found that some types of reinforcement are not effective to the uneven load distribution, although they are effective to the even distribution. Finally, a three-dimensional analysis is carried out with a three dimensional frame model. The structure consists of arch pipes arranged in parallel and connected with each other by horizontal tie-beams (circular pipes). Discussion is made of the effect of three-dimensionality of the frame on the maximum load capacity.

## 1 Introduction

Pipe-framed greenhouses (Figure 1(a)), widely used in the agricultural and horticultural industries in Japan, are generally designed to a lower level of structural safety than conventional buildings, because of the need to minimize capital costs, the demand for a higher level of light transmission and so on. Being inherently light and flexible, they are vulnerable to snow loading and often experience damage due to heavy snowfall (see Figure 1(b), provided by Dr. Moriyama, National Institute for Rural Engineering, Japan). Indeed, many pipe-framed greenhouses were collapsed by heavy snowfall in Kanto District, Japan, during February 14 to 16 of 2014. Depression of arch pipes is the most popular type of collapse [1, 2].



(a) Example      (b) Collapse due to heavy snow
**Figure 1.** Pipe-framed greenhouse.

In Japan, pipe-framed greenhouses are usually designed based on allowable stress or deformation limit following the structural guidelines [3, 4]. In the allowable deformation design, it is assumed that the structure will not lose the resistance because of the restraint effect given by the surrounding members, even if the stresses of some members exceed the elastic range. However, such an assumption has not been verified yet. Furthermore, it is not clear how much safety margin they have against the collapse, when they are designed based on the allowable stress.

The present paper investigates the collapse process of pipe-framed greenhouses under snow loading based on a non-linear finite element analysis. In the analysis, both the geometrical and the material non-linearity are considered because of large deformation and plastic range of stress. Uneven snow accumulation on the roof may be induced by wind (snow drift). Furthermore, snow sliding may occur on the south roof due to solar radiation. Therefore, both even and uneven distributions of snow load are considered.

First, two-dimensional analysis is carried out in order to understand the fundamental characteristics of the collapse process of the basic frame. Then, the effect of reinforcement on the maximum load capacity of the frame is discussed; six types of reinforcements are investigated.

It should be mentioned that the present paper is an extended version of our previous paper [6], focusing on the snow reistance. Furthermore, discussion is made of the effect of reinforcement on the strength of the frame.

## 2 Finite element analysis

### 2.1. Analytical model

The analytical model is schematically illustrated in Figure 2. The span $S$, height $H$, eaves height $h$, and length $L$ are 5.4 m, 3.0 m, 1.55 m and 14.4 m, respectively. The arch pipes are carbon steel tubes for general structural purpose (JIS G3445 STKM11A) with Young's modulus of $E =$
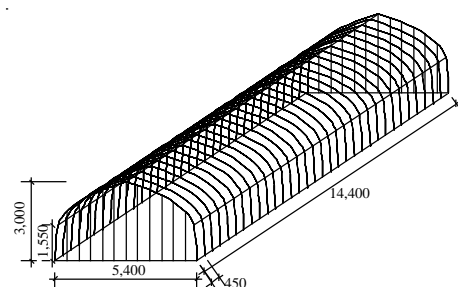


**Figure 2.** Analytical Model (Perspective) : unit mm.

---

[a] Corresponding author: yu@archi.tohoku.ac.jp

$2.05 \times 10^5$ N/mm$^2$, Poisson's ratio of $\nu = 0.33$, and yield stress of $\sigma_y = 175$ N/mm$^2$. The external diameter $\phi$ and thickness $t$ of the arch pipes are 22.2 mm and 1.2 mm, respectively. The arch pipes are arranged in parallel with a spacing of $d = 0.45$ m and connected with each other by horizontal tie-beams (circular pipes with the same dimension as that of the arch pipes). The connection of the arch pipes and tie-beams is assumed 'rigid' or 'hinged' for the purpose of simplicity; the actual condition is complicated depending on the construction method. The column base is assumed to be fixed to the ground.

The resistance of pipe-framed greenhouses against snow load can be improved by adding members to the frame. Figure 3 shows a schematic illustration of the reinforcements made on the frame. The members for reinforcement are the same as that of the arch pipes. The boundary condition of these added members are assumed 'rigid' or 'hinged'; the practical condition is thought to be in-between. In Case 5, temporary vertical supports are installed at intervals of 3.15 m ($= 7d$) when heavy snowfall is forecast. Diagonal arches are installed in Case 6, as shown in Figure 4. Note that this figure shows the development view of the frame. In Cases 1 to 4, both two-dimensional and three-dimensional analyses are made, and the effect of three-dimensionality on the maximum load capacity is discussed. In Cases 5 and 6, on the other hand, three-dimensional analysis is made, because the structures are basically three dimensional.



(a) Case 1    (b) Case 2    (c) Case 3

(d) Case 4    (e) Case 5
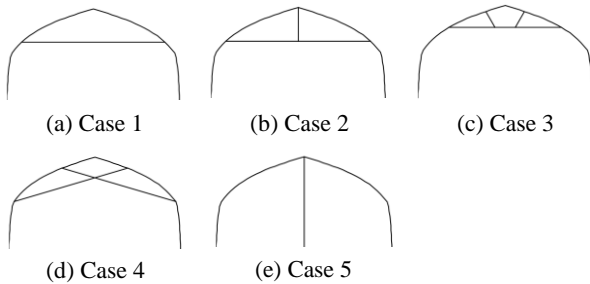
**Figure 3.** Reinforcement methods (Cases 1 to 5).
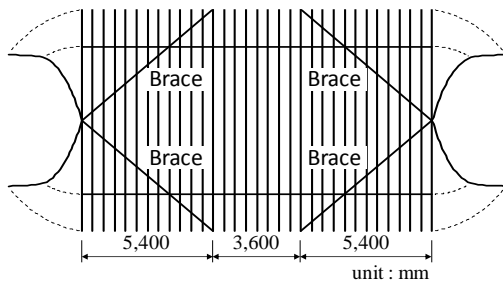


**Figure 4.** Reinforcement method (Case 6).
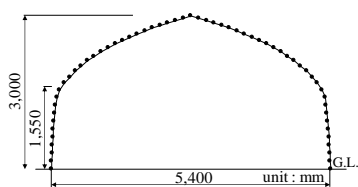


**Figure 5.** Finite element model of the arch pipe.

## 2.2. Method of analysis

A nonlinear finite element analysis is made by using a commercial software 'ABAQUS 6.13'. The arch pipe is divided into 58 beam elements (see Figure 5). The relationship between stress ($\sigma$) and strain ($\varepsilon$) of the material is assumed to be represented by a bi-linear model as shown in Figure 6, according to Ogawa et al [5]. The slope of the second polygonal line is approximately 1/420 of that of the first polygonal line. In the analysis, both the geometric and the material non-linearity are considered. The arc-length method is used, in which the arc length is controlled so that the equilibrium path of the structure up to the collapse can be obtained.

Buckling may occur before reaching the maximum load. Therefore, buckling analysis is also carried out by solving an eigenvalue problem. Buckling load and mode are given by the eigenvalue and eigenvector, respectively.
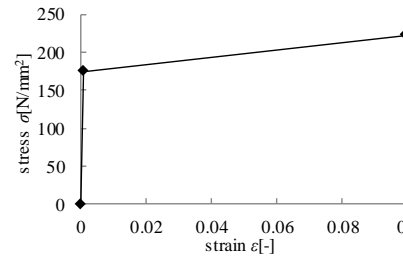


**Figure 6.** Stress-strain relationship of the material.

## 2.3. Load distribution

As mentioned above, uneven snow load distribution may occur due to the effects of wind and snow sliding. Therefore, not only even but also uneven distributions of snow load are considered. The snow loads per unit area, $S_W$ and $S_L$, on the windward and leeward roofs are assumed constant over each area, but the ratio of $S_W$ and $S_L$ is changed so that the total load is kept constant. The snow load per unit area is represented by the product of average snow density $\rho_s$ (assumed 9.8 N/m$^2 \cdot$ cm according to Ref. [3]) and snow depth $d_s$. Figure 7 shows three typical distributions of snow loads; i.e. $S_W : S_L = 1 : 1$ (Type 1), 0.5 : 1.5 (Type 2) and 0 : 2 (Type 3). The total snow load on the structure is the same for all distribution types. The snow loads are applied to the nodes as concentrated loads evaluated by considering the tributary area of each node. For the purpose of simplicity, the loads are assumed to act in the vertical direction despite the deformation of the frame. This assumption is not practical when the deformation becomes large, resulting in the redistribution of snow accumulation due to sliding and others.



(a) Type 1    (b) Type 2    (c) Type 3
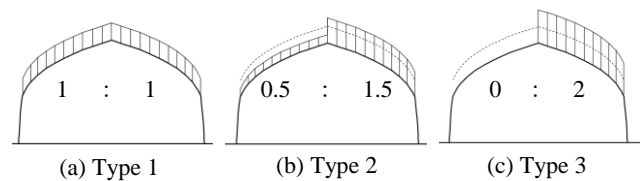
**Figure 7.** Typical load distributions.

# 3 Results on 2-D frames

## 3.1. Collapse process of the basic frame

First, the fundamental characteristics of collapse process of the basic two-dimensional frame with no reinforcement are investigated. Figures 8 shows the transition of the equilibrium configuration of the frame under uniform snow load (Type 1) when the snow load is increased up to
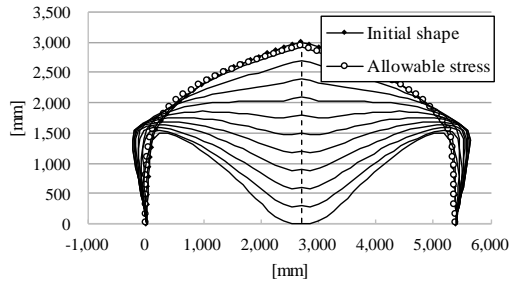


**Figure 8.** Collapse process for even load distribution (Type 1, $S_W : S_L$ =1 : 1).
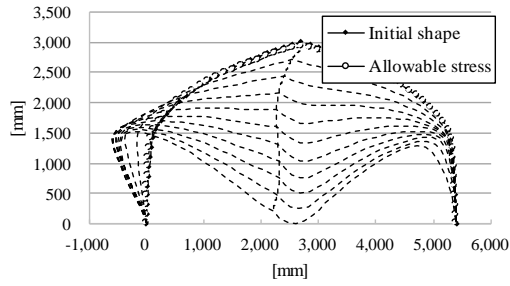


**Figure 9.** Collapse process for even load distribution with consideration of initial imperfection (Type 1, $S_W : S_L$ =1 : 1).
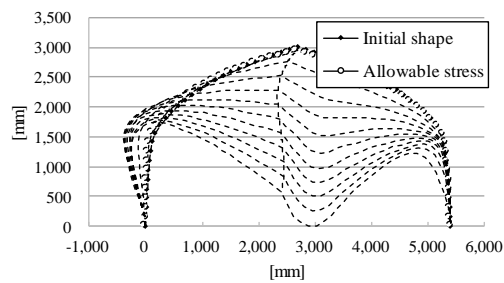


**Figure 10.** Collapse process for uneven load distribution (Type 2, $S_W : S_L = 0.5 : 1.5$).
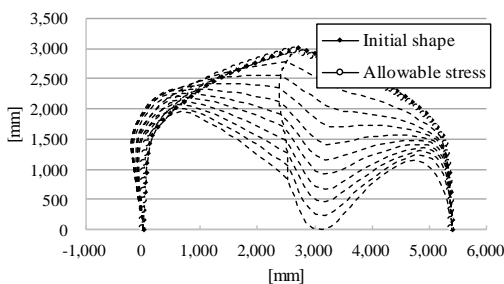


**Figure 11.** Collapse process for uneven load distribution (Type 3, $S_W : S_L = 0 : 2$).

the maximum value, beyond which the structure collapses. The figure with smal open circles represents the deformation of the frame when the maximum stress induced in the frame attains the allowable stress (yield stress). The deformation is relatively small. The dashed line shows the trace of the ridge. In this case, the deformation is always symmetric with respect to the centerline. However, when a small geometric imperfection similar to the buckling mode is introduced, the deflection becomes asymmetric with respect to the centerline, as shown in Figure 9. Note that the maximum imperfection is as small as $0.01\phi$, with $\phi$ being the external diameter of the arch pipes. Similar collapse process is observed for uneven snow load, as shown in Figures 10 and 11. These results imply that the collapse pattern may become asymmetric with respect to the centerline in most cases. However, almost symmetric patterns are often observed in the damage investigations. This discrepancy may be related to the restraint effect of horizontal members connecting the arch pipes and the gable walls (a kind of 3D effect).

## 3.2. Maximum load capacity of the basic frame

Because the snow density $\rho_s$ is assumed constant despite the snow depth $d_s$, the snow load $S$ per unit area is proportional to $d_s$. Therefore, the snow load is represented by a reference snow depth $d_{ref}$ in the present paper. That is, the frame is subjected to uniform snow load of $\rho_s \times d_{ref}$ in Type 1. On the other hand, the windward and leeward halves are respectively loaded by $0.5\rho_s \times d_{ref}$ and $1.5\rho_s \times d_{ref}$ in Type 2. Only the leeward half is loaded by $2\rho_s \times d_{ref}$ in Type 3 (see Fig. 7).

Table 1 shows the snow depths, $d_{ref,a}$ and $d_{ref,u}$, providing the allowable stress (yield stress) and the ultimate strength, respectively. The flowing features can be observed from the results.

1) The $d_{ref,u}/ d_{ref,a}$ ratio for the frames subjected to uniform snow load (Type 1) is relatively small compared with those for uneven distributions (Types 2 and 3). This feature implies that the safety margin of this frame up to the collapse is not so large when the frame is designed based on the yield stress as the allowable stress. It may be more reasonable to design the pipe-framed greenhouses based on the ultimate strength.

2) The value of $d_{ref,a}$ for uniform snow load is decreased by a small initial imperfection. This is due to the effect of additional bending moment induced by the initial imperfection. Because some initial imperfection is unavoidable in practice, the snow resistance of the structures should be evaluated by considering such a feature. On the other hand, the $d_{ref,u}$ value seems less sensitive to the initial imperfection. This feature implies again that the design based on the ultimate strength is more reasonable.

3) The unevenness in load distribution affects the $d_{ref,a}$ value significantly. Such an uneven distribution of snow load induces larger bending moments, resulting in a decrease in $d_{ref,a}$. However, the effect on $d_{ref,u}$ is relatively small. It is interesting to note that the $d_{ref,u}/ d_{ref,a}$ ratio is almost the same, approximately 1.5, both for Types 2 and 3.

**Table 1.** Snow depth providing the allowable stress and the ultimate strength.
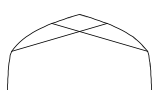
| Load distribution | Snow depth (cm) | | $d_{ref,u}/d_{ref,a}$ |
|---|---|---|---|
| | $d_{ref,a}$ | $d_{ref,u}$ | |
| Type 1 (No initial imperfection) | 14.71 | 19.82 | 1.35 |
| Type 1 (Initial imperfection) | 14.66 | 19.74 | 1.33 |
| Type 2 (No initial imperfection) | 11.91 | 18.11 | 1.52 |
| Type 3 (No initial imperfection) | 10.13 | 14.97 | 1.48 |

### 3.2. Effect of reinforcement

As mentioned above, the boundary condition of the added members for reinforcement is assumed 'rigid' or 'hinged'. It was found that the bound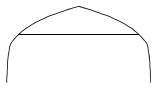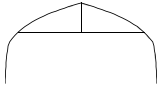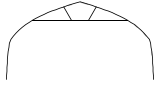ary condition does not affect the results significantly. This is because the members are relatively thin and subjected to tension in most cases. Therefore, the results for 'rigid' will be shown hereafter.

Table 2 summarizes the results of $d_{ref,a}$ and $d_{ref,u}$ for all reinforcement methods and load distributions obtained from the two-dimensional analysis. It is clear that the snow resistance of pipe-framed greenhouses can be improved by adding members to the frame. The improvement is fairly significant in Cases 1 and 2, particularly when the snow load is uniform, due to the effect of the horizontal member that is subjected to tension. The effect becomes smaller with an increase in the unevenness of load distribution. The horizontal member may interference with the work inside the greenhouse. Then, the horizontal member is moved upward in Case 3. It is found that the improvement

**Table 2.** Effect of reinforcement on the ultimate snow depth.

| Reinforcement | Load type ($S_W : S_L$) | Snow depth (cm) | | $d_{ref,u}/d_{ref,a}$ |
|---|---|---|---|---|
| | | $d_{ref,a}$ | $d_{ref,u}$ | |
| Case 1 | 1 (1.0:1.0) | 47.10 | 58.73 | 1.25 |
| | 2 (0.5:1.5) | 29.53 | 35.40 | 1.20 |
| | 3 (0.0:2.0) | 19.41 | 24.07 | 1.24 |
| Case 2 | 1 (1.0:1.0) | 56.46 | 65.10 | 1.16 |
| | 2 (0.5:1.5) | 34.33 | 41.18 | 1.20 |
| | 3 (0.0:2.0) | 21.41 | 29.05 | 1.36 |
| Case 3 | 1 (1.0:1.0) | 28.52 | 33.67 | 1.18 |
| | 2 (0.5:1.5) | 20.95 | 24.03 | 1.15 |
| | 3 (0.0:2.0) | 16.08 | 18.93 | 1.18 |
| Case 4 | 1 (1/0:1.0) | 28.12 | 35.77 | 1.27 |
| | 2 (0.5:1.5) | 28.67 | 35.06 | 1.22 |
| | 3 (0.0:2.0) | 27.77 | 34.21 | 1.23 |

on the strength is limited compared with that in Cases 1 and 2. Case 4 seems to be the best among the four cases tested from the viewpoints of both strength and workability. This structure provides similar maximum load capacity for all load distributions. Even in this case, the $d_{ref,u}/d_{ref,a}$ ratio is not so large, approximately 1.2.

## 4 Results on 3-D frames

In the three-dimensional model, the arch pipes are arranged in parallel with a spacing of $d = 0.45$ m and connected with each other by horizontal tie-beams at the ridge and eaves (see Figure 2). As mentioned above, two kinds of joint conditions are considered; i.e. 'rigid' and 'hinged'. Buckling analysis is also carried out.

The results for the two joint conditions are summarized in Tables 3 and 4. The results for the basic frame with no reinforcement are almost the same as those obtained from the two-dimensional analysis despite the boundary condition. When the joint is 'rigid', the critical loads of buckling, not shown in the table, are generally much larger than the maximum loads obtained from the non-linear analysis. When the joint is 'hinged', on the other hand, the buckling load becomes smaller than the maximum load in some cases. The snow depth corresponding to the buckling is represented by $d_{ref,b}$ in the table. Figure 12 shows the buckling mode in Case 4. The buckling mode is dominated by the displacements in the longitudinal direction with almost no in-plane deformation of the frame. This is due to low horizontal stiffness of the structure. Similar failure modes are often observed in the snow-induced damage to greenhouses, as shown in Figure 13. This greenhouse is not pipe-framed greenhouse but a reinforced pipe-framed greenhouse, in which the frame is constructed of square steel tubes (about 50 mm × 500 mm) and the roof is constructed of arch pipes. Because the horizontal stiffness of this kind of structure is rather low, the structure tends to be collapsed by snow load, as shown in Figure 13.



(a) Perspective



(b) Side view
**Figure 12.** Buckling mode (Case 4).



**Figure 13.** Collapse of a reinforced pipe-framed greenhouse due to snow load.

**Table 3.** Snow resistance of 3D frames: the connection of arch pipes and tie-beams is assumed 'rigid'.
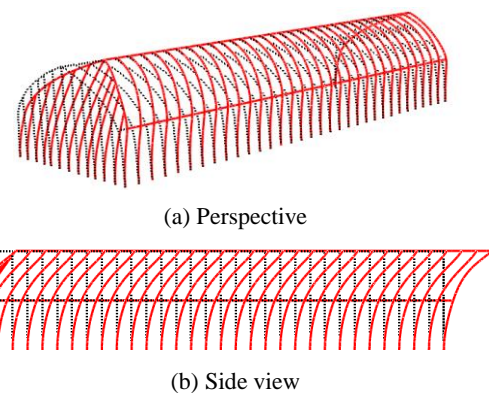
| Frame | Load type ($S_W$ : $S_L$) | Snow depth (cm) $d_{ref,a}$ | Snow depth (cm) $d_{ref,u}$ | $d_{ref,u}$/ $d_{ref,a}$ |
|---|---|---|---|---|
| Basic | 1 (1.0:1.0) | 14.56 | 20.44 | 1.40 |
|  | 2 (0.5:1.5) | 11.81 | 18.85 | 1.60 |
|  | 3 (0.0:2.0) | 10.03 | 15.40 | 1.54 |
| Case 1 | 1 (1.0:1.0) | 45.32 | 58.89 | 1.30 |
|  | 2 (0.5:1.5) | 29.52 | 35.73 | 1.21 |
|  | 3 (0.0:2.0) | 19.36 | 24.24 | 1.25 |
| Case 2 | 1 (1.0:1.0) | 55.15 | 65.45 | 1.19 |
|  | 2 (0.5:1.5) | 33.30 | 41.46 | 1.25 |
|  | 3 (0.0:2.0) | 22.53 | 29.27 | 1.30 |
| Case 3 | 1 (1.0:1.0) | 28.14 | 33.79 | 1.20 |
|  | 2 (0.5:1.5) | 20.88 | 24.47 | 1.17 |
|  | 3 (0.0:2.0) | 14.84 | 19.39 | 1.31 |
| Case 4 | 1 (1.0:1.0) | 14.94 | 36.06 | 2.41 |
|  | 2 (0.5:1.5) | 12.20 | 35.55 | 2.91 |
|  | 3 (0.0:2.0) | 10.43 | 34.92 | 3.35 |
| Case 5 | 1 (1.0:1.0) | 12.52 | 39.65 | 3.17 |
|  | 2 (0.5:1.5) | 12.25 | 28.44 | 2.32 |
|  | 3 (0.0:2.0) | 12.12 | 19.81 | 1.63 |
| Case 6 | 1 (1.0:1.0) | 15.19 | 22.08 | 1.45 |
|  | 2 (0.5:1.5) | 13.24 | 20.05 | 1.51 |
|  | 3 (0.0:2.0) | 11.35 | 16.33 | 1.44 |

**Table 4.** Snow resistance of 3D frames: the connection of arch pipes and tie-beams is assumed 'hinged'.

| Frame | Load type ($S_W$ : $S_L$) | Snow depth (cm) $d_{ref,a}$ | Snow depth (cm) $d_{ref,u}$ | Snow depth (cm) $d_{ref,b}$ | $d_{ref,u}$/ $d_{ref,a}$ |
|---|---|---|---|---|---|
| Basic | 1 (1.0:1.0) | 13.99 | 19.61 | 28.41 | 1.40 |
|  | 2 (0.5:1.5) | 11.17 | 17.82 | 27.50 | 1.60 |
|  | 3 (0.0:2.0) | 9.40 | 14.82 | 25.39 | 1.58 |
| Case 1 | 1 (1.0:1.0) | 41.83 | 51.45 | 26.24 | * |
|  | 2 (0.5:1.5) | 21.70 | 25.07 | 25.57 | 1.16 |
|  | 3 (0.0:2.0) | 13.96 | 17.07 | 23.93 | 1.22 |
| Case 2 | 1 (1.0:1.0) | 42.19 | 50.72 | 26.23 | * |
|  | 2 (0.5:1.5) | 21.66 | 25.07 | 25.56 | 1.16 |
|  | 3 (0.0:2.0) | 13.95 | 17.08 | 23.92 | 1.22 |
| Case 3 | 1 (1.0:1.0) | 23.56 | 30.82 | 27.00 | ** |
|  | 2 (0.5:1.5) | 17.60 | 22.91 | 25.99 | 1.30 |
|  | 3 (0.0:2.0) | 13.68 | 17.83 | 23.74 | 1.30 |
| Case 4 | 1 (1.0:1.0) | 14.34 | 35.26 | 26.65 | ** |
|  | 2 (0.5:1.5) | 11.57 | 34.81 | 25.25 | ** |
|  | 3 (0.0:2.0) | 9.79 | 34.08 | 22.65 | ** |
| Case 5 | 1 (1.0:1.0) | 10.44 | 26.56 | 29.06 | 2.54 |
|  | 2 (0.5:1.5) | 10.25 | 22.90 | 28.36 | 2.23 |
|  | 3 (0.0:2.0) | 10.16 | 17.59 | 26.55 | 1.73 |
| Case 6 | 1 (1.0:1.0) | 13.71 | 19.41 | 43.21 | 1.42 |
|  | 2 (0.5:1.5) | 11.34 | 17.75 | 43.20 | 1.57 |
|  | 3 (0.0:2.0) | 9.42 | 14.67 | 43.08 | 1.56 |

\* $d_{ref,b}$ is the lowest.
\*\* $d_{ref,b}$ is larger than $d_{ref,a}$ but smaller than $d_{ref,u}$.

Because the diagonal arches introduced in Case 6 increases the horizontal stiffness of the frame with 'hinged' joints, the value of $d_{ref,b}$ increases significantly.

The following features can be observed from Tables 1 to 3:

1) The values of $d_{ref,a}$ and $d_{ref,u}$ for 'rigid' connection are generally larger than those for 'hinged' connection. This is related to the stiffening effect of tie-beams on the arch pipes in the case of 'rigid' connection.

2) In the case of 'hinged' connection, the value of $d_{ref,b}$ is generally small except for Case 6 where the horizontal stiffness of the frame is increased by the diagonal braces. The value of $d_{ref,b}$ is comparative to or smaller than $d_{ref,u}$ in many cases.

3) The value of $d_{ref,u}$ for the 'rigid' connection is generally larger than that for the 2D frame. However, the difference is only a little, which indicates that the 3D effect on the maximum load capacity is relatively small.

4) The value of $d_{ref,a}$ for the 3D frame is not necessarily larger than that for the corresponding 2D frame. This feature is contrary to our expectation that the constraint of tie-beams would decrease the stress induced in the members and increase the load capacity. Careful investigation of the results on the stresses induced in the members of the 3D model indicates that the location of $d_{ref,a}$ is different from that for the 2D model. For example, in Case 4, $d_{ref,a}$ occurs at the top of the arch pipe in the 2D model, while at the column base of an arch pipe in the 3D model. In Case 5, $d_{ref,a}$ occurs in the tie-beam at the top of the arch pipes in the 3D model. The 3D effect induces additional stresses in the members and the maximum stress is induced at some point different from that in the 2D frame. In such a case, 2D analysis is not appropriate, because it will underestimate the snow resistance of the structure, when designing it based on the allowable stress.

5) The value of $d_{ref,u}$ is less sensitive to the analytical model. Therefore, it is more desirable to design the structure based on the maximum load capacity not on the allowable stress.

# 5 Concluding remarks

First, the two dimensional analysis shows the fundamental characteristics of the collapse process of pipe-framed greenhouses under snow loading. Both initial imperfection and uneven load distribution decrease the snow depth providing the allowable stress (yield stress) in the member, significantly. Therefore, the snow resistance of the structure should be evaluated by considering these factors, when the structural design is carried out based on the allowable stress. On the other hand, the maximum load capacity of the frame seems less sensitive to these factors.

Then, the effects of various reinforcements on the snow loads providing the allowable stress and the maximum load were investigated. The boundary condition of the added members minutely affects the load capacity of the frame. Generally speaking, the reinforcements tested in the present paper increases the snow resistance of

the structures significantly. However, some of them are not so effective for uneven load distribution.

Finally, three-dimensional frames with and without reinforcement were analysed. The structure consists of arch pipes arranged in parallel and connected with each other by horizontal tie-beams. When the horizontal stiffness of the frame is low, the buckling provides the critical condition. However, in the practical condition, where the connection between the arch pipe and tie beam is regarded as 'rigid', the buckling load is much larger than the maximum load obtained from the non-linear analysis. The maximum load is not so sensitive to the analytical model that the snow resistance of the frames can be evaluated based on the maximum load not on the allowable stress.

# 6 Acknowledgement

# References

1.  Y. Uematsu, Damage to structures due to heavy snow during February 14 to 16, 2014 – Mainly on the damage to carports and greenhouses in Gunma Prefecture -, Tohoku Journal of Disaster Science, Vol.51, pp.165-170 (2015). (in Japanese)
2.  M. Hideki, S. Inoue, I. Kamiishi, Damage to Greenhouses by Heavy Snow in Feb. 2014, JSSI & JSSE Joint Conference – 2014/Hachinohe (2014). (in Japanese)
3.  Japan Greenhouse Horticulture Association, Horticultural facility safety structural criteria, (1997). (in Japanese)
4.  Japan Greenhouse Horticulture Association, Underground push-fit pipe-framed greenhouse safety structure guideline, (1988). (in Japanese)
5.  H. Ogawa, I. Tsuge, Y. Sato, S. Hoshiba, S. Yamashita, Experimental analysis on strength of pipe-houses with ground anchoring (1) – Actual size experiment -, The Journal of the Society of Agricultural Structures, Japan, Vol. 9, No.3, pp.29-38 (1989). (in Japanese)
6.  K. Takahashi, Y. Uematsu, Collapse processes of pipe-framed greenhouses under wind and snow loads, The Journal of the Society of Agricultural Structures, Japan, Vol.47, No.1, pp. 108 (2016). (in Japanese)

# Study on evaluation of roof snow load considering rain-on-snow surcharge: Statistical evaluation of snow cover and precipitation in winter in Japan

Masaya Otsuki[1,a], Toru Takahashi[2], Yoshihiko Saito[1], Takuya Tsutsumi[3] and Kikitsu Hitomitsu[4]

[1]Yukiken Snow Eaters Co., Ltd., 5-6, Nishi-7, Minami-2, Chuo-ku, Sapporo 060-0062, Japan
[2]Department of Architecture, Chiba University, 1-33 Yayoicho, Inage-ku, Chiba 263-8522, Japan
[3]Northern Regional Building Research Institute, Higashi-1-3-1-20, Midorigaoka, Asahikawa 078-8801, Japan
[4]National Institute for Land and Infrastructure Management, Tachihara-1, Tsukuba 305-0802, Japan

**Abstract.** To examine regions for which the roof snow load, influenced by rain after snow, has to be estimated, a statistical evaluation of snow cover and rainfall during the winter period in Japan was conducted to examine the calculation method. In a comparison of daily and two-day rainfall, the latter was slightly greater without substantial difference in the distribution. The two-day rainfall is considered to be an appropriate data for considering the rain load. Investigation of areal distribution of rainfall revealed that the rainfall for an entire winter was greater in regions that received large amounts of rainfall in summer. The extreme values of rainfall on snow cover were found to be higher in regions with a long snow-cover period, ranging from Hokuriku to Tohoku and southern Hokkaido as well as the Kanto-Koshin region. The load conversion value of the rainfall is often relatively higher in general areas with snow cover depth of less than 1 m, such as the Pacific Ocean side of Tohoku and the Kanto-Koshin region, compared with their roof snow load. In such regions, there is a concern that the rain-on-snow surcharge, when added to the roof snow load, will exceed the design load.

## 1 Introduction

From February 14–16, 2014, the Kanto region of Japan was hit by heavy snow caused by a rapidly developing low-pressure system. A large number of buildings were damaged. The roof snow-load increase owing to a rain-on-snow surcharge was indicated as the main cause of the damage. Figure 1 shows the weather time series observed at Tokyo District Meteorological Observatory in one of the regions that sustained damage. The snow started on February 14, accumulated 27 cm, and then turned to rain after 2:00 a.m. on February 15. The snowfall was approximately 42 mm, and the rainfall was 54 mm, for a total precipitation of 96 mm. Since the design load of the region is 0.6 kN/m$^2$, a roof snow load of approximately 0.42 kN/m$^2$ was within the permissible range. Subsequently, as shown in the time-series graph, a rainfall of approximately 20 mm (0.2 kN/m$^2$) led to the collapse of buildings. It is suspected that the snow on the roofs absorbed the rain and that a load of 0.62 kN/m$^2$, exceeding the design load, was applied to the roof and led to the collapse. (Since this precipitation does not consider the capture rate owing to the wind velocity, the actual precipitation may have been greater).
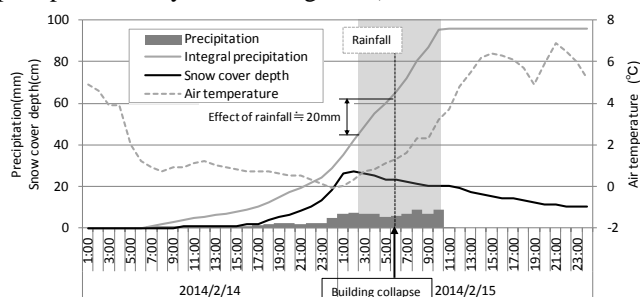


**Figure 1.** Weather time series of Tokyo at time of damage owing to rainfall increasing the load (February 15, 2014).

In the United States, the rain-on-snow surcharge of a roof snow load is specified in ASCE7 [1]. In regions where the roof snow load is 0.96 kN/m$^2$ or less, all roofs with a slope angle of less than W/15.2º are required to allow for a surcharge of 0.24 kN/m$^2$. [W refers to the roof span (m).] In Canada, NBC sets the roof snow load $S_S$ and rain load $S_R$ for each city, and the sum of these is to be used [2]. Values for both countries are based on a 50-year return period, but they can be considered as precautionary values if snowfall and rainfall are perceived not as individual events but as interdependent events. On the other hand, there has not been any clear regulation in Japan. This study examines the effect of the rain-on-snow surcharge on the roof snow load, and analyzes the characteristics of snow cover and rainfall in winter using the daily snowfall data. The goal is to establish a calculation method for the surcharge load.

## 2 Data used and methods of analysis

Precipitation, air temperature, and snow depth data measured by meteorological stations of the Japan Meteorological Agency were used for analysis. The meteorological stations include manned meteorological offices (142 locations) and 1500 unmanned AMeDAS (195 of which measures snow depth) (Figure 2). All data from the beginning of the observation period until 2014 (from December to March only) were used. Okinawa was excluded because snow does not fall in this region.

Rainfall and snowfall were distinguished according to the daily average temperature based on the precipitation data to extract the daily precipitation data of the days when rain was determined to have fallen. Winter daily rainfall was then calculated using the assumption that snow changes to rain when the daily average air temperature rises above 2ºC [3] among various proposed methods of rain/snow determination. Similarly, the

[a] Corresponding author: otsuki@snow-eaters.com

maximum rainfall for each winter was obtained by extracting the rainfall precipitation data of only the stations where snow cover was observed (snow depth of more than 1 cm). To take into account the nighttime rainfall events that may continue to the next day, two-day rainfall data were also compiled. Further, the extreme value of the snow depth during rain was statistically analyzed to evaluate the roof snow load, as it is necessary to understand the snow depth characteristics during rain in winter.
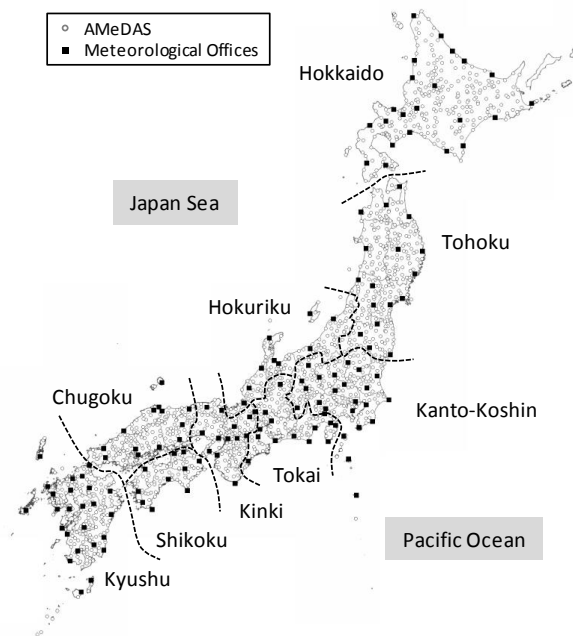


**Figure 2.** Meteorological stations whose data were analyzed.

# 3 Statistical evaluation of daily and two-day rainfall

## 3.1 Occurrence frequency of daily and two-day rainfall

Figures 3 and 4 show the ranked averaged winter maximum daily and two-day rainfall by number of stations. In the graph, the white bars represent the values for the entire winter, and the black bars represent the collected statistics of the rainfall on days when there was snow cover. The number of observation stations with snow cover is less than the total number for the entire winter because the former is the statistic for only the points where snow cover was observed. According to the graph, the greatest number of stations observed 10–20 mm as the multiyear average of the maximum winter daily rainfall in the case of snow cover, with the highest values at 40–50 mm. In case of the entire winter period, the highest number of stations observed 30–40 mm. The data for which the number of observation stations peak for the two-day rainfall are 10–20 mm and 40–50 mm, respectively. Compared with the daily data, two-day rainfall precipitation tends to be higher, but the difference is not significant. This means that a rainfall event usually

takes no more than two days, and a substantial amount of rain does not fall on both days.

Figures 5 and 6 show the ranked daily and two-day extreme rainfall by number of observation stations. In the case of snow cover, the extreme value distribution of the daily rainfall peaks at 50–60 mm, while the two-day data is distributed throughout a range of 40–90 mm without a distinguishing peak. For the entire winter period, the extreme values of the daily rainfall are in the range of 60–70 mm. For two-day rainfall, the extreme values are in the range of 80–90 mm. This shows a tendency that the peak values are higher by approximately 30–40 mm over
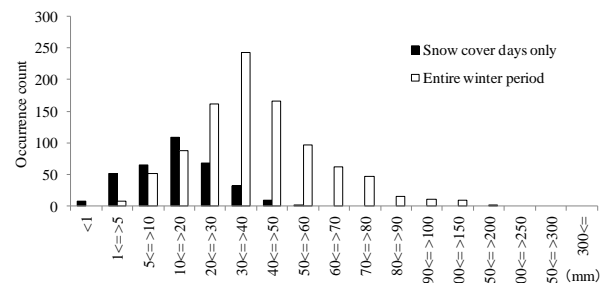


**Figure 3.** Ranked averaged winter maximum daily rainfall by number of observation stations.
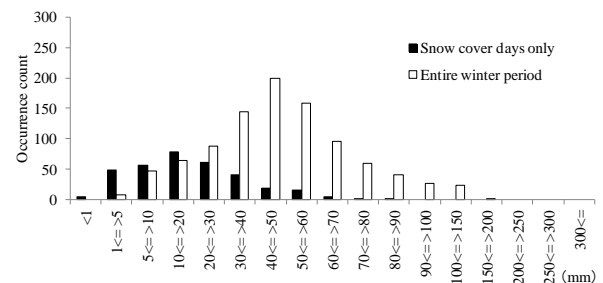


**Figure 4.** Ranked averaged winter maximum two-day rainfall by number of observation stations.
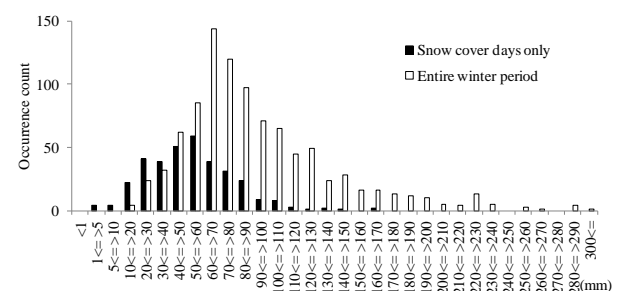


**Figure 5.** Ranked extreme winter maximum daily rainfall by number of observation stations.
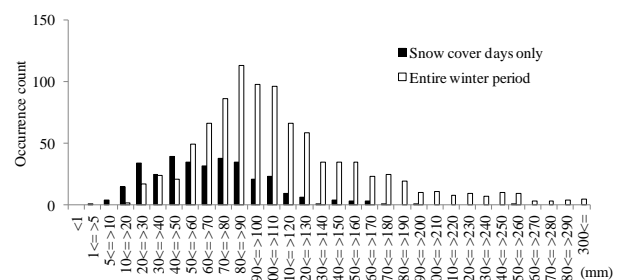


**Figure 6.** Ranked extreme winter maximum two-day rainfall by number of observation stations.

those of the multiyear averaged values. In terms of the peak occurrence of observation stations, the rainfall for the entire winter period tended to be greater by a range of 10–20 mm for daily rainfall and approximately 30 mm (although the distribution is unclear) for two-day rainfall than that with snow cover.

## 3.2 Areal distribution of daily and two-day rainfall

### 3.2.1 Precipitation distribution in Japan

Regional distribution of rainfall in winter is examined in this section. First, Figure 7 shows the mesh climatic data of precipitation from the Japan Meteorological Agency. Values tend to be higher on the Japan Sea side from
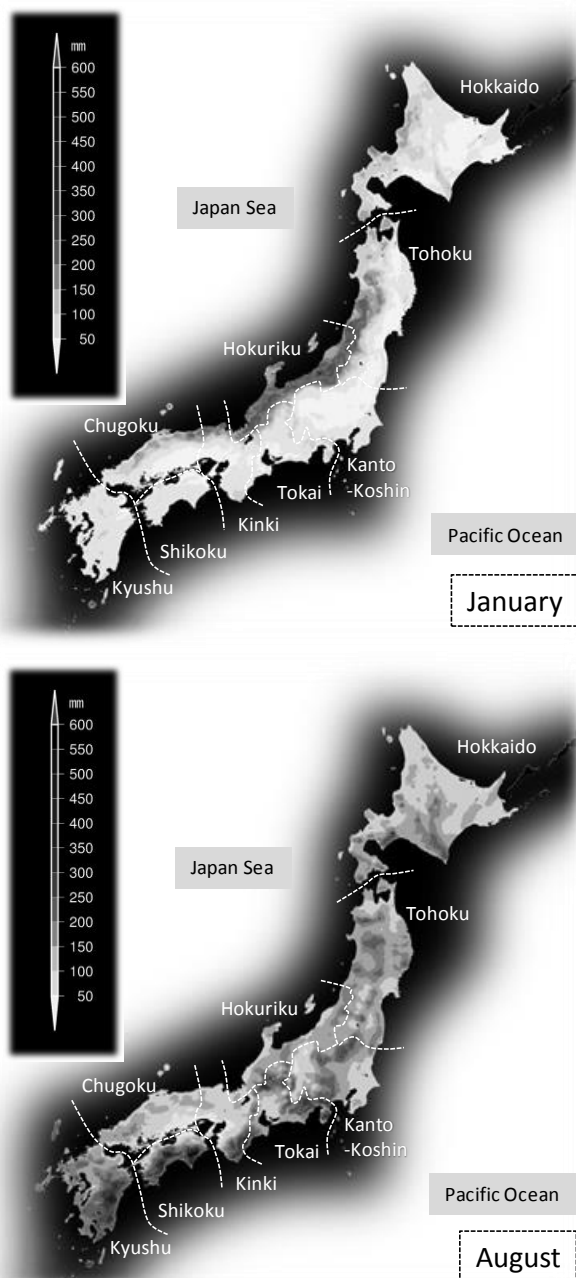


**Figure 7.** Mesh climatic data of monthly precipitation (Japan Meteorological Agency).

Tohoku to the Hokuriku-Chugoku regions in winter (January), and extremely low along the coast of the Pacific Ocean from Hokkaido to Kyushu. This is a result of the typical winter pressure pattern (east: high pressure, west: low pressure), where snow clouds bring heavy snow to the coast of the Japan Sea. In summer (August), on the other hand, the coast of the Pacific Ocean from Kanto to Kyushu regions receives considerable rain owing to substantial rainfall from typhoons and stationary fronts.

### 3.2.2 Rainfall distribution for the entire winter period

With the above facts in mind, the multiyear average and extreme distribution of winter rainfall (two-day data, the entire winter period), shown in Figures 8 and 9 are examined. The distribution of average values overall is smaller in northern Japan and greater in southern Japan. Values tend to be higher on the Pacific Ocean side from the Tohoku to Shikoku regions, Kyushu, and the Japan Sea side from the Hokuriku to Chugoku regions (in the range of 70–150 mm). On the other hand, the values are smaller in Hokkaido and the inland part of Tohoku in the range of 20–30 mm, unlike the distribution of the winter precipitation according to the mesh climatic data. It is thought that most of the precipitation in winter is snowfall, that most of it falls on the Japan Sea side, and that two-day rainfall is often observed on the Pacific Ocean side as well, similar to the precipitation characteristics in summer.

Extreme values appear to indicate that the overall rainfall is increasing compared with the average, and that the difference in the area distribution of rainfall is narrowing. The values for inland Hokkaido are similarly low at approximately 20 mm as is the multiyear average, but those on the Pacific Ocean side from Tohoku to Kyushu exceed 100 mm. The rainfall on the Pacific Ocean side of Hokkaido and inland Tohoku where the
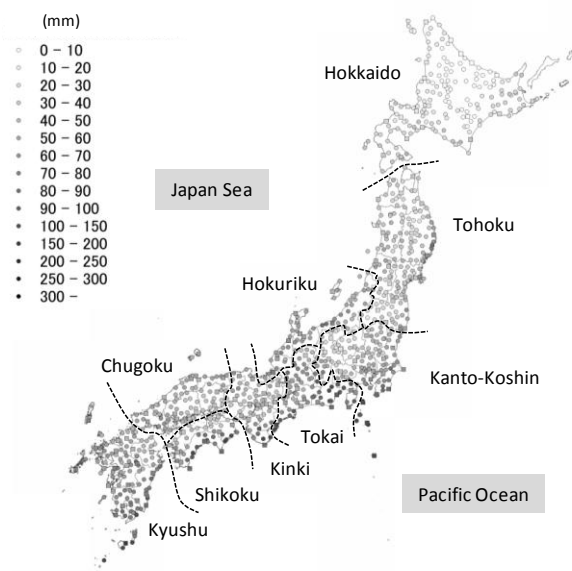


**Figure 8.** Average distribution of winter maximum rainfall (two-day data, entire winter period).
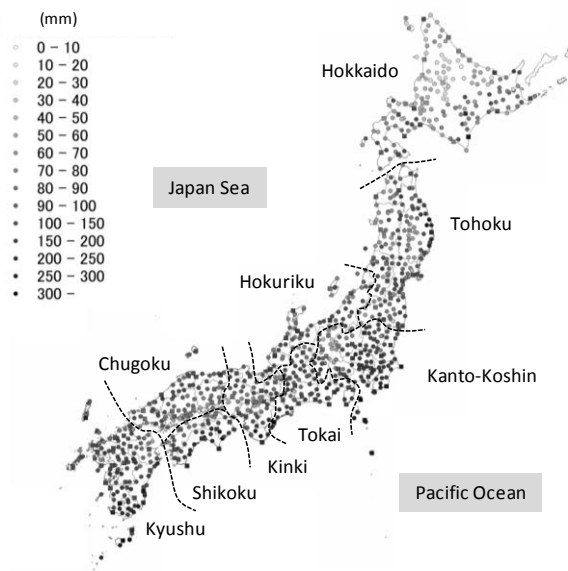
**Figure 9.** Extreme value distribution of winter maximum rainfall (two-day data, entire winter period).

average values were relatively small is just as high as other regions with regard to the extreme values. The reason for this is probably that substantially large rainfall events are recorded in these regions depending on the year. Such records become apparent by plotting the extreme values, but they do not stand out when averaged over multiple years.

### 3.2.3 Distribution of rainfall in snow cover period

In this section, the distribution of the multiyear average and extreme values of two-day rainfall on snow cover are examined (Figures 10 and 11). The number of plots is smaller than that for the entire winter because only the stations that measure snow depth are included, and the distribution trend is completely different. Regarding the multiyear average, the values are high at 30–60 mm on the Japan Sea side from the Tohoku to Chugoku regions, but small at 30 mm or less in other regions. The regions where the average values are high roughly overlap the regions of high rainfall in the winter period, and the rainfall during this period is more likely to be reflected in the statistics because the snow cover exists for a longer time in these regions. In regions with less precipitation and almost no snow cover period in winter, on the other hand, the two-day rainfall is expected to be extremely small when there is snow cover.

According to the extreme value results, the majority of stations recorded 50 mm or more, and values for the Pacific Ocean side of the Hokkaido, Tohoku, and Kanto-Koshin regions tended to be high, in addition to the stations on the Japan Sea side where the average values were high. While the values for the average were high only on the Japan Sea side, plotting the extreme values reveals large values in the range of 100 mm even in the Tohoku and Kanto-Koshin regions. This suggests that heavy rainfall events occasionally occur once every few years in such regions. From the extreme value distribution of two-day rainfall on snow cover, heavy

rainfall events are likely to be extracted on the Japan Sea coast because the snow cover exists for a longer time between December and March. On the other hand, conditions for snow cover forming are rare in Kanto-Koshin and the Pacific Ocean side of the Tohoku region, but it is thought that meteorological disturbances are likely to occur in these areas, causing heavy rainfalls during the snow cover periods.
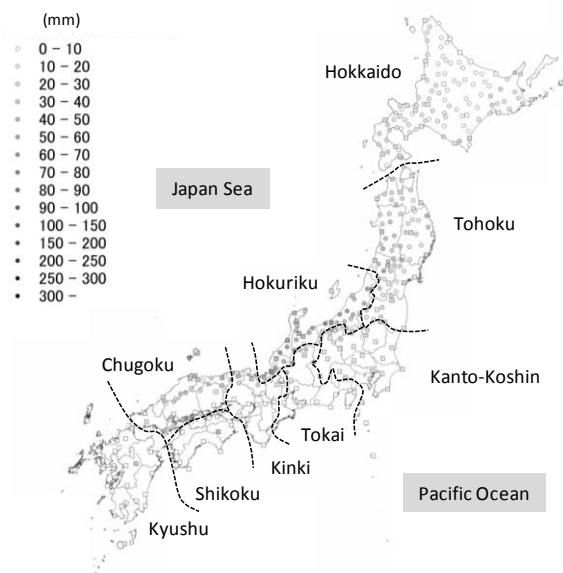


**Figure 10.** Average distribution of winter maximum rainfall (two-day data, snow cover days only).
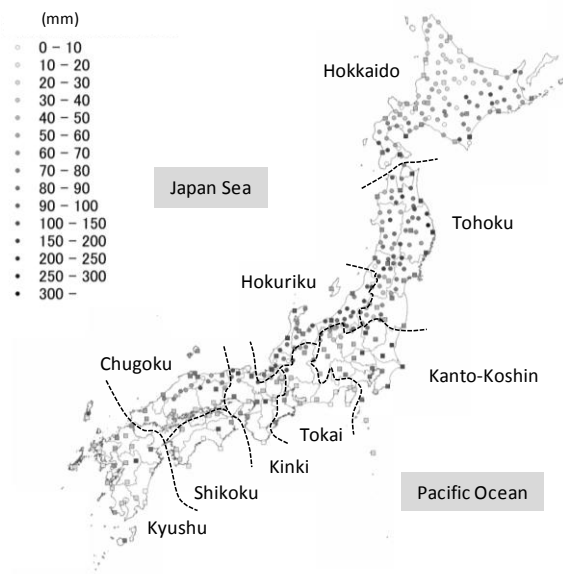


**Figure 11.** Extreme value distribution of winter maximum rainfall (two-day data, snow cover days only).

### 3.3 Summary

To summarize up to this point, the regions with more rainfall in summer tend to have higher daily and two-day rainfall during the entire winter period, while the

multiyear average is high in the Hokuriku region for snow cover. Extreme values are recorded in a relatively wide area, including the Pacific Ocean side of the Tohoku and Kanto-Koshin regions, where it snows little. In other words, snowfall and rainfall events occur occasionally in the regions with little snow cover and a small roof snow load, and dangerous conditions easily exceeding the roof snow load could occur depending on the amount of snow cover and rainfall. Thus, for the regions that need to allow for a rain-on-snow surcharge, the rainfall ratio for the original roof snow load is important.

## 4 Extreme value analysis of snow depth and rain load ratio

According to the 50-year probability [3] distribution of the annual maximum snow depth, snow cover is as deep as 150–200 cm in the Hokuriku region and on the Japan Sea side of Hokkaido (Figure 12). The roof snow load for these regions is known to be very high. Therefore, even if a rainfall event occurs, the relative load would not increase much. By contrast, the roof snow load is small in the coastal part of Tohoku and in the areas west of Kanto-Koshin. There, the relative load would increase substantially during rainfall. Considering this, the two-day rainfall load conversion value ratio (multiyear average and 50-year return period) in relation to the roof snow load is shown in Figures 13 and 14. The roof snow load here is the product of the snow cover depth shown in Figure 12 and the snow cover density of 0.3 kN/m³ in heavy snow areas that recorded a snow depth of 1 m or more, and of 0.2 kN/m³ in other general areas. The unit load of snow cover can be specified as 20 N/m²/cm in general areas, and more for the heavy snow areas [4]. The ratio is 1 or more at locations with a two-day rain load exceeding the roof snow load. These regions are consistent with those having less snow cover such as Kanto on the Pacific Ocean side of Kinki, and the Shikoku and Kyushu regions.
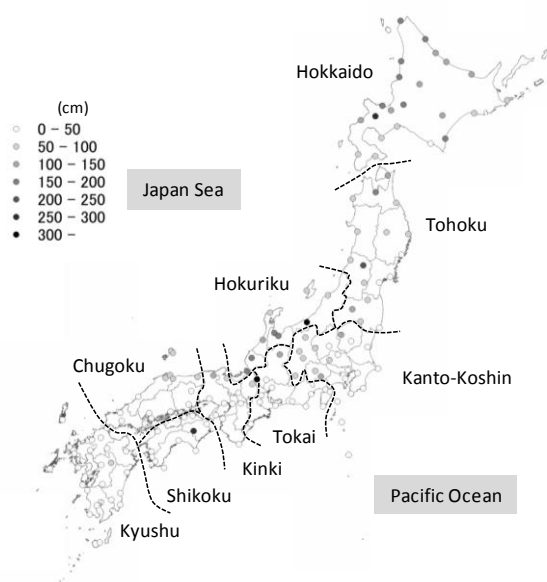


**Figure 12.** 50-year probability of snow depth distribution (according to Japan Meteorological Agency) [3].
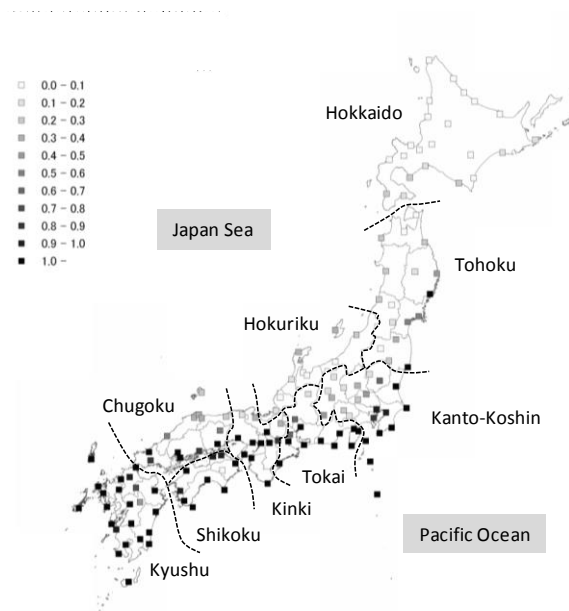


**Figure 13.** Ratio between two-day rainfall-equivalent load(average) and roof snow load.
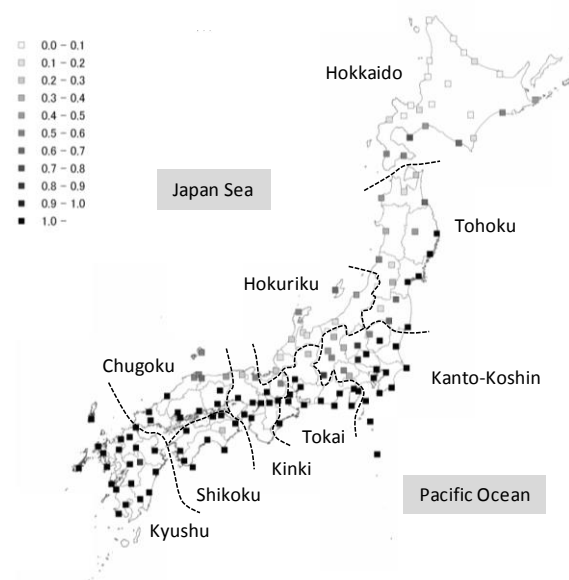


**Figure 14.** Ratio between two-day rainfall-equivalent load(50-year return period) and roof snow load.

By contrast, the ratio is relatively small in regions with heavy snowfall such as the Hokkaido, Tohoku, and Hokuriku regions. Figure 15 shows the number of occurrences ranked by ratio. In heavy snow areas, the ratio for many stations is 0.3 or less in the 50-year probability values for two-day rainfall precipitation, and that for most stations is 2.0 or less for multiyear average values. On the other hand, the ratio for 70% and 50%, respectively, of the observation stations exceeds 1.0 (the rain load exceeding the roof snow load) in the general areas with less snow cover. Further, although the occurrence numbers are small, there are occurrences that appear evenly in the 0.3 to 0.9 range, and it is possible that the risk of rain-on-snow events applying a load far greater than the bearing strength of the structure is quite high. An inference can be made from these data that rain-on-snow surcharge must be considered in general areas

with a snow cover depth of less than 1 m in Japan. However, because snow is not thought to absorb much rain unless there is deep snow cover, general areas with less snow cover, many of which are expected to be stations with the above ratio of 1 or higher, should be excluded from consideration.
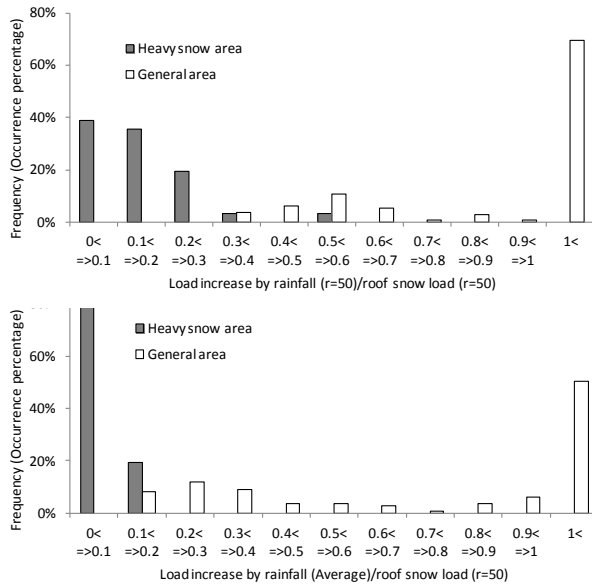


**Figure 15.** Occurrence percentage ranked by ratio between two-day rainfall-equivalent load and roof snow load.

# 5 Conclusion

In this study, the snowfall and rainfall characteristics of winter in Japan were investigated.

– Statistics of maximum annual daily rainfall and two-day rainfall in the winter period based on precipitation data from the Japan Meteorological Agency revealed that the occurrence count peaked at 30–40 mm for the average daily rainfall during the entire winter period, and at 10–20 mm when there was snow cover. With regard to extreme values, peaks were observed at 60–70 mm and 50–60 mm, respectively.

– A comparison of daily and two-day rainfall showed that two-day rainfall was slightly greater without a substantial difference in the distribution. Thus the two-day rainfall is considered to be appropriate for examining the rain load.

– The number of data for the entire winter period naturally tended to be greater than those with snow cover in the processing of maximum values for statistics. The statistical values of rainfall during the entire winter period as a precautionary measure may be applied to a surcharge load. If there is a strong dependency and connection between snowfall and rainfall, however, the use of rainfall on snow cover is a possibility, and further investigation into the relationship between rainfall and snowfall is necessary.

– An investigation of the areal distribution of rainfall revealed that the rainfall for the entire winter was greater in regions where summer rainfall was high. The extreme values of rainfall on snow cover were

found to be higher in regions with a long snow cover period, ranging from Hokuriku to Tohoku and southern Hokkaido as well as the Kanto-Koshin regions.

– The load conversion value of the two-day rainfall is often relatively higher in the general areas on the Pacific Ocean side with snow cover depth of less than 1m, such as the Kanto-Koshin region, in relation to their snow load. In such regions, there is a concern that the roof snow load exceeds the design load owing to the rain-on-snow surcharge.

# 6 Future Challenges

The actual degree of load increase during continuous rainfall on snow on sloped roofs is still not known. According to Otsuki (2015) [5], the rain-on-snow load peaks when rainfall becomes heavy, the water starts to drain, and the speed of the rainfall becomes roughly equal to that of the drainage. Figure 16 shows how the load increases when a constant strength of rain (10 mm/h) falls on snow on four different roof models. The dashed line in the figure indicates the load conversion of the cumulative rainfall, and the load is plotted on this line when there is no drainage.

According this figure, the greater the span and the smaller the slope of the roof, the less rainfall it takes to reach the peak. The load on all roofs shifts slightly to the right of the dashed line by a few tens of millimeters before reaching the peak, indicating that the water started to drain during the rain. The drainage further accelerated after the peak load was reached on all roofs, and the load continued to decrease (the 50-m roof reached its peak at approximately 70 mm). In other words, reflecting all of the rainfall in the surcharge is too much. By continuing this experiment, the roof shape, snow depth, peak load, and their relationship to rainfall precipitation at that time will be clarified. Further, the amount of this rainfall will be compared with the rainfall distribution during the winter period to examine the regions where it is
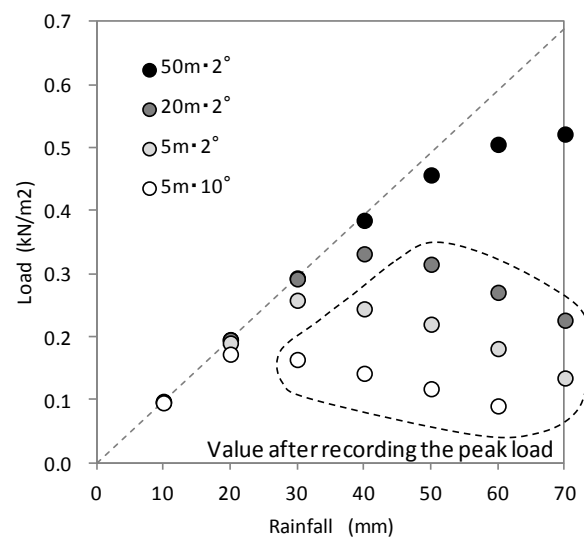


**Figure 16.** Load change over time owing to rainfall (example of snow depth at 50 cm) [5].

necessary to consider the effect of rain on the roof snow load. In addition, the roof-snow-load calculation method considering rain on snow will be examined.

## Acknowledgments

## References

1.  ASCE, *Minimum Design Loads for Buildings and Other Structures* (ASCE/SEI 7-10) (2010, 2013)
2.  *National Building Code of Canada* (NRCC53301) (2010)
3.  Architectural Institute of Japan, *Recommendations for Loads on Buildings* (2015)
4.  *The Building Standard Law of Japan* (2013)
5.  M. Otsuki et al., *Evaluation of Roof Snow Load Considering Rain-on-Snow Surcharge; Summaries of JSSI & JSSE Joint Conference on Snow and Ice Research*, 283 (2015)

# Structural damage caused by rain-on-snow load in Japan

Toru Takahashi[1,a], Takahiro Chiba[2] and Kazuki Nakamura[3]

[1]Department of Architecture, Chiba University, 1-33 Yayoicho, Inage-ku, Chiba, Japan
[2]Department of Architecture, Hokkaido University of Science, 7-15-4-1, Maeda, Teine-ku, Sapporo, Japan
[3]National Research Institute for Earth Science and Disaster Prevention, 3-1 Tennodai, Tsukuba, Japan

**Abstract.** In February 2014, heavy snow and additional rain led many large span structures and carports to collapse in Kanto region, Japan. We had almost the same depth of heavy snow one week before the event, but no structural damage was reported. Therefore, the authors focused on precipitation data and estimated roof snow load for each structure that collapsed time was clarified. As a result, it was clarified that designers would better to use precipitation data for design snow load.

## 1 Foreword

In February 2014, we got heavy snow twice with interval of one week in Japan. Both of snowfall was caused by low-pressure system that approached over the south coast of Japan, but only the second one led many large span structures to collapse.

In this paper, the authors checked time history data of weather stations and estimated the snow load for each structure that collapsed time was clarified. Then, problem of ordinary design method for snow load in Japan was discussed.

## 2 Outline of damage

Table 1 shows outline of damaged buildings during the disaster and Figure 1 shows distribution of collapsed large span structures in Kanto region. This was the first time in Kanto region to have such a number of structures' collapse. Besides, large numbers of carports with lightweight and simply supported as cantilever were collapsed but the authors do not discuss the issue.

**Table 1.** Outline of snow disaster in February 2014 in Japan[1)]

| | residential house | | | non-residential buildings | |
|---|---|---|---|---|---|
| Prefecture | fully damaged | half damaged | partially damaged | public buildings | other |
| Hokkaido | | | 2 | | 1 |
| Aomori | | | 2 | | |
| Iwate | | | 3 | 1 | 7 |
| Miyagi | | | 25 | 6 | 60 |
| Akita | | | | | 1 |
| Fukushima | 1 | | 3 | 7 | 34 |
| Tochigi | | 2 | 24 | | |
| Gumma | 2 | | 27 | | 16 |
| Saitama | | 1 | 19 | 3 | 45 |
| Tokyo | | 1 | 76 | 20 | 72 |
| Kanagawa | | | 21 | 2 | 41 |
| Yamanashi | 13 | 42 | 357 | | |
| Nagano | | | 14 | | 24 |
| Gifu | | | | | 1 |
| Shizuoka | | | 4 | | 39 |
| Aichi | | | 3 | | 1 |
| Kyoto | | | 3 | | 1 |
| Oita | | | 2 | 1 | 4 |
| Miyazaki | | | | | 1 |

[a] Corresponding author: takahashi.toru@faculty.chiba-u.jp

As shown in Figure 1, it looks like there is a zone of collapse. There seems to have had heavier roof snow load than design value in the zone.
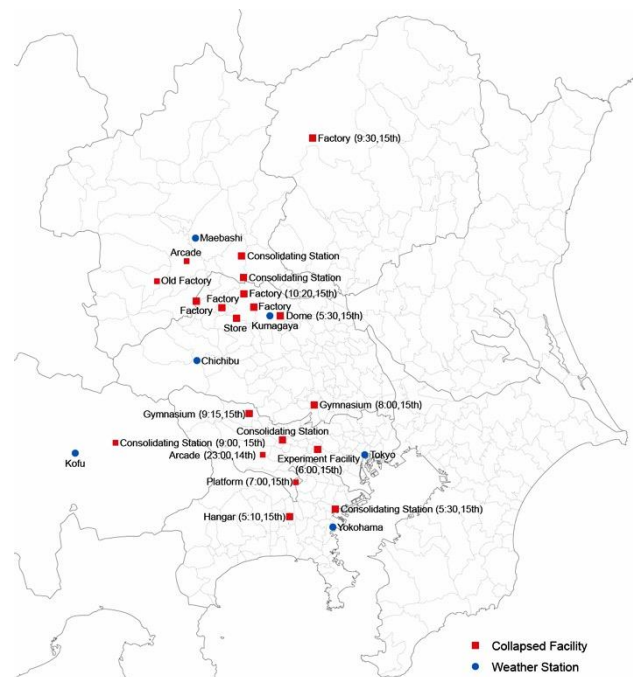


**Figure 1.** Distribution of collapsed structures in Kanto region.

**Table 2.** List of structure whose collapsed time was clarified.

| No. | Date | Time | Place | Damaged system |
|---|---|---|---|---|
| 1 | 14th Feb. | 23:00 | Hachioji | Arcade |
| 2 | 15th Feb. | 05:10 | Yamato | Diamond truss |
| 3 | 15th Feb. | 05:30 | Kumagaya | Membrane |
| 4 | 15th Feb. | 05:30 | Yokohama | Prefab. truss |
| 5 | 15th Feb. | 06:00 | Mitaka | Parallel truss |
| 6 | 15th Feb. | 07:00 | Yokohama | Cantilever roof |
| 7 | 15th Feb. | 08:00 | Fujimi | Parallel truss |
| 8 | 15th Feb. | 09:00 | Yamanashi | Parallel truss (old) |
| 9 | 15th Feb. | 09:15 | Ome | Full web frame |
| 10 | 15th Feb. | 09:30 | Nikko | Parallel truss |
| 11 | 15th Feb. | 10:20 | Fukaya | Unknown (factory) |

Table 2 shows the list of collapsed large span structure whose collapsed time was clarified[2]. The snowfall began in Kanto region in the morning of February 14th, 2014 and changed to rain in the next morning. Structure No.1 collapsed midnight of February 14th and the others collapsed in the morning of February 15th. Photos 1, 2, 3 and 4 show examples of collapsed buildings. Investigation reports of the accidents say these structures were safe for design snow load level (600 N/m²)[3]. In the figure, collapsed time shown in table 2 and expected accumulated precipitation i.e. snow load on the roof are plotted with triangle mark. Because 1.0 mm of precipitation means 9.8 N/m² of roof snow load if its shape factor is 1.0, expected snow load on the roof might be heavier than design snow load level and it might be 800 to 900 N/m² as shown in Figure 2, except of structure No.1. In Figure 2, catch ratio of precipitation gauge was corrected after Yokoyama et al[4]. In the figure, it can be seen that snow load on the roof might exceed at 4 o'clock in the morning at Tokyo, and after that, additional rain-on-snow load might be affected.

This time series investigation results of roof snow loads are consistent with results of structural analyses in the accidents investigation reports of collapsed structures.



**Photo 1**. Example of collapsed building. (No.7 in Table 1.)



**Photo 2**. Internal view of Photo 1.



**Photo 3**. Example of collapsed building. (No.9 in Table 1.)
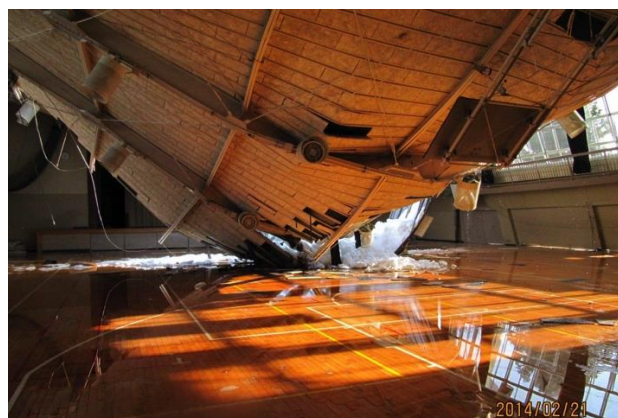


**Photo 4**. Internal view of Photo 3.

# 3 Statistical data study

Conventionally, in Japan, roof snow load of the general area, which is defined by building code, is calculated by multiplying the annual maximum snow depth of return period 50 years in the region and the unit snow weight (2.0 kN/m³). By the damage of this heavy snow accident, the influence of rainfall has become clear. Therefore, in the following clause, the authors verify the influence of rainfall using a method of snow layer model, which has been proposed by the authors to estimate the ground snow depth and the ground snow weight by using precipitation and temperature[6], and extreme value statistics.

## 3.1 Longitudinal data

Figure 3 shows longitudinal data of annual maximum snow depth (left hand) and annual maximum snow weight on the ground (right hand), which were estimated by the snow layer model, for Tokyo, Yokohama, Kumagaya and Kofu from 1962 to 2014 seasons. In the figure, design levels of snow depth and snow weight are also shown for the convenience.

When we focus attention on snow depth, the latest value was not the largest one, for Tokyo and Yokohama. In the case of Tokyo, snow depth in 2014 (0.27 m) was second deepest value and was less than design snow

depth (0.3 m). On the other hand, at Kumagaya and Kofu, snow depth in 2014 was enormously high. The value reaches almost twice of design value. If we consider only this value, it is difficult to describe why no structure (except of the deteriorated old one) was collapsed around there.

Therefore, next, the authors evaluated annual maximum ground snow weight by snow layer model and compared them with snow depths. Even in Tokyo and Yokohama, the value of 2014 has become the largest. In Kofu, there appeared large value in 1998. There was a snow disaster in 1998 around Kofu region[7]. The values are consistent with structural damage.

## 3.2 Extreme value statistics

Figure 4 shows plots of annual maximum ground snow depth (left hand) and annual maximum ground snow weight (right hand) for Tokyo, Yokohama, Kumagaya and Kofu on the Gumbel probability paper. In the figure, design values of snow depth and snow weight are also shown for the convenience. Triangle plots are data based on 1962 to 1999, which was used in the AIJ recommendation 2004[8] version, and circle plots are data based on 1962 to 2014[9].

Comparing with these plots, the effect of 2014 data was clarified. For snow depth of Tokyo and Yokohama, there is no difference between both regression formula,

can also be understood that the snow depth 0.3 m that has been used in the design is a value that corresponds to return period 50 years. In Kumagaya, although 0.3 m was a value exactly corresponding in recurrence interval 50 years in the data by 1999, by regression including the data in 2014, it would be the evaluation 17.8 years. On the other hand, if observed value 0.62 m in 2014 was applied to this regression, it would become the evaluation of recurrence interval 272 years. In Kofu, although 0.5 m was a value exactly corresponding in recurrence interval 74 years in the data by 1999, by regression including the data in 2014, it would be the evaluation 18.2 years. On the other hand, if observed value 1.14 m in 2014 was applied to this regression, it would become the evaluation of recurrence interval 353 years.

When attached to the ground snow weight, as long as it has been based on the data by 1999, it has turned out that using 0.6 kN/m$^2$ for a design value of recurrence interval 50 years in Tokyo, Yokohama, and Kumagaya has been almost comparable. However, if based on the data by 2014, the recurrence interval that 0.6 kN/m$^2$ corresponds would become 24 years in Tokyo, 26 years in Yokohama and 16 years in Kumagaya. On the other hand, in Kofu, if based on the data by 1999, 1.0 kN/m$^2$ corresponds in 138 years, and even if it uses the data by 2014, it would become 67 years. This result was also considered as the circumstantial evidence that the damage of large span structure was little in Yamanashi.
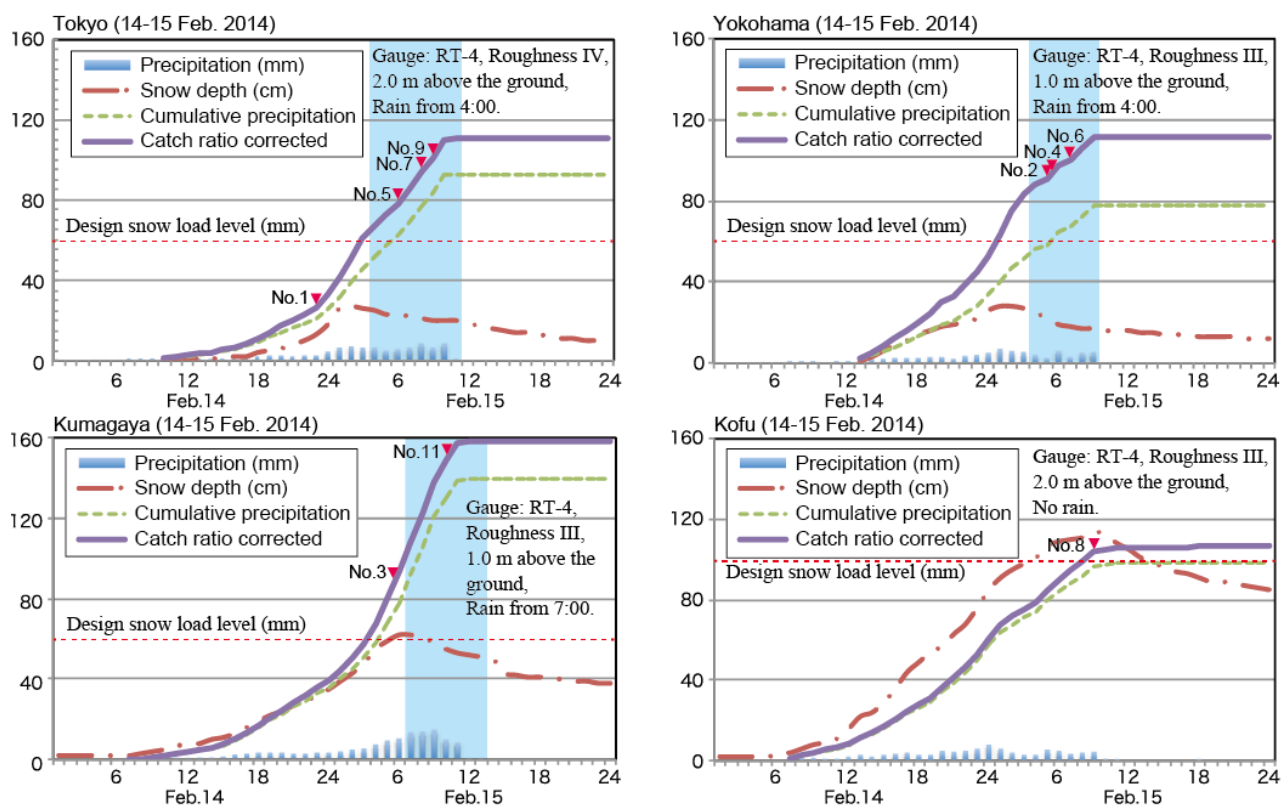


**Figure 2.** Example of weather data during the disaster[5].

(a) Annual maximum snow depth

(b) Annual maximum snow weight on the ground
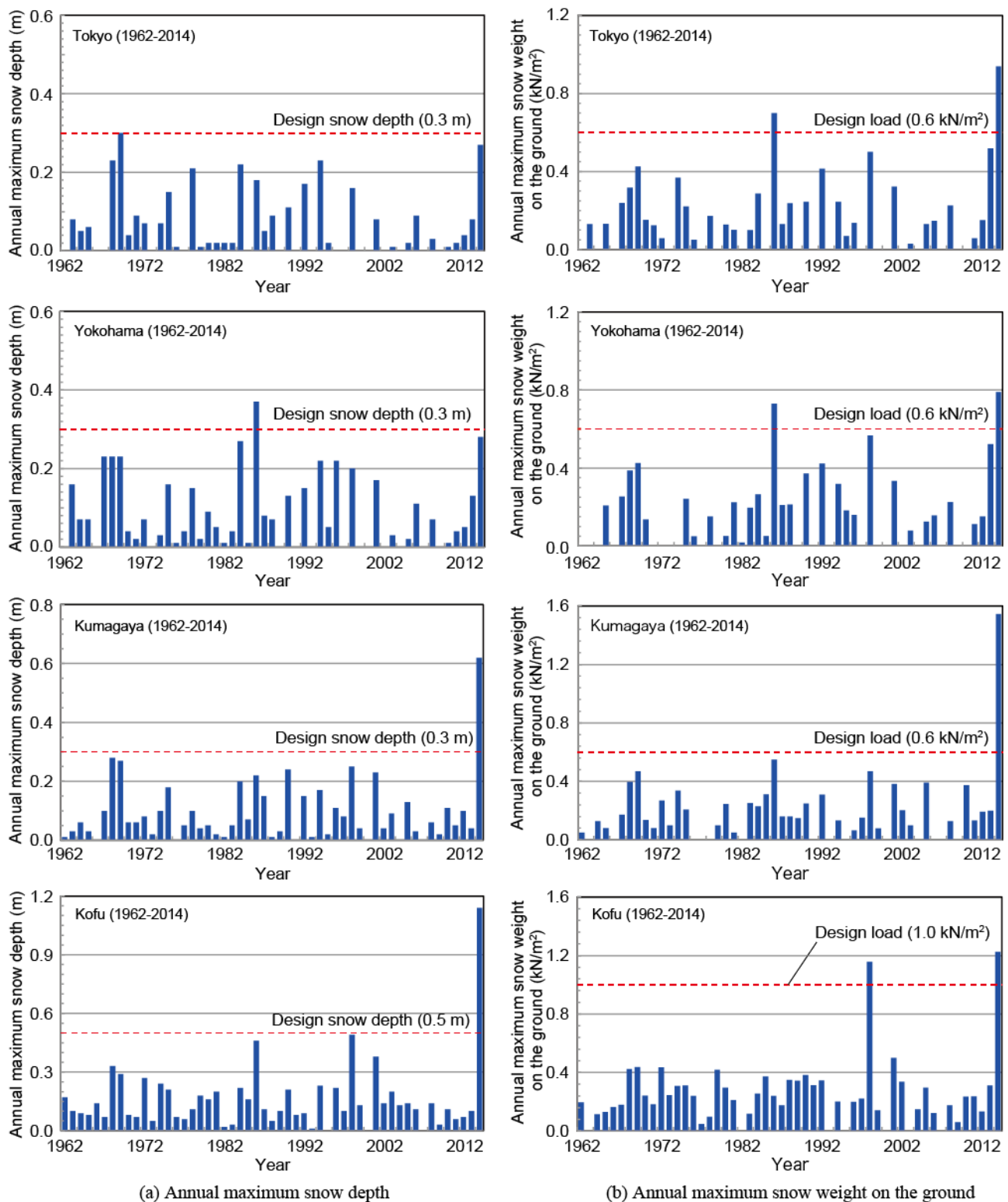
**Figure 3.** Longitudinal data of annual maximum snow depth and annual maximum snow weight on the ground.
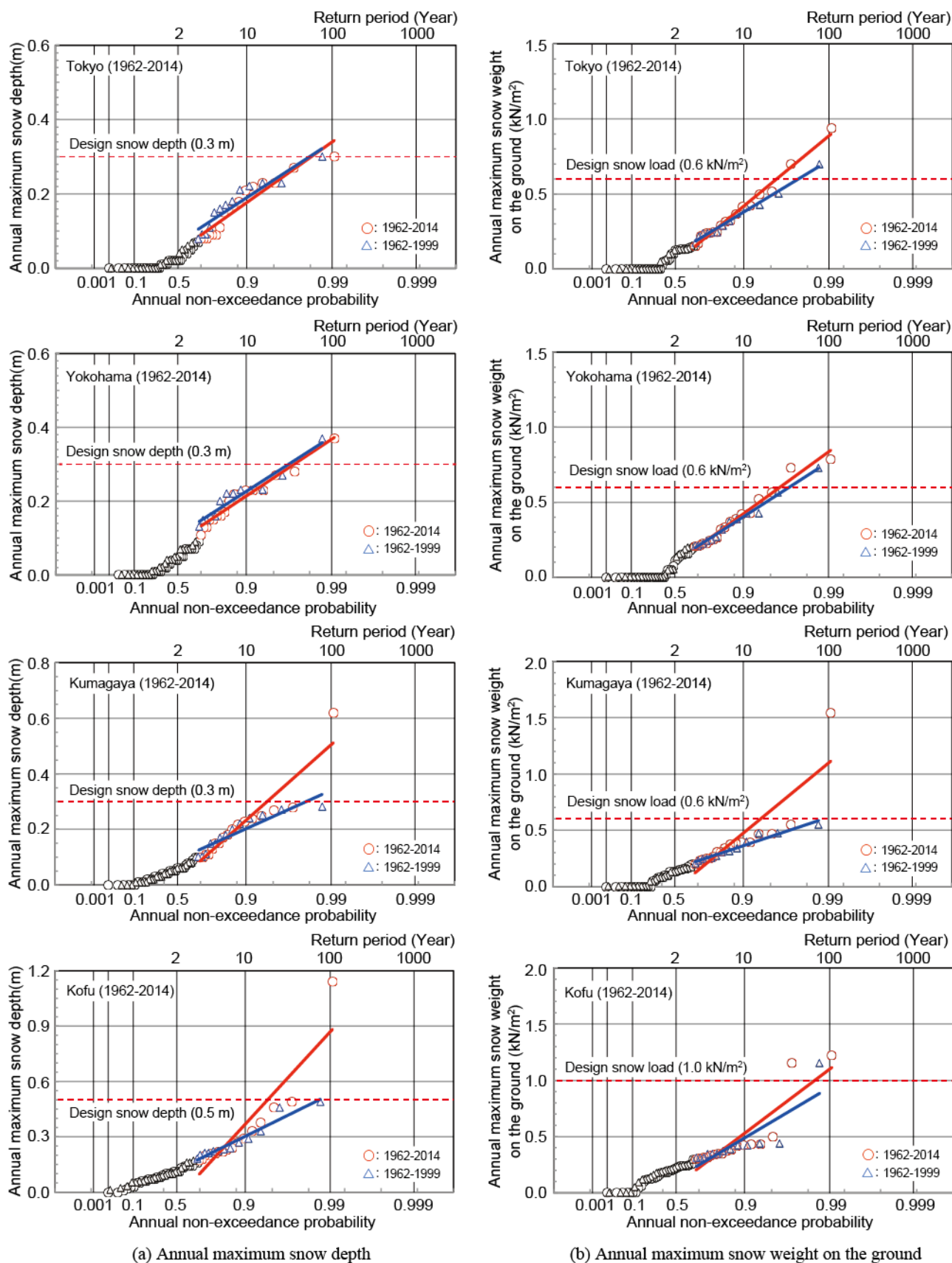
**Figure 4.** Plots on Gumbel probability paper of annual maximum snow depth and annual maximum snow weight on the ground.

## 4 Equivalent snow density

Figure 5 shows the relation between annual maximum snow depth and equivalent unit snow weight (snow density). Ordinary Japanese design sequence (building code) needs snow depth first, then requests equivalent unit snow weight. 2.0 kN/m$^3$ is normally used in general region and 3.0 kN/m$^3$ is used for heavy snow region. AIJ (Architectural Institute of Japan) recommends equation 1 for the equivalent unit snow weight $p_s$ [kN/m$^3$] based on observations in heavy snow region[8)9)].
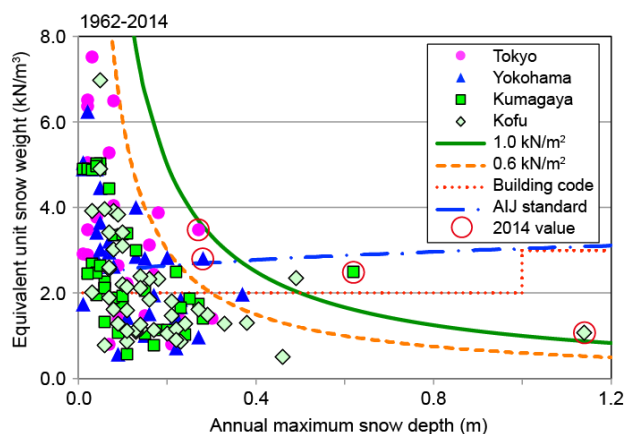


**Figure 5.** Relation between annual maximum snow depth and equivalent unit snow weight.

$$p_s = 0.72\sqrt{d/d_{ref}} + 2.32 \qquad (1)$$

where, $d$ [m] is snow depth on the ground and $d_{ref}$ [=1 m] is standard snow depth for make it non-dimensional number. Figure 5 shows that snow density for small snow depth could be very large based on precipitation data. In such a case, even if we use equation 1, it could not be expounded. It seems better to use precipitation data directly. For 2014 value, it could be said that the ground snow weight might be around 1.0 kN/m$^2$. It includes rain-on-snow surcharge. The value exceeded design load in Tokyo, Yokohama and Kumagaya, and led to structural damage. On the other hand, in Kofu, it was almost even with design load, and little damage for large span structure was reported.

## 5 Results

Almost of structural damage in 2014 heavy snow might occur because snow load on the roof exceeded their design snow load. It could be said that total precipitation during the event largely 1.0 kN/m$^2$ in Kanto region. It could be said that we would be better to use precipitation data directly to decide design snow load value that including rain-on-snow surcharge.

In Kofu, it was happy that design snow load had sufficient margin (long return period) against actual load, and it led little damage for large span structures.

## References

1. Fire and Disaster Management Agency: Heavy Snow Disaster Report during February 14 to 16, (2014) http://www.fdma.go.jp/ (in Japanese)
2. *Asahi-shimbun* newspaper, Feb. 17th, 2014, *Nikkei-shimbun* newspaper, Feb. 17th, 2014, etc. (2014)
3. For example, Investigation Board on Collapse of Fujimi Arena: *Investigation Report on Collapse of Fujimi Arena* (2014) (in Japanese)
4. Yokoyama K., Ohno H., Kominami Y., Inoue S. and Kawakata T.: Performance of Japanese Precipitation Gauges in Winter, *Seppyo* (Journal of Snow and Ice), **65**, 303-316 (2003)
5. Japan Meteorological Agency: Observations at each weather station (as of February 2014) http://www.data.jma.go.jp/obd/stats/etrn/index.php
6. Takahashi, T., Kawamura, T., Kuramoto K.: Estimation of Ground Snow Load Using Snow Layer Model, *Journal of Structural and Construction Engineering* (*Transactions of AIJ*), **66**, No.545, 35-41 (2001)
7. Takahashi, T., Kawaguchi, K., Ohi, K.: Snow Disaster in Yamanashi Prefecture in January, 1998, *Journal of Snow Engineering of Japan*, **14**, 141-144 (1998)
8. Architectural Institute of Japan: *Recommendations for Loads on Buildings (2004)*, AIJ, Tokyo (2004)
9. Architectural Institute of Japan: *Recommendations for Loads on Buildings (2015)*, AIJ, Tokyo (2015)

# A new method of predicting slide snow load for sloped roofs

Xuanyi Zhou[1,a], Jialiang Li[1], Peng Huang[1], Ming Gu[1] and Lulu Sun[1]

[1]State Key Laboratory of Disaster Reduction in Civil Engineering, Tongji University, Shanghai, China

**Abstract.** This study applies a new method to simulate sliding snow load on sloped roofs based on the snowmelt model for two regions in China. The positive energy absorbed by snowpacks on sloped roofs is regarded as a key indicator of snow sliding based on a previous snowmelt model for building roofs and based on field observation results from the previous literature. The impacts of roof slope, shielding effect of neighbouring buildings and heat gained from within buildings are analysed. And, this study presents a simplified formula of sliding snow load as a function of roof slope, shielding effect of neighbouring buildings, and heat transfer coefficients for convenient application of structural engineers.

## 1 Introduction

Snow can accumulate easily on the roofs of buildings in cold regions. When the weather warms up, snowpack often becomes unstable sliding drops. When two buildings with different heights are adjacent to each other, the snowpack sliding from the upper roof can aggravate the snow load on the lower one.The prediction of slide snow/ice loads on roofs is vital for structure design in heavy snowfall regions. Some studies have been conducted on the snow-slide loads on roofs. Sack et al. (1987) [1] developed a method to calculate the accumulation of snow on unobstructed, slippery roofs and pointed out that snow sliding on the roof—snow interface is initiated by either a reduction in resistance or shear failure. Lepage and Schuyler (1988) [2] presented a numerical simulation method that is combined with a scale model test to predict the quantity of snow that could eventually slide off sloped roofs. The simulation method considered several years of historical observations of wind, temperature, precipitation, and solar radiation. The scale model tests included a water flume and a wind tunnel experiment. Takakura et al. (2000) [3] reported that snowslide is affected not only by roof slope, but also by the temperature characteristics in each region. Based on the available historical weather data, Isyumov and Mikitiuk (2008) [4] developed a numerical method to predict the frequency of snow sliding from the surfaces of sloped buildings. In this method, 0 °C was the prerequisite air temperature in snowpack sliding. To explore the relationship between temperature characteristics and snow-slide, Chiba et al. (2012) [5] presented the snow-slide probabilities of different roof slopes as a function of the accumulated temperature above freezing .However, most of them do not provide a practical method for structural engineers. Current load codes and Zhou et al. (2013) [6] established calculation methods that disregard some crucial effects of key factors. For example, these load codes generally regard the slide snow/ice load coefficient as fixed. Zhou et al. (2013) considered the effects of heat obtained from within buildings and the shielding effect of neighbouring buildings, but they ignored the effects of roof slope. Further, Zhou et al. (2015) [7] developed a new method to simulate sliding snow load loads on sloped roofs. The positive energy absorbed by snowpacks on sloped roofs was regarded as a key indicator of snow sliding based on a previous snowmelt model for building roofs and based on field observation results from the previous literature. In this study we adopted the new method developed by Zhou et al. (2015) to analyse the characteristics of slide snow in some regions in China

## 2 Snowmelt model on building roofs

The snowmelt model of Zhou et al. (2015) includes the energy and mass balance equations.

The energy balance equation can be described as follows,

$$\frac{dU}{dt} = S_n + L_a - L_t + H + E_l + Q_p + Q_r \qquad (1)$$

where, $S_n$ denotes the solar radiation absorbed by snow on roofs; $L_a$ the atmospheric longwave radiation, $L_t$ the terrestrial longwave radiation; $H$ sensible heat; $E_l$ latent heat; $Q_p$ the heat advected by precipitation (rainfall or snowfall); and $Q_r$ the heat obtained from within the building. The unit of the energies above is $kJm^{-2}hr^{-1}$.

The mass balance equation in the snow layer (Zhou et al., 2015) can be expressed as follows,

$$\frac{dW}{dt} = P_r + P_s - M_{out} - W_E$$

(2)

where $P_r$ denotes the precipitation as rainfall; $P_S$ the precipitation as snowfall; $M_{out}$ the rate of snowmelt; $W_E$ the sublimation or condensation from the snowpack. The unit of the variables on the right side of Equation (2) is $mhr^{-1}$.

## 3 Method of predicting slide snow load for sloped roofs

The concept of accumulated temperature above freezing was proposed by Chiba et al. (2012) [5]. Chiba et al.

believed that the data of the accumulated temperature above freezing follows log-normal distribution and summarized the relationship between snow-slide probability and the accumulated temperature above freezing. In Zhou et al.'s (2015) study, snow sliding is closely related to the internal physical states of snowpack, which is determined by the absorption of energy by snowpack on roofs. The energy absorbed by the snowpack reflects the essence of snow slide more effectively than air temperature does. In especial, the positive energy absorbed from the surrounding environment can alter snow phases and induces further snow slide. The concept of the positive energy that is shadowed is shown in Fig. 1.
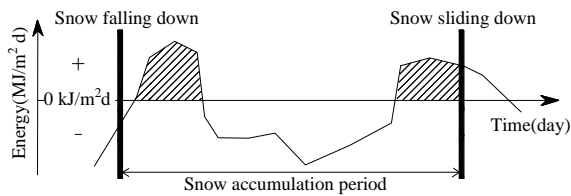


**Fig. 1.** Accumulated positive energy

**Table 1** Comparison of sufficient condition between field observation and simulated result (Chiba et al., 2012; Zhou et al., 2015)

| Roof slope α (1) | Critical accumulated temperature above freezing (Chiba et al., 2012) (2) | Critical accumulated positive energy (simulated results) (3) | Critical accumulated temperature above freezing (simulated results) (4) |
|---|---|---|---|
| 1.4 | 33°C·hr | 1.0 MJ/m² | 33°C·hr |
| 1.0 | 46°C·hr | 1.3 MJ/m² | 43°C·hr |
| 0.7 | 72°C·hr | 2.0 MJ/m² | 70°C·hr |
| 0.5 | 110°C·hr | 2.8 MJ/m² | 115°C·hr |
| 0.4 | 161°C·hr | 4.1 MJ/m² | 165°C·hr |
| 0.3 | 314°C·hr | 8.8 MJ/m² | 310°C·hr |
| 0.2 | 480°C·hr | 15.0 MJ/m² | 482°C·hr |

Chiba et al. (2012) built several roof models with different slopes in Sapporo, Japan. Field observations were performed from 2001 to 2008. For every snow-sliding event, the accumulated temperature above freezing was analyzed based on eight years' data of field observation. Chiba believed that the data of the accumulated temperature above freezing follows log-normal distribution and summarized the relationship between snow-slide probability and the accumulated temperature above freezing. Column 2 of Table 1 lists the accumulated temperatures above freezing under a 95% sliding probability for different roof slopes. The accumulated temperature above freezing can be regarded as a sufficient condition for snow sliding on sloped roofs because the values correspond to a high sliding

probability. Thus, they are labeled in Table 1 as critical accumulated temperature above freezing. The assumed critical values in Column 3 of Table 1 are adjusted through trial and error until the differences between Column 2 and Column 4 are minimized. After continuous trials, the preset critical accumulated positive energy depicted in Column 3 reduces the differences between Columns 4 and 2, which suggests that Column 3 of Table 1 can reflect the results of the field observation in Sapporo. The critical accumulated positive energy increases significantly as roof slope decreases; thus, snowpacks on low-sloped roofs can be expected to slide down with more difficulty. In the following simulations, the values of critical accumulated positive energy as listed in Column 3 of Table 1 are applied as the thresholds of sufficient condition for snow sliding on differently sloped roofs.

# 4 Simulation of sliding snow loads for two regions in China

The following part would apply the method described above to predict the slide snow loads for sloped roofs in China.

## 4.1 Effect of geographic differences on the energy exchange

This study analysed the meteorological data of several representative regions with snowfall in Jiamusi and Nanchang, which represent the northern region and southern region of China, respectively. The meteorological data of the two regions were collected from the China Meteorological Data Sharing Service System and included the daily average wind speed, average temperature, daily maximum temperature, daily minimum temperature, relative humidity, and amount of snowfall or rainfall during 62 winters from November 1, 1951 to March 31, 2013. Figure 2 depicts the meteorological data on the representative regions in a certain winter. All meteorological data include four measured values at some fixed time every day and the data were linearly interpolated to obtain the hourly data. As shown in Figure 2, Jiamusi experiences evenly distributed snowfall and little rainfall in winter, whereas Nanchang encounters concentrated snowfall and heavy rainfall. Moreover, the winter temperature in Jiamusi mainly ranges between -30 °C and -10 °C, whereas that in Nanchang usually exceeds 0 °C. Even during snowfall, the temperature is greater than -5 °C in Nanchang. In addition, wind speed in Jiamusi is slightly higher and fluctuates more than that in Nanchang. The humidities of both regions are similar, although that in Nanchang fluctuates more.

Figure 3 and Figure 4 exhibit the energy absorbed/released by snowpacks on roofs in Jiamusi and Nanchang during a certain winter. These figures were drawn based on the hypothesis that the snow on the roof does not slide down. Thus, they can reflect the entire process of energy absorption/release in winter. In these figures, short wave radiation Sn, sensible heat, and heat

transfer are positive. Net longwave radiation is generally negative, but it may also be positive on occasion. The latent heat and energy from precipitation are positive at times and negative at others. Their absolute values are smaller than those of other energies. Radiation energy including short wave and longwave radiation dominates the energy, followed by that obtained from sensible heat and the heat transfer from within buildings. The remaining energies only contribute a small proportion. The proportion of Sn in total energy is lower in Jiamusi than in Nanchang mainly because of the low latitude of Nanchang, which enhances solar radiation in Nanchang. The proportion of the net longwave radiation is lower in Nanchang compared with that in Jiamusi. This is because southern China experiences rainy days in winter more frequently than northern China, resulting in an increase in cloudy sky emissivity and decrease in the absolute value of net longwave radiation.
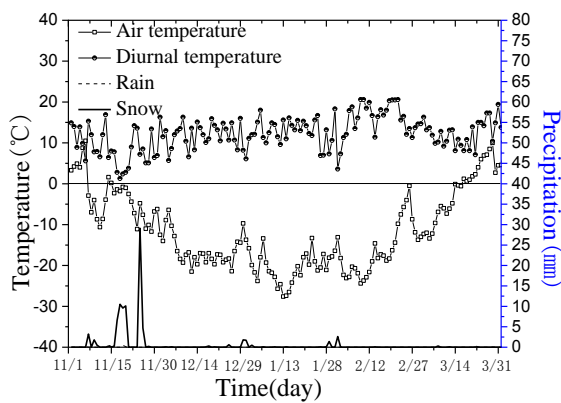


Nanchang

**Figure 2.** Meteorological data in a certain winter
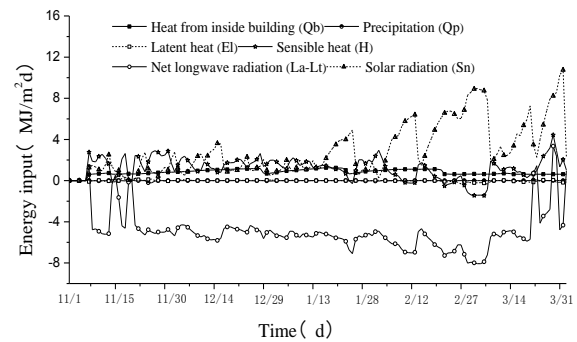


**Figure 3** Energy absorbed/released in a certain winter of Jiamusi
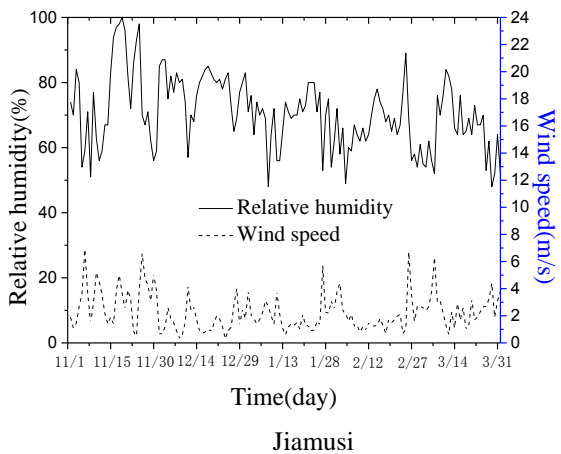


**Figure 4** Energy absorbed/released in a certain winter of Nanchang
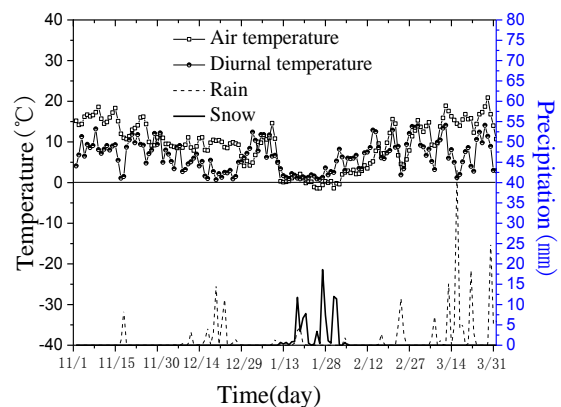


Jiamusi



Figure 5 depicts the air and snow temperatures in Jiamusi and Nanchang. It can be seen that snow temperatures variation differs from that of external air temperature to a certain extent. This result can be attributed to the influence of radiation, wind speed, and humidity on snow energy content, although air temperature does affect it significantly. Throughout winter, the air temperature in Jiamusi is significantly lower than 0 °C according to Figure 5, which facilitates the accumulation of snow on roofs. The mean temperature of snow fluctuates with air temperature. Snow is a poor heat conductor. When external temperature is lower than 0 ℃, snow temperature is relative higher for most of time. From the figure, Nanchang has a short snow accumulation period for its winter temperature is high.

**Figure 6.** Accumulated positive energy and events of snow sliding in Jiamusi



**Figure 7.** Accumulated positive energy and events of snow sliding in Nanchang
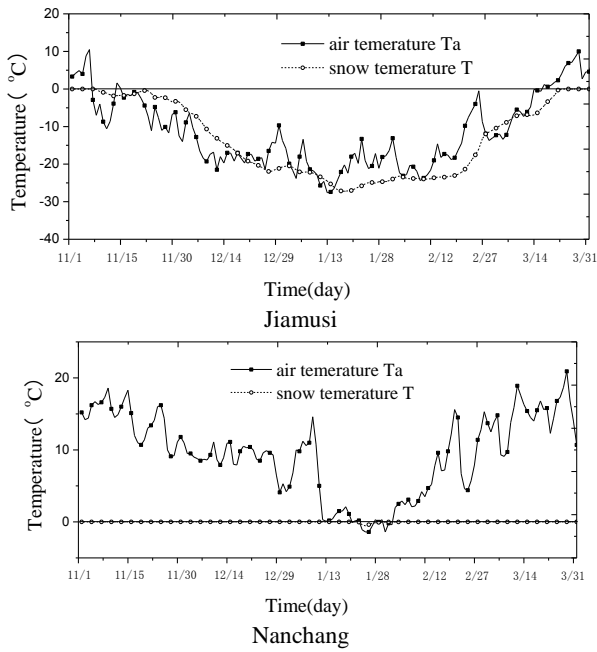
**Figure 5** Air temperature and snow temperature in a certain winter

## 4.2 Characteristics of snow sliding

The developed method is used to simulate the slide snow loads on several sloped roofs. The differences in snow-slide mechanisms between Jiamusi and Nanchang were analysed. Fig. 6 and Fig. 7 present the simulated results for accumulated positive energy and events of snow sliding in two presentative regions. From Figure 6 and Figure 7, we can compare the snow-sliding events in Jiamusi and Nanchang under the same roof slope. The sliding events in Jiamusi were found more evenly distributed than those in Nanchang. And these sliding events of Jiamusi were uncorrelated with snowfall. However, the sliding events in Nanchang were relatively concentrated and mainly occurred several days after snowfall. After snowfall, the air temperature in Nanchang generally increases, which induces the snow-slide. In addition, high-sloped roofs easily facilitated snow-sliding events so that the mass of sliding decreases significantly. The phenomenon corresponds to the proposed sufficient condition on sloped roofs, in which roofs with high slopes facilitate sliding events for small accumulated positive energy is needed.

As roof slope increases, sliding events remain still concentrated in Nanchang compared with those in Jiamusi. This difference is not only related to the concentrated snowfall in Nanchang, but also to their varied positive energy absorptions. According to Figure 6 and Figure 7, the positive energy absorption of snow after snowfall is much more in Nanchang than that in Jiamusi. Thus, snow accumulates for only a short period in Nanchang, whereas Jiamusi enjoys a long accumulation period.
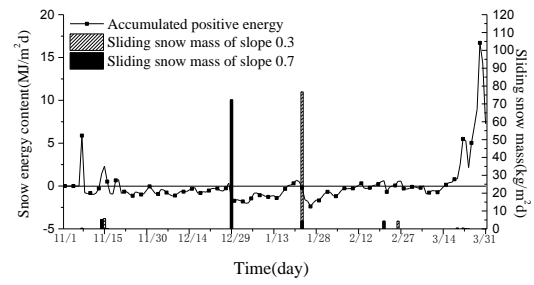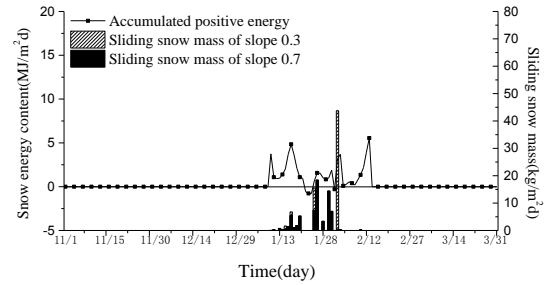
## 5 Simplified formula of sliding snow load coefficient

The sliding snow load coefficient is defined as the ratio of the snow load that slides from the upper roof to the total snow load on the upper roof. Figure 8 depicts the effect of roof slope on the sliding snow load coefficient. The heat transfer coefficient of the roof is 0.4 W/m$^2$·k, and PSA is 0. PSA is defined as the ratio of the blocked area on a roof to the entire roof area. The coefficients obtained from the Canadian code (National Research Council of Canada, 2005), European code (British Standard Institution, 2003), and ASCE standard (American Society of Civil Engineers, 2010) are constant at 0.5, 0.5 and 0.4, respectively. The sliding snow load coefficients decrease quickly with the increase in roof slope when roof slope is lower than 0.5 (26.6°); when roof slope is larger than 0.5 (26.6°), these values decrease gradually. In general, the sliding snow load coefficients of both the northern and southern regions vary significantly with the change of roof slope.
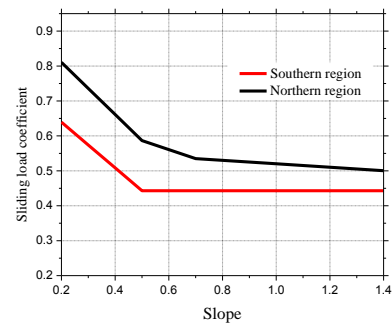


**Figure 8.** Sliding load coefficient as a function of slope

Given the differences in the sliding snow load coefficients between the northern and southern regions of China, the following simplified formula was obtained [3]. For northern regions,

$$
\begin{cases}
(0.45-0.35\times\alpha)\times(1.35+0.15\times PSA)\times(1.7-0.3\times K) & 0\le\alpha\le0.5 \\
(2.88-0.25\times\alpha)\times(0.43+0.02\times PSA)\times(0.5-0.1\times K) & \alpha>0.5
\end{cases}
\tag{3}
$$

For southern regions,

$$
\begin{cases}
(0.4-0.34\times\alpha)\times(1.8+0.4\times PSA)\times(1.15-0.2\times K) & 0\le\alpha\le0.5 \\
0.23\times(1.8+0.4\times PSA)\times(1.15-0.2\times K) & \alpha>0.5
\end{cases}
\tag{4}
$$

where $\alpha$ is the roof slope, which is defined as the change in the vertical direction divided by the corresponding change in the horizontal direction; PSA is the shield rate at which adjacent buildings shield the upper roof; $K$ is the heat transfer coefficient of the roof (W/m$^2$k).

# 6 Conclusions

This study applies a new method to simulate sliding snow load on sloped roofs based on the snowmelt model for building roofs presented by Zhou et al. (2015). The simulation of sliding snow loads for two regions in China was performed and their characteristics of representative regions were analyzed. The sliding events in the northern regions, which were uncorrelated with snowfall, were more evenly distributed than those in the southern regions. However, the sliding events in the southern regions were relatively concentrated and mainly occurred several days after snowfall. The distribution of these events in the southern regions remained concentrated even with an increase in roof slope.

# Acknowledgements

# References

1. Sack RL, Arnholtz D, Haldeman JS, Sloped roof snow loads using simulation. Journal of Structural Engineering, ASCE, 113 (8): 1829-1833 (1987)
2. Lepage MF, Schuyler GD, A Simulation to Predict Snow Sliding and Lift-off on Buildings, Proceedings of the Engineering Foundation Conference on a Multidisciplinary Approach to Snow Engineering. Santa Barbara, California (1988)
3. Takakura M, Chiba T, Ito T, Tomabechi T, On the Term Controlled by Snow Load: Practical Use of Snow Sliding on Pitched Roof. Journal of Structural and Construction Engineering, Transactions of AIJ 528: 53-57. (2000)
4. Isyumov N, Mikitiuk M, Sliding Snow and Ice from Sloped Building Surfaces: Its Prediction, Potential Hazards and Mitigation. The 6th Snow Engineering Conference, Whistler B.C., Canada (2008)
5. T. Chiba, T. Tomabechi, T. Takahashi, Study on evaluation of snow load considering roof snow-slide on gable roofs. *Snow Engineering VII*, Fukui, Japan, 231-241, (2012).
6. X.Y. Zhou, Y.Q. Zhang, M. Gu, J.L. Li, Simulation Method of sliding Snow Load on Roofs and its application in Some Representative Regions of China. Nat. Hazards **67**, 2: 295-320, (2013).
7. X.Y. Zhou, J.L. Li, M. Gu, L.L.Sun, A new simulation method on sliding snow load on sloped roofs, Nat. Hazards, **77**, 1 : 39-65, (2015).

# Experimental study of the distribution of snow deposits on the surface of structures with complex three-dimensional shape of the roof

Poddaeva Olga[1], Pavel Churin[1a]

[1]Moscow State University of Civil Engineering (Mgsu) Yaroslavskoe shosse, 26, Moscow, 129337, Russian Federation

**Abstract.** Currently, due to the modern trends of architecture in our country unique buildings such as trade, exhibition and business centres, sports arenas, airport complexes, and others are being actively constructed. One of the key features of such structures is a complex spatial geometric shape of the roof, which together with the peculiarities of the Russia climate make the need for accurate accounting snow load at design significantly increase. This article describes an experimental study of the snow deposits distribution on the structures surface with complex three-dimensional roof shape by the example of the airport complex in the Rostov-on-Don city, which is being built for the World Cup.

## 1 Investigated object and problem analysis

A site is located at Russian Federation, Rostov region. A new terminal construction is associated with the air network expansion and provides international passenger transport services.

As it seen from Figure 1, the most difficult and interesting airport terminal part in terms of aerodynamics and the snow load studying is the roof as it has a complex three-dimensional shape with a bending in all the directions, the exact reproduction of such forms is possible only by using the advantage of 3D printing.





**Figure 1.** Airport complex in the city of Rostov-on-Don

Snow cover consists of solid precipitation in winter and ice crust and the water formed during the thaw. Depending on climatic conditions, snow can have a

different thickness and density. The product of thickness and density gives the snow mass on area unit, i.e. snow load on the ground that defines a basis for snow load on the roof.

The normative document that regulates the accounting impact of snow on structures in the Russian Federation is the SP 20.13330.2011 "Loads and effects"[1]

Statistical methods allow establishing design values of snow load on the ground by the results of meteorological observations. Snow load on the roof is formed by a number of additional factors, them interconnection is needed to be taken inter account. Full snow load acts on buildings and structures, where snow accumulates throughout the winter. Let's consider the four main factors that determine the value of the snow load on the buildings surfaces:

- amount of falling in the winter solid precipitation (details are provided in Annex G SP 20.13330.2011);
- snow falling from the inclined surfaces;
- melting snow on the surfaces of heated buildings
- transport of snow as a result of wind action, leading to non-uniform deposits on the coating surface and the demolition of some fallen snow from a coating.

Moving snow under the wind influence is a major factor, due to which the level of the snow load is not the same for the cover area. As a result of snow transport the places where snow imposed and places with snow accumulation (the so-called snow bags) arise. The location of these sites is due primarily to the configuration of the surface coating (his profile) and with the wind direction on the other hand. These phenomena are studied by simulation in the wind tunnel, as well as through natural observations of snow deposits on real roofs. The research results are displayed in the norms given load factor of transition from the ground to the load to the load on the cover.

Schemes of snow deposits distribution which listed in Annex G to SP 20.13330.2011 (as, indeed, in other standards, such as Eurocodes [2]) cover only a limited set of the most common forms of coatings, while often problems arise on account of the snow load on other forms of roofing or clarify the data provided in norms due

[a] Corresponding author: pashok_@inbox.ru

to the need of specification of bearing ability. It is necessary to take into account two factors that have been used in the preparation contained in the norms unified design schemes of loading the snow:

− it assumed approximately uniform distribution of the winds from the characteristic directions;
− it used the balance ratio, which consists in the fact that the amount of snow in a snow bag equal to the volume of snow, demolished with the overlying section.

Based on these assumptions and the provisions of the regulations set out below in difficult cases we can recommend an approach to the estimation of the maximum possible value of the snow bag, based on the completely filled it with snow.

The obvious unpredictability of the snow cover value has led to an understanding of its random nature and the need to use statistical methods for the design values of snow loads determination on the basis of natural observations and modeling in a wind tunnel.

Current regulations SP 20.13330.2011 "Loads and effects" were developed on the methodological basis, where as the raw statistical data used yearly highs weight of snow cover according to the data snow surveys at sites protected from the effects of wind. Full standard value of snow load on the horizontal projection of the cover is equal $S = S_0\mu$, where $S_0$ is a standard value of snow cover weight per 1 $m^2$ of horizontal earth surface; $\mu$ is a conversion factor from the weight of snow cover on the ground surface to the snow load on the cover.

In the formation of snow load even on the covers single-span buildings there is a nonuniform deposition of snow on the bi-coatings, as well as deflation and falling from the snow surface coatings. These phenomena are taken into account by means of the coefficients $\mu$ listed in the regulations of most countries, depending mainly on the slopes of coatings and present differences of heights.

Determination of snow loads on structures nontraditional forms and/or unusual scales may lead to a number of new issues. A wind tunnel simulation is used for the snow load determination. Based on the results of physical experiment a zoning of complex roof for primitives that are presented in the regulations [1] is performed.

According to SP 20.13330.2011 - "Loads and effects." P. 10 "Snow load", p. 10.1, Note 2: for spatial coatings of complex geometric shapes and coatings having the largest characteristic dimension in the plane of more than 100 m, their snow load distribution scheme is necessary to determine with test data based on a specially developed recommendations.

## 2 Layout

For experimental studies a model of the passenger terminal of the airport complex was designed and manufactured. Considering the wind tunnel working part size, the best possible scale of layout was chosen that is 1: 250.

**Table 1.** Comparison of the main characteristic of the model and the size of the full-scale object.

| Overall dimension | Model | Full-scale object |
|---|---|---|
| length, mm | 1322 | 331200 |
| width, mm | 906,5 | 226700 |
| height, mm | 132 | 33213 |

The main requirement to the model for aerodynamic testing is a strict observance of the geometric similarity of the object under study. To meet this requirement at the stage of layout design based on the raw data provided by the customer the album design drawings was created.

Walls of model are made of plywood. Columns and roof support are made of a steel wire and aluminum plates (Figure 2).



**Figure 2.** Layout framework

Elements of the roof due to the complex spatial geometric forms were made on 3D printer Cube Pro (Figure 3).



**Figure 3.** 3D Printer Cube Pro and roofing element.

After the assembly of all the elements of the layout, the layout was painted matt black to enhance the results of photographic phenomena snow transport and snow deposits (Figure 4).



**Figure 4.** Painting layout.

# 3 Test procedure

Research was carried out in the Boundary Layer Wind Tunnel of Moscow State University of Civil Engineering (Figure 5). This plant has a closed circulation loop and modular fan unit of the nine units, with the length of the working zone of 18.9 meters.



**Figure 5.** Boundary Layer Wind Tunnel of Moscow State University Of Civil Engineering

The research method of the main regularities experimental determination of snow transport and snow deposits formation on roofing construction objects coverings is based on the following actions:

1. The model is rigidly mounted in the working area of the wind tunnel on the turntable;
2. Rotation angle of the relative to the direction of the oncoming flow is set to mark 0˚;
3. The surface model is cleaned of extraneous elements such as dust, sawdust, wood flour residues and so forth.
4. The uniform layer of model material (brand 200 wood flour, bulk density – 200 kg/m$^3$, humidity – 3,5-4%) with 1 to 1,5 mm thick is applied on model;



**Figure 6.** Model of the airport complex coated with a layer of modeling material

5. Engines start of a wind tunnel is made. The flow velocity increases uniformly from 0.1 to 7.6 m/s After the beginning of the phenomenon emergence the transport model material the speed of a stream is established by a constant and the purge proceeds before formation of characteristic snow deposits. The control of the beginning transport moment and the moment of snow deposits characteristic forms formation is carried out visually;

6. The work of engine wind tunnel stops, the experimental group captures results using a camera;
7. Position model changes according to the experimental plan. Repeat steps 3-6.

Characteristic speeds of a wind at which investigated snow transport on model in the range from 3,4 to 8 m/s. Modeling of snow is carried out by wood flour with a size of particles from 50 micron to 250 microns at humidity of 3,5-4% which is displaced from a smooth colored surface at a speed of wind of 3,4 m/s [3]. As a result of a long exposition of the model covered with a thin layer of wood flour in an air stream with a speed of 6-7 m/s the picture of snow deposits is formed. An analysis of the snow bags forms was performed for the zoning of the roof at the elementary entities for which the standard calculation of snow load [4].

Tests were carried out on a model scale of 1: 250 (Figure 3). When the model was under blowing from different directions the wind effect on creating of snow deposits was simulated in accordance with the wind rose for the region. In the experiment complete circular exposure to the wind direction with a step 45° was performed. Pictures at different wind directions were proposed (Figure 7-8), that can be used for data obtaining about the snow deposits phenomenon, directions and volumes of transported snow.



**Figure 7.** Model of airport complex



**Figure 8.** Typical areas of snow deposits, the angle of the incoming flow is 45°

# 4 Analysis of the results

Analysis of snow deposits allows to select specific zones as a result of increased snow deposits. On the surface of the roof there are always areas with elevated snow deposits determined by wind direction. Any portion of the roof may be in the area of high snow deposits depending on wind direction.

On the basis of the data provided by the Customer and data of the carried-out climatic analysis, the characteristic directions of wind in the Rostov region during the winter period are eastern (the angle of statement of model is 315˚) and western (the angle of statement of model is 135˚). For those directions and also for the direction 0˚, schemes of snow deposits at the airport complex roof surface are made.
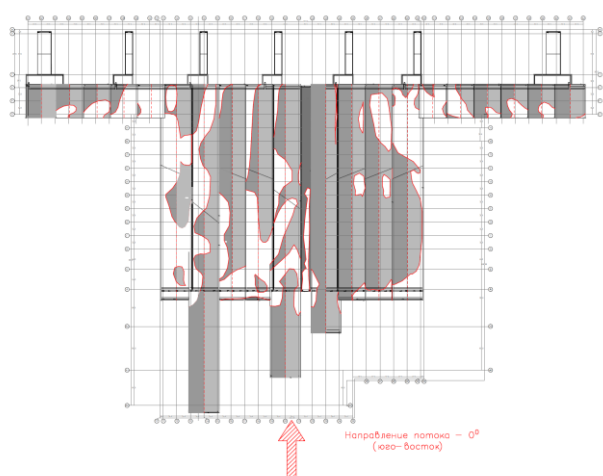


**Figure 9.** The scheme of distribution of snow deposits, flow direction - south-east - 0˚

Analysis of the results shows that for all elements of the roofing there is a flow direction in which this element will carry the maximum of snow load. Based on this, for the calculation of the snow load is necessary to consider the full picture of the snow covered roof. Figure 6 shows the zones indicating the wind direction at which the element receives the maximum snow load.
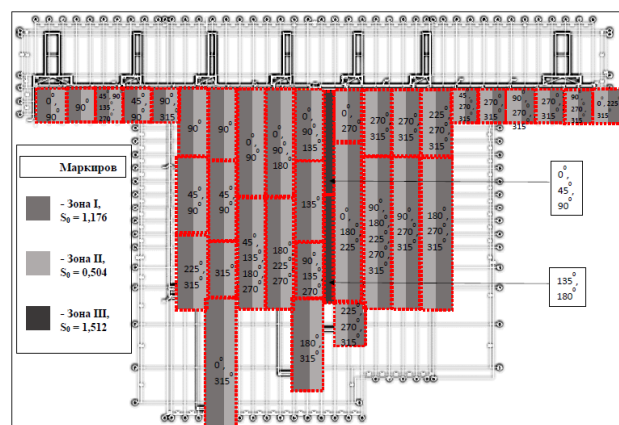


**Figure 10.** Zones indicating the wind direction at which the element receives the maximum snow load

# References

1. SP 20.13330.2011 - "Loads and effects."
2. EN 1991 Eurocode 1: Actions on structures
3. Xuanyi Zhou, Jinhai Hu, Ming Gu. Wind tunnel test of snow loads on a stepped flat roof using different granular materials // Natural Hazards. 2014. Volume 74, Issue 3, pp 1629-1648
4. E. Hjorth-Hansen, I. Holand, S. Loset, H. Norem Snow Engineering 2000: Recent Advances and Developments // CRC Press, 2000

# Theoretical and experimental study of ice accretion due to freezing rain on an inclined cylinder

Krzysztof Szilder

*Aerospace, National Research Council, Ottawa, ON, K1A 0R6, Canada*

**Abstract.** This paper reports on an investigation of ice formation on a cylinder exposed to freezing rain. Freezing rain icing is characterized by supercooled raindrop impingement, with vertical and horizontal velocity components, water flow over the surface driven by aerodynamic and gravity forces, and freezing or shedding of the surface water. In the first part of the paper, a novel, three-dimensional analytical model of ice growth on a cylinder is derived and the results are discussed. This is followed by a discussion of experimental tests in the NRC Altitude Icing Wind Tunnel. The experiments were constrained to horizontal drop impingement, and we encountered difficulties delivering large drops at low speed to the test section. Hence, the experiments were used primarily to validate the NRC morphogenetic ice accretion model. The morphogenetic model is a discrete element, random walk model that emulates the motion and freezing of individual fluid elements on the accretion surface. After validating the numerical methodology against the wind tunnel experiments, the model could be used to simulate ice formation under more realistic and general geometrical configurations and environmental conditions.

## 1 Introduction

Freezing rain consists of raindrops that become supercooled while passing through a sub-freezing layer of air. When these drops impact a surface at a sub-zero temperature, they partly freeze. The resulting ice can accumulate to a thickness of many centimetres during severe freezing rain events called ice storms. Although ice storms are not violent, they often cause power outages and tree damage, because of the weight of the ice accretions and wind-on-ice loads. In addition, the shape of ice accretions may alter the aerodynamics of transmission lines and bridge cables, causing large amplitude vibrations called galloping. Finally, pieces of ice falling from structures such as overhead transmission lines, wind turbines and telecommunication masts can cause serious injuries and property damage.

In order to better understand the physics of freezing rain and its consequences for engineered structures, more observations and controlled experiments are needed. In aeronautical icing wind tunnels, tiny drops are delivered to the test section by the horizontal flow and the drop trajectories are almost horizontal. In nature, however, freezing precipitation drops are larger and have a substantial vertical velocity component. Thus, there are limits to how accurately one can simulate ice formation due to freezing rain in a horizontal icing wind tunnel, designed for simulating in-flight icing. This discrepancy leads to different ice shapes in a wind tunnel and nature. In addition, in aeronautical icing wind tunnels, one encounters great difficulty delivering large drops characteristic of freezing rain to the test section. These differences lead to a different drop impingement domain and distribution than in the natural environment. Consequently, wind tunnel experiments can simulate only the "boundary conditions" of the environmental parameter space to which engineered structures are exposed.

Existing freezing rain ice accretion models are quite simplistic, often consisting of a couple of algebraic equations [1] and assuming simple two-dimensional geometry [2]. These models do not reflect the complexity of the ice accretion process. Instead of computing it, the ice accretion shape is assumed to have a simple geometrical form. Recognizing the scarcity of ice accretion experimental data [3-4] and the oversimplification of existing predictive models, the objective of this work is to develop a validated numerical model that can predict realistic ice accretion shapes under diverse freezing rain conditions. The focus of our current analysis is ice formation on a simple, but common, three-dimensional cylindrical geometry. Such a geometry can be found in a variety of engineered structures, such as transmission lines, telecommunication masts and bridge cables. In the future, the model can be readily extended to include more complex substrate shapes.

This contribution consists of three sections: development and analysis of an analytical ice accretion shape model that yields back-of-the-envelope estimates, experimental data collection in the National Research Council (NRC) Altitude Icing Wind Tunnel (AIWT), and validation of NRC's 3D morphogenetic icing model for experimental conditions.

Corresponding author: Krzysztof.Szilder@nrc-cnrc.gc.ca

# 2 Analytical model of ice accretion on a cylinder in 3D space

In this section, we examine the ice mass, its shape and its location on a cylinder under freezing rain conditions, in a three-dimensional configuration. We assume that the freezing rain drops are large enough to follow straight-line trajectories. In addition, the impinging precipitation is assumed to freeze promptly upon impact. There is no surface flow of liquid. These assumptions give a zero-order model of impingement and the ice accretion processes. This model can help identify where the freezing rain impinges and estimate extreme ice shapes, sizes and loads, under general geometrical configurations. Comparison between the predictions of this simple model and experimental or numerical results from more complex models will allow identification of the influence of physical processes, such as surface water flow, gradual water freezing, water shedding, and the formation of rough ice surfaces or voids in the ice structure. Such processes might occur in nature but they are not included in this zero-order approximation.

## 2.1 Freezing precipitation with vertical and horizontal velocity components

The drop trajectory direction is given by the droplet velocity, $\vec{V}$, which is the vector sum of the drop terminal velocity, $V_Z$, and the horizontal wind velocity with components $V_X$ and $V_Y$, Fig. 1. The effect of turbulence and slower changes in wind speed and direction are neglected here but they could be incorporated in the future. The present values could be considered as mean values, and a fluctuating or time dependent term could be added to each velocity component.

In order to represent the most general configuration of the cylinder relative to the precipitation impingement direction, we establish the coordinate system shown in Fig. 1. Without loss of generality, the axis of the cylinder lies in the y-z plane, but it is inclined to the x-y plane at the inclination angle $\omega$. It varies from 0° to 90°. The angle between the drop velocity vector and the vertical is called the precipitation angle, $\varepsilon$.

The impinging freezing rain mass per unit length of cylinder, m (kg/m), is given by:

$$m = P \sin \delta \; 2R \, \rho_w \qquad (1)$$

where: P is the equivalent depth of the approaching precipitation, (m) (depth if it accumulated uniformly on a plane perpendicular to its velocity vector); $\delta$ is the approach angle between the drop impingement direction and cylinder axis; R is cylinder radius, (m); and $\rho_w$ is water density, (kg/m$^3$).
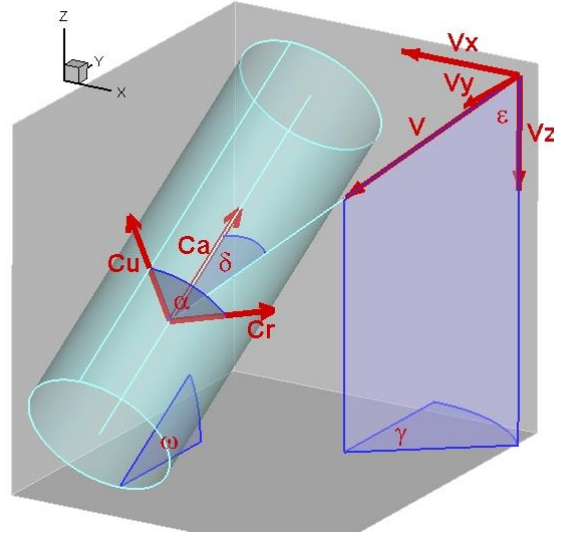


**Figure 1.** A sketch of the general geometry for freezing rain impinging on a cylinder.

The equivalent depth of precipitation P can be considered to be a vector with direction along the precipitation trajectory. It has vertical, $P_V$, and horizontal, $P_H$, components. The horizontal and vertical components are related by the precipitation angle:

$$P = \sqrt{{P_V}^2 + {P_H}^2} = \frac{P_V}{\cos \varepsilon}$$
$$where \qquad \tan \varepsilon = \frac{\sqrt{V_X^2 + V_Y^2}}{V_Z} \qquad (2)$$

It can be shown that the negative unit drop velocity vector, $-\widehat{V}$, and unit cylinder axis vector, $\widehat{C_A}$, are given by:

$$-\widehat{V} = [\sin \varepsilon \sin \gamma, \; \sin \varepsilon \cos \gamma, \; \cos \varepsilon \,]$$
$$and \qquad \widehat{C_A} = [0, \; cos\omega, \; sin\omega] \qquad (3)$$

where the yaw angle, $\gamma$, is defined as the angle between the projection of the precipitation velocity vector and the projection of the cylinder axis onto a horizontal plane. It varies from 0° to 180°.

The dot product of these two unit vectors gives the approach angle:

$$\cos \delta = \sin \varepsilon \, \cos \gamma \, \cos \omega + \cos \varepsilon \, \sin \omega \qquad (4)$$

Combining Equations (1) and (2) gives the expression for ice accretion mass as a function of precipitation and cylinder characteristics:

$$m = \lambda \, P_V \, 2R \, \rho_w \quad where \quad \lambda = \frac{\sin \delta}{\cos \varepsilon} \qquad (5)$$

where $\lambda$ is the overall impingement coefficient and the approach angle is given by Eq. (4). It should be noted that the impingement coefficient has the same value as the local collision efficiency at the stagnation point.

The cylinder area where ice forms can also be identified. Since the drop trajectories are assumed to be straight lines, impingement occurs on the half of the cylinder circumference that is exposed to drops. We will call the angle between the uppermost location on the cylinder cross-section, perpendicular to its axis, and the middle of the ice semicircle the maximum impingement angle, α, see Fig. 1. This angle is in a plane perpendicular to the cylinder axis and it should be also noted that ice accretion is homogenous along the length of the cylinder.

In order to find the maximum impingement angle, we examine the components of the negative drop velocity vector along the cylinder axis, $\overrightarrow{C_A}$ , and perpendicular to it, $\overrightarrow{C_R}$:

$$-\overrightarrow{V} = -[V_X, \ V_Y, \ V_Z] = \overrightarrow{C_A} + \overrightarrow{C_R} \tag{6}$$

Using second term of Eq. (3) and eliminating the magnitude of the cylinder axis vector gives components of the vector perpendicular to the cylinder axis:

$$\overrightarrow{C_R} = [-V_X, \quad (V_Z \cos \omega - V_Y \sin \omega) \sin \omega, \\ - (V_Z \cos \omega - V_Y \sin \omega) \cos \omega ] \tag{7}$$

The dot product of $\overrightarrow{C_R}$ and a vector perpendicular to the cylinder axis in the y-z plane $\widehat{C_U} = [0, -\sin\omega, \cos\omega]$ gives, with the help of first term of Eq. (3), the maximum impingement angle:

$$\cos \alpha = sign \left[ \left( \frac{\sin \gamma}{\cos \gamma \sin \omega - \cot \varepsilon \cos \omega} \right)^2 + 1 \right]^{-0.5} \\ where \\ sign = \begin{cases} -1 & when \ \tan \varepsilon \cos \gamma \tan \omega > 1 \\ 1 & when \ \tan \varepsilon \cos \gamma \tan \omega < 1 \end{cases} \tag{8}$$

From this location, the mass impingement amount decreases, following a cosine function of an angle in a plane perpendicular to cylinder axis, to vanish at the ± 90° locations.
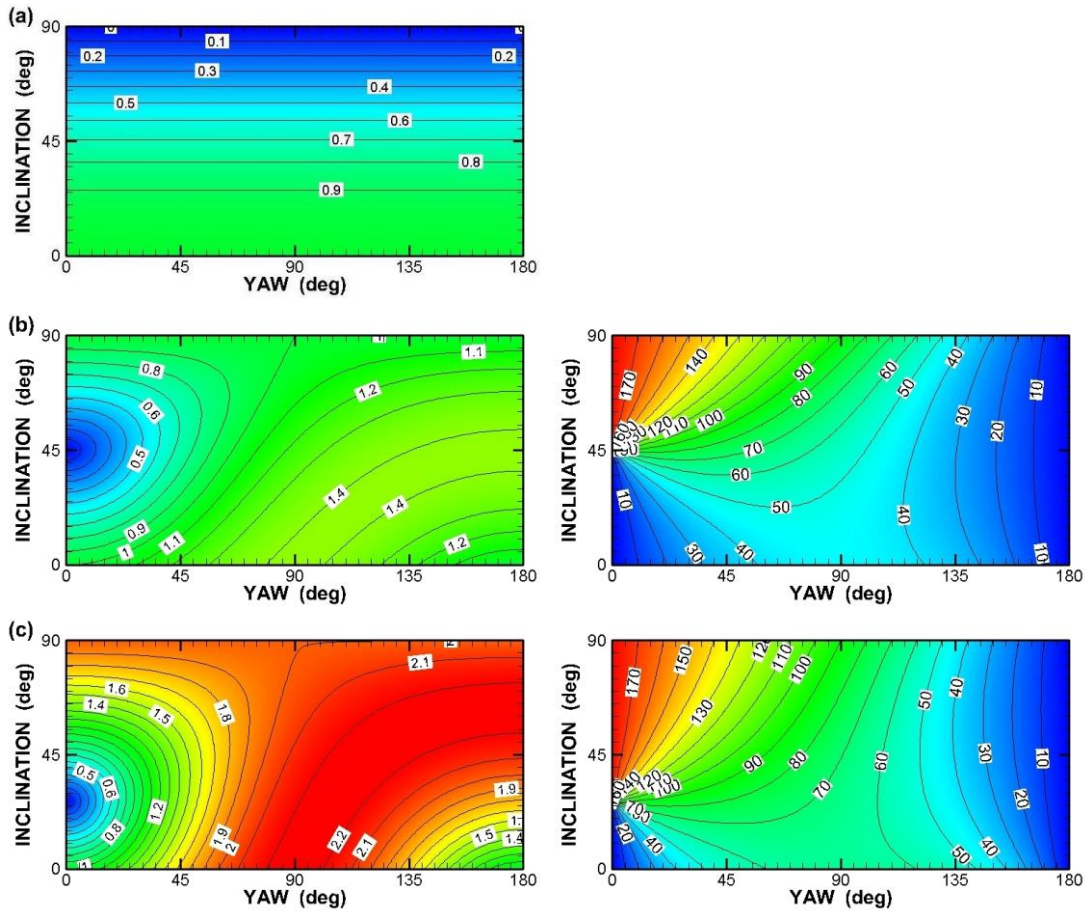


**Figure 2.** Impingement coefficient, λ, (left column) and maximum impingement angle, α, (right column) as a function of yaw, γ, and inclination, ω, angle.
    (a)   vertical precipitation, ε = 0°.
    (b)   horizontal speed equal to terminal speed, ε = 45°.
    (c)   horizontal speed twice terminal speed, ε = 63.4°.

Equations (5) and (8) have been used to examine ice accretion mass, shape and its location as a function of the precipitation angle, $\varepsilon$, yaw angle, $\gamma$, and inclination angle, $\omega$. Three cases have been considered: vertical precipitation, $\varepsilon = 0°$, Fig. 2a; horizontal velocity equals terminal velocity, $\varepsilon = 45°$, Fig. 2b; and horizontal velocity twice the terminal velocity, $\varepsilon = 63.4°$, Fig. 2c. Since the typical fall speed for drizzle is around 3.5 m/s and for rain is 6.5 m/s, in the extreme case, the wind speed would be approximately 50 km/h. For vertical precipitation, the precipitation yaw angle is meaningless and $\lambda = \cos\omega$, Fig. 2a. In addition, the maximum impingement angle is always 0°. When the cylinder is horizontal, $\omega = 0°$, the precipitation impinges perpendicular to the cylinder axis, and consequently, the impingement coefficient is unity. An increasing cylinder inclination angle leads to a decrease in the impingement mass per unit length of the cylinder. When the cylinder is vertical, $\omega = 90°$, drops do not impinge on the cylindrical surface (impingement on the cylinder ends is not included in this analysis), resulting in an impingement coefficient of zero.

Horizontal airflow enhances the impinging precipitation amount, P, for a given value of raingauge-measured precipitation, $P_v$, as given by Eq. (2). The case when the precipitation horizontal speed (which is assumed to equal the wind speed) equals the vertical terminal drop speed has been examined in Figure 2b. In addition, the ice shapes have been plotted for four inclination angles, Fig. 3, for a vertical precipitation amount equal to the cylinder radius, $P_V = R$. In order to obtain the ice shape it has been assumed that the initial growth rate does not change with time and that the ice grows radially away from the cylinder surface. For given inclination angle, the ice shape is displayed for varying yaw angle with five enhanced cross-sections at 0°, 45°, 90°, 135° and 180° that are depicted with a different circumference colour. The ice surface colour, with corresponding contour lines, depicts the local ice thickness. It should be noted that the accretion shape and thickness for given conditions is uniform along the length of the cylinder and the apparent longitudinal variations on Fig. 3 are the result of yaw angle variations.
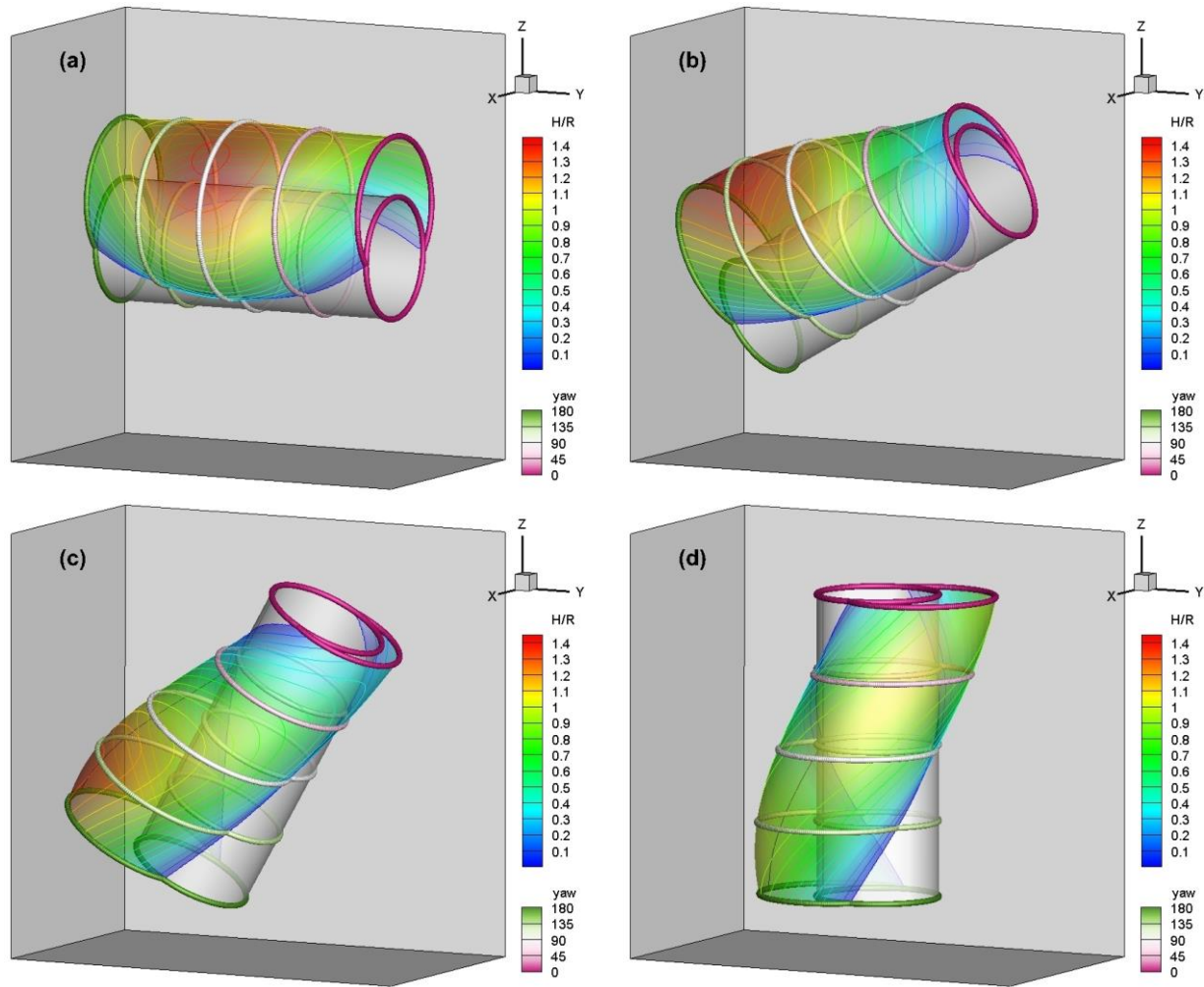


**Figure 3.** Schematic illustration of the influence of yaw angle on ice accretion shape for four inclination angles, assuming $\varepsilon = 45°$. H/R is the relative ice accretion thickness.
(a) $\omega = 0°$,  (b) $\omega = 30°$,  (c) $\omega = 60°$,  (d) $\omega = 90°$
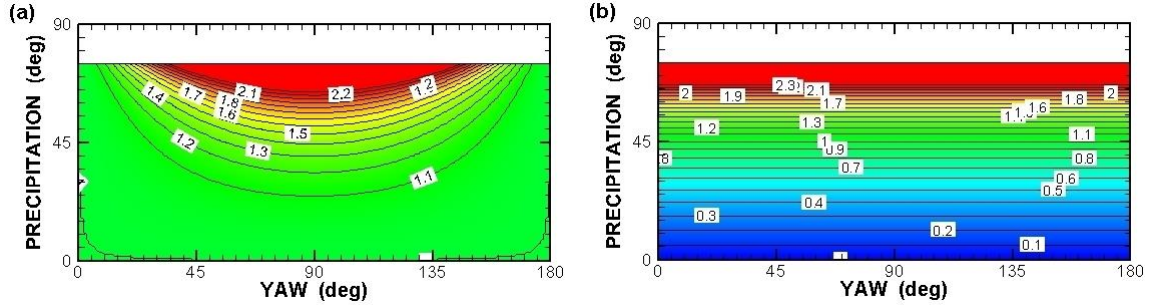
**Figure 4.** The impingement coefficient, $\lambda$, as a function of yaw angle, $\gamma$, and precipitation angle, $\varepsilon$.
(a) horizontal cylinder, $\omega = 0°$, (b) vertical cylinder, $\omega = 90°$.

For a precipitation angle of 45°, Fig. 2b, and for a horizontal cylinder, Fig. 3a, the solution is symmetrical about a 90° yaw angle. When the yaw angle is 0° or 180°, the impingement coefficient is unity since the impinging mass flux is enhanced by $\sqrt{2}$ but diminished by $\sqrt{2}$ because of the approach angle. For these two limiting cases, maximum impingement occurs at the uppermost point of the cylinder, Fig. 3a. When the yaw angle is 90°, the impingement coefficient is $\sqrt{2}$, because the approach angle is 90°, but since $\varepsilon = 45°$, the vertical precipitation is enhanced by a factor of $\sqrt{2}$. For this case, the maximum impingement occurs 45° from the vertical, as can be seen in the right-hand image of Fig. 2b. The ice shapes and thickness for all yaw angles are depicted in Fig. 3a.

For a cylinder inclination angle of 30°, Fig. 3b, changes of yaw angle have a more pronounced effect on accretion mass and shape than in the horizontal cylinder case, Fig. 3a. When the yaw angle is 0°, the impinging water mass is small, since the incoming drop direction lies only 15° from the cylinder axis. Increasing the yaw angle leads to an ice mass increase; it reaches a maximum for a yaw angle of approximately 125°, Fig. 2b, when the maximum impingement angle is approximately 35°. A further increase of yaw angle diminishes the impinging mass; for a yaw angle of 180°, the ice accretion is symmetrical about a vertical plane. Associated ice shape changes are depicted in Fig. 3b. For a cylinder inclination angle of 60°, variations in the impinging mass are somewhat similar to the $\omega = 30°$ case, but the ice location is markedly different for yaw angles smaller than 90°. For low yaw angles, ice forms underneath the cylinder. Finally, for a vertical cylinder, a change of yaw angle leads only to a change in the ice location, but the ice mass is independent of yaw angle, Fig. 3d.

When the horizontal velocity is increased twofold, $\varepsilon = 63.4°$, the impingement coefficient increases, Fig. 2c. The precipitation amount is enhanced by a factor of $\sqrt{5}$, see Eq. (2). When the cylinder is horizontal and the yaw angle is 90°, the impingement coefficient has a maximum value of $\sqrt{5}$. For a vertical cylinder, the impingement coefficient decreases to 2. For a yaw angle of 180°, the maximum precipitation occurs when $\omega = \varepsilon$. Conversely, for a yaw angle of 0°, zero precipitation occurs when $\omega = 90°-\varepsilon$. These last two statements are valid for any precipitation angle.

Horizontal and vertical cylinder configurations have also been analysed as a function of yaw and precipitation angle, Fig. 4. The horizontal case is symmetrical about a yaw angle of 90°, for which $\lambda = 1/\cos \varepsilon$. A high value of horizontal velocity leads to a precipitation angle increase and rapidly increasing impingement coefficient. However, when the wind blows along the cylinder, corresponding to yaw angle of 0° or 180°, the impingement coefficient remains unity. For a vertical configuration, the impingement coefficient is not a function of yaw and $\lambda = \tan(\varepsilon)$, Fig. 4b. Consequently, an increase of precipitation angle leads to an initially gradual but then a more dramatic increase in impinging precipitation mass.

The above analysis is valid for an outdoor environment where it can be assumed that vertical precipitation is the input parameter. However, in order to examine ice accretion in a horizontal wind tunnel configuration, the above analysis has been modified.

## 2.2 Freezing precipitation with only horizontal impingement

Since the experimental validation was performed in a horizontal icing wind tunnel, we will now consider the analytical model for horizontally incoming precipitation. We assume now that horizontal precipitation, $P_H$, is the input parameter and $\varepsilon = 90°$. An analysis similar to that described in the previous section, which led to Eq. (5), now gives:

$$m = \lambda \, P_H \, 2R \, \rho_w \tag{9}$$

$$where \quad \lambda = \sin \delta \quad and \quad \cos \delta = \cos \gamma \cos \omega$$

In addition, the maximum impingement angle function assumes the following simpler form:

$$\cos \alpha = sign \left[ \left( \frac{\tan \gamma}{\sin \omega} \right)^2 + 1 \right]^{-0.5} \tag{10}$$

$$where \quad sign = \begin{cases} -1 & when \quad 0° \leq \gamma \leq 90° \\ 1 & when \quad 90° < \gamma \leq 180° \end{cases}$$

Graphics of the solutions to Eqs. (9) and (10) are given in Figures 5 and 6. When the yaw angle is 90°, the cylinder inclination angle does not influence the impingement coefficient. It is equal to its maximum value of unity,

since the impingement direction is always perpendicular to the cylinder axis, Fig. 5. The maximum impingement angle also remains constant at 90°. The resulting ice shapes can be seen in Fig. 6, for four different cylinder inclination angles, for the case when $P_H = R$. It may be noted that the ice shape is independent of inclination angle for a 90° yaw angle. Figure 5 shows that the solution is symmetrical about a yaw angle of 90°.

However, when the yaw angle is less than 90°, impingement occurs on the lower part of the cylinder. Consequently, the maximum impingement angle varies between 90° and 180°. For a yaw angle larger than 90°, impingement occurs on the upper surface. For a horizontal cylinder with a precipitation yaw angle of 0° or 180°, drops do not impinge on the cylinder and consequently, the impingement coefficient is zero.
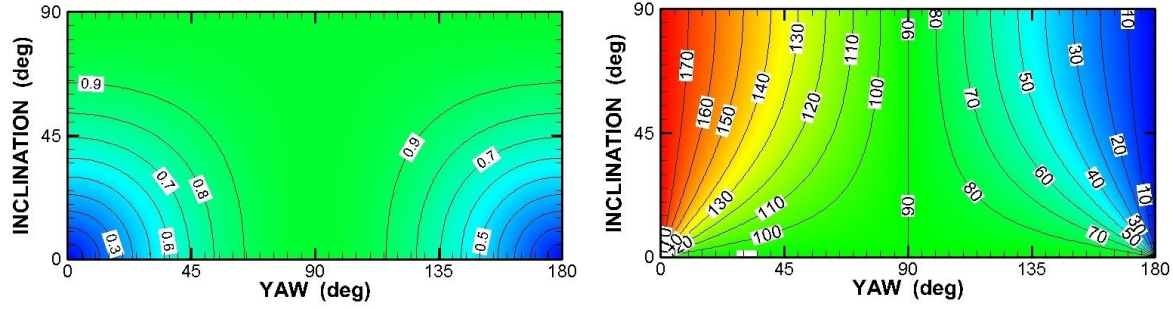


**Figure 5.** The impingement coefficient, λ, (left) and maximum impingement angle, α, (right), as a function of yaw, γ, and inclination, ω, angle for horizontal precipitation.



**Figure 6.** Schematic illustration of the influence of yaw angle on ice accretion shape, for four inclination angles, assuming horizontal precipitation impingement. H/R is the relative ice accretion thickness.
(a) ω = 0°,  (b) ω = 30°,  (c) ω = 60°,  (d) ω = 90°.

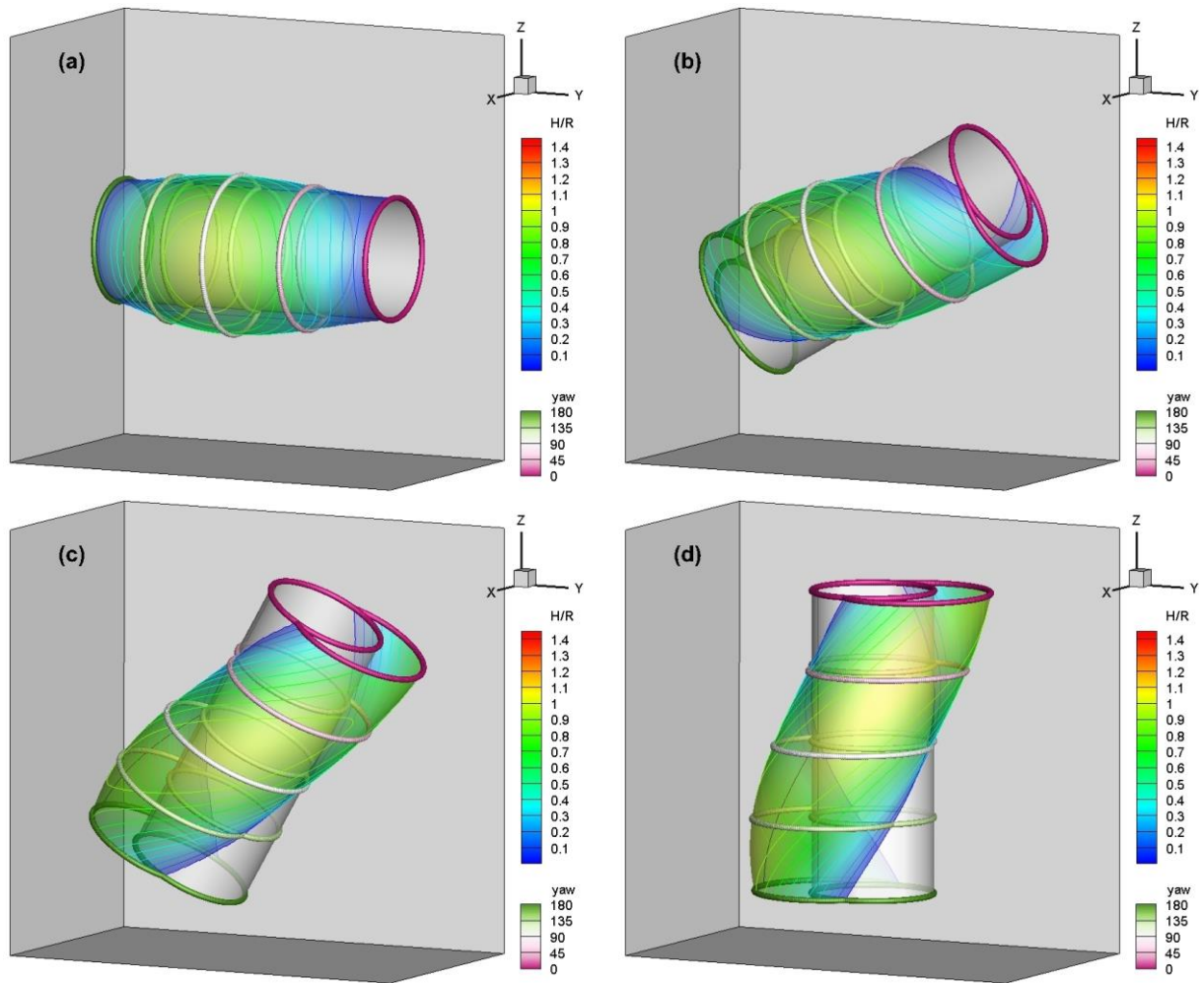Figure 6 depicts the ice shape profiles/cross-sections for four cylinder inclination angles and a continuously varying yaw angle.

# 3 Ice accretion laboratory experiments

The ice accretion experiments were performed in the NRC Altitude Icing Wind Tunnel (AIWT), which is a specialized, closed-loop wind tunnel designed to simulate an in-flight atmospheric icing environment [5]. In the tunnel test section of 57 by 57 cm, a cylinder of diameter 5.08 cm was placed vertically and at an inclination angle of 30° with varying yaw angle with respect to practically horizontally incoming precipitation. All horizontal icing wind tunnels, including AIWT, have difficulties to deliver large drops that are characteristic of freezing rain to the test section. Consequently, smaller drops of volume median diameter of 120 μm were produced and delivered to the cylindrical surface in an airflow of 20 m/s. The air relative humidity was 80%, the airstream liquid water content was 0.26 g/m$^3$, and the tests were run at atmospheric pressure. The ice was grown for 30 min and the ice accretion shapes were observed and documented. The aim of these tests was to collect a sample of data that could be used to validate our analytical and numerical models. A more extensive experimental campaign with varying inclination angle, yaw angle and larger air temperature range is planned in the future.

In this section, the focus is on the experimental rate of ice growth at the stagnation line and its comparison with a simple thermodynamic model outlined below. In the subsequent validation section, we will describe other characteristics of the experimental ice shapes. Since the analytical model described in the previous section assumes instant drop freezing upon impingement, it is applicable only for very cold conditions. However, when water flows on the surface during warmer conditions, a model that includes thermodynamics should be applied. Figure 7 shows the ice growth rate at the stagnation line for all of the experimental cases. For each experimental test, the ice thickness was measured at three locations spaced 5 cm apart along the cylinder axis. The experimental results for a vertical cylinder are depicted as points in Fig. 7a. Decreasing air temperature leads to a gradual increase of the ice growth rate, which is consistent with the observation that, at lower air temperatures, less water is shed from the cylinder. When the air temperature was -15°C, no water shedding was observed and the ice thickness reached a maximum value. The inclined cylinder at 30° was exposed to incoming precipitation at various yaw angles and tests were run for air temperatures of -2°C and -5°C, Fig. 7b. The experimental results show limited variability as a function of yaw angle. However, the strong influence of air temperature could be seen, lower temperatures being associated with greater ice growth rates.

These experimental results were compared with a simple thermodynamic ice accretion model outlined below. It has been assumed that freezing is determined by convective and evaporative heat fluxes. Hence the rate of ice growth, $\dot{H}$ (m/s), is determined by the following heat balance equation:

$$\dot{H}\,\rho_I\,L_F = h(T_S - T_A) + h\,\frac{\varepsilon L_V}{pc_P}(e_S - RH\,e_A) \qquad (11)$$

where: $\rho_I$ is the glaze ice density, $L_F$ is the specific latent heat of freezing, $L_V$ is the specific latent heat of vaporization, $\varepsilon$ is the ratio of the molecular weights of water vapour and dry air, p is the static pressure in the freestream, $c_P$ is the specific heat capacity of dry air at constant pressure, $T_S$ and $T_A$ are respectively the ice accretion surface temperature and the air temperature, $e_S$ and $e_A$ are the saturation vapour pressures at $T_S$ and $T_A$, and RH is the air relative humidity. The convective heat transfer coefficient, h, is computed using the Frossling number, Fr, defined as the ratio of the Nusselt number to the square root of the Reynolds number, $Fr = Nu/\sqrt{Re}$. Based on the experimental results [6], we assume that for comparatively low Reynolds number and a realistic range of surface roughness, the Frossling number is equal to unity. The sloped line in Fig. 7a and the horizontal lines in Fig. 7b are graphical representations of Eq. (11) assuming a glaze density of 900 kg/m$^3$ and a surface temperature of 0°C. The agreement between the experimental points and this simple thermodynamic model is satisfactory.
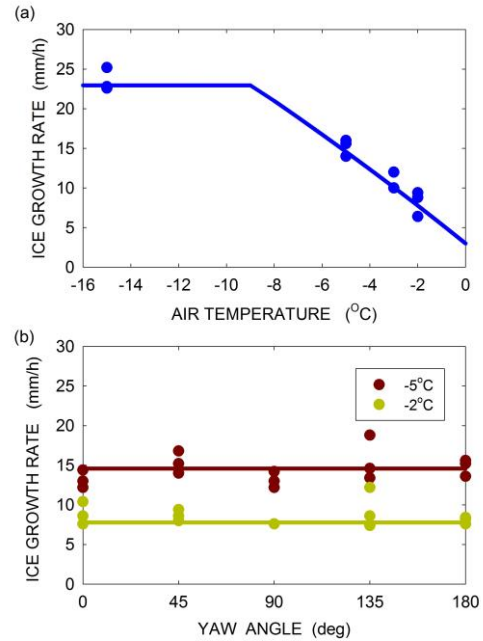


**Figure 7.** Experimental ice growth rate (points) and simple thermodynamic model prediction (lines) for the stagnation point.
(a) vertical cylinder, ω = 90º
(b) inclined cylinder, ω = 30º

Equation (11) gives the growth rate of ice thickness when there is sufficient water available to freeze. The maximum possible ice growth rate, $\dot{H}_M$, at the stagnation point is determined by the impinging liquid flux and given by:

$$\dot{H}_M\,\rho_{IR} = \beta_M\,V\,LWC \qquad (12)$$

where: $\rho_{IR}$ is the rime ice density at the stagnation point, $\beta_M$ is the collision efficiency at the stagnation point, and LWC is the liquid water content of the airstream. We have estimated a rime density of 750 kg/m$^3$ [7] and calculated $\beta_M = 0.92$ based on drop trajectory calculations for the experimental volume median drop diameter, air speed and cylinder radius. Equation (12) is depicted as the horizontal line on Fig. 7a. It, too, gives a reasonable agreement with experiments in the rime ice growth range.

## 4 The morphogenetic model and its validation for horizontal precipitation

We have already examined two models: the analytical model capable of ice mass and shape prediction when drops freeze on impact, and the thermodynamic model that predicts ice thickness at the stagnation line for rime and glaze conditions. Now we will discuss the NRC morphogenetic ice accretion model, which has a prediction domain that includes both mentioned models. In addition, the morphogenetic model can analyse cases with complex water flow and freezing on the surface, and it also predicts three-dimensional details of the ice accretion shape, mass and structure.
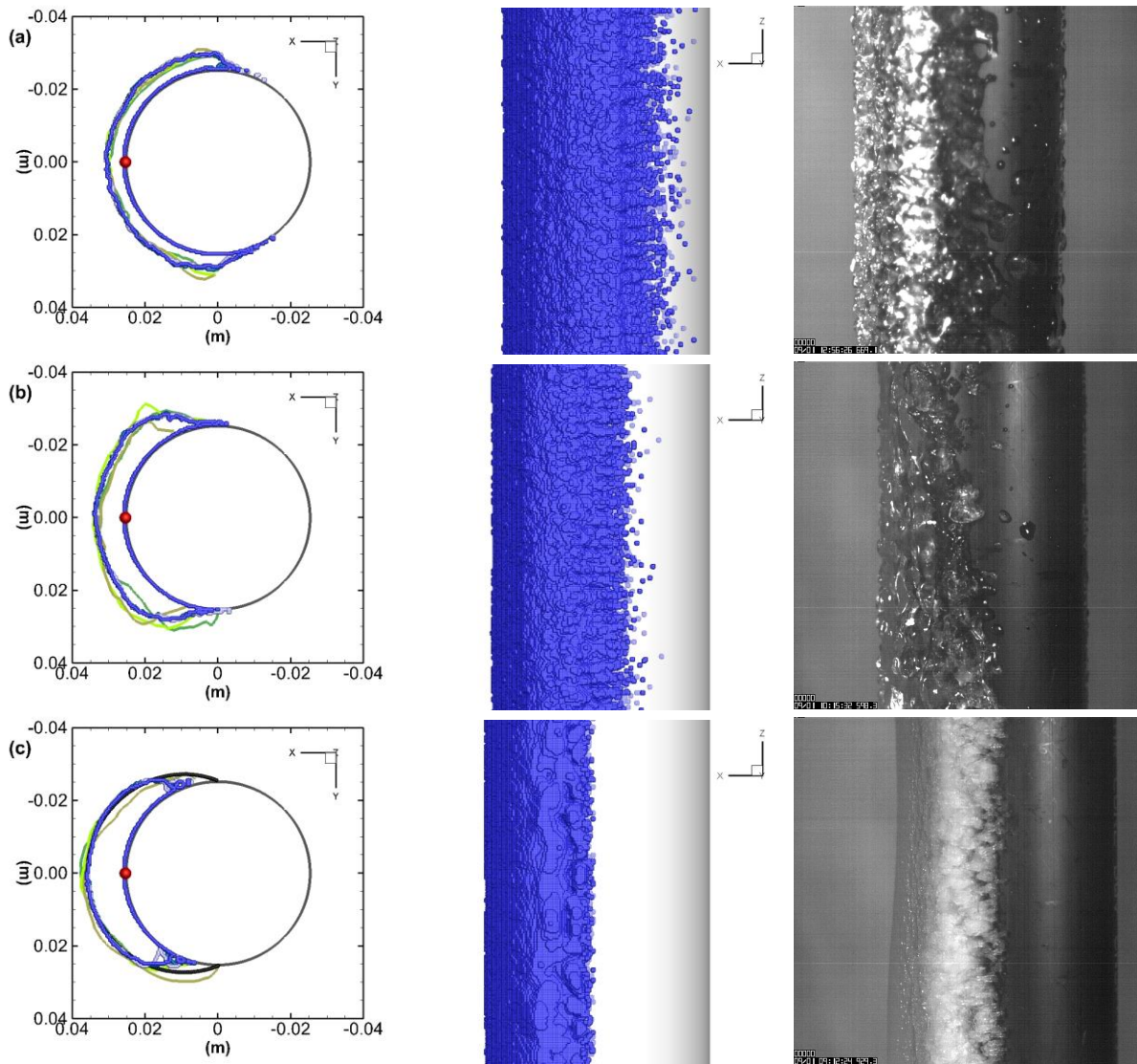


**Figure 8.** Comparison between morphogenetic model prediction and experimental ice accretion on a vertical cylinder. The first column shows three cross-sections, spaced 5 cm apart, produced by the morphogenetic model and depicted by the blueish lines. Three experimental ice cross-sections with the same spacing are represented by greenish lines. The red dot represents the stagnation line. The black line in (c) is the analytical model prediction. Side views of the numerical prediction and experimental ice are shown in the second and third columns, respectively.
(a) air temperature -2ºC, (b) air temperature -5ºC, (c) air temperature -15ºC.

The morphogenetic model was originally developed for aerospace in-flight icing applications (2D and 3D versions are described in [8] and [9], respectively). It has recently been modified to predict ice accretion shapes due to freezing rain precipitation. The main characteristics of our novel approach are described below. The morphogenetic model is a discrete element, random walk model that emulates the motion and freezing of individual fluid elements arriving at the accretion surface. Individual model fluid elements may be imagined to consist of an ensemble of drops, all of which undergo identical histories. However, each fluid element has a different history on the surface because of the stochastic nature of the model. A 3D rectangular lattice defines the accretion domain. Each fluid element begins a stochastic motion downstream along the surface from its initial impact location, which is also determined stochastically. At each step in the process, a random number is generated, and, according to its value, the element either freezes or moves along the surface. The model is sequential, so that as soon as a particular fluid element freezes, the behaviour of the next fluid element is considered.

Most of the results presented in this paper were obtained for a fluid element size of $0.4 \times 0.4 \times 0.4$ mm and a morphogenetic model domain of $200 \times 600 \times 600$ elements, giving $8 \times 24 \times 24$ cm in the horizontal x and y, and vertical directions, respectively. The fluid element size was chosen as a compromise between model resolution and computational effort. An extensive sensitivity analysis to fluid element size has not yet been performed for the three-dimensional version of the model. However, a sensitivity analysis for the two-dimensional version of the model [8] suggests that the principal, large-scale features of the ice accretion are not sensitive to a reduction in fluid element size. However, with smaller elements, additional, fine-scale details of the ice structure are revealed.

In this section, the NRC morphogenetic model is validated for ice-on-cable applications, using the experimental results described above for horizontal airflow and drop impingement. In this version of the morphogenetic model, we assume that the impinging fluid elements move along straight lines. The precipitation flux is given by the right hand side of Eq. (12). Using our experimental values, the flux is 4.78 g/m²-s. The duration of the simulation for all examined cases is 30 min. We also assume a Frossling number of unity, which determines the convective heat transfer coefficient.

Results of the numerical prediction and laboratory tests of ice formation on a vertical cylinder for three air temperatures of -2°C, -5°C and -15°C are depicted in Fig. 8. The morphogenetic model shows that, when the air temperature is -2°C, the heat transfer is sufficient to freeze approximately 35% of the impinging liquid at the stagnation point. The unfrozen water flows downstream and freezes gradually. Because the aerodynamic drag acting on the surface liquid greatly exceeds gravity, the water flows nearly horizontally on the surface. Once the drops reach locations beyond 90° from the stagnation point, they are gradually shed. For the -2°C case, 72% of the impinging water mass freezes on the cylinder and the

remaining water is shed. Our comparison between the numerical ice accretion cross-sections and the experimental cross-sections shows good agreement. However, the experimental results exhibit higher variability than numerical prediction. The comparison between the side views of numerical and experimental ice accretions is also good. When the air temperature is -5°C, freezing is enhanced, leading to greater ice thickness on the upwind side of the cylinder. In the model, approximately 70% of the impinging water at the stagnation line freezes instantly, and only 0.2% of the impinging water is shed from the cylinder. Once again, the agreement between numerical and experimental ice cross-sections and side views is good. For an air temperature of -15°C, all impinging drops freeze instantly in the model, and there is no flow of liquid on the surface. In this case, the cross-section comparison is confirmed by the analytical model, where all impinging water freezes instantly. The agreement between the morphogenetic, analytical and experimental results is good.

Figure 9 shows a comparison between the model and experiments for ice forming on a 30° inclined cylinder, at a yaw angle of 0°. Since the collection efficiency at the stagnation point for this case is 0.5, see Fig. 5, the total impinging liquid mass is half that for the vertical case. When the air temperature is -2°C, 70% of the impinging water at the stagnation line freezes instantly. Drops that do not freeze immediately upon impingement freeze downstream and there is no water shedding. In addition, the rapid freezing and the low approach angle of 30° lead to the formation of a rough ice surface. The numerical and experimental ice cross-sections exhibit diverse ice surface irregularities, but the overall agreement between them is good. These ice shape anomalies can also be seen in the three-dimensional numerical and laboratory ice accretion views, the second and third columns in Fig. 9. Since the model ice features are best seen in profile, we show profile images, despite the different angle of view for the experimental ice accretions. The model accretions show the three-dimensionality of the ice accretion process, with ice rivulets aligned with the external airflow. They also show the variability of the ice accretion shape on different geometrical scales. When the air temperature is -5°C, all impinging drops freeze almost instantly upon impact. However, due to the shadowing effect of the ice irregularities, the resulting ice shapes are rather complex. In the aircraft icing literature, this type of accretion is sometimes called "lobster tail" [9]. It is encouraging to note that the predicted and observed 3D features are similar, inasmuch as the cross-sections are rather "jagged" in both the model and experiment. Both the morphogenetic model and experimental ice structures are full of cavities, which increase the ice structure thickness. However, the analytical model, depicted by the black line in the first (b) column, predicts a smaller ice thickness, since it assumes solid ice (high density) without voids.
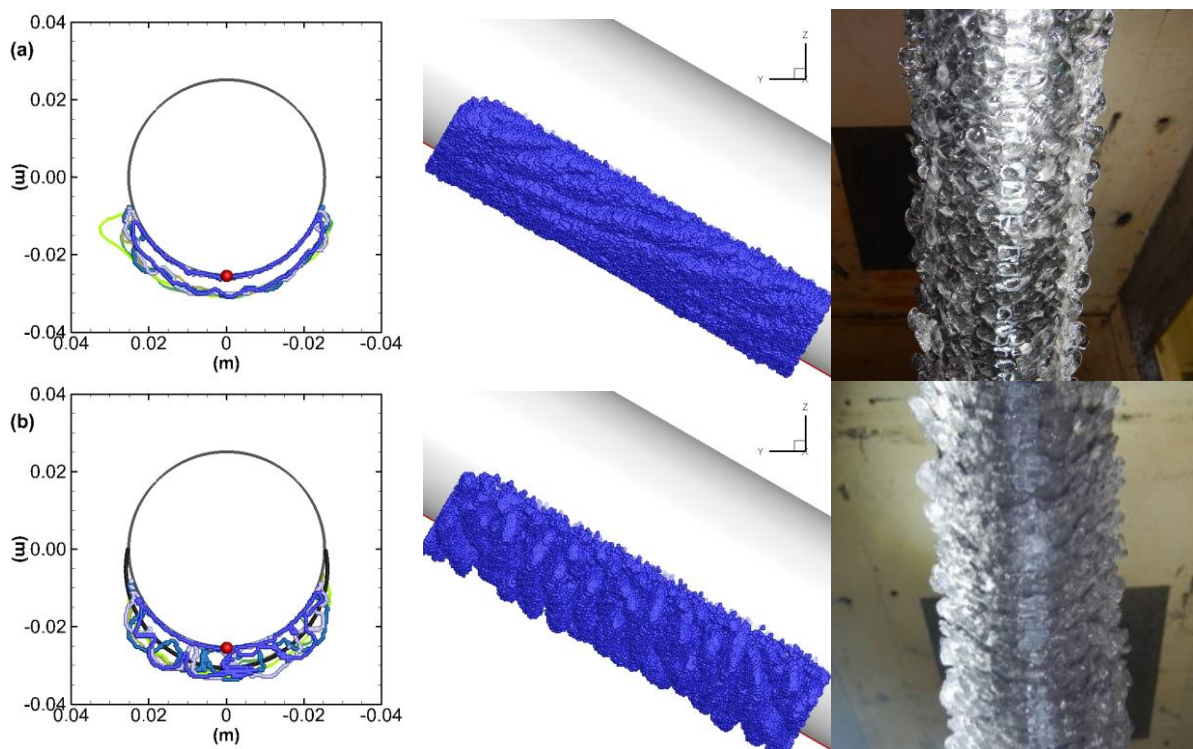
**Figure 9.** Comparison between morphogenetic model prediction and experimental ice accretion on an inclined cylinder (30° inclination angle) and with a yaw angle of 0°. The first column is described in the caption of Figure 8. The second column depicts side views of a 10 cm segment of the morphogenetic model simulation, and the third column shows the corresponding experimental ice accretions, seen from below.
(a) air temperature -2ºC, (b) air temperature -5ºC.

# 5 Conclusions

We have developed a morphogenetic numerical model that can simulate ice accretions on arbitrarily oriented cylinders exposed to freezing rain precipitation. This predictive model has been validated experimentally for a limited number of conditions in an aeronautical icing wind tunnel under horizontal droplet impingement. We have also developed a zero-order analytical model that identifies the location and size of freezing rain ice formation on a cylinder in a fully 3D geometrical space. This comparatively simple model assumes droplet freezing on impact, allowing swift identification of limiting ice shapes in a cold environment. The agreement between predictions of the morphogenetic and the analytical model for considered limiting conditions is satisfactory.

The validated morphogenetic model can be used to predict complex three-dimensional ice accretion shapes on overhead transmission lines, bridge cables, telecommunication masts or any other cylindrical objects exposed to freezing rain. This morphogenetic numerical model is not subject to the limitations of aircraft icing wind tunnels in trying to simulate freezing rain conditions. Although the model presented here was developed and validated for a cylindrical geometry, it could be easily extended to more complex geometries of engineering interest.

# Acknowledgement

# References

1. K. Jones, Ice Storms in the St. Lawrence Valley Region, ERDC/CRREL TR-03-1 (2003)
2. P. Fu, M. Farzaneh, G. Bouchard, Cold Reg. Sci. Technol. **46**, 132-146 (2006)
3. C. Demartino, H.H. Koss, C.T. Georgakis, F. Ricciardelli, J. Wind Eng. Ind. Aerodyn. **138**, 98 (2015)
4. L. E. Kollar, M. Farzaneh, Int J. Heat Mass Transfer, **53**, 849-861 (2010)
5. M. Oleskiw, F. H. Hyde, P.J. Penna. AIAA-2001-094 (2001)
6. E. Achenbach, Int. J. Heat Mass Transfer, **20**, 359-369 (1977)
7. W.C. Macklin, Q. J. R. Meteorol. Soc, **88**, 30-50 (1962)
8. K. Szilder, E.P. Lozowski. J. Aircraft, **41**, 834 (2004)
9. K. Szilder, E.P. Lozowski, SAE 2015 Int. Conf. Icing Aircraft, Engines, and Structures, 2015-01-2162 (2015)

# Parametric approach for assessing risks due to falling ice and snow

Jan Dale[1,a], Scott Gamble[1], Albert Brooks[1] and Jill Bond[1]

[1]*Rowan Williams Davies & Irwin Inc., 650 Woodlawn Road West, Guelph, Ontario, Canada N1K 1B8*

**Abstract.** Falling ice and snow from structures presents a significant challenge for building design in cold climate regions. The variables involved in the accumulation and subsequent shedding of snow and ice from a structure include building and feature geometry, thermal and surface characteristics, melt-water drainage paths, ambient air temperature fluctuations, solar radiation and wind forces. The transient and combined effect of these variables does not facilitate a discrete probabilistic prediction of the associated risks. As a result, there are no known standards or codes available to designers to provide guidance on addressing these concerns in design. This paper outlines a parametric approach for assessing the relative risks associated with falling ice and snow hazards for a range of façade details and climatic variables. The approach has been developed through a combination of scale model testing within a boundary layer wind tunnel, full scale testing in a climatic wind tunnel and numerical snow and ice accumulation models. The aim is to provide designers with a reliable approach to understand the risks associated with a particular design and the level of on-going maintenance efforts that will be required over the life of the structure to manage these risks and maintain a safe environment.

## 1 Introduction

Snow and ice accumulations which are shed from buildings and structures pose a significant hazard to pedestrians and property due to the associated large impact forces. However, snow and ice falling from structures into pedestrian areas remains a commonplace occurrence in cold climates. The key factors regarding whether the accumulations that are shed from a structure pose a serious risk are related to how massive the falling accumulations are and how often the events happen.

Ice and snow collection and the subsequent shedding can be influenced by, but is not limited to, air temperature, solar radiation and heat loss, insulation properties of accumulated snow, the cyclical freeze and thaw process created by daily temperature cycles and the orientation and surface friction properties of the materials. The transient and combined effects of these variables do not easily facilitate discrete quantification of all potential falling ice and snow scenarios. As a result, to the knowledge of the authors, there are no known criteria or guidelines for designers to assess acceptable performance considering falling ice and snow hazards. Rather, it is necessary to balance effective design detailing with on-going maintenance efforts over the life of the structure to effectively mitigate falling ice and snow concerns.

An approach for assessing the performance of a structure has been developed whereby building features that are identified through experience as sensitive to snow and ice accretion and shedding are evaluated. The approach relates the severity of a potential shedding scenario relative to that of a reference façade detail. The methodology involves an assessment of the magnitude of potential falling accumulations for a range of mean recurrence intervals. This is then combined with an estimate of the probability that a falling accumulation will impact either pedestrians or property before coming to rest to estimate the probability of a problematic shedding event. An estimate of the potential magnitude of this event relative to that of the reference façade detail is

used to determine a severity index associated with each façade detail. An example assessment result is shown in Figure 1. The following outlines the methodology proposed to provide design teams with adequate information to assess the performance of a structure.
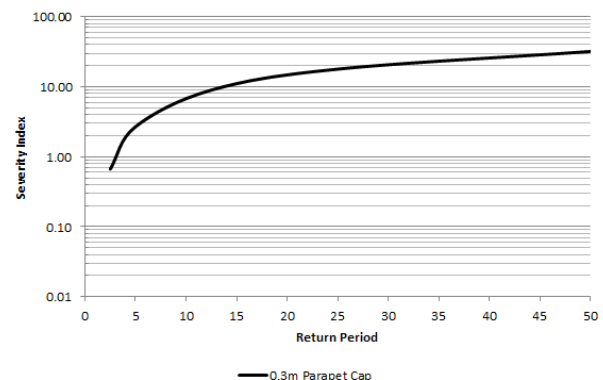


**Figure 1.** Example assessment result.

A combination of scale model testing within a boundary layer with tunnel, full scale testing in a climatic wind tunnel and numerical snow and ice accumulation models are used to provide insight into the relative risks.

## 2 Assessment of shedding severity

The random nature of many of the variables involved in the accumulation and subsequent shedding of snow from a building façade makes a deterministic solution to the mass and frequency of shedding almost impossible to achieve. Further, there needs to be the presence of pedestrians or property in the location of impact in order for an accumulation to pose a significant risk when shed from a structure. As such, the relative risks associated with falling accumulations are assessed through the introduction of a severity index. A probabilistic approach has been used to estimate the severity index at a level of

risk consistent with the design snow loading provisions for structural design.

## 2.1 Relative volume of accumulations shed from a façade surface

### 2.1.1 Accumulation magnitude

The potential risks associated with a falling snow event are directly related to the mass of the accumulation being shed. A relatively small accumulation falling from a building surface poses significantly less risk than a large dense accumulation. As a result, an estimate of the relative volume of potential falling accumulations has been used as the basis for the estimation of the severity of a shedding event.

As outlined in further detail in Sections 3 and 4, the effective depth of an accumulation is estimated based on the geometry and location of a particular façade detail on the building. Estimates of the effective depth of accumulation are derived based on the anticipated snow load combined with an average snow density of 3 kN/m$^3$. This density is representative of an aged or wind driven snow accumulation. The resulting effective cross section is then used to estimate the potential volume of an accumulation that may be shed from the façade.

The key uncertainty associated with the volume of an accumulation that may be shed from a structure it the length of piece that falls. Given the range of conditions that may lead to the shedding scenario, accumulations may be shed in relatively small pieces, or as a consistent mass equal to the length of the façade detail. For the purposes of comparison, it has been assumed that the potential length of accumulation that is shed from a façade detail is proportional to the effective cross sectional area moment of inertia of the accumulation.

## 2.2 Reference severity index

The shedding performance model relates the severity of a potential shedding scenario relative to that of a reference façade detail. For the purposes of this research, a 10cm wide horizontal ledge surface has been used as the reference as accumulations shedding from ledges of this size have historically been considered acceptable by building owners. While surfaces of this nature will collect and potentially shed snow and ice accumulations, the size and consistency of these are not known to have been problematic. Larger accumulations that fall from larger ledges have increased tendency to be considered inappropriate, and mitigation investigations are commonly sought as a result.

As the potential risk associated with a falling accumulation is dependent on the presence of pedestrians or property in the vicinity of the impact area, probability of hazardous conditions is the combined probability of having an accumulation and an estimate of the probability of impacting something of significance. As a reasonable estimate of an average condition for reference, it has been assumed that the probability of occupancy in the impact area is 0.25. Given this, the resulting reference return

period for snow accumulation to achieve an effective 50-year return period falling snow hazard event is 12.5 years. This is determined as follows:

$$R_A = R_{FH} * 1 / P_P \qquad (1)$$

Where : $R_A$ is the mean recurrence interval of the snow accumulation;

$R_{FH}$ is the mean recurrence interval of a falling snow hazard; and,

$P_P$ is the probability of persons or property in the impact area during a falling event.

The accumulation cross section for a 10cm wide ledge representative of a 12.5-year return period was determined based on historical meteorological information. The product of this cross section and associated moment of inertia was used as the reference for a severity index of unity. The ratio of the product of the effective cross sectional area and moment of inertia associated with other return periods and façade details to this reference magnitude is then used as the basis for comparison. This ratio is then scaled to account for the slope of the surface. A linear scale factor ranging from 1.0, for horizontal surfaces, to 10 for vertical surfaces has been introduced to account for the anticipated increase in shedding frequency for steeply sloped surfaces. The resultant is the severity index associated with a particular façade element.

Figure 2 shows a plot of the relative change in severity index for a 10cm ledge as a function of the return period of snow accumulation. As outlined, the effective 50-year return period falling snow event for the 10cm ledge, given a 12.5 year snow accumulation and 25% chance of having something of significance at the point of impact, has a severity index of 1.0. It should be noted that, the severity index of the same ledge detail would be increased if it were assumed that the ledge was located above an area where the probability of impacting something of significance was higher. For example, if it is assumed that an accumulation falling from the ledge would always impact something of significance, the severity index would be increased to approximately 3.5.
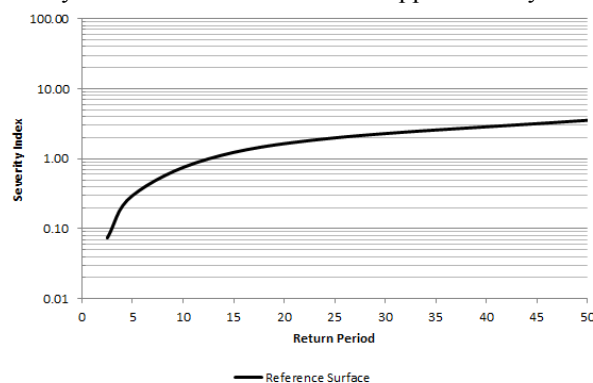


**Figure 2.** Severity index plot for reference surface.

The severity index may be associated with approximate operational impacts for the purpose of comparison of the performance of various façade details. In general, severity indices of 1.0 or less may be

considered to be indicative of small falling accumulations that are likely to be considered a nuisance, but not likely to cause harm. Façade details with severity indices ranging from 1.0 to 5.0 are considered to be small enough to be handled through effective operational and maintenance procedures such as clearing operations and reduced access to the impact areas. Larger chunks that could be expected to cause some safety issues or property damage are expected from façade details with severity indices ranging from 5.0 through 10. Façade details with severity indices above 10 are expected to experience large chunks that may be considered a significant risk to life safety or extensive property damage. Clearly, the better performing building would shed smaller chunks and/or shed less frequently.

# 3 Model simulation techniques

## 3.1 Climatic wind tunnel simulations

Climatic wind tunnel simulations are conducted on building façade mock-up sections to observe the accumulation and shedding characteristics of snow on various details. A range of variables including temperature, snow and ice consistency, effects of wind and façade geometry can be varied to gain an understanding of the overall performance of a particular design. Figure 3 shows an example of wet snow accumulations on a horizontal sunshade element during a climatic wind tunnel simulation.
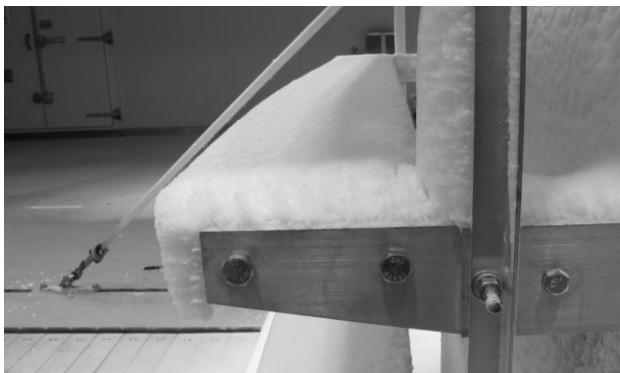


**Figure 3.** Example of snow accumulation on a sunshade during a climatic chamber simulation.

It should be noted that although there is a difference in simulated to natural snow, ice particles from the snow gun were assumed to attach to surfaces in a similar manner to the ice at the end of the fingers of a snow flake. The ambient temperature, snow gun air pressure and water discharge were varied to give a range of conditions to simulate the various types of frozen accumulations. Observations of snow accumulations on various full scale mock-up façade details were used throughout this research.

### 3.1.1 Effect of snow consistency

As it is not practical to simulate all of the combinations of frozen precipitation that may occur, a range of

conditions that bound the general range of snow characteristics are modelled. Simulations considering relatively dry snow and wet snow are typically conducted to observe any variation in accumulation and shedding characteristics.

As shown in Figure 4, dry snow simulations do not show significant accumulations. While accumulations are often observed, they tend to be limited in depth and not well adhered to the façade surface. As a result, these accumulations are expected to be either melted or shed from the surface in a manner that does not pose a significant concern.
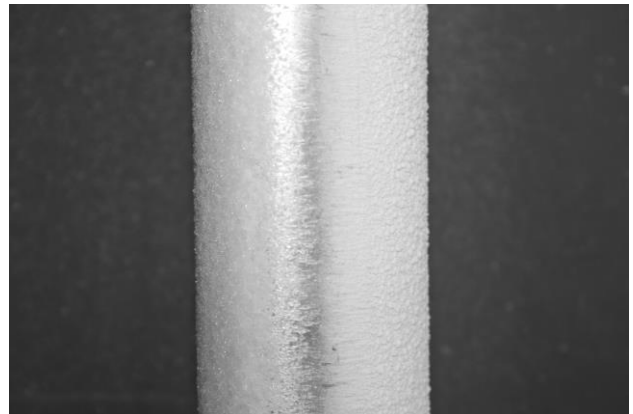


**Figure 4.** Example of dry snow accumulation on a mullion in a climatic chamber simulation.

In contrast, the observations in wet snow simulations, as shown in Figure 5, are significantly different. Windward façade details readily accrete snow. Further, the accumulations tend to be relatively dense. When shed from the façade sections, the accumulations that form as a result of wet snow applications tend to remain relatively well intact. As a result, accumulations under these conditions are likely to be relatively more severe than those for dry snow events.



**Figure 5.** Example of wet snow accumulation (after partial shedding) on a mullion in a climatic chamber simulation.

It should be noted that, the simulations shown in Figures 4 and 5 were conducted using similar snow application rates and durations. The only significant change to the simulation was the consistency of the applied snow.

### 3.1.2 Capture efficiency

While it is common knowledge that snow will accumulate on horizontal surfaces such as ledges and parapet caps, accumulations on steeply sloped or even vertical surfaces are often overlooked. This is likely due to the fact that most building codes and standards assume snow loading to be negligible for steeply sloped surfaces. However, the aerodynamics of many façade details, particularly those that are separated from the heated interior of a building by a thermal break, can accrete significant quantities of snow. The key difference is the duration that the accumulation will be present on the structure. For most cold climate regions, the structural loading due to snow is generally the combination of accumulations that occur over an entire winter. In the case of vertical façade details, the accumulations typically would only remain on a structure for a period of days or potentially weeks. As a result, the impact on structural loading may be considered to be negligible. However, falling accumulations can be of sufficient size to cause significant damage or injury and are shed from the structure potentially many times in a given winter.

The observations from climatic chamber simulations have been used as the basis for assessing the potential magnitude of accumulations on steeply sloped and vertical façade details. Figure 6 shows accumulations on a flat vertical façade during a climatic chamber simulation. It can be seen that, while accumulations do form on the façade surface, they are not densely packed and uniformly distributed. This is due to the redirection of wind flows along the surface of the façade. As a result, the shedding of these accumulations is generally not problematic.
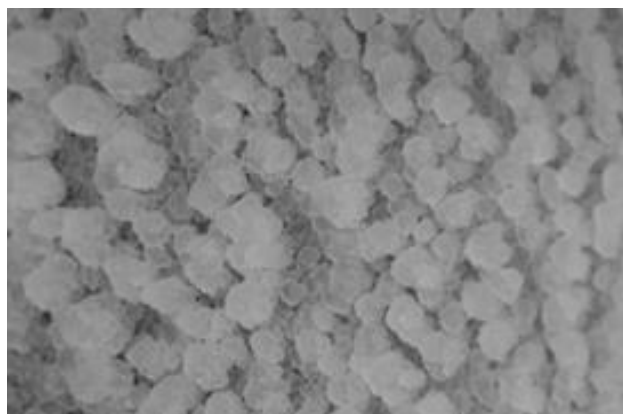


**Figure 6.** Example of wet snow accumulation on a flat vertical façade during a climate chamber simulation.

Alternatively, as seen previously in Figure 5, vertical projections from a façade surface do have the potential for significant, dense accumulations. These accumulations form on projections from the façade or other relatively narrow surfaces such as signs or other decorative façade elements as winds are not redirected to the same extent as with the main façade. As a result, there is the need to determine the potential magnitude of accumulation on these features to facilitate an estimate of the associated risks. The simulation parameters and observations from multiple climatic chamber simulations

of various façade projections were used to estimate the effective capture efficiency for this type of detail. This capture efficiency is analogous to the basic reduction factors used by most building codes and standards for deriving roof snow loading distributions from ground snow load estimates. The capture efficiency was defined as the ratio of the average depth of accumulation on the façade detail to the effective depth of snow falling on an unobstructed horizontal surface. Based on the observations, a capture efficiency of 0.8 was found to be a reasonable assumption.

## 3.2 Finite area element (FAE) modelling

The Finite Area Element (FAE) methodology [1] was employed to investigate the contribution to snow accumulations and potential shedding from independent variables. The FAE method includes a detailed computer simulation of the hour-by-hour deposition, drifting and melting of snow on building roofs and façade details. The absorption of rain and melt water into the snowpack as well as the thermal characteristics of the façade are also considered throughout each of the simulations. Entire winters are simulated, including the cumulative effects of successive storms and melting periods. Available meteorological records such as daily snowfall, hourly snowfall intensity, hourly wind speeds and directions, rainfall, temperature, solar radiation and thermal performance of the façade may be altered to observe their overall effect on snow accumulation magnitude.

### 3.2.1 Effects of wind directionality

Some façade details can be sensitive to wind exposure when considering the potential accumulations that may form. In many instances, such as with vertical mullions on a particular façade of a building, significant accumulations will only form for precipitation events associated with winds from a particular sector of directions. To account for this variability, the meteorological data used in the FAE assessment of snow accumulation were filtered to include only storm events from the sector of interest. In this way, the reduced frequency of a problematic shedding event was assessed.

The plot in Figure 7 shows the snowfall for the winter of 1995-96 based on meteorological data collected at LaGuardia International Airport in New York, NY. This figure is considering all snowfall events regardless of wind directionality. In comparison, the plot in Figure 8 shows the snow fall events for the same winter considering only events that occur when winds would impact the west façade of a subject building. It is evident in comparing these two plots that considering all snowfall events equally will over-estimate the total amount of snow when assessing the potential for wind driven accumulations.

The FAE methodology was used with the various filtered meteorological data sets to estimate the magnitude of potential accumulations. Figure 9 outlines the variation in snow load on a building surface if all winds are considered, while Figure 10 presents the

loading magnitude if only westerly winds are considered. It can be seen in comparing these two figures that there is a significant difference in potential loading for building features prone to accumulations from all wind directions compared to features limited to wind-driven accumulations from particular directional sectors.
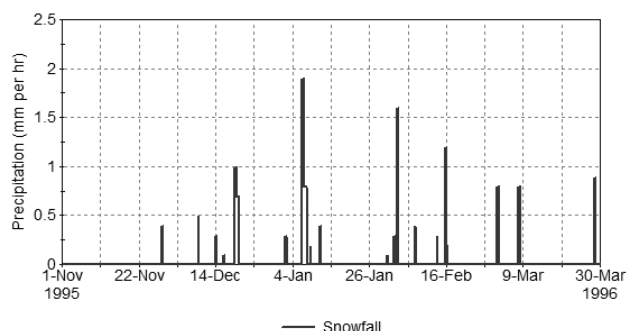


**Figure 7.** Snowfall at LaGuardia International Airport during the winter of 1995-96 considering all winds.
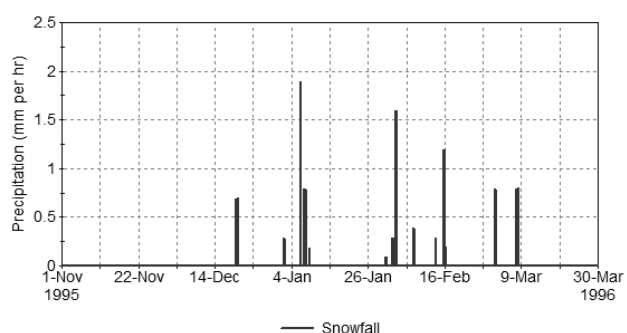


**Figure 8.** Snowfall at LaGuardia International Airport during the winter of 1995-96 considering only westerly winds.
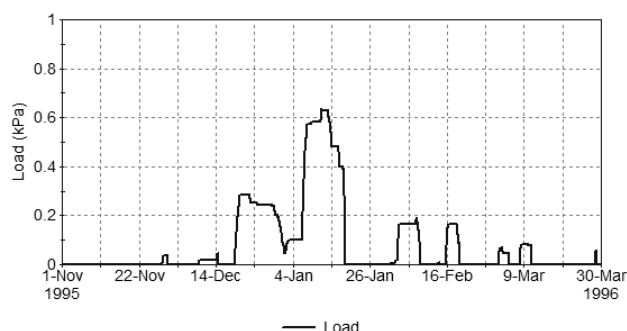


**Figure 9.** Snow load variation at LaGuardia International Airport during the winter of 1995-96 considering all winds.



**Figure 10.** Snow load variation at LaGuardia International Airport during the winter of 1995-96 considering only westerly winds.

### 3.2.2 Snow consistency consideration

Similar to the effect of wind directionality, some accumulations are sensitive to the consistency of the snow. This is particularly true for wind driven accumulations. As discussed based on observations in the climatic wind tunnel simulations, wind driven dry snow accumulations do not tend to build to problematic magnitudes and are generally shed from the façade in small amounts that would not pose a significant risk to pedestrians or property. However, wet snow accumulations tend to be more cohesive and can experience significant hardening through repetitive freeze thaw cycles before being shed from a building. As with the wind directionality assessments, the meteorological data were filtered to assess accumulations within a range of snow consistency. For the purposes of this research, snow occurring at temperatures less than -2.5° Celsius was considered to be dry, while that occurring at or above -2.5° Celsius was considered to be wet.

Similar to the consideration for wind directionality, the meteorological data were filtered to consider only wet snow precipitation events. Figure 11 shows an example of the wet snow precipitation events in New York. The corresponding snow accumulation magnitudes are presented in Figure 12.



**Figure 11.** Wet snow precipitation events at LaGuardia International Airport during the winter of 1995-96.



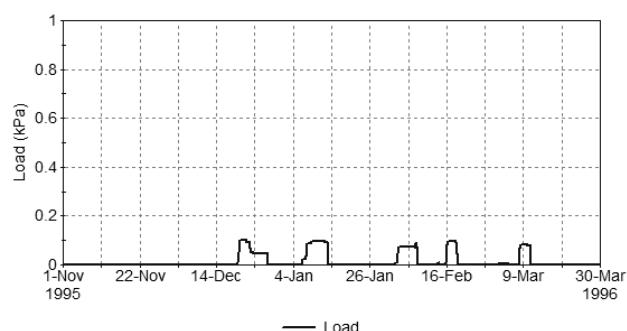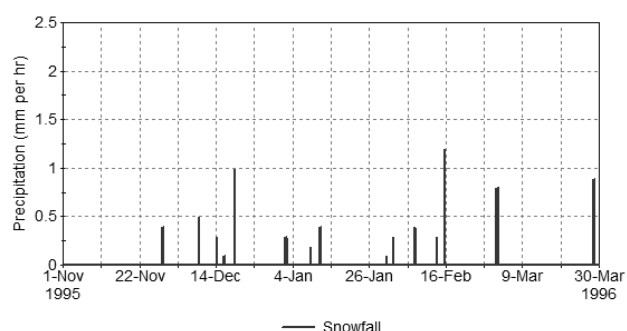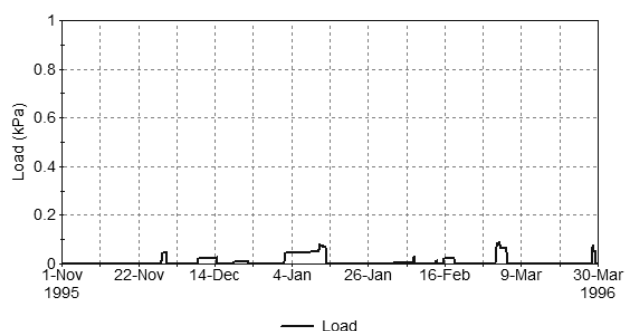**Figure 12.** Snow load variation at LaGuardia International Airport during the winter of 1995-96 considering only wet snow events.

### 3.2.3 Effects of snow sliding

In addition to the ability to parametrically assess the impact of the climate variables associated with snow loading, the FAE methodology was used to assess the potential loading magnitude for sloped surfaces that will regularly shed accumulations. For simplification, the specific coefficient of friction and the resulting slipperiness of the roof were not included in these analyses. Rather, weather conditions such as rain and melting that encourage sliding from generally smooth surfaces were focussed on. This provided a starting point for the resulting snow load reduction due to sliding since the basic assumption was that low friction between the building surface and snow pack would be produced by liquid water at this interface, not the material itself. Sliding was assumed to occur whenever there was sufficient melt water produced in the snowpack or rain water draining through the snow pack. Note that this could happen multiple times a winter in some areas.

## 4 Parametric assessment of shedding magnitude

### 4.1 Façade geometry

To facilitate the parametric assessment, building details have been categorized as being horizontal, sloped or vertical. Each of these classifications has a fundamental difference in the relative amount of snow or ice that will accumulate during a precipitation event. The present work outlines the key concerns with respect to falling ice and snow for these generalized classifications and how the parametric analysis has been developed to estimate the risks associated with each.

### 4.1.1 Horizontal surfaces

The FAE methodology was employed directly to determine the magnitude of accumulations on horizontal building surfaces accounting for wind scouring and potential drift accumulations.

### 4.1.2 Sloped façade surfaces

Further, the effects of snow sliding from a building surface have been estimated. The formation of melt water is monitored throughout the FAE analysis process. An accumulation was considered to be able to slide given the condition that melt water is at the interface between the building façade and the accumulated snow. A probability of slide was applied in the analysis to determine the effects of sliding on sloped building façade details. An appropriate probability of slide was determined such that the 50-year accumulation of snow equalled that of a horizontal building surface, reduced by an appropriate slope reduction factor as obtained from building codes and standards.

### 4.1.3 Vertical façade surfaces

For vertical accumulations, the probability of slide given the condition of melt water at the façade-accumulation interface was set to be unity. In addition, the rate of accumulation was adjusted based on observations of vertical façade elements in climatic wind tunnel simulations.

## 5 Example assessment

A generic building incorporating various façade details and located in New York has been used as the basis for an example use of the proposed methodology. The building incorporates 0.3m wide sunshade elements on all facades; 0.3m wide parapet caps around the perimeter of the roof; 0.3m deep vertical mullions on the north façade; and 0.3m wide sills sloped at 45° on the north façade. The following outlines the use of the proposed assessment methodology.

Each of the building details highlighted in this example are sensitive to a different set of loading assumptions. The parapet cap would be susceptible to all snow consistencies and exposed to all wind directions. Similarly, the sunshade elements will collect snow during all snowfall events, but significant accumulations would be limited to events that occur from wind directions approaching the building façade. The sloped sill accumulations are similar to the sunshade elements, but are further reduced due to the relative increase in the frequency of shedding throughout the winter months. It has been assumed that the vertical mullion details would only have accumulations during wet snow events that are associated with winds blowing into the façade. These accumulations were assumed to shed when there was water present at the interface of the mullion and the snow. The resulting severity indices of these elements based on these assumptions is presented as a function of snow accumulation return period in Figure 13. It should be noted that, although the accumulation magnitude associated with the sloped surfaces are expected to be less than the horizontal surfaces, the relative severity indices could exceed that of other façade features as a result of the increased frequency of shedding.

With the severity index relationships determined for each of the façade details, one can readily assess the relative risks associated with falling snow. For example, if there are minimal pedestrian areas along the north, it may be assumed that the probability of persons or property in the impact area during a falling event is relatively low. If it is assumed to be 10%, the corresponding snow accumulation corresponding to the 5-year mean recurrence interval would yield the 50-year falling snow hazard. As the parapet cap would potentially be adjacent to a major urban pedestrian thoroughfare, the probability of persons in the impact area could be considered to be much higher. If it is assumed to be 100%, the severity index associated with the 50-year snow accumulation would be assessed. The assessment would yield severity indices of 1.2, 2.2, 6.2 and 32 for the vertical mullion, horizontal sunshade, sloped sill and parapet cap, respectively.
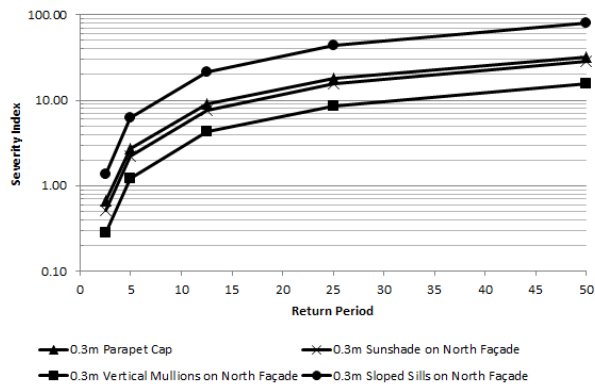
**Figure 13.** Effect of geometry on the severity index of a façade detail.

In addition to the relative performance of different façade details, the proposed methodology may be used to optimize the design of the façade features and focus mitigation expenses on the areas that pose the most significant risk. As outlined in Figure 14, the same façade detail mounted on different building faces can yield significantly different severity indices. The plot is showing the variation in severity indices for a 0.3m wide sunshade mounted on the north, east, south, and west facades. If the probability of persons or property in the impact zone is assumed to be 50%, then the resulting severity indices would be 0.01, 0.3, 7.5 and 15.6 for the south, west, east and north facades, respectively. Effectively, the sunshades mounted on the south and west facades would be expected to shed accumulations that could be considered a nuisance, but not posing a significant risk to safety. However, the sunshades mounted on the east and north facades would be expected to pose a concern for public safety. As a result, it may be appropriate to focus mitigation efforts on the north and east facades, or eliminate these features from those facades all together. Ultimately, this methodology provides the design and ownership teams with the information required to make an educated decision on the risks associated with a particular design.
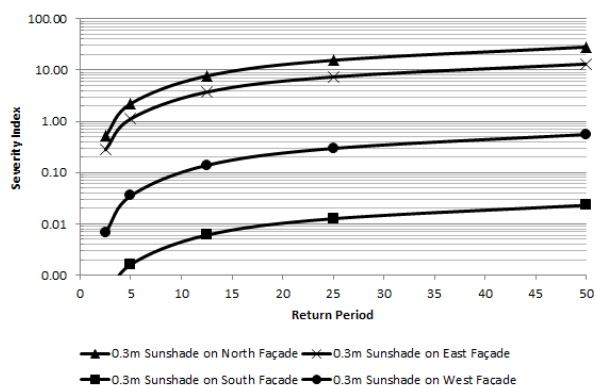


**Figure 14.** Effect of wind directionality on the severity index of a façade detail.

# 6 Conclusions

Even though snow accumulations that fall from structures present a significant risk to pedestrians and property, there are no known standards or codes available to assist designers in addressing these concerns in design. The wide range of variables involved in the accumulation and subsequent shedding of snow from a structure does not facilitate a discrete probabilistic prediction of the associated risks. The presented methodology outlines a parametric approach for assessing the relative risks associated with falling snow hazards for a range of façade details and climatic variables. The approach was developed through a combination of boundary layer wind tunnel and climatic wind tunnel simulations in addition to numerical snow accumulation models. The result is a reliable approach for designers to understand the risks associated with a particular facade detail. Variations in façade details and pedestrian usage of the areas around a particular building are accounted for through the proposed methodology. This will allow building designers and owners to focus mitigation and maintenance efforts on the building details that pose the most significant risk of a falling snow hazard.

# References

1.     Gamble, S.L., Kochanski, W.W. and Irwin, P.A. *Finite Area Element Snow Loading Prediction – Applications and Advancements*. Journal of Wind Engineering and Industrial Aerodynamics, 41-44: 1537-1548 (1992)
2.     ASCE 7-10, 2010. *Minimum Design Loads for Buildings and Other Structures*. American Society of Civil Engineers, Reston, Virginia.
3.     National Research Council of Canada. *National Building Code. 2010. Vol.2 Section 4.1.6.* Ottawa, ON.

# Building / Simulation

# Prediction of snow loads: past, present and future

Peter A. Irwin[1a]

[1]*Rowan Williams Davies and Irwin Inc., 650 Woodlawn Road West, Guelph, Ontario, N1K 1B8, Canada.*

**Abstract.** : The evolution of building code provisions is reviewed, with a main focus on Canada, and the development of physical and computational modeling methods for studying snow accumulation, melting and sliding are described. Physical models in water flumes and wind tunnels using various particles to represent snow can provide useful guidance on the locations and forms of snow drifts, particularly when snow loads are dominated by a single event. Computational Fluid Dynamics with particles can provide similar guidance. To go beyond a single event it is necessary to numerically track the multiple processes of snowfall, rainfall, melting, and sliding over extended periods. Therefore numerical methods are needed that make full use of the meteorological records and the building's geometry and thermal characteristics. Some of these methods are described in the paper. With the trends towards better energy efficiency and more varied building shapes, buildings are being designed that increasing are in need of more sophisticated methods for predicting snow and ice behavior.

## 1 Introduction

In snowy countries there are many impacts of snow loads on buildings and on the infrastructure that we rely on. An important one is the extra gravity load that snow causes on a roof. The load can be relatively uniform or it may be redistributed by the wind and by ponding of melt water. In drifts it may result in loads that are several times the snow load on the ground. Therefore snow loading has always been of concern to designers, and building codes have long specified minimum design snow loads. In Canada, up until 1960, the specified roof loads were equal to the 30 year ground load applied uniformly over the roof (Allen [1]; Shriever et al [2]), but they evolved subsequently so as to make allowance for reduced loads due scouring of snow off roofs by wind, and increased loads that occur in areas of aerodynamic shade such as in roof steps, roof valleys, the downwind sides of gable, arch and dome roofs and around rooftop projections such as mechanical units (Taylor [3]). They also make allowance for sliding of snow off sloped roofs, both in reducing the snow on an upper roof and increasing loads on a lower roof.

Another effect of snow or ice is that it can alter the shape of a structure seen by the wind. The electrical power industry have learned how the accumulation of ice on power transmission lines can lead to large amplitude wind-induced galloping oscillations and have developed measures to deal with this problem. Another example is snow, ice or freezing rain accumulating on and blocking up an otherwise very porous fence at the edge of a bridge deck. Wind tunnel tests show this increases aerodynamic drag and can amplify the problems of vortex excitation, flutter and galloping. The reliability of the structure needs to be assessed with such possibilities in mind.

There are other practical issues that must be addressed in building design and operations. The sliding of snow and ice off a building can cause a hazard to pedestrians below. Lawsuits have been launched in some cases due to injury or death that resulted. The measures that have been employed to avoid the adverse effects of sliding are varied, ranging from melting the snow, to holding it on the roof, to treating it as an operational problem and simply fencing off hazardous areas until the threat has diminished (Williams et al [4], Isyumov [5]). The same type of problem has occurred on cable supported bridges where snow and ice falling off the cables has impacted vehicle or pedestrian traffic below.

In this paper the focus will be on snow loading and how methods of prediction have evolved and will probably continue to evolve in future.

## 2 Snow loading viewed as a chain

In wind engineering the problem of wind loading is often represented as a chain. In fact the chain has been formally named the Alan G. Davenport wind loading chain. A somewhat similar concept can be applied to snow loading and is depicted in Figure 1.
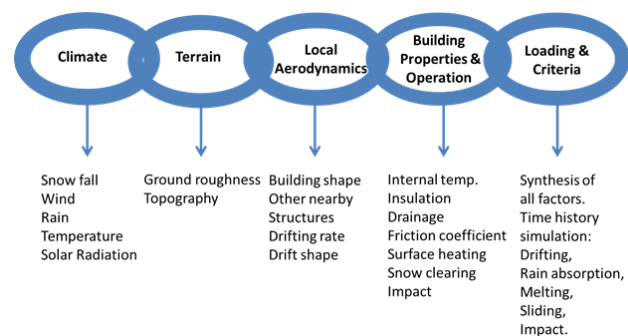


**Figure 1.** Snow loading viewed as a chain

The chain has five main links. Starting at the left hand end, the first is the climate. Right from this starting point one realises that snow loading is more complex in many ways than wind. We see that whereas for wind we only need concern ourselves with the statistics of wind speed and direction, for snow we need to know about the statistics of snow fall, wind, rain, temperature and solar radiation. Therefore there are many more variables to keep track of compared with wind loading. The second link in the chain is the terrain surrounding the site. Like in wind engineering the ground roughness and topography affect the wind's mean velocity profile and

turbulence at the site which in turn affect air flow patterns over the building and the resulting drifting. The next link in the chain is the local aerodynamics of the building, which is a function of the building's shape and the shapes of other buildings in the immediate neighbourhood. One additional factor for snow in this link is that the formation of drifts or ice accumulations can alter the shape of the structure and this in turn affects the air flow. Some drifts such as those at roof steps "fill in" areas of aerodynamic shade and are thereby limited as to how deep they can get.

The fourth link in the chain for wind is the influence of the properties of the building. For wind loading these would primarily be the dynamic properties, i.e. the frequencies of the natural modes of vibration, the mass distribution and the damping. For snow the dynamic properties of the building are not relevant but several other properties can be very important. Two of these are the internal temperature and thermal resistance of the roof since these affect melting rate. Two more are the slope and slipperiness of the roof in so far as they affect re-distribution of the load through sliding, which may also result in impact loads on lower level roofs. For some buildings snow accumulations are countered by operational measures. Operational measures can involve surface heating to melt the snow, or procedures to remove snow manually or mechanically before it can accumulate excessively. Another very important property of the building is drainage. The drainage system needs to be able to be of an appropriate capacity to rid the building of melt water without blocking or re-freezing.

The final link in the chain is to meet criteria for structural safety and serviceability. For snow this involves synthesizing the effects of all the parameters that affect snow loading so that quantities such as the 50 or 100 year return period loads can be determined and serviceability problems kept to an appropriate low level of probability.

## 3 Codes and standards

Because of the large number of factors that influence snow loads to estimate loads appropriate for use in design with any precision is very complex. However, codes and standards must attempt to reduce the complexities and provide relatively simple rules for designers. The author's experience with snow loads is primarily in Canada and the USA. The National Building Code of Canada (NBCC [7]) has evolved considerably since the 1940's. In the 1940's simple uniform loads were specified as a blanket provision (Allen [1]). By 1980 drift loads and shifting of loads due to sliding had been introduced (Taylor [3]) and by 1995 the effect of roof size on both uniform and drift loads had been introduced (Irwin, et al [8]). Similar developments were taking place in the USA, (O'Rourke et al [9]). Through involvement in the ISO Standard the author has become more familiar with practices in other snowy countries such as Norway, Japan, Germany, Poland and Russia. Interesting differences in approach can be seen in different countries. For example in Japan snow removal is recognized as a method of controlling

snow loads whereas in Canada, for example, it is not. The ISO Standard was updated in 2013 and, as with the national codes and standards contains provisions for uniform loads, drift loads and sliding. Building codes and standards use the recorded ground snow loads (or depths as substitute, along with assumptions concerning density) and then develop factors that are applied for exposure, drifting, and sliding. In some codes the effect of the internal temperature of the building is accounted for by a thermal factor.

It should be mentioned that many building codes and standards permit and encourage special, project specific studies to determine wind loads by wind tunnel testing as an alternative to using the standard analytical provisions. In 2012 the American Society for Civil Engineers published a standalone standard, ASCE/SEI 49-12 [6], covering the requirements for the wind tunnel testing methods. It is noteworthy that the ASCE 49-12 Standard also covers use of scale model testing and associated analysis methods for establishing snow loads on buildings.

## 4 Physical modeling and computer modeling of particle drifting

Because drifting has been the cause of many roof failures (O'Rourke and Wikoff [10]) a number of researchers have investigated methods to simulate the particle drifting process using physical models in wind tunnels and water flumes (Isyumov [11], Iversen [12], Irwin and Williams [13], Anno [14], Peterka and Petersen [15], O'Rourke et al [16]. The scaling principles were discussed by Kind [17]. It is quite difficult to match all the required scaling parameters but nonetheless useful information can be obtained on typical drift patterns and on potential methods for mitigating drifts.
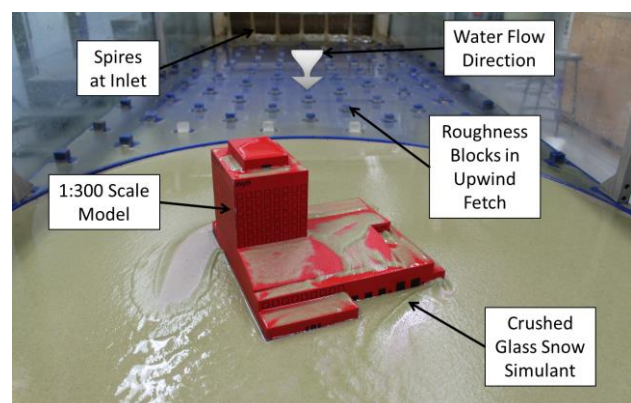


**Figure 2.** Physical modeling in water flume

Figure 2 shows an example of a drifting study in RWDI's water flume using crushed glass as the model particles. The physical model approach is best suited to the situation where drifts are formed by wind from a single direction in a single event. They are also useful in showing the limiting shapes for drifts as they fill in areas of aerodynamic shade. However, modeling the cumulative effects of different wind directions and speeds becomes cumbersome to implement on physical models.

Computational Fluid Dynamics (CFD) methods have also be applied to the particle drifting process: Beyers et al [18], Thiis and Ramberg [19]. As with physical models the CFD approach is easiest to implement for a single event with a predominant wind direction. However, it does in principle have some flexibility to examine the cumulative effects of varying directions and speeds.

## 5 Full time history modeling

To estimate extreme snow loads corresponding to a given return period requires that the cumulative effects of all the parameters listed in Figure 1 be evaluated with reasonable precision over a sufficient number of winters to obtain statistically meaningful results. The statistics of ground loads have themselves been analyzed by many researchers and meaningful relationships developed for ground loads as a function of return period. Building codes and standards rely on these relationships. However, notwithstanding the assumptions of building codes, the true relationship between 50 year ground load and roof load is not one to one and varies widely depending on circumstances.

In Canada, Isyumov and Davenport [20] made the first serious attempt to simulate the detailed processes of snow accumulation and melting on roofs over protracted periods using statistical methods. They examined the case of flat roofs in different regions of Canada using a Monte Carlo simulation method based on the statistics of snow fall, wind and temperature. Further work along these lines was reported by Isyumov and Mikitiuk [21]. The numerical approach, although approximate, allowed the importance of various parameters to be identified. For example in less cold areas peak snow loading is more likely to be associated with a single event, whereas in cold areas the prolonged sub-freezing temperatures meant that peak snow accumulations were more likely to be due to cumulative effects over many weeks.

Subsequently Irwin and Gamble [22] developed what they named the Finite Area Element (FAE) method, which allowed the numerical approach to be extended to roofs of any shape. They developed the method during the design of the 208 m span retractable roof of the Toronto SkyDome (now named the Rogers Centre), using wind tunnel measurements of wind velocities near the roof as input into their numerical simulations of snow fall, drifting, and melting. The following description of the FAE method is taken largely from Irwin et al [8]. In the FAE method the roof is divided into a grid forming a large number of small area elements, Fig. 3, and the mean wind velocity vectors at the grid node points at height about 1 m (or other similar value) above the roof are determined by wind tunnel tests, Figure 4 (or alternatively by CFD). This is done for wind direction intervals such as 10, 15, or 22.5 degrees and empirical relationships based on field data are used to relate drift rate to wind velocity and direction. All velocities are determined as a fraction of a reference value, high above the building. When the results of the wind tunnel tests are combined with the hourly meteorological wind records, a

set of velocities over the roof corresponding to any particular date and time can be established. Alternatively, for approximate studies on simple shapes such as flat roofs the velocities can be estimated, without wind tunnel tests, directly from the meteorological records and general knowledge of wind flow over buildings.
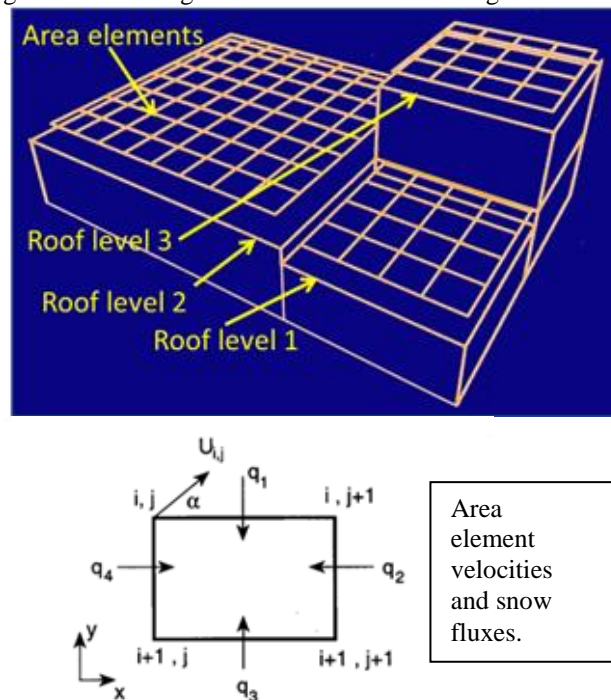




**Figure 3.** Finite area element (FAE) method



**Figure 4.** Measurement of surface wind velocities in an RWDI wind tunnel for FAE method

In the FAE method the computations are completed for every area element and, by evaluating the snow fluxes into and out of each area, the change in snow mass contained within each element during a selected time interval, usually 1 hour, is determined. This procedure is repeated for a whole series of time steps, covering first one winter, and then a whole series of winters. If the meteorological records show that, in addition to drifting, snow was falling during a particular time interval, the change in snow mass in each element due to this is incorporated. Likewise, if the heat balance within the snowpack permits melting, then the mass of snow turning to the liquid state is computed. If the snow is saturated,

liquid water is allowed to drain out; otherwise it is held within the snowpack. Rain falling onto the snow is treated as additional liquid water in this calculation. Refreezing when the temperature drops is also computed. There is also an on-off switch that monitors whether the snow has been rained upon or has melted, in which case drifting is turned off. If new snow subsequently arrives, then drifting is turned back on, at least until all the new snow has drifted away and the old layer of snow below is reached again. The end result of an FAE simulation is a complete time history of the average snow load in each area element on the roof for every hour for about 30 to 50 winters typically. Then the output is analyzed statistically to determine extreme snow loads or extreme values of other meteorological quantities. This allows computation of quantities such as 50 year return period uniform and drift loads. It is worth noting that if wind pressure coefficients are measured on the wind tunnel model in addition to wind velocities then the FAE method lends itself to the evaluation of wind and snow load combinations.
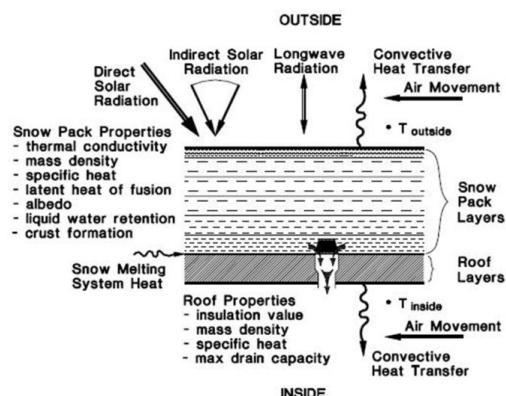


**Figure 5.** Heat transfer parameters for a roof

The evaluation of melting and water retention in the snow pack is complex. Figure 5 illustrates the various factors affecting melting. They include direct and indirect solar radiation, long- wave radiation, convective heat transfer, internal temperature, roof insulation value, and various snow pack properties such as thermal conductivity, latent heat, liquid water retention, albedo, crust formation etc. Typically the FAE simulation is run on the ground load initially for a specific project and is calibrated to the code ground load. The calibration is accomplished through adjustments of the assumed snow pack computer model until a good alignment with the code ground load is achieved. Then the FAE simulation is applied to the roof and snow load factors developed. Figure 6 shows a time history of simulated ground load in Montreal for the winter of 1981 – 1982 which was a fairly typical winter. It can be seen that the ground load builds up and reduces several times during the winter due to snow falls followed by melting. In contrast the winter of 1977-1978 shown in Figure 7 was much colder and the ground load continued to build up over almost the entire winter. There were a large number of roof collapses in the Northeastern part of North America in that year. At locations where snow does not stay for long such as Denver, Colorado, studies using the FAE method have

shown that heat transfer through the roof has much less influence on the snow load since the snow arrives in a large fall and heat transfer, although it may reduce the time the snow stays on the roof, does not have time to have much influence the maximum load. In an area like Montreal heat transfer through the roof is more likely to affect the maximum load.
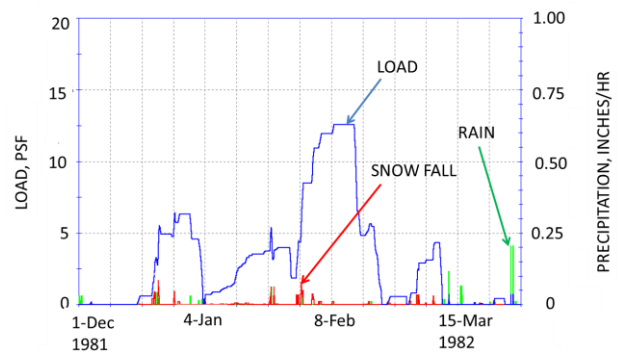


**Figure 6.** Ground load simulation for Montreal for the winter of 1981-1982
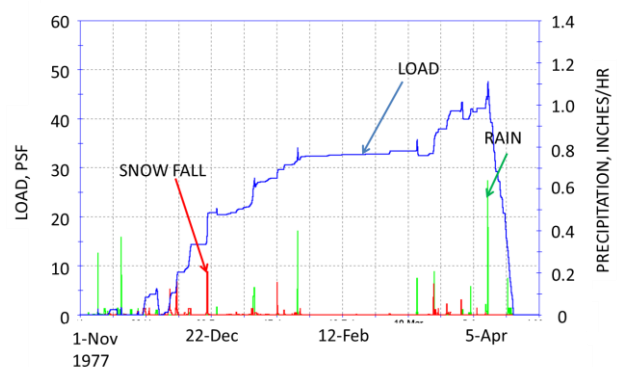


**Figure 7.** Ground snow load simulation for Montreal for the winter of 1977-1978

Figure 8 shows as an example the application of the FAE method to the roof of Terminal 1at Toronto's Pearson International Airport. The snow load in each area element is colour coded so that areas of heavy snow load (red in the diagram) can be seen at a glance. Figure 9 shows a photograph of actual snow accumulations on the roof seen during construction. The FAE method gives a good indication of the location and magnitude of snow loads that a large area roof such as this can experience.

Although the FAE method was developed initially for large one-of-a-kind projects, it was subsequently applied to the development of improved provisions in the 1995 edition of the NBCC, specifically to account for the effect of roof size on loads on flat roofs and in roof steps (Irwin et al, [8]). Later the method was also used to improve the NBCC load provisions on arch roofs (Hochstenbach et al [23]). More recently Dale et al [24] have used the parametric modeling capabilities of the FAE method to examine the effect of building orientation and height on roof step loads, as well as the effects of

internal temperature and roof thermal resistance, and the variation of loads averaged over different roof areas.
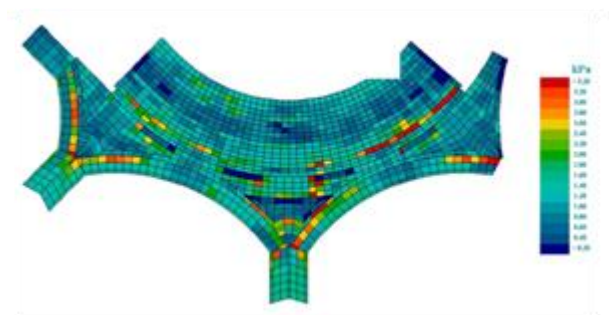


**Figure 8.** Output from and FAE study on Terminal 1 at Pearson International Airport, Toronto



**Figure 9.** Observed snow on Terminal 1 at Pearson International Airport, Toronto

Figures 8 and 9 are both snapshots in time of roof loading, as simulated and as seen on a real roof. For design extreme value analysis of the annual maxima is needed. Figure 10 shows and example of extreme value analysis of the load in one of the valleys on the fabric roof of Denver International Airport. The analysis uses the simulated highest annual load from about 30 winters.
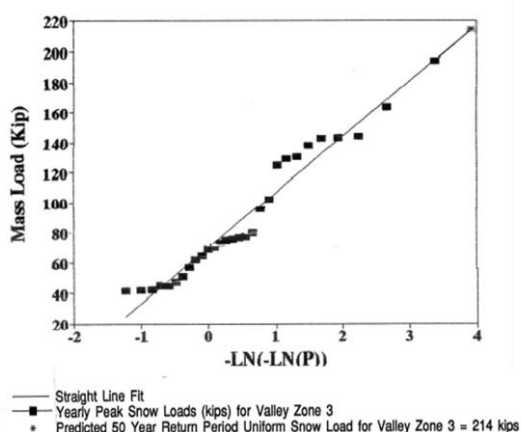


**Figure 10.** Example of extreme value analysis of snow load on a portion of roof

# 6 Future directions

Because of the issue of climate change the energy consumption of buildings has become an increasing preoccupation of building designers. At the turn of this century buildings were responsible for approximately 35% of greenhouse gas emissions (Battles and Burns, [25]). Since then the rapid trend towards more energy efficient buildings implies reduced heat loss. This has the potential to increase snow loads and designers are becoming more aware of the need for more detailed studies to address this issue.

Another trend is the use of external shading devices to reduce solar energy input into buildings. These features can attract snow and ice accumulations and increase the likelihood of falling snow and ice. Care is required to examine this problem during design and, if necessary, develop appropriate solutions, such as heat tracing to cause melting, snow retention devices, and devices to break ice into small pieces less likely to cause injury or damage. Tests in climatic simulation chambers (such as the Jules Verne facility here in Nantes) that can generate both snow and wind can be very instructive in identifying problems and developing solutions for architects, Fig. 10 shows an example of such testing in the test facilities at the University of Ontario Institute of Technology.



**Figure 11.** Example of tests in a climatic simulation chamber for wind, snow and ice

The clean energy trend has also led to the installation of solar panels on many buildings, in some cases in large arrays. The snow load patterns induced by the collectors are different from a bare roof and can be usefully studied using scale models, Irwin et al [26], Brooks et al. [27]. An array of solar panels greatly alters the air flow patterns on roofs which leads to different drift formations.
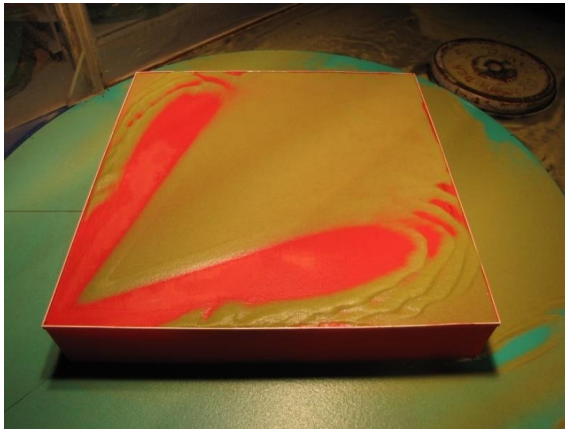
**Figure 12.** Water flume simulation of snow drifting on a bare flat roof for quartering winds
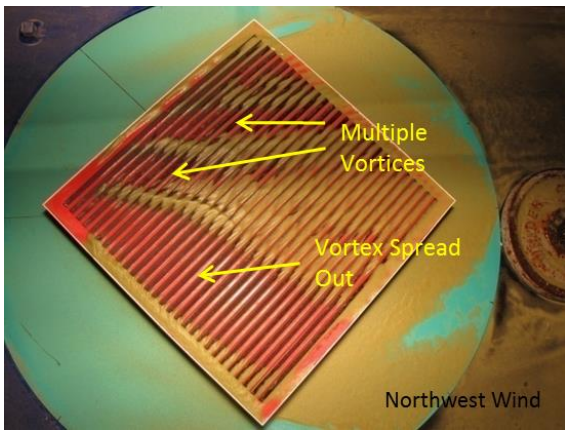


**Figure 13.** Modification of drifts due to a solar panel array for quartering winds from the northwest

Figure 12 shows a water flume simulation of snow drifting and scouring for quartering winds. A dominant feature for this wind direction is the scouring that occurs under the vortices generated by the upwind corner. Figure 13 shows the change in drift patterns due to the solar panel array for winds from the northwest. The single vortex on the northeast side of the roof breaks into multiple vortices and the vortex on the southwest half of the roof tends to be spread out more. The gap beneath a solar panel can be blocked off by sliding snow which can cause further changes in snow load distribution. Further research into the interaction of snow with solar panels is needed.

As indicated earlier the combination of wind and snow loads can benefit from time history simulation methods since both wind and snow loads can be tracked simultaneously. Bond et al [28] describe studies along these lines and more can be expected in future. Although snow loads on roofs act downwards and in most cases the dominant wind loads are upwards there can be some situations, such as a roof next to a taller building, or a roof with unbalance snow, where the snow and wind combination might govern.
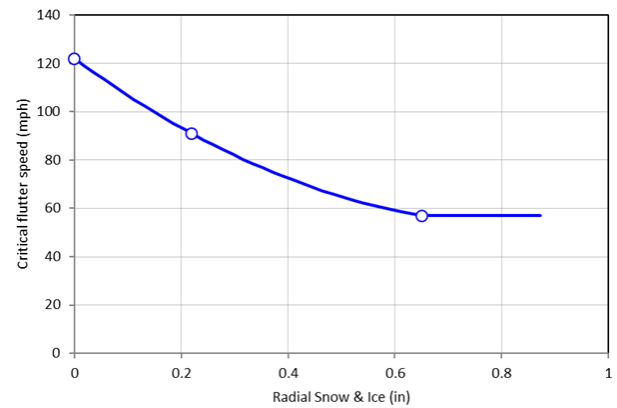


**Figure 14.** Variation of critical speed for flutter with radial snow and ice thickness

Combined wind and snow loads are an example of a multi-hazard situation. Besides loading, aerodynamic stability can also be influenced by snow and ice accumulations. For example the aerodynamic stability of flexible structures such as long span bridges can be affected by snow or ice accumulations. The current trend in North America is for long span bridges to have tall "anti-climb" fences at the deck edges. These are designed to be very porous, having no more than about 10% to 15% solidity, but snow or ice accumulations can greatly increase their solidity which can then adversely change the aerodynamic behaviour of the deck, making it far less stable against vortex excitation and flutter. This is illustrated in Fig.14 where the critical speed, as determined by sectional model tests, for the onset of flutter is plotted versus radial thickness of ice on the fence elements. It can be seen that the ice thickness can have a very adverse effect in reducing the flutter speed substantially.

In these situations a combined risk approach based on historical records of wind, snow and freezing rain, as well as wind tunnel tests of aerodynamic stability with and without fences blocked to varying degrees, can help determine the true risk of problems occurring. Table 1 illustrates the risk associated with ice being left on the fence for different numbers of days. The target return period for flutter was 10,000 years in this case. Therefore if a maintenance protocol can ensure ice does not remain for more than four days then the risk of flutter is acceptable.

**Table 1.** Effect of number of days of exposure to icing on return period for flutter of a bridge

| Assumed Exposure (days) | Return Period of Flutter (years) |
|---|---|
| 1 | 30,000 |
| 4 | 10,000 |
| 7 | 6,300 |
| 10 | 4,500 |
| 15 | 3,000 |

The sliding of snow off roofs is still an area of significant uncertainty. The NBCC simply classifies roofs as slippery or non-slippery. Further research is needed into the sliding process. What may be a conservative assumption for an upper roof is non-conservative for a lower roof. Lepage and Schuyler [29] described the development of computer and scale model simulation methods for predicting the sliding of snow off sloped roofs or the lifting off of snow mass by wind forces. These phenomena are of particular concern on high rise buildings because of the hazard to pedestrians below. The simulation techniques enable the effectiveness of various mitigation measures to be assessed. The sliding snow and ice problem has been more recently discussed by Williams et al [4] and by Isyumov [5].

An important continuing task is the validation of simulation methods. These include scale model simulations, CFD simulations, and full time history methods such as FAE. Here field data is invaluable as a means of calibrating their accuracy. Irwin [30] describes comparison of the FAE method with field observations on a large area stepped roof in Canada. The observations were taken shortly after a heavy snow loading event that caused part of the roof to collapse. During its investigations the FAE method was run for the winter months leading up to the collapse and was used to estimate the loads in the collapsed part. It was calibrated by comparing it with observations of load in roof steps in un-collapsed parts of the roof. The indications were that the FAE method tended to overestimate the capture efficiency of the step by about 20% and this allowed the results in the collapsed portion to be refined. This illustrates the importance of capitalizing on any full scale data that becomes available.

# 7 Conclusion

Snow loads continue to cause roof failures and we still have much to learn. Snow engineering is in many ways similar to wind engineering, only more complex due to the increased number of variables involved and the fact that in many cases cumulative effects over time must be accounted for. In wind engineering the forces are generated over a short interval but in snow engineering the load is affected by the history of snow fall, wind speed and direction, temperature, heat transfer through the building, sliding and retention of melt water and rain by the snow pack. In some cases the history leading up to the maximum load can be many weeks long. The concept of the A.G. Davenport wind loading chain used in wind engineering can nonetheless serve as a good guide as to what needs to be taken into account. There has been progress in developing both physical and CFD models to simulate single events of drifting, and numerical techniques to track the multiple climatic variables and their effects on the snow. These modeling techniques, although often approximate can nonetheless provide good guidance on probable extreme loads and on ways of avoiding problems of overloading and sliding hazards. Much of what has been learned about snow loading has

come from case histories and field observation. It cannot be emphasized enough how important it is that information continue to be gathered from case histories and field observation. Only with such data can prediction methods continue to be improved in future.

# References

1. Allen, D.E., *Snow loads on roofs*, National Research Council of Canada, DBR Internal Report 106, 1956.
2. Schriever, W.R., Lutes, D.A., and Peter, B.G.W., *Snow Loads*, National Building Code of Canada, Supplement No. 4., Commentary No.2, pp. 568-573, 1970.
3. Taylor, D.A., *Roof snow loads in Canada*, Canadian Journal of Civil Engineering, Vol. 7, No.1, pp.1-18, 1980.
4. Williams, C.J., M. Carter, M., Hochstenbach, F., and Lovlin, T., *Sliding snow and ice on Buildings: a balance of risk cost and aesthetics*, Proceedings of Snow Engineering V, 5th International Conference on Snow Engineering, Davos Switzerland, p. 59, 2004
5. Isyumov, N., *Sliding Snow from Sloped Roofs: Its Prediction, Potential Hazard and Mitigation*, Proceedings of Snow Engineering VI sixth International Conference on Snow Engineering, Whistler, British Columbia, Canada, 2008.
6. ASCE/SEI 49-12, Wind tunnel testing for buildings and other structures, American Society for Civil Engineering/ Structural Engineering Institute, Standard 49-12, 2012.
7. NBCC, National Building Code of Canada, Various Editions, published by the National Research Council, 1970, 1975, 1980, 1985, 1990, 1995, 2005, 2010, 2015.
8. Irwin, P.A., Gamble, S.L and Taylor, D.A. 1995. *Effects of Roof Size, Heat Transfer, and Climate on Snow Loads: Studies for the 1995 NBC*. Canadian Journal of Civil Engineering, Vol. 22: 770-784.
9. O'Rourke, M., Tobiasson, W., and Wood, E., *Proposed code provisions for drifted snow loads*, ASCE J. Structural of Engineering, Vol. 112, No. 9, 1986.
10. O'Rourke, M., and Wikoff, J., *Snow related collapse and implications for building codes*, Structure Magazine, pp. 18-21, January 2013.
11. Isyumov, N., *An approach to the prediction of snow loads*, PhD Thesis, University of Western Ontario, 1971.
12. Iversen, J.D., *Drifting snow similitude – transport rate and roughness modeling*, Scientific Symposium on Snow Motion, Fort Collins, Colorado, August 12-17, 1979.
13. Irwin, P.A., and Williams, C.J., Application of snow simulation model tests to planning and design, Proceedings of the Eastern Snow Conference, Vol. 28, 40th Annual meeting, pp. 118-130, 1983.
14. Anno, Y., *Snow drift wind tunnels in Japan,* Proceedings First International Conference on Snow

Engineering, Santa Barbara CA, USA, publ. by CRREL, Hanover NH, p. 191, 1988.

15. Peterka, J., and Petersen, R. L. *On the Relaxation of Saltation Length as a Modeling Criteria for Particulate Transport*, J. Wind Engineering and Industrial Aerodynamics, 36, 867-876, 1990.

16. O'Rourke, M., DeGaetano, A., and Derjue Tokarczyk, J., *Snow drifting transport rates from water flume simulation*, J. Wind Engineering. And Industrial Aerodynamics, Vol. 92, 14-15, pp. 1245-1264, 2004.

17. Kind, R.J., *Snow drifting: A review of modelling methods*, Cold Regions Science and Technology, 12, pp.217-228, Elsevier, 1986.

18. Beyers, M., Sundsbo, P.A., and Harms, T.M., (2004), *Numerical simulation of three-dimensional, transient snow drifting around a cube*, J. Wind Engineering and Industrial Aerodynamics, 92(9):725-747, 2004.

19. Thiis, T.K., and Ramberg J.F*., Measurements and numerical simulation of development of snow drifts on curved roofs*, Proceedings of Snow Engineering VI, Whistler, BC, Canada, ECI, 2008.

20. Isyumov, N., and Davenport, A.G., *A probabilistic approach to the prediction of snow loads*, Canadian Journal of Civil Engineering, Vol.1, Number 1, pp. 28-49, 1974.

21. Isyumov, N., and Mikitiuk, M., *Wind tunnel modeling of snow accumulations on large area roofs*, Proceedings of Second International Conference on Snow Engineering, Santa Barbara CA, publ. by U.S. Army Cold Regions Research and Engineering Laboratory, Hanover NH, July, 181-193, 1992.

22. Irwin, P.A., and Gamble, S.L. *Prediction of Snow Loading on the Toronto SkyDome*, Proceedings First International Conference on Snow Engineering, Santa Barbara CA, USA, publ. by CRREL, Hanover NH, p. 118, 1988.

23. Hochstenbach, F.M., Baker, H.A., Gamble, S.L., and Irwin, P.A., *Unbalanced snow loads on arched roofs- research for the National Building Code of Canada*, Proceedings of the Annual Conference of the Canadian Society for Civil Engineering, June 4-7, 2003.

24. Dale, J., Gamble, S., Brooks, A., *Design snow load refinement using modeling and analysis techniques*, Proceedings of the Canadian Society for Civil Engineering 4th International Structural Specialty Conference, May 28-31, Halifax, NS, p. CST-88-1, 2014.

25. Battles, S.J., and Burns, E.M., *Trends in building-related energy and carbon emission: actual and alternate scenarios,* American Council for an Energy-Efficient Economy summer study on energy efficiency in buildings, August 2001.

26. Irwin, P.A., Gamble, S.L., and Lepage, M.F., *Snow and wind loads resulting from roof mounting of solar collectors*, Report prepared by Morrison Hershfield Limited for the National Research Council Canada, Solar Energy Program, Contract 04SX. 31155-2-2701, April 1984.

27. Brooks, A., Gamble, S., Dale, J., and Gibbons, M., *Determining snow loads on buildings with solar arrays*, Proceedings of the Canadian Society for Civil Engineering 4th International Structural Specialty Conference, May 28-31, Halifax, NS, p. CST-49-1, 2014.

28. Bond, J.V., Brooks, A.J., Gamble, S.L., and Dale, J.C., *Combined probabilities of peak wind and snow load events*, Canadian Society for Civil Engineering, Conference on Resilient Infrastructure, London ON, Canada, June 1-4, 2016.

29. Lepage, M.F., and Schuyler, G.D., *A simulation tom predict snow sliding and lift-off on buildings*, Proceedings First International Conference on Snow Engineering, Santa Barbara CA, USA, publ. by CRREL, Hanover NH, p. 128, 1988.

30. Irwin, P.A., *Snow loads in roof steps*, Proceedings of the Third International Conference on Snow Engineering, May 26-31, Sendai, Japan 1996.

# CFD simulation of drift snow loads for an isolated gable-roof building

Yoshihide Tominaga[1,a], Tsubasa Okaze[2] and Akashi Mochida[3]

[1]Niigata Institute of Technology, 1719 Fujihashi, Kashiwazaki, Japan
[2]Tokyo Institute of Technology, 4259 Nagatsuta-cho, Midori-ku, Yokohama, Japan
[3]Tohoku University, 6-6-11 Aoba, Sendai, Japan

**Abstract.** Unbalanced snow accumulation on an isolated gable-roof building with different roof pitches was modeled using computational fluid dynamics (CFD). First, we confirmed CFD prediction accuracy for the velocity and pressure fields around the building by comparing simulated results with results obtained in prior wind tunnel experiments. Next, the unbalanced roof snow accumulation was predicted for different wind velocities using a snowdrift model previously proposed by the authors. The predicted drift coefficients were compared with observational data and resultant design codes developed by ISO4355. Finally, we confirmed that the observational data could generally be reproduced using the proposed CFD simulation method.

## 1 Introduction

When predicting snow loads on building roofs, unbalanced snow accumulation due to wind flow is a difficult problem. Accumulation occurs because of a complex interaction between snow particle motion and fluid flow affected by building geometry. Through field observations, much has been learned about this phenomenon [1–3]. Observation of specific cases in which impacts of various parameters on snow accumulations can be considered under controllable conditions (e.g., wind or water tunnels) has also been effective in advancing the knowledge [4–6]. Although these efforts have greatly contributed to improvements in building design [7, 8], their applicability has been limited to specific geometries and weather conditions. Recently, computational fluid dynamics (CFD) has been applied to model snowdrift around buildings [9]. However, few studies have applied CFD to model roof snow. Thiis et al. [10, 11] predicted snow distribution on a sports hall with a curved roof located in Oslo, Norway, and compared the simulated results with field measurements. They focused primarily on reproducing the snow distributions observed on the actual building caused by the specific weather conditions. Few prior studies have applied CFD to model snowdrifts with a generic configuration.

This study aimed to clarify the fundamental performance and limitations of CFD in roof snow prediction. First, we confirmed the prediction accuracy of CFD on the flowfield by comparing simulation results with experimental wind tunnel results for a gable roof with different pitches. Next, we applied a proposed snowdrift model to predict snow distribution on the roof. For this application, drift coefficient data measured in Norway [2, 3]—the data used for snow load design by the ISO4355 'Bases for design of structures - Determination of snow loads on roofs' [8]—was compared with the simulated results.
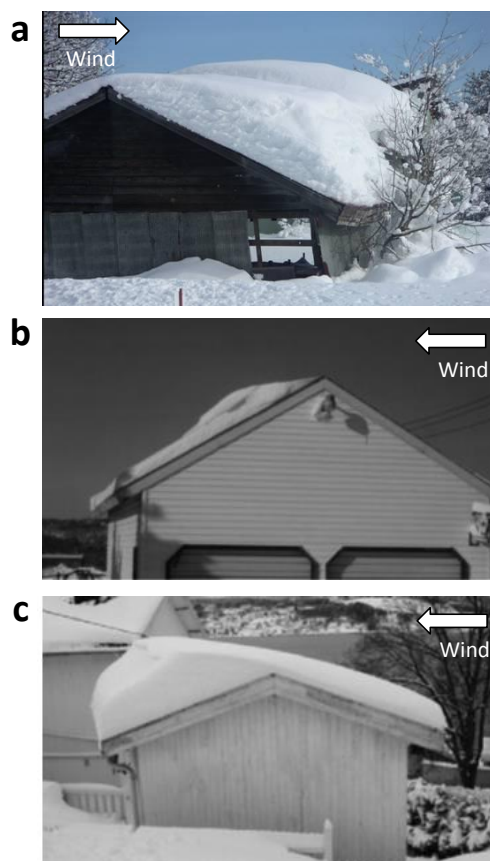


**Figure 1.** Field observation of unbalanced roof snow on gable roofs: (a) courtesy of Dr. T. Tomabechi, (b, c) courtesy of Dr. T. Thiis [7]
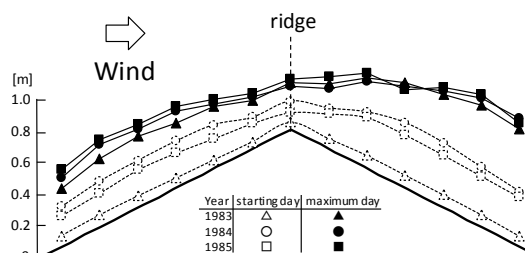


**Figure 2.** Snow depth for 5:10 roof pitch obtained by field observation (modified from [12])

---

[a] Corresponding author: tominaga@abe.niit.ac.jp

## 2 Snow accumulation on gable roofs

Gables are a common roof shape for single-family residences, garages, barns, etc. Figure 1 shows examples of unbalanced snow accumulations on various gable roofs. Snow blown by incoming flow on the windward side of the roof can accumulate on the leeward side of the roof, where the wind velocity is sufficiently low allowing snow to settle out and form a drift. As a result, the snow load on the leeward side is larger than the snow load elsewhere on the roof and, in some cases, is even larger than the ground snow load [7].

Figure 2 shows accumulated snow depth on a gable roof with a 5:10 roof pitch obtained by field observation [12]. The larger snow accumulations on the leeward side of the roof are clearly demonstrated. O'Rourke and Auren [13] suggested that roof slope, roof width, and ground snow load are key parameters affecting drift size on gable roofs. The American Society of Civil Engineers (ASCE) [14] considered uniform surcharges that extend downwind from the roof ridge for some specified distance (related to the eave-to-ridge fetch distance and the roof slope) and noted a smaller downwind extent for shorter fetch distances and steeper roof slopes. Measurements obtained by Høibø [2, 3] indicated that both the mean and standard deviation of the differences and drift coefficients increase with roof slope [7]. Therefore, gable roofs with different roof pitches that experience unbalanced snow accumulations are good candidates for investigating the complex interaction between snow particle motion and fluid flow affected by building geometry. This roof type is deemed suitable to validate the CFD numerical methods proposed in this study.

## 3 CFD simulation method

### 3.1 Building configuration

Figure 3 provides a schematic view of the building model used in this study. An isolated gable-roof building, with an eave height ($H_e$) of 6 m and a width (W) of 6.6 m, was placed perpendicular to the approaching wind flow. The model singularly considered three different roof pitches: 3:10 (16.7°), 5:10 (26.6°), and 7.5:10 (36.9°). The eave height ($H_e$) was constant for the three model scenarios. Tominaga et al. [15] performed a detailed investigation on



Ground and building surfaces

Central section of building

**Figure 4.** Plan and cross-sectional grid overlay for the building model (5:10 roof pitch)
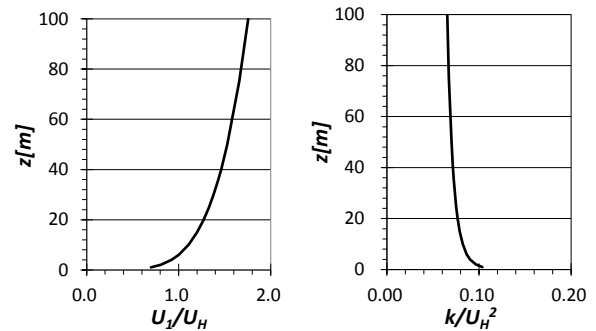


**Figure 5.** Inflow boundary conditions (actual scale)
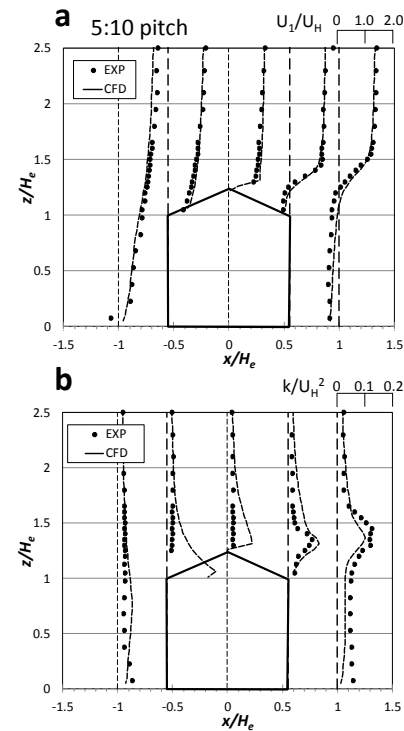


**Figure 6.** Comparison of simulated and measured (a) mean streamwise velocity ($U_1$) and (b) turbulent kinetic energy ($k$) (5:10 roof pitch)



**Figure 3.** Schematic view of building model

CFD prediction accuracy for this type of configuration.

## 3.2 Numerical methods

### 3.2.1 Flowfield

The ANSYS FLUENT 14.5 commercial software was used to perform steady-state Reynolds-averaged Navier-Stokes (RANS) equation computations based on a control volume approach for solving the flow equations.

Grid generation is an important consideration when applying CFD to predict roof snow. If structured grids consisting of rectangular cells are used for slanted roofs (such as a gable), prediction of friction velocity and snow distribution on the roof surface may be inaccurate. Tetrahedral and pyramid cells are superior in reproducing complicated shapes, but controlling appropriate grid resolution to ensure accurate prediction of surface velocity and calculation convergence is difficult. In this study, special care was taken to allocate an adequate number of hexahedral cells along the oblique roof to preclude tetrahedral and pyramid cells. Figure 4 shows example grid resolutions for the plan-view building and ground surfaces, and for the building cross section for the 5:10 roof pitch. One side of each roof pitch was divided into approximately 20 cells. For the 5:10 roof pitch domain, the computational grid comprised 2,355,280 cells; other roof pitches had similar grid sizes. In a prior study [15], a grid-sensitivity analysis showed that grid refinement did not significantly affect the results. The realizable $k$-$\varepsilon$ model [16] was used as the turbulence model.

The computational conditions used in this study were based on guidelines from the Architectural Institute of Japan (AIJ) [17]. The computational domain comprised a volume measuring 16 H (x-axis) × 12 H (y-axis) × 7 H (z-axis). For the flowfield validation study, the profiles of the streamwise velocity ($U_1$) and turbulent kinetic energy ($k$) were imposed at the inlet, based on experimental data. For the snowdrift study, a power law profile with an index of 0.20 was assumed for $U_1$; the profile for $k$ was determined using a turbulent intensity equation proposed by the AIJ [18]. Figure 5 shows the $U_1$ and $k$ profiles for the snowdrift study. The $\varepsilon$ values were determined from the local equilibrium assumption, $P_k = \varepsilon$, where $P_k$ is the production term in the $k$ equation.

### 3.2.2 Drifting snow field

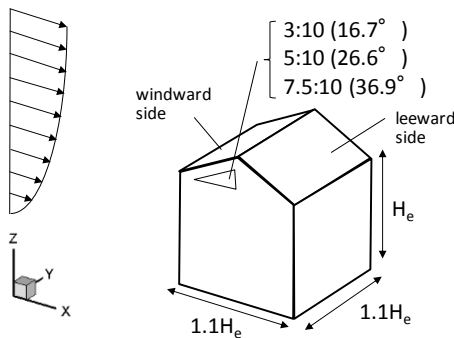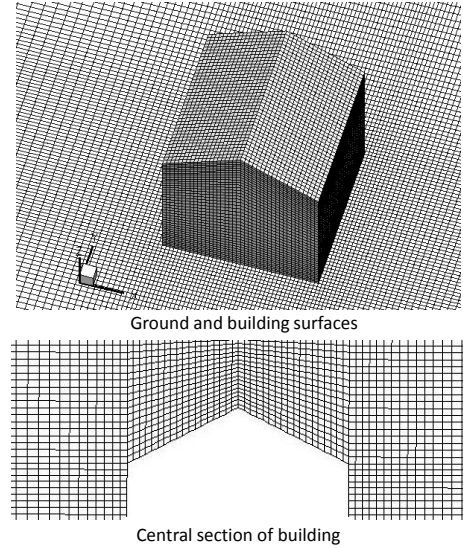The snowdrift model previously proposed by the authors [9] was implemented in CFD code as a user-defined function. To model suspension, the transport equation for snowdrift density ($\Phi$) [kg/m³] was solved, where $W_f$ is the snowfall settling velocity assumed to be -0.5 m/s.

$$\frac{\partial \Phi}{\partial t} + \frac{\partial U_i \Phi}{\partial x_i} + \frac{\partial W_f \Phi}{\partial x_3} = \frac{\partial}{\partial x_i}\left(\frac{\nu_t}{\sigma_s}\frac{\partial \Phi}{\partial x_i}\right) \tag{1}$$

The snowdrift density at the inflow and top boundaries ($\Phi_{in}$) was $7.5 \times 10^{-4}$ kg/m³, calculated using the amount of snowfall per unit time and snowfall velocity ($W_f$). The turbulent Schmidt number ($\sigma_s$) was 0.7 [19].

The deposition flux on the snow surface ($q_{dep}$) [kg/m²s] and the erosion flux on the snow surface ($q_{ero}$) [kg/m²s] are determined as follows using Eqs. (2) and (3):

$$q_{dep} = W_f\,\Phi_P\left(\frac{U_{*t}^2 - U_*^2}{U_{*t}^2}\right) \qquad (U_* \le U_{*t}) \tag{2}$$

$$q_{ero} = -A_e\rho_i U_*\left(1 - \frac{U_{*t}^2}{U_*^2}\right) \qquad (U_* > U_{*t}) \tag{3}$$

where $\Phi_P$ is the drift density at the first grid adjacent to the snow surface, $U_*$ is the friction velocity at the snow surface, $U_{*t}$ is the threshold friction velocity (0.2 m/s), $A_e$ is a proportional constant ($1.0 \times 10^{-5}$), and $\rho_i$ is the density of ice. This model differs from the prior study's model [9] because friction velocity effects on the snow surface were included in not only erosion but also deposition fluxes [20]. The net deposition flux ($q_{total}$) [kg/m²s] is given by Eq. (4).

$$q_{total} = q_{dep} + q_{ero} \tag{4}$$

When erosion occurs ($U^* > U_t^*$), $q_{ero}$ is given as the surface boundary condition for the $\Phi$ transport equation.

Friction velocity ($U^*$) was calculated using a generalized log law adopted in CFD code [21] as follows:

$$U_*^2 = \frac{\kappa C_\mu^{1/4} k_P^{1/2} U_P}{ln\left(\frac{E C_\mu^{1/4} k_P^{1/2} y_P}{\nu}\right)} \tag{5}$$

where

$U_P$ is mean velocity of the fluid at point P
$k_P$ is the turbulent kinetic energy at point P
$y_P$ is the distance from point P to the wall
$\nu$ is the kinematic viscosity of the fluid
E = 9.793
$\kappa$ = 0.4187
$C_\mu$ = 0.09

### 3.2.3 Snow accumulation

In this study, snow depth was not calculated directly. The snow depth ratio was defined as the ratio between the standard deposition flux ($q_{sta} = \Phi_{in} \times W_f$) and net deposition flux ($q_{total}$). The drift coefficient (described later in Section 4.3) was calculated using the net deposition flux at the reference point, which was not affected by the building.

The snowdrift analysis was performed using steady-state CFD, in which the flowfield is unaffected by snow accumulation. Thus, the results of this analysis express the potential for snow deposition or erosion due to the flowfield determined by the building geometry without snow. Although, surface change effects can be considered using sequential predicted snow surface levels and grid deformation [10, 11, 22, 23], such an approach is time-consuming and complicated. In this study, the applicability of the *one-way* method that does not consider the influence of surface change on the flowfield was examined from a practical viewpoint.

In steady-state CFD simulation, a mean wind velocity is applied as a boundary condition. In a real environment,
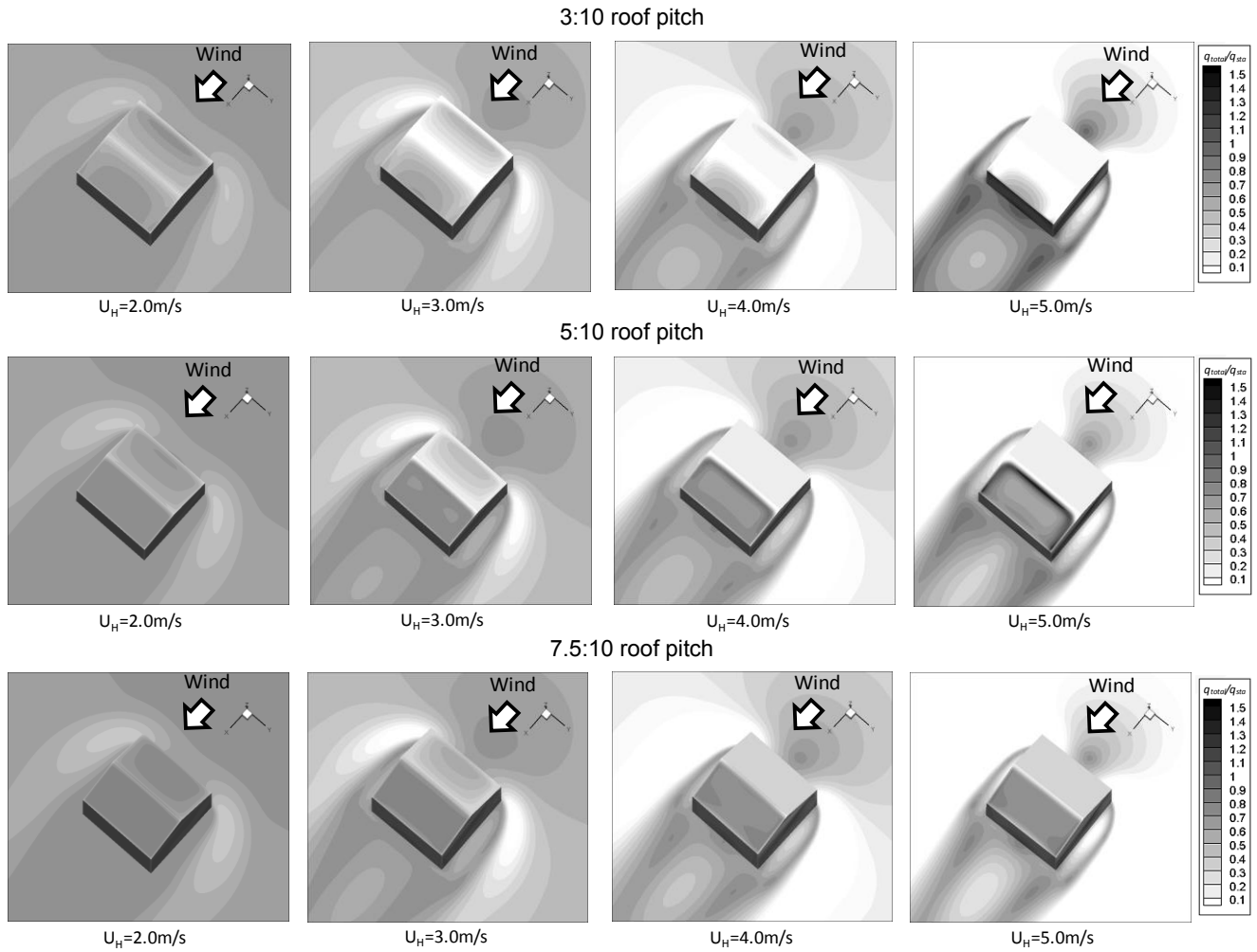
**Figure 7.** Snow depth ratio for different wind velocities

wind velocity fluctuates over time during snowdrift formation; erosion and deposition do not occur continually. This real phenomenon is difficult to reproduce accurately using steady-state CFD. In this study, a simplified method to reproduce this process was proposed for steady-state CFD. Specifically, the weighted average of prediction results for different wind velocities were used to obtain the snowdrift result at a specific reference velocity. In this study, the occurrence frequency of the wind velocities was assumed to follow normal distribution. Accordingly, the occurrence probabilities of $U_{ave}$, $U_{ave} \pm 1$ m/s, and $U_{ave} \pm 2$ m/s were assumed as 40%, 25%, and 5%, respectively, to obtain the averaged snowdrift result for $U_{ave}$ at the eave height.

# 4 Results and discussion

## 4.1 Velocity field validation

Figure 6 compares the vertical distributions of the mean streamwise velocity ($U_l$) and the turbulent kinetic energy ($k$) obtained using CFD simulation with the measured results obtained from the wind tunnel experiment [15] for 5:10 roof pitches. The agreement between the simulated and experimental results is generally good. Similar agreement was observed for the other roof pitches

considered. Generally, the steady RANS CFD results agreed well with the measured data for $U_l$ and $k$, although the predicted values were overestimated near the windward roof and ridge of the building [15]. The average deviation between the simulated and measured results was typically less than 10%; the deviation increased to 30% in the lower wind speed region behind the building.

## 4.2 Roof snow accumulation

Figure 7 indicates the contours of the snow depth ratio ($q_{total}/q_{sta}$) on the roof and ground for three different roof pitches and different wind velocities. Results for $U_H = 1.0$ m/s are omitted in Figure 7 because only very small undulations were observed. Figure 8 compares the snow depth at the vertical center section on the various roof pitches for different wind velocities. For $U_H = 2.0$ m/s, erosion occurred only near the ridges of each roof pitch. Large snow depths were observed near the middle of the windward side of the roof for $U_H = 3.0$m/s. For $U_H \geq 4.0$ m/s, the windward side of the roofs were eroded and snow depths converged to 0 for each roof pitch. Concurrently, snowdrifts were formed on the leeward side of the roof. For the 5:10 roof pitch, an extraordinarily sharp peak of snow depth was observed on the leeward side of the ridge for $U_H = 4.0$ and 5.0 m/s.

This snow depth overestimation is likely caused by the standing vortex behind the ridge specific to this roof pitch that is attributed to the failure of the turbulence model.

Figure 8 also shows results using the weighted averages of $U_{ave}$ = 2.0 and 3.0 m/s. The results from these averaged velocities were consistent with other observed results; snow depth on the leeward side of the roof tended to increase with increasing wind velocity and roof pitch. Results were also consistent with snow load codification [8, 18]. Therefore, the efficacy of the simplified averaging method proposed in this study was confirmed. Further, the superiority of CFD simulation over traditional experimental approaches was demonstrated through the unique visual display of detailed snow depth distributions shown previously in Figure 7.

## 4.3 Drift coefficient comparison

Table 1 lists the drift coefficients ($C_d$) calculated using Eq. (6) as follows:

$$C_d = \frac{S_l - S_w}{S_g} \qquad (6)$$

where $S_w$ and $S_l$ are the snow load on the windward and leeward sides, respectively, and $S_g$ is the ground snow load, which is unaffected by the building. Only values at the center section were used, along with wind direction, for averaging each side of the roof. In the CFD simulation, these snow loads were replaced by the net deposition fluxes at each position.

**Table 1.** Drift coefficient ($C_d$) at different wind velocities

|  | 3:10 pitch | 5:10 pitch | 7.5:10 pitch |
|---|---|---|---|
| $U_H$ = 1.0 m/s | 0.02 | 0.05 | 0.04 |
| $U_H$ = 2.0 m/s | 0.15 | 0.27 | 0.23 |
| $U_H$ = 3.0 m/s | 0.41 | 0.79 | 0.74 |
| $U_H$ = 4.0 m/s | 0.90 | 2.07 | 2.00 |
| $U_H$ = 5.0 m/s | * | * | * |
| $U_{ave}$ = 2.0 m/s | 0.18 | 0.35 | 0.32 |
| $U_{ave}$ = 3.0 m/s | 0.39 | 0.82 | 0.77 |

*Not calculated due to zero net deposition flux on the ground

The results listed in Table 1 further confirm observations made in Figures 7 and 8; the drift coefficient increases with increasing wind velocity and roof pitch. Drift coefficients for the 5:10 pitch are larger than coefficients for the 7.5:10 pitch. The relative differences in drift coefficient magnitude for roof pitches remain similar for different wind velocities.

Figure 9 shows the predicted drift coefficients ($C_d$) for $U_H$ = 1.0 m/s, $U_H$ = 2.0 m/s, and $U_{ave}$ = 2.0 m/s (from Table 1) plotted against a scatter plot of observational results [7]. The observational data comprised approximately 1,300 examples of snowdrift formation on gable roofs in Norway [2, 3]. This data also supported development of various models (normal, sheltered, exposed) in *ISO 4355 Bases for Design of Structures—Determination of Snow Loads on Roofs* [3]. For $U_{ave}$ = 2.0 m/s (▲), simulation results generally corresponded well with the ISO model (exposed), but values for the 5:10 pitch were overestimated. Deviations from ISO model were within 5% for the 3:10 and 7.5:10 roof pitches, and were approximately 40% for the 5:10 roof
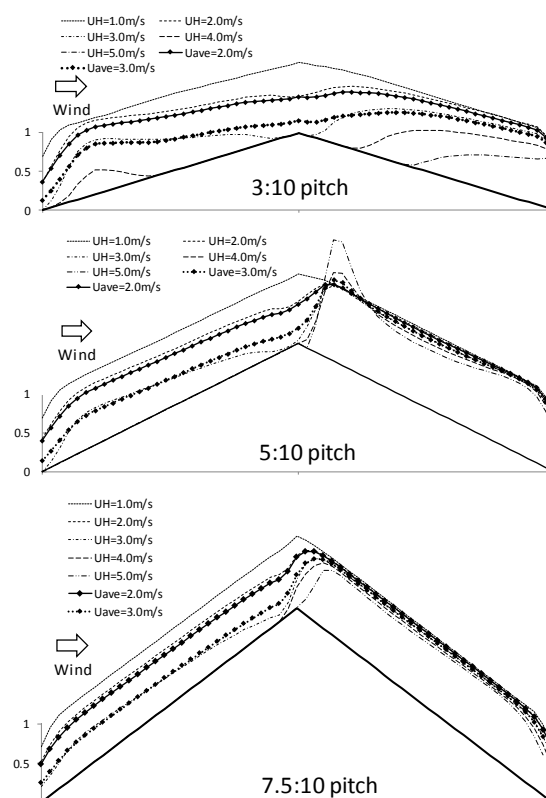


**Figure 8.** Normalized snow depth along roof centerline
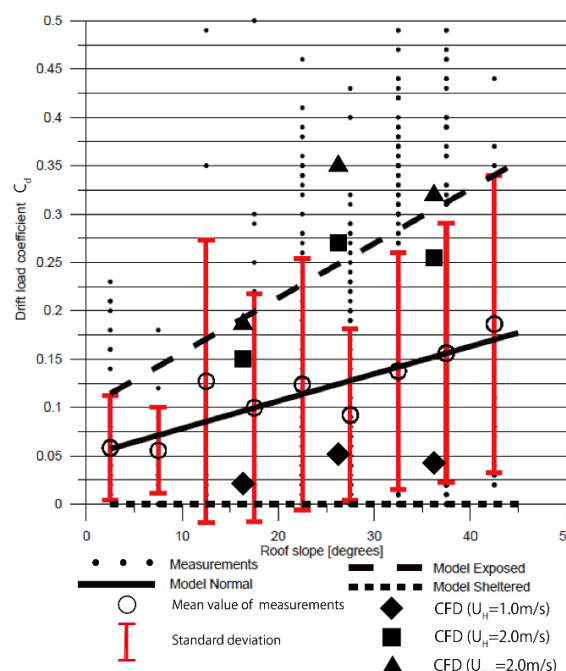


**Figure 9.** Comparison of CFD simulated drift coefficients with measured and ISO model results

pitch. Comparatively, the ISO model (normal) corresponded well to intermediate values between $U_H$ = 1.0 m/s (♦) and $U_H$ = 2.0 m/s (■). Values with $U_H$ = 2.0 m/s at the eave height are somewhat smaller than the established threshold velocity for drifting snow. This difference may be caused by overestimation of turbulent kinetic energy ($k$) as an intrinsic defect of the turbulence model used. Furthermore, the validity of the existing

threshold friction velocity ($U*_t$) for slanting snow surfaces (such as gable roofs) is unconfirmed and should be considered for future study.

# 5 Conclusions

In this study, CFD simulations of unbalanced snow accumulation on roofs were conducted for an isolated gable-roof building. The simulated results were compared with observational data.

As a result of this work, the following conclusions can be drawn:

– The proposed CFD simulation method was generally able to reproduce observational results. Consistent with prior results, the model showed that the snow depth on the leeward side of the roof increases with increasing wind velocity and roof pitch.
– Further, snow depth distributions can be visually captured and displayed using CFD simulation; such visualization is not provided in traditional experimental approaches.
– A prediction method, in which results obtained for different wind velocities are combined assuming a normally distributed occurrence frequency for wind velocities, was proposed and verified.
– For $U_{ave}$ = 2.0 m/s, the predicted drift coefficients generally corresponded well with the ISO Model (Exposed) [3], but values for the 5:10 pitch were overestimated. Deviations from the ISO Model were within 5% for the 3:10 and 7.5:10 roof pitches, and were approximately 40% for the 5:10 roof pitch.

The current study has the following limitations that will be addressed in future work:

– Although three different roof pitches were used, this study considered only an isolated gable-roof building. Applicability of the proposed CFD method should be examined for other configurations, such as flat and step roofs.
– The validity of the model parameters, such as threshold friction velocity and snowfall settling velocity, should also be examined and optimized for various conditions.
– This study considered wind direction only perpendicular to the windward facade. The effect of wind direction variations should be considered.

# Acknowledgements

# References

1. D. A. Taylor, Roof snow loads in Canada, Canadian J. of Civil Eng. **7**, 1, 1-18 (1980)
2. H. Høibø, Form factors for snow load on gable roofs - Extending use of snow load data from inland districts to wind exposed areas, *11th International Congress on Agricultural Engineering*, Dublin, Ireland, Balkema (1989)
3. H. Høibø, Snow Load on Gable Roofs - Results from Snow Load Measurements on Farm Buildings in Norway, *First International Conference on Snow Engineering*, Santa Barbara, CA, USA, CRREL, Special Report 89-6, 95-104 (1988)
4. N. Isyumov, M. Mikitiuk, Wind tunnel model tests of snow drifting on a two-level flat roof, J. Wind Eng. Ind. Aerodyn. **36**, 893-904 (1990)
5. M. Dufresne de Virel, P. Delpech, C. Sacre, Wind tunnel investigation of snow loads on buildings, *Snow Engineering, Hjorth-Hansen, Holand, Loset & Norem (Eds)*, 171–178 (2000)
6. M.J. O'Rourke, P. Wrenn, Water flume evaluation of snowdrift loads on two-level flat roofs, *Snow Engineering: Recent Advances, Izumi, Nakamura & Sack (Eds)*, 321–328 (1997)
7. T.K. Thiis, M. O'Rourke, Model for snow loading on gable roofs, J. Struct. Eng. **141**, 12 (2015) 10.1061/(ASCE)ST.1943-541X.0001286 , 04015051.
8. ISO 4355 'Bases for design of structures - Determination of snow loads on roofs' (2013)
9. Y. Tominaga, T. Okaze, A. Mochida, CFD modeling of snowdrift around a building: An overview of models and evaluation of a new approach, Build Environ **46**, 4, 899–910 (2011)
10. T.K. Thiis, J.F. Ramberg, Measurements and numerical simulations of development of snow drifts of curved roofs, *Proceedings of Snow Engineering VI*, Whistler, Canada (2008)
11. T. K.Thiis, J. Potac, J. F. Ramberg, 3D numerical simulations and full scale measurements of snow depositions on a curved roof. *In 5th European & African Conference on Wind Engineering*, Florence, Italy (2009)
12. T. Tomabechi, M. Izumi, A. Endo, A fundamental study on the evaluation method of roof-snowfall-distributions of buildings, J. Struct. Eng. **32B**, 49-62 , (1986) (in Japanese)
13. M.J. O'Rourke, M. Auren, Unbalanced snow loads on gable roofs, *Snow Engineering: Recent Advances, Izumi, Nakamura & Sack (Eds)*, 201–208 (1997)
14. ASCE, Minimum design loads for buildings and other structures, ASCE/Structural Engineering Institute (SEI) 7-19, Reston, VA. (2010)
15. Y. Tominaga, S. Akabayashi, T. Kitahara, Y. Arinami, Air flow around isolated gable-roof buildings with different roof pitches: Wind tunnel experiments and CFD simulations, Build Environ, **84**, 204-213 (2015).
16. T.H. Shih, W.W. Liou, A. Shabbir, Z. Yang, J. Zhu, A New k-ε Eddy Viscosity Model for High Reynolds Number Turbulent Flows—Model Development and Validation. Comput Fluids **24**, 3, 227-238 (1995)
17. Y. Tominaga, A. Mochida, R. Yoshie, H. Kataoka, T. Nozu, M. Yoshikawa, T. Shirasawa, AIJ guidelines for practical applications of CFD to pedestrian wind environment around buildings, J. Wind Eng. Ind. Aerodyn. **96**, 10-11, 1749-1761 (2008)

18. Architectural Institute of Japan, *AIJ Recommendations for Loads on Buildings (2004Edition)* (2006)
19. Y. Tominaga, T. Stathopoulos, Turbulent Schmidt numbers for CFD analysis with various types of flowfield, Atmos Environ **41**, 37, 8091-8099 (2007)
20. M. Naaim, F. Naaim-Bouvet, H. Martinez, Numerical Simulation of drifting snow - erosion and deposition model, Ann Glaciol **26**, 191-196 (1998)
21. ANSYS Fluent, *ANSYS Fluent Theory Guide, Release 14.5*, ANSYS Inc., Canonsburg, PA. (2012)
22. P.A. Sundsbø, Numerical simulations of wind deflection fins to control snow accumulation in building steps, J. Wind Eng. Ind. Aerodyn. 74-76, 543-552 (1998)
23. J.H.M. Beyers, P.A. Sundsbo, T.M. Harms, Numerical simulation of three-dimensional transient snow drifting around a cube, J. Wind Eng. Ind. Aerodyn. **92**, 725-747 (2004)
24. Y. Tominaga, A. Mochida, S. Murakami, S. Sawaki, Comparison of various revised k-ε models and LES applied to flow around a high-rise building model with 1:1:2 shape placed within the surface boundary layer, J. Wind Eng. Ind. Aerodyn. **96**, 4, 389-411 (2008)

# Analysis of snow drifts on arch roofs

Michael O'Rourke[1,a], Jan Potac[2] and Thomas K. Thiis[3]

[1] Rensselaer Polytechnic Institute, New York, USA
[2] Multiconsult ASA, Tromsø, Norway
[3] Norwegian University of Life Sciences, Norway

**Abstract.** ASCE provisions for unbalanced loads on arch roofs have remained nominally unchanged since the 1982 predecessor to ASCE 7. This was due to the lack of snow load case histories for these iconic roof shapes. Fortunately, drift load case histories for three large arch roofs in Norway have recently become available. In this paper, the observed arch roof snow drifts will be compared to unbalanced load provisions in current model codes and load standards in Europe and North America, specifically the ASCE 7 load standard, ISO and NBCC.

## 1. Introduction

Due to their structural efficiency and ability to economically span large distances, arches are frequently the preferred roof shape for large indoor sports facilities. They are particularly effective for symmetric loads (e.g. nominally uniform snow loads from eave to eave). Arches are not as efficient for asymmetric or unbalanced loads. Examples of asymmetric loads include across-the-ridge drift loads and differential sliding resulting from one side directly facing towards the sun. Furthermore, the shorter structural components which span between arches are particularly sensitive to localized drift surcharge loads.

In the U.S., drift loads in general and unbalanced loads for common gable roofs shapes have undergone modification and improvement based upon analysis of case histories. Provisions for unbalanced loads on arch roofs however have remained nominally unchanged since the 1982 predecessor to ASCE 7. This was due to the lack of snow load case histories for these iconic roof shapes. Fortunately drift load case histories for three large arch roofs in Norway have recently become available.

In this paper, the observed arch roof snow drifts will be compared to unbalanced load provisions in current model codes and load standards in Europe and North America, specifically the ASCE 7 load standard, ISO and NBCC.

## 2. Study sites and analysis

Potac (2013) measured snow drift accumulation on several roofs over a period of several years. In this study the snow drift loads on three arch roofs are analyzed. An overview of the roofs in the study is given in Figure 1. A total of 9 measurements were made at the Vallhall Arena over 4 winter seasons. The roof itself is a quarter cylinder with a radius of 198.5 ft (60.5 m) and a 45° roof slope at the eaves. Two measurements were made at Ekeberghallen during the 2009-10 winter. The roof was also a quarter cylinder (i.e., roof slope of 45° at the eaves). The arch roof radius at Ekeberghallen was 105.6

ft (32.2 m). Finally one measurement was made at Byggmakker (arch roof radius = 59.7 ft (18.2 m)) during the 2009-10 winter. Although the Byggmakker structure consisted of three arches, only data from the windward arch (arch #1) is analyzed herein.
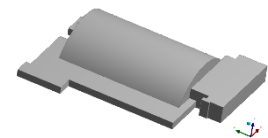


a) Neighborhood          Building shape
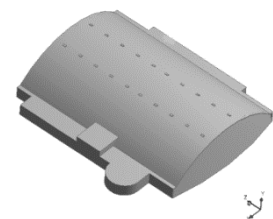


b) Neighborhood          Building shape
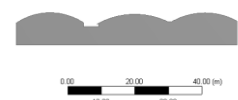


c) Neighborhood          Building shape

**Figure** 1. The three buildings in the study a) Ekeberghallen sports hall, b) Vallhall sports hall and c) Byggmakker shopping mall.

---

[a] Corresponding author: orourm@rpi.edu

Figure 2 is a sample of the arch measurements. They consisted of a plot of roof snow depth (in meters) as a function of the horizontal distance (in meters) from the top (ridgeline) of the arch.

The snow load atop the downwind portion of the arch is taken to be a nominally uniform (balanced) load plus a drift surcharge. The depth of the balanced load is taken to be 70% of the ground snow depth at a nearby location on the date of the measurement. In some cases the snow load at the ridgeline was zero, increasing with location downwind. In such cases, the location of the start of the surcharge is taken to be the location where the roof snow depth first reaches $0.7 \, h_g$.
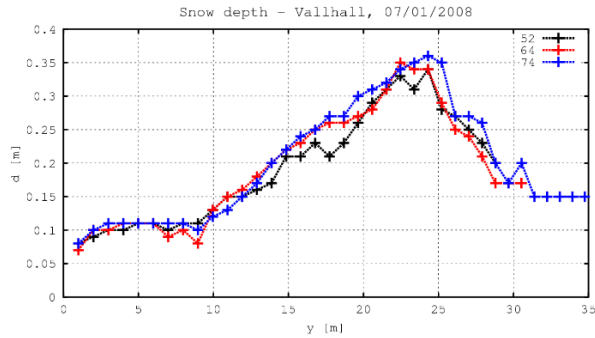


**Figure 2.** Roof snow depth measurements for Vallhall on 1/7/08

Since the three circular arch roofs had different radii, and the location of the peak roof snow depth moves during development of the snow drift (Thiis et al., 2009), the nominally triangular drift surcharge will be characterized by 4 angles as sketched in Figure 3. The first is the angle $\theta_1$ from vertical to the start of the drift surcharge (thought to be the initial flow separation point). The second is the angle $\theta_2$ to the end of the drift surcharge (thought to be the drifted snow angle of repose, or the angle corresponding to snow sliding). The next angle $\beta$ is the initial slope of the top surface of the drift surcharge (thought to correspond to the top of the aerodynamic shade region downwind of the ridge). While the final angle characterizing the surcharge geometry, $\theta_p$, is the angle from vertical to the location of the peak roof snow depth. Furthermore, the angle $\theta_p$ also corresponds to the flow separation point for a roof with a developed drift surcharge. At the start of the drift accumulation process, the angle $\theta_p$ equals $\theta_1$ and moves further downwind as the drift surcharge grows.
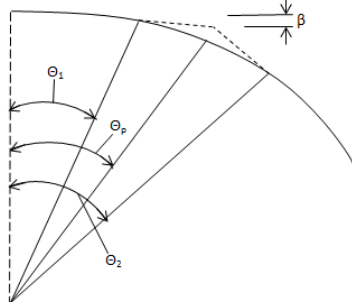


**Figure 3.** Four angles characterizing the arch roof drift surcharge.

Table 1 presents the location, measurement date and the 2 snow depth measurements for the Norwegian arches. Table 2 presents the 4 angles for the 12 sets of measurements. The ground snow depth $h_g$ ranged from 0.59 to 1.64 ft (0.18 to 0.5 m) with an average of 0.98 ft (0.3 m). The peak roof depth $h_{max}$ (balanced plus surcharge) ranged from 1.15 to 3.94 ft (0.35 to 1.2 m) with an average of 2.52 ft (0.77 m). The location of the start of the drift surcharge, $\theta_1$, ranged from 4.7 to 14.4° with an average of 8°. The peak drift location, $\theta_p$, ranged from 20.9 to 29.7° with an average of 24.5°. The end point of the surcharge, $\theta_2$, (point where the roof snow depth returned to $0.7 \, h_g$) ranged from 25.8 to 34° with an average of 28.6°. Finally, the initial slope of the top surface of the drift ranged from 2.4 to 16.9° with an average of 13.6°.

**Table 1.** Norwegian Arch Depth Measurements

| No. | Location | Date | Ground Snow Depth $h_g$ [ft] ([m]) | Peak Roof Snow Depth $d_{max}$ [ft] ([m]) |
|---|---|---|---|---|
| 1 | Vallhall | 2/27/07 | 0.66 (0.20) | 2.46 (0.75) |
| 2 | Vallhall | 1/7/08 | 0.59 (0.18) | 1.15 (0.35) |
| 3 | Vallhall | 1/20/09 | 0.89 (0.27) | 1.48 (0.45) |
| 4 | Vallhall | 1/25/09 | 0.59 (0.18) | 2.95 (0.90) |
| 5 | Vallhall | 2/8/09 | 1.44 (0.44) | 2.79 (0.85) |
| 6 | Vallhall | 2/23/09 | 1.64 (0.50) | 2.63 (0.80) |
| 7 | Vallhall | 1/5/10 | 0.72 (0.22) | 1.80 (0.55) |
| 8 | Vallhall | 2/5/10 | 0.95 (0.29) | 2.30 (0.70) |
| 9 | Vallhall | 2/23/10 | 1.02 (0.31) | 3.44 (1.05) |
| 10 | Ekeberg | 1/12/10 | 0.89 (0.27) | 2.30 (0.70) |
| 11 | Ekeberg | 2/5/10 | 1.21 (0.37) | 2.95 (0.90) |
| 12 | Byggmakker | 2/8/10 | 1.18 (0.36) | 3.94 (1.20) |

**Table 2.** Norwegian Arch Angle Measurements

| No. | $\theta_1$ [°] | $\theta_p$ [°] | $\theta_2$ [°] | $\beta$ [°] |
|-----|------|------|------|------|
| 1 | 9.5 | 27.6 | 34.0 | 16.8 |
| 2 | 11.0 | 23.4 | 29.7 | 16.9 |
| 3 | 4.7 | 24.4 | 29.7 | 13.9 |
| 4 | 14.4 | 26.5 | 29.7 | 17.0 |
| 5 | 4.74 | 23.4 | 27.0 | 14.4 |
| 6 | 4.74 | 21.8 | 27.0 | 12.0 |
| 7 | | | | |
| 8 | 9.5 | 24.4 | | 15 |
| 9 | 9.5 | 29.7 | | 17.5 |
| 10 | 5.34 | 21.9 | 25.8 | 10.4 |
| 11 | 10.7 | 25.8 | | 13.9 |
| 12 | 6.3 | 20.9 | 26.1 | 2.4 |

Since the overall objective is to investigate arch loads for design purposes, particular attention was paid to the larger drifts. The drifts were subdivided into three groups based upon relative drift size, specifically the ratio of peak snow depth to balanced depth,

$$RDS = \frac{h_{max}}{0.7\,h_g} \qquad (1)$$

For group A, the ratio was less than 3. For group B the ratio was between 3 and 4, while for group C the ratio was greater than 4, as shown in Table 3.

**Table 3.** Relative Drift Size classes

| A | B | C |
|---|---|---|
| $RDS < 3$ | $3 < RDS < 4$ | $RDS > 4$ |

The starting angle, $\theta_1$, was found to be an increasing function of relative drift size. The value chosen for $\theta_1$ was 9.2°, the average for groups B and C. Similarly the peak location, $\theta_p$, was found to be an increasing function of relative drift size. The value chosen for $\theta_p$ was 25.1°, again the average for groups B and C. On the other hand, there was no apparent variation of $\theta_2$ or $\beta$ with relative drift size. For these parameters, the average of all three groups was chosen that is $\theta_2 = 28.6°$ and $\beta = 13.6°$.

The cross-sectional area of the drift surcharge and the location of the surcharge center of gravity were determined from the surcharge geometry given above. The drift surcharge area $A_d$ was

$$A_d = 0.00416\,R^2 \qquad (2)$$

and the location of the surcharge center of gravity was

$$\chi = 0.354\,R \qquad (3)$$

where R is the radius of the circular roof. Note that the values in (2) and (3) are based on circular arch roofs with the radius roughly in the 65.6 to 196.85 ft (20 to 60 m) range. One expects for a given amount of wind, the percentage of the upwind snow that is transported onto the leeward side (hence eligible for drift formation) is a decreasing function of roof radius. That is, one expects that the constant 0.00416 in (2) would be larger for smaller radius roofs and smaller for larger radius roofs.

The size and location of the observed drift surcharge is quantified by (2) and (3). Since the size is provided as an area, one needs a snow density to convert into load. Herein the ASCE 7 empirical relation between snow density $\gamma$ (lb/ft$^3$) and ground snow load $p_g$ (lb/ft$^2$) is used

$$\gamma = 0.13\,p_g + 14$$
$$\text{in SI: } \gamma = 0.426\,p_g + 2.2 \qquad (4)$$

For a quarter cylinder roof (eave roof slope = 45°) the total downwind load (lb/ft) from (2) thru (4) is presented in Table 4 for four values of the roof radius $R$ and the ground snow load $p_g$. Also presented in Table 4 is the location of the center of gravity $\chi$ of the total (balanced plus surcharge) downwind (ridge to eave) load. These parameters, the total snow load on the downwind side of the arch and its center of gravity would be needed for the structural design of the arch spanning from eave to eave. However, for the in-fill beams which span between adjacent arches, the peak localized load is the key parameter. Based upon the Norwegian measurements, this peak pressure occurs at $\theta_p$ (25.1°). The drift surcharge depth at this peak load location is $0.026\,R$ based upon geometry.

**Table 4.** Total downwind load and center of gravity (distance from ridge) based upon Norwegian observed geometry.

| Arch radius R [ft] ([m]) | Total Downwind Load [lb/ft] ([kN/m]) | | | $\chi$ [ft] ([m]) |
|---|---|---|---|---|
| | $p_g$ = 20 lb/ft$^2$ (1 kN/m$^2$) | $p_g$ = 50 lb/ft$^2$ (2.4 kN/m$^2$) | $p_g$ = 100 lb/ft$^2$ (4.8 kN/m$^2$) | |
| 20 (6.1) | 226 (3.3) | 529 (7.7) | 1035 (15.1) | 7.1 (2.2) |
| 50 (15.2) | 668 (9.8) | 1452 (21.2) | 2756 (40.2) | 17.7 (5.4) |
| 100 (30.5) | 1681 (25.5) | 3328 (48.6) | 6073 (88.6) | 35.4 (10.8) |
| 200 (61) | 4741 (69.2) | 8361 (122) | 14380 (210) | 70.8 (21.6) |

Table 5 presents the peak localized pressure (surcharge plus balanced) for various values of $R$ and $p_g$. Note in this regard that for the Norwegian observations,

the ratio of the peak roof snow depth to the ground depth for the 12 measurements in Table 1 ranged from 1.6 to 5.0 with an average of 2.71.

**Table 5.** Peak Localized Pressure (drift surcharge plus balanced) based upon observed geometry of Norwegian Arches.

| Arch radius R [ft] ([m]) | Peak Pressure [lb/ft²] ([kN/m²]) | | |
|---|---|---|---|
| | $p_g = 20$ lb/ft² (1 kN/m²) | $p_g = 50$ lb/ft² (2.4 kN/m²) | $p_g = 100$ lb/ft² (4.8 kN/m²) |
| 20 (6.1) | 22.6 (1.1) | 45.7 (2.2) | 84.0 (4.0) |
| 50 (15.2) | 35.6 (1.7) | 61.7 (2.9) | 105.1 (5.0) |
| 100 (30.5) | 57.2 (2.7) | 88.3 (4.2) | 140.2 (6.7) |
| 200 (61) | 100.3 (4.8) | 141.6 (6.8) | 210.0(10.1) |

# 3. Comparison to ASCE 7 provisions

ASCE 7-10 (ASCE 2010) provides curved roof unbalanced loads for three groups of roof slope at the eave. Specifically the unbalanced load for an eave roof slope of 45°, corresponding to the quarter cylinder roofs in the Norwegian measurement program, is shown in Figure 4. The roof snow load at the ridge is half the so-called flat roof snow load $0.5\,p_f$, while the load at the 30° roof slope point is $2\,p_f\,C_s^{**}/C_e$ and $2\,p_f\,C_s^{*}/C_e$ at the eave (45° roof slope point). In ASCE 7 the flat roof load is a function of the structures importance factor $I_s$, the roof exposure factor $C_e$, and the roof thermal factor $C_t$. Herein it is assumed that the roof is of ordinary importance ($I_s = 1.0$), has normal wind exposure ($C_e = 1.0$) and is heated ($C_t = 1.0$). For these conditions, the flat roof load is $0.7\,p_g$ where $p_g$ is the ground snow load with a 50 year mean recurrence interval.
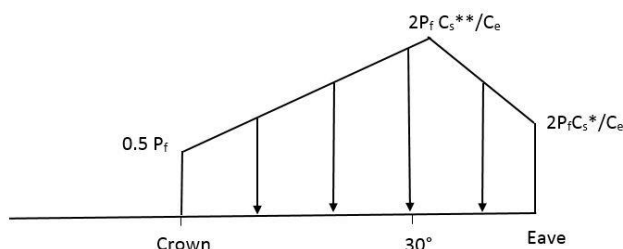


**Figure 4.** Unbalanced load in ASCE 7 for an arch roof with eave slope of 45°.

$C_s^{**}$ is the slope factor at the 30° point and $C_s^{*}$ is the slope factor at the eave (45° point for our quarter cylinder roofs). For slippery roof surfaces, corresponding to the Norwegian arches with plastic membrane roof material, the slope factors at 30 and 45° are 0.615 and 0.385 respectively. As such the load at the ridge is $0.35\,p_g$ while the loads at the 30° point and the eave are $0.861\,p_g$ and $0.53\,p_g$.

The total downwind load from the ASCE 7 provisions is shown in Table 6 for an arch radius ranging from 20 to 200 ft (6.1 to 61 m), and a ground snow load ranging from 20 to 100 lb/ft² (1 kN/m² to 4.8 kN/m²). A comparison of the total loads in Table 4 and Table 6 show that the ASCE 7 load is smaller than that suggested by the observed geometry of the Norwegian arch measurements. The ratio of ASCE 7/Norwegian observed ranged from 38% to 86% with the lowest percentage (38% - most unconservative) occurring for the low ground snow loads (20 lb/ft² (1 kN/m²)) and large arch radius (200 ft (61 m)). The highest ratio (86% - slightly unconservative) occurs for the high ground snow loads (100 lb/ft² (4.8 kN/m²)) and small arch radius (20 ft (6.1 m)).

**Table 6.** Total Downwind Load and center of gravity (distance from ridge) based upon ASCE 7 provisions.

| Arch radius R [ft] ([m]) | Total Downwind Load [lb/ft] ([kN/m]) | | | $\chi$ [ft] ([m]) |
|---|---|---|---|---|
| | $p_g = 20$ lb/ft² (1 kN/m²) | $p_g = 50$ lb/ft² (2.4 kN/m²) | $p_g = 100$ lb/ft² (4.8 kN/m²) | |
| 20 (6.1) | 179 (2.6) | 447 (6.5) | 894 (13.1) | 7.7 (2.4) |
| 50 (15.2) | 447 (6.5) | 1118 (16.3) | 2235 (32.6) | 19.3 (5.9) |
| 100 (30.5) | 894 (13.1) | 2235 (32.6) | 4470 (65.2) | 38.6 (11.8) |
| 200 (61) | 1788 (26.1) | 4470 (65.2) | 8940 (130) | 77.2 (23.5) |

In terms of the location of the total unbalance load, the Norwegian measurements suggest that the center of gravity is at $0.354\,R$ from the ridge, while the ASCE 7 provisions have the center of gravity at $0.386\,R$ – a difference of 9%.

For the design of the in-fill beams which span between adjacent arches, the peak localized pressure as per the ASCE 7 provisions is $0.86\,p_g$ or 17.2, 43.1 and 86.1 lb/ft² for $p_g$= 20, 50 and 100 lb/ft² respectively. In comparison to the peak local pressures in Table 4, the ASCE pressures are arguably reasonable for an arch radius of 20 ft (6.1 m) but are low by roughly a factor of 2 to 5 for an arch radius of 200 ft (61 m).

In relation to the location of the peak localized pressures the Norwegian measurement program suggests it occurs at $\theta_p = 25.1°$, while the peak localized pressure in the ASCE 7 provisions occurs at 30° or a difference of about 20%.

## 4. Comparison with ISO 4355 provisions

Provisions in the International Standards Organization (ISO 4355) provide unbalanced snow loads for curved roofs, pointed arches, and domes. For a quarter cylinder (circular arch with eave slope of 45°), the unbalanced snow load is

$$s_d = s_0\, \mu_b\, \mu_d(x) \qquad (5)$$

where $s_0$ is the 50 year design ground snow load, $\mu_b$ is a slope coefficient and $\mu_d(x)$ is a drift coefficient given by

$$\mu_d(x) = \begin{cases} 2\, x/x_{30} & x \le x_{30} \\ 2 & x \ge x_{30} \end{cases} \qquad (6)$$

where $x$ is the horizontal distance from the ridge and $x_{30}$ is the horizontal distance to the location where the roof slope is 30°.

The slope coefficient for a slippery roof surface over a heated space (i.e., characteristics for the Norwegian Arches) is shown in Figure 5.
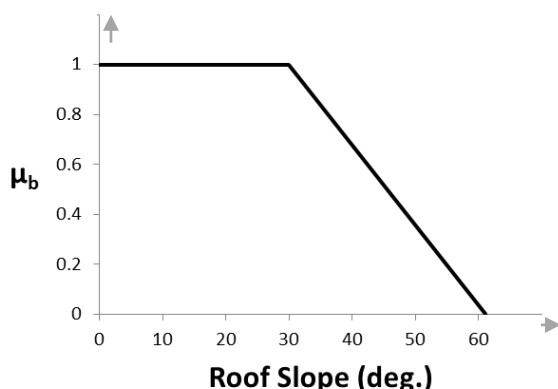


**Figure 5.** Slope Coefficient in ISO 4355 for slippery roof surface over a heated space

As such, the unbalanced snow load in the ISO provisions for a quarter cylinder roof increases from zero at the ridge to $2\, s_0$ at the 30° roof slope point and then decreases to $s_0$ at the eave (45° roof slope point). This unbalanced load is sketched in Figure 6.
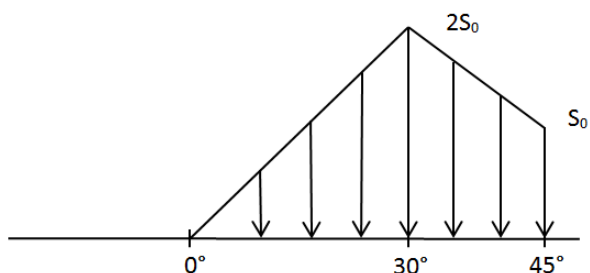


**Figure 6.** Unbalanced Snow Load for Quarter Cylinder Arch in ISO

The total downwind snow load in Figure 6 is $0.8R\ s_0$ and its center of gravity is at $0.437\,R$ from the ridge.

Table 7 presents the total downwind load and location of the center of gravity for the ISO provisions for the same range of arch radius and ground snow loads as Table 4 and Table 6.

**Table 7.** Total Downwind Load and center of gravity (distance from ridge) based upon ISO provisions

| Arch radius R [ft] ([m]) | Total Downwind Load [lb/ft] ([kN/m]) | | | $\chi$ [ft] ([m]) |
| --- | --- | --- | --- | --- |
| | $p_g = 20$ lb/ft$^2$ (1 kN/m$^2$) | $p_g = 50$ lb/ft$^2$ (2.4 kN/m$^2$) | $p_g = 100$ lb/ft$^2$ (4.8 kN/m$^2$) | |
| 20 (6.1) | 320 (4.7) | 800 (11.7) | 1600 (23.4) | 8.74 (2.7) |
| 50 (15.2) | 800 (11.7) | 2000 (29.2) | 4000 (58.4) | 21.90 (6.7) |
| 100 (30.5) | 1600 (23.4) | 4000 (58.4) | 8000 (117) | 43.70 (13.3) |
| 200 (61) | 3200 (46.7) | 8000 (117) | 16000 (234) | 87.40 (26.6) |

In terms of total downwind load, the ISO provisions provide a much better match to the observed Norwegian values (Table 4) than the ASCE 7 provisions (Table 6). For most combinations of R and $s_0$ (i.e. $p_g$), the ISO loads are larger than the observed with ISO overestimating the observed by roughly 55% for the case of small arch radius (R = 20 ft (6.1 m)) and large ground snow load ($p_g = s_0 = 100$ lb/ft$^2$ (4.8 kN/m$^2$)). For a large arch radius (R = 200 ft (61 m)) and small ground snow loads ($p_g = s_0 = 20$ lb/ft$^2$), the ISO underestimate the expected (Table 4) loads by roughly 50%.

In terms of the location of the center of gravity, the Norwegian measurements suggest that the center of gravity, $\chi$, is at $0.36\,R$ while the ISO provisions yield $\chi$ at $0.44\,R$, roughly a 20% difference.

Finally, in terms of the peak pressure need for design of the in-fill beams which span between arches, the ISO provisions specify a peak pressure of $2\, s_0$ (twice the design ground snow load). In comparison to the observed Norwegian values in Table 5, the ISO values overestimate the peak pressures for eight of the 12 combinations of $R$ and $p_g$. The worst underestimation is for $p_g = 20$ lb/ft$^2$ (1 kN/m$^2$) and R = 200 ft (61 m), for which the peak pressure based upon the observed Norwegian geometry is about 2.5 times larger.

## 5. Comparison with NBCC provisions

The National Building Code of Canada (NBCC, 2010) provides unbalanced snow load provisions for arch roofs, curved roofs and domes. For a quarter cylinder arch of ordinary importance, the unbalanced load is

$$S = C_b\, C_w\, C_s\, C_a\, S_s \qquad (7)$$

where $C_b$ is the basic snow factor, $C_w$ is the wind exposure factor specified as 1.0 for the unbalanced case, $C_a$ is shape factor, $C_s$ is the slope factor, and $S_s$ (i.e., $p_g$) in the 50 year ground snow load. In the Canadian provisions, the product $C_b\, C_a$ is identical to the ISO drift coefficient $\mu_d(x)$ in (5). The slope factor $C_s$ in NBCC for unobstructed slippery surfaces is similar to the ISO $\mu_b$ shown in Figure 5, except that the transition from flat to sloped (uniform to linearly decreasing) occurs at the 15° roof slope location.

As a result, the unbalanced snow load in NBCC for a quarter cylinder arch with a slippery unobstructed roof surface is as sketched in Figure 7.
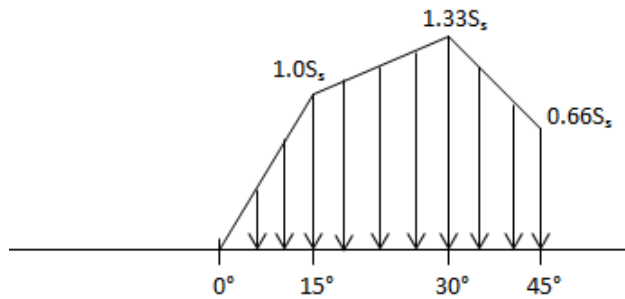


**Figure 7.** Unbalanced Snow Load for Quarter Cylinder Arc in NBCC

The total downward load in Figure 7 is $0.618\, S_s^*\, R$ (roughly 75% of that in ISO), while the center of gravity is located at $0.408\, R$ from the ridge. Table 8 presents the total downward load and location of the center of gravity for the same range of roof and ground load parameters as Table 4.

**Table 8.** Total Downwind Load and center of gravity based upon NBCC provisions.

| Arch radius R [ft] ([m]) | Total Downwind Load [lb/ft] ([kN/m]) | | | $\chi$ [ft] ([m]) |
|---|---|---|---|---|
| | $S_s = 20$ lb/ft$^2$ (1 kN/m$^2$) | $S_s = 50$ lb/ft$^2$ (2.4 kN/m$^2$) | $S_s = 100$ lb/ft$^2$ (4.8 kN/m$^2$) | |
| 20 (6.1) | 247 (3.6) | 617 (9.0) | 1236 (18.0) | 8.2 (2.5) |
| 50 (15.2) | 618 (9.0) | 1545 (22.6) | 3090 (45.1) | 20.4 (6.2) |
| 100 (30.5) | 1236 (18.0) | 3090 (45.1) | 6180 (90.2) | 40.8 (12.4) |
| 200 (61) | 2472 (36.1) | 6180 (90.2) | 12360 (180) | 81.6 (24.9) |

Fifty percent of the downwind load values in Table 8 are larger than the Norwegian values in Table 4. Like the ASCE 7 (Table 6) and ISO (Table 7), the worst performance is for low ground snow loads and large arch radius (NBCC load ~50% of expected load at $S_s$ (i.e., $p_g$) of 20 lb/ft$^2$ (1 kN/m$^2$) and $R$ of 200 ft (61 m)).

Considering the design load for in-fill beams, the peak local pressure on the roof for the NBCC provisions is $1.33\, S_s$ or 26.6, 66.5, and 133 lb/ft$^2$ for $S_s$ of 20, 50 and 100 lb/ft$^2$ respectively (1.33, 3.19, and 6.38 kN/m$^2$ for $S_s$ of 1.0, 2.4, and 4.8 kN/m$^2$ respectively) . In comparison to Table 5, NBCC underestimated the peak local pressure for seven of the twelve radius and ground load combinations. This performance (7 of 12 underestimated) was better than ASCE 7 (11 of 12 underestimated, but not as good as ISO (4 of 12 underestimated).

# 6. Conclusions

A series of full scale measurements on circular arch roofs in Norway were analyzed to determine the downwind snow surcharge corresponding to the unbalanced load case. The Norwegian arches were quarter cylinders (constant radius, 45° roof slope at the eaves) with roof radius ranging from 60 to 198.5 ft (18.2 to 60.5 m). The drift surcharge typically began at 9.2° and terminated at 28.6° with the peak surcharge occurring at 25.5°. The initial slope of the drift surcharge had a slope of 13.6°.

Based upon the observed geometry, the expected load for a series of quarter cylinder arches were determined and compared to current provisions in ASCE 7, ISO 4355 and NBCC.

Unbalanced loads from the ASCE 7 provisions generally underestimated the magnitude of the leeward load. The poorest performance occurred for a low ground snow load and a large arch radius where the expected load was more than 2.5 times the load prescribed by the ASCE 7 provision.

The ISO provisions faired much better in comparison to the Norwegian observation. In about 66% of the comparisons the ISO loads were larger than those based upon the Norwegian observations. However, like the ASCE 7 provisions, ISO underestimated the expected loads for low ground snow loads and large arch radii.

In relation to the peak roof pressure needed to design the in-fill beams which span between arches, ISO again did a better job than ASCE. However, all these sets of provisions performed poorly in relation to the expected peak pressure for arches with a large radius in a low ground load location.

The NBCC provisions resulted in larger loads (better performance) than the ASCE 7 provisions but lower loads (poorer performance) than the ISO provisions.

Finally, the Norwegian measurements were for arch roofs with arch radius ranging from 60 to 198.5 ft (18.2 to 60.5 m). The ground snow depths ranged from 0.59 to 1.64 ft (0.18 to 0.5 m). Since the unbalanced load case is the result of snow drifting, one expects that the

normalized drift size as characterized by the ratio of peak roof snow depth to ground snow depth ($d_{max}/h_g$ ranged from 1.6 to 5.0 with an average of 2.71) would decrease for larger values of the arch radius and increase for smaller values of the arch radius. Similarly, one also expects that the $d_{max}/h_g$ ratio will decrease for larger values of the ground snow load and increase for smaller values of the ground snow load.

## References

"ASCE (American Society of Civil Engineers) (2010)" Minimum design loads for buildings and other structures (ASCE/SEI 7-10). American Society of Civil Engineers, Reston, VA, USA.

ISO (International Standards Organization) (2013), "ISO 4355 Bases for design of structures, Determination of snow loads on roofs".

NRCC (National Research Council of Canada) (2010) "National Building Code of Canada," Institute for Research in Construction, Ottawa, Ontario, Canada.

Potac, J. (2013) Field measurements and numerical simulations of snow transport and deposition around structures and into ventilation intakes. PhD Thesis Norwegian University of Life Sciences ISSN 1503-1667 ISBN 978-82575-1180-7

Thiis, T.K., Potac, J., Ramberg, J.F. 3D numerical simulations and full scale measurements of snow deposition on a curved roof. 5th European and African conference on Wind engineering, EACWE 5, Florence, Italy, 2009
http://www.iawe.org/Proceedings/5EACWE/104.pdf

# Falling snow and ice from buildings and structures: risk assessment and mitigation – two case studies

Stefan Margreth[1,a]

[1]*WSL Institute for Snow and Avalanche Research SLF, 7260 Davos Dorf, Switzerland*

**Abstract.** Falling snow and ice from buildings can be extremely dangerous for pedestrians or traffic. This paper describes the factors contributing to hazardous snow and ice accumulations and shows how the risks can be assessed. Two case studies are presented to demonstrate how the adverse effects of snow and ice accumulations on buildings are identified and minimized. An important conclusion is to involve snow experts in an early planning stage of complex buildings in snowy areas.

## 1 Introduction

Snow loads on buildings, including the load of snow overhangs, are comprehensively regulated in different standards (e.g. Swiss Code 261 [1]). Few documents, however, exist concerning how to handle the risk of falling ice and snow from buildings or facades. Falling snow and ice from buildings can be extremely dangerous for pedestrians or traffic [2]. Even a small piece of ice can be dangerous if it hits a sensitive area such as a person's eye [3]. Snow accumulates not only on roofs but also to some extent on exterior architectural features such as window sills, solar shades or fins especially in snowy areas. Deposited snow can become unstable and meltwater can contribute to ice accumulations [4]. The normal approach to handle the risk of falling ice and snow is to specify safety zones covering the endangered areas or to optimize the design of the structure. The latter includes, for example, adaptations of the roof geometry, minimizing horizontal structural features such as window sills where snow can accumulate, reducing the size of drift areas or improving drainage systems to prevent dripping of meltwater. Sometimes the risk can be minimized with the installation of mitigation measures such as snow fences, snow barriers, snow drift measures or heating systems. Building designers are often not aware of the danger of falling snow or ice leading to expensive, post-construction design modifications.

## 2 Assessment of risk

The amount of snow and ice which accumulates on a building depends mainly on the geographic location, climate, wind exposure, geometry and structure of building, solar exposure and heat losses. Whether accumulated snow stays stable or not depends on many factors, such as strength of snow, width of snow overhang, relation of snow thickness to supporting surface or inclination and surface roughness. A chunk of snow typically falls if overhanging snow breaks off (case 1, Figs. 1 and 2) or if a mass of snow becomes unstable (case 2, Figs. 1 and 4). Case 1 occurs often in snowdrift situations if the weight of the overhanging snow mass is greater than its strength. Case 2 is especially relevant if the height of

the accumulated snow is greater than the width of the supporting surface or if the supporting surface is inclined and smooth. The equilibrium of an accumulated snow mass can become unstable due to unfavourable deformation processes because of settlement of the snow and melting processes which reduce friction.
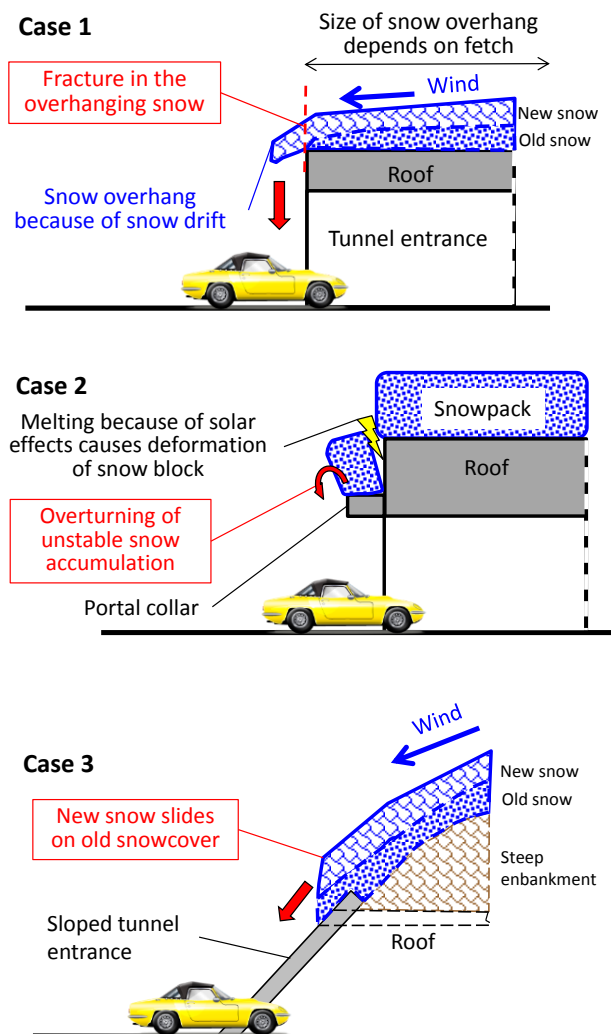


**Figure 1.** Hazard scenarios for falling and sliding snow masses from tunnel entrances.

---

[a] Corresponding author: margreth@slf.ch

If a tunnel portal is sloped snow can slide off like an avalanche (case 3, Figs. 1 and 5) and hit the road. Snow can slide directly on the structure if the surface roughness is low. This case is mostly decisive if the slope of the structure is relatively low [5]. In snowy climates and on steep surfaces snowslides can release as well on or in between the snow cover (Fig. 5). Such snowslides happen especially during snow storms and warming periods if the stability of the snow cover is very poor.

The resulting risk of falling snow depends mainly on the likelihood that a snow accumulation breaks off or slides, the weight of the falling chunk of snow, the drop height, the width of the danger zone and the presence of persons and objects. Very crucial is the geometry of the structure and conditions of the area where snow can accumulate. The annual snowfall controls the risk. For a structure located at high elevation with a great annual snowfall (see case study A) the risk of falling snow is much higher compared to a low elevation with a small annual snowfall.

Icicles typically form on buildings because of freezing or dripping water. The roof or facade of a building can warm up because of heat transfer or solar radiation. Deposited snow melts and dripping water freezes if the air temperature is below 0 °C. The growth of an icicle on a building is a complicated process, which is very sensitive to the atmospheric conditions and the water flux. The growth is faster if the air temperature is below -5 °C than if the air temperature is between 0 °C and -5 °C. The growth rate is increasing with strong winds and low melting water flux [6]. For Switzerland maps exist which show the frequency of meteorological icing at 10 and 100 m height above ground [7]. For the Central Plateau, the meteorological icing frequency at a height of 10 m is low, about 4 days/year. The maximum simulated icing frequency at a height of 10 m is found in the area of the Central Alps and is about 100 days/year. These icing maps were elaborated with focus on ice accretion on powerlines and wind turbines.

Little information is available on the problem of icing on buildings because of dripping water or melted snow. We tried to quantify the probability of potential icing and formation of icicles by analysing the combination of days per winter with a snow height of more than 10 cm and mean negative temperatures. We named such a day an "icicle day". Because a single "icicle day" is often not sufficient to form a large icicle we looked as well at the number of "icicle periods". We named a time period an "icicle period" if the snow height is more than 10 and 20 cm respectively and the mean air temperature is lower than 0 °C during three consecutive days and lower than -5 °C respectively during two consecutive days. We think that the number of "icicle days" and "icicles periods" per winter allows to assess for a certain location the potential risk of icing and icicle formation. An icicle breaks off when its weight is greater than its strength. This occurs typically if the air temperature is above 0 °C or if the structural component where the icicle is fixed warms up. Strong winds combined with warm temperatures increase the risk that an icicle falls. The risk is reduced if the air temperature is below -5 °C [4]. Icicles do not build without dripping water. The risk of icicle formation can be minimized by preventing the snow from melting (e.g. cold roof), by draining melting water with structural adaptations (e.g. rain pipes) or by installing combined heating and drain systems.

The following two case studies on risk and mitigation of falling snow and ice from buildings and structures are based on consulting mandates we recently completed.

# 3 Case study A: Tunnel entrances along San Bernardino highway (Switzerland)

The San Bernardino national highway is 58 km long and connects eastern Switzerland with the Canton of Ticino. The highway is the second most important transit axis, after the Gotthard route, crossing the Swiss Alps for freight and private transport. The culmination of the highway is a 6.6 km long road tunnel at an elevation of 1650 m a.s.l. On 1 February 2014, strong southerly winds on the San Bernardino national highway led to the formation of snow drifts at different tunnel entrances. The new snow height in the area was about 35 cm. In the late afternoon, a chunk of snow weighing approximately 10 kg broke off from the northern entrance of the San Bernardino tunnel and struck a passing car with an approximate impact force of 900 N.



**Figure 2.** North entrance of the San Bernardino tunnel on 1 February 2014 with the fractured snow overhang (Photo Tiefbauamt Graubünden).



**Figure 3.** Damaged front shield of a car hit by a falling chunk of snow on San Bernardino national highway, on 1 February 2014 (Photo Kantonspolizei Graubünden).

We calculated the impact force as a function of the falling snow mass, the drop height, the velocity of the car and the deceleration time [8]. Although the impact caused heavy damage to the vehicle, the passengers were unharmed (Figs. 2 and 3). The maintenance personnel checked the portal two hours before the accident without spotting a dangerous snow overhang. A similar accident happened in 2012 at the southern entrance of the Cassanawald tunnel when a chunk of snow weighing approximately 15 kg hit the windshield of a passing car. Luckily there was also only material damage. A survey in Switzerland showed that no other similar incidents are documented.



**Figure 4.** Entrance of the Cassanawald tunnel with portal collar in winter 2014, San Bernardino national highway. The width of the portal collar is 50 cm and the depth of the accumulated snow is about 80 cm.

The SLF was asked to investigate how and where dangerous snow overhangs form on tunnel entrances and to evaluate possible measures for avoiding accidents in the future. The analysis of snow data shows that the 100-year snow height varies along the San Bernardino national highway between 90 cm at an elevation of 400 m a.s.l. and 340 cm at an elevation of 1650 m a.s.l. The return period of a snowfall of 40 cm varies between 4 and 50 years. Based on a daily traffic of 5000 vehicles, a vehicle velocity of 70 km/h and the assumption that every winter five times a snow chunk breaks off we calculated an occurrence probability of 0.03 per year that a vehicle is hit along the San Bernardino national highway. With the assumption that every tenth hit ends deadly the risk of death of a commuter who travels the road four times a day is $2.4 \times 10^{-6}$ which is a little lower than the threshold value of $1 \times 10^{-5}$ accepted in Switzerland [9].

We analysed the geometry and design, the local amount of snow and the exposure to snowdrift of 38 tunnel entrances for the risk assessment and the possible planning of mitigation measures. Five of the tunnel entrances which are all situated above an elevation of 1500 m a.s.l. were found to be particularly endangered due to high exposure to snowdrift and portal collars where snow accumulations can get easily unstable (Figs. 1 and 4).



**Figure 5.** South entrance of the San Bernardino tunnel in winter 2014. The snow cover was removed around the sloped tunnel portal. Snow drift accumulations or new snow can easily slide (see case 3, Fig. 1). The old snow cover is stabilized by knee pines which are overfilled with snow.

The normal procedure to prevent the formation of dangerous snow accumulations on tunnel portals is to visually check the situation within the scope of the winter maintenance and to remove manually hazardous snow masses if necessary. At some tunnel portals up to 30 clearing operations were performed in the snow rich winter 2013/14. The maintenance personnel climb on the portals and remove the snow with shovels. Such operations can be very dangerous and time consuming. We recommended in particular that access for maintenance personnel be improved with fixed installed ladders and guardrails. Furthermore, we proposed installing heating bands on the portal collars at three critical entrances (Fig. 6). The heating band prevents the accumulation of snow by continuous melt. Heating bands worked well on a portal collar with a width of 50 cm in winter 2014.
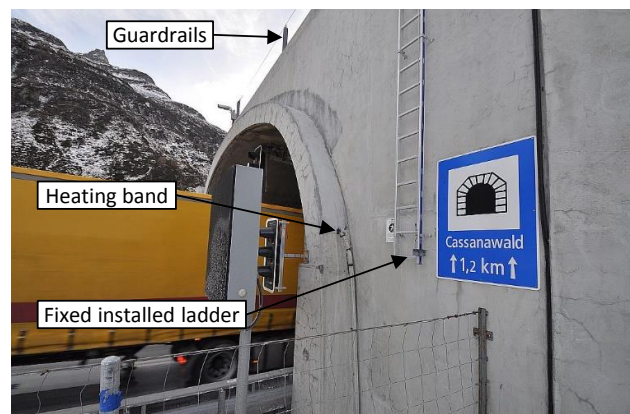


**Figure 6.** North entrance of the Cassanawald tunnel, San Bernardino national highway. In fall 2014 an electrical trace heating system was installed on the portal collar to prevent hazardous snow accumulations. A fixed installed ladder and guardrails allow an easier access to the roof of the tunnel and safer work conditions to remove snow accumulations.
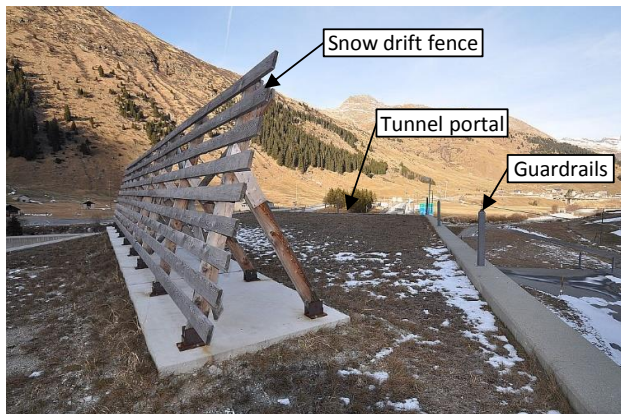
**Figure 7.** Snowdrift fence on the north entrance of the San Bernardino tunnel (Fig. 2). The fence which is anchored on prefabricated concrete slabs is made out of wooden boards and trusses. The snowdrift fence can relatively easily be displaced if necessary. In addition, guardrails were installed to allow a safe removal of snow overhangs.

The northern portal of the San Bernardino tunnel has a 40 m long horizontal roof. Southerly winds transport snow towards the portal. We proposed to build a snowdrift fence with a height of 2.5 m and a length of 12 m to prevent dangerous snowdrift accumulations (Fig. 7). The goal of a snowdrift fence is to restrain the wind so that the force of the wind on the snow surface is reduced allowing moving snow particles to come to rest [10]. Most of the drifted snow is deposited on a limited area on the downwind side of the fence. The fence should be oriented perpendicular to the predominant wind direction. We proposed a porosity of the fence of 30% and a bottom gap of 30 cm. The fence was designed on a wind force of 1.6 kN/m². So far not much experience on the effectiveness of the installed snow fence could be gained because the winters 2015 and 2016 were not very rich in snow.

# 4 Case study B: Facades of a planned four-story office building in St. Gallen (Switzerland)

The planned building, resting on two mighty cones, forms the main entrance to the Helvetia Insurance building complex (Fig. 8). The building is the last stage of three similar extensions which were as well planned by the architects Herzog & de Meuron and completed in 2004. The facades of the buildings consist of room-height windows, mounted with a slight twist from their vertical or horizontal axis (Fig. 9). The window boxes overhang the facade by 20 to 30 cm.

Observations demonstrate that dangerous snow and ice accumulations can form on the window boxes and roof parapets. On 10 February 2015 the snow height in St. Gallen varied between 20 and 30 cm. About 20 cm of snow accumulated on the roof and the top most window boxes (Fig. 10). The snow masses accumulated in the facade were about ten times smaller compared to the roof.
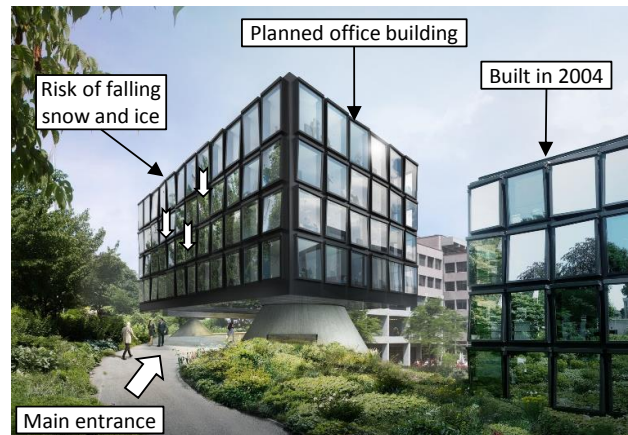


**Figure 8.** The planned new west wing of the Helvetia Insurance building complex in St. Gallen towers above the main entrance (planning architects Herzog & de Meuron, Basel, Switzerland). Falling snow and ice from the 17 m high building can be a risk. The identity of the entire complex is shaped by the uniform facade treatment of all four extensions (Visualisation Herzog & de Meuron).



**Figure 9.** Snow accumulations on the window boxes of the existing Helvetia building on 10 February 2015.

**Figure 10.** Snow accumulations on the window boxes of the existing Helvetia building on 10 February 2015. The snow height is about 20 to 40 cm.
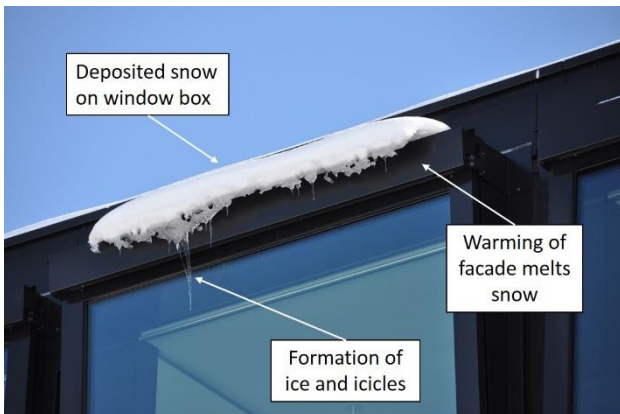


**Figure 11.** Formation of small icicles on the window boxes of the existing Helvetia building on 10 February 2015.

A chunk of snow weighing approximately 10 to 20 kg broke off from a window box and hit the ground. Our evaluation showed that the break off was caused by tipping of the snow mass due to uneven melting (case 2, Fig. 1). Solar radiation considerably warms the facade and window boxes. This can cause additional meltwater which can refreeze as ice accumulations or icicles (Fig. 11). The cover of each window box is designed with a slight slope towards the outer facade. Rain water and meltwater drops uncontrolled along the facade. Falling snow chunks or icicles were so far not a problem because green areas surrounded the buildings. However, the newly planned main entrance will be situated directly below the facade.

The SLF was mandated to evaluate the risk of falling snow and ice masses and to propose mitigation measures for the planned new west wing to decrease the risk. The 50-year snow height in St. Gallen (776 m a.s.l.) is 90 cm. The 50-year snow height on the roof of the planned building is estimated to be 70 cm. The maximum recorded new snow depth in 24 hours is 60 cm and the 50-year total new snow sum is 375 cm. The long-term average number of ice days with maximum temperatures below 0 °C is 35. The number of "icicle days" is 28 with a mean temperature below 0 °C and a snow height of 10 cm or 14 with a snow height of 20 cm (Fig. 12). Furthermore, we evaluated the number of "icicle periods". On average, 2 to 3 "icicle

periods" per winter with a minimal snow height of 10 cm and a length of 7 days must be expected in St. Gallen. Our analysis demonstrated that nearly every winter dangerous snow and ice accumulations have to be expected on the planned office building. We concluded that the risk of falling snow and ice is unacceptable without further structural adaptations and mitigation measures. Without such measures the access to the building would have to be closed every winter for certain time periods.
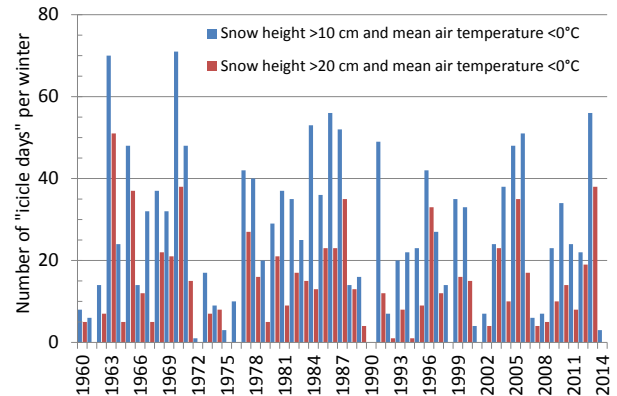


**Figure 12.** Number of "icicle days" per winter in St. Gallen, 776 m a.s.l.

The installation of a porch roof above the main entrance would be the most simple and most effective mitigation measure. However such a porch roof was out of the question because of the architectural design concept of the whole building complex. The uniform shape of the facade could not be changed. Therefore we proposed comprehensive mitigation measures which include heating systems on all window boxes above the entrance area and the roof parapets, heated rain pipes and an enlargement of the roof parapets to 65 cm (Fig. 13). Furthermore, we recommended planning the ledges of the facade to be inclined towards the roof to prevent that snow masses slide outward and endanger the entrance area. In addition, we suggested to connect the drainage of the window boxes with continuous heated rain pipes over the whole width of the entrance area. The heat capacity should be planned so that about 10 cm of new snow with a density of 150 kg/m$^3$ can be melted per hour.

We concluded that the risk of falling snow and ice is acceptable with the proposed mitigation measures for a normal winter scenario with an estimated return period of 50 years. Additional temporary measures such as closures or snow and ice removal were considered to be only necessary in exceptional meteorological situations. We proposed to inspect the completed new building after ice and snow events to verify the performance of the proposed measures.
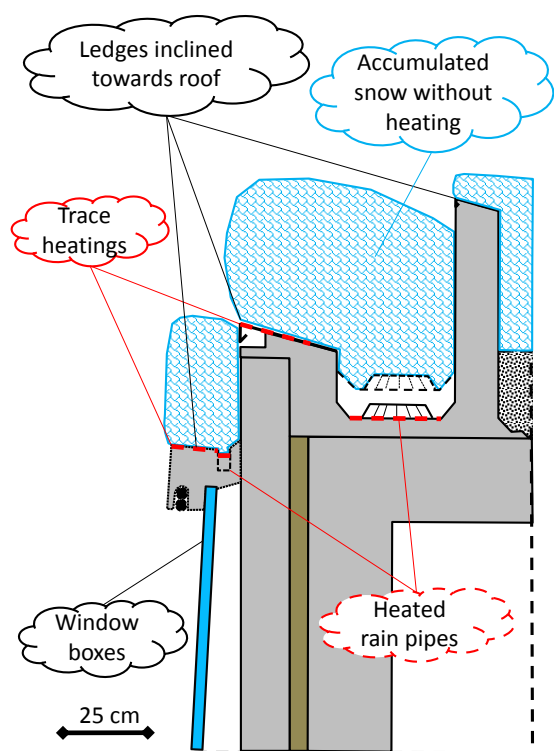
**Figure 13.** Facade and roof parapet of the planned new west wing building with the proposed mitigation measures for the new building.

# 5 Conclusions

The risk of falling snow and ice accumulations depends strongly on the building design and the snow climate. It is very important to involve snow experts in an early planning stage. If problematic accumulation surfaces for snow such as small ledges, window sills or roof parapets are identified their adverse effect can be often minimized with small adaptations to the design. An important point is to inspect a completed building after ice and snow events to verify the performance of the proposed measures. According to experience it is much more complex and costly to improve the design of an existing building or structure. The quantification of the adverse effect of snow and ice accumulations is very difficult and has to be assessed mostly by expert judgment. Therefore the documentation of incidents or interesting winter observations is very valuable for a better understanding of the interaction between snow, ice and buildings.

# References

1. SIA, *Actions on structures*, Swiss Code 505 261 (2014).
2. M. Carter, R. Stangl, *Increasing Problems of Falling Ice and Snow on Modern Tall Buildings*. CTBUH Journal 2012 Issue IV. 24-28 (2012).
3. C.J. Williams, M. Carter, F. Hochstenbach and T. Lovlin. *Sliding snow and ice on buildings: a balance of risk, cost and aesthetics.* Proceedings of the Fifth International Conference on Snow Engineering, 5-8 July 2004, Davos, Switzerland. Edited by E. Adams, P. Bartelt, R. Sack, A. Sato, and M. Christen. Taylor & Francis 2004, 59–66 (2004).
4. A. Nielsen, *Snow, Ice and Icicles on Roofs – Physics and Risks*, Sixth Nordic Conference on Building Physics in the Nordic Countries, Reykjavik, 562-569 (2005).
5. D.A. Taylor, *Sliding Snow on Sloping Roofs*. Canadian Building Digest (1983).
6. L. Makkonen, *A model of icicle growth*. J. Glaciol. **34**, 64-70 (1988).
7. T. Grünewald, S. Dierer, R. Cattin, P. Steiner, W. Steinkogler, F. Fundel and M. Lehning. *Mapping frequencies of icing on structures in Switzerland*. J. Wind Eng. Ind. Aerodyn. **107–108**, 76-82 (2012).
8. R. Perla, T. Beck and J. Banner, *Impact Force of Snow*. NHRI Paper No. **2**, IWD Sci. Ser. No. 97. Natl. Hydrology Research Institute, Ottawa, Canada (1979).
9. Federal Roads Office FEDRO, *Natural hazards on national roads: Risk concept. Methodology for risk-based assessment, prevention and response to gravitative natural hazards on national roads*. ASTRA 89001 (2012).
10. R.D. Tabler, *Snow fence guide*. SHRP-W/FR-91-106 (1991).

# Capture of windward drift snow

Jan Potac [1,a], Michael O'Rourke [2] and Thomas K. Thiis [3]

[1]*Multiconsult AS, Tromsø, Norway*
[2]*Rensselaer Polytechnic Institute, Troy, NY USA*
[3]*Norwegian University of Life Sciences, Ås, Norway*

**Abstract.** A new taller building adjacent to an existing building with a lower roof is a relatively common situation. The new building provides a snow source area, which results in snow drift atop the lower roof which likely was not anticipated in its original design. Since it is usually difficult to retrofit the existing roof structure, a solid wall can be considered to capture the expected snow transport on the upper roof. Using field measurement on snowdrift development, ASCE 7 provisions and Drift Ratio parameter, two approaches based on average or conservative values are studied to determine the required height of the solid wall.

## 1. Introduction

Building roofs are generally designed to carry snow loads prescribed in snow load standards. Shape factors have been used to describe the snow distribution for various roof shapes. However, a snow drift load not anticipated in original design can appear, for example, in case of a new higher building adjacent to an existing lower roof building, as show in Figure 1. In this example, the uniform distribution on the lower roof would alter to the triangular distribution due to the effect of the upwind building. It is difficult to retrofit the existing roof, in general. Therefore, to avoid the snowdrift on the lower roof, a solid wall could be erected on the upper roof to capture the expected upwind snow and thus avoid the snowdrift built-up on the lower roof.
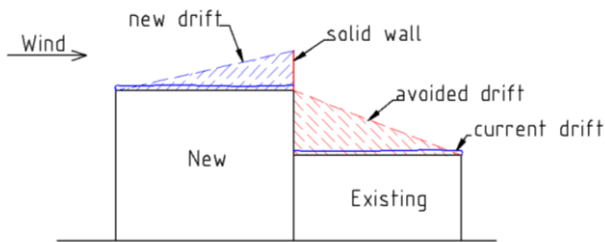


**Figure 1.** Scheme of load situation

In this paper, two approaches are evaluated to determine the relation between the upper roof fetch, and the solid wall height to capture the snow on the upper roof. Potac [1] conducted measurements on snowdrift development around solid fences of various heights and shapes. This experimental data and data on drift loads from Cocca and O'Rourke [3] together with ASCE 7 provisions [2] are utilized to evaluate the required height of the solid wall.

## 2. Method

The snow load is commonly considered to consist of balanced and drifted components. Therefore, the minimum wall height $h_w$ that would capture the expected upwind snow can be expressed as the sum of the heights of the balanced and drifted snow $h_b$ and $h'_d$, respectively.

In addition, one needs to consider a height characterizing the required freeboard $h_s$ (distance from top of the drift to top of wall) to avoid snow particles hopping over the wall. Therefore, an expression for $h_w$ can be written as

$$h_w = h_b + h'_d + h_s \qquad (1)$$

The height of balanced drift $h_b$ can be obtained using the expression for flat surface loads and snow density as

$$h_b = \frac{0.7p_g}{\gamma} \qquad (2)$$

Where $p_g$ is the ground snow load and $\gamma$ (lb/ft$^3$) is the snow density determined as

$$\gamma = 0.13p_g + 14$$
$$\text{in SI}: \gamma = 0.426p_g + 2.2 \qquad (3)$$

To evaluate the drift component $h'_d$, two approaches are introduced. The first, Approach 1, adopts the ASCE 7 relation for a leeward drift of characteristic slope $s = 0.25$ (rise to run of 1:4). Furthermore, it is assumed that the trapping efficiency, which lead to the drift is 0.5. That is, the total amount of snow transport is twice the area of the ASCE 7 leeward drift. Comparing the area of the ASCE 7 drift with the area of measured drifts, one can obtain the drift height $h'_d$ as a function of $h_d$ defined in ASCE 7 as

$$h_d = 0.43\sqrt[3]{l_u}\sqrt[4]{p_g + 10} - 1.5 \qquad (4)$$

where $l_u$ is the length of the roof upwind the drift.

The second approach utilizes Drift Ratio (DR) [3], which is defined as a percentage of the snow in the snow source area that contributes to drift formation. Drift Ratio can be expressed as

$$DR = \frac{L_d}{p_g l_u} \qquad (5)$$

where $L_d$ is the annual maximum drift load. Similarly to Approach 1 above, trapping efficiency of 0.5 is assumed. Then, the annual maximum drift load $L_d$ is compared to the load from drift measurements. As a result, a relation for drift height $h'_d$ is obtained as a function of $DR$, $p_g$ and $l_u$.

---

[a] Corresponding author: jan.potac@gmail.com

The height characterizing the required freeboard $h_s$ should correspond to a height when snow particles are not able to hop over the wall. Its value is to be determined from measurements. In both approaches, average or maximum (conservative) values of drift parameters and Drift Ratio are considered.

## 3. Field data

Three solid wall fences (I) and two solid wall fence with lee-overhang (Γ) are analyzed. The schematic overview of the geometries studied is given in Figure 2.
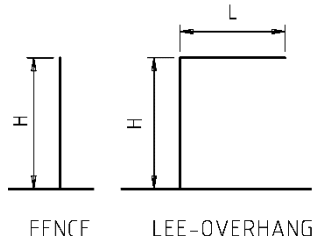


**Figure 2.** Snow fence geometries

The measurements show that the snowdrift starts developing first on the windward side of the fence. When the windward side is partially filled, the leeward snowdrift starts developing, as shown in Figure 3.
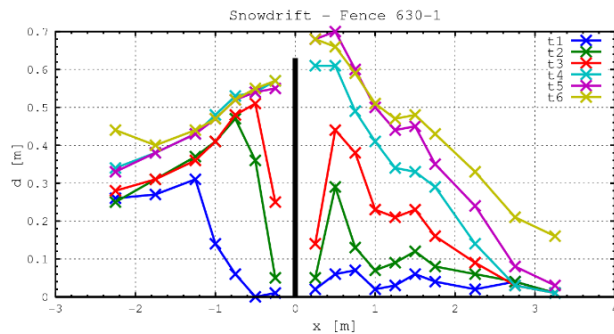


**Figure 3.** Snowdrift development [1]

The geometry of windward snowdrift is characterized by four parameters: solid wall height $h_0$, windward drift height for no leeward drift $h_1$, windward drift height for substantial leeward drift $h_2$, and slope parameter for windward drift $s$. The height parameters are summarized in Table 1.

**Table 1.** Snowdrift parameters

| Fence type | $h_0$ [ft] ([m]) | $h_1$ [ft] ([m]) | $h_2$ [ft] ([m]) |
|---|---|---|---|
| I | 2.07 (0.63) | 0.98 (0.30) | 1.57 (0.48) |
| I | 2.95 (0.90) | – | 1.87 (0.57) |
| I | 4.26 (1.30) | 2.36 (0.72) | 2.36 (0.72) |
| Γ | 2.3 (0.70) | 1.31 (0.30) | 1.31 (0.40) |
| Γ | 3.44 (1.05) | 1.97 (0.52) | 1.97 (0.60) |

Since the snow transport along a surface is primarily given via saltation, one expects that the odds that a saltating snow particle will hop over the wall is related to the height difference. Height difference obtained from the measurements is shown in Table 2.

Later on in this study two sets of slope $s$ and height difference $h_s = h_0 - h_1$ are employed. While Approach 1 uses average values, the second, Approach 2 uses maximum, thus conservative values.

**Table 2.** Height difference

| Fence type | $s$ [-] | $h_0 - h_1$ [ft] ([m]) | $h_0 - h_2$ [ft] ([m]) |
|---|---|---|---|
| I | 0.14 | 1.08 (0.33) | 0.49 (0.15) |
| I | 0.09 | – | 1.08 (0.33) |
| I | 0.08 | 1.90 (0.58) | 1.90 (0.58) |
| Γ | 0.06 | 1.31 (0.40) | 0.98 (0.30) |
| Γ | 0.16 | 1.74 (0.53) | 1.48 (0.45) |
| Avg. | 0.107 | 1.51 (0.46) | 1.19 (0.36) |
| Max. | 0.16 | 1.90 (0.58) | 1.90 (0.58) |

## 4. Analysis

In the section above, the minimum wall height was derived as a function of two parameters: $p_g$ and $l_u$. Therefore, for further analysis we consider the following ranges of $p_g$ = 10, 20, 50, 100 lb/ft$^2$ and $l_u$ = 50, 100, 250, 500 and 1000 ft.

### 4.1. Approach 1

As described in 2, using this approach, the minimum solid wall height is determined using ASCE 7 drift area, trapping efficiency of 50% and drift height $h_d$, in comparison to geometric properties of the snowdrift from measurements. For further analysis average values of geometrical properties of measured drifts, i.e. $s = 0.1$ and height difference $h_s = h_0 - h_1 = 1.5$ ft (0.46 m) are considered. Comparing the ASCE 7 drift area with the area of drift measurements, one obtains the relation for $h_d'$ as

$$h_d'^2 = \frac{4}{5} h_d^2 \Rightarrow h_d' = 0.90 h_d \qquad (6)$$

Employing Equation 2, 3, 4 and 6 into Equation 1 together with the average value of $s$ and $h_s$, the minimal wall height $h_w$ for given ranges of ground snow load and fetch is calculated in Table 3.

**Table 3.** Minimum wall height, Approach 1

| $h_w$ [ft] ([m]) | | $l_u$ [ft] ([m]) | | | | |
|---|---|---|---|---|---|---|
| | | 50 (15.2) | 100 (30.5) | 250 (76.2) | 500 (152.4) | 1000 (304.8) |
| $p_g$ [lb/ft$^2$] ([kN/m$^2$]) | 10 (0.5) | 3.62 (1.10) | 4.41 (1.34) | 5.76 (1.76) | 7.10 (2.17) | 8.79 (2.68) |
| | 20 (1) | 4.33 (1.32) | 5.20 (1.58) | 6.70 (2.04) | 8.18 (2.49) | 10.05 (3.06) |
| | 50 (2.4) | 5.83 (1.78) | 6.86 (2.09) | 8.64 (2.63) | 10.41 (3.17) | 12.63 (3.85) |
| | 100 (4.8) | 7.36 (2.24) | 8.56 (2.61) | 10.64 (3.24) | 12.69 (3.87) | 15.28 (4.66) |

Values from Table 3 are visualized in Figure 4. It is shown that for given parameters of $l_u$ and $p_g$ the minimal wall height ranges from 3.62 ft to 12.69 ft for ground snow load 10 lb/ft$^2$ and fetch 50 ft, and 100 lb/ft$^2$ and 500 ft, respectively.

**Figure 4.** Minimum wall height, Approach 1



**Figure 5.** Minimum wall height, Approach 2

## 4.2. Approach 2

Cocca and O'Rourke [3] present plots of DR as a function of ground snow load for upwind fetches 50, 250, 500 and 1000 ft. These figures can be used to establish conservative DR values for Approach 2. Table 4 shows conservative values of DR assigned to upwind fetches according to the plots in Cocca and O'Rourke.

**Table 4.** Fetch and conservative DR values

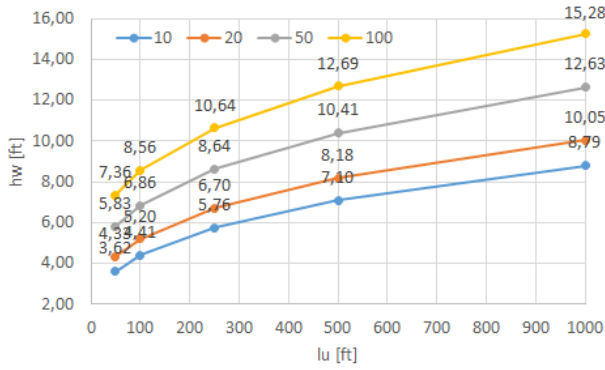| $l_u$ [ft] ([m]) | $DR$ [-] |
|---|---|
| 50 (15.2) | 0.35 |
| 250 (76.2) | 0.30 |
| 500 (152.4) | 0.25 |
| 1000 (304.8) | 0.20 |

Furthermore, conservative values of slope and height difference from measurements are considered, i.e. $s = 0.16$ and $h_s = 2$ ft. Then, the annual maximum drift load $L_d$ can be obtained from Equation 5 and equated to load calculated from trapping efficiency 50%, conservative drift parameters and snow density $\gamma$. Hence, the expression for the drift height $h'_d$ is obtained as

$$h'_d = \sqrt[2]{\frac{2}{3}\frac{DR\,p_g\,l_u}{\gamma}} \qquad (7)$$

Then, considering the conservative value of $h_s$, the minimum wall height can be determined from Equation 1. Calculated values are shown in Table 5 and plotted in Figure 5.

**Table 5.** Minimum wall height, Approach 2

| $h_w$ [ft] ([m]) | | $l_u$ [ft] ([m]) | | | |
|---|---|---|---|---|---|
| | | 50 (15.2) | 250 (76.2) | 500 (152.4) | 1000 (304.8) |
| $p_g$ [lb/ft$^2$] ([kN/m$^2$]) | 10 (0.5) | 5.22 (1.59) | 8.17 (2.49) | 9.84 (3.00) | 11.79 (3.59) |
| | 20 (1) | 6.59 (2.01) | 10.60 (3.23) | 12.86 (3.92) | 15.52 (4.73) |
| | 50 (2.4) | 9.04 (2.76) | 14.75 (4.50) | 17.96 (5.48) | 21.74 (6.63) |
| | 100 (4.8) | 11.17 (3.40) | 18.20 (5.55) | 22.16 (6.75) | 26.81 (8.17) |
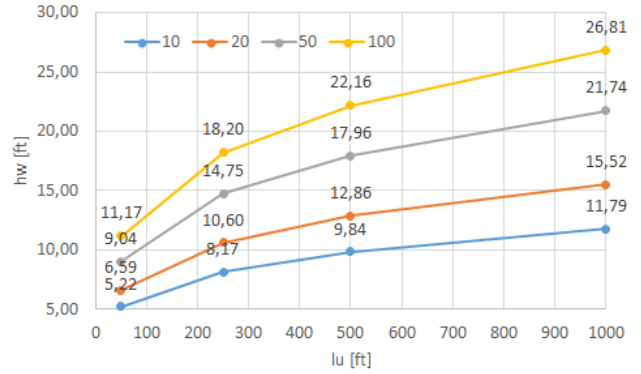
Comparing values of $h_w$ for both approaches, Figure 4 with Figure 5, values of approximately 30% larger are obtained using Approach 2 than by Approach 1.

Since the second approach uses both conservative (i.e. "not likely to be exceeded") values for DR and for drift parameters, it is found that Approach 2 arguably provides unrealistically large values for $h_w$.

Hence, two other scenarios are considered. First scenario combines conservative values for DR (Table 6) and average windward drift parameters. Alternately, the second combination uses average value of DR and conservative windward drift parameters. The larger of these two combinations is expected to provide reasonably safe values for $h_w$.

**Table 6.** Conservative (maximum) values of DR

| $DR$ [-] | | $l_u$ [ft] ([m]) | | | |
|---|---|---|---|---|---|
| | | 50 (15.2) | 250 (76.2) | 500 (152.4) | 1000 (304.8) |
| $p_g$ [lb/ft$^2$] ([kN/m$^2$]) | 10 (0.5) | 0.37 | 0.30 | 0.25 | 0.20 |
| | 20 (1) | 0.25 | 0.20 | 0.20 | 0.20 |
| | 40 (1.9) | 0.25 | 0.22 | 0.20 | 0.18 |

Similarly to previous calculation, using the average value of $s = 0.106$, drift density, trapping efficiency of 50%, the drift load can be compared to the load obtained by using conservative values of DR (Table 6), which results in expression for $h'_d$ as

$$h'_d = \sqrt[2]{0.377\frac{DR\,p_g\,l_u}{\gamma}} \qquad (8)$$

Using the average value of $h_0 - h_1$ and $h_0 - h_2$ from Table 2 $h_s = 1.33$ ft, the minimum wall height is obtained from Equation 1 and shown in Table 7.

**Table 7.** Minimum wall height, Approach 2, combination 1

| $h_w$ [ft] ([m]) | | $l_u$ [ft] ([m]) | | | |
|---|---|---|---|---|---|
| | | 50 (15.2) | 250 (76.2) | 500 (152.4) | 1000 (304.8) |
| $p_g$ [lb/ft$^2$] ([kN/m$^2$]) | 10 (0.5) | 3.92 (1.2) | 6.09 (1.86) | 7.34 (2.24) | 8.81 (2.68) |
| | 20 (1) | 4.56 (1.39) | 6.94 (2.11) | 8.91 (2.72) | 11.70 (3.57) |
| | 40 (1.9) | 5.92 (1.8) | 9.36 (2.85) | 11.65 (3.55) | 14.68 (4.47) |

In second combination, maximum value of height difference $h_s$= 1.90 ft (0.58m) is employed together with the maximum slope $s$ = 1.6. Comparing the measured drift load with the load obtained using DR, and assuming trapping efficiency 50%, the drift height $h'_d$ can be calculated as

$$h'_d = \sqrt[2]{0.63 \frac{DR\, p_g\, l_u}{\gamma}} \qquad (9)$$

The resulting values of minimal wall height $h_w$ are show in Table 8.

**Table 8**. Minimum wall height, Approach 2, combination 2

| $h_w$ [ft] ([m]) | | $l_u$ [ft] ([m]) | | | |
|---|---|---|---|---|---|
| | | 50 (15.2) | 250 (76.2) | 500 (152.4) | 1000 (304.8) |
| $p_g$ [lb/ft²] ([kN/m²]) | 10 (0.5) | 4.55 (1.39) | 6.31 (1.92) | 7.14 (2.18) | 8.47 (2.58) |
| | 20 (1) | 5.23 (1.59) | 7.33 (2.23) | 8.61 (2.62) | 10.05 (3.06) |
| | 40 (1.9) | 6.30 (1.92) | 9.39 (2.86) | 11.48 (3.5) | 12.25 (3.73) |

Table 9 show maximum values of minimum wall height from Table 7 and Table 8. Values are plotted in Figure 6.

The combination of average and conservative values of drift parameters and DR shows more realistic values than in the case of conservative values only. The minimum wall height in this case are close to values obtained by Approach 1, that is based on average values of drift parameters and ASCE 7 drift.

**Table 9**. Minimum wall height, Approach 2, maximum of combination 1 and combination 2

| $h_w$ [ft] ([m]) | | $l_u$ [ft] ([m]) | | | |
|---|---|---|---|---|---|
| | | 50 (15.2) | 250 (76.2) | 500 (152.4) | 1000 (304.8) |
| $p_g$ [lb/ft²] ([kN/m²]) | 10 (0.5) | 4.55 (1.39) | 6.31 (1.92) | 7.34 (2.24) | 8.81 (2.68) |
| | 20 (1) | 5.23 (1.59) | 7.33 (2.23) | 8.91 (2.72) | 11.7 (3.57) |
| | 40 (1.9) | 6.30 (1.92) | 9.39 (2.86) | 11.65 (3.55) | 14.68 (4.47) |
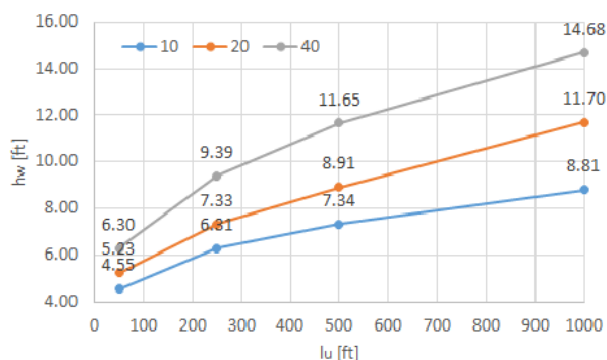


**Figure 6.** Minimum wall height, Approach 2, maximum of combination 1 and combination 2

Comparison of all three sets of calculation for ground snow load of 20 lb/ft² (1 kN/m²) is shown in Figure 7. It shows that the minimum wall height values are relatively similar for Approach 1 and Approach 2 using combinations of average and conservative parameters.
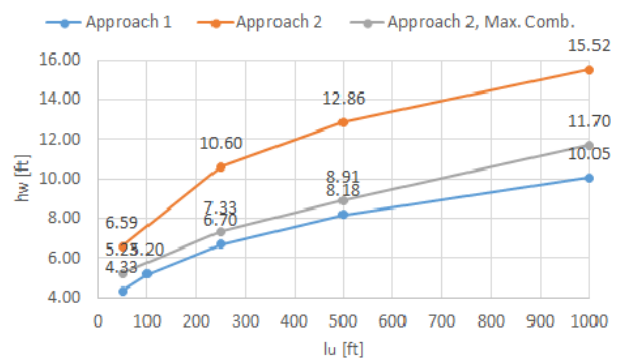


**Figure 7.** Summary of all three approaches for ground snow load of 20 lb/ft²

## 5. Conclusions

Field measurements of snowdrift around solid snow fences were analyzed, and characteristic drift properties (slope and height difference) were determined. For further analysis, average and conservative values were considered. In first set of calculations, average drift parameters $s$ = 0.1 and $h_s$=1.5 ft (0.46 m) were compared to ASCE 7 drift relation resulting in minimum wall height ranging from 4.33 ft (1.32 m) to 10.05 ft (3.06 m) for a location with ground snow load of 20 lb/ft² (1 kN/m²) and fetch of 50 ft (15.24 m) and 1000 ft (304.8 m) respectively.

The second set of calculations employs conservative values of drift parameters ($s$ = 0.16 and $h_s$= 2 ft (0.58 m) and conservative values of Drift Ratio DR. This approach leads to arguably unrealistic large values. The minimum wall height ranged from 6.59 ft (2.01 m) to 15.52 ft (4.73 m) for a location with ground snow load of 20 lb/ft² (1 kN/m²) and fetch of 50 ft (15.24 m) and 1000 ft (304.8 m) respectively. It is approximately 30% lagrer than values obtained from first set of calculations.

Finally, two combinations of average and conservative values of DR and drift parameters are considered. Resulting values of minimum wall height lead to more realistic values ranging from 5.23 ft (1.59 m) to 11.7 ft (3.57 m) for a location with ground snow load of 20 lb/ft² (1 kN/m²) and fetch of 50 ft (15.24 m) and 1000 ft (304.8 m) respectively. These values are relatively similar to values obtained using by Approach 1.

## 6. References

1. Potac, J. (2013) Field measurements and numerical simulations of snow transport and deposition around structures and into ventilation intakes. PhD Thesis Norwegian University of Life Sciences ISSN 1503-1667 ISBM 978-82575-1180-7
2. American Society of Civil Engineers (2013) Minimum Design Loads for Buildings and Other Structures ASCE 7-10, New York, NY
3. Cocca, J. and O'Rourke, M. (2008) Mathematical Simulation of 50-Year Snow Drift Loads. Structures Congress 2008: pp. 1-9. doi: 10.1061/41016(314)150

# Wind tunnel tests and analysis of snow load distribution on three different large size stadium roofs

Andrzej Flaga[1], Łukasz Flaga[2]

[1]Prof.D.Sc.Eng. Andrzej Flaga, Wind Engineering Laboratory, Faculty of Civil Engineering, Cracow University of Technology, Poland
[2]Ph.D.Eng.Arch. Łukasz Flaga, Faculty of Civil Engineering, Department of Technology of Building and Materials Processes, Częstochowa University of Technology, Poland

**Abstract.** The article contains comparison and analysis of snow load tunnel tests for three different roofs of sport facilities. Tests were performed in a wind tunnel with boundary layer modelling. Snow precipitation and redistribution tests were performed using powdered polystyrene foam as artificial snow. The results of snow load distributions were presented as dimensionless roof shape factor of snow load for both the precipitation and redistribution simulations.

## 1 Introduction

The paper deals with snow load tunnel tests for three different roof constructions of sport facilities. Test were performed for: Municipal Stadium in Łódź, Poland [1] (study case L), Municipal Stadium in Poznań, Poland [2] (study case P), and multi-purpose sports and entertainment hall in Krakow (study case K) [3] (comp. Fig. 1, 2 & 3).



a)

b)

c)
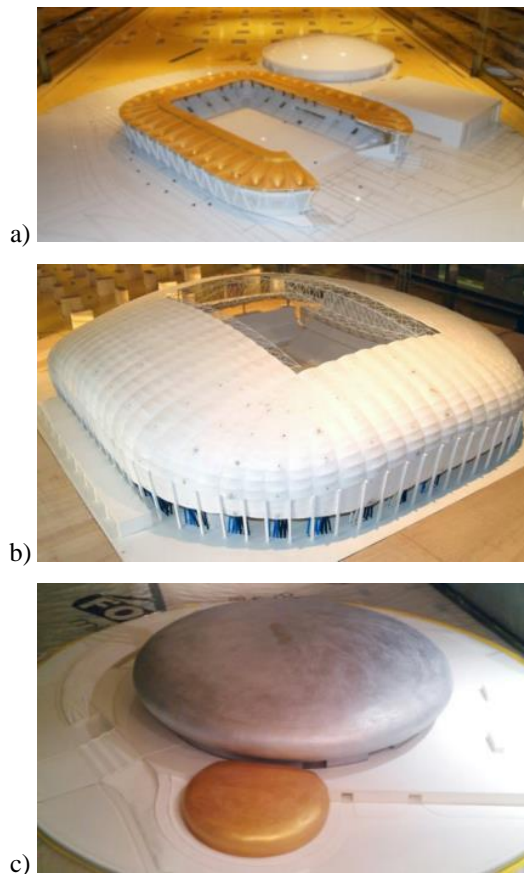
**Figure 1.** Model of the: Municipal Stadium in Łódź, Poland (a), Municipal Stadium in Poznań, Poland (b) and multi-purpose sports and entertainment hall in Krakow, (Poland) (c) in working section of the wind tunnel [1, 2, 3]

[a] Corresponding author: lukasz.flaga@interia.pl

Experimental works were made in a boundary layer wind tunnel, which allowed proper creation of natural wind speed and turbulence profile. Wind tunnel facility belongs to the Wind Engineering Laboratory at the Cracow University of Technology. Main goal of the paper is to compare and analyse results of snow load tunnel tests for three geometrically different roofs of sport facilities.

The geometry of each roof shape as well as its construction is different (comp. Fig. 2). It is obvious that the unique shape of the roof substantially affect the shape of the snow cover. Key differences in the form of roof structures are: study case L – concave membranes (comp Fig. 2 a); study case P – convex membrane (comp Fig. 2 b); study case K – dome – (comp Fig. 2 c). Comparison between influences of snow load distribution schemes on each construction was not a part of this article.

Initially, for each of tested cases similarity criteria were elaborated. The powdered polystyrene foam was used to simulate snow for each study case (P, L & K). It was powdered on a belt sander. Detailed description of the adopted similarity criteria and bases for experimental works are presented in [4, 5, 6].

## 2 Experimental setup

### 2.1 Wind tunnel

The flow structure inside working section of the tunnel was established using floor blocks, spires and fence (Fig. 3). Wind speed was measured in several vertically aligned points with the use of hotwire thermo-anemometers. From the regression of the mean speed measurement, exponent of the power-law wind speed profile in model situation was obtained for both precipitation and redistribution experiments.

a)



b)



c)
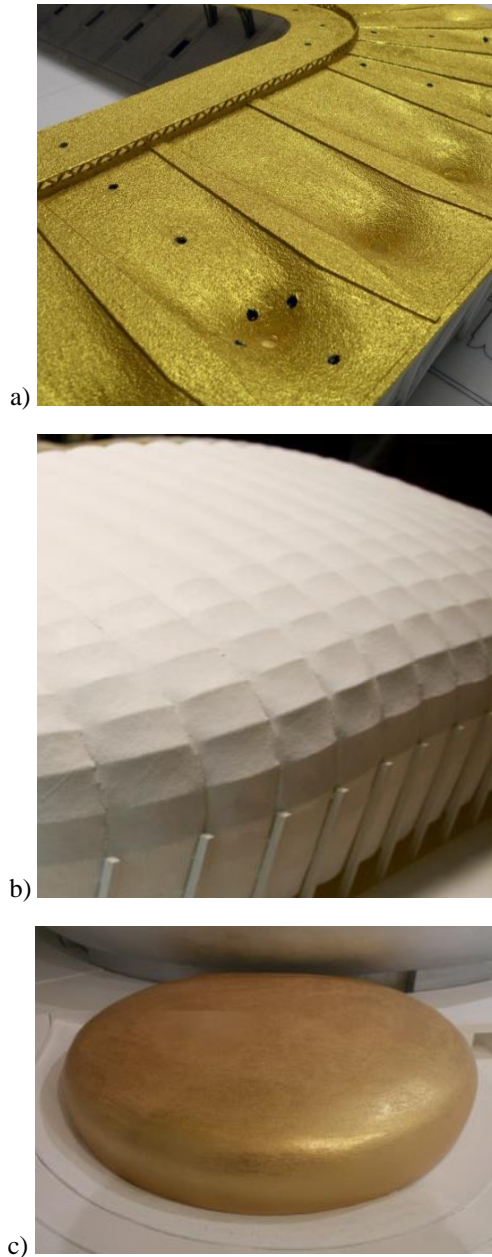
**Figure 2.** Key differences in the form of roof structures: study case L – concave membranes (a), study case P – convex membranes (b), study case K – dome (c) [1, 2, 3]

## 2.2 Artificial snow

Substance: grinded styrofoam (Fig. 4):
• $\rho_c$ – particle bed density: ~10 kg/m$^3$
• $d$ – mean particle diameter: 0,43 mm
• $v_t$ – terminal speed: 0,3 m/s
• $\chi$ – kinematical cohesion: 0 m$^2$/s$^2$

Density was measured with help of laboratory scales and cylinder. Diameter was measured with help of 100x microscope. Terminal speed was obtained by measurement of artificial snow falling time from 1m height. Because artificial snow is a loose material the kinematical cohesion is nearly zero.
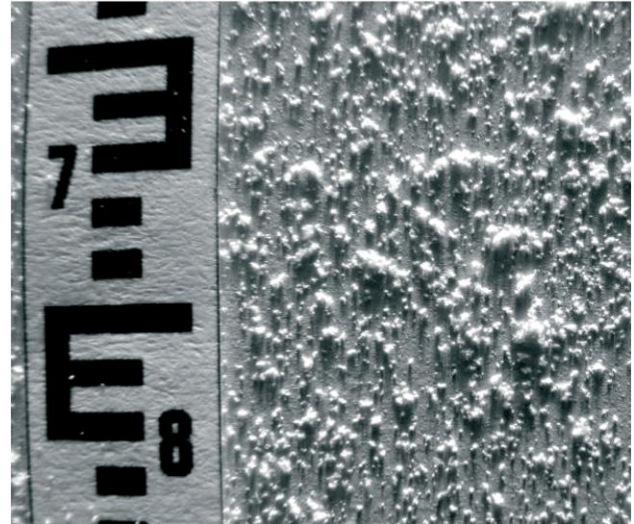


**Figure 4.** A sample of "artificial snow" made of styrofoam (numbers on the scale denote centimetres) [5]

## 2.3 Artificial snow supply (feeder)

A feeder is presented in Figure 5. The device consists of stable sieve – steel frame 108x220 cm, with perforated bottom 6x20 mm and movable sieve – steel frame 100x210 cm, identical perforated bottom. Movable sieve is suspended on slide bearing. Sieve is moved by a motor with continuous regulation of speed. It is possible to stop the sieve in closed position.
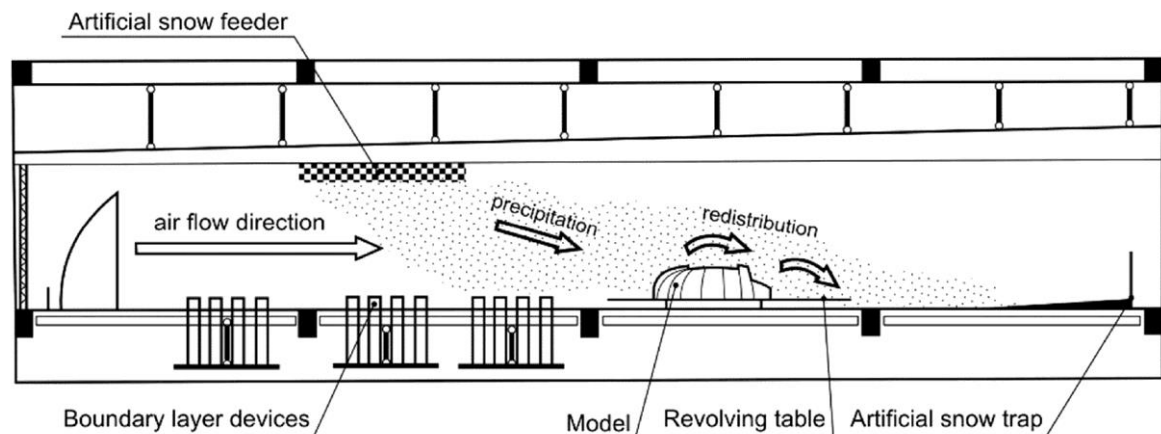


**Figure 3.** Experiment implementation [4]

## 2.4 Photogrammetry method

The measurement of snow cover thickness was done by a single frame photogrammetry method for case study P and K. For the case study L an optical scanning method was used. The results were elaborated as diagrams that can be used during design process. Scheme of photogrammetry arrangement schematic diagrams and method used in experiments are presented in Figure 6 (a) and (b).

a)



Top view



b)
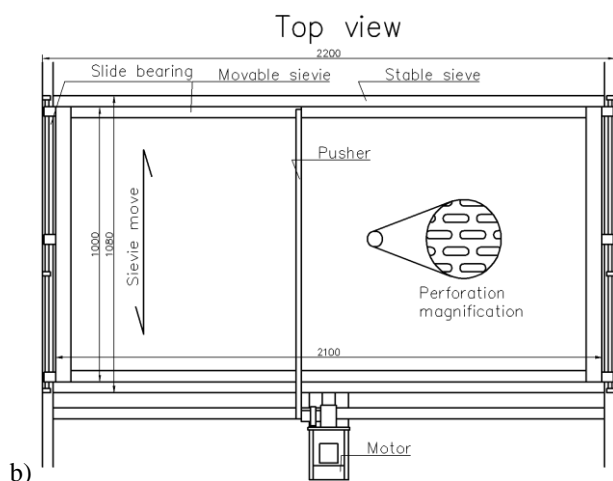
**Figure 5.** Experimental setup – feeder [5]

## 2.5 Tests algorithm

In snow load tunnel tests following algorithm was assumed:
– Model preparation;
– Setting the direction of inflowing air;
– Setting a proper wind speed;
– Precipitation;
– Measurement of thickness of snow cover after precipitation;
– Setting a proper wind speed for redistribution:
– Redistribution;
– Measurement of thickness of snow cover after redistribution;
– Removing layer of artificial snow.

## 3 Comparison of setup parameters values

### 3.1 Precipitation simulation

The main similarity criteria numbers according to [4, 5] for each of model situations are as follows:

$$\Pi_t = \frac{v_{ref}}{v_t}; \qquad Stk = \frac{\frac{v_t}{g}}{\frac{L}{v_{ref}}} = \frac{v_t \cdot v_{ref}}{g \cdot L}; \qquad (1)$$

where: $\Pi_t$ - speed ratio similarity number; $Stk$ - Stokes number; $v_{ref}$ - average reference horizontal flow speed (at $z_{ref}$); $z_{ref}$ - reference height; $v_t$ – terminal velocity of powdered polystyrene foam particle (dispersion terminal speed); $g$ – acceleration due to gravity; $L$ – reference length;

a)



b)



$$x = k \cdot a \cdot \tan \varphi; \qquad y = 0; \qquad z = z_b + k \cdot \left( b \cdot \cos \varepsilon \cdot \tan \varphi - \sin \varepsilon \right);$$
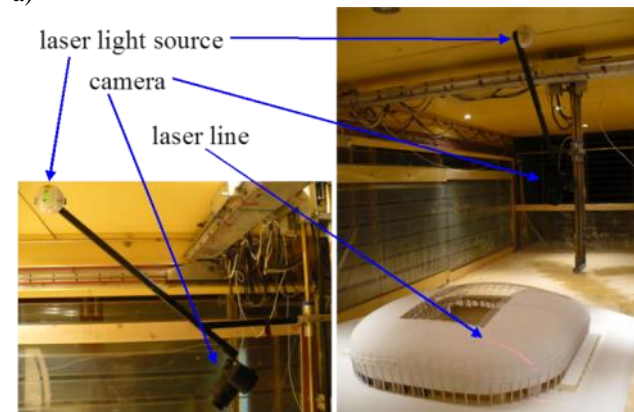
$$k = \frac{y_b}{\cos \varepsilon + b \cdot \sin \varepsilon \cdot \tan \varphi}.$$
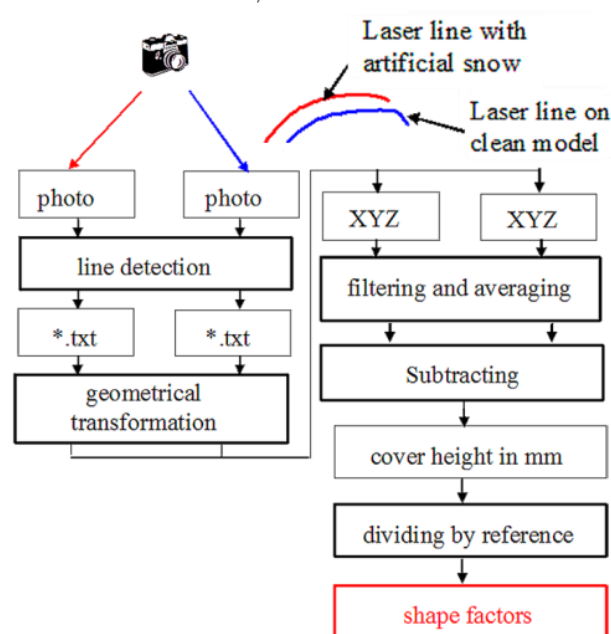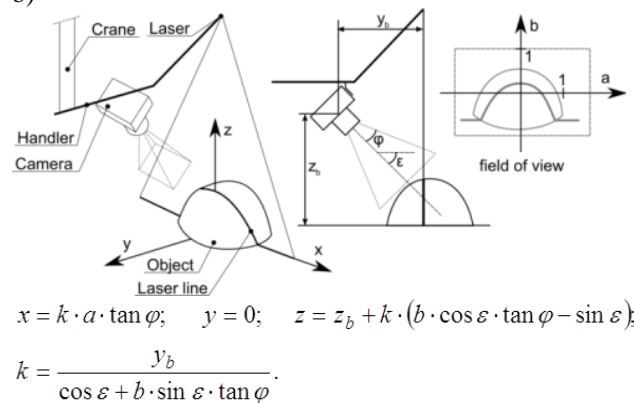


**Figure 6.** Experimental setup – photogrammetry (a) and photogrammetry algorithm diagram (b) [5]

These two quantities are called "ballistic" because they describe airborne particles behavior. The $\Pi_t$ is responsible for the particle movement in the free fall state. The *Stk* is responsible for the dispersion particles inertial movement. It is a ratio of the particle movement characteristic time to the fluid flow characteristic time. Comparison of setup parameters values for precipitation situation is given in Table 1.

**Table 1.** Comparison of setup parameters values for precipitation situation

|  | Study case L | | Study case P | | Study case K | |
|---|---|---|---|---|---|---|
|  | (M) | (P) | (M) | (P) | (M) | (P) |
| *scale* | 1:200 | - | 1:200 | - | 1:150 | - |
| *a* | - | - | 0,22 | 0,19 – 0,24 | 0,224 | 0,19-0,24 |
| $z_{ref}$ | 12,5 cm | 20 m | 40 cm | 80 m | 27,2 cm | 40,8 m |
| $\Pi_t$ | 3,13 | 3,13 | 3,0 | 3,0 | 3,05 | 3,05 |
| $v_{ref}$ [m/s] | 0,94 | 4,7 | 0,9 | 4,5 | 0,914 | 4,6 |
| $v_{10}$ [m/s] | - | 3,83 | - | 2,85 | - | 3,38 |
| $I_u$ [%] | 25,8 | 23,8 - 33,4 | 12,6 | 17,9 - 22,8 | 14,0 | 20,4-27,0 |

where: (M) – Model ; (P) – Prototype ; α – velocity profile power law coefficient; $I_u$ - intensity of turbulence.

Eight precipitation tests were conducted for different wind angle in 45° interval. For each test after establishing steady flow, 60 litres of powdered polystyrene foam was poured into the working section of the wind tunnel from a sieve-like feeder during 5 minutes (comp. Figure 5). The particle cover reference height samples were collected from the wind tunnel floor and the height of the particle cover on the model roof was measured with photogrammetry method. The particle cover shape factor $\mu_{pre}$ was determined as dimensionless height of the cover.

### 3.2 Redistribution simulation

For each wind direction, redistribution test of particle cover was performed. The reference flow velocity was increased in regard to precipitation simulation up to $v_{ref}$. Tests at this velocity were performed until equilibrium state was obtained after about 20 minutes. Assuming the air density $\rho_f = 1.23$ kg m$^{-3}$, following similarity numbers according to [4, 5, 6] are as follows:

$$\Pi_g = \frac{(\rho_c - \rho_f) \cdot d_{cl} \cdot g}{v_{ref}^2 \cdot \rho_f} ; \quad \Pi_\chi = \frac{\chi \rho_c}{v_{ref}^2 \cdot \rho_f} \qquad (2)$$

where: $\Pi_g$– particle bed gravitational number; $\Pi_\chi$ - particle bed cohesive number; $\chi$ – "kinematical" cohesion of the particle bed; $\rho_c$ – particle cover density, $\rho_f$ - fluid (air) density; $d_{cl}$ – mean "cluster" diameter (or simply, mean particle diameter); $g$ – acceleration due to gravity;
Comparison of setup parameters values for redistribution situation is given in Table 2.

**Table 2.** Comparison of setup parameters values for redistribution situation.

|  | $\Pi_t$ | $\Pi_g$ | $v_{ref}$ |
|---|---|---|---|
| Study case L (M) | 4,95 | 0,0137 | 1,48 m/s |
| Study case P (M) | 8,33 | 0,00482 | 2,5 m/s |
| Study case K (M) | 5,67 | 0,0104 | 1,7 m/s |

## 4 Snow load distribution formulation



a)



b)



c)
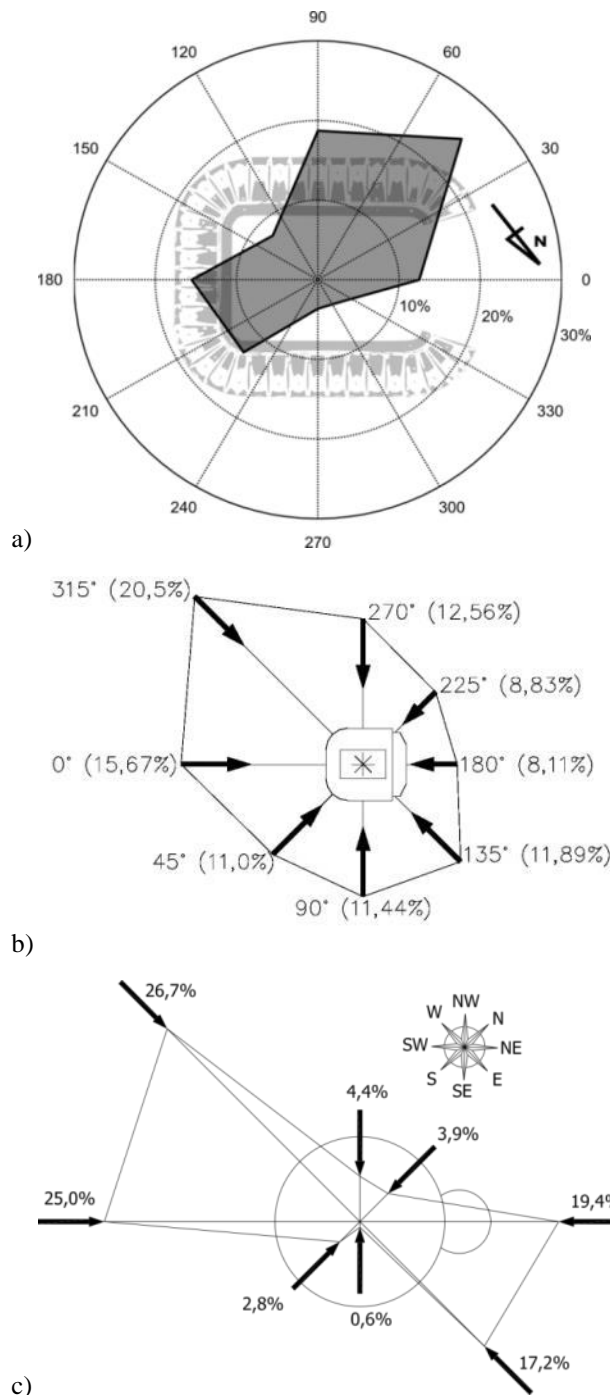
**Figure 7.** Wind rose for the study case L (a), study case P (b), study case K (c) localization [1, 2, 3]

Procedure of assembling results from wind-tunnel experiments into recommended load distributions took into account different wind directions. So called "base scheme" (Fig. 7) was obtained by determining the weighted mean from precipitation simulation results for different wind directions:

$$\mu_{base} = \sum p_i \mu_{i.pre} \qquad (3)$$

where $\mu_{base}$ is shape factor for base scheme, $p_i$ is probability of the wind from $i$th direction (obtained from local wind rose, comp. Fig. 7), $\mu_{pre}$ is shape coefficient obtained from single precipitation simulation. Resultant redistribution patterns were calculated for each direction from the formula:

$$\mu_{i.drift} = \mu_{base} + \Delta\,\mu_{i.drift} = \mu_{base} + (\mu_{i.red} - \mu_{i.0}) \qquad (4)$$

where $\mu_{i.drift}$ is the drift scheme shape factor for $i$th wind direction, $\mu_{red}$ is the shape coefficient obtained from single redistribution simulation, $\mu_{i.0}$ is the initial shape factor for redistribution test.

## 5 Comparison of selected experimental results

Selected examples of basic snow load distributions - $\mu_{base}$ shape factor of snow load for precipitation and redistribution simulation for each study case is presented in Fig. 8 - 15.



a)

b)
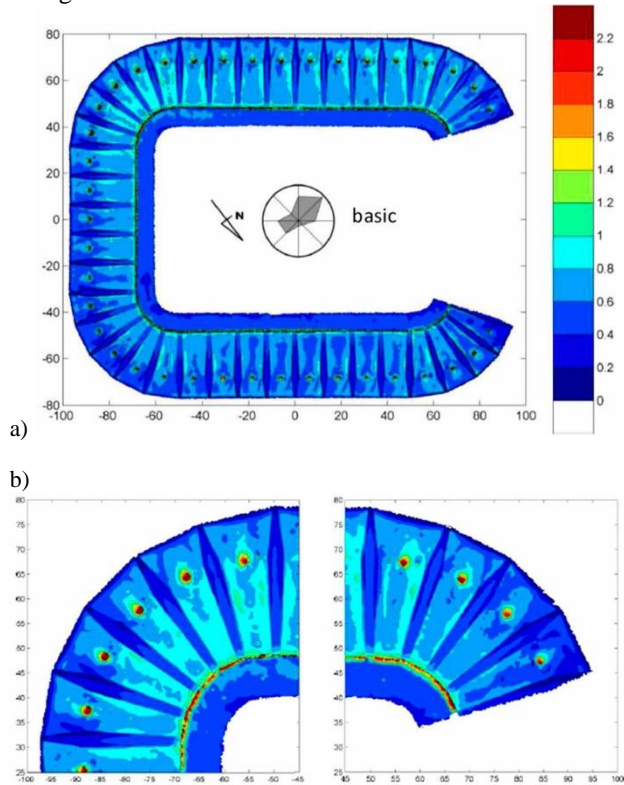
**Figure 8.** Basic snow load distribution - $\mu_{base}$ shape factor of snow load for precipitation simulation for the study case L: (a) whole model; (b) close-ups of selected roof parts [1]
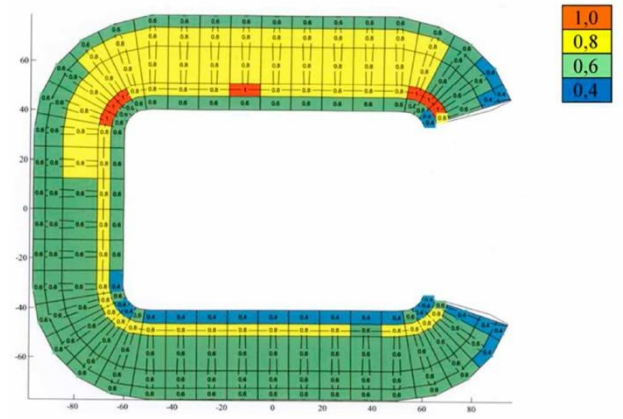


**Figure 9.** Characteristic basic snow load distribution [kN/m²] with use of - $\mu_{base}$ shape factor for structure division into fields, in which an averaging process has been done [1]



a)

b)
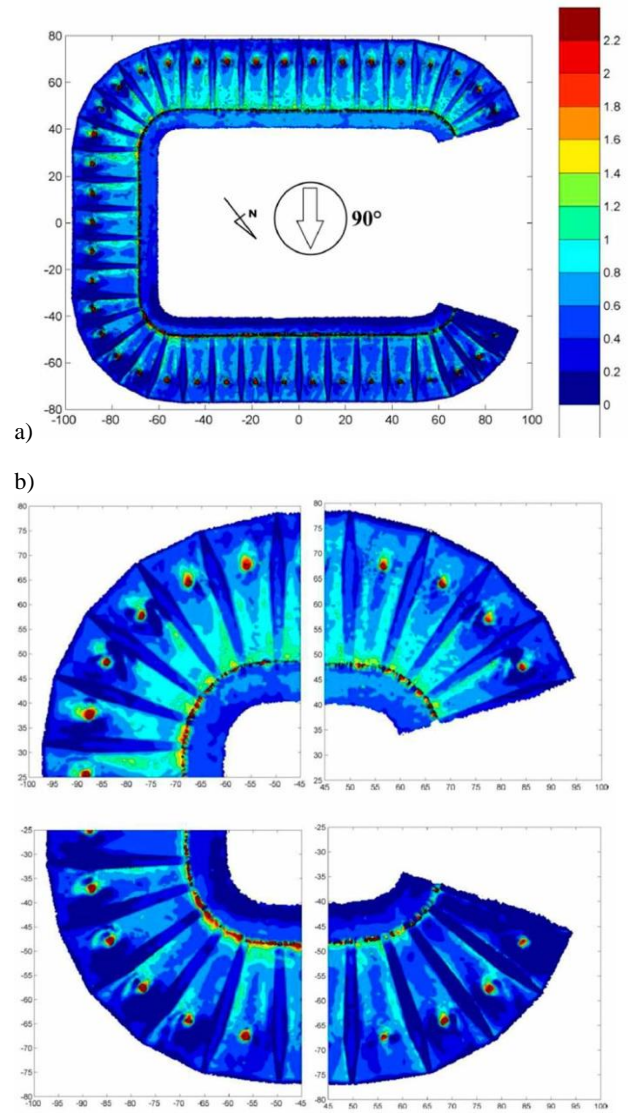


**Figure 10.** Snow load distribution - $\mu_{drift}$ shape factor of snow load for the 90⁰ redistribution simulation for the study case L: (a) whole model; (b) close-ups of selected roof parts [1]
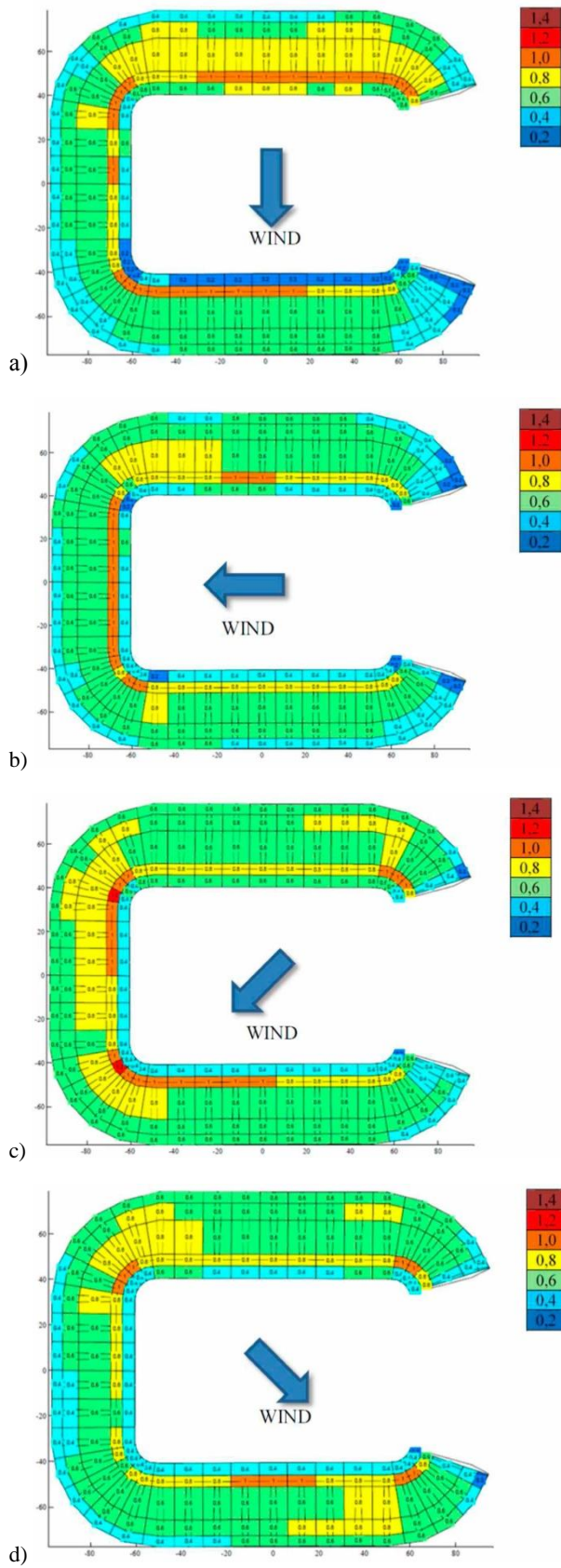
Figure 10. Characteristic snow load distribution [kN/m$^2$] with use of - $\mu_{drift}$ shape factor of snow load (for structure division into fields, in which an averaging process has been done) for the study case L for the: $90^0$ (a), $0^0$ (b), $45^0$ (c),$135^0$ (d) redistribution simulation [1]
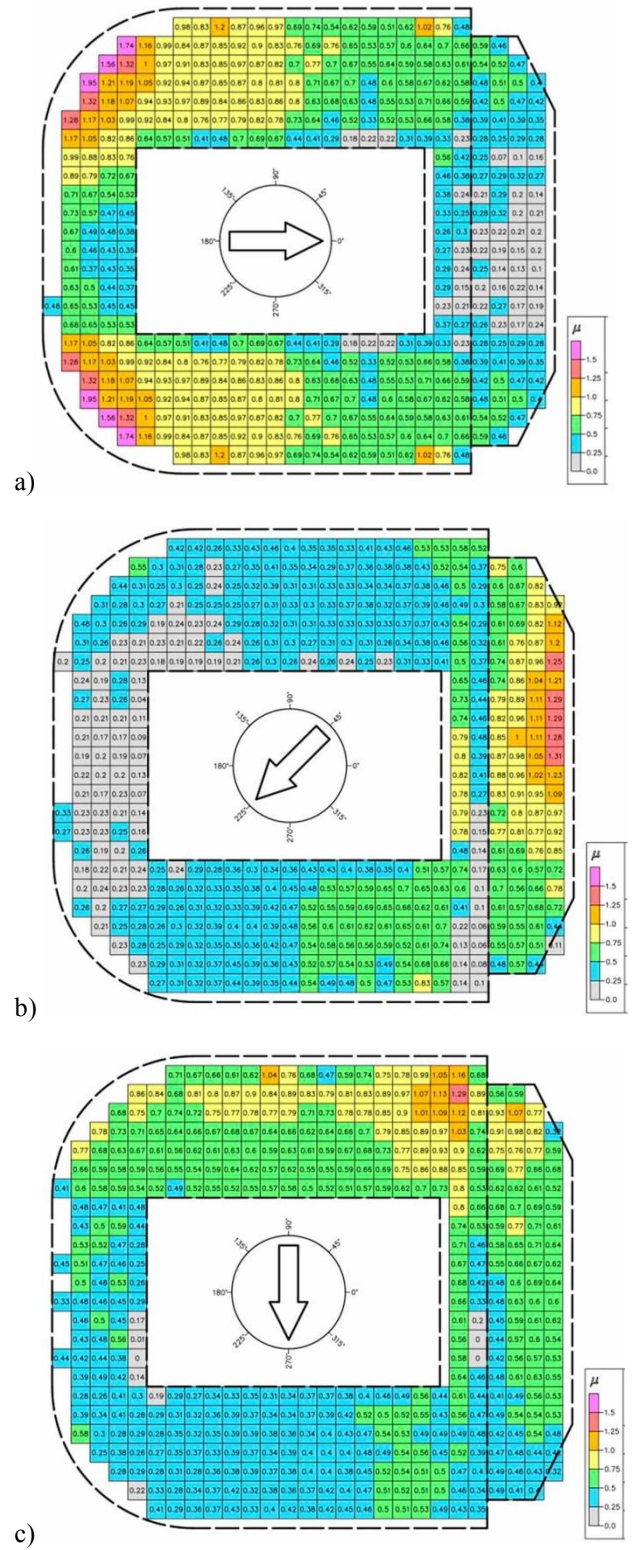


Figure 11. Snow load distribution - $\mu_{pre}$ shape factor of snow load for the study case P for the: $0^0$ (a), $225^0$ (b), $270^0$ (c) precipitation simulation [2]

a)



b)



c)



d)
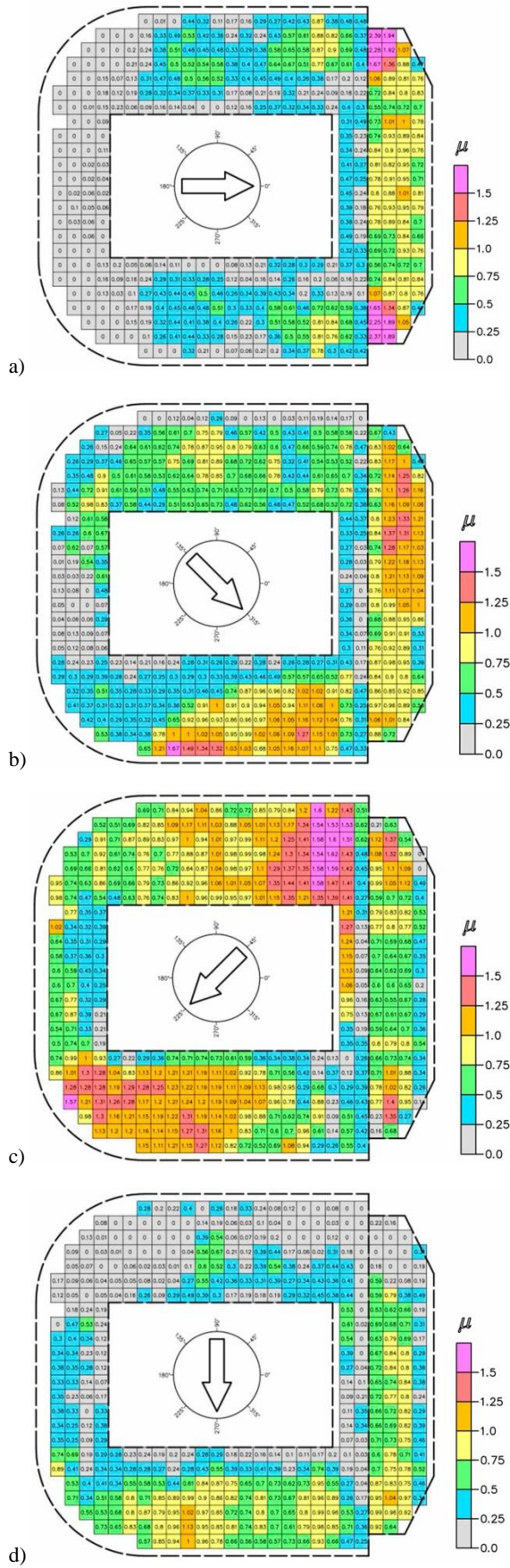
**Figure 12.** Snow load distribution - $\mu_{drift}$ shape factor of snow load for the study case P for the: $0^0$ (a), $315^0$ (b), $225^0$ (c), $270^0$ (d) redistribution simulation [2]



a)
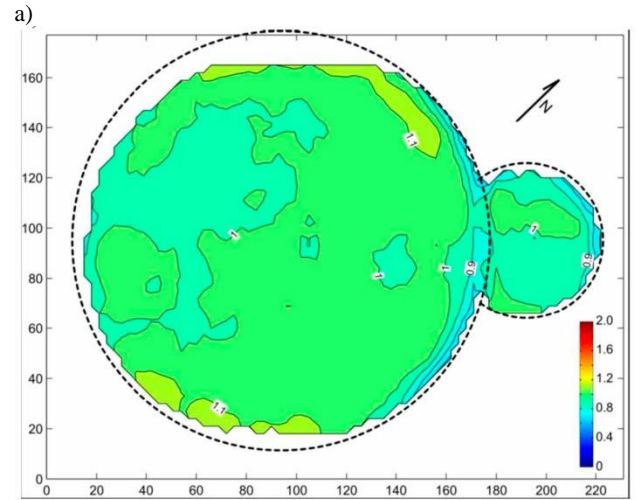
**Figure 13.** Example of basic snow load distribution - $\mu_{base}$ shape factor of snow load for precipitation simulation for the study case K



a)



b)
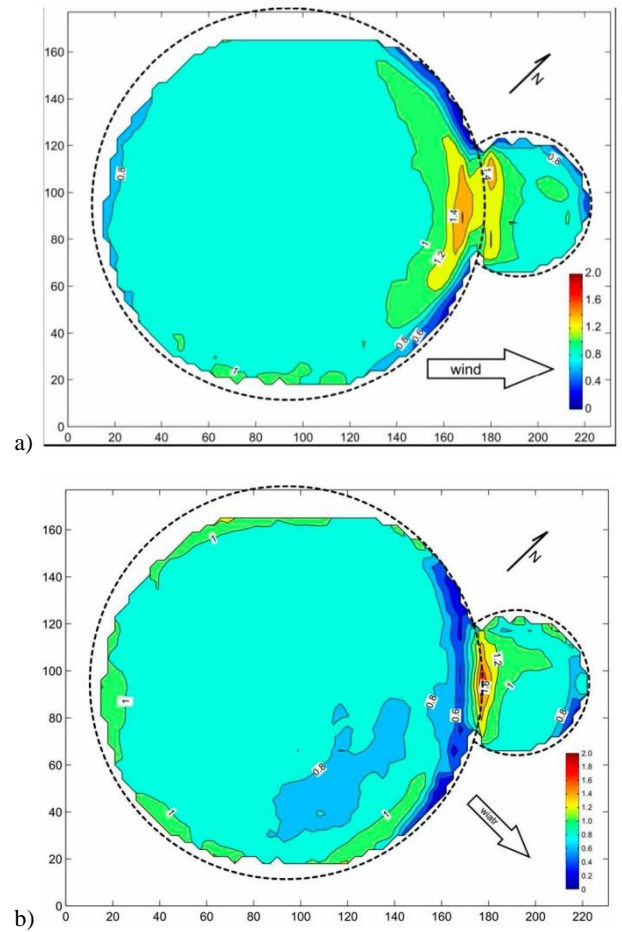
**Figure 14.** Snow load distribution - $\mu_{drift}$ shape factor of snow load for the study case K for the: $0^0$ (a), $45^0$ (b), redistribution simulation [3]
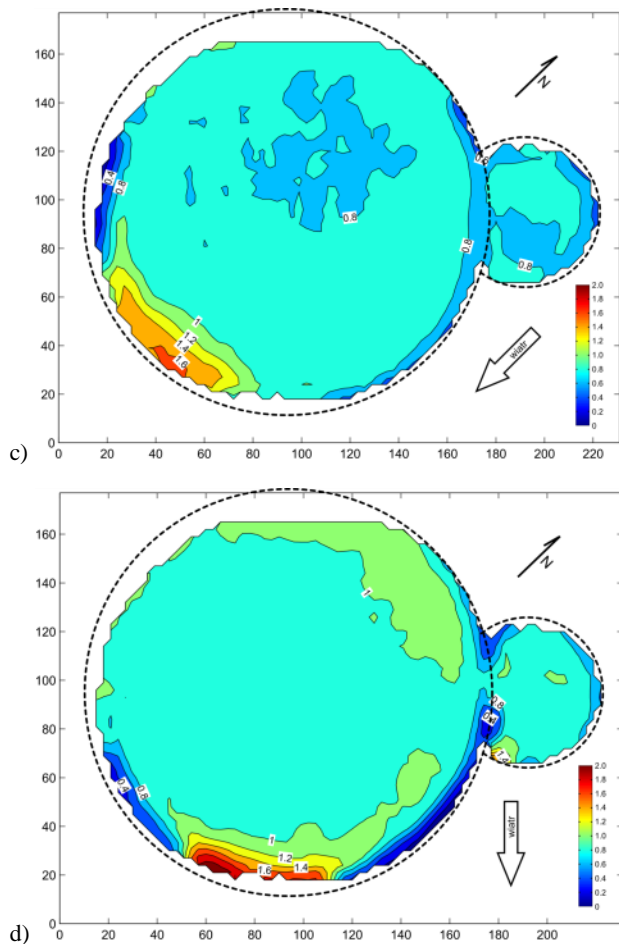
**Figure 15.** Snow load distribution - $\mu_{drift}$ shape factor of snow load for the study case K for the: $135^0$ (a), $90^0$ (b) redistribution simulation [3]

## 6 General conclusions

All presented snow load distributions, both in the precipitation and redistribution simulations, differ significantly each other. Roof shapes of selected cases differ as well. So, in such cases no convergence features were noticed. Each case should be treated separately with respect to local conditions.

Shape factor distribution results are reasonable. These distributions diverge substantially from results which could be obtained by extrapolation of rough shape factor distribution in Eurocode [8] for cylindrical and abutting roofs. Peak values of obtained shape factors are lower than ones that could be derived from abovementioned code schemes.

## 7 References

1. A. Flaga, G. Bosak, G. Kimbar, R. Kłaput, Ł. Flaga, P. Matys, *Wind tunnel tests of snow load distribution and wind action on the roof of the municipal stadium in Łódź, Kraków* (in Polish) (2012)
2. A. Flaga, G. Kimbar, *Wind tunnel tests for snow load prediction on the roof of the Municipal Stadium in Poznań*, Snow Engineering VI, Whistler, Canada, Conference Proceedings. (2008)
3. A. Flaga, G. Bosak, G. Kimbar, R. Kłaput, Ł. Flaga, P. Matys, *Study work: Wind tunnel tests of snow load distribution on the roof of the New Krakow Arena.* Cracow University of Technology, Kraków (2009).
4. G. Kimbar, A. Flaga, *A new approach to similarity criteria for predicting a snow load In wind tunnel experiments*, Snow Engineering VI, Whistler, Canada, Conference Proceedings. (2008)
5. G. Kimbar, A. Flaga, *Similarity criteria of snow precipitation and redistribution and snow load simulation in wind tunnel*, 6th International Symposium on Environmental effects on buildings and people Actions, influences, interactions, discomfort, EEBP VI, Tomaszowie near Cracow, Poland, (2010)
6. A. Flaga, *Wind engineering – bases and applications* (in Polish)*,* Arkady, Warsaw (2008)
7. M. Mellor, *Cold regions Science and Engineering Part III, Section A3c: Blowing Snow*; Cold Regions Research & Engineering Laboratory, Hanover New Hampshire (1965)
8. *PN-EN 1991-1-4: Actions on structures - General actions - Part 1-4: Wind actions* (in Polish)

# Comparison of physical snow accumulation simulation techniques

Albert Brooks[1,a], Scott Gamble[1], Jan Dale[1] and Jill Bond[1]

[1]Rowan Williams Davies and Irwin (RWDI), Guelph, Ontario, CA

**Abstract.** Simulated snow accumulation patterns are presented using two methods: scale model testing in a water flume and wind tunnel testing of a model combined with numerical simulations of snow accumulation and depletion. The results of these two approaches are compared using a calibration building with features that demonstrate the complexity of building aerodynamics and resulting snow accumulation patterns. This paper identifies the strengths and limitations of each method and provides recommendations for future research initiatives.

## 1 Introduction

The ability to predict the distribution of snow accumulations on a structure is important for determining structural requirements and to address building serviceability challenges in cold regions.

Simulations using a water flume or a wind tunnel have been preferred methods since the 1970s for investigating snow drifting using scale models of an existing or proposed building or development. Where problematic snow accumulations are observed, remedial solutions can be readily developed.

However, these simulation approaches can be limited due to the challenge of directly simulating the effects of multiple meteorological events that occur in succession over a winter. More recently, simulation methods using the combination of numerical modelling and wind tunnel testing or computational fluid dynamics (CFD) have been developed, such as the finite area element (FAE) method.

These approaches, while accounting for the varying nature of snow accumulation, are more computationally intensive and may not account for the iterative time-varying aerodynamic changes that result during the accumulation of drifting snow.

This paper compares the snow accumulation patterns obtained using water flume and FAE simulation methods with partial scale field observations. Strengths and limitations of each approach are identified from the perspectives of structural snow load design and building serviceability.

## 2 Snow simulation methods

### 2.1 Simulation scaling

A great deal of detailed, fundamental research has been conducted to assess the applicability of scale model testing within wind tunnels and water flumes. Although scaling laws are important, exact matching is difficult so the summation of similitude relationships for saltation drifting may be simplified down the variable of particle trajectory length to the selected model scale. Most model scales used by researchers and industry have been derived through qualitative methods such as the visual comparison of drift patterns on simple model geometries

like building roof steps, snow fence accumulation patterns and through experience.

Tests conducted within wind tunnels have used glass spheres or sodium borate simulation materials at scales of around 1:20 [1, 2, and 3]. Successful tests have been conducted using water as the working fluid and crushed walnut shells at 1:30 [4], and using sand at 1:300 model scales in literature [5, 6, and 7]. Table 1 provides a summary of historical simulate materials, simulation methods, and approximate geometric model scales.

Model scale studies conducted in both air and water have provided valuable snow accumulation distribution information to researchers and designers. However, the applicability of testing models of larger scales, for example 1:10 to 1:20, for large commercial structures is of limited practicality due to the physical size of the models and test facilities required, and the overall volume of simulation material needed to conduct a test. As a result, smaller model scale testing is required, placing greater demand on matching the simulated particle trajectory length to the model scale. For these types of structures, testing within water using a sand particle or in a wind tunnel with a heavier particle with a shorter particle trajectory length carries great appeal, even if all similitude requirements are not strictly met.

**Table 1.** Simulation modelling materials and scale.

| Simulate Material | Simulation Method | Approx. Model Scales |
|---|---|---|
| Real/Artificial Snow | Field, Wind Tunnel [1,8] | 1:1 - 1:150 |
| Borax | Wind Tunnel [1,3] | 1:20 - 1:50 |
| Glass Spheres | Wind Tunnel [1] | 1:20 - 1:50 |
| Crushed Glass | Water Flume [5,6,7] | 1:200 - 1:500 |
| Crushed Walnut Shells | Water Flume [4] | 1:30 |

### 2.2 Water flume simulation

Scale model simulation of snow drifting and accumulations using a water flume has a long history in snow engineering, having many practical design uses

a Corresponding author: Albert.Brooks@rwdi.com

including the identification of snow drift patterns at ground level, unusual roof drifts, and snow infiltration problems [2, 5, 6, 7, and 9].

Although the strict requirements for dynamic similarity are not met, it appears that in many cases, the main features of full scale drifts are adequately represented on a model [1, 2, and 4].

The water flume simulations described in this paper were conducted with building models at a 1:300 model scale. Snow drifting is simulated using finely crushed glass particles with sizes ranging from 60 through 120 sieve size, which is commonly used as a sand blasting material in industry. The crushed glass particles carried by the water simulate snow particles saltated by the wind over the actual site. Like drifting at full scale, the drifting particles are deposited in regions of flow deceleration on a scale model building. Snow simulation depths and patterns can be varied by modifying the application rate of crushed glass snow simulate material and water flow rates. These settings are commonly varied on a case-by-case basis to account for differences in local meteorological climates, or to provide greater volumes of simulated snow to calibrate to building code or field measurement based drift accumulations [7].

## 2.3 Finite Area Element (FAE) method

The FAE method numerically simulates the hour-by-hour deposition, drifting, and melting of snow and absorption of rain and melt water into a snow pack within a grid system that divides the roof into a large number of finite areas. Entire winters are simulated on an hour-by-hour basis using historical meteorological data, including the cumulative effects of successive storms, drifting events and melting periods.

As part of the simulation process, physical scale models are instrumented and tested within a boundary layer wind tunnel to obtain the aerodynamic flow patterns that are required as an input into the snow flux, redistribution and melting models used within the FAE numerical simulation [5, 11, and 13].

# 3 Simulation of roof step surcharge accumulation

Of the snow loads recommended by building codes and standards, snow accumulations located within roof steps tend to govern the design of a structural system for many buildings.

Generically speaking, most commercial building stock contains large flat roof surfaces on the order of 10s of metres in roof length and width, with roof steps on the order of 3000 mm in height or greater. A simple building roof step described by Brooks et al., 2016 has dimensions that are considered representative of commercial buildings, and is illustrated in Figure 1 [13].
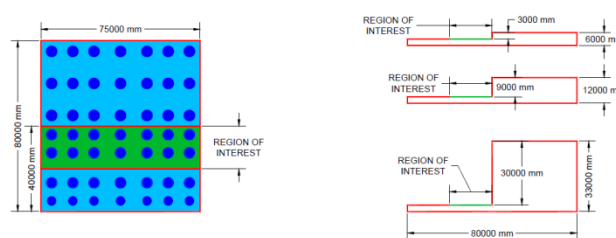


**Figure 1.** Plan and elevation views of the roof step model. Dimensions are given in full-scale millimetres. Wind tunnel velocity sensor locations are indicated by the dark blue circles.

Field observations of snow drifts on a simple roof step model of comparable geometry are described in detail by Tsuchiya et al., 2002 [14]. Valuable snow drift geometry information was obtained for both upwind and downwind drift formations on a roof step 4500 mm in total width, 1800 mm high and 5400 mm long with a roof step height of 900 mm. It is assumed that these dimensions were selected due to practical construction and measurement reasons. As this roof step is much smaller than typically seen on commercial buildings, the model used by Tsuchiya et al 2002 may be considered a 1:3 scale model for practical application. The findings described by Tsuchiya et al., 2002 will serve as a point of reference for each of the modelling techniques further described in this paper. Two roof step models were used to illustrate downwind and upwind roof step drifts by orienting the buildings perpendicular to prevailing winds.

## 3.1 Reference meteorological events

Meteorological data recorded in Sapporo, Hokkaido Prefecture, Japan covering the period of record described by Tsuchiya et al., 2002 is used as a reference climate for comparison purposes. An analysis of winter winds determined that the predominate direction and frequency of winds in January and February are from the west through west-northwest and southeast through northeast directions. The snowfall and resulting snow drift patterns were recorded following events on January 31st, February 20, and February 25, 2001, resulting in uniform snow accumulation depths on the ground of 70 mm, 150 mm and 200 mm, respectively over the duration of each event. During these events, winds were blowing from the northwest. Each test event started with the model cleared of snow. This represents a limited meteorological data set, and does not include the effects of multiple successive snowfall, drifting, rain and melting events over the course of the winter. Most of these events are also of relatively small snowfall amounts and low wind speed (between 2.9 and 3.5 m/s being referenced). Of this data set, the 200 mm snowfall event on February 25, 2001 is considered most valuable for comparison purposes.

## 3.2 Water flume simulation

Water flume simulations were conducted using the 1:300 scale models described in Figure 1 with roof step heights of 3000 mm, 9000 mm and 30000 mm, respectively, at full scale. Although the model roof described in Figure 1

is much larger than that described by Tsuchiya et al., 2002, the aerodynamic wind flow patterns are expected to be similar for winds perpendicular to the step.

Photographs of snow accumulation and scour patterns are shown in Figure 2 for each roof step model when winds approach from over the upper roof and when winds approach from over the lower roof. Wind flow is from left to right in each photograph.

A great deal of useful design information can be gleaned through inspection and comparison of scour and deposition patterns for each image. For example, as the upper roof height is increased, wind exposure and scour unsurprisingly increased. Step accumulation patterns vary with roof step height as well. When winds flow over the upper roof, a downwind drift is formed within the roof step. As the step height is increased, the resulting accumulation patterns indicate that there is greater turbulent mixing within the downwind flow, leading to more uniform and smaller accumulation depths. Within the lower 3000 mm roof step, localized wind accelerations and scour patterns can be seen at the outer edges of the lower roof at the vertical wall of the roof step. Review of these patterns indicates that although the geometry of the model is simple, the simulated wind flow patterns at work are not.

When wind flows over the lower roof toward the step face, snow deposition patterns are equally complex, with evidence of strong flow separations and recirculation patterns on both the lower and upper roof surfaces. Greater downwash and recirculating wind flows tend to relocate snow to the middle of the lower roof surface in a roll back drift, with greater snow movement and localized drift accumulation with greater roof step heights.



**Figure 2.** Snow accumulation patterns when winds approach from over the upper roof (top images) and over the lower roof (bottom images).

## 3.3 Finite Area Element (FAE) method

### 3.3.1 Ground snow accumulation simulation

24-hour meteorological data from the Sapporo reference winter of 2000-2001 was used to simulate the ground snow load. The resulting time history of snow accumulation and depletion for the winter has been plotted in Figure 3 with the corresponding snow and rainfall rates plotted on the secondary axis. The snow load is presented in kilopascals (kPa) and precipitation in millimetres (mm/hr) of water equivalent. The maximum simulated snow load for this year occurred on March 18, 2001 and corresponds to a ground snow load of 3.5 kPa. As can be seen, the peak snow load is the result of numerous freezing precipitation events with little opportunity for melting earlier in the winter.

Tsuchiya et al., 2002 identified three significant snowfall and drifting events occurring on January 31st, February 20 and February 25, 2001 with uniform ground snow depths of 70 mm, 150 mm and 200 mm, respectively occurring over the course of each event. These events have been identified in Figure 3.

Of these events, the February 25th event has been selected for comparison as it features the largest snow accumulation when winds occurred from a narrow range of directions. The increase in simulated ground snow accumulation over the February 24/25 event was 0.17 kPa using the FAE procedure, suggesting an average storm snow density of 0.85kN/m$^3$.
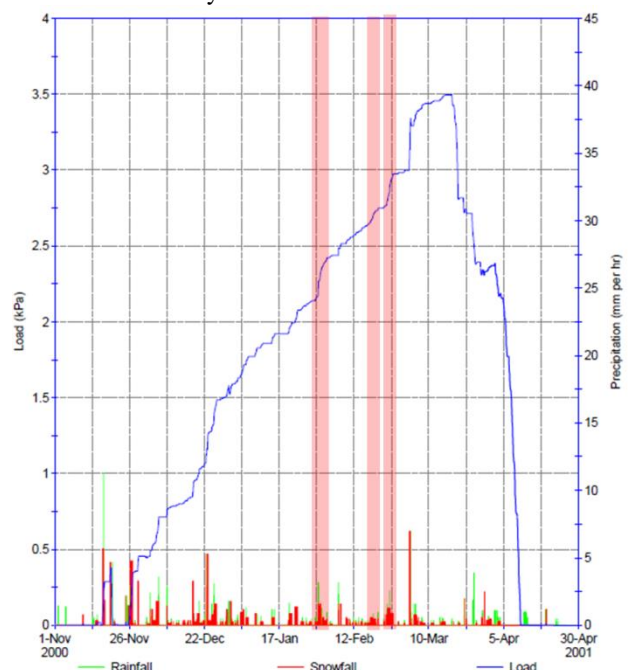


**Figure 3.** Example simulated ground snow load for the winter of 2000-2001 with the reference snowfall events identified.

### 3.3.2 Roof step snow accumulation - Single event simulation

Identical physical and numerical models of the roof steps presented in Figure 1 and Figure 2 were created using the FAE methodology. This required each model to be instrumented and tested within a boundary layer wind

tunnel. A standard suburban wind velocity and turbulence profile was used to obtain the required aerodynamic flow patterns.

Figure 4 and Figure 5 illustrate the distribution of area averaged snow load in kilopascals for each area element after the February 25th event beginning with a bare roof. These distributions of snow loads represent single instances in time during the event, as the peak snow load in each element can vary due to the meteorological history and building roof step aerodynamics. For the 3000 mm step, the FAE method predicted an accumulation of load within the first row of area elements as indicated in Figure 4. With higher roof steps, similar to the water flume simulations, the load was more distributed over the lower roof surface.
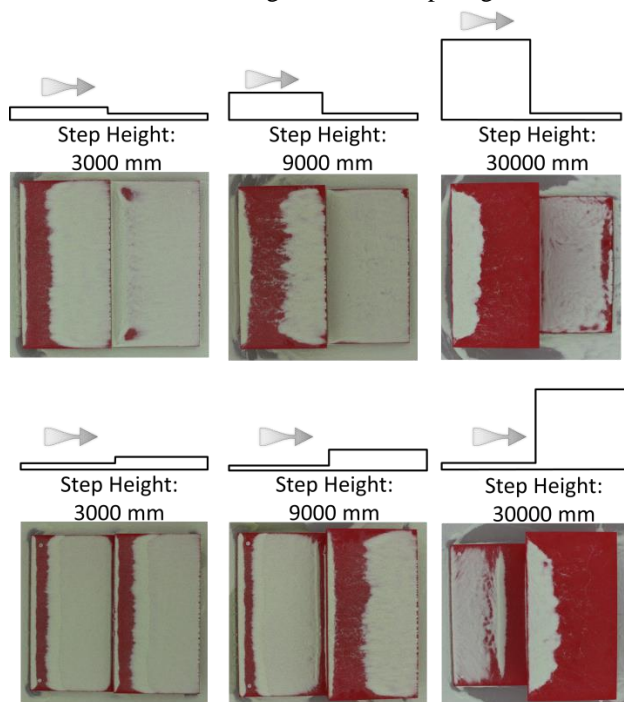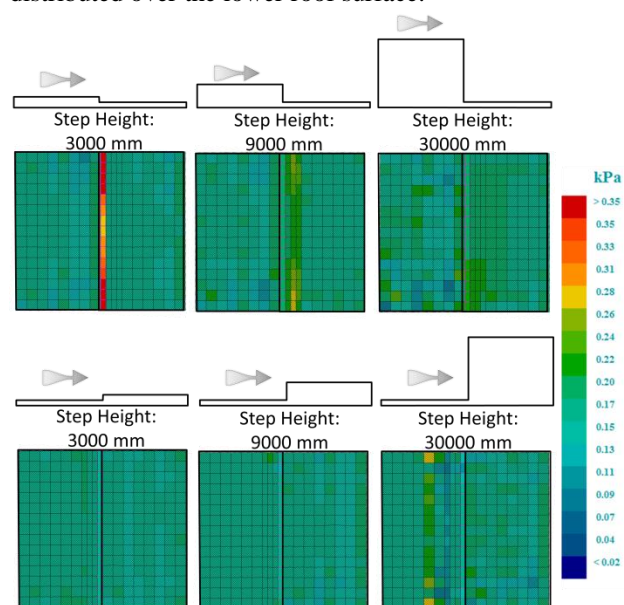


**Figure 4.** FAE-predicted snow accumulation patterns when winds approach from over the upper roof (top images) and over the lower roof (bottom images).

The snow distribution for the 3000 mm roof step when winds flow over the upper roof are illustrated in the top and bottom images in Figure 5 when simulated using the FAE and water flume, respectively. In this wind flow and drifting scenario, the FAE method predicts an accumulation of load within each element located closest to the roof step. The distribution in load along the width of this zone appears to vary, with the greatest loading occurring closer to the outer ends of the roof. The corresponding water flume simulations provide evidence of similar accumulation patterns, where localized wind flow recirculation has drawn snow towards the ends of the roof step region.

When winds flow over the lower roof, the FAE method results indicate smaller drift loads within the roof step regions than when winds flow over the upper roof using the reference meteorological data. These simulations also indicate that increasing the roof step height leads to an increase in snow redistribution on the lower roof, with evidence of a localized increase in accumulation in the middle of the roof, similar to the trends observed within the water flume simulations.
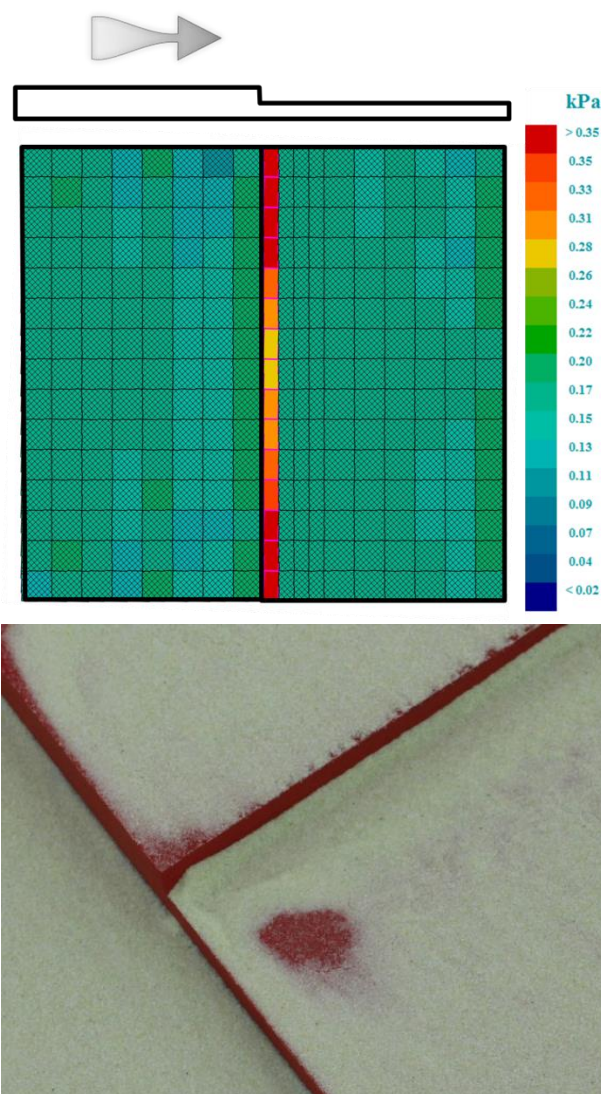


**Figure 5.** Comparison of FAE simulated of snow load (top) with water flume pattern (bottom).

## 3.4 Comparison of simulation methods

The plots in Figure 6 and Figure 7 contain the geometric distribution of snow within the simple building roof step for each of the snow simulation methods including field observations [14], and via water flume and FAE simulation methods. The direct geometric comparison of simulated snow accumulations required rescaling of the field measurements to the 3000 mm roof step height. The geometry of the snow accumulations obtained from field observations and each simulation method are presented as normalized ratios where s is the measured depth or load, and Sd is the uniform depth or load on the ground.
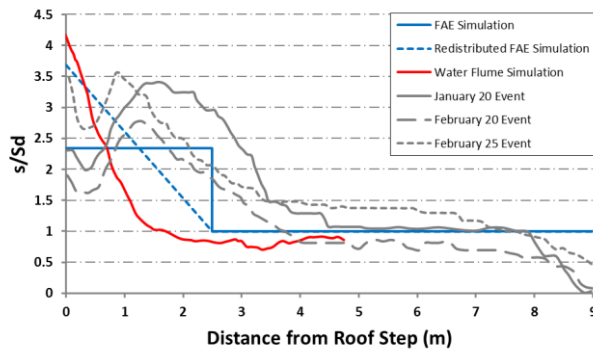
**Figure 6.** Normalized field measurements of snow accumulation (s/Sd) [14] and predictions from water flume and FAE simulation techniques for when wind blows over the upper roof.



**Figure 7.** Normalized field measurements of snow accumulation (s/Sd) [14] and predictions from water flume and FAE simulation techniques for when wind blows over the lower roof.

As indicated in Figure 6, snow accumulation depths are greatest using the water flume technique. In addition, some subtleties in the cross-section of the downwind accumulation have not been explicitly captured, such as the small trough and second peak moving away from the vertical wall. When winds flow over the lower roof, Figure 7, field observations provided evidence of a strong recirculation zone which swept snow into a tight roll back drift with a high angle of repose removed from the vertical wall of the roof step. The results of the water flume simulations indicate the presence and location of these flow patterns, but at a lower magnitude and angle of repose of the drift.

Two distribution geometries have been presented in Figure 6 for the loads predicted by the FAE: one as a uniform accumulation as predicted by the FAE, and one as a tapering snow load by redistributing the area averaged load as a triangular load over the width of the area element. In general, the magnitude and distribution in load appear to be within reason when compared to the field observations. However, when winds blow over the lower roof, Figure 7, the FAE method predicted a uniform distribution in snow load and misses the formation of the roll back drift for the single event scenario.

This may be due to the meteorological data used within the simulation, and the assumptions in local site exposure. The tendency to form greater loads in the middle of the roof is however captured with increased step heights as illustrated in Figure 4. It is suspected that the roll back drift in the 3000 mm step was not captured for this particular case due to the implementation of a fixed threshold velocity for drifting that was perhaps not appropriate for the specific snow characteristics of the chosen event. An event with a slightly higher wind speed is expected to have produced the roll back drift.

Review of the simulated distributions in snow for the entire reference year containing a variety of snow events more faithfully illustrates the roll back drift for the 3000 mm step model (see Section 3.5).
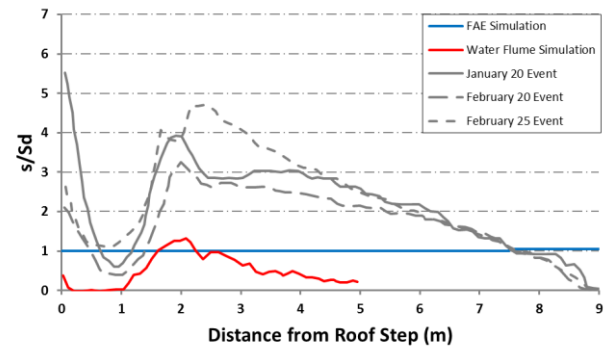
For the simple case of a building roof step, the water flume method captured a great deal of high resolution information regarding wind flow patterns and the bulk movement and deposition of snow, as evidenced by the photographs in Figure 2 and Figure 5, although snow distribution patterns show some variability as compared with field data. The inability to physically simulate successive meteorological events, such as winds from multiple approaching directions, represents a significant practical limitation to the direct application of this modelling technique to providing snow loads.

The FAE method provides reasonable estimations of the transport and accumulation of snow, but lacks the high resolution and visual nature of a physical simulation, such as the subtleties in drift shape that may be provided by the water flume modelling technique. However, the FAE approach overcomes the limitations of a single wind direction event simulation technique by accounting for the time-varied nature of snow accumulation and depletion.

These simulation approaches can therefore be considered synergistic, where each method can be used to overcome some of the shortcomings and uncertainties inherent in snow simulation. Despite some limitations in modelling, it should be noted that each simulation technique represents an extremely powerful tool for modelling snow. These tools can and should be used for researchers and designers as they provide a great deal of information and insight that is currently beyond building code recommendations [5, 7, 11, 12, and 13].

### 3.5 Multiple event simulation

Within most cold climate regions, the peak snow load is seldom the result of a single storm event, as illustrated by the increase and depletion of snow load within the simulated 2000-2001 time history shown in Figure 3. Exposure to successive events can cause snow to be scoured and relocated when in a driftable state.

Figure 8 presents the distribution in snow load at a single instance in time when the peak load is at its greatest. Review of the distribution of snow load when the upper roof surface is oriented to the northwest indicates the presence of a large roof step accumulation. When the upper roof is oriented towards the southeast,

prevailing winter winds from the northwest appear to create strong flow recirculation which result in a roll back drift. A comparison with the loads presented in Figure 4 indicates that the trends in snow accumulation patterns are similar, although more redistribution in snow has occurred, which is likely the result of multiple wind events. This is due to the highly directional nature of winds around Sapporo; however this is not the case for many other snow-prone regions of the world.
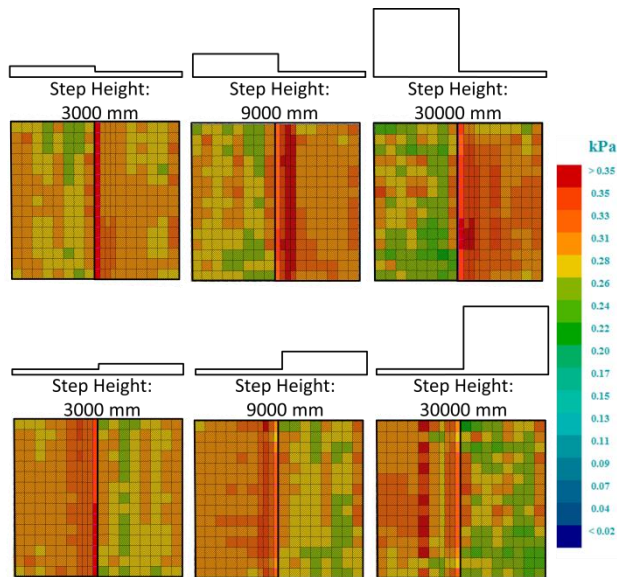


**Figure 8.** Peak snow accumulation patterns as a result of numerous successive precipitation events for the winter of 2000-2001 when the upper roof surface is oriented towards the northwest (top) and to the southeast (bottom).

## 4 SPACE model simulations

The tests conducted using a building roof step provides a good geometry for evaluating simulation methods. However, for a simulation approach to be robust and applicable, it must be able to simulate the deposition and scour of snow on complex building geometries that are likely to be encountered in practice.

To test and refine various simulation approaches, the authors created the Snow Precipitation and Accumulation Calibration Experiment (SPACE) model, as illustrated in Figure 9. This building includes geometries that result in complex building aerodynamics and resulting snow accumulation patterns. A detailed description of the SPACE model and the water flume simulation method can be found in Brooks et al, 2015 and Brooks et al 2016 [7, 13].

### 4.1 Water flume simulation

The top two images shown in Figure 10 are photographs taken from above the SPACE model, where the simulated snow drifts can be seen on and surrounding the scale model. A heavy drifting scenario was performed to provide greater visual detail.
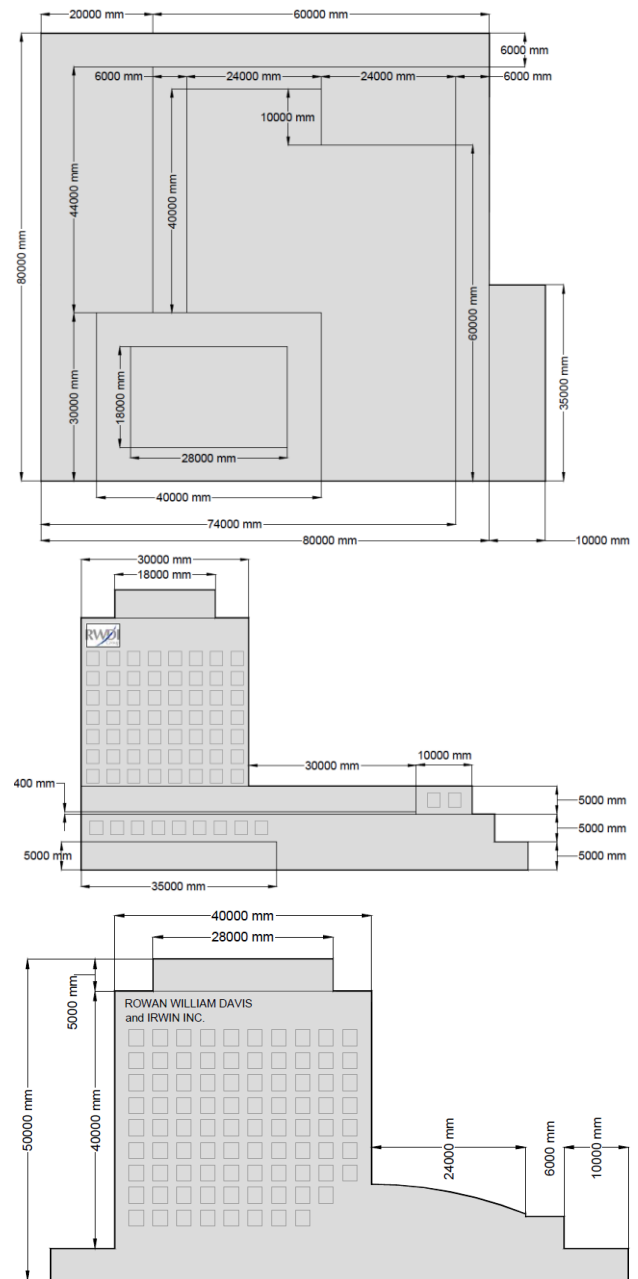


**Figure 9.** Plan and elevation views of the SPACE model building. Dimensions are given in full-scale millimetres (Brooks et al, 2015).

The distribution of simulated snow on the SPACE model is shown in Figure 10 when winds are from the northwest. Wind flow flows from left to right in the top image. The bottom photograph in Figure 10 is a close up of the roof step located mid-span of the arched roof.

Regions of interest to practitioners may include the well exposed upper roof, regions of wind flow acceleration and scour across the arched roof and the corresponding location of snow on the arched roof.

Also of interest is the location and relative magnitude of roof step surcharges, as these types of accumulations are highly dependent on wind directionality [13]. It should also be noted that most of these snow accumulation patterns are not well addressed by current building codes and standards.

As can be seen in Figure 10, the water flume simulation provides a very detailed picture of the wind flow patterns across the structure, with well exposed areas being scoured of snow and depositions where wind flows decelerate. Visual comparison between the wind velocity vectors obtained through the boundary layer wind tunnel testing shown in Figure 11 and the regions of scour and depositionshow good agreement.
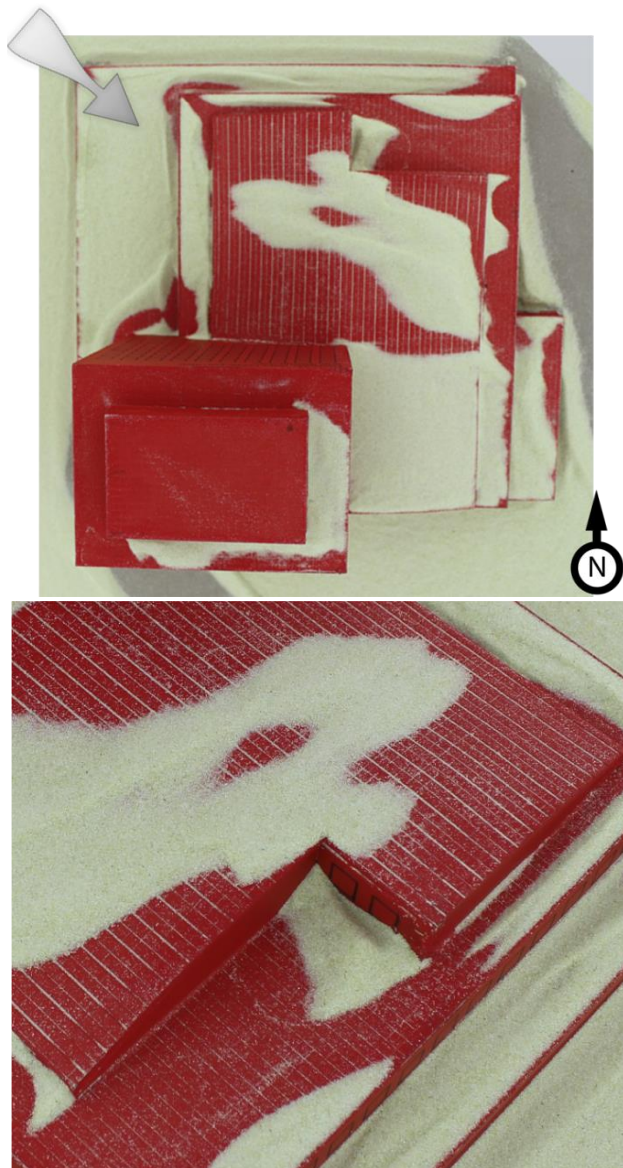




**Figure 10.** Photograph of the SPACE model when winds were approaching from the northwest direction (top). Distribution of snow in the roof step region of the arched roof (bottom).

## 4.2 Finite Area Element (FAE) simulation

The FAE simulation method required detailed wind flow velocity information. This information was obtained through boundary layer wind tunnel testing of a 1:300 scale model identical in geometry to the water flume model (top photograph in Figure 11). Velocity data (magnitude and direction) were measured with a high degree of spatial resolution using 253 surface velocity vector (SVV) sensors [11] (middle photograph in Figure 11). A standard suburban wind and turbulence profile

was used for each of the 24 equally incremented test directions.

The velocity at each sensor was linearly interpolated to each of the nodes of the area elements used to define the geometry of the model. An example of the direction and relative magnitude of wind flows are presented in the bottom image in Figure 11 when winds are from the northwest (315°).
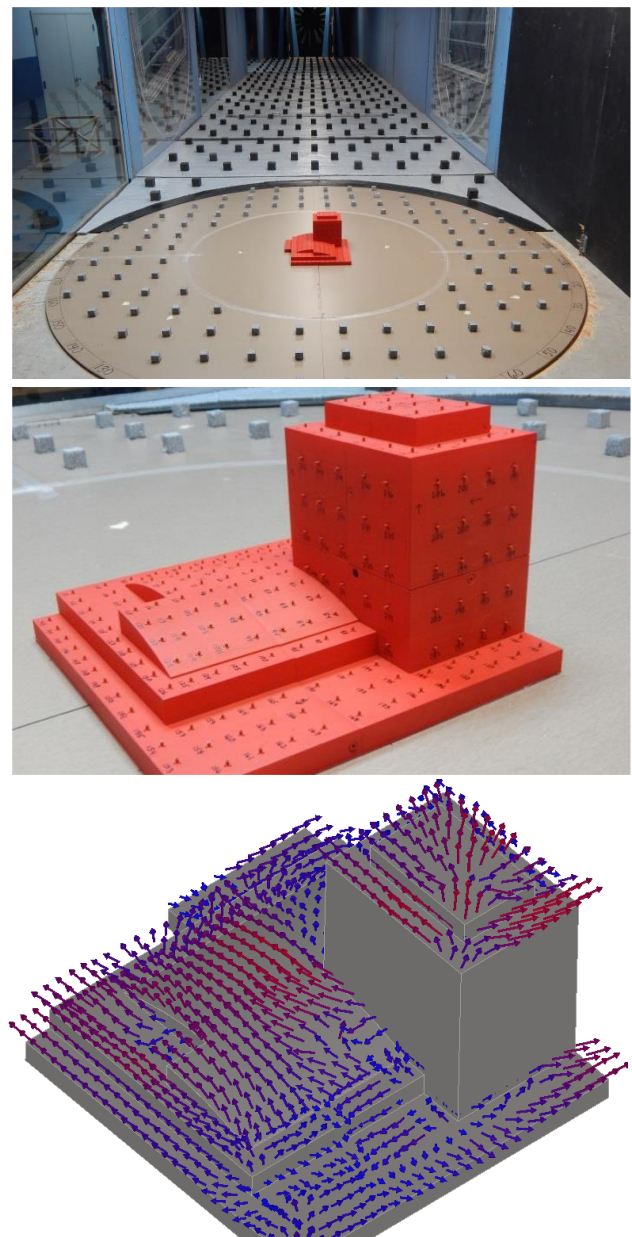


**Figure 11.** SPACE model within a boundary layer wind tunnel (top) instrumented wind tunnel model with surface velocity vector (SVV) sensors (middle) and resulting wind velocity vector field when wind is from the northwest (bottom).

### 4.2.1 Single event accumulation distributions

The distribution of snow load using the FAE method using meteorological data encompassing the February 25th snowfall event in Sapporo, Hokkaido Prefecture, Japan can be seen in Figure 12. Visual comparison of the distribution patterns of snow between Figure 10 and

Figure 12, indicate that the water flume and FAE simulations are in quite good agreement.

Areas of uniform snow depth are consistent, for example the snow accumulations along the lower roof surface at the northeast corner of the building, and within the wake region west of the tower. Regions with greater accumulation are also well replicated, such as the tapering drift accumulation on the leeward side of the arched roof, and the accumulations within roof step areas.

However, there are some minor differences between the simulations; the FAE model illustrates the presence of uniform snow loads at the northeast corner of tower, where the water flume simulations indicate the presence of a roll back drift at the base of the tower. It is expected that these minor differences are primarily the result of the discretized nature of the FAE approach and due to area averaging of the loads, removing the localized minimums and maximums that normally occur due to the aerodynamic shape of drifts.
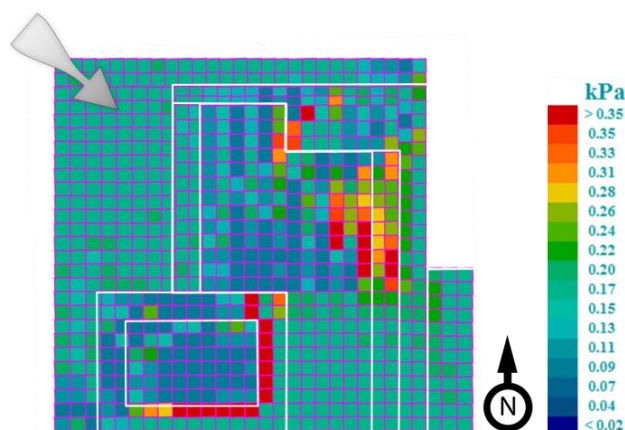


**Figure 12.** Plan view of the SPACE model building illustrating the distribution of snow load using meteorological data from February 24-25, 2001. Loads presented in kilopascals (kPa) for February 25 at 23:00 hours. Prevailing approaching wind direction is indicated by the arrow at top-left in the image.

### 4.2.2 Multiple event accumulation distributions

As previously discussed, peak snow accumulations in most cold climate zones are the result of multiple successive events. The simulation presented in Figure 13 is the result of the hour by hour simulation of the winter of 2000-2001 using the meteorological data described in Section 3.3.3. To illustrate the range of various wind directions and speeds within this data set, an analysis of the directional distribution of winds was performed, which are presented in the wind rose (bottom image of Figure 13).

Within this meteorological data set, the majority of strong winds occur from the west through north, with weaker winds occurring from the southeast through south-southeast. Inspection of the snow drift patterns with those presented in Figure 10 and Figure 12 clearly illustrate that the majority of scour and redistribution is the result of these northwest winds.
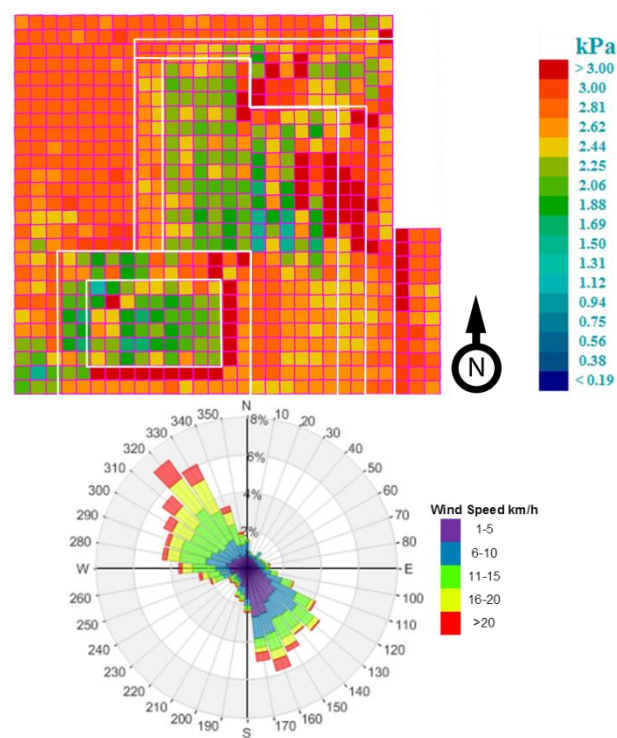


**Figure 13.** Snow accumulation distribution using meteorological data from the winter of 2000-2001 (top). Accumulations presented in kilopascals (kPa) on March 8 at 02:00 hours. Directional distribution of winds (blowing from) as recorded in Sapporo, Hokkaido Prefecture, Japan of the months of November through April for the winter or 2000-2001(bottom).

The effect of variable wind directionality can be better illustrated through the use of a climate other than the Sapporo, Japan, such as Toronto, Canada. Figure 14 illustrates the predicted distribution of snow while accounting for a climate where winds occur from many directions. As can be seen within the wind rose, winds in this example winter occur from a wide variety of directions and are quite strong. As a result, snow drift and scour zones are more varied, with drifts occurring within multiple roof step zones in patterns very different than the patterns driven by the highly directional wind climate of Sapporo.

Currently, accounting for the time varying nature of snow drifting when approaching winds occur from a variety of directions is not practical within a wind tunnel or water flume. Although individual test directions provide excellent information regarding aerodynamics and snow accumulation geometry, the use of the FAE method provides additional advantages, particularly for these more challenging meteorological climates.
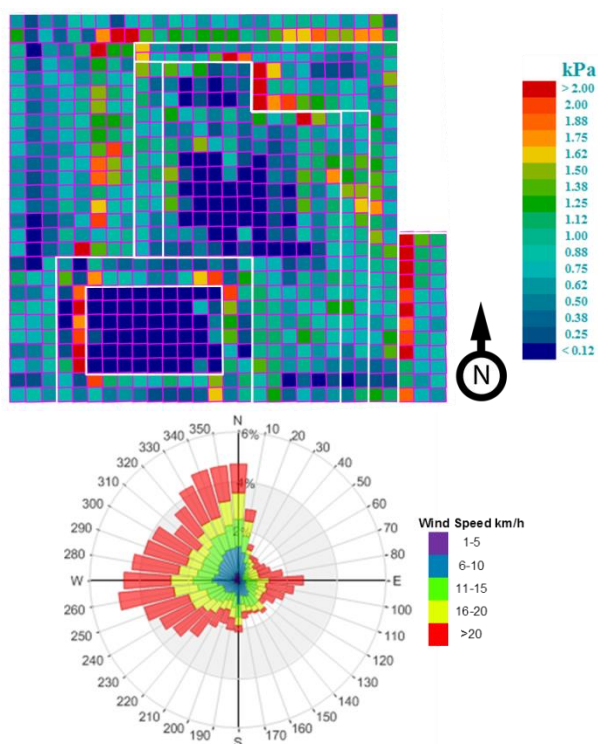
**Figure 14.** Snow accumulation distribution using meteorological data from the winter of 1970-1971 (top). Accumulations presented in kilopascals (kPa) on February 23, 1971 at 23:00 hours. Directional distribution of winds (blowing from) as recorded at Pearson International Airport in Toronto, Canada for the months of November through April for the winter of 1970-1971 (bottom).

## 5 Conclusions and recommendations

Predicting the accumulation, movement and depletion of snow on a building is a very complex process that is a challenge to model despite decades of continued reseach. The findings presented in this paper illustrate some of the many physical and numerical simulation challenges. Pricipal findings and recommendations for future work include:

- When comparing field observations on a partial scale model to water flume simulations, the resulting drift accumulations tend tobe varied in predicting snow accumulation depths. The large scale features of the drift patterns are well represented, such as regions of scour and deposition. Therefore, water flume simulations provide invaluable wind flow information, as well as useful information regarding the geometry of resulting snow accumulations.

- Water flume simulations provide excellent information to designers regarding wind flows and resulting snow redistributions for a single wind direction at a time. This can provide resonable approximations within a highly directional climate, but cannot simulate the time history of numerous wind and precipitation events.

- The trends in the distribution in snow load agree well between water flume, FAE and field observations. However, the detailed geometry of the FAE-generated snow accumulations is generally of lower

resolution due to area averaging within each simulation element. For the purpose of stuctural design, such small scale geometries are generally not as significant since a structural system is not as sensitive to point loads due to load sharing. Some drift accumulations may not be predicted due to the size of the elements, or when suffcient wind velocity information is not available.

- The FAE method can simulate the time history of entire winters and can account for the effects of multiple wind events from different directions, temperature variables, heat loss and the driftability of snow.

- Where the FAE method lacks the ability to determine the geometry of a drift at high resolution, the water flume simulation technique can provide some of this information, while compensating for the inability of the water flume technique to simulate multiple events. These approaches should be considered synergistic and should be applied together to determine the most efficient and applicable estimations for snow distribution on a building.

- Advancing the science of snow accumulation techniques for structures requires validation through partial and full scale field observations. Models should include a simplied roof step of various heights and a more complicated geometry such as the SPACE model. Not only should the geometry of snow accumulation be studied, but also the time history of the increase and decrease in structural load. To provide a more robust data set, a long term monitoring and data collection program should be initiated for a variety of climate zones.

## Acknowledgments

## References

1. J.D. Iverson. Drifting-snow similitude – transport-rate and roughness modelling. Journal of Glaciology. Vol. **26**, no. 94 (1980).

2. J.D. Iversen. Development of Small-Scale Snowdrift Simulation. Western Snow Conference. Reno, NV, USA, (1982) 112-119.

3. R.W. Gerdel, G.H Strom. Wind Tunnel Studies with Scale Model Simulated Snow.

4. M. O'Rourke, A. DeGaetano, J.D. Tokarczyk. Snow Drifting Transport Rates from Water Flume Simulation. Journal of Wind Engineering and Industrial Aerodynamics. **92**, (2004) 1245-1264.

5. P.A. Irwin, C.J. Williams. Application of snow simulation model tests to planning and design. 40th Eastern Snow Conference. Toronto, Ontario, Canada. (1983) 118-130.

6.  C.J. Williams. Field Observations of Wind Deflection Fins to Control Snow Accumulations on Roofs. Proc. 1st Int. Conf. on Snow Eng., Santa Barbara, California, USA, (1986) 307-314.

7.  A.J. Brooks, J.C. Dale, S.L. Gamble, S, F. Kriksic. The Rapid Assessment of Snow Drifting Conditions using Physical Model Simulations. American Society of Civil Engineers Cold Regions Conference. Salt Lake City, UT (2015).

8.  R.B. Haehnel, CPT., J.H. Wilkinson, J.H. Lever. Snowdrift Modeling in the CRREL Wind Tunnel. 50th Eastern Snow Conference. 61st Western Snow Conference. Quebec City (1993).

9.  J.D. Iverson. Development of snow-scale snowdrift simulation. Western Snow Conference (1982).

10. A.J. Brooks, S.L. Gamble, J.C. Dale, M.P. Gibbons. Determining Snow Loads on Buildings with Solar Arrays. CSCE 2014 4th International Structural Specialty Conference. Halifax, NS (2014).

11. S.L. Gamble, W.W. Kochanski, P.A. Irwin. Finite Area Element Snow Loading Prediction – Applications and Advancements. Journal of Wind Engineering and Industrial Aerodynamics, **41**(1992)

12. P.A. Irwin, S.L. Gamble, D.A. Taylor, D.A. Effects of Roof Size, Heat Transfer, and Climate on Snow Loads: Studies for the 1995 NBC. Canadian Journal of Civil Engineering. **22** (1995).

13. A.J. Brooks, J.V. Bond J.C. Dale, S.L. Gamble. Parametric Simulation of Roof Structural Snow Loads. Canadian Society of Civil Engineers. CSCE2016 Resilient Infrastructure Specialty Conference. London, ON (2016).

14. M. Tsuchiya, T. Tomabechi, T. Hongo, H. Ueda. Wind effects on snowdrift on stepped flat roofs. Journal of Wind Engineering and Industrial Aerodynamics, **90**(2002) 1881-1892.

# Snowdrifts on two-level building roofs and modeling of snow density at Harbin

Guolong Zhang [1, 2], Yu Zhang [1, 2] and Feng Fan [1, 2]

[1]School of Civil Engineering, Harbin Institute of Technology, Harbin 150090, China
[2]Key Lab of Structures Dynamic Behavior and Control of China Ministry of Education, Harbin Institute of Technology, Harbin 150090, China

**Abstract.** Outdoors measurements on snowdrifts on two-level building roofs and an equation for predicting snow density by the use of meteorological data are presented. The measurement was undertaken within the campus of Harbin Institute of Technology (HIT), during the period 2014-2015. The models were two-level buildings, with angles of the upper roof being 0º, 15º, 30º and 45º. The observations were undertaken directly after snowfall. The results show that the critical angle of the upper roof that affects the snow distribution on lower roofs is 30º. In addition, the critical angle that causes snow sliding from upper roofs is 30º. The snow density and meteorology measurements for the period 2010–2013 were taken by authors. With an analysis of variance, a relationship of snow density with various predictor variables was explored, That is, the snow depth and temperature have a significant effect on the snow density, while velocity, humidity and precipitation have a weak influence. Based on the various predictor variables, a fitting equation of snow density was developed with a coefficient of determination equaling 0.90.

## 1 Introduction

Snow load on building roofs is calculated based on the snow distribution and the regional mean snow density. For many years, lots of research has been carried out on both issues.

In the aspect of the snow distribution. Thiis [1] investigated the snowdrifts around three different model buildings in a valley in Spitsbergen, Norway. The different roof designs proved to have a significant influence on the size of the snowdrifts produced. A flat roof gives a larger snowdrift than a single pitch roof, and a single pitch roof, tilted upstream the wind, gives a larger snowdrift than a single pitch roof tilted downstream the wind. Oikawa [2] explored the snowdrift around a cubic model on open ground. The results showed that a deep snowdrift was encountered windward of the cube, followed by large snowdrifts on each lateral side and leeward of the cube. Strong erosion areas were observed nearly surrounding the cube. Beyers [3] evaluated the snowdrift characteristics surrounding the research station of the South African National Antarctic Expedition, SANAE IV. In this research, a 1:25 scale model of the research station was constructed and mounted on a large flat snow covered area. The wind profiles of the prevailing winds were measured with a 6-m wind mast positioned near the model. The characteristic surface roughness and shear velocity functions were derived and analyzed. From the results, a new velocity profile function was established with additional parameters to account for the effects of surface roughness and saltating snow.

In the aspect of the snow density. Meløysund [4] presented a simple method for predicting snow density using weather data, and pointed out that the snow density values suggested in the Norwegian code are, in most cases, overestimated. Bruland [5] modified Sturm's model of snow density by extending predictor variables. The final model improved the snow density predictions for the Norwegian data, compared to the model of Sturm, by up to 50%. McCreight [6] developed a new model of the bulk density for a daily time step, and demonstrated its improved accuracy over existing models.

Although many researches on snow distributions on building roofs have been carried out, more details need determinations, like the critical angles, the amount of sliding snow from upper roofs, the relationship between the angle and the distribution coefficient, etc. Furthermore, the snow load on building roofs, in China, is calculated based on the regional mean snow density, which may cause a doubtful estimated load. Therefore, an accurate estimation equation for snow density is needed.

## 2 Outdoor experiments of snow distributions on building roofs

### 2.1 Study site and setup

The outdoor experiments were undertaken on an open flat base within the campus of Harbin Institute of Technology (HIT), China (Figure 1). It was part of a large snow engineering program. The wind pattern in this area has been previously found to be constant during the winter (Figure 2). The uniform wind direction makes this area ideal for snowdrift experiments.
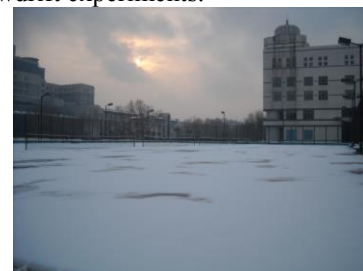


**Figure 1.** Location where outdoor experiments were conducted

Corresponding author: zhanggl_hit@126.com
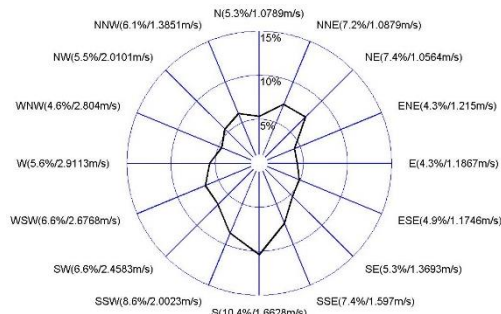
Figure 2. Wind frequency diagram in the winter of 2012-2013

The models were two-level buildings, with angles of the upper roof being 0º, 15º, 30º and 45º. The snow distribution on each roof was observed right after snowfall (Figure 3).
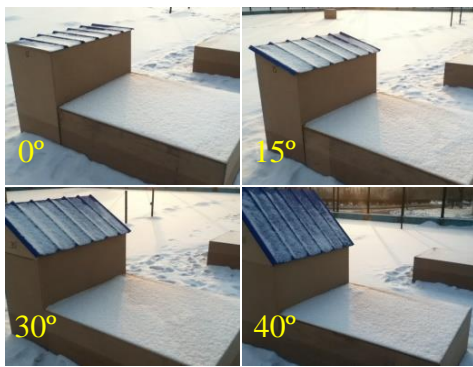


Figure 3. Photos of snow distribution on two-level roofs

The models were installed on December 15th on flat bare ground. In the following 3 months. The wind speed and direction were measured at 1.8 m on a PC-4 automatic weather station and the sampling interval was 1min.

## 2.2 Results

The two-level buildings had four kinds of upper roofs, namely, 0º, 15º, 30º and 45º slopes. Each slope pattern was made twice, and positioned face to face to investigate the snow distribution windward and leeward. The measurements on lower roofs were untaken simultaneously with those on upper single pitch roofs.

The results on 2014/12/29 have been selected for this investigation. The incidence angle of wind was 22.5° on the windward wall. The mean wind speed in dominant direction was approximately 0.7m/s (at 1.8m) and the maximum was 1.6m/s, as indicated in Figure 4.
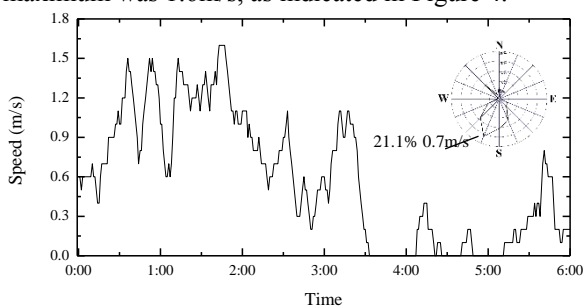


Figure 4. Wind speed and rose map for the whole period on 2014/12/29 at Harbin
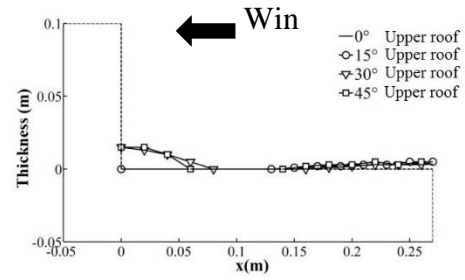


a) Snow profiles on the lower roofs in windward
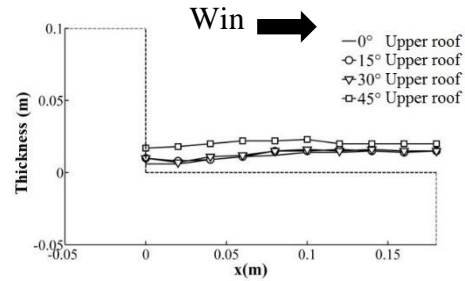


b) Snow profiles on the lower roofs in leeward

Figure 5. Snow profiles on the lower roofs with four upper slope roofs in windward and leeward on 2014/12/29

Figure 5 gives a thickness-profile for different upper slopes. In the windward condition, deposition occurs close to the foot of the upper wall, then erosion extends along the width direction, due to the strong vortex at the corner of the upper wall. In the leeward condition, the snow distribution has a gradual rising pattern along the width side. Instead of the deposition next to the wall, there exists a slight erosion.

The results presented in Figure 5 and Figure 6 illustrate that, when the slope of upper roofs is less than 30º, its influence on the snow distribution can be neglected. Furthermore, a similar pattern exists with a higher thickness value, when the upper slope exceeds 30º. In addition, the critical angle that causes snow sliding from upper roofs is 30º.
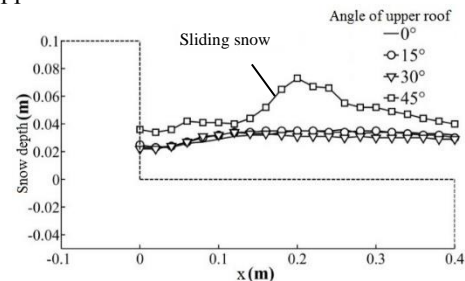


Figure 6. Profiles of model snowdrift formed on two-level roofs with sliding snow on 2015/01/02

## 3 Analyses of snow density

### 3.1. Data

The snow density and meteorological data were measured directly after each snowfall. No measurements were undertaken when the maximum snow depth on the ground was less than 5mm. Snow density measurements

were undertaken using a sharp-edged tube with an internal cross-section of 1135mm2. The snow inside the tube was weighed and the density calculated. The meteorological data were measured by a PC-4 automatic weather station. Air temperature and humidity were measured at 1.5 m above the ground, with an accuracy of 0.1 °C and 0.1%, respectively. Precipitation (mm water equivalent) was measured with fresh snow. Snow depth was measured using a yardstick simultaneously with snow density. This was a measure of the accumulated snow depth (not only precipitation as snow was present since the last measurement). In the period 2012-2013, a total of eight sets of data were collected. The mean temperatures, mean wind velocities, precipitations and maximum snow depths during the measurement period are given in Table 1.

**Table 1.** Snow and meteorological data for the measurement period of 2012–2013

| Time | Temperature (℃) | Humidity (%) | Wind velocity (m/s) | Precipitation (mm) | Snow depth (mm) | Snow density (kg/m$^3$) |
|------|-----------------|--------------|---------------------|--------------------|-----------------|-------------------------|
| 2012/11/26 | -12.0 | 79.8 | 2.0 | 7.0 | 7.3 | 86.6 |
| 2012/11/27 | -8.5 | 80.2 | 2.7 | 51.0 | 57.8 | 106.4 |
| 2012/12/03 | -13.9 | 82.5 | 2.3 | 37.0 | 94.0 | 136.4 |
| 2012/12/15 | -17.1 | 78.1 | 1.8 | 40.0 | 133.2 | 150.8 |
| 2012/12/21 | -20.1 | 71.5 | 1.8 | 20.0 | 149.6 | 156.4 |
| 2012/12/29 | -19.4 | 78.3 | 2.4 | 24.0 | 173.6 | 144.7 |
| 2013/01/23 | -12.5 | 79.5 | 2.0 | 18.0 | 185.8 | 154.6 |
| 2013/02/28 | -10.0 | 58.2 | 1.3 | 100.0 | 267.4 | 154.6 |

## 3.2 Analyses and result

Analysis of variance (ANOVA) is a procedure for assigning sample variance to different sources and deciding whether the variation arises within or among different population groups. ANOVA can be used to identify sources of variability in a response variable Y and determine which factors affect the output in a design of experiment (DOE). This method contains One-Way ANOVA, Two-Way ANOVA and N-Way ANOVA. The model of Two-Way ANOVA may be described by the linear equation:

$$Y_{ijk} = \mu + \tau_i + \beta_j + (\tau\beta)_{ij} + \varepsilon_{ijk} \begin{cases} i = 1, 2, ..., a \\ j = 1, 2, ..., b \\ k = 1, 2, ..., n \end{cases}$$

Here, $\mu$ is the overall mean effect, $\tau_i$ is the effect of the i th level of factor A, $\beta_j$ is the effect of the j th level of factor B, $(\tau\beta)_{ij}$ is the effect of the interaction between A and B. $\varepsilon_{ijk}$ is a random error component, having a normal distribution with mean zero and variance $\sigma^2$. The ANOVA was used to identify qualitatively the effect of meteorological variables on snow density.

Each variable had two levels, i.e. H (High) and L (Low). Three variables were selected in each analysis, because of the limited amount of data. As the snow depth and the temperature are the main contribution factors proposed in literature, the analyses were divided into three groups, as shown in Table 2.

**Table 2.** The group information of meteorological variables in each analysis

| | meteorological variable | | | | | | | | |
|-------|-------|-------------|----------|-------|-------------|----------|-------|-------------|---------------|
| | Group 1 | | | Group 2 | | | Group 3 | | |
| | Depth | Temperature | Velocity | Depth | Temperature | Humidity | Depth | Temperature | Precipitation |
| Level | L | L | L | L | L | L | L | L | L |
| | H | L | L | H | L | L | H | L | L |
| | L | H | L | L | H | L | L | H | L |
| | L | L | H | L | L | H | L | L | H |
| | H | H | L | H | H | L | H | H | L |
| | H | L | H | H | L | H | H | L | H |
| | L | H | H | L | H | H | L | H | H |
| | H | H | H | H | H | H | H | H | H |

Note: H denotes high; L denotes low.

Note: Dep. denotes snow depth; Tem. denotes temperature; Var. denotes velocity, humidity and precipitation respectively in Group 1, 2 and 3

The results of ANOVA are shown in Table 3. According to this method, the effect is significant with a lower p value. If the significance level is 0.05, the snow depth and temperature have a significant effect, while velocity, humidity and precipitation have a weak influence. Considering interaction effects, depth & temperature, depth & precipitation and temperature & velocity, all have obvious influences. Furthermore, the

**Table 3.** The results of ANOVA

| Variable | $p$-value（%） | | |
|----------|---------|---------|---------|
| | Group 1 | Group 2 | Group 3 |
| Dep. | 0.00 | 0.00 | 0.00 |
| Tem. | 0.00 | 0.00 | 0.00 |
| Var. | 0.67 | 0.48 | 0.12 |
| Dep.&Tem. | 0.00 | 0.00 | 0.00 |
| Dep.&Var. | 0.24 | 0.97 | 0.00 |
| Tem.&Var. | 0.00 | 0.08 | 0.23 |

effect of temperature & humidity is relatively high. Therefore, snow depth, temperature, depth & temperature, depth & precipitation, temperature & velocity and temperature & humidity are chosen for the regression analysis.

### 3.3 Multiple regression analyses

Multiple regression analyses are suitable for predicting snow density by the use of meteorological data. The parameters investigated as predictors in this study are those discussed in 3.2. The analyses were performed using the statistical software program MATLAB. During the period of 2012-2013, there were 50 observations. If the significance level is set to 0.05, the function is as follows with a high coefficient of determination equaling 0.90:

$$\rho = 45.02 + 0.88D - 0.01D^2 - 2.97T$$
$$+ 0.02D \cdot T + 0.30T \cdot V - 0.01T \cdot H$$

Here, $\rho$ is the snow density. D is the snow depth. T is the air temperature. V is the wind velocity. H is the humidity.

## 4 Conclusions

This study has investigated the characteristics of drifting snow on some typical roofs and developed a method for estimating snow density using meteorological data. The following results have been obtained:

1) For two-level roofs, when the angle of the upper roof is smaller than 30º, its influence on the snow distribution on the low roof can be neglected. In addition, the critical angle that causes snow sliding from the upper roof is 30º.

2) In the aspect of influence factors of the snow density, Snow depth and temperature are the main influencing factors. In the aspect of the effect of the interaction, depth & temperature, depth & precipitation and temperature & velocity also have an obvious influence. Furthermore, the regression equation, presented in 3.3, could predict the snow density accurately with a high coefficient of determination equaling 0.90.

## References

1. T. K. Thiis, Y. Gjessing. J. Cold Reg. Sci. Technol. 30, 175 (1999)
2. S. Oikawa. J. J. of Snow Eng. of Japan. 5, 3 (2000)
3. J.H.M. Beyers, T.M. Harms. J. J. Wind Eng. Ind. 91, 551 (2003)
4. V. Meløysund, B. Leira, K. V. Høiseth, K. R. Lisøa. J. Meteorol. Appl. 14, 413 (2007)
5. O. Bruland, Å. Færevåg, I. Steinsland, G. E. Liston. J. HYDROL RES. 46, 494 (2015)
6. J. L. McCreight, E. E. Small. J. TC. 8, 521 (2014)

# Advantages and features of four different snow utilizing facilities

Seiji Kamimura[1, a], Yoshiomi Ito[2] and Junki Zen[3]

[1]*Nagaoka University of Technology, Department of Mechanical Engineering, 1603-1 Kamitomioka, Nagaoka, Japan*
[2]*Yuki-daruma (snowman) Foundation, 722-3 Yasuzuka, Jo-etsu, Niigata 942-0411, Japan*
[3]*Nagaoka University of Technology, Graduate School of Engineering, 1603-1 Kamitomioka, Nagaoka, Japan*

**Abstract.** In the summer of 2014, the air-conditioning performance of four different snow-utilizing facilities in Niigata and Nagano Prefectures in Japan were evaluated. Systems with a snow storeroom, a rice depot and spa resort, showed the advantages of stable and flexible air temperature control with high deodorizing and dedusting effects. The investment will be earned back in less than 10 years. The system with a snow mound, shiitake mushroom greenhouses, showed that the annual cost is cheaper than that of the heat pump unit. A highway lavatory with daily snow delivery was not cost effective.

## 1 Introduction

In Japan, the northwestern region bordering the Sea of Japan receives heavy snows not seen in other locations worldwide. Therefore, a traditional but unique culture using natural snow for daily life and industry has developed. From the late 1980s, traditional snow utilization applications and facilities have been upgraded with modern technology and revitalized in Japan. Currently, more than 150 facilities are utilizing snow and/or ice in Japan[1].

In Niigata Pref., two trials were conducted in 1998[1]: a refrigerated vegetable warehouse in Tokamachi City was covered with snow and a residential house in Uonuma City was cooled by deposited snow sliding down from a roof. These challenging applications showed many advantages, such as much lower energy consumption, greater and longer crop freshness, high comfort, and so on. Government support since 2002 has also helped with the development of snow-utilizing facilities, and their applications have been diversifying.

From the late 1980s to the early 1990s, the first stage of snow utilization was to verify the technical possibilities and to develop the basic technologies. After that, snow utilization was applied as alternatives to air-conditioners and refrigerators. The second stage, from the late 1990s to the early 2000s, concentrated on the energy saving effect. The authors assume that we are now in the third stage, which focuses on the advantages of snow, such as an extremely stable temperature of around 0 °C, high relative humidity of around 100%, and high absorptivity of odor and dust[2, 3]. In this third stage, many effects have been demonstrated in succession: taste improvement of root vegetables, maintaining freshness of green-leaved crops and fruit, and high-quality aging of meat, coffee, sake, wine, and so on. There are now a wide range of applications for snow storage[4].

Snow cooling/refrigerating systems mainly consist of three sections: snow storing, cold heat extraction and delivery, and snow use. The methods for storing snow are classified into two types: snow mound and snow storeroom. In the snow mound, naturally accumulated snow is collected and piled up outside, then covered with special insulation material, such as rice shells, wood

chips/bark or an industrial insulation sheet. The initial cost of a snow mound is relatively low, but a snow mound has some disadvantages, such as poor insulation performance, slightly higher running cost and larger space requirements, as compared to a snow storehouse[5].

Two major methods are used to extract and deliver cold heat to the cooling target: cold-air circulation and cold-water circulation. In the cold-air circulation method, dust, odor and humidity in the circulating air are expected to be removed as they contact the wet snow surface. The water-circulation method offers no air-purifying effect, but it only requires piping with a small diameter and does not transmit noise through this piping.

The most simple and inexpensive way to use snow is the snow/ice house method, which puts both snow and stored goods in a room. The natural convection of air results in a temperature of about 5 °C and a humidity of 70 to 100%. The air-circulation and water-circulation systems can produce any temperature condition if the control equipment is well designed.

Now, the number of snow-utilizing facilities is over 150 in Japan and the application of snow utilization has diversified for various purposes and industries. In 2014, we had an opportunity to investigate four snow-utilizing
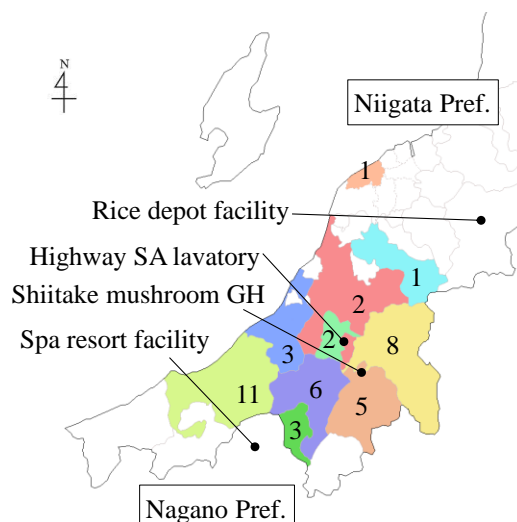


**Figure 1.** Locations of snow-utilizing facilities.
(Numeral is number of facilities in each municipality)

[a] Seiji Kamimura: kami@nagaokaut.ac.jp

facilities in Niigata and Nagano Prefectures, Japan. The facilities are shown in **Figure 1**. Temperature, humidity, amount of heat used, and the air purifying effect of all the facilities were observed during the entire summer of 2014. In this study, the advantages, characteristics, performance, and stability of these four snow-utilizing facilities were evaluated.

## 2 Facilities and evaluation

### 2.1 Outline of facilities

The four snow-utilizing facilities are as follows: (1) a rice depot having a snow storeroom with cold-air circulation, (2) a spa resort having a snow storeroom with cold-water circulation, (3) shiitake mushroom greenhouses having a snow mound covered by rice shells with cold-water circulation, and (4) a highway service area (SA) lavatory with daily snow delivery from a snow mound covered by wood chips with a simplified cold-water circulation unit. A summary of these systems is listed in **Table 1**. Schematic layouts and pictures of the systems are shown in **Figures 2**, **3**, **4,** and **6**.

### 2.2 Rice depot having a snow storeroom with cold-air circulation

The rice depot was constructed in Aga town, Niigata Pref. in January 2014 and utilizes snow for cooling. The depot has two rice storage rooms of different temperatures, 5 and 15 °C, for paddy rice and brown rice, respectively. The storage room for the paddy rice (PR room) has the following dimensions: width 13 m, depth 15 m and height 8 m. The PR room can store 4,000 bales of paddy rice (1 bale is equal to 60 kg). The storage room for brown rice (BR room) has dimensions 15 x 20 x 8 m. The BR room can store 6,000 bales of brown rice. The snow storeroom has dimensions of 10 x 7 x 8 m and can store 545 tons of snow, as calculated from the capacity multiplied by the packing rate of 0.8 under the assumption that the average snow density is 0.5 t/m³. Snow collecting/throwing is combined with the snow removal operation for parking lots neighboring the facility.

The aim of storing rice in a cooling room less than 15 °C is to suppress infestation by insects and microbes, and to lower the physical activity to keep the rice fresh. A lower temperature may give better results but a control temperature of 15 °C is normally chosen to reduce operating costs. In the case of the snow-cooling room, a lower temperature, such as 5 or 10 °C, can easily be realized and, moreover, it can avoid the temperature fluctuations associated with electric coolers. Such temperature fluctuations may increase the fatty acid content. For the above reasons, the control temperature of the rice depot with the snow storeroom is set to 5 °C for the paddy rice room for long-term storage and to 15 °C (12°C from 1 May to 11 July) for the brown rice room based on demand/supply regulations.

The depot has two sets of blowers (send and return) and electric dampers (send, return and bypass). The output of the blowers is 1.5 and 3.7 kW for the PR room and the BR room, respectively. All blowers are generally operating all the time, while the dampers are controlled to maintain a predetermined room temperature. The snow-cooling system began on 16 April 2014 for the BR room, then the PR room was added from 1 May to 19 Nov. 2014.
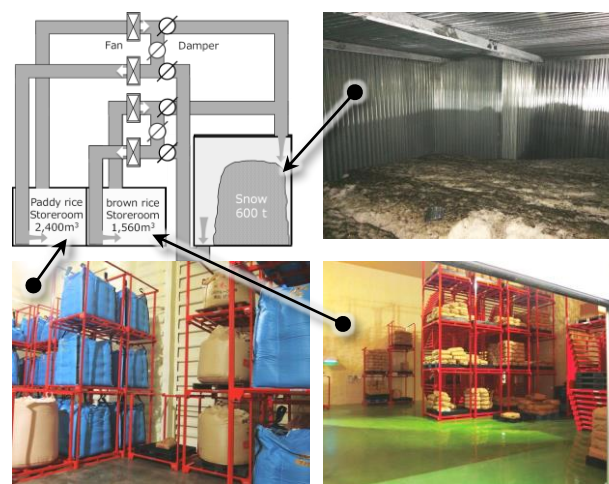


**Figure 2.** Snow-cooling system for the rice depot.

**Table 1.** Outline of four snow-utilizing facilities.

| | Cooling space [m³] | Set temperature [°C] | Purpose | Snow storage [tons] | Extraction of cold heat | Operating period |
|---|---|---|---|---|---|---|
| (1) Rice depot    for paddy rice    for brown rice | 1,560 2,400 | 5 12, 15 | Refrige- ration | 545 in storeroom | Cold-air circulation | 5 months |
| (2) Spa resort    lounge and    cafeteria | 741 716 | 25 25 | Space cooling | 263 in storeroom | Cold-water circulation | 3 months |
| (3) Mushroom    greenhouses | 1,463 | 10–20 (budding) 20–30 (growing) | Space cooling | 1,000 mound covered with rice shells | Cold-water circulation | 3 months |
| (4) Highway SA    lavatory | 289 / 289 for M and F | No control (25) | Space cooling | 1,000 mound covered with wooden chips | Daily delivery, Cold-water circulation | 1 months |

## 2.3 Spa resort having snow storeroom with cold-water circulation

The spa resort facility was reconstructed in Nozawa-onsen village, Nagano Pref. in July 2014. At that time, the space-cooling system utilizing snow was added to the facilities. The site is a very famous ski area in winter, but few tourists visit in summer because skiing is the main attraction. Therefore, snow cooling is expected to be a summer tourist resource. The resort lounge of 741 $m^3$ and the cafeteria of 716 $m^3$ are cooled by fan coil units (FCUs) connected to the snow storeroom through a pipeline.

The resort has two heat exchanging circuits, which are primary and secondary. In the primary circuit of water, warm water sprays onto the snow, then the resulting cooler water, including melt water, flows down to the water reservoir, and then is pumped up to the heat exchanger (HE) and returns to the snow storeroom. In the secondary circuit, warm water returned from the FCUs release heat at the HE, and then is sent to the FCUs again.

The snow storeroom has dimensions of 15 x 10 x 5 m, and can store 241 tons of snow, as calculated from the capacity multiplied by the packing rate of 0.7. Snow collecting/throwing work is combined with the snow removal operation for a parking lot neighboring the facility. The volumes of the lounge and cafeteria are 741 and 716 $m^3$, respectively. The experiment ran from 16 June to 2 Sept. 2014. The FCUs during this time were manually operated by the users.



**Figure 3.** Snow-cooling system for a spa resort.

## 2.4 Shiitake mushroom greenhouse having snow mound covered by rice shells with cold-water circulation

A farmers association in Minami-Uonuma City in Niigata Pref. is cultivating shiitake mushrooms in greenhouses (GHs) in a year-round operation. To cultivate mushrooms all through the year, the temperature in the GHs must be kept constant, and so they require heating in winter and cooling in summer. The annual cost of heating and cooling is about 500,000 yen/y (approx. 4,600 USD) for a greenhouse. In particular, the electricity cost for cooling accounts for two-thirds of the whole energy cost. Therefore, reduction of the cooling cost is very effective for improving profitability. Since summer 2011, farmers

have tried to use a snow mound system for GH cooling. After trial and error for three seasons, a practical way to use snow for the GHs was established. The snow mound shown in **Figure 4** was heaped up by using a rotary snow blower of 10 horsepower for one day. After forming a snow mound of about 1000 tons, rice shells partly mixed with snow were also blown up to the snow surface to a thickness of 20 to 30 cm. Finally, an anti-scattering net was put on the surface.

The bed of the snow mound is 30 x 30 m with a water gradient. **Figure 5** shows the layout of the snow mound, pipeline, and GHs. Melt water in the reservoir pit from the snow mound is pumped up and sent through a PVC pipe to the FCUs in the GHs and then heat is exchanged and cold air is blown in. The warmed-up water returns to the upper end of the snow mound and is cooled down again under the snow mound. FCUs are installed in GHs Nos. 3, 4, 5 and 6 of the six GHs. In addition, the No. 3 GH only has two FCUs due to its large room volume. Because each GH is also equipped with an electric cooler unit, the snow-cooling system is constantly working for the base demand in the summer. The electric coolers are controlled by room temperature to adapt to the fluctuating demand.

The snow-cooling system operation for Nos. 3, 4, and 5 started on 6 June 2014 and ran until 9 Sept., while No. 6 started on 11 July. The control temperatures in the room were between 10 to 20 °C for cultivating the mushroom beds, and 20 to 30 °C for the development.
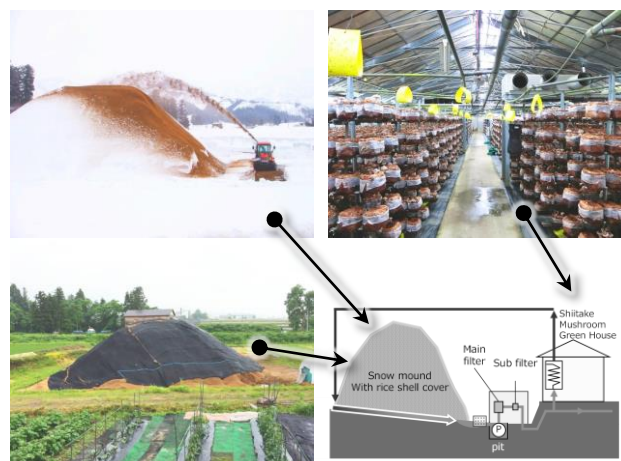


**Figure 4.** Snow-cooling system for the shiitake mushroom Greenhouse.
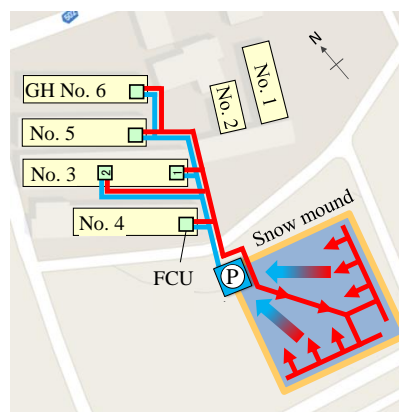


**Figure 5.** Layout of a snow mound, GHs and piping.

## 2.5 Highway SA lavatory with daily snow delivery from a snow mound covered by wooden chips with simplified cold-water circulation unit

A trial experiment of snow cooling for a lavatory of a highway service area (SA) was conducted in July and Aug. 2014 in Kawaguchi, Niigata Pref. **Figure 6** shows delivery procedure from the snow mound to lavatory. Because the



**Figure 6.** Snow cooling system for Highway SA lavatory.
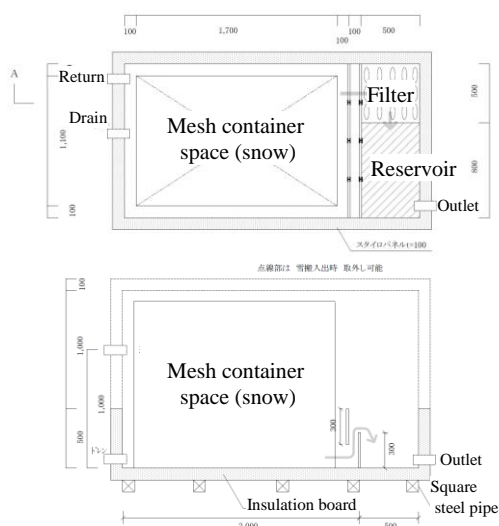


**Figure 7.** Simple Snow Cooling Unit (SSCU).
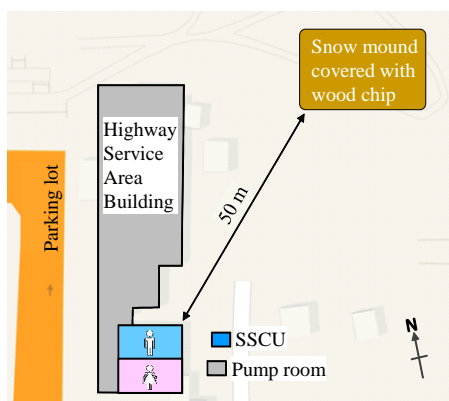


**Figure 8.** Plan view of snow mound and Service Area building.

highway SA has a large parking lot, much of the SA budget in winter is snow removal, and the resulting piles of snow take up a large area. In addition, a sudden increase of melt water containing antifreezing salt from the snow piles in the spring may adversely affect the neighboring rice paddy.

For three days in the middle of March, 2014, a snow mound was shaped into a pyramid in a back area of the SA by using a backhoe. For two days after shaping, the mound was covered by crushed chips of wood. The mass of the snow mound was estimated to be 866 t, as calculated from the measured volume of 1732 m³ under the assumed snow density of 0.5 t/m³. The stored snow was also used for an event in the summer.

Because the snow mound was 50 m away from the lavatory, we decided to deliver 1 ton of snow every morning from the snow mound to a simple snow-cooling unit (SSCU), which was newly designed and assembled for the project, as shown in **Figure 7**. The SSCU (2.5 x 1.3 x 1.6 m) was composed of an insulated chassis, a filtering tank (bag of crushed shells), a melt-water reservoir, and a cold water outlet. In addition, it had a mesh container (1.7 x 1.1 x 1.4 m) inside for storing the snow. The amount of snow packed in the mesh container was about 0.9 tonnes, which was estimated from the volume of 2.05 m³ under the assumed snow density of 0.5 t/m³ and packing factor of 0.9. Every morning, an operator brought snow down from the snow mound with a backhoe and then packed snow into the mesh container. The container packed with snow was transported by a dump truck with a crane and stored in the SSCU.

The cold water outlet of the SSCU was connected to an insulated PVC pipeline and pump, and the melt water was sent to the FCUs in both the men's and women's lavatories, and then returned to the SSCU again. The FCUs were placed around the entrance of each lavatory. The pump operated 24 hours a day from 18 July to 20 Aug. 2014. On average, 1 ton of snow was carried at 8 am and remained until approximately 8 pm.

## 3 Evaluation of facilities

The cooling performance of these facilities was evaluated by the coefficient of performance (COP) calculated from the amount of cold heat extracted from the stored snow (GJ), $Q$, and the electric power consumption for system operation (GJ), $P$, as follows:

$$\text{COP} = Q/P.$$

$Q$ is calculated by the following equation,

$$Q = \int \rho C_p (T_{out} - T_{in}) G \, dt$$

where $\rho$ is the density of circulating fluid (kg/m³), $C_p$ is the isobaric specific heat (kJ/kg*K), $T_{in}$ and $T_{out}$ are the fluid temperature of the supply and return, respectively, and $G$ is the mass flow rate of fluid (m³/s). $P$ is the sum of the products of electric current $I$ and electric voltage $V$:

$$P = \int IV dt.$$

The profitability of these facilities is discussed with the simple cost calculation denoted in the following equation,

$$C_a = \frac{C_i}{L} + C_r$$

**Table 2.** Observation items.

| | (1) Rice depot | (2) Spa resort | (3) Mushroom GH | (4) SA lavatory |
|---|---|---|---|---|
| Room temp. & humid. | ○ | ○ | ○ | |
| Blowing air temp. | | | ○ | ○ |
| Fluid temp. of inlet | ○ | ○ | ○ | ○ |
| Fluid temp. of outlet | ○ | | ○ | ○ |
| Fluid velocity | ○ | ○ | ○ | |
| Calories | | ○ | | ○ |
| Electric current | | | ○ | ○ |
| Electric power | ○ | | | |
| Snow-room temp. | | ○ | | |
| Water tank temp. | | ○ | | |
| Outside temp. & humid. | ○ | ○ | ○ | ○ |
| Dust concentration | ○ | | | |
| Odor level | ○ | | | |

where $C_a$ is the annual cost of the system, $C_i$ and $C_r$ are the initial and running costs, respectively. $L$ is the lifetime of the components of the system. The cost of these facilities is compared with a commercial air-coupled heat pump system, and then the break-even point is discussed.

# 4 Experimental result

## 4.1 Rice depot having a snow storeroom with cold-air circulation

**Figure 9** shows the observed outdoor temperatures and room temperatures. The temperature in the BR room was followed well at the pre-set temperature of 12 °C from 1 March to 11 July and 15 °C after 12 July. The standard deviation for the BR room was 0.4 °C even in the middle of summer. The temperature in the PR room varied around 7 °C after the end of May despite the pre-set temperature of 5 °C. The reason for the higher temperature difference after the beginning of June is considered to be the lower heat exchanging efficiency in the snow storeroom due to the short circuit of the air flow. The standard deviation from the pre-set temperature for the PR room was 2.1 °C. After mid-September, the temperature varied widely because it was the harvesting season and the door was often opened. The humidity in both rooms had been kept at about 70% and the standard deviations were 4.4% and 3.5% for the PR room and the BR room, respectively.

In the case of the air-circulation system, it is known that the effect of air-purifying and deodorizing is promising. **Figure 10** shows the dust concentration in the PR room. The suspended dust concentration was far below the environmental standard of 0.10 mg/m³. The odor level was about 160, which corresponds to that of a kitchen or laundry machine and is less than that in a factory of plastic products. This beneficial effect was confirmed by a facility operator's comment that "There is no rice bran smell."

## 4.2 Spa resort having snow storeroom with cold-water circulation

**Figure 11** shows the air temperature of the lounge and cafeteria of the spa resort. The snow cooler operated from 9 am to 8 pm, so the air temperature was quite low in the daytime and relatively high in the night time. Therefore, the following analysis takes into account the daytime result. The temperature in the lounge and cafeteria was kept in the range between 20 to 25 °C even when the outside temperature exceeded 30 °C. Especially, the
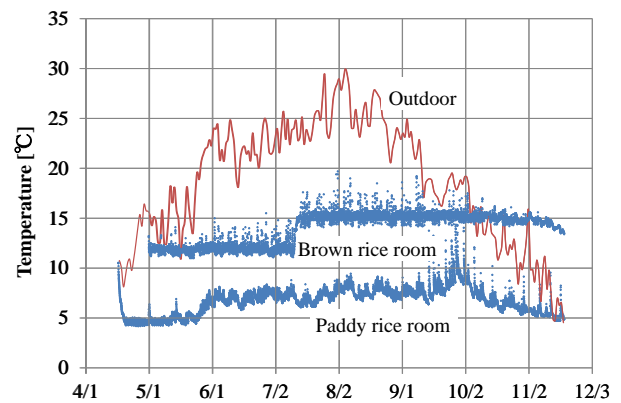


**Figure 9.** Observation result of temperature in the rice depot.
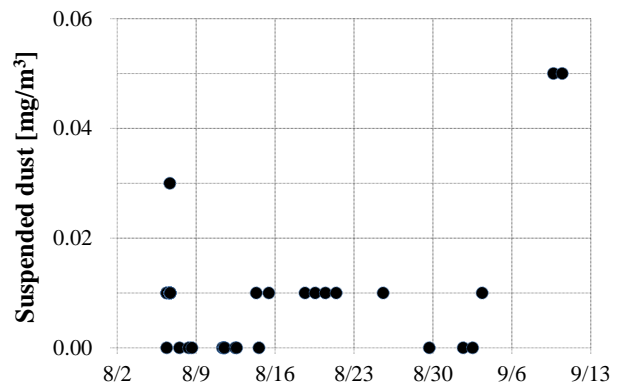


**Figure 10.** Concentration of suspended dust in the PR room.

cafeteria temperature sometimes reached 22 °C, so the snow cooler was shown to be effective. The snow cooler operated until the end of Sep., when the outside temperature became lower than the room temperature.
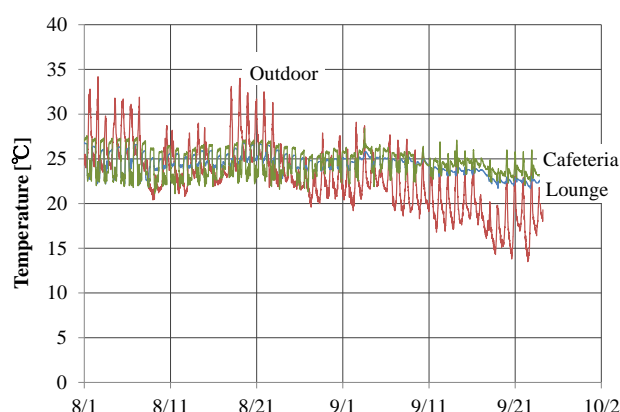


**Figure 11.** Observed temperature of the spa resort.

## 4.3 Shiitake mushroom greenhouses having snow mound covered by rice shells with cold-water circulation

**Figure 12** shows the water temperatures of the inlet and outlet of the FCU in the No. 4 GH. The daily fluctuation of the curve corresponds to the outdoor temperature. The temperature difference, which corresponds to the amount of heat released at the FCU from the beginning of Aug. to the beginning of Sept. was around 5 °C in the daytime, so this shows that the snow-cooling system worked well. After 10 Sept. the volume of the snow mound shrank and the heat exchange at the snow mound did not work well. The average temperature differences for the whole period were 3.4, 4.1, 3.1 and 2.2 for Nos. 3, 4, 5 and 6 GHs, respectively.
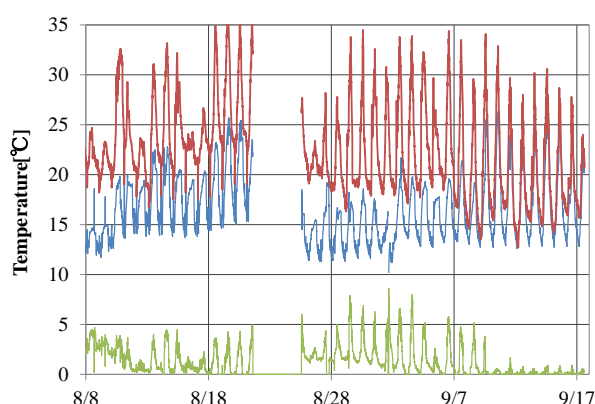


**Figure 12.** Observed temperature of the No. 4 GH.

Some problems were explained by the experiment in 2014. For the GHs except No. 4, which was the closest to the snow mound, the flow rate of the circulated water was insufficient, because the piping design of the distribution to that branch was inappropriate and two filters often had troubles. In addition, the storage capacity of the snow mound was too small, because two FCUs were added to the No. 3 and No. 6 GHs, even though the volume of the snow mound in 2014 was the same as in the previous year. The number of FCUs in the 2013 season was three each for the Nos. 3, 4 and 5 GHs, while it increased to five each in the 2014 season.

The maximum cooling energy per day extracted from the snow mound was 3.0 GJ, which is equal to 9.1 tons of snow. By assuming no filter problems, the total cooling energy was estimated as 219 GJ, which corresponds to 654 tons of snow. This estimate suggests that 65% of the stored energy from a snow mound of 1000 tons can be used.

## 4.4 Highway SA lavatory with daily snow delivery from a snow mound covered by wooden chips with simplified cold-water circulation unit

**Figure 13** shows the wind temperature at an FCU outlet at the SA lavatory. The average temperatures were 17.3, 22.5 and 26.1 °C for the men's lavatory, the women's lavatory, and the outside air, respectively. The temperature of the women's lavatory was about 5 °C higher than the temperature of the men's lavatory. The assumed reason is the length of piping was 1.5 times longer and was affected by solar radiation and heat convection from the outside hot air.
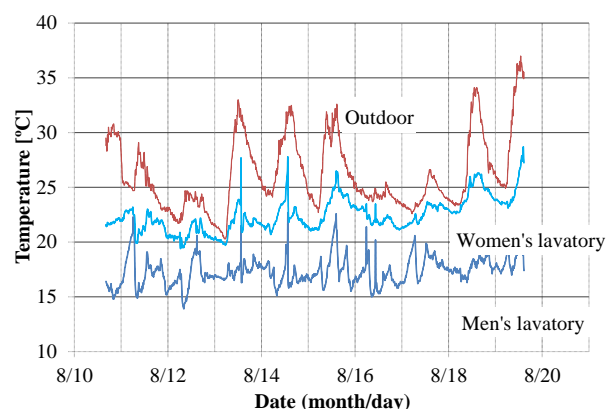


**Figure 13.** Wind temperature at FCU outlet of SA lavatory.

# 5 Consideration

## 5.1 Cool energy utilization

The effective cool energy used for the facility was estimated from the temperature difference, flow rate of circulation and specific heat of the media. The amounts of electricity consumed for the snow-cooling system operations are summarized in **Table 3**.

In the rice depot, the COP of the PR room was 5.3, which is somewhat better than that of a commercial electric cooling unit of equivalent capacity, whereas the COP of the BR room was 2.5, which is about that of an ordinary electric cooler that has a COP of 3. The values of *P* in parentheses in Table 3 are for the snow-cooling operations and do not consider the electricity consumption for air circulation. As shown, the 4.9 GJ in Table 3 lead to an improved COP of 7.3 in the snow-cooling operation.

The COP of the spa resort, 4.8, is also an improvement. Both systems of the rice depot and the spa resort represent the first year after opening the facility, so it is considered that the optimization of system control was insufficient. The COPs might become better as the operation of the system is improved.

For the shiitake mushroom GHs, excellent energy efficiency was verified. Even though some problems occurred, such as filter clogging and inappropriate piping design, the COP exceeded 10. The last year of data, which are the values in parentheses, show better results because of fewer problems.

**Table 3.** Coefficient of performance (COP) of four systems.

| | $Q$ [GJ] | $P$ [GJ] | COP |
|---|---|---|---|
| Rice depot PR room | 71.9 | 13.7 | 5.3 |
| BR room | 36.0 | 14.4 ( 4.9) [*1] | 2.5 ( 7.3) [*1] |
| Spa resort | 36.8 | 7.6 | 4.8 |
| Shiitake GHs | 37.1 (77.0) [*2] | 3.3 ( 5.4) [*2] | 11.2 (14.3) [*2] |
| SA lavatory | 11.5 | 2.3 | 4.9 |

*1 only for snow-cooling operation.
*2 experimental results in 2013 summer.

For the SA lavatory cooling considering only the electricity consumption of the FCUs and pumps, the COP was 4.9, which is almost equal to a high-ranking electric cooler. In this case, because the pump operated during the night time, the system can be improved. If the pump stopped during the night time, the COP could be improved to 8.08. However, if accounting for the energy consumption for snow-packing and transportation every morning, the energy efficiency of the snow delivery cooling system may not be acceptable.

## 5.2 Cost performance

Evaluations of the cost performance of the four snow-cooling facilities are summarized in **Table 4** by comparing the equivalent electric cooling units. In the case of the rice depot, the initial cost (IC) was estimated by the average

construction cost of a mid-scale snow storehouse of 80 x $10^3$ yen/t. The statutory durable years of steel-framed reinforced concrete constructions is 38 years. The running cost (RC) included the electricity cost and excluded the snow-throwing cost, because it is the ordinary snow-removal operation cost of parking lots. For an equivalent electric cooler, the IC was estimated from the price of a commercial cooler (not including installation cost). The RC is taken as 13 years from the statute. By assuming running hours and electricity cost, the RC was calculated.

At the spa resort facility, the IC of the snow-cooling system was estimated as the sum of the snow storehouse, 45,000 x $10^3$ yen, and the air-conditioning equipment, 5,000 x $10^3$ yen. The lifetime (L) and RC values were given in the same manner. The total cost, TC, which was the cost of the first year of the snow cooler, was about 4 times greater than that of the electric cooler, whereas the RC of the snow cooler was about one-fourth; therefore, the break-even point (BEP), is 10.5 years after construction. It can be said that the BEP of the rice depot of 2.7 shows an excellent cost performance. This result means facilities with lower control temperatures may achieve better cost effectiveness.

The IC of the snow-cooling system of the shiitake GH assumed the anti-scattering net, piping material, pump and FCUs have a lifespan of 2 years. The RC included snow mound construction, insulation covering work and electricity consumption. As shown in the table, the TC of the snow-cooling system is less than that of an electric cooler from the first year. The reason for such a cost advantage is that it did not require construction of a snow storehouse, which is the main factor contributing to the cost of a snow-cooling system. Another contributing factor is that the site of the snow mound was a rice paddy, where it was not required to remove rice shells as insulation material after the snow-cooling operation.

The IC of the SA lavatory snow cooler takes into account the FCUs of 150 x $10^3$ yen, a pump of 105 x $10^3$ yen and the SSCU of 1,000 x $10^3$ yen. The durable years of the FCUs and pump are taken as 13 and 7, respectively, and that of the SSCU is 7. The RC of the lavatory snow cooler must include the snow-packing and transportation cost. The rental fee for a backhoe and a dump truck with a crane for 34 days was estimated as 762 x $10^3$ yen. Because of the high packing/transportation cost, the BEP is not

**Table 4.** Cost estimation and break-even point of four sysytems.

| | | IC [$10^3$ Yen] | L [y] | IC/L [$10^3$ Yen/y] | RC [$10^3$ Yen/y] | TC [$10^3$ Yen/y] | BEP [y] |
|---|---|---|---|---|---|---|---|
| Rice depot | Snow cooler | 48,000 | 38 | 1,263 | 122 | 1385 | 2.7 |
| | Electric Cooler | 2,400 | 13 | 184 | 524 | 708 | |
| Spa resort | Snow cooler | 50,000 | 38 | 1,320 | 34 | 1,354 | 10.5 |
| | Electric Cooler | 3,400 | 13 | 262 | 135 | 397 | |
| Shiitake GHs | Snow cooler | 1,120 | 2 | 560 | 42 | 602 | 0.5 |
| | Electric Cooler | 5,200 | 13 | 400 | 354 | 754 | |
| SA lavatory | Snow cooler | 150/1104 | 13/7 | 179 | 122+762 | 1063 | – |
| | Electric Cooler | 450 | 13 | 35 | 523 | 558 | |

shown. It was concluded that snow cooling with daily delivery is not cost effective. But, if the snow is also used for summer events, the value of the snow must not be evaluated only in terms of energy saving. Summer snow events are popular all over Japan, and the snow could be used in such events.

## 6 Conclusion

In the summer of 2014, four different snow-utilizing facilities in Niigata and Nagano Prefectures in Japan were evaluated by their air-conditioning performance.

The systems with a snow storeroom, a rice depot and spa resort, had advantages such as stable and flexible air temperature control. Especially, the air circulation system achieved high deodorizing and dedusting effects. Moreover, the energy efficiency of both systems was better than that of an equivalent electric heat pump unit, and the cost of investment will be earned back in less than 10 years.

The system with the snow mound, which was the shiitake mushroom greenhouses, showed that the annual cost will be cheaper than the heat pump unit starting in the first year. It was concluded that the snow-cooling of the greenhouses was highly suitable for the agricultural industry. For the SA lavatory system, it was concluded that snow cooling with daily delivery is not cost effective.

## Acknowledgements

## References

1. Hokkaido Bureau of Economy, Trade and Industry, Cool Energy 5. (2012) (in Japanese)
2. Kamimura, S. and Ito, Y., A simple air-conditioning system with built-in snow storeroom, Proceedings of 6th Int'l Conf. on Snow Engineering in Whistler. (2008)
3. Kamimura, S., Kato, R., and Kamiura, K., Evaluation of air-conditioning performance of an ice cooling system, J. of SHASE Japan, **201** (2013) (in Japanese)
4. Yuki-daruma Foundation, Research review and prospect of quality keeping and improvement effect on food stored in Snowroom. (2015) (in Japanese)
5. Y. Nakamura, H. Sugiyama and S. Kamimura, Experimental Study on Open Air Storage of Snow with Simple Insulation Using Agricultural Wastes, , Proc. 5th Int'l Conf. on Snow Eng. in Davos. (2004)

**Session 7**

# Transport

# Modelling the thermal conductivity of melting snow layers on heated pavements

Anne Nuijten[1,a], Knut Vilhelm Høyland[1,2], Cor Kasbergen[3] and Tom Scarpas[3]

[1]NTNU, Department of Civil and Transport Engineering, Trondheim, Norway
[2] Sustainable Arctic Marine and Coastal Technology (SAMCoT), Centre for Research-based Innovation (CRI), Norwegian University of Science and Technology, Trondheim, Norway
[3]TU Delft, Department of Structural Engineering, Delft, the Netherlands

**Abstract.** A snow layer on a heated pavement largely affects the energy balance at the pavement surface. Its physical properties are not constant, but a function of the thermal properties and snow microstructure. This study looks into the change in thermal conductivity during the melting process of snow on heated pavements. The energy balance of the heated pavement system is described and the effective thermal conductivity of the melting snow layer during the melting process of snow on a heated pavement system are calculated based on pavement properties and measured temperatures and meteorological data. The results show that the effective thermal conductivity of a melting snow layer on a heated pavement can be best described a combination of a parallel and series system where ice and air are modelled as a series system and water and the combination of the ice and air system are modelled in parallel.

## 1 Introduction

A snow layer on a heated pavement largely affects the energy balance at the pavement surface and its physical properties are not constant, but a function of the thermal properties and snow microstructure. They vary greatly during the melting process.

The thermal conductivity is one of the most fundamental properties determining the rate of snow metamorphism [1]. The thermal conductivity of the snow layer seems to be mostly affected by the density and by the snow microstructure. It can vary from 0.025 W $m^{-1}K^{-1}$ to 0.56 W $m^{-1}K^{-1}$ for densities varying from 10 to 550 kg $m^{-3}$ [2].

Various methods have been developed to model the effective thermal conductivity of snow. The effective thermal conductivity is often described as a function of the density [3-6]. Most relationships are based on data retrieved from thermal conductivity measurements of various types of seasonal snow with densities up to 600 kg $m^{-3}$. The increase of density of melting snow on heated pavements differs from the density increase of snow packs. On heated pavements the snow density increases up till a value of 999.8 kg $m^{-3}$ (density of water), mostly due to changes in the moisture content, while snow in a snow pack increases in density over a longer time without necessarily the same increase in moisture content.

Alternatively the effective thermal conductivity can be modelled based on the volume fractions of ice, water and air. The ice, water and air layers can either be modelled in parallel, in series or in another configuration, such as the model by Schwerdtfeger [7] in which dense snow is modelled as ice containing air bubbles and air spaces in light snow are modelled as parallelepipeds or the SNOWPACK model [8] which is based on the work of Adams and Sato [9]. In later developed models the effective thermal conductivity is modelled based on the snow microstructure where x-rays of snow samples are used [6].

This study looks into the change in thermal conductivity during the melting process of dry uncompressed snow on heated pavements. A snow melting experiment was done to gain a better understanding of the snow melting process on heated pavements. The energy balance of the heated pavement system is described and the effective thermal conductivity of the melting snow layer during the melting process of snow on a heated pavement system is calculated based on the volume fractions of ice, water and air. The results show that the thermal conductivity of a melting snow layer on a heated pavement can be best described a combination of a parallel and series system where ice and air are modelled as a series system and water and the combination of the ice and air system are modelled in parallel.

## 2 Experimental setup and procedure

The snow melting experiment was executed in the cold laboratories at the NTNU in Norway. An experimental setup of a heated pavement system was built, representative for an asphalt road with a heated pavement system. On the bottom side of the 5cm thick asphalt plate heating films were connected to the slabs. On the top side the slabs were covered with a 4mm thick binder layer to make the structure water tight (Figure 1). To minimize heat losses insulation was placed to the side as well as under the slabs. The setup was equipped with sensors measuring the pavement (nr. 1 in Figure 1), snow (nr. 2) and air (nr. 3) temperatures, the humidity (nr. 3), incoming longwave radiation (nr. 4) and wind speed (nr. 5). Additionally the height was measured and the surface condition was registered (nr. 6).

A clouded winter night with temperatures around -5°C and low wind speed was simulated. The pavement was covered with approximately 4 cm of dry snow at the

---

[a] Corresponding author: anne.nuijten@ntnu.no

start of the experiment. For a detailed description of the experimental setup and method is referred to [10].
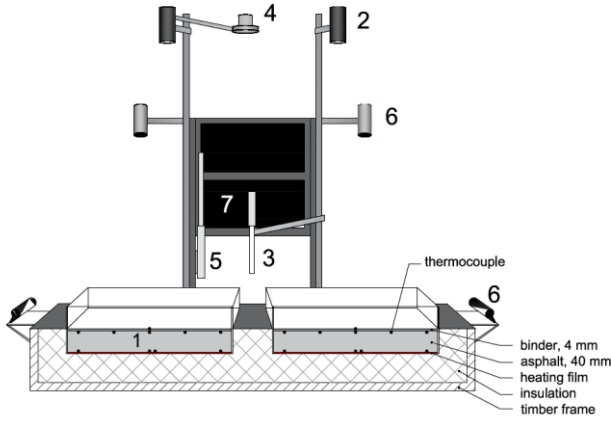


**Figure 1.** Overview of the experimental setup

# 3 Thermal conductivity model

Based on the heat balance of the snow melting system the mass fluxes of ice and water and consequently the volume fractions of ice, water and air in the snow layer are calculated. The change of the snow properties is calculated based on the volume fractions.

## 3.1 Heat balance

The heat balance of the snow melting system is described as:

$$q_m = q_h - q_s - \rho_1 c_1 \left( \frac{\partial T}{\partial t} \right)_1 z_1 - \rho_2 c_2 \left( \frac{\partial T}{\partial t} \right)_2 z_2 \\ - \rho_3 c_3 \left( \frac{\partial T}{\partial t} \right)_3 z_3 \tag{1}$$

where $q_m$ is the energy used to melt the snow (W m$^{-2}$), $q_h$ is the heat flux from the heating film (W m$^{-2}$), $q_s$ is the surface heat flux, $\rho$ is the density (kg m$^{-3}$), $c_p$ is the specific heat capacity (J kg$^{-1}$K$^{-1}$), $\partial T / \partial t$ is the rate of temperature difference (°C s$^{-1}$) and $z$ is the height of the layer (m). The subscripts 1, 2 and 3 are used to indicate the different layers from top to bottom; the surface layer (snow/water), the binder layer and the asphalt layer. The heat flux at the top of the surface layer q$_s$ is given as:

$$q_s = q_{LW} + q_{conv} + q_{evap} + q_{subl} \tag{2}$$

where q$_{LW}$ is the longwave radiation, q$_{conv}$ is the convective heat flux, q$_{evap}$ is the heat flux due to evaporation and q$_{subl}$ is the heat flux due to sublimation.

### 3.1.1   Longwave radiation

The longwave radiative heat flux $q_{LW}$ (W m$^{-2}$) can be calculated as:

$$q_{LW} = \varepsilon_s \cdot \sigma \cdot T_s^4 - \varepsilon_s \cdot \varepsilon_{eff} \cdot \sigma \cdot T_{sky}^4 \tag{3}$$

where the first term is the amount of energy that the pavement surface radiates and the second term the amount of incoming radiation. In this formula $\varepsilon_{eff}$ and $\varepsilon_s$ are the effective and surface emissivity respectively (-), $\sigma$ is the Stephan-Boltzmann constant, which is 5.68·10$^{-8}$ W·m$^{-2}$ K$^{-4}$, $T_s$ is the surface temperature (K) and $T_{sky}$ is the sky temperature (K). $\varepsilon_{eff}$ can be calculated as [11, 12]:

$$\varepsilon_{eff} = \varepsilon_{cs} \left( 1 - n_c^2 \right) + \varepsilon_{cl} n_c^2 \tag{4}$$

where $\varepsilon_{cs}$ is the clear sky emissivity (-), $\varepsilon_{cl}$ is the cloud sky emissivity (-) and $n_c$ is the cloud cover which can be taken as 1 for this experiment. Denby et al. [11] used a constant value for cloud sky emissivity, $\varepsilon_{cl}$, of 0.97, as suggested by Konzelmann et al. [12]. The values used for the emissivity coefficient used during this study are given in Table 1.

**Table 1** Emissivity coefficient for different surface conditions

| Condition | Surface emissivity $\varepsilon_s$ |
|---|---|
| Dry asphalt | 0.85 – 0.90 |
| Wet asphalt | 0.90 – 0.96 |
| Wet snow / slush | 0.90 |
| Dry snow | 0.97 |

### 3.1.2   Convection

The convective heat flux $q_{conv}$ (W m$^{-2}$) is given by (Incropera, 2013):

$$q_{conv} = h_c \cdot (T_s - T_a) \tag{5}$$

where $h_c$ is the convection heat transfer coefficient (in W m$^{-2}$ K$^{-1}$) and $T_a$ is the air temperature (°C). $h_c$ is given as:

$$h_c = \rho_a \cdot C_p / r_T \tag{6}$$

where $\rho_a$ is the atmospheric density (kg m$^{-3}$), $C_p$ is the heat capacity of dry air (J kg$^{-1}$ K$^{-1}$) and $r_T$ is the aerodynamic resistance for temperature (s m$^{-1}$).

### 3.1.3   Evaporation

The heat flux for evaporation and condensation $q_{evap/cond}$ (W m$^{-2}$) is described as:

$$q_{evap/cond} = L_v \cdot \dot{m}_{wc} \tag{7}$$

where $L_v$ is the latent heat of vaporization (J kg$^{-1}$) and $\dot{m}_{wc}$ is the mass flux of condensation and evaporation (kg m$^{-2}$ s$^{-1}$).

### 3.1.4 Sublimation

The heat flux of sublimation $q_{depo/subl}$ (W m$^{-2}$) can be calculated by:

$$q_{depo/subl} = L_i \cdot \dot{m}_{id} \qquad (8)$$

where $L_i$ is the latent heat of sublimation (J kg$^{-1}$) and $\dot{m}_{id}$ is the deposition and sublimation flux (kg m$^{-2}$ s$^{-1}$).

### 3.2 Mass fluxes

The mass flux of water $\dot{m}_w$ (kg m$^{-2}$ s$^{-1}$) is determined by adding the flux of condensation and evaporation $\dot{m}_{wc}$ and the mass flux of melting $\dot{m}_m$ (kg m$^{-2}$ s$^{-1}$):

$$\dot{m}_w = \dot{m}_{wc} + \dot{m}_m \qquad (9)$$

$\dot{m}_{wc}$ is given by [11]:

$$\dot{m}_{wc} = \rho_a \cdot (q_a - q_s) / r_q \qquad (10)$$

where $\rho_a$ is the density of the air (kg m$^{-3}$), $r_q$ is the aerodynamic resistance for water vapour (s m$^{-1}$) and $q_a$ and $q_s$ are the atmospheric and surface specific humidity respectively. $\dot{m}_m$ is given by:

$$\dot{m}_m = \frac{q_m}{L_f} \qquad (11)$$

where $L_f$ is the latent heat of fusion.

The mass flux of ice is determined by subtracting the mass flux of melting and freezing $\dot{m}_m$ (kg m$^{-2}$ s$^{-1}$) from the deposition and sublimation flux $\dot{m}_{id}$ (kg m$^{-2}$ s$^{-1}$):

$$\dot{m}_i = \dot{m}_{id} - \dot{m}_m \qquad (12)$$

where $\dot{m}_{id}$ is calculated according to equation (11).

### 3.3 Volume fractions

Based on the densities and mass fluxes of snow, water and air and the height of the surface layer the volume fractions of ice, water and air are calculated as follows:

$$1 = \theta_i + \theta_w + \theta_a \qquad (13)$$

where $\theta i$, $\theta w$ and $\theta a$ are the volume fractions of ice, water and air. $\theta i$ and $\theta w$ are given as:

$$\theta_i = \frac{M_i \cdot \rho_1}{M_s \cdot \rho_i} \qquad (14)$$

$$\theta_w = \frac{M_w \cdot \rho_1}{M_s \cdot \rho_w} \qquad (15)$$

where $M_i$, $M_w$ and $M_s$, are the mass of ice, water and the surface layer, $\rho_1$ is the density of the surface layer and $\rho_i$, $\rho_w$ and $\rho_a$ are the density of ice, water and air.

### 3.4 Snow properties

The specific heat capacity of the surface layer $c_1$ can be calculated as follows [13]:

$$c_1 = \frac{1}{\rho_1} \left( \rho_i \cdot c_i \cdot \theta_i + \rho_w \cdot c_w \cdot \theta_w + \rho_a \cdot c_a \cdot \theta_a \right) \qquad (16)$$

where $c_i$, $c_w$ and $c_a$ are the specific heat capacities of ice, water and air.

The thermal conductivity of the surface layer is calculated based on the volume fractions and the thermal conductivity of ice, water and air in the following ways:
As a parallel system:

$$\lambda_1 = \lambda_i \cdot \theta_i + \lambda_w \cdot \theta_w + \lambda_a \cdot \theta_a \qquad (17)$$

As a series system:

$$\lambda_1 = \frac{1}{\left( \dfrac{\theta_i}{\lambda_i} + \dfrac{\theta_w}{\lambda_w} + \dfrac{\theta_a}{\lambda_a} \right)} \qquad (18)$$

Additionally a combination of a parallel and series system is proposed in which ice and air are modelled as a series system and water and ice/air in parallel:

$$\lambda_1 = \frac{\theta_i + \theta_a}{\left( \dfrac{\theta_i}{\lambda_i} + \dfrac{\theta_a}{\lambda_a} \right)} + \lambda_w \cdot \theta_w \qquad (19)$$

An explicit finite difference method is used to solve the equations and to calculate the heat and mass fluxes and snow properties.

## 4 Input parameters

Input parameters for the model not yet described in section 2 are the pavement properties and the height of the surface layer as was measured during the test.

### 4.1 Pavement properties

The density of the asphalt and binder layer is taken as 2100 kg m$^{-3}$ [14] and the specific heat capacity is taken as 0.92 kJ kg$^{-1}$ °C$^{-1}$.

## 4.2 Height and density of the surface layer

Figure 2 shows the height profiles of the snow layer found during the tests and the change of the surface condition as was visible from the top. The same trend is visible for all tests; during the first 40 minutes the height did not change much. After an hour the height started to decrease linearly till it reached a height of 4-5 mm after which it stayed more of less constant. This decrease happened when the snow changed from dry snow into slush.
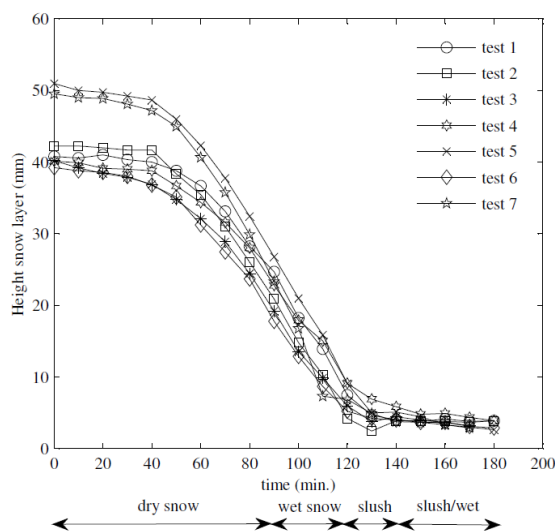


**Figure 2.** Change in height of the snow layer

Figure 3 shows the average change in density of one of the tests (continuous thin line) and the average density including the measuring error of 1 mm (dotted line). The density is calculated by dividing the weight of the snow on the plate by the volume.

The calculated average density at the end of the test was 800 kg m$^{-3}$. Since at the end of the test all snow was melted and only melt water was left the actual density was 999.8 kg m$^{-3}$. Towards the end of the experiment the formula for calculating the density becomes very sensitive for small changes in the height. The height of the surface layer at the end of the experiment is 3-4 mm and the accuracy of the measuring method was around 1 mm. To increase the accuracy of the input data, the value at the end of the density curve is replaced with the value
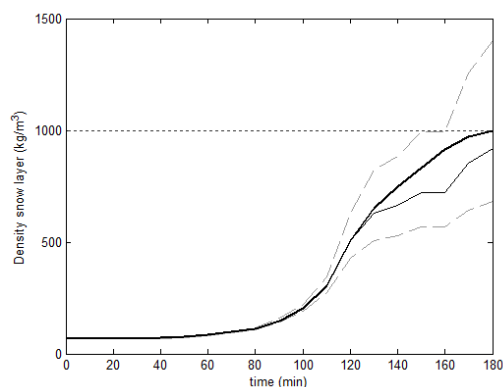


**Figure 3.** Average change in density of the surface layer during one of the tests (continuous thin line), average +/- measuring error (dotted line) and an adjusted curve which ends at the density of water (continuous thick line)

for the density of water (999.8 kg m$^{-3}$) and the curve is fitted for the last part of the test. The adjusted curve used for the model is shown as a continuous thick line in Figure 3.

## 5  Results

### 5.1 Volume fractions

The volume fractions are the main input parameters for the effective thermal conductivity. The accuracy of the results depends on the accuracy of the input parameters, e.g. the accuracy of the meteorological data, temperatures, the pavement properties, the height and density of the snow layer and possible heat losses near the heating film.

A sensitivity study is done to look into the effect of the following parameters on the volume fractions and melting time: 1) the height of the snow layer (which also affects the density), 2) the surface heat flux ($q_s$), 3) the pavement heat flux ($q_p$), 4) the heat from the heating film ($q_h$).

Table 2 shows the results of the sensitivity analysis. The model originally predicts that all ice is melted after 101 minutes while as can be seen in Figure 2 the surface condition consists at that moment of wet snow. Changing the height of the snow layer with 1 mm (the measuring error) and changing the density accordingly does not seem to have an effect on the melting time. A change in the surface heat flux of 20% does not seem to affect the melting time either. An increase in the pavement flux by 20% or a decrease of 20% of the heat generated by the heating film, e.g. due to heat losses, increases the melting time with respectively 5 and 17 minutes. Figure 4 shows the range of volume fractions of ice, water and air during the melting process and the effect of the accuracy of the pavement and heating film flux on the accuracy of the results. By combining an increase in the pavement flux and a decrease in the amount of heat coming from the heating film the melting time is increased till 126 minutes which is the transition phase from wet snow into slush.
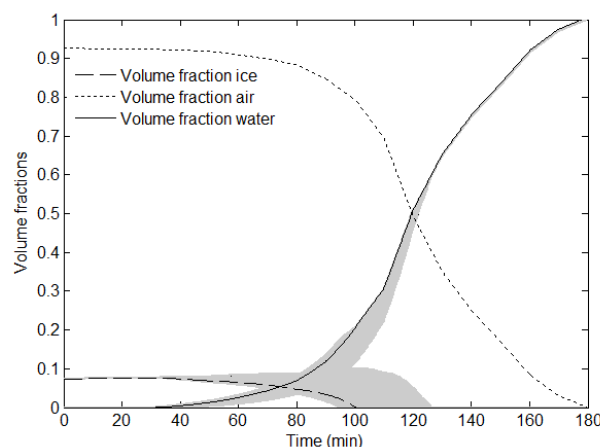


**Figure 4.** Change of the volume fractions of ice, water and ice during the melting process, based on the values used in the sensitivity analysis. The inaccuracy of the results based on the sensitivity analysis done is marked in grey.

**Table 2** Effect of the accuracy of various input parameters on the melting time

| height snow layer | | | surface flux | | pavement flux | | heating film | | melting time (min) |
|---|---|---|---|---|---|---|---|---|---|
| -1 mm | mean | + 1 mm | 0.8 qs | qs | qp | 1.2 qp | 0.80 qh | qh | |
| | x | | | x | x | | | x | 101 |
| x | | | | x | x | | | x | 101 |
| | | x | | x | x | | | x | 101 |
| x | | | x | | x | | | x | 101 |
| x | | | | x | | x | | x | 106 |
| x | | | | x | x | | x | | 118 |

## 5.2 Thermal conductivity

Figure 5 shows the change in effective thermal conductivity during the melting process of dry uncompressed snow on a heated pavement. The effective thermal conductivity is calculated with a parallel system, a series system and a combined parallel/series system. The effective thermal conductivity formulas which are based on the volume fractions are compared to the formulas based on the density by Yen [3], Sturm et al. [4] and Calonne et al. [6] which were developed for snow with density values up till 600 kg m$^{-3}$.

The series and the combined parallel/series system start around the same values as the curves by Yen [3], Sturm et al. [4] and Calonne et al. [6]. Only the parallel system starts at a higher value.

At the end of the test the effective thermal conductivity of the surface layer goes towards the thermal conductivity of water for the parallel and series systems.

The formulas by Yen [3], Sturm et al. [4] and Calonne et al. [6] give much higher values towards the end of the test. Those formulas are based on measurements on seasonal snow from a snow pack with densities up to 600 kg m$^{-3}$ where the snow density often increases due to settling and to a lesser extent due to an increase in moisture content.

Figure 6 shows the effect of the accuracy of various input parameters on the accuracy of the modelled effective thermal conductivity. Height measurements have an effect on the accuracy of the modelled effective thermal conductivity, especially towards the end of the test when the snow has changed into slush. The accuracy of the pavement flux and the accuracy of the heat from the heating film affect the accuracy of the result for the parallel system during the change from dry snow to slush. It slightly affects the accuracy of the modelled effective thermal conductivity with the combined parallel/series system.
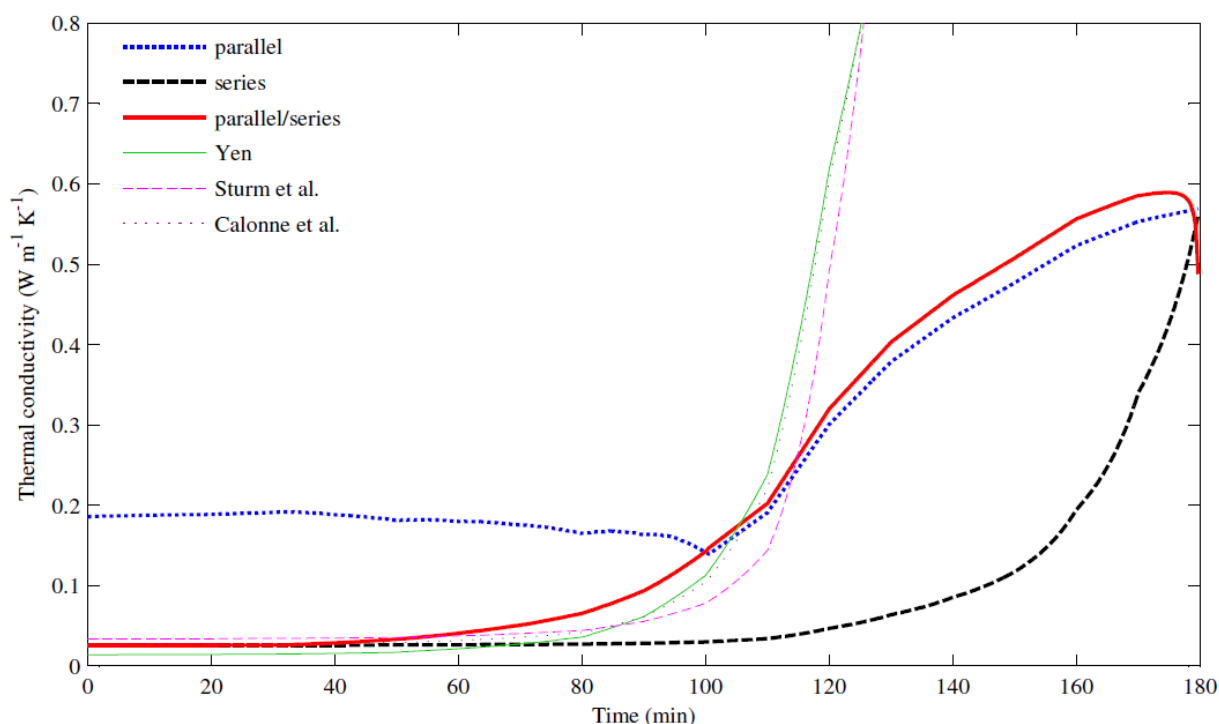


**Figure 5.** Effective thermal conductivity during the melting process of dry uncompressed snow calculated based on the volume fractions of ice, water and ice with a parallel system, a series system and a combined parallel/series system and compared to the curves by Yen [3], Sturm et al. [4] and Calonne et al. [6]

a)



b)



c)
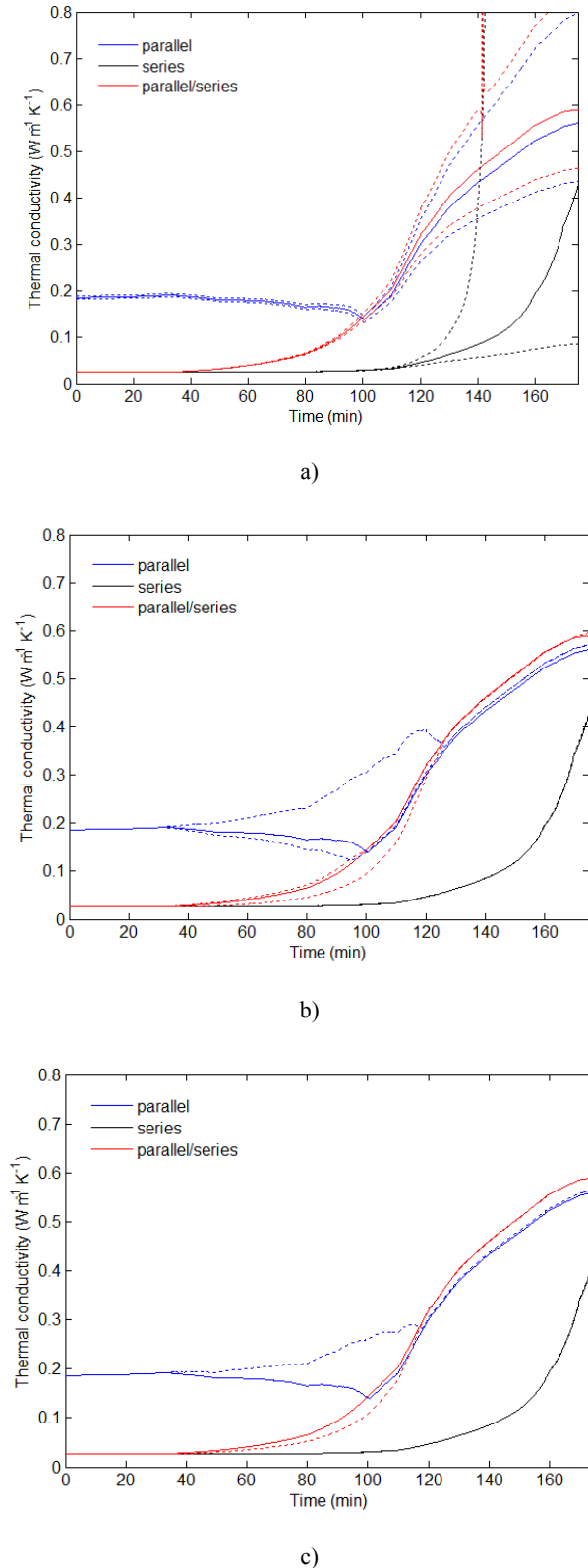
**Figure 6.** The effect of a) the accuracy of the height measurements, b) the accuracy of the heat flux from the heating film and c) the accuracy of the pavement heat flux on the modelled effective thermal conductivity during the melting process of dry uncompressed snow, where the mean value is presented as a continuous line and the effect of the various input parameters with dotted lines.

## 6 Discussion

During the first 40 minutes the snow has not started to melt and the surface condition consisted of dry snow. During this period the predicted thermal conductivity based on the volume fractions should give comparable results compared to the curves by Yen [3], Sturm et al. [4] and Calonne et al. [6]. The series and the combined parallel/series system correspond well with these curves.

After 90-120 minutes the snow is wet. Since in the curve of Calonne et al. [6] melt forms are included with densities around 500 kg m$^{-3}$ it is expected that the formulas based on the volume fractions should approach this curve for wet snow values. The parallel and a combined parallel/series correspond better to this data than the series system. The series system gives a very low thermal conductivity at the end of the test while during that period the snow has transformed into slush and thermal conductivity values around that of water are expected.

The model predicts a faster snow melt than is observed during the experiment. The two main parameters affecting this prediction are the heating film heat flux and the pavement heat flux. In the model no heat losses are included, while these are expected to occur. Including these fluxes seem to have a positive effect on the results. The pavement flux depends largely on the thermal properties of the pavement which are estimated based on literature. Using measured properties would improve the accuracy of the results.

The accuracy of the height measurements and the accuracy of the surface flux barely affect the calculated melting time. The height measurements do however affect the results of the prediction of the volume fractions and effective thermal conductivity (Figure 6 a). Towards the end of the test, when the surface layer becomes very thin, the density is more difficult to estimate based on the height measurements, as can be seen in Figure 3. During this last part of the test the effect of the height measurements on the accuracy of the effective thermal conductivity prediction becomes larger.

## 7 Conclusion

The effective thermal conductivity of a melting snow layer on a heated pavement can be best described a combination of a parallel and series system, based on the volume fractions and the thermal conductivity of ice, water and air. In the proposed combined parallel and series system ice and air are modelled as a series system and water and ice/air are modelled in parallel.

## Acknowledgements

# References

1. F. Riche, M. Schneebeli, Thermal conductivity of snow measured by three independent methods and anisotropy considerations, The Cryosphere, **7**, 217-227 (2013)

2. J. Cote, M. Rahimi, J.-M. Konrad. Thermal conductivity of compacted snow, *Proceedings of the 15th International Specialty Conference on Cold Regions Engineering* (2012)

3. Y.C. Yen, Review of the thermal properties of snow, ice and sea ice, *Cold Reg. Res. and Eng. Lab.* (1981)

4. M. Sturm, J. Holmgren, M. König, K. Morris, The thermal conductivity of seasonal snow, J. Glaciol., **43**, 26-41 (1997)

5. R.K. Aggarwal, P.S. Negi, P.K. Satyawali, New density-based thermal conductivity equations for snow, Defence Sci. J., **59**, 126-130 (2009)

6. N. Calonne, F. Flin, S. Morin, B. Lesaffre, S. Rolland du Roscoat, C. Geingreau, Numerical and experimental investigations of the effective thermal conductivity of snow. Geophys. Res. Lett., **38** (2011)

7. P. Schwerdtfeger, Theoretical derivation of the thermal conductivity and diffusivity of snow *(*1963)

8. M. Lehning, P. Bartelt, B. Brown, C. Fierz, P. Satyawali, A physical SNOWPACK model for the Swiss avalanche warning, Part II. Snow microstructure. Cold Reg. Sci. Technol., **35**, 147-167 (2002)

9. E.E. Adams, A. Sato, Model for Effective Thermal Conductivity of a Dry Snow Cover Composed of Uniform Ice Spheres. Ann. Glaciol., **18,** 300-304 (1993)

10. A.D.W. Nuijten, K.V. Høyland, Comparison of melting processes of dry uncompressed and compressed snow on heated pavements (manuscript submitted for publication)

11. B.R. Denby, I. Sundvor, C. Johansson, L. Pirjola, M. Ketzel, M. Norman, K. Kupiainen, M. Gustafsson, G. Blomqvist, M. Kauhaniemi, G. Omstedt, A coupled road dust and surface moisture model to predict non-exhaust road traffic induced particle emissions (NORTRIP). Part 2: Surface moisture and salt impact modelling, Atmos. Environ., **81**, 485-503 (2013)

12. T. Konzelmann, R.S.W. van de Wal, W. Greuell, R. Bintanja, E.A.C. Henneken, A. Abe- Ouchi, Parameterization of global and longwave incoming radiation for the Greenland ice sheet, Global Planet. Change, **9,** 143-164 (1994)

13. P. Bartelt, M. Lehning, A physical SNOWPACK model for the Swiss avalanche warning, Part I: numerical model. Cold Reg. Sci. Technol., **35,** 123-145 (2002)

14. O.B. Andersland, B. Ladanyi, *Frozen Ground Engineering*, John Wiley & Sons, Inc, New York (2004)

# Snow engineering questions related to road and rail vehicles

Jean-Paul Bouchet[a], Sylvain Aguinaga, Pierre Palier and Philippe Delpech

*Centre Scientifique et Technique du Bâtiment (CSTB), CAPE Department, 11 rue Henri-Picherit 44300 Nantes, France*

**Abstract.** Snow falls induce many constraints on road and rail vehicles as well as helicopters. A selection of questions from snow engineering is presented in the paper. The experimental method that was undertaken to investigate these questions makes use of a large climatic wind tunnel, partly designed to address snow engineering problems at full scale: snow ingress in engine compartments, into ventilation systems of vehicles and snow or ice accretions on vehicles bodies.

## 1 Introduction

Snow may interact in different ways with transport systems and can induce many dysfunctions to vehicles and infrastructures exposed to atmospheric conditions. The multiform nature of snow, the deposition process and the mechanical and thermal properties of snow, bring potential problems which, in some cases, may have tragic consequences both for equipment and unfortunately users.

Beyond local mechanical constraints induced by snow accumulations and accretions, the accidental risk is increased if the accumulations occur on fast moving vehicles with possible detachments of these snow accretions due to temperature raise, vibrations or relative air velocity.

To reproduce and understand the interaction phenomena as they are observed in nature, it is valuable to implement an experimental approach that allows control of the main climatic parameters as air temperature, wind velocity, concentration of snow/ice particles and the liquid water ratio (LWR). These possibilities are offered by large climatic wind tunnels where it is possible to reproduce the phenomena at full scale or moderately reduced scale.

## 2 Snow simulation in the Jules Verne climatic wind tunnel (CWT)

The thermal circuit of Jules Verne climatic wind tunnel (Figure 1), with artificial snow making capabilities, can reproduce various kinds of snowstorm events. Wind velocity, ambient air temperature and air/water ratio in the installed snow guns are fully controllable to determine the snow properties (dry or wet snow). The appropriate thermodynamic conditions (air temperature and humidity) can be controlled by two heat exchangers (cold and warm) across the section of the wind tunnel.

The large dimension of the test chamber, 25 m long, 10 m wide and 7 m high, enables simulation of mechanisms of snow/vehicle interaction at full scale.

Snow guns (high pressure air and water technology) can be fitted in any location in the test section. They are used to generate a freezing water spray (Figure 2). The typical grain flake diameters produced by the snow guns in the wind tunnel range from 0.150 to 0.450mm (Figure 3).



**Figure 1.** The thermal circuit of the Jules Verne CWT



**Figure 2.** Snow guns in operation in the thermal circuit of the Jules Verne CWT
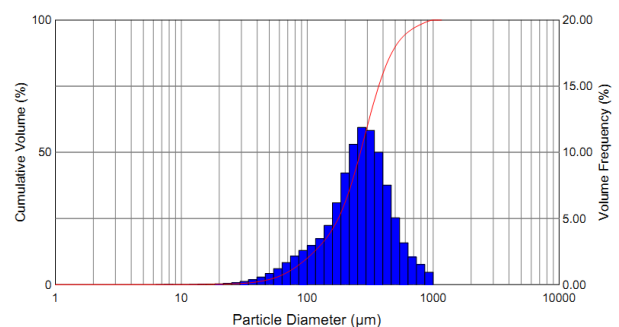


**Figure 3.** Particles diameter distribution (Malvern Spraytec)

The air temperature, and air/water ratio in the snow guns, can be set to control the LWR of snow which determines the quality of the snow from dry to wet snow. LWR of the deposited snow is measured by using either a

---

[a] Corresponding author: jean-paul.bouchet@cstb.fr

calorimeter [1, 2] or by measuring the dielectric property of wet snow [3].

The measurement of the air flow snow concentration is conventionally measured by net collectors of snow on the duration of the test (Figure 4). The collected mass of snow can be converted into concentration ($g/m^3$) knowing the wind velocity, the diameter of the snow collector and sampling time.



**Figure 4.** Measurement of the snow concentration in the airflow by net snow collectors

Comparisons were made with an isokinetic sensor wherein the air input speed is controlled to be equal to the wind speed in order to avoid snow particles bypass effects due to aerodynamic forces.

For example in the case of vehicle rolling simulation at 80km/h with one snow gun in operation, the concentrations measured on the side of the vehicle by isokinetic sampling or by net collectors are close to $4.5 g/m^3$ ( +/- $0.5 g/m^3$).

# 3 Snow ingress in the engine compartment and air intake of HVAC of vehicles

Snow ingress and accumulation under the bonnet of road vehicles and in particular into the air intake of engines can cause severe damages. Amongst the most critical conditions for road vehicles, let us mention the follow-up configuration where a vehicle follows one or several other vehicles (Figure 7). The snow falling is added to the snow picked-up by vehicles ahead made of fine particles. When combined to cold atmospheric conditions the ingress capacity of the fine and dry particles is high and can impact several systems as engine air intake and cabin HVAC system. The main induced problems could be engine dysfunctions (power loss) due to snow accumulation on the air filter or in its supply duct (air supply deficit) or severe damage to the HVAC fan due to the water ingress into the air circuit (melting of the snow collected on the cabin air filter, Figure 5).
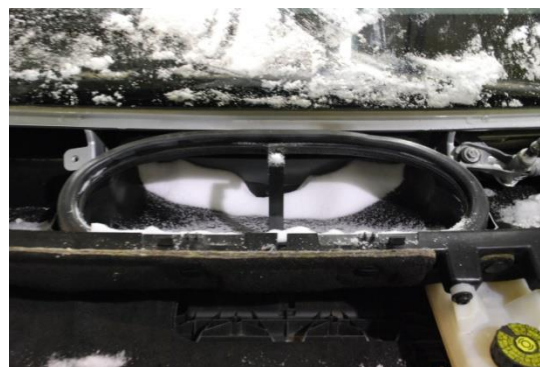


**Figure 5**. Dry snow ingress in the HVAC air intake of a road vehicle

When the weather is warmer and Liquid Water Ratio of the snow is higher (wet snow), these driving conditions (follow-up of vehicles) can generate significant accumulations of snow on the front face of the car. This is also the case when the roads are treated with snow melting additives (salt). The problems induced by with these conditions are: snow accretion on vehicle lights (safety issue), blockage of the radiator fans and blockage of motorized air intake panels etc. (Figure 6).



**Figure 6**. Wet snow accretion on the front panel of a road vehicle

Similar situations are experienced by helicopters that can be maintained in stationary flight over snow covered ground. In this case, it is important to locate and assess the quantity of snow that accumulates in the heated air intake channel of the turbine engines. The risk is to observe a local snow accumulation that could be released in large blocks and damage the turbine. The remedial strategy involves fitting of heating mats inside the air intake which efficiency needs to be assessed according standard procedures.
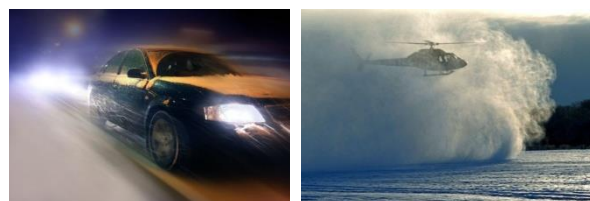


**Figure 7**. Operation of vehicles in snow conditions

For driving snow tests, the wind tunnel is operated in a way, which enables the assessment of the air filter efficiency in severe conditions. Since the making of snow

is made while the wind is blowing at the appropriate test velocity, the location of the snow gun behind the test vehicle allow the freezing particles to go all along the wind tunnel circuit before reaching the model. This trajectory is long enough to freeze the water droplets producing dry snow (Figures 8 and 9).
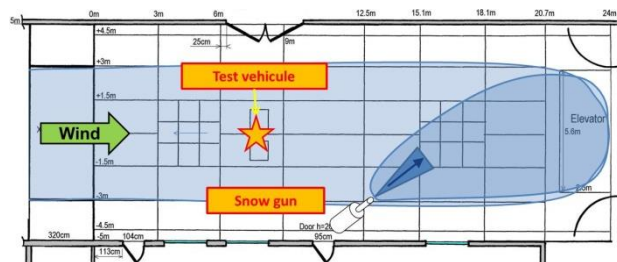


**Figure 8** – Top view of the thermal unit test section, experimental setup for dry snow tests

The experimental set-up enables the operation of the vehicle, engine on, fitted on a roll chassis dynamometer that simulates the resistant force (aerodynamic drag and rolling resistance).



**Figure 9**. Snow test of vehicles in the wind tunnel

The test in snow storm conditions is carried for a significant duration or driving distance or until an observed breakdown. Sensitivity to high snow concentration in the air is assessed by weighing the snow collected in the air filters or others observations as snow accumulation in the electronic or cooling devices (Figure 10). In parallel measurements of pressure drop increase across the air filter are made.



**Figure 10**. Snow ingress under the bonnet of a road vehicle at the end of a wind tunnel test

## 4 Braking and wiper blocking by snow

Apart of these snow accumulations under the bonnet, other types of deposition may occur on moving or stationary vehicles. One can mention:
- Snow deposition on the back of vehicle (due to turbulent drag flows) that may induce visibility problems of the rear lights,
- Accumulations on the roof of parked vehicles with sliding risk towards the windshield in case of sudden braking, which can lead to breakage of the wiper systems,
- Accumulations on A pillars or windshield base due to wipers operation under wet snow storm resulting in malfunction or blockage of these wiping mechanisms.

Similarly, the heat from engine components leads to snow melting at hot spots with possible re-icing at cold spots. This can be found on clutch components and more dangerously on the brake calipers by snow accumulation on the inside of the wheel rims. This aspect has been studied in the Climatic Wind tunnel Jules Verne and correlation test campaigns have been carried out between observations in proving ground (Kiruna site in Sweden) and in wind tunnel (Figures 11 and 12).



**Figure 11**. Snow braking test on a frozen lake in Kiruna
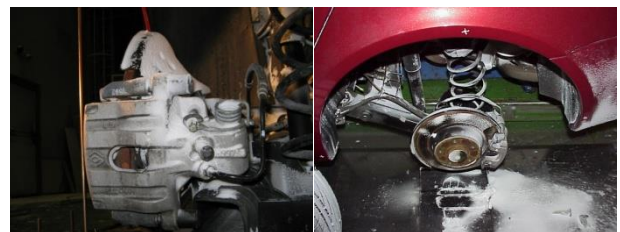


**Figure 12**. Snow braking test in wind tunnel

As achieved on real outdoor conditions on test site similar to Kiruna, tyre adherence tests can be undertaken in the wind tunnel. For this purpose, one needs to reproduce a homogeneous stratified and compacted snow layer in the entire test section, similar to the one observed on the snowy roads (Figure 13). This is made by a succession of snow making and compacting steps.

**Figure 13**. Tyre adherence tests on a stratified and compacted road snow layer in the wind tunnel

# 5 Wet snow accretions on high speed trains bodies

To maintain the development of the high-speed train traffic, railway operators have to face extreme conditions, in particular during winters, with impacts on both infrastructure and rolling stock, and associated maintenance. Usual major consequences of snowfalls are both on traffic regulation with cruising speed reductions and on rolling stock with severe damages (underbody structure, windows) due to ice and snow accretions and shedding, leading for instance to ice-drop ballast projection.

In order to minimize the impacts of winter conditions on high-speed trains, wind tunnel experiments were undertaken as a part a research program conducted by the French railway company SNCF. The aim was to explore solutions to reduce the snow accumulation on trains. The first part of the study was dedicated to collect data and to identify the mechanism of snow accumulation by performing tests in a climatic wind tunnel.

Most of the tests were performed with one snow gun located on the central axis of the test section (Figure 14). The snow gun was set up in a counter-current configuration to enhance the spatial uniformity of particle concentration in the air flow. This configuration also ensures that particles are carried out to the test structure in equilibrium with the air flow.
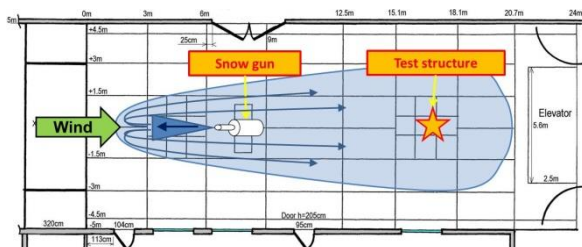


**Figure 14** – Top view of the thermal unit test section, experimental setup for the snow tests

Generic simple-shaped prisms and a railway shape geometry at 1/2 reduced scale were used. The obtained results consist in snow and ice growths and localizations, with the influence of different parameters, with particular attention to the wind speed, air flow temperature, characteristics of snow particles (LWR and snow concentration) and their behavior on various angles of impact.

Two superimposed planes were used to support the prisms outside the boundary layer of the wind tunnel air flow. The prims were located underneath the supporting planes to include the impact of the horizontal plane on the accretion phenomena to the vertical surfaces of the prisms in the simulation. This arrangement intended to mimic the volume locations under a TGV floor (Figure 15).
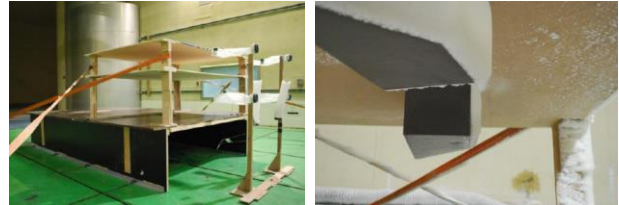


**Figure 15:** Experimental set-up supporting the simple-shaped prisms in the wind tunnel test section (the wind comes from the right of the picture)

The snow concentration was derived from the collected snow mass regarding the collection area, the local wind velocity and the test duration.

The prisms have been designed to explore various inclination angles of the walls, two sizes, from 0 to 90°, in respect with the main flow. The measurement of the mass of snow captured by each face, during a run, allowed to get a table of mass flux expressed in kg/m²-s depending on the faces area and the duration of the run.

The second part consisted in reproducing these mechanisms by numerical simulations which methodology has been validated by comparing computational results to measurements on both the prisms and the railway mock-up [3].

In order to supplement the prism measurements with results on a more realistic train geometry, a railway vehicle model at 1/2 reduced scale was designed. The model simulates two parts of a TGV body including the connection between two railroad cars (Figure 16). The overall train model was 8m long. A bluff body shape upstream the bogie was designed in order to model the aerodynamic influence of the front part of the train.
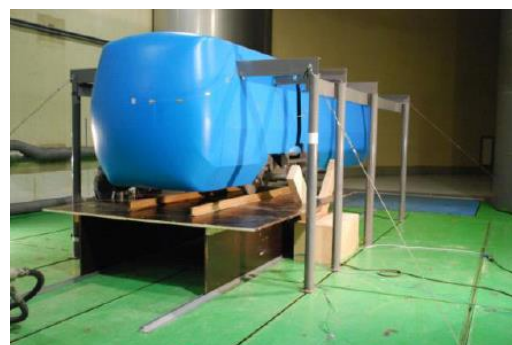


**Figure 16**: TGV model set-up in the climatic wind tunnel (the box on the side of the model shelters the belt drive system for the rotation of the wheels).

An entire boogie was reproduced. The boogie model was simplified compared to a real one, but the main elements which may collect snow were reproduced, including the brake system (Figure 17).



**Figure 17**: TGV bogie model including anti-roll bar and the bogie-car drive system

In order to reproduce the air flow underneath the train body, the model was suspended. An additional floor simulating the track was fitted 70cm above the wind tunnel floor. The height of the floor was intended to maintain the area of interest outside the boundary layer of the wind tunnel. The rotation of the wheels was simulated by a belt drive system and an electric engine located on the side of the model.

At the end of each test period, the measurements of accumulated snow were made and photographs were taken at predefined locations and angles of view (Figure 18). The snow accumulated on specific spots was collected and weighed.



**Figure 18**: Snow accumulation in the bogie cavity (wind tunnel model and real TGV train)

A CFD methodology has been developed concurrently with wind tunnel experiments [3]. The measurements made on the prismatic bodies with various sizes and shapes allowed fast and precise tuning with the exploration of a large panel of parameters. The resulting simulation chain has been deployed on the more complex geometry, reproducing the TGV car details, and the workflow has been enriched with the mesh growing, in respect with the snow accretion rate obtained, and the associated volume of snow calculated.

# 6 Experimental and numerical modeling of snow accretion

There is no doubt about the usefulness of a model able to realistically assess the accretion of snow and ice on vehicle components.

The implementation of this type of modeling requires knowledge of climate constraints. In addition the simulation must be tuned to include the effect of the body shapes and the incident direction of the flow on the elementary surfaces of the structure for computing the accretion mass. From this point of view, wind tunnel experiments with a cylindrical shape allow the analysis of accretion over a wide range of angle of impact.

The analysis must be complemented by a criterion that includes the sticking capacity of the freezing particles at time of impact to make the model truly operational.

Such a modelling is possible if one can assess the LWR of the snow at the impact time. Recent works have shown the primary effect of the LWR of snow on the snow accretion mass and volume [5]. The experimental approach was based on the assessment of wet snow accretion formation on simple geometric shapes. Cylinders were placed in the snow particle flow produced in the climatic wind tunnel. If all other parameters were kept constant, the ambient temperature setting (from -10°C to -2°C) allows to modify the thermodynamic state of the snow particle at time of impact. It is then possible to assess the effect of the liquid water ratio on the accretions and perform a parametric study.

A numerical model for two-phase flows simulation has also been developed in parallel. The study conducted, has been setup mainly to identify the most important parameters that drive the accretion phenomenon (Figure 19).

The results obtained with -10°C and -2°C experimental tests provided the limiting cases of the study as being the conditions were the accretion was either very thin and could not be weighted or too humid and could no longer be considered as actual snow.
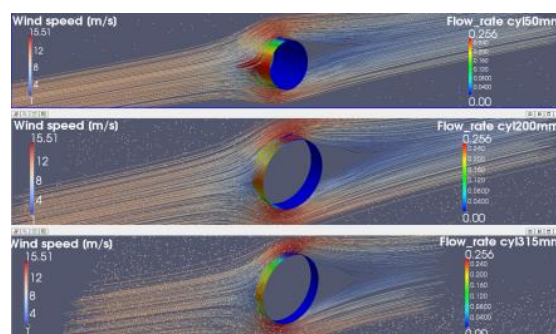




**Figure 19.** Experimental and numerical modeling of wet snow impact and accretion cylinders of various diameters (diam. 50, 200 and 315mm)

With the three intermediate ambient temperatures, 6°C, -5°C, -4°C, one can observe the evolution of the accretion sizes to the structures (Figure 20).
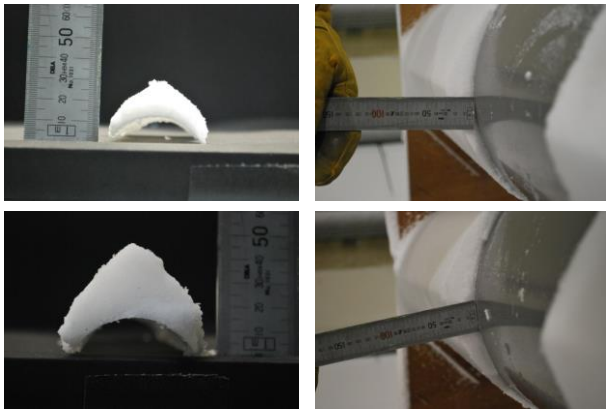
**Figure 20**: Examples of wet-snow accretion (ambient temperature -6°C top and -4°C bottom, left: from a 50mm cylinder, right : from a 315mm cylinder)

The comprehension of the parameters which govern wet snow accretion, leads to the possibility to undertake a numerical study to characterize the different accretions by using a so called "stick-function" for wet snow particles. The study will also aim at producing an experimental database of climatic wind tunnel icing simulations for comparisons with outdoor real-scale phenomena.

The criterion implemented in the numerical modeling of accretion takes into account the angle between the particle path at the impact with the surface and the normal to the surface, i.e. if this angle $\alpha_{imp}$ is lower than a threshold angle $\alpha_t$ the particle sticks to the surface. The approach has simulated accretion shapes showing fair similarities with the experimental. However it fails to predict accretion on the upper and lower part of the cylinder. This might lead to a more comprehensive model to take into account the particle energy, the LWR and the angle of impact that have been identified as the crucial aspects involved in wet snow accretion process (Figure 21).
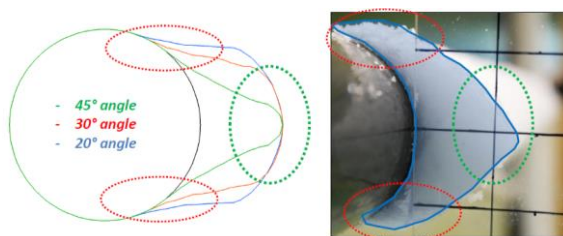


**Figure 21**: Comparison of accretion shapes obtained by numerical modelling with experimental results, analysis of the upper and lower part of a cylinder $d_{cyl} = 50mm$: (a) numerical simulation $\alpha_t = 20°, 30°$ and $45°$ (b) experimental result,

# 6 Perspectives

Due to the diversity of situations, i.e. snow ingress or accretion and accumulation in vehicles, there is not a unique approach to investigate these situations and assess the measures to alleviate the risks. But in all cases the use of experimental facilities that provide controlled ambiances and snow making capacities is valuable.

The climatic wind tunnel provides the controlled ambient environment which allows isolating influencing variables and analyses the causes of phenomena. Nevertheless, a wind tunnel remains a simulating situation of natural environment. From this point of view natural field experiments are useful to validate lab simulations. Although the wide range of potentialities of climatic wind tunnels, many conditions remain absent from material and financial possibilities. In some cases, numerical modelling can supplement the experiments in wind tunnels. A parallel approach, experimental and experimental field tests, seems the most productive way since it enables to avoid the pitfalls of each method. It seems this should be the way to favour in the future.

Common to all of the examples given in this paper is that no absolute solution has been proposed. The presented results provided the basis of analysis for future developments. The main benefit of the experimental work, and that seems crucial, is the ability to predict the severity of the observed phenomena. This is an essential first step whatever are the corrective actions further considered, improvement of design or preventing measures.

An interesting protecting strategy is provided by ice-phobic coatings. If these kinds of coating do not yet fully prevent ice and snow deposition, they greatly reduce the adhesion. Hence, the mechanical movements of the iced structures enable the fall of the accretion. Similarly, during the melting phase, the protective coatings allow to reduce the icing cover more quickly.

With regard to the snow ingress in the engine compartment and air intake of HVAC of vehicles, optimization of air inlets is needed. Similarly, reducing the risk of snow accretion on vehicles may be due to a better design of heating de-icing system and shape optimization. But in any case, it is not certain that this eliminates the problem permanently.

# Acknowledgments

# References

1. Boisson-Kouznetzoff S., Palier P., Caractérisation de la neige produite en souflerie climatique, *Int. J. of Refrigeration* 24, 302-324, (2001)
2. Boyne H.S., Fisk D.J., A Laboratory comparison of field technique for measurement of liquid fraction of snow. CRREL Spec. Rep 90.3, (1990)
3. Denoth A. Snow dielectric measurements, Adv. Space Res. Vol 9, No1, pp 233-243, (1989)
4. Allain E., Paradot N., Ribourg m. Delpech P., Bouchet JP., De la Casa X., Pauline J. Experimental and numerical study of snow accumulation on high speed trains. Proceedings of the 49th International Symposium on Applied Aerodynamics, Lille, France, 2014
5. Vigano A. Experimental and Numerical modelling of wet snow accretion on structures. PhD thesis, France, 2012.

# Anti- and de-icing of walking and cycle paths – Field trials of new follow-up techniques for quantifying salt amount and resulting ice quality

Göran Blomqvist[a], Bengt Lindström, Ida Järlskog, Emelie Karlsson and Anna Niska

*Swedish National Road and Transport Research Institute (VTI), SE-581 95 Linköping, Sweden*

**Abstract.** New follow-up methods for evaluating winter maintenance of walking and cycle paths have been developed and tested. The effects of different anti- and de-icing methods, salt qualities and doses as well as the processes behind salt loss are fairly well known after decades of studies on runways, highways and roads. Those relationships are, however, not valid on walking and cycle paths, since these lacks the action of high speed car tyres on the road surface. Therefore methods for quantifying the amount of residual salt on walking and cycle path surfaces before a weather event and the resulting quality of the frost or ice after the event would be a good help in order to enable follow-up of anti-icing actions taken. By manually dissolving the salt within a confined area of the pathway and measure the electric conductivity of the liquid, the salt dose on the pavement may be established and by inflicting a mechanical angular impact on the ice surface after the weather event, the quality of the ice may be established. Knowledge of the salt dose and the resulting ice quality then enables the road keeper to evaluate the efficiency of the winter maintenance actions taken.

## 1 Need for follow-up methods

There is a rapid development of methods for winter operation of pedestrian and bicycle paths. Many Swedish cities are committed to transferring car trips to cycling even in winter, which places great demands on achieving satisfactory friction for cyclists. Eight out of ten bicycle accidents are single vehicle accidents and among these, the most common cause is slipperiness caused by ice, snow or remaining gritting sand. Therefore most of the new methods developed are gritting free, usually combining a rotating brush with salting equipment for brine or pre-wetted salt, so-called sweep salting [1, 2].

The city road keepers and their contractors, however, often lack possibilities to effectively evaluate the efficiency of the actions taken, since:
• Existing knowledge and evaluation methods are taken from the highway and airport experiences and therefore need to be downscaled to walking and cycle paths,
• There can be a big difference between the pedestrian and bicycle sections within the same walking/cycle path,
• Standard friction measurements does not represent the forces that a cyclist or pedestrian is exposed to.

Therefore a new follow-up methodology based on measurements of the salt dose on the surface and the resulting ice quality was developed.

## 2 Salt measurements

Commercially available salt measurement devices, be it manually held salt sensors like the SOBO20 or sensors installed in the pavement, may be very accurate, but when it comes to salt that is undissolved, either because it is spread dry and there is not enough salt on the surface to dissolve it, or the liquids have dried up due to evaporation, such devices will inevitably underestimate the amount of salt on the road surface.

Therefore a portable device where a known amount of liquid is applied manually within a confined area and the surface is brushed, also manually, until all salt within the area is dissolved has been developed (Figure 1).



**Figure 1.** Portable salt measuring and sampling device.

In order to decide when all the salt on the investigated surface is dissolved, the salt measuring and sampling device is equipped with two electrodes connected to a 54€ conductivity circuit (Atlas Scientific EZO™) communicating with a 30€ digital microcontroller (Arduino UNO), presenting the calculated salt amount on an OLED graphic display in front of the operator.

Depending on the situation the operator may decide to leave the liquid and just use the calculated salt amount, or take the sample back to the laboratory for further analyses by sucking it up with a suction device and transfer it from the confined area to the sample cup. The relation between the electric conductivity and chloride concentration is

---

[a] Corresponding author: goran.blomqvist@vti.se

known from field and laboratory trials within the Nordic research project NordFoU-MORS (Modelling Residual Salt) [3].
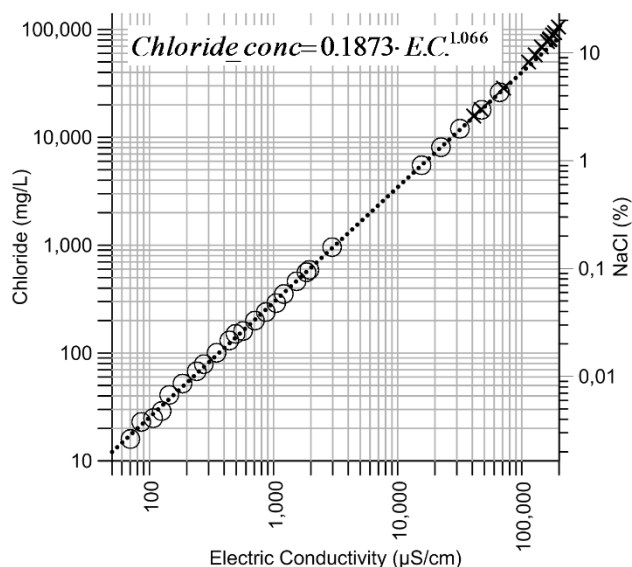


**Figure 2.** Relation between the electric conductivity and chloride concentration.

## 3 Ice quality measuring device

In order to inflict a repeatable angular impact on the ice surface investigated, an ice-hammer-pendulum was constructed (figure 3).



**Figure 3.** Ice quality measuring device.

The pendulum head is equipped with a 32€ 9-DOF absolute orientation sensor (Adafruit BNO055) combining three axis accelerometer, gyroscope and magnetometer into the actual 3D space orientation with a 100Hz time

resolution communicating with a 30€ digital micro-controller (Arduino UNO).

By adjusting the height of the pendulum over the ice-layer tested, the impact is intended to be repeatable.

Analyses will include the hardness of the ice as calculated from the registered forces and the effect of the impact by visual inspection of the surface after the pendulum is dropped. A crucial issue is to establish whether the formed ice has bonded to the pavement or not.

## 4 Combined experiments

The combination of salt and ice impact measurements will be performed in a climate chamber during November–December 2015 where rain will be simulated on five different pavements (Table 1) at different freezing temperatures and with different anti-icing salt doses applied.

**Table 1.** Pavements used for salting/freezing tests in the climate chamber.

| Pavement type | Stone size (mm) | Stone mineral | Road surface texture (mm) |
|---|---|---|---|
| SMA | 16 | Porphyry | 2.1 |
| SMA | 11 | Quartzite | 1.6 |
| AC | 11 | Limestone | 1.4 |
| SMA | 8 | Porphyry | 2.1 |
| SMA | 16 | Quartzite | 1.3 |

SMA = Stone Mastic Asphalt, AC = Asphalt Concrete

During January–March, 2016, the same equipment will be used in field trials under real conditions in order to follow-up different winter maintenance techniques used in the City of Stockholm where the relation between salt dose, ice quality and efficiency of different salt sweepers will be addressed.

## Acknowledgments

## References:

1. A. Bergström [Niska], PhD Thesis, Royal Institute of Technology, Stockholm (2002),
2. J. Jansson & S. Kok, Master Thesis Linköping University (2015)
3. G. Blomqvist, M. Eram, M. Gustafsson & S. Thordarson, PIARC XIV International Winter Road Congress (2014)

# Shallow geothermal switch point heating system

Lars Staudacher[1], Damian Schink[2], Dr. Roman Zorn[3], Dr. Hagen Steger[4]

[1]*Bavarian Center for Applied Energy Research, 85748 Garching, Germany*
[2]*Pintsch Aben geotherm GmbH, 46537 Dinslaken, Germany*
[3]*European Institute f. Energy Research (EIFER), 76131 Karlsruhe, Germany*
[4]*Karlsruher Institut für Technologie (KIT) Institut für Angewandte Geowissenschaften, 76131 Karlsruhe, Germany*

**Abstract.** For safety reasons railroad switches are heated in winter to prevent malfunction due to snow or ice. Typically electric resistance heating or gas burners are applied. In Germany about 490 MW electric power are installed at German Railways and approximately 186 GWh of electric energy are consumed per year by these systems. Within the project "Geothermal Zero Emission Switch Point Heating" a low temperature heating system has been developed that runs solely using shallow geothermal energy. Low temperature heat is extracted from the ground by a $CO_2$ thermosyphon which consists of a borehole heat exchanger working as evaporator and condensers placed at the switch point. The whole system has been developed, tested in laboratory and finally 3 pilot plants have been built.

## 1 Principle

A geothermal switch point heating system working solely with shallow geothermal energy requires that the heat transfer between the ground and the switch point is working with a very low temperature difference. A thermosyphon is a heat exchanger which fulfils this requirement and furthermore does not require any additional energy for operation. The heat carrier is filled into a closed pipe system such that it is in a two phase state. In our case $CO_2$ has been chosen because of its environmentally uncritical characteristics. As the condensers are cooled due to environmental conditions the gaseous $CO_2$ starts to condense inside the condenser. The resulting pressure drop in the system leads to evaporation of the liquid phase in the pool (see Figure 1).
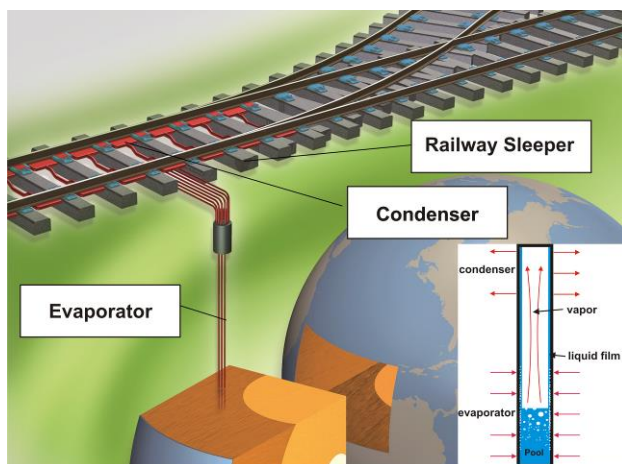


**Figure 1.** Principle of the switch point heating system

Once the circuit has started to operate the back flowing liquid phase from the condenser wets the tube walls of the evaporator and leads to a heat flux from the entire borehole to the switch as long as the condenser surface is cooler than the evaporator surface. Thus no additional control system is necessary to start or shut down the heating system. The unique requirement that has to be fulfilled is that the supply temperature of the gaseous $CO_2$ is always high enough to melt all the snow or ice that has to be expected at the site of installation.

## 2 Determination of load profiles

A load profile of the switch point heating system is necessary for dimensioning of the borehole heat exchanger. Hereby the essential heating power as a function of environmental circumstances has to be determined. In order to get this correlation two steps have been carried out [1]. First the heat transfer of a flat plate to environment has been calculated. Second the correlations have been validated at an outdoor test facility as the geometry of the heating system differs from that of a flat plate.

Figure 2 shows the heat transfer terms which are of interest.
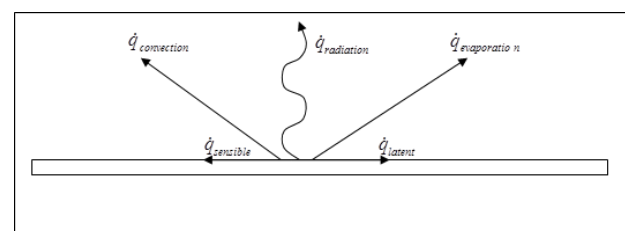


**Figure 2.** Heat transfer at the surface

As the plate is heated continuously there are convective losses at the surface when the plate is warmer than the surrounding air. There are also radiation losses especially at cloudless nights. If snow falls down to the plate it will be heated up to zero degrees (sensible heat) and then be melted (latent heat). There are also losses due to evaporation when the plates are wet because of rain or melted snow. All this terms together give a correlation which describes the heating power of the plate as a function of environmental conditions.

The problem of the heat demand of a surface heating system has already been investigated by different authors [2-6]. Aberrations of the results of this calculation in our case are mainly due to the fact that some of the models

---

[a] Corresponding author: lars.staudacher@zae-bayern.de

are specially designed for certain applications and do not account for all physical parameters like absorption and emission coefficients. Nevertheless all correlations lead to results of the same order. Aberrations of the yearly energy demand are within a range of ±15% based on the average value. The result of this calculation for standard weather data are illustrated in Figure 3 and Figure 4.
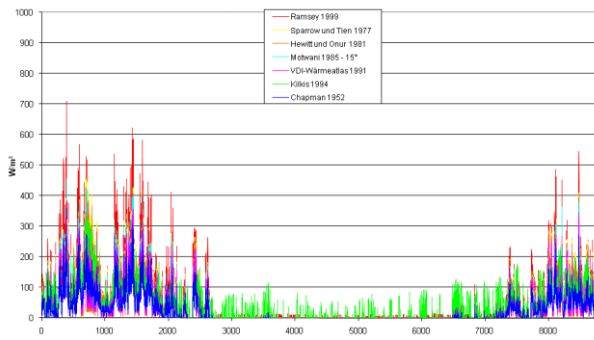


**Figure 3.** Exemplary Load Profile of the switch point heating system [2-6]
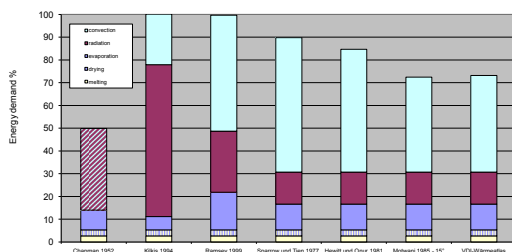


**Figure 4.** Comparison of the yearly energy demand calculated with different models [2-6]

The results strongly depend on the site. If the surface is heated continuously as in our case most of the heating demand are losses. Only around 5% of the yearly consumed energy is necessary to melt snow. Most of the energy is lost by convection. This is around 55 – 60% of the total heat demand. The rest are evaporation and radiation losses that are more or less of the same order. Simple control strategies taking into account air temperature can lead to energy savings around 25% compared to a not controlled system. If an ideal control strategy could be applied which detects exactly when heating is necessary due to snow fall up to 65% of the energy demand could be saved.

# 3 Development of the condensers

## 3.1 Design of the condensers

In order to fulfil the requirement to melt snow and ice at a very low temperature level the integration of the heating system into a railroad switch point has been the major challenge. First numerical simulations have been carried out in order to investigate if a simple coupling of heat exchangers to a switch is possible. A first prototype of the heating system was build and tested (see Figure 5). This prototype was mounted above the slide plate with a condenser on each side. Heat transfer into the slide plate was solely by conduction.

Although this prototype worked quiet well the design had to be improved in terms of thermal and mechanical characteristics and especially costs.



**Figure 5.** First prototype of the switch point heating system

The main improvement of the next prototype was to integrate the condenser into the slide plate. This leads to a much better coupling of the heating system to the slide plate and therefore to a better performance of the heating system. As a consequence of this the slide plate had to pass through all the safety tests that are necessary to get a permission for the German railways. Beneath a numerical stress analysis also experimental tests had to be carried out. Figure 6 shows some results of the stress analysis of the slide plate.
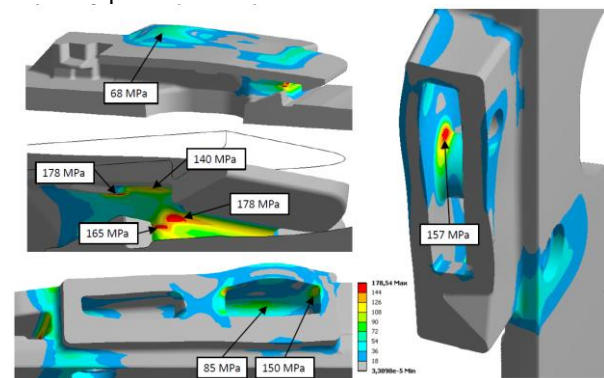


**Figure 6.** Stress analysis of the slide plate (Source: Pintsch Aben Geotherm)

On the right side of the figure the hollow space of the condenser is visible in which the gaseous $CO_2$ condenses. Between the slide plates a melting device has been developed that also works as a condenser (see figure 7). It is made out of aluminium as an extrudet section. The channels are closed afterwards through cover plates that are welded at the melting plates. To protect the condenser but also the pipping a safety box made out of stainless steel was constructed. One part of this box is also illustrated in figure 7.
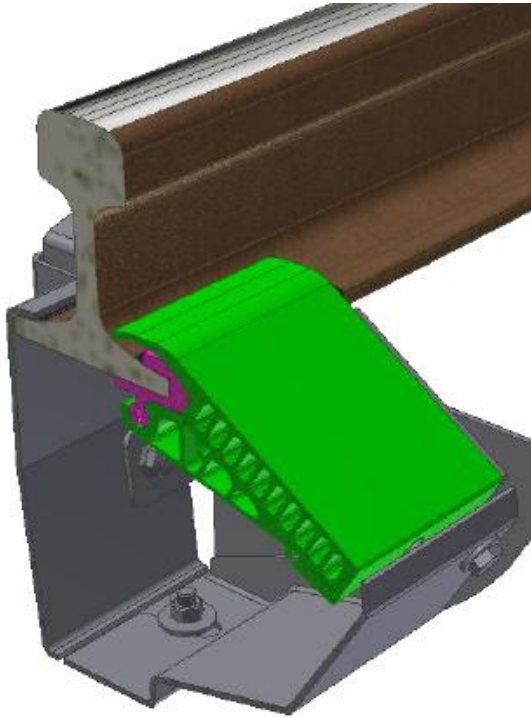
**Figure 7.** Melting plate mounted at the rail base
(Source: Pintsch Aben Geotherm)

This aluminium condenser together with respectively one left and one right condenser of the slide plate is connected to one evaporator in a borehole. Figure 8 shows the mounted heating system but without the stock rail. The service pipe including its protective pipe is also visible.
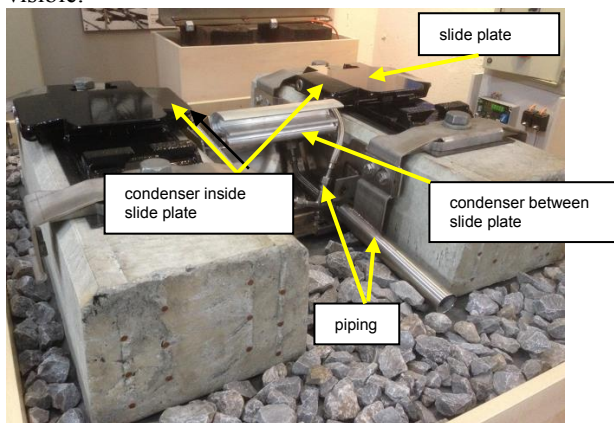


**Figure 8.** Slide plate with integrated condensers and melting condenser between slide plates (Source: Pintsch Aben Geotherm)

## 3.2 Laboratory test of the heating system

For this prototype laboratory tests have been carried out in order to identify weaknesses of the heating system and measure the minimum supply temperature as a function of peak power. Figure 9 shows a picture of the heating system when it starts to fail. Snow starts to accumulate at the middle of the slide plate. This is one of the most critical parts of a switch point in terms of snow or ice and it has therefore to be avoided.



**Figure 9.** Laboratory test of the heating system

Beneath this stationary test also shock tests have been carried out in order to investigate the system behaviour in the case of big ice lumps falling inside the switch point. The new heating system passed all these tests nevertheless there is still potential for optimization.
In order to supply snow to this relatively small area of about 0.3x1.5m a little snow machine has been developed as no commercial system was available (see figure 10).
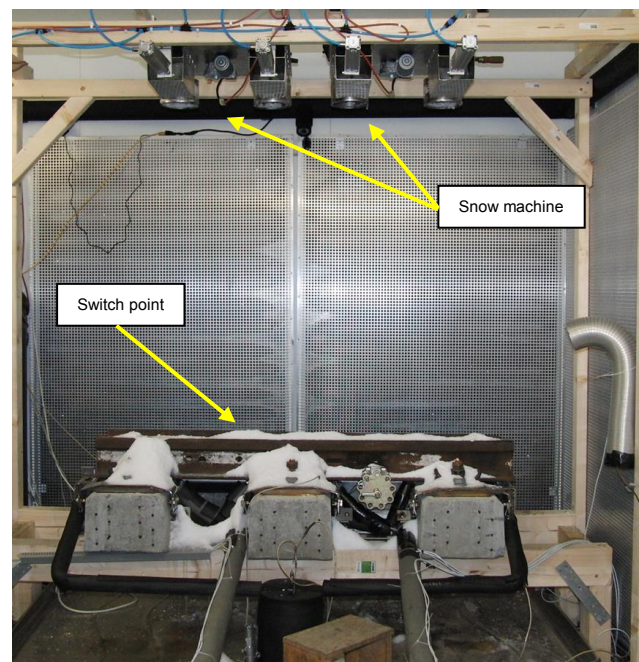


**Figure 10.** Switch point test facility inside climate chamber

With this machine a maximum snow load of 1000W/m² can be applied for approximately 4 hours exactly at the place where the heating system has to prove its functionality. Due to its modular composition this snow machine can be extended easily to bigger areas. The whole system is located in a climate chamber that is cooled through natural convection. This is necessary in order not to blow the snow away.

# 4 Development of the evaporator

## 4.1 Phenomenological discussion of heat transfer inside of a thermosyphon

Heat transfer inside of a geothermal $CO_2$ earth probe is a very complex process. Different hydrodynamic and heat transport phenomena occur inside of the evaporator thus predictability of heat transfer is highly uncertain [7]. Inside of the evaporator there is a liquid pool at the bottom of the earth probe. If a temperature difference is applied to it the liquid starts to boil. At small temperature differences there is convective boiling inside of the pool. If the temperature difference increases nucleate boiling will be encountered and the heat transfer coefficient will rise at this part of the evaporator. In parallel the liquid phase that flows back from the condensor to the pool evaporates along the way in the probe as long as the wall temperature is higher than the saturation temperature of the liquid. Depending on the wetting conditions of the inside surface the heat transfer in this part is better or worse. As the evaporator of a CO2 earth probe is very long one could encounter different forms of boiling at the same time because of the backpressure inside of the pool. In the upper part there might be nucleate boiling, deeper there might be convective boiling and even deeper the pressure might be too high to even boil. How the different parts perform also depends on the applied load. Back pressure inside of the pool is principally negative as the saturation temperature rises inside of the pool. Anyway a certain pool should be assured to ensure start up and to realize a satisfactory heat transfer behaviour. Beneath different forms of boiling and flow regimes nucleate boiling strongly depends on surface properties. Exact predictions concerning heat transfer coefficients inside of a thermosyphon is therefore difficult.

## 4.2 Heat transfer limits

There are three different phenomena that limit the heat transfer inside of a thermosyphon:

•  burn out limit

•  boiling limit

•  flooding and entrainment limit

At small filling amounts the burn out limit has to be taken into account. It occurs when the liquid film does not reach the bottom of the evaporator and no pool exists anymore. All the heat carrier is circulating inside the themosyphon at this state. A further increase of the heat flux leads to a burn out of the evaporator. The boiling limit occurs, when the radial heat flux is so high that a closed blanket of vapour covers the inside surface of the evaporator. This vapour film increases the resistance between the heat carrier and the evaporator wall. An increase of temperature difference will not lead to a rising power but an increasing vapour film. Flooding and entrainment in thermosyphons occurs at high axial heat flux. The reason for this limitation is the shear force between the liquid and vapour phase that flow counter current. If the transferred power is increased the shear force increases until the downward flowing liquid phase is stopped. This phenomenon is called "flooding limit" if the thermal fluid conditions are still steady and stable. Further increase of the heat input will lead to unstable and unsteady conditions in the liquid film. In this case liquid droplets are entrained from the liquid film and transported to the condenser. Both phenomena lead to an accumulation of heat carrier in the condenser section and can lead to a dry out of the evaporator.

## 4.3 Experimental results at ZAE Bayern

Aim of this experiment was to measure the power of a $CO_2$ evaporator as a function of the applied temperature difference between surface and outlet of the evaporator with a high accuracy of measurement. The test facility consists of three coupled circuits. One circuit to cool the condenser, one circuit to heat the evaporator and one circuit that contains the themosyphon. The evaporator section of the themosyphon was heated by a water quench circulating at hight velocity around the evaporator tube. This setup was necessary to determine the surface temperature of the evaporator accurately. The power of the evaporator was determined by a mass flow meter that measured the mass flow rate coming back from the condenser. Together with the measured temperature at the outlet of the evaporator the power could be calculated. The experiment was carried out using a plain tube with a length of 9.22 m and an inside diameter of 11.2 mm. At the bottom of the evaporator was a liquid pool with a height of 3.4 m. The investigation of this evaporator tube showed a clear dependence of the operation behaviour on the way the evaporator is heated. Depending on how DT is changed one can observe significant differences of the output power at the same temperature difference. Figure 11 shows the relative power of this tube versus the applied DT for three different operation conditions. At small temperature differences one can observe a linear behaviour between the applied DT and the output power which is practically independent of the operation conditions. After that the power strongly depends on how the operation conditions have been before and how they are changing. For example if we start at a power of 0 W and increase the temperature difference stepwise through a decrease of the outlet temperature of the evaporator while the surface temperature is maintained at a constant level one will observe a behaviour as it is illustrated by the black crosses in figure 11. The same procedure just the other way around starting at maximum power and decreasing DT through a stepwise increase of the outlet temperature of the evaporator will lead to a behaviour illustrated by the black squares in figure 11. Another possible way of changing the operation conditions is to start at maximum power and decrease DT through an increase of the surface temperature of the evaporator

while keeping the outlet temperature constant. This behaviour is illustrated by the grey triangles in figure 11. All these different ways of changing the operation conditions have in common that one can observe two transition points. At this points is found an immediate change of the transferred power at nearly the same temperature difference. This transition points indicate that there is a change of flowing, wetting or boiling behaviour inside of the evaporator. The transition points itself depend on the operation conditions. Another interesting result is that the maximum power of the evaporator could not be reached at small temperature differences starting at a power of 0 W. To reach the maximum power starting from zero a DT of about 7 K was necessary. Temperature differences higher than 7 K did not lead to an increase of the transferred power anymore.



**Figure 5.** First Pilot Plant – Grünberg (Germany)
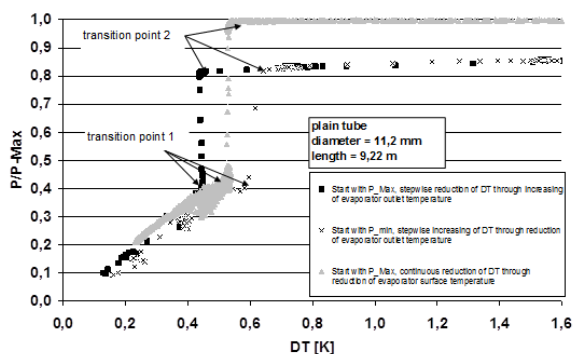


**Figure 11.** Operation behaviour of a plain tube working as a $CO_2$-evaporator

As a result of these experiments the entrainment limit, the essential temperature difference and the necessary filling amount of the refrigerant could be determined for this special case of evaporator tube.

## 5 Pilot plants

3 pilot plants have been built up to now using this technique. The first one was built 2012 in Grünberg for DB (German Railways). The second plant was built 2013 in Hamburg for the Harbour Railway. The third pilot plant was build 2014 in Sponholz also for DB. The heating System works reliable (see figure 5) and measurements show that the ground temperature at the borehole recovers completely during summer so that from this side no limit of lifetime is expected.

One critical point that has to be improved is leak-tightness. Some of the heating circuits loose $CO_2$ which has to be refilled once in a while. From a technological point of view this problem can be solved as much lower leakage rates are achieved in chiller technology. Nevertheless leak-tightness is a challenge as mounting, linking of components and filling of the system has to be done at installation site.

## References

1. L. Staudacher, M. Reuß, D. Schink, Geothermal Zero Emission Switch Heating, Proc. Effstock 2009, Stockholm
2. AMERICAN SOCIETY OF HEATING, REFRIGERATING AND AIR-CONDITIONING ENGINEERS (Hrsg.): 1999 ASHRAE Handbook – HVAC Applications. In: The ASHRAE HandbookCD, Atlanta: American Society of Heating, Refrigerating and Air-Conditioning Engineers Inc., 1996-1999
3. CHAPMAN, W.P.: Calculating the Heat Requirements of a Snow Melting System. In: Air Conditioning Heating and Ventilating Vol. 53 No. 9, 1956
4. KILKIS, I.B.: Desining of Embedded Snow Melting Systems: Part 1, Heat Requirements – An Overall Assessment and Recommendations. In: ASHRAE Transactions/100.1994, 1
5. RAMSEY, J.W.; HEWETT, M.J.; KUEHN, T.H.; PETERSEN, S.D.: Updated Design Guidelines for Snow Melting Systems. In: ASHRAE Transactions/105.1999, 1
6. VEREIN DEUTSCHER INGENIEURE (Hrsg.): VDI-Wärmeatlas : Berechnungsblätter für den Wärmeübergang. 6., erw. Aufl., Düsseldorf: VDI-Verlag, 1991
7. L. Staudacher, M. Reuß, $CO_2$-Thermosysphon Borehole Heat Exchanger, Proc. Innostock 2012, Lleida

# A Method for estimating road friction coefficients with ice film subjected to melting by de-icing agents

Akihiro Fujimoto[1,a], Shunsuke Tanaka[1], Kenji Sato[1], Roberto Tokunaga[1], Naoto Takahashi[1], Tateki Ishida[1] and Kiyoshi Takeichi[2]

[1]PWRI, CERI, Hiragishi 1-3-1-34, Toyohira-ku, Sapporo, 062-8602, Japan
[2]Hokkai-Gakuen University, 1-1, Nishi 11, Minami 26, Chuo-ku, Sapporo, 064-0926, Japan

**Abstract.** In this study, to achieve the efficient use of the de-icing agents that are spread on icy-covered roads, we developed a method for estimating the road friction coefficient ($\mu$) after de-icing agent spreading on such roads. A theory for estimating $\mu$ and the results of an experiment conducted in a constant low-temperature room to estimate $\mu$ for stone mastic asphalt pavement and porous asphalt pavement are described. Also, the estimated $\mu$ between the different pavement types are compared.

## 1 Introduction

Resources for guidance on the spreading of de-icing agents include the Snow and Ice Databook[1] and Clear Roads[2]. However, methods to determine the appropriate amount of de-icing agent application and its timing that give due consideration to weather conditions and the state of ice and snow on the road have not been established. In addition, various types of pavement have been constructed in cold, snowy regions as well as in other regions in recent years. Porous asphalt (PA) pavement and stone mastic asphalt (SMA) pavement (pavement that affords both the surface texture of PA pavement and the durability of mastic asphalt pavement) have rough surface textures. Such textures mean that less moisture remains on road surface, which makes them less prone to surface freezing than dense-graded asphalt (DGA) pavement is. However, their rough surface texture and drainage function make the effectiveness of de-icing agent spreading unclear because they cause a loss of de-icing agents along with the loss of moisture from the pavement surface.

With the continuing diversification of pavement types, the texture and drainage function of pavements should be taken into consideration in efforts to make de-icing agent spreading more optimal than ever. Also needed is an evaluation method for the effectiveness of spreading of de-icing agents using objective indices such as road friction coefficient (hereinafter: $\mu$). In other words, a method for estimating $\mu$ after de-icing agents are spread needs to be established.

An experiment on the spreading of de-icing agents on icy roads was conducted in a constant low-temperature room with DGA pavement, SMA pavement, and PA pavement. By measuring the ice thickness on each pavement specimen before and after the spreading of de-icing agents and $\mu$, a method for estimating $\mu$ after de-icing agents are spread was established [3-4], which will be introduced in this paper.

## 2 $\mu$ estimation method

### 2.1 Assumptions and conditions of the study

The method for estimating $\mu$ after de-icing agent spreading that is proposed in this paper makes the following assumptions.
i) No consideration is given to the possibility that de-icing agents can be dispersed while being spread, dispersed by passing vehicles after spreading, or effused from the sloped pavement.
ii) The melting of the ice film on the road surface caused by the spreading of de-icing agents occurs evenly to the same degree all over the road surface. In practice, the melting of the ice film on the road surface occurs unevenly and some areas of pavement surface retain ice film on them after the spreading of solid de-icing agents on roads covered with thin ice. To distinguish between the ice thickness on road surface in real situation and the ice thickness referred to in this study based on the assumption (ii) above, the latter will be called mean ice thickness $H_i$ (mm) hereinafter.

### 2.2 Estimation method

Our $\mu$ estimation method is described here (Also see the diagram in Figure-1). The upper part of the diagram shows the state of the pavement surface on which de-icing agents have not been spread (hereinafter: State 1). The lower part of the diagram shows the state of the pavement surface for which sufficient time has passed after de-icing agent spread for ice to melt (hereinafter: State 2). Thermodynamic equilibrium is reached in State 2. Where the input conditions are mean ice thickness ($H_i$ (mm), i.e., $H_{i-1}$), road surface temperature ($T$ (°C)), amount of de-icing agent spreading ($M_{ss-in}$ (kg/m$^2$)), and pavement types for State 1. The $\mu$ of State 2 ($\mu_2$) is determined by the following five steps.
1: Determine the $T$ and then estimate the concentration ($C$ ($C_2$)) of salt solution for State 2 by using the freezing-point curve.
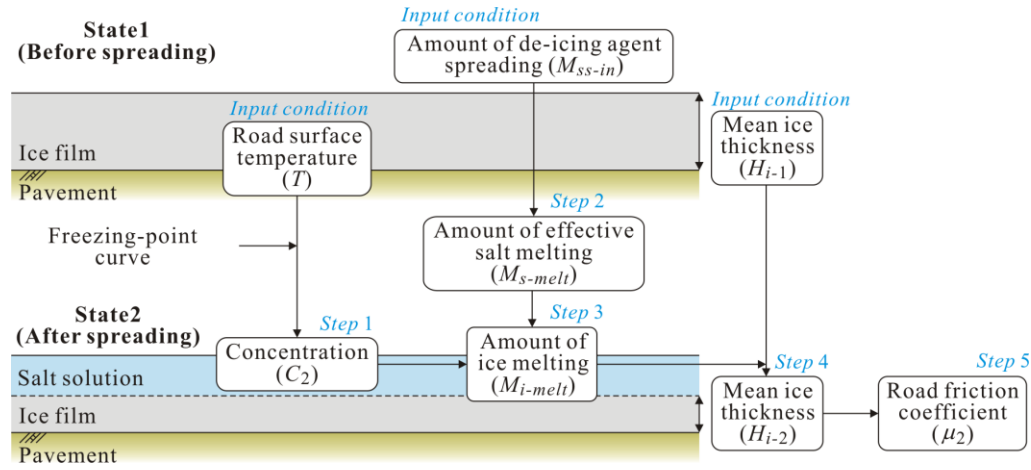
**Figure 1.** Schematic of the $\mu$ estimation method.

2: Because there is a loss of de-icing agents on the pavement, to determine that loss, we define the mass per square meter of de-icing agent acting to melt ice on the pavement as the amoumt of effective salt melting ($M_{s\text{-}melt}$ (kg/m$^2$)). The amount is determined by Equation (1).

$$M_{s-melt} = M_{ss-in}(1-R_z)(1-R_v)(1-R_x) \qquad (1)$$

Where, $R_x$ is the ratio of the mass per square meter of de-icing agents effused away from the sloped pavement to $M_{ss\text{-}in}$. $R_z$ is the ratio of the mass per square meter of de-icing agents infiltrated into and accumulated inside the pavement to $M_{ss\text{-}in}$ (hereinafter: the ratio of salt loss in the vertical direction). $R_v$ is the ratio of the mass per square meter of de-icing agents dispersed by passing vehicles to $M_{ss\text{-}in}$. Because our focus of this study is $R_z$ (described in **4.4**), $R_x$ and $R_v$ are regarded as zero.

3: The amount of ice melting for State 2 ($M_{i\text{-}melt}$ (kg/m$^2$) is determined from the following equation.

$$M_{i-melt} = M_{s-melt} \cdot (1-C)/C \qquad (2)$$

4: The mean ice thickness of State 2 ($H_i$ ($H_{i\text{-}2}$)) is determined by subtracting the thickness of melted ice ($H_{i\text{-}melt} = M_{i\text{-}melt}/\rho_i$, where $\rho_i$ is ice density (kg/m$^3$)) from $H_{i\text{-}1}$.

5: Finally, $\mu_2$ is calculated from the $\mu$-$H_i$ relational equation (described in **4.3**).

## 3 Indoor experiment

### 3.1 Experiment procedure and conditions

The laboratory experiment was conducted in a constant low-temperature room. Figure 2 shows pavement specimens after the formation of an ice film. As shown in the photo, three types of pavement specimens were used: PA pavement (top), SMA pavement (middle) and DGA pavement (bottom). Three specimens per type were used.
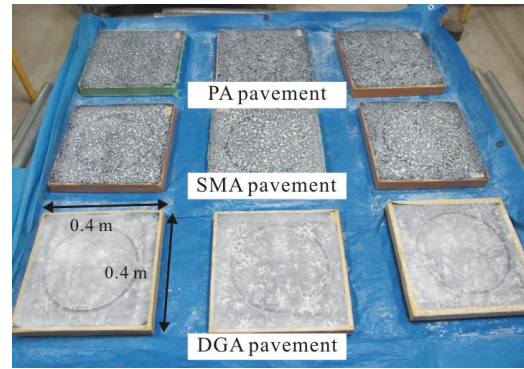


**Figure 2.** Specimens of indoor experiment

Each specimen is 0.40m in width, 0.40m in length, and 0.05m in height. The maximum size of coarse aggregate is 13mm. The void ratio of the PA pavement is 17%. The circle marks on the ice film on specimens in the photo were made by the Dynamic Friction Tester used for measuring $\mu$.

Following is the experiment procedure. (i) Pavement specimens are placed in the constant low-temperature room. They are left until their temperature falls to that of the room. (ii) Fresh water is sprayed on the specimens. (iii) They are left until an ice film forms on their surface. (iv) Sodium chloride is sprinkled on the ice film. (v) The specimens are left until the sodium chloride dissolves completely. (vi) $T$, $\mu$, $C$, and $H_i$ are measured in that order. In procedure (v), $T$ was regularly measured to determine the completion of sodium chloride dissolution. It was determined when $T$, which had dropped due to the endothermic reaction from the spreading of sodium chloride, returned to that of before the spreading.

Table 1 shows the experiment conditions.

### 3.2 Measurement items

$T$ was measured with a radiation thermometer for 5 seconds, and the average value was adopted. The measurement accuracy was ±2.0°C at $T = 0$°C. A Dynamic Friction Tester was used to measure $\mu$. $\mu$

measured at a travel speed of 40km/h is adopted in this paper. The salt solution on the road surface was sampled using water-absorbent paper in order to measure $C$ with a refraction salinity concentration meter. $H_i$ was measured using our ice film thickness meter, which uses weight of meltwater on pavement surface (the ice film thickness meter hereinafter). The meter was made on our own referring to ideas in Haavasoja, T et al. [5]. The following is the procedure for measuring $H_i$ by using the ice film thickness meter.

The ice film thickness meter consists of a box and water absorbing paper that is placed between the box and a road surface covered with thin ice, as shown in the upper picture in Figure 3. For this experiment a box was made with easily moldable laminate sheet. It was 220mm in width, 230mm in length and 100mm in height. $H_i$ is measured in the following procedure. (i) Remove moisture from the road surface by using absorbent paper. (ii) Place the ice film thickness meter on pavement specimens and pour hot water (about 95°C) into the box. (iii) 15 seconds later, detach the meter and measure the weight of the absorbent paper that has taken in the snowmelt. (iv) Repeat (ii) and (iii) until the amount of snowmelt falls below the lower limit of the amount of snowmelt. (v) Calculate $H_i$ from the total weight of snowmelt. The lower limit of the amount of snowmelt water taken by the absorbent paper to conclude the procedure (iii) was set based on the $\mu$ of the wet surface. The following is the background and procedure for setting the lower limit. By repeating (iii), the ice that fills voids inside pavement will also melt and be absorbed, but such ice does not affect $\mu$. To avoid overestimating $H_i$ due to the situation above, a preliminary experiment was conducted to measure the amount of snowmelt when $\mu$ was that of wet surface, and this amount was designated as the lower limit of snowmelt. Accordingly $H_i$ means the spatial average thickness of ice on the pavement that will affect $\mu$.

The lower photo in Figure 3 shows the difference between the area of pavement after $H_i$ is measured (left side of the photo) and the area of pavement for which measurement was not conducted (right side of the photo). As shown in the photo, the surface of coarse aggregate becomes dry after $H_i$ is measured.

# 4 Experiment results

## 4.1 Road surface conditions

Figure 4 shows the surface of the pavement specimens after the removal of surface moisture from the specimens in State 2 using absorbing paper. Photos in (a) in Figure 4 show pavement specimens on each of which 1.0kg/m² of water was sprinkled ($M_{w\text{-}in}$ = 1.0kg/m²) and the photos in (b) show pavement specimens on each of which 2.0kg/m² of water was sprinkled ($M_{w\text{-}in}$ = 2.0kg/m²). The left side photos in both (a) and (b) show specimens over each of which 20g/m² of de-icing agent was spread ($M_{ss\text{-}in}$ = 20g/m²) and the right side pictures of both (a) and (b) show specimens over each of which 60g/m² of de-icing

**Table 1**. List of experiment conditions

| ・ Environmental conditions | |
| --- | --- |
| Room temperature | -5°C |
| ・ Water sprinkling conditions | |
| Amount of water sprinkled | ・ kg/m² (sprinkle twice, 0.5 kg/m² each time) <br> ・ kg/m² (sprinkle 4 times, 0.5 kg/m² each time) <br> ・ 3.0 kg/m² (sprinkle 6 times, 0.5 kg/m² each time) |
| Temperature of sprinkled water | 0 - 1.0°C |
| Coloring | ・ White (aqueous acrylic paint) <br> ・ Mass ratio (100:1 // fresh water : |
| ・ Conditions of de-icing agent spreading | |
| Type of de-icing agent | Sodium chloride |
| Amount of de-icing agent spreading | 0, 20, 40, 60, 80 g/m² |
| Form | Powder |
| ・ Conditions of pavement specimens | |
| Type of de-icing agent | ・ DGA pavement <br> ・ SMA pavement <br> ・ PA pavement |
| Size | 0.40m in width, 0.40m in length, 0.05m in height |
| Number of specimens | 3 for each pavement type |
| Specifications | ・ Maximum size of coarse aggregate: 13mm <br> ・ Void ratio: 17% (for PA pavement) |
| ・ Measurement items | |
| Items | ・ Road surface temperature <br> ・ $\mu$ <br> ・ Concentration of salt solution <br> ・ Mean ice thickness |
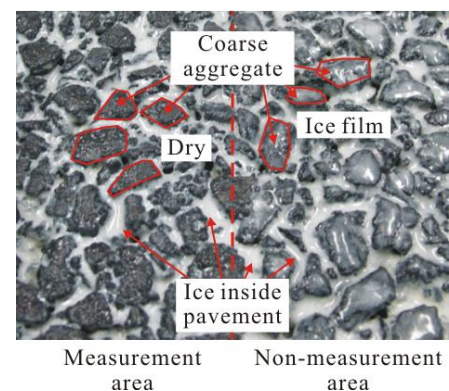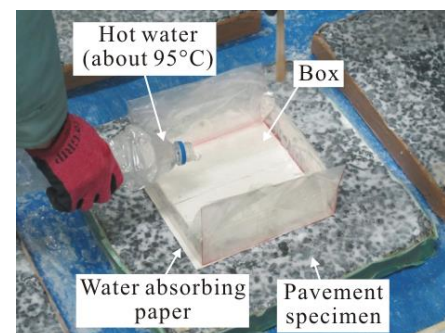


**Figure 3.** Measurement of ice film thickness

| Amount of de-icing agent spreading = 20 g/m² | Amount of de-icing agent spreading = 60 g/m² | Amount of de-icing agent spreading = 20 g/m² | Amount of de-icing agent spreading = 60 g/m² |

(a) Amount of water sprinkled = 1.0 kg/m²    (b) Amount of water sprinkled = 2.0 kg/m²
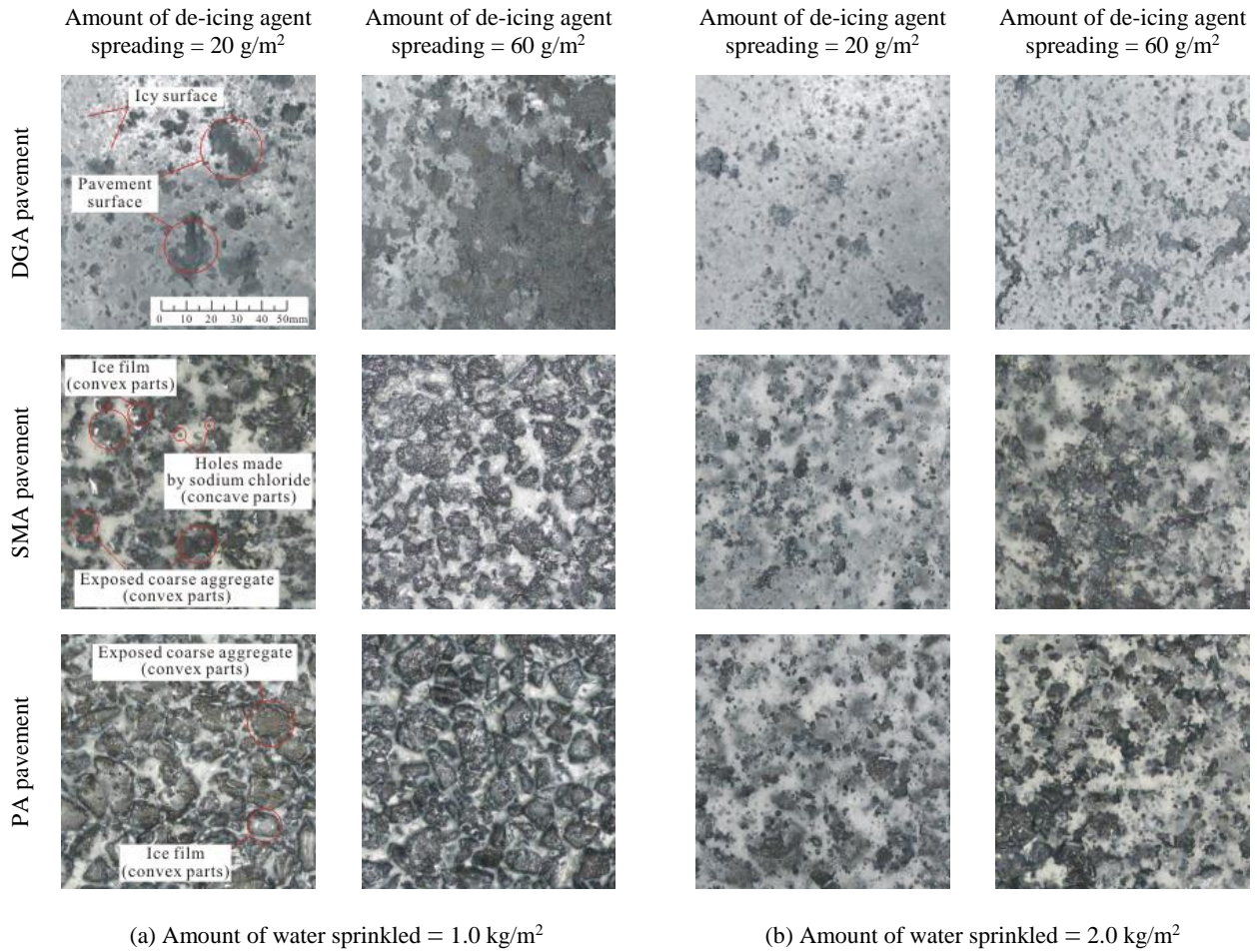
**Figure 4.** Surface of pavement specimens after removal of surface moisture

agent was spread ($M_{ss\text{-}in}$ = 60g/m²). The upper photos show the road surface conditions for DGA pavement, the middle photos show those for SMA pavement and the lower photos show those for PA pavement.

First, look at the photos in (a) of $M_{w\text{-}in}$ = 1.0kg/m². When $M_{ss\text{-}in}$ = 20g/m², pavement surface and icy surface existed intermingled for DGA pavement since parts of the ice film that had been in contact with sodium chloride melted. As for the SMA pavement, aggregate was exposed on convex parts of the surface of the specimens due to contact with sodium chloride, and indentations on the surface of the pavement specimens that had ice in voids had holes in places made by sodium chloride. The road surface condition for the PA pavement specimen was similar to that for the SMA pavement specimen, but ice on the PA pavement seems thinner than that on the SMA pavement. For DGA pavement, the area where pavement was revealed on the surface was greater horizontally at $M_{ss\text{-}in}$ = 60g/m² than at $M_{ss\text{-}in}$ = 20g/m². As for SMA pavement and PA pavement, the area where the aggregate of convex parts of pavement was revealed was greater at $M_{ss\text{-}in}$ = 60g/m² than at $M_{ss\text{-}in}$ = 20g/m².

Photos in (b) of $M_{w\text{-}in}$ = 2.0kg/m² are described next. When $M_{ss\text{-}in}$ = 20g/m², the degree of ice melting by sodium chloride was just enough to make holes in the ice

film and the exposure of the pavement surface was limited for the DGA pavement. Although aggregate was partially exposed on the surface of the SMA pavement and the PA pavement, most of the pavement surface was covered with the ice film, and the rough surface texture was hardly recognized. For DGA pavement, the pavement surface had more holes in places made by sodium chloride at $M_{ss\text{-}in}$ = 60g/m² than at $M_{ss\text{-}in}$ = 20g/m². As for the SMA pavement and the PA pavement, ice film which did not have contact with sodium chloride remained the states before the spreading of de-icing agent, though parts of surface of the SMA pavement and the PA pavement were revealed.

## 4.2 Influence of the amount of de-icing agent spread on $\mu$ and on mean ice thickness

Figure 5 shows the influence of $M_{ss\text{-}in}$ on $\mu$ and on $H_i$. (a) and (b) in the figure show the results for $M_{w\text{-}in}$ = 1.0kg/m² and $M_{w\text{-}in}$ = 2.0 kg/m², respectively. The upper tables show $\mu$, and the lower tables show $H_i$.

$\mu$ will be described. First, the results of $M_{w\text{-}in}$ = 1.0 kg/m² are described. When no de-icing agent was spread, (i.e., when $M_{ss\text{-}in}$ = 0 g/m²), the $\mu$ for DGA pavement, SMA pavement and PA pavement was 0.03, 0.11 and 0.16, respectively. $\mu$ for DGA pavement increased

(a) Amount of water sprinkled = 1.0 kg/m²



(b) Amount of water sprinkled = 2.0 kg/m²
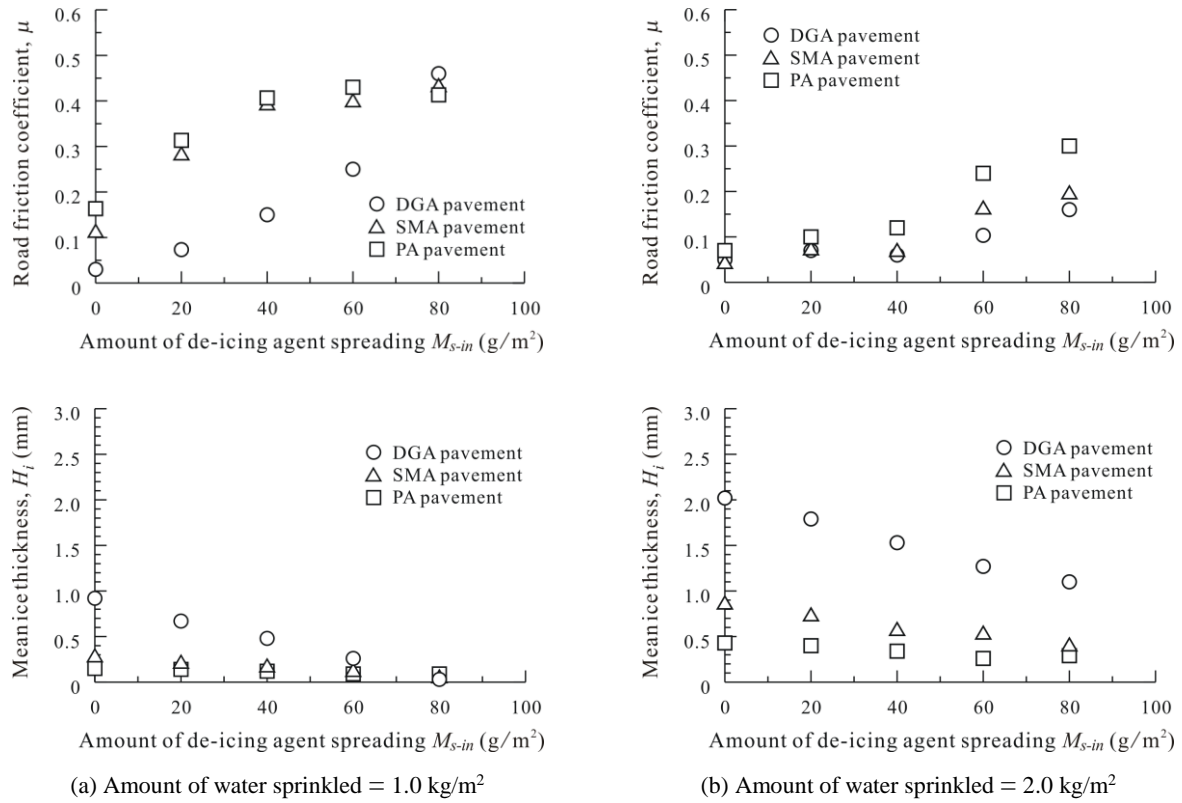
**Figure 5.** Influence of amount of de-icing agent spreading on $\mu$ and on an ice thickness
(upper table: $\mu$, lower table: mean ice thickness)

exponentially with increases in $M_{ss\text{-}in}$, and the value was 0.46 at $M_{ss\text{-}in} = 80$ g/m². By contrast, $\mu$ for the SMA pavement and the PA pavement increased logarithmically with increases in $M_{ss\text{-}in}$, and at $M_{ss\text{-}in} = 80$ g/m², the values were 0.43 and 0.41, respectively. $\mu$ for PA pavement changed at slightly higher values than the values for SMA pavement. Next, when $M_{ss\text{-}in} = 2.0$ kg/m², the values of $\mu$ for all pavement types increased exponentially with increases in $M_{ss\text{-}in}$. The rate of increase was the greatest for the specimens of PA pavement, followed by those for SMA pavement and DGA pavement. Reasons for the difference in distribution of $\mu$ for SMA pavement and PA pavement by the amount of $M_{w\text{-}in}$ are assumed to have come from differences in the pavement exposure seen in Figure 4. That is, when $M_{w\text{-}in} = 1.0$ kg/m², portions of the exposed surface of coarse texture increased with increases in $M_{ss\text{-}in}$, but when $M_{w\text{-}in} = 2.0$ kg/m², the slight increase in portions with exposed coarse texture was observed along with increases in $M_{ss\text{-}in}$ due to relatively thick $H_i$.

$H_i$ will be described now. The values of $H_i$ for DGA pavement, SMA pavement and PA pavement without the spreading of de-icing agent were 0.92mm, 0.27mm, and 0.15mm, respectively, at $M_{w\text{-}in} = 1.0$kg/m². The values of $H_i$ for the respective pavements were 2.02mm, 0.85mm, and 0.43mm at $M_{w\text{-}in} = 2.0$kg/m². $H_i$ for DGA pavement was the greatest, and $H_i$ for PA pavement was the least. Regardless of $M_{w\text{-}in}$ or the pavement types, the values of $H_i$ decreased linearly with increase in $M_{ss\text{-}in}$. The rate of decrease was the greatest for specimens of DGA

pavement, followed by those for SMA pavement and PA pavement.

### 4.3 Relationship between $\mu$ and mean ice thickness

Figure 6 shows the relation between $\mu$ and $H_i$. $\mu$ of all the specimens decreased exponentially with increase in $H_i$. The rate of decrease was the sharpest for the specimens of PA pavement, followed by those of SMA pavement and DGA pavement. The range of the data in the figure is $H_i < 0.85$ mm for SMA pavement and $H_i < 0.43$ mm for PA pavement. It is assumed that $H_i$ values greater than these would cause the pavement surface texture to exert less influence and that the values of $\mu$ for both SMA pavement and PA pavement would gradually get closer to 0.05 (which is the $\mu$ for the ice surface). Note that the value of $\mu$ when $H_i = 0$ was measured under the conditions of $T = 20$°C and $M_{w\text{-}in} = 1.0$ kg/m².

The relational equation of $\mu$-$H_i$ above mentioned is as follows.

$$\mu = a\,exp(bH_i) + c \qquad (3)$$

Figure 6 shows coefficients $a$, $b$, and $c$ corresponding to $\mu$ for each pavement specimen.
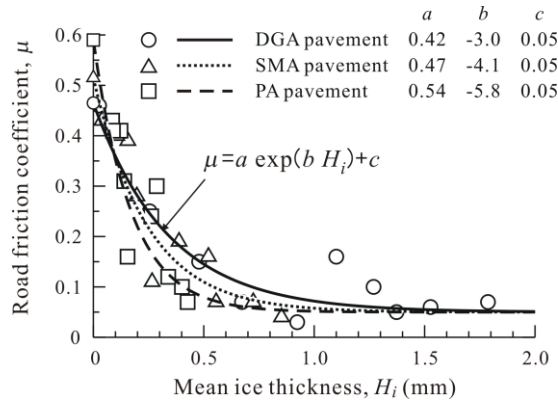
**Figure 6.** Relation between $\mu$ and the mean ice thickness



(a) Amount of water sprinkled = 1.0 kg/m²    (b) Amount of water sprinkled = 2.0 kg/m²

**Figure 7.** Ratio of salt loss in vertical direction

## 4.4 Ratio of salt loss in the vertical direction

In this section, $R_z$ will be calculated from the results of the experiment. This paper defines $R_z$ as the ratio of the amount of salt which did not act in melting ice film on the road surface and was lost from the road surface ($M_{ss\text{-}in}$ - $M_{s\text{-}melt}$) to $M_{ss\text{-}in}$.

$$R_z = 1 - \frac{M_{s-melt}}{M_{ss-in}} \qquad (4)$$

$M_{s\text{-}melt}$ was calculated as follows: $H_{i\text{-}melt}$ was divided by $\rho_i$ to obtain $M_{i\text{-}melt}$. Then $M_{i\text{-}melt}$ and $C_2$ were assigned to Equation (2) to get $M_{s\text{-}melt}$. $H_{i\text{-}melt}$ means the ice thickness that was melted by the spreading of de-icing agent, that is, the difference between $H_i$ obtained from the experiment without de-icing agent spreading ($H_{i\text{-}1}$) and $H_i$ obtained from the experiment with de-icing agent spreading ($H_{i\text{-}2}$).

Figure 7 shows the relation between $R_z$ and $M_{ss\text{-}in}$. Table (a) shows when $M_{w\text{-}in}$ = 1.0 kg/m² and table (b) shows when $M_{w\text{-}in}$ = 2.0 kg/m². The figure reveals that $R_z$ is independent of $M_{ss\text{-}in}$. It can be concluded that, for DGA pavement, moisture or de-icing agents were not effused away from the pavement surface during the experiment and almost all of the de-icing agents spread worked to melt the ice film on the pavement specimens. As for SMA pavement and PA pavement, it is assumed that large portions of the de-icing agents spread on the pavement specimens moved into holes in the pavement surface and inside the pavement as solids or as highly concentrated salt solution. $R_z$ for DGA pavement was independent of $M_{w\text{-}in}$; the values were mostly around 0 and hardly changed. $R_z$ for SMA pavement and PA pavement decreased with increase in $M_{w\text{-}in}$.

Figure 8 shows the relation between $R_z$ and $H_i$ [3]. Each $R_z$ of SMA pavement and PA pavement declined linearly with increase in $H_i$. The relation is expressed in the following equation.
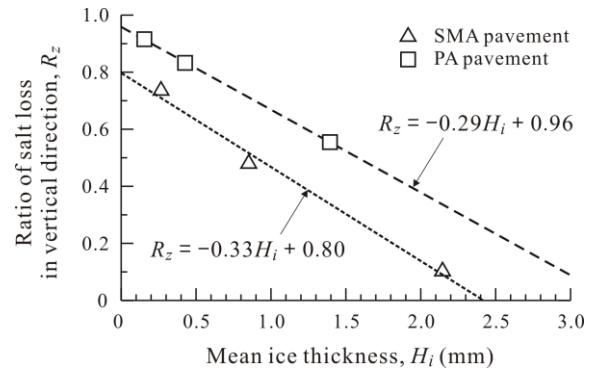


**Figure 8.** Relation between the ratio of salt loss in the vertical direction and the mean ice thickness

$$R_z = \begin{cases} -0.33H_i + 0.80 \\ -0.29H_i + 0.96 \end{cases} \qquad (5)$$

## 5 Discussion on $\mu$ after spreading

First, this chapter will show examples of estimating $\mu$ for DGA pavement, SMA pavement and PA pavement using the estimation method described in 2.2. The calculation conditions were $M_{ss\text{-}in}$ = 30 g/m², $M_{w\text{-}in}$ = 1.0 kg/m², and $T$ = -3°C. Next, changes in $\mu$ were examined for each pavement specimen when only $T$ was varied from 0°C to -8°C. $H_i$ values used in the estimation were the values obtained from the results of experiments: 0.92 mm for DGA pavement, 0.27 mm for SMA pavement, and 0.15 mm for PA pavement.

Table 2 shows the estimation results for $\mu$. When $T$ = -3°C, $C_2$ = 4.7% is obtained from the freezing-point curve for sodium chloride (Step 1). Multiplying $M_{ss\text{-}in}$ = 30g/m² by 1-$R_z$ produces an $M_{s\text{-}melt}$ of 30.0g/m² for DGA pavement, 7.8g/m² for SMA pavement and 2.4g/m² for PA pavement (Step 2). Calculating $M_{i\text{-}melt}$ using equation (2) (Step 3) produces a $H_{i\text{-}melt}$ of 0.66 mm for DGA pavement, 0.17mm for SMA pavement, and 0.05mm for PA pavement. Consequently $H_{i\text{-}2}$ is 0.26mm for DGA

**Table 2.** Results of $\mu$ estimation

| | Items | Symbols | DGA pavement | SMA pavement | PA pavement |
|---|---|---|---|---|---|
| Input conditions | Mean ice thickness in State 1 (before the spreading of de-icing agents) | $H_{i\text{-}1}$ | 0.92 | 0.27 | 0.15 |
| | Road surface temperature | $T$ | -3°C | | |
| | Amount of de-icing agents spreading | $M_{ss\text{-}in}$ | 30 g/m² | | |
| Step 1 | Concentration of salt solution | $C_2$ | 4.7% | | |
| Step 2 | Ratio of salt loss in the vertical direction | $R_z$ | 0 | 0.74 | 0.92 |
| | Effective salt melting rate | $M_{s\text{-}melt}$ | 30.0 g/m² | 7.8 g/m² | 2.4 g/m² |
| Step 3 | Thickness of ice melted | $H_{i\text{-}melt}$ | 0.66 mm | 0.17 mm | 0.05 mm |
| Step 4 | Mean ice thickness in State 2 (after the spreading of de-icing agents) | $H_{i\text{-}2}$ | 0.26 mm | 0.10 mm | 0.10 mm |
| Step 5 | Tire-road friction coefficient | $\mu$ | 0.24 | 0.37 | 0.36 |

pavement, 0.10mm for SMA pavement, and 0.10 mm for PA pavement (Step 4). Lastly, assigning $H_{i\text{-}2}$ to equation (3) will produce $\mu$ of each type of pavement in State 2; 0.24 for DGA pavement, 0.37 for SMA pavement, and 0.36 for PA pavement.

Figure 9 shows the relation between $\mu_2$ and $T$ under the conditions of $M_{ss\text{-}in} = 30$ g/m² and $M_{w\text{-}in} = 1.0$ kg/m². All $\mu$ values for the wet specimens decreased exponentially with decrease in $T$. As shown in the figure, it is suggested that $\mu_2$ possibly varied by pavement type, even though $M_{ss\text{-}in}$, $M_{w\text{-}in}$, and $T$ are the same. In other words, the $M_{ss\text{-}in}$ that is required to achieve a certain $\mu_2$ may vary by pavement type. Because the authors excluded $R_x$ and $R_v$, the experimental results cannot necessary be applied to actual roads.

# 6 Conclusions

In this study, an experiment on the spreading of de-icing agents on ice-filmed pavement specimens was conducted in a constant low-temperature room. The pavements were DGA pavement, SMA pavement and PA pavement. The ice thickness and the $\mu$ after the spreading of anti-icing agents were examined for each pavement specimen. Based on the results, an estimation method for $\mu$ after the spreading of de-icing agent was developed, and the values of $\mu$ for each pavement type after the spreading of de-icing agents at a given road surface temperature were compared.

The following are the findings.

(1) Values of $\mu$ increased exponentially with decrease in mean ice thickness. The relationship between $\mu$ for each pavement type and mean ice thickness was formulated.

(2) For DGA pavement, the ratio of salt loss in the vertical direction was zero, independent of the amount of sprinkled water. For SMA pavement and PA pavement, the ratio decreased with increase in the amount of sprinkled water. SMA pavement had a greater rate of decrease than that of PA pavement. These relationships could be formulated.

(3) Although the study cases were limited to thin ice-covered roads without the passing of vehicles and without slopes in the longitudinal or lateral directions, from (1) and (2), it was found to be

possible to estimate $\mu$ after de-icing agent spreading
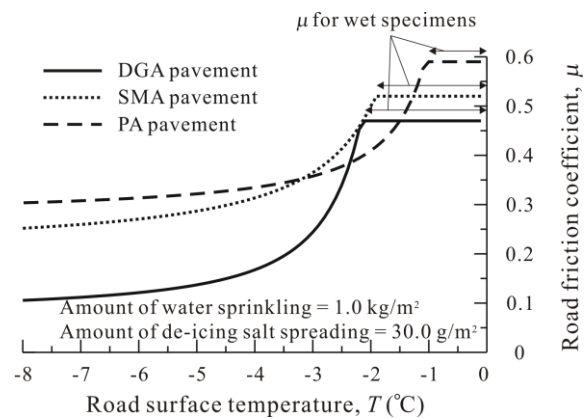


**Figure 9.** Relation between $\mu$ and road surface temperature for State 2

for DGA pavement, SMA pavement and PA pavement.

(4) It was shown that $\mu$ after de-icing agent spreading could differ depending on the pavement type, even for a same given temperature, same amount of sprinkled water, and same amount of de-icing agent.

Challenges left behind regarding the method of estimating road surface friction explained in this paper are described below. The method of estimating road friction developed in this study has not taken into consideration aging-related changes in road surface texture and in drainage function of pavement, or the dispersion of de-icing agents by passing vehicles. To take into account changes in pavement texture and in drainage function, additional experiments need to be conducted to identify various parameters. Regarding $R_v$, please refer to Fujimoto et al., 2015 [6].

When this study further develops and the $\mu$ estimation method proposed in this study becomes applicable to real roads, the method is expected to contribute to the optimization of de-icing agent spreading (amount, timing and location), improvements in winter road safety and reductions in winter road management costs.

## References

1. SNOW AND ICE DATABOOK – 2010 Edition, PIARC Technical Committee B5 Winter Service, 70, (2014).
2. L. Fay, M. Akin, S. Wang, X. Shi and D. Williams, Correlating Lab Testing and Field Performance for Deicing and Anti-icing Chemicals (Phase 1), Final Report, Western Transportation Institute, College of Engineering, Montana State University (2010).
3. A. Fujimoto, Y. Yamamoto, S. Tanaka, Y. Kawabata, and K. Takeichi, *Journal of Japan Society of Civil Engineers* , E1, **70**, 3, I_173-I_180 (2014).
4. A. Fujimoto, S. Yamada, S. Tanaka, N. Takahashi and K. Takeichi, *Journal of Japan Society of Civil Engineers*, E1, **71**, 2, 81-96 (2015).
5. T. Haavasoja, J. Nylander, and P. Nylander: Relation of road surface Friction and salt concentration, SIRWEC 2012, **16**, (2012).
6. A. Fujimoto, S. Yamada, S. Tanaka, N. Takahashi and K. Takeichi, *Journal of Japan Society of Civil Engineers*, E1, **71**, 3, (2015).

# Airplane braking friction on dry snow, wet snow or slush contaminated runways

Alex Klein-Paste[a,1]

[1]NTNU, dept. of Civil and Transport Engineering, Winter Maintenance Research Group, Høgskoleringen 7A, N-7491 Trondheim, Norway

**Abstract.** Airplanes need tire-pavement friction during taxiing, take-off and landing. The presence of snow reduces the friction and therefore there is need to understand how much friction can be expected on the different types of snow. This study analyses the braking performance of Boeing 737 airplanes on snow or slush contaminated runways. Airplane braking performance on runways contaminated with dry snow, wet snow and slush as analysed. The main finding is that airplanes experienced wet snow covered runways more often as very slippery, compared to slush covered runways. The fraction of the landings experiencing the conditions as "poor" or "less than poor" was significantly higher on wet snow (21%), compared to landings on slush (11%). This can be caused due to higher precipitation intensity during wet snow precipitation, or possibly because wet snow, in contrast to slush, is a compressible material that gets compacted and fills the underlying pavement texture.

## 1 Introduction

Airplanes need a certain amount of tire-pavement friction for retardation and directional control during taxiing, take-off and landing. The magnitude of the required friction depend mainly on the aircraft type, gross weight, runway length, cross wind, reversed engine thrust usage and pilot skills. The presence of snow or ice on runways reduces the available friction and therefore it is important that pilots get correct information on the prevailing runway conditions.

In aviation, snow and ice is considered as a type of runway contamination (such as oil, sand and rubber deposits) and are therefore referred to as "winter-contaminants". The available braking friction for airplanes is called the "braking action". Historically, the term originated from the subjective feeling of the pilots how well the aircraft responds (decelerates) when pressing the brake pedals. The braking action was expressed in a scale from 1 to 5, ranging from "poor" to "good" [1]. More recently the scale have been extended from 0 to 6 to indicate "less than poor" and "dry runway" respectively [2]. Nowadays it is possible to measure the braking action during the parts of the landings where the frictional conditions limit the total stopping distance [3].

Before operating on winter-contaminated runways, pilots calculate the required stopping distance based on the landing weight, wind and runway conditions. These calculations are known as performance calculations. To make the performance calculations pilots need accurate information on how much braking action can be expected. Historically, airports have estimated the braking action by conducting measurements with ground friction measurement devices (GFMD's) [4]. Unfortunately, it has proven difficult to establish a reliable correlation between actual aircraft braking performance and the readings of GFMD's on winter contaminated runways [5]. An alternative approach is to estimate the braking action based on descriptive data,

such as the type, depth and spatial coverage of the contamination. This data is collected by means of a visual inspection, conducted by the ground personnel of the airport. The Talpa-Arc matrix [2] uses type, depth and temperature to estimate the braking action. Another model, known as the IRIS runway model also includes other parameters such as coverage, use of sand and chemicals, runway temperature and dew point [6]. To support further development of these models and provide a correct situation awareness, there is still a need for better understanding how aircraft perform under real-life operational winter conditions.

The Norwegian aerodrome operator Avinor performed a five-year R&D project, called IRIS (Intelligent Runway Information System) where it collected landing data and coupled this with reported runway condition information and weather data. The present paper presents a study using this dataset to investigate the differences in braking performance on dry snow, wet snow or slush.

## 2 Method

Data was collected during the winters 2008/2009 to 2012/2013 at different airports in Norway The number of airports increased from two in 2008/2009 to 15 in 2012/2013. Data from the Quick Access Recorder (QAR) was obtained from all landings of Boeing 737-600, 700, 800, 900 models that were operated by Scandinavian Air Services (SAS) and Norwegian Air Shuttle AS.

The airplane braking coefficient $\mu_B$ was determined by a methodology described earlier [3]. In short, the total retardation force during landing is measured and the contribution of wheel braking is determined. This provides an estimate of the used friction during the landing. Only when the airplane's anti-skid system becomes activated it is certain that the airplane utilized all of the available friction and $\mu_B$ can be determined. In these cases the landing distance is limited by the

[a] Corresponding author: alex.klein-paste@ntnu.no

frictional conditions of the runway, hence denoted a friction limited landing (FL-landing). The obtained $\mu_B$ of the FL landings were interpreted into the common scale braking action scale, according to Table 1.

**Table 1.** Conversion of measured airplane braking coefficient into the common braking action scale [3].

| airplane braking coefficient | Braking action |
|---|---|
| $\mu_B > 0.2$ | 5 – good |
| $0.15 < \mu_B \leq 0.2$ | 4 – medium / good |
| $0.10 < \mu_B \leq 0.15$ | 3 – medium |
| $0.075 < \mu_B \leq 0.10$ | 2 – medium / poor |
| $0.05 < \mu_B \leq 0.075$ | 1 – poor |
| $\mu_B \leq 0.05$ | 0 – less than poor |

During operation under winter conditions, runway inspectors regularly enter the runway and report the surface conditions for each third of the runway length (called a RWY section). The frequency of these inspections varies with the conditions, but typically range in Norway between 30 minutes and eight hours. The type of the contamination (dry, wet, rime, dry snow, wet snow, slush, compacted snow, or ice), the depth (in mm), the spatial coverage (in %) and other relevant information such as the use of sand or anti-/de-icing chemicals is registered. Weather stations placed near the runway (within 500 meters) measured air temperature, runway temperature, dew point temperature and wind at one-minute intervals.

The GPS data from the QAR was used to identify on which runway section the FL state occurred and the braking friction coefficient $\mu_B$ was coupled with the observed runway condition of that section. The current size of the database is shown in Table 2. Only data from runways contaminated with dry snow, wet snow or slush with 100 % spatial coverage were used for the present analysis.

**Table 2.** Size of the landing database.

| | |
|---|---|
| Number of winter seasons | 5 |
| airports | 15 |
| landings | 117849 |
| FL-landings | 5097 |
| RWY sections* | 353547 |
| RWY sections with FL-landing | 6418 |
| Number of FL-landings on | |
| dry snow, 100% coverage | 135 |
| wet snow, 100% coverage | 382 |
| slush, 100% coverage | 221 |

# 3 Results

The measured aircraft braking coefficient on dry snow, wet snow and slush contaminated runways is plotted against runway temperature in Figure 1.
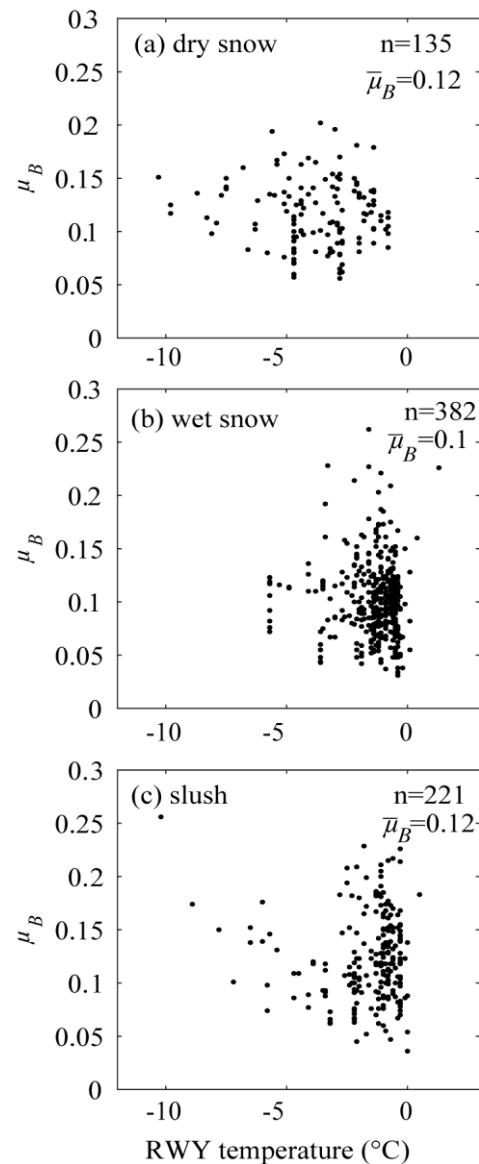


**Figure 1.** Airplane braking friction coefficient of FL landings on (a) dry snow, (b) wet snow, and (c) slush contaminated runways.

Figure 1 shows that there is a large scatter present for each type of runway contamination. The aircraft braking friction can range from below 0.05 (less than poor) to above 0.2 (good) in all three types of runway contamination. The average braking friction coefficient is very similar (ranging only between 0.1 and 0.12), but due to the large scatter, an average number has little value/meaning.

There is no clear temperature dependency visible for any of the contamination types. Again, the scatter in the data dominates the picture. Naturally, wet snow and slush mostly occur around 0°C. However, also at lower

temperatures wet snow and slush can be present due to the usage of anti-/de-icing chemicals on runways.

Figure 2 presents the distribution of the $\mu_B$, converted into the braking action scale (0-5) and the percentage of landings experiencing the runway as 0 (less than poor) or 1 (poor) is highlighted by the dashed rectangles.
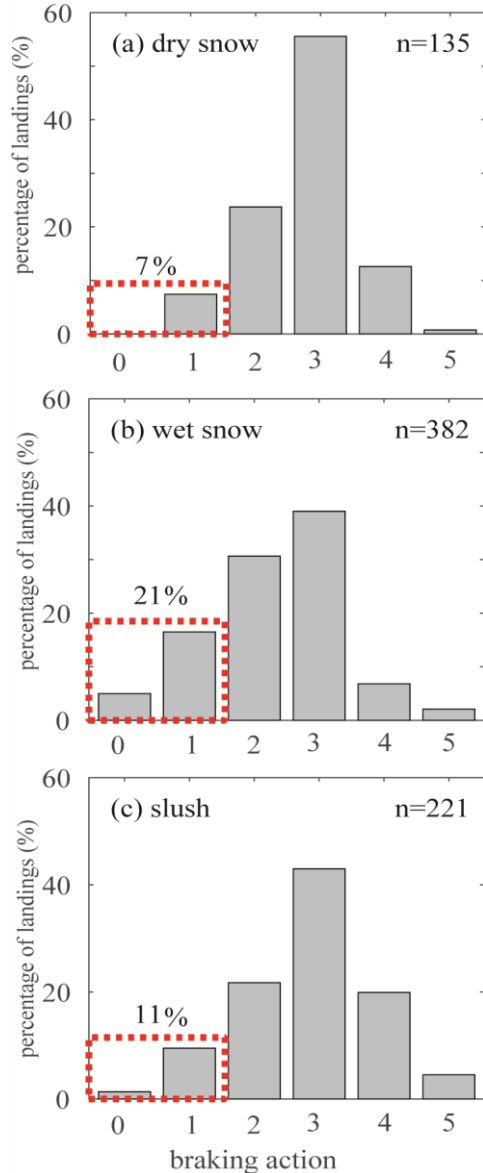


**Figure 2.** Distribution of braking action for landings on (a) dry Snow, (b) wet snow, (c) slush. The red rectangles highlight the percentage of landings experiencing the runway as "less than poor" or "poor".

On wet snow, 21 % of the landings experienced the runway as 0 or 1 (less than poor or poor). This percentage is significantly higher than on dry snow (7%) or slush (11%). Hence, the runways contaminated with wet snow were more often experienced as very slippery, compared to slush.

During operation under snowfall, airports have to close the runway regularly to perform snow clearance operation. In Norway, the runway inspector determines the need for a snow clearance operation. After the

snow/slush is removed the runway is inspected before it re-opens for air traffic. The time difference between runway inspection and landing is called the report age and expresses how long snow can have accumulated before the landing took place. The report age distribution of landings on dry snow, wet snow and slush are shown in Figure 3.
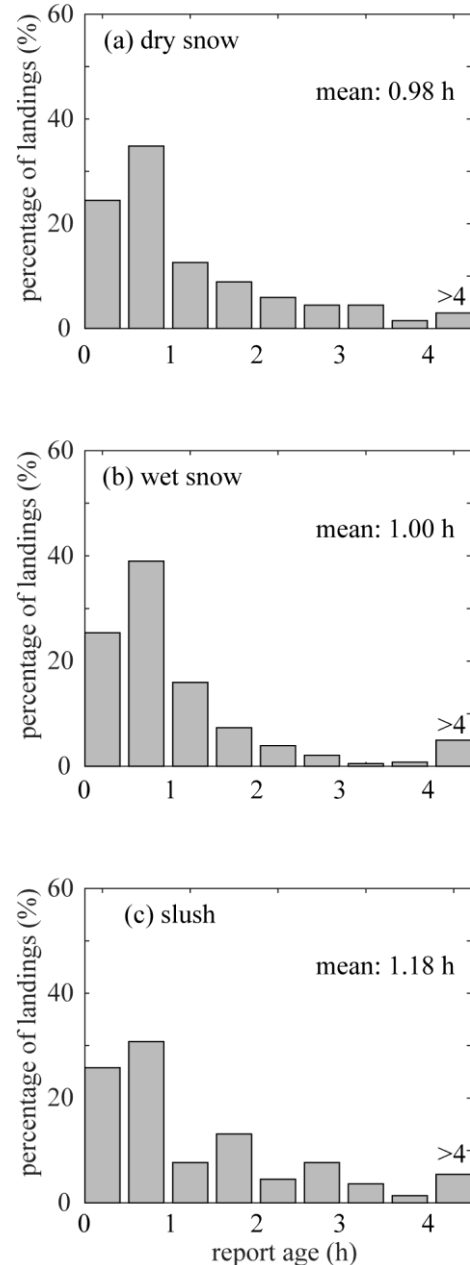


**Figure 3.** Distribution of the report ages (in hours) for the landings on (a) dry snow, (b) wet snow, and (c) slush.

Figure 3 shows that the distributions of the report ages are very similar. The average report time on slush is slightly higher (1.18 h), compared to dry snow (0.98 h) and wet snow (1.0 h). This means that there are no large differences in how long the airports maintain a runway open during precipitation of dry snow, wet snow or slush.

To calculate the amount of precipitation (in mm snow height) that had fallen between the last snow clearance and landing one needs high-resolution precipitation

intensity data and integrate the intensity over the time between snow clearance and landing. One-minute precipitation intensity data (Optic Eye precipitation sensor) was only available for 207 landings on snow/slush. For these landings the accumulated precipitation (in geometrical snow/slush depth) was calculated and presented in Figure 4. One needs to bear in mind that there are uncertainties connected to measuring precipitation rates in geometrical snow depths, particularly on such short time scales of 0-4 hours. Hence, Figure 4 cannot give a definite answer, but should be viewed as an indication based on the available information.
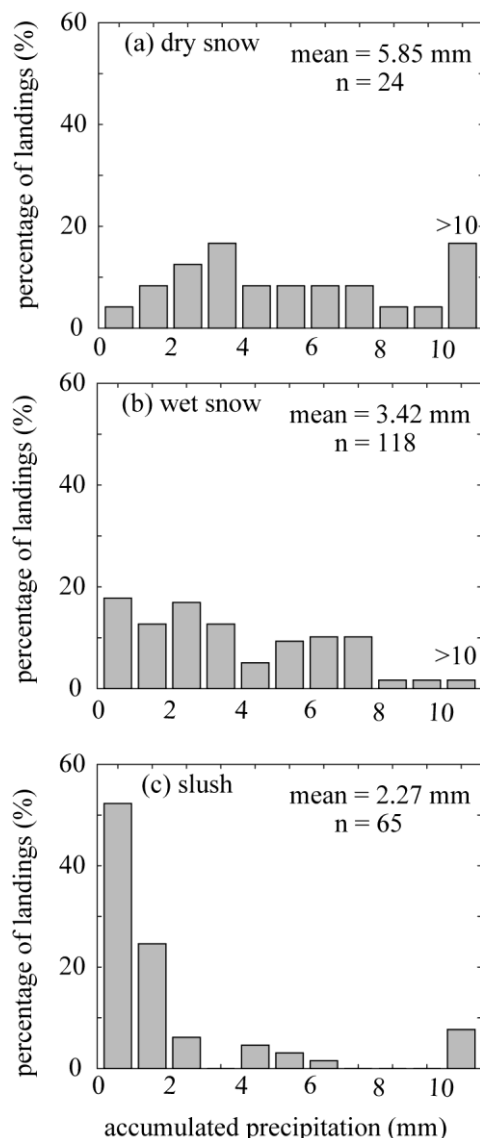


**Figure 4.** Distribution of the precipitation accumulated after the last runway condition report (in mm snow/slush depth) for the landings on (a) dry snow, (b) wet snow and (c) slush.

Figure 4 suggests that more dry snow was allowed to accumulate (on average about 6 mm), compared to wet snow (on average about 3 mm) and slush (on average about 2 mm).

# 4 Discussion

The main question that arises from this study is "why the airplanes experienced wet snow more often as "poor" or "less than poor", compared to slush?"

One explanation can be that more wet snow was allowed to accumulate, compared to slush, as suggested by Figure 4. If this is true, it is due to higher precipitation intensities, not because the airports kept the runways longer open when wet snow was present, as shown in Figure 3.

Another explanation can be that given amount wet snow on a pavement is in fact experienced more slippery, compared to the same amount of slush. This may be counter-intuitive within the aviation community, because slush has historically received more attention than wet snow. Slush mainly consists of water and ice particles and behaves like an incompressible fluid. The braking action on slush is mainly reduced because of hydroplaning. When a tire rolls on a pavement covered with an incompressible fluid, it is squeezing the fluid from under the footprint. This squeezing process generates pressures on the surface of the tire footprint [7], delaying or preventing it to get into contact with the underlying pavement. When full hydroplaning occurs it provides almost no braking action as the tire slides over the fluid film without reaching the pavement texture at all. Hydroplaning is largely speed dependent since the speed determines how much time is available for the squeeze out. However, it is also largely dependent on the fluid thickness. As long as the thickness is limited, the tire will be able to get at least partly in contact with the pavement texture and reasonably high amounts of braking action will be experienced. Since runways are regularly cleared and the accumulation of slush is limited, the danger of hydroplaning is effectively reduced.

But for wet snow, on the other hand, the way friction is lost differs from the case of slush. Wet snow is a compressible material, consisting of ice particles, water and considerable amounts of air. Being compressible, wet snow is much more difficult to squeeze out under the footprint. It rather compacts and fills the pavement texture when an external pressure is applied. An example of a thin layer of wet snow that was compacted by an aircraft tire is shown in Figure 5. The picture was made after the runway was cleared using a runway sweeper. All uncompressed wet snow was removed but the snow compacted by the tire was firmly attached to the pavement. Hence on wet snow, runways get slippery not because of hydroplaning, but because friction is created between the compacted wet snow and the tire.

**Figure 5.** Example of a thin layer of wet snow compressed by a single aircraft tire passage. The runway sweeper was able to remove all loose wet snow, but not the snow compressed by the tire. The longitudinal grooves present in the aircraft tire can be recognized in the track.

Historically, the aviation industry have had more focus on slush-contaminated runways, compared to runways contaminated with wet snow. This is partly due to the issue of increased rolling resistance and impingement drag [8], hampering take-off. But slush seems also to be considered more slippery as wet snow. This is for example reflected in the Talpa Arc matrix [2] where slush greater than 1/8 inch (approximately 3 mm) is considered as "medium-poor" whereas wet snow of the same depth is considered as "medium". This study suggest that that view may need reconsideration.

Dedicated studies under controlled conditions, comparing the reduction of braking action on similar amounts of wet snow and slush would be very helpful to understand further how and how severely braking action can be reduced due to the presence of wet snow and slush.

## 5 Conclusion

Airplane braking performance on runways contaminated with dry snow, wet snow and slush as analysed. The main finding is that airplanes experienced wet snow covered runways more often as very slippery, compared to slush covered runways. The fraction of the landings experiencing the conditions as "poor" or "less than poor" was significantly higher on wet snow (21%), compared to landings on slush (11%).

One reason for this difference can be that more wet snow had accumulated since the last snow clearance operation, as compared to slush. The airports did not keep runways contaminated with slush longer open, but the precipitation rates may have been higher during wet snowfall.

Another explanation for the difference can be that a limited amount wet snow can be experienced more slippery by airplanes, compared to the same amount of slush because the compressible wet snow gets easily compacted in the pavement texture.

## References

1. ICAO, International standards and recommended practice, Annex 15 Aeronautical Information Services Chapter 5 NOTAM. Eleventh edition ed. 2003: International Civil Aviation Organization.
2. Subbotin, N. and S. Gardner, Takeoff and Landing Performance Assessment Validation Effort of the Runway Condition Assesment Matrix. 2013.
3. Klein-Paste, A., et al., Braking performance of commercial airplanes during operation on winter contaminated runways. Cold Regions Science and Technology, 2012. 79-80: p. 29-37.
4. Andresen, A. and J.C. Wambold, Friction Fundamentals, Concepts and Methodology. 1999.
5. Boccanfuso, A. History of the Joint Winter Runway Friction Measurement Program. 2004. Transportation Development Centre, Transport Canada.
6. Klein-Paste, A., H.-J. Bugge, and A.B. Huseby, A decision support model to assess the braking performance on snow and ice contaminated runways. Cold Regions Science and Technology, 2015. 117: p. 43-51.
7. Van Es, G.W.H., Hydroplaning of modern aircraft tires. 2001, National Aerospace Laboratory NLR.
8. Giesberts, M.K.H., Test and evaluation of precipitation drag on an aircraft caused by snow and standing water on a runway. 2001.

# Engineered pavements of snow and ice

Adrian McCallum[1] and Greg White[1]

[1]University of the Sunshine Coast, Queensland, Australia

**Abstract.** The complex mechanical behaviour of snow and its propensity to vary temporally and spatially makes the engineering of pavements of snow and ice challenging. Current technologies and design methods for snow and ice runways remain largely reliant on work performed in the 1950s and 1960s. This paper examines the evolution of techniques for the engineering of runways constructed using snow and ice. It is recommended that modern engineering approaches based on conventional rigid and flexible pavement design principles be considered for ice and snow runway design. The adoption of such methods requires the development of an analytical model for the prediction of snow strength, based on snow age, temperature history and density. The use of such a model would allow contemporary engineered pavements of snow and ice to be efficiently sited and constructed. This would increase the viability and reliability of engineered snow and ice pavements across the polar regions of the world.

## 1 Introduction

Polar operations depend heavily on air transportation and support for personnel and equipment [1]. However, polar terrain, climate and material availability do not generally allow for conventional runway construction [2]. Therefore, most polar runways are constructed of ice or snow, or a combination of the two. The current technologies and design methods for snow and ice runways remain largely reliant on the work performed by the Cold Regions Research and Engineering Laboratory (CRREL) of the US Army Corps of Engineers, undertaken primarily in the 1950s and 1960s. Since that time, polar exploration, research, tourism and general interest has expanded.

Current challenges for air transportation in Antarctica include the short period for wheeled aircraft operations [3], the complex mechanical behaviour of snow and ice materials [4], the risk of short annual periods of above-freezing temperatures causing localised melting [1], glacial flow that occurs in many areas of Antarctica [5], the inability to bind compacted snow at very cold temperatures [6] and the high cost of fuel in polar areas. The limited imperative to understand snow and ice mechanics for governmental or private activities limits the motivation to address these challenges [7].

This paper examines the evolution of techniques for the engineering of runways constructed using snow and ice. Snow and ice mechanics are discussed then material characterisation and site investigation is briefly considered. Finally, historical snow and ice runway design methods are contrasted with contemporary conventional pavement design. Future work including the development of an analytical model for the prediction of snow strength, based on snow age, temperature history and density is then considered.

## 2 Historical perspectives

Aviation has existed in Antarctica since the early 1900s. However, only recently has it been considered as a possible replacement for traditional ship-borne logistics. Permanent Antarctic stations require significant volumes of large cargo that are necessarily supplied by sea. However, large numbers of personnel and lighter equipment can more efficiently be transported by air. The development of air transport systems and supporting infrastructure, especially runways, is therefore assuming greater importance [8, 9].

Both blue ice and rock runway sites have been identified in Antarctica. However, the majority of the Antarctic continent is a snow accumulation area [2] and methods to allow aircraft access to these areas is desirable. Ski-equipped aircraft for use on areas of snow have operated on the continent since the 1930s [2] and continue to be used by most Antarctic operators today. However, the advent of retractable aircraft landing gear, and the added engineering complications and expense means that equipping a modern aircraft with skis is an expensive modification; retractable skis can be used, but the use of wheeled aircraft on suitable snow runways is preferable. Unfortunately, the majority of natural snow covered areas do not provide a suitable surface for the operation of wheeled aircraft and the snow needs to be processed in order to obtain sufficient bearing capacity for wheeled aircraft.

Contemporary polar runway options include wheeled aircraft on thick (permanent) bay ice, wheeled aircraft on annual sea ice, wheeled aircraft on glacial ice, wheel aircraft on prepared snow and skiways on semi-prepared snow for use by aircraft fitted with skis [10]. Russian Ilyushin 76T aircraft have been successfully used by commercial operators at the Russian developed Novolazarevskaya and more recently at Union Glacier (originally Patriot Hills) by Antarctic Logistics and Expeditions. Australia operates a commercial A320 annually into Wilkins ice runway near Casey Station [11] and has recently completed five proof of concept flight to the Wilkins ice runway using a Royal Australian Air Force (RAAF) C-17A Globemaster. The C17A already operates into the USA controlled McMurdo Ice runway

and provides a significant increase in cargo/freight capacity compared to the A320.

The US Antarctic Program desires the construction of a wheeled C17A capable runway at the South Pole (US Antarctic Program 2012). However, techniques to develop such a runway at this location have not yet been developed.

## 3 Snow mechanics

Snow is a three-phase geomaterial consisting of ice (solid), pore water (liquid) and void air (gas). Polar snow is generally a two-phase material consisting of ice and air.

Fresh snow density is around 100 kg m$^{-3}$. As surface snow is buried, it gradually compacts, eventually becoming ice. Throughout this process the snow is increasing in both density and strength. As soon as snowflakes hit the surface, the free energy of the system tends towards a minimum, such that dendritic and irregularly shaped crystals with a large surface area are gradually transformed to rounded particles [12]. This reduction in system surface energy is the primary driving force for the process of sintering: ``a thermal treatment for bonding particles into a coherent, predominantly solid structure via mass transport events that often occur on the atomic scale'' [13]. Because the radius of an ice particle is larger than the concave radius of the bond joining it to an adjacent ice particle, there is a driving force to move mass to this concave neck area. So two previously spherical particles start tending towards a `dumb-bell' shaped particle joined by a neck, as shown in Figure 1.
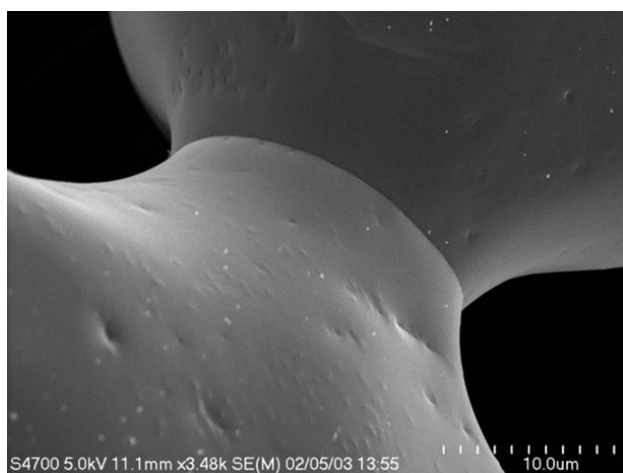


**Figure 1.** A low temperature SEM image of two ice grains, made by spraying water into liquid nitrogen, sintered at -25ºC for 216 h. The grain boundary can be seen at the neck between the particles; the particles are single crystals [13].

The bonding leads to improved strength and a lower energy system [14]. Mass redistribution occurs throughout the densification process and when occurring under additional pressure such as when snow is buried owing to accumulation, it is termed pressure sintering, and the sintering rate is increased. Although numerous processes occur throughout the pressure sintering process, not all contribute to densification [15]. Three main phases have been identified in the densification process [16]:

Stage 1. Settling and packing. Particles of ice are displaced relative to their neighbours. Bonds may initially be broken but eventually stable bonds begin to form. Alley [15] determined grain boundary sliding to be the primary mechanism during this process. The average number of bonds between ice grains (coordination number = N) has been observed to become constant (N = 6) at a relative density of approximately 0.6 [15]. This corresponds to a density of approximately 550 kg m$^{-3}$. After this, the size and strength of the bonds increase, without additional bonds being formed. Neck growth occurs rapidly initially (explaining why snow develops some strength quickly) and smaller grains sinter at a larger rate than larger grains [17]. The strongest bonds and thus strength ultimately occur from small rounded grains, which grow at a slow rate.

Stage 2. The second stage of the process occurs from a density of 550 kg m$^{-3}$ through to about 840 kg m$^{-3}$ and involves a decrease in pore space within the snow, such that interconnected pore spaces become closed. This occurs through a process of plastic deformation via power law creep combined with recrystallization [13]. Necks between grains continue to grow. However, the rate of growth decreases, and no new bonds are formed.

Stage 3. During the third stage, pores within the snow are closed and the snow is generally considered as an isothermal system; it may be described as bubbly [13] or closed-cellular [18] ice. The density during this phase increases from about 840 kg m$^{-3}$ through to the density of pore free ice at -25 ºC, 919 kg m$^{-3}$. Densification proceeds primarily by the same mechanisms as stage 2, but at a reduced rate. As the bubbles are compressed, this opposing pressure causes the process to slow.

The densification process progresses at a decreased rate in each stage, and occurs at different times throughout the year, commensurate with times of increased accumulation [19]. During densification, the microstructure or the nature of the ice grains and the physical bonding between them evolves. This evolution is influenced by the initial thermal regime within the snow, and two distinct processes have historically been used to describe this effect on grain size down to a depth of approximately 2.5 m [15].

Temperature gradient metamorphism (more recently *kinetic growth)* [20] occurs when a strong temperature gradient exists and results in rapid non-linear grain growth and a lack of cohesion. Over time this will result in coarse-grained layers with reduced density [21]. This type of snow is often seen at depth as a seasonal layer of buried surface-hoar, which has formed during a previous surface summer season when temperatures were high. When a strong temperature gradient is absent, equitemperature metamorphism (more recently *equilibrium growth*) [20] occurs. This results in surface layers experiencing slower, more linear grain growth, resulting in a finer grained layer of increased density.

Abele [22] in examining snow runway construction identified that although temperature gradient metamorphism results in an increased rate of densification and an increase in short-term strength, it is

equitemperature metamorphism that will ultimately produce a stronger pavement even though the rate of strength increase will be less. Thus although the initial strength of the snow may be less than rapidly sintered snow (nearer to 0°C), the ultimate bond strength over time will be greater. At temperatures typical at the South Pole (-25°C to -50°C) significant sintering can take months or years [22].

The primary mechanical observation is that the strength of snow is controlled by the size of the bonds between grains [17]. This is the *microstructure* of the snow, defined as the configuration of the ice and air spaces within the snow incorporating, density, porosity, specific surface area, curvature, tortuosity and coordination number [20]. The evolution of microstructure over time can be seen in Figure 2.
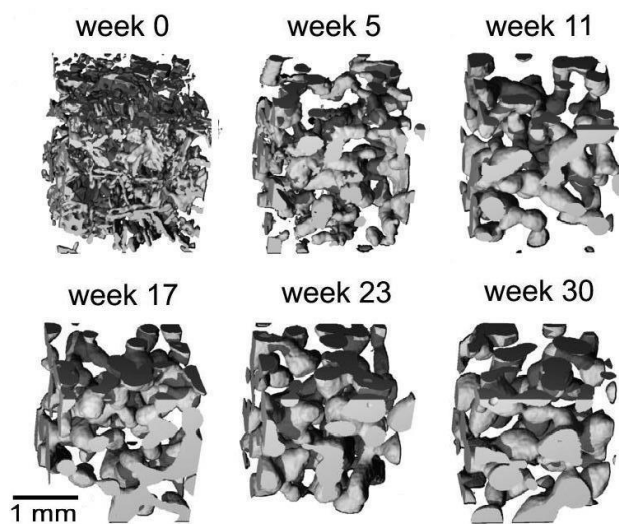


**Figure 2.** Evolution of the 3D structure of the ice matrix during isothermal metamorphism at - 1.6°C over a 30-week period. Adapted from Kaempfer [23].

It is the strength provided by this bonded microstructural matrix and not solely the density that will account for snow's mechanical behaviour. Therefore, any attempt to understand the mechanical behaviour of snow must consider both bulk density and microstructure.

Snow properties complicate snow runway design. At the South Pole, snow density rarely exceeds 360 kg m$^{-3}$ regardless of treatment or age [3]. This reflects the cold and dry nature of the snow particles at typical South Pole temperatures [6].

Snow is one of the most brittle materials known [24]. The fracture toughness of snow is two to three orders of magnitude lower than that of ice and the tensile strength of snow is also much lower than that of ice [18].

In summary, sintered snow is an aggregated mass of bonded particles of crystallized pure-water ice. The properties of snow are dependent upon the strain rate, temperature, particle size distribution and density. In turn, the density of snow is influenced by the age and temperature history throughout the sintering process. This complex mechanical behavior complicates the development of micromechanical models for snow. For practical purposes, snow remains characterised as an aggregated mixture with interdependent age, temperature and stress dependent properties.

# 4 Ice mechanics

The nature of ice reflects the mode of formation [25]. Blue ice is formed by top-down freezing of lake water and white ice results from the flooding of snow [26]. Solid sea ice is porous due to trapped air [1] and contains brine of salt water.

Pure air-free ice has a density of 920 kg m$^{-3}$ [27] and despite its freezing point, a thin layer of water-like material can be identified on the surface of ice down to -40°C [28]. Understanding this water-like film is important for explaining many other ice properties.

Like concrete, ice is strong in compression and weak in tension [29] (Figure 3). Pure ice has a tensile strength generally between 0.7 and 3.1 MPa, with an average of 1.43 MPa between -10°C and -20°C. In contrast, compressive strength is between 5 and 25 MPa over a similar temperature range [18]. Ice modulus also increases with decreasing temperature [1].
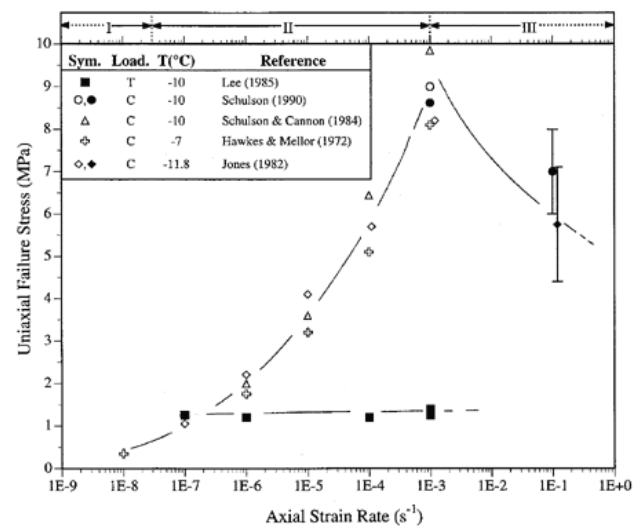


**Figure 3.** Tensile and compressive strengths of equiaxed and randomly oriented fresh-water ice of about 1 mm grain size vs. strain rate. At the top of the figure, I, II, and III denote low-, intermediate-, and high-strain rates [29].

The strength of ice is dependent upon density, temperature, grain size, brine content and strain rate. As the temperature of ice increases from -40°C to near the freezing point, the compressive strength of ice decreases by 75%. The influence of temperature on tensile strength is less, with a decrease of 25% over the same temperature increase [18]. Between -5°C and the melting point, ice is ductile and becomes prone to rapid creep during sustained strain [26]. At lower temperatures, ice has high resistance to creep [30]. However, ice is brittle. Its fracture toughness is low, at around 10% of that of glass [18].

Trapped air reduces the density of ice. At lower density, ice strength decreases, as does the modulus [1]. Increasing brine content also reduces ice modulus [1]. Brine volume is the portion of the ice that contains liquid

brine. Ice grain size also affects ice properties with a smaller grain size providing a significant increase in compressive strength [31]. In contrast, Petrovic [18] reported a decrease in tensile strength with smaller grain size.

Strain rate affects ice mechanics. Like many engineering materials, quickly loaded ice fractures while slowly loaded ice creeps [32]. The compressive strength of ice is dependent upon the strain rate ([18], [29], [33]) in contrast to the tensile strength, which is independent of strain rate ([18], [29]).

Ice is similar in many respects to other engineering materials. Like concrete, it is much stronger in compression than in tension. Similar to asphalt, ice creeps when loaded slowly, but when loaded fast, it fractures. Mechanical characterisation of ice is complicated by the proximity of polar temperature fluctuations to its melting point and the broad range of properties determined by the way in which it was formed.

# 5 Pavement design

Conventional (non-polar) runways are designed by one of two general approaches. Flexible pavements are designed based on protection of the subgrade or foundation. A combination of cover material stiffness and thickness is determined to reduce the vertical strain at the subgrade to a level that is (empirically) not expected to result in excessive permanent vertical deformation (ie. rutting).

Rigid pavements are designed similar to a floating beam or slab, using Westergaard's equations to limit the flexural stress within the slab. Protection of the subgrade is of less importance, although the subgrade provides support to the concrete base.

Snow is similar to a bonded particulate. Ice is not unlike concrete, a solid material of high compressive strength and relatively low tensile strength. It follows that snow and ice runways are designed using similar principles to conventional flexible and rigid pavements. However, unlike conventional runways, the ability to 'construct' a pavement in polar environments is limited. Importation of material is not feasible and the cost of energy is high, making any energy-intense construction method logistically difficult and cost prohibitive [10]. Further, seasonal changes and prevailing weather conditions limit constructability. For example, the thickness of some Antarctic sea ice runways is determined by the medium-term prevailing conditions. Increasing the structural capacity of such runways is impractical. Similarly, short annual periods of above-freezing temperature result in snowmelt that affects the structural capacity of coastal snow runways in Antarctica. Significant temperature differences between the Antarctic interior (generally -25°C to -50°C) and coastal areas (generally -10°C to -30°C) necessitates substantially different construction processes.

## 5.1 Historical snow pavement design

Numerous authors have shown that because of its high compressibility, the typical shear failure mechanism for snow is punching shear ([34], [35], [36]). However, traditionally, snow pavement design is founded upon the distribution and spreading of applied stresses, similar to conventional flexible pavements. Boussinesq's equation is used to estimate stress dissipation with depth [1]. Failure due to generated shear stresses must be defined; Abele et al. [38] suggesting that a 5 cm rut depth indicates a failed pavement. Although aircraft can continue to operate on snow pavements with greater rut depths, 5 cm was selected as it discriminated between stable pavement performance and rapidly accelerating failure [38].

Like flexible pavements, the contact stress at the pavement surface is critical to pavement performance. In recognition of the rapid dissipation of shear stress with depth, materials of reducing shear strength are acceptable as the depth from the pavement surface increases [38]. For conventional flexible pavements this results in lower quality materials being selected. For snow runways, the same snow is accepted at a reduced density. However, deeper snow is generally older and of higher density so without mechanical improvement, desired shear strengths are inverted with depth. This is not conducive to efficient snow runway construction.

Using empirical data derived from full scale testing, Abele and Frankenstein [1] concluded that necessary snow strength must extend to a depth equal to the radius of the tyre contact area. Repeated loading trials determined a 50% increase in snow strength was required for two aircraft repetitions within an hour. Ten repetitions required a 100% increase in snow strength [38[. Design charts were developed for common aircraft and snow strengths (Figure 4). This is similar to the US Army Corps of Engineers approach to the early design of conventional runway pavements.
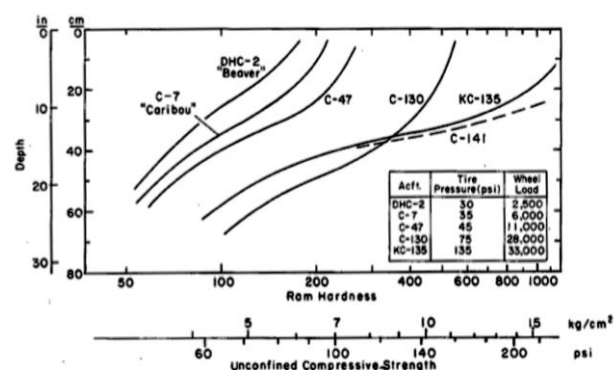


**Figure 4.** Example of snow hardness with depth required for various aircraft [22].

## 5.2 Contemporary Snow Pavement Design

Traditional snow runway design uses flexible pavement design methods developed for conventional roads and runways. Alternative stress estimation methods have

been considered for the design of polar infrastructure ([37], [38], [39] etc.). However, snow runway design still relies on estimating stresses under an aircraft tyre using Boussinesq's equation.

In contrast, conventional flexible pavement design has progressed to using layered elastic and finite element stress calculation tools. These modern layered elastic pavement design tools are yet to be applied to the design of contemporary snow runways. Such application would require an analytical method for the characterisation of snow incorporating temporal changes in snow density and microstructure. WSL Institute for Snow and Avalanche Research SLF, Davos Dorf, Switzerland has progressed large amounts of research into the temporal evolution of snow microstructure ([23] etc.) However, this work has yet to be incorporated within the contemporary design of polar snow runways.

## 5.3 Ice pavement design

Ice pavement design varies depending on the type of ice. Ice-on-ground pavement is designed to dissipate loads within the ice, thereby protecting the underlying subgrade [26]. This is similar to snow pavement design except the ice is working in flexure rather than as an aggregate mass.

However, runways on (floating) sea ice, are designed to resist tensile stresses at the bottom of the ice layer [26]. This is analogous to conventional rigid (concrete) pavement design methods. Either way, runway strength increases as ice flexural strength or thickness increases. As a 'rule of thumb' Arctic sea ice should be greater than ~70 cm for a ski-equipped Twin Otter to safely land and taxi. However, thinner ice can be viable if thicker ice can be taxied onto for parking/loading etc.

Because of the large number of variables incorporated within formal ice runway design and the contrastingly low number of ice runways in use, nomographs for ice runway design are generally runway specific. An example Landing and Take-off Nomograph for the United States' McMurdo Sound Sea Ice Runway is shown [30] (Figure 5).
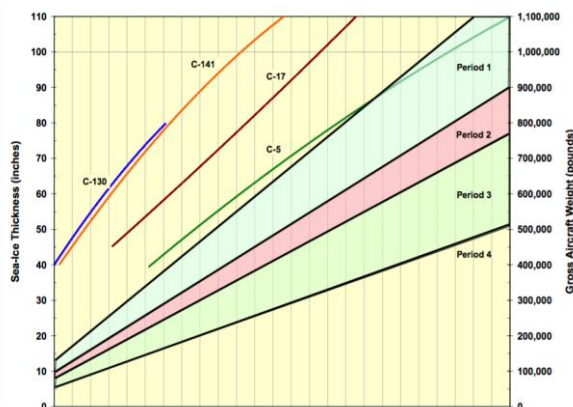


**Figure 5.** Landing and Take-off Nomograph for the McMurdo Sound Sea Ice Runway [30].

The design of McMurdo Station's annual sea ice runway is based on wheel load and contact pressure [30]. Estimated stresses are compared to the flexural strength determined from laboratory testing of extracted samples. Proof rolling is then performed to confirm pavement structural capacity. At temperatures greater than -5°C, re-testing of ice samples occurs to confirm adequacy of pavement strength.

For ice runways constructed over shallow water, the increase in pressure induced by the moving aircraft load must be considered. The shallow water pressure wave increases the stress in the ice layer by up to 50% [26]. Thicker or stronger ice is required for the portion of the runway located over the shallower water.

Ice runways are also constructed on glaciers or ice caps. Union Glacier runway in East Antarctica moves approximately 20 m per year and Wilkins glacial ice runway near Australia's Casey Station moves around 12 m per year as the ice flows downhill [40]. Differential movement at this runway is shown (Figure 6).
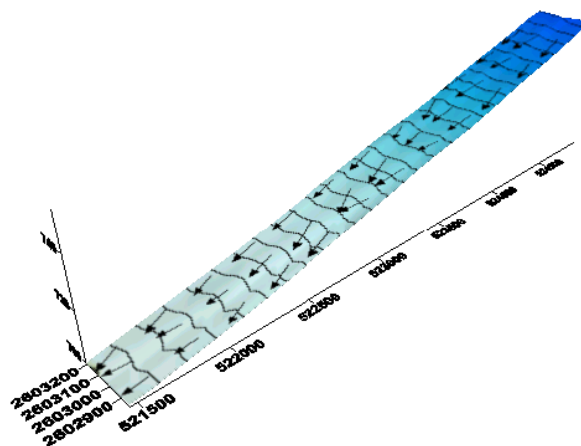


**Figure 6.** Down slope velocity vectors indicating areas of surface tension and compression within the Wilkins glacial ice runway [40].

The flow of the variable depth ice over the bedrock also distorts the runway surface, requiring periodic correction by ice milling [11]. The ice milling also reinstates frictional properties when aircraft land directly on the ice surface. Proof rolling and testing of removed samples also generally occurs on glacial ice runways.

It is also general practice to surface ice runways with a layer of snow [5]. The snow insulates the ice from solar radiation. Rubber deposits, engine soot and other small dark particles deposited on the surface cause pitting. The regular removal of this low albedo material is necessary to reduce potential for time-consuming surface repairs.

# 6 Site investigation and material characterisation

Traditionally snow has been characterised by its bearing or shearing strength. Recent attempts to develop mechanical models for snow have achieved limited success. The specific properties of snow make

micromechanical model development challenging [41]. Like bitumen and asphalt, snow behaves in a viscous or viscoplastic manner during short duration tests at natural density [4]. However, for high stress conditions of compacted and aged snow, linear elastic models are more appropriate [7]. For most polar applications, snow transitions from one state to the other and back [7]. A unified constitutive model of snow would likely be so complex that it would also be applicable to many other engineering materials [19]. As a result, the bulk density of snow is commonly used for characterisation similar to fine crushed rock for conventional pavement design [41]. Mohr-Coulomb shear-based failure models are employed by designers and engineers of snow structures ([19], [39]).

There are three primary measurement techniques for assessing the strength of snow: surface loading, sample strength testing, or probing [22]. The applicability of the test and the usefulness of the result is inversely proportional to the convenience of the test method. For example, the Australian-developed surface loading device known as the Clegg Hammer is easy and fast to operate, but its effective measurement depth is very limited. Whereas the in situ California Bearing Ratio (CBR) test is applied internationally for assessing granular material bearing capacity, but it is impractical to perform regularly in the field.

The Swiss Rammsonde has been used to estimate the strength of snow for many years [42]. More recently, numerous mini-penetrometers have been used, primarily for avalanche research and the detection of weak layers ([43], [44], [45], [46] and [47]; Floyer [48] provides a review. McCallum [49] described the use of a modified, friction-sleeve-equipped, commercial cone penetrometer to efficiently assess the strength and physical characteristics of polar snow to depths of 10 m or more and McCallum [39] examined the direct derivation of snow density and microstructure using this device. Since its development in the 1970s the Clegg Hammer, a 4.5 kg flat-faced hammer and electronic decelerometer [27] has been a valuable addition for near-surface snow bearing capacity assessment [50]. It is easy to operate in the field and has been used extensively in Antarctica ([22], [51]). The Clegg Impact Value (CIV) is calculated by the rate of deceleration of the hammer.

Correlation between Ram hardness and UCS was presented by Abele [52] and Lee at el. [6] developed relationships between Ram hardness, CBR and CIV. More recently, McCallum [39] proposed a model for direct derivation of snow compressive strength from CPT data. For significant works, a site-specific conversion between the various strength measuring devices is desirable. For example, CBR and Ram hardness may be used for design purposes, with CIV from the Clegg Hammer used for construction quality control.

Spatial extrapolation of identified snow physical properties is also possible using geophysical methods such as Ground Penetrating Radar (GPR). McCallum [53] examined the correlation between CPT tip resistance data and GPR amplitude information and Fitter et al. [54] investigated the development of UAV-mounted GPR for the rapid spatial extrapolation of point CPT resistance

data. Additionally, McCallum [55] presented a method for the direct assessment of surface snow dielectric and density values using the surface reflection method [56].

# 7 Material processing and construction

Similar to conventional pavement construction, processing the naturally occurring material is an efficient method to improve material properties and pavement performance. Such processing can be problematic because for ice runways little gain can generally be achieved and for snow pavements, acceleration or modification of the material density or microstructure can be resource intensive. However, processing techniques are proven in the particular optimisation of snow pavements.

## 7.1 Snow processing

Techniques for building runways from processed snow have been practised for more than 50 years. When snow is disturbed by agitation or disaggregation, it begins to sinter and densify at a greater rate than undisturbed snow [6] and it is this behaviour that is exploited in the construction of compressed-snow roads and runways.

Mechanical disaggregation of snow increases the density to between $250 \, \mathrm{kg} \, \mathrm{m}^{-3}$ and $500 \, \mathrm{kg} \, \mathrm{m}^{-3}$ [58]. Optimum snow strength is achieved when the snow reaches around $700 \, \mathrm{kg} \, \mathrm{m}^{-3}$ [31]. The disaggregation process improves the distribution of the snow particle size and allows sintering to occur rapidly. Snow bearing strength can be further improved by mechanical compaction during the sintering process. Timely compaction is equivalent to six days of sintering [57]. The most efficient and effective approach to snow processing is to disaggregate and compact around -2°C, followed by sintering below -10°C. However, the inability to control the snow temperature complicates snow runway construction.

To reduce reliance on favorable weather conditions there have been attempts to temporarily and artificially warm snow during the disaggregation and compaction process. A heated snow processing capability was developed but was restricted to 45 cm processing depth and fuel requirements were logistically prohibitive [57]. Localised snow warming by watering at a rate of 3 cm per 25 cm of snow thickness was found to be more efficient than direct heating of snow, but remained logistically problematic.

The first equipment developed for snow disaggregation was a modified mechanical pulveriser, capable of processing to a depth of 45 cm. The Peter Plow was introduced in the 1960s and has the capability to process snow up to 130 cm thick [1]. The Peter Plow remains the primary equipment for snow processing during runway construction [11].

Snow has also been reinforced with sawdust to improve the physical properties. Around 3 cm of sawdust was added to 15 cm of snow with some success [57]. Dark sawdust resulted in localised snow melting and white sawdust was preferred [6]. More recently snow has

been compacted into ice bricks. A pressure of 6.9 MPa was applied to a 15 cm diameter round mould filled with snow. The resulting ice bricks were strong and durable with a density of 800-900 kg m$^{-3}$ [31]. Despite these processes being viable, practical limitations have seen almost all snow runways constructed by disaggregating and compaction of naturally occurring snow [22].

## 7.2 Ice processing

There is little that can be done to improve or process ice. Fissures or cracks are filled with a slurry of ice, snow and water, that rapidly freezes. Such repairs are usually denser and stronger than the surrounding naturally occurring ice [11]. Ice has also been made by the flooding of snow with water. Although effective, it is prohibitively costly and logistically challenging to melt water in polar regions.

## 7.3 Runway construction

Ice runway construction generally includes the levelling of the existing ice and correction of cracks and fissures. Ice mills are used to provide a smooth and flat surface [11]. Across broader areas a bulldozer with a laser guided and chisel-tooled blade is common [5]. Runways with ice surfaces are maintained and corrected for changes in the ice surface level. Regular treatment with an ice mill, to provide surface texture for friction as well as the continuous removal of rubber deposited during aircraft landing, is also common [11]. During temperatures above -5°C, an insulating layer of snow is used to protect the ice against melting [30]. In areas of ample annual snow fall, the insulating layer of snow is maintained as a wearing course, negating the need to create texture and friction in the underlying ice.

Snow runway construction remains more common. This reflects the majority of Antarctica being covered with significant thickness of snow. Despite this, some areas of Antarctica are snow 'shadows' and blue ice runways are constructed, such as Australia's Wilkins Runway near Casey Station. Snow runway construction is a multiple step process including disaggregation, compaction, leveling and then sintering time. The essential construction technique is summarised by Russell-Head and Budd [27]:

1. Process the snow to depth. This disaggregation reduces the size of the ice particles within the snow to aid in more rapid densification;
2. Compaction. This process further assists in the densification and strength-gaining process; and
3. Levelling. The pavement is levelled for vehicle use.

A combination of the above construction processes may be performed at different time intervals depending on the runway location and specific site characteristics including surface temperatures, accumulation, and snow pack initial conditions. Lang et al. [58] in examining the characteristics of processed snow concluded that the generation of a robust snow pavement is best expedited by producing a well-graded, small-grained and firmly compacted section of snow.

Snow disaggregation is most commonly performed by Peter Plow for the increased processing depth capability. The Peter Plow has a closed drum with rotating cutting blades over 1.2 m in diameter and 2.7 m wide. It rotates between 225 and 305 rpm and can cut up to 1.5 m deep [57].

Planing and compacting must be performed immediately behind the processing [57]. A laser guided fine grader is used with a large volume blade. For compaction, a D8-sized bulldozer with crawler tracks has long been found to be effective [59]. Australian engineers developed a 38 tonne towed proof roller for deep snow compaction [3]. During the construction of Wilkins Runway, a larger, 60 tonne, proof roller was used [11].

The key to snow runway construction is timing [3]. Processing and compaction must be performed during periods of warm weather and then sintering permitted to occur during the colder weather. The strength of the snow must be monitored throughout the sintering process [22] and whenever the temperature or conditions change significantly.

# 8 Future needs and opportunities

The introduction of larger and more demanding aircraft creates a challenge for the operation of runways constructed from snow and ice. The empirical basis for design and performance of Antarctic runways was developed for aircraft significantly smaller than the A320 and C17A that will form the basis of future Australian aircraft operations in Antarctica [11]. Reliance on the work performed in the 1960s and 1970s requires supplementation to reflect the equipment and aircraft technology advances that have occurred since that time.

The ultimate goal for Antarctic aviation is the development of a wheeled aircraft snow runway at the South Pole [10]. This would revolutionise polar logistic capability [3]. An all-year wheeled A320 (or equivalent) capable runway anywhere in Antarctica would also be of great benefit [3]. However, the low summer temperatures (below -25°C) inhibit snow sintering. At temperatures below -18°C snow processing and compaction alone cannot produce snow capable of resisting heavy aircraft operations [6].

Any technology that allows construction of a C17A capable snow runway to be built at the South Pole would likely also provide significant capability to build and maintain coastal Antarctic airfields. Alternate methods to induce sintering at temperatures below -25°C appear to be the most viable opportunity. Laser treatment, heated roller tyres and chemical additives have been trialed, all with success. However, overcoming the logistical burden of operating in such a remote location has resulted in technically viable options remaining impractical.

# 9 Summary and recommendations

Snow and ice runway design is similar in principle to that of conventional runway pavement design: snow runways are like flexible pavements; ice runways are like rigid pavements. Challenges for polar runway design include the complicated nature of snow and ice mechanics, particularly near the melting point, as well as the inability to control or predict the temperature or thickness of the snow and ice comprising the runway pavement.

It is recommended that an analytical model for snow strength be developed from existing data. This would be age, temperature-history and density dependent. The model would form a key element in the development of a modern layered elastic design tool for snow runways. A similar ice runway design tool, based on conventional rigid pavement design, is also recommended. Finally, it is recommended that the feasibility of constructing a snow runway at the South Pole be revisited, in light of contemporary snow sintering methods. Such a runway would represent a revolutionary advance in the logistical support of Antarctic research efforts.

## References

1. G. Abele & G. Frankenstein, *Snow and ice properties as related to roads and runways in Antarctica*, Technical Report 176, Cold Regions Research and Engineering Laboratory, US Army Corps of Engineers, Hanover, New Hampshire, USA, October (1967).
2. M. Mellor, *Notes on Antarctic Aviation*, Cold Regions Research and Engineering Laboratory, Special Report 88-13, US Army Corps of Engineers, Hanover, New Jersey, USA (1993).
3. M. Mellor, *Hard-surface runways in Antarctica*, Special Report 88-13, Cold Regions Research and Engineering Laboratory, Special Report 88-13, US Army Corps of Engineers, Hanover, New Jersey, USA, August (1998).
4. J. K. Landauer, *Creep of snow under combined stress*, Research Report 41, US Army Snow Ice and Permafrost Research Establishment, US Army Corps of Engineers, Wilmette Illinois, USA, December (1957).
5. G. L. Blaisdell, R. M. Land, G. Crist, K. Kurtti, R. J. Harbin & D. Flora, *Construction maintenance and operation of a glacial runway, McMurdo Station, Antarctica*, Monograph 98-1, Cold Regions Research and Engineering Laboratory, US Army Corps of Engineers, Hanover, New Hampshire, USA, March (1998).
6. S. M. Lee, W. M. Haas & A. F. Wuori, *Improved techniques for construction of snow roads and airstrips*, Special Report 88-18, US Army Corps of Engineers, Hanover, New Jersey, USA, August (1988).
7. L. H. Shapiro, J. B. Johnson, M. Sturm & G. L. Blaisdell, *Snow mechanics: review of the state of knowledge and applications,* CRREL Report 97-3, Cold Regions Research and Engineering Laboratory,

US Army Corps of Engineers, Hanover, New Jersey, USA, August (1997).
8. A. Bergin & M. Haward, "Frozen assets: Securing Australia's Antarctic future", Technical Report 34, Australian Strategic Policy Institute, Canberra (2007).
9. E. Fogarty, "Antarctica: Assessing and Protecting Australia's National Interests", Tech. rep., Lowy Institute for International Policy (2011).
10. US Antarctic Program, *More and Better Science in Antarctica through increased Logistical Effectiveness*, Blue Ribbon Panel Report, Washington, DC, USA, July (2012).
11. M. Filipowski, 'Building and maintaining a runway in the Antarctic', *Australian Airports Association National Conference*, Hobart, Tasmania, Australia, 12-16 October, Australian Airports Association (2015).
12. W. Paterson, The Physics of Glaciers, 3rd ed., Elsevier Science Ltd., Oxford (1994).
13. J. R. Blackford, "Sintering and microstructure of ice: a review", Journal of Physics D - Applied Physics, 40(21), R355–R385 (2007).
14. R. M. German, Sintering Theory and Practice, Wiley Interscience, New York (1996).
15. R. B. Alley, "Firn Densification by Grain-boundary sliding - A 1st Model", Journal De Physique, 48(C-1), 249–256 (1987).
16. M. M. Herron & C. C. Langway, "Firn Densification - An empirical model", Journal of Glaciology, 25(93), 373–385 (1980).
17. S. C. Colbeck, "Sintering in a dry snow cover", Journal Of Applied Physics, 84(8), 4585–4589 (1998).
18. J. J. Petrovic, 'Review of mechanical properties of ice and snow', *Journal of Materials Science*, no. 38, pp. 1-6 (2003).
19. M. Mellor, *A review of basis snow mechanics*, Cold Regions Research and Engineering Laboratory, Special Report 88-13, US Army Corps of Engineers, Hanover, New Jersey, USA (1974).
20. C. Fierz, R. L. Armstrong, Y. Durand, P. Etchevers, E. Greene, D. M. McClung, K. Nishimura, P. K. Satyawali and S. A. Sokratov, "The International Classification for Seasonal Snow on the Ground", IHP-VII Technical Documents in Hydrology 83, UNESCO-IHP, Paris. IACS Contribution No. 1 (2009).
21. U. Rick, & M. Albert, "Microstructure of West Antarctic Firn and Its Effect on Air permeability", Technical Report 04-16, US Army Cold Regions Research and Engineering Laboratory, Hanover (2004).
22. G. Abele, *Snow roads and runways, Monograph 90-3*, Cold Regions Research and Engineering Laboratory, US Army Corps of Engineers, Hanover, New Hampshire, USA, November (1990).
23. T. U. Kaempfer & M. Schneebeli, "Observation of isothermal metamorphism of new snow and interpretation as a sintering process", Journal Of Geophysical Research- Atmospheres, 112(D24). 0148-0227 D24101 (2007).

24. H. O. K. Kirchner, "Brittle fracture of snow", Physical Aspects of Fracture. Proceedings of the NATO Advanced Study Institute on Physical Aspects of Fracture, 47–57 (2001).

25. S. R. Stearns, *Flexural properties of snow and snow-ice*, Special Report 59, US Army Corps of Engineers, Hanover, New Jersey, USA, October (1964).

26. D. M. Masterson, 'State of the art of ice bearing capacity and ice construction', *Cold regions Science and Technology*, no. 58, pp. 99-112 (2009).

27. D. S. Russell-Head & W. F. Budd, *Compacted-snow runways: guidelines for their design and construction in Antarctica*, Special Report 89-10, US Army Corps of Engineers, Hanover, New Jersey, USA, April (1989).

28. D. Szabo & M. Schneebeli, 'Subsecond sintering of ice', *Applied Physics Letters*, no. 90, paper 151916, pp. 1-3 (2007).

29. E. M. Schulson, *Creep and Fracture of Ice*, JOM, 51 (2) (1999), pp. 21-27 (1999).

30. J. L. Greene, W. G. Schauz & G. L. Blaisdell, *Design construction, maintenance and evaluation of the McMurdo Sound (Antarctica) sea ice runway for heavy wheeled aircraft*, Engineering Technical Letter, AFCESA-TR-2006-0012, Air Force Civil Engineering Support Agency, Tyndall Air Force Base, Florida, USA, July (2006).

31. D. Diemand & V. Klokov, *A method for producing fine-grained ice from snow by compaction*, ERDC/CRREL TR-01-12, Cold Regions Research and Engineering Laboratory, US Army Corps of Engineers, Hanover, New Hampshire, USA, August (2001).

32. E. M. Schulson & P. Duval, *Creep and Fracture of Ice*, Cambridge University Press, Cambridge, UK (2009).

33. H. Kim & J. N. Keune, 'Compressive strength of ice at impact strain rates', *Journal of Material Science*, no. 42, pp. 2802-2806 (2007).

34. G. J. Irwin, A. M. O. Mohamed, S. Alammawi & R. N. Yong, "Prediction of load carrying capacity of deep snow by rammsonde hardness", Journal of Terrame- chanics, 28(2-3), 167 (1991).

35. S. A. Shoop & R. Alger, "Snow deformation beneath a vertically loaded plate formation of pressure bulb with a limited lateral displacement", in: "Ninth International conference on Cold Regions Engineering", American Society of Civil Engineers, Duluth, pp. 143 – 150 (1998).

36. J. H. Lee & W. Wang, "Characterization of snow cover using ground penetrating radar for vehicle trafficability - Experiments and modeling", Journal Of Terramechanics, 46(4), 189–202. ISI Document Delivery No.: 491NE Times Cited: 0 Cited Reference Count: 28 English Proceedings Paper 0022-4898 Sp. Iss. SI (2009).

37. J. Weale & G. L. Blaisdell, Settlement of a Large Structure on Polar Firn. Cold Regions Engineering 2006: pp. 1-11 (2006).

38. M. Geduhn & D. Enss, "Bearing capacity of 20 single column shallow foundations of the Antarctic Station Neumayer III over 30 years service life", in:

"The 25th International Conference on Offshore Mechanics and Arctic Engineering OMAE, CCH Hamburg", American Society of Mechanical Engineers, Hamburg (2006).

39. A. B. McCallum, 'Cone Penetration Testing (CPT): a valuable tool for investigating polar snow', Journal of Hydrology (NZ), Vol. 52, No. 2, pp. 97-113 (2013).

40. A. B. McCallum, 'Movement and Expected Lifetime of the Casey ice runway', *13th International Conference on Cold Regions Engineering*, Orono, Maine, USA, 23-26 July, American Society of Civil Engineering, pp. 1-19 (2006).

41. C. Scapozza & P. Bartelt, 'Triaxial tests on snow at low strain rate: part II constitutive behaviour', *Journal of Glaciology*, vol. 49, no. 164, pp. 91-101 (2003).

42. R. Haefeli, "Beitrge zur Gologie der Schweiz Geotechn.", Serie-Hydr, 3 (1936).

43. T. Dowd & R. L. Brown, "A New Instrument For Determining Strength Profiles In Snow Cover", Journal Of Glaciology, 32(111), 299–301. 0022-1430 (1986).

44. R. L. Brown & K. W. Birkeland, "A comparison of the digital resistograph with the ram penetrometer", in: "International Snow Science Workshop", Bigfork, Montana, pp. 19–30 (1990).

45. M. Schneebeli & J. B. Johnson, "A constant-speed penetrometer for high- resolution snow stratigraphy", Annals of Glaciology, 26, 107–111 (1998).

46. R. Mackenzie & W. Payten, "A Portable, Variable-Speed, Penetrometer for Snow Pit Evaluation", in: "International Snow Science Workshop", Penticton, p. 7 (2002).

47. J. Christian, S. Whittemore, B. Markle, T. Laakso & A. Sohn, Avatech: The first portable, web connected snow penetrometer for professionals, Proceedings, International Snow Science Workshop (2014).

48. A. J. Floyer, "An update on digital penetrometer technology", University of Calgary, Applied Snow and Avalance Research (2006).

49. A. B. McCallum, 'Cone Penetration Testing (CPT) in Antarctic firn: an introduction to interpretation', *Journal of Glaciology*, vol. 60, no. 219, pp. 83-93 (2014).

50. B. Clegg, 'An impact testing device for in situ basecourse evaluation', 8th Australian Road Research Board Conference, Perth, Western Australia, Australia, pp. 1-6, Australian Road Research Board (1976).

51. S. Shoop, M. Knuth & J. Crandell, 'Using a Clegg Impact Hammer to Measure Snow Strength', In *Proceedings of the 15th International Specialty Conference on Cold Regions Engineering*, Quebec City, Canada, 19-22 August, Morse, B & Dore, G (eds), pp. 811-822 (2012).

52. G. Abele, A correlation between unconfined compressive strength and Ram hardness of processed snow, Technical Report 85, Cold Regions Research and Engineering Laboratory, US Army Corps of

Engineers, Hanover, New Hampshire, USA, January (1963).

53. A. B. McCallum, Cone Penetration Testing in Polar Snow, PhD Thesis, University of Cambridge (2012).

54. J. Fitter, A. B. McCallum & J. L. Patino, UAV-mounted GPR for remote area site investigation, Proceedings 5th International Conference on Geotechnical and Geophysical Site Characterisation, Gold Coast, Australia, September (2016).

55. A. B. McCallum, 'Estimating snow density from dielectric values measured using the surface reflection method', Journal of Hydrology (NZ), Vol. 53, No. 2, pp.179-183, (2014b).

56. T. Sarrenketo & T. Scullion, Road evaluation with Ground-Penetrating Radar, Journal of Applied Geophysics, 43, 119–138 (2000).

57. G. Abele, R. O. Ramseier & A. F. Wuori, *Design criteria for snow runways*, Technical Report 212, Cold Regions Research and Engineering Laboratory, US Army Corps of Engineers, Hanover, New Hampshire, USA, November (1968).

58. R. M. Lang, G. L. Blaisdell, C. Durso, G. Reinemer & M. Lesher, "Processing snow for high strength roads and runways", Cold Regions Science and Technology, 25(1), 17–31 (1997).

59. A. F. Wuori, *Snow stabilization using dry processing methods*, Technical Report 68, USA Snow, Ice and Permafrost Research Establishment, July (1960).

# Performance of remote road surface sensor on different pavement types

Naoto Takahashi [a], Kenji Sato and Roberto Tokunaga

*Civil Engineering Research Institute for Cold Region, Traffic Engineering Research Team, 1-3 Hiragishi, Toyohira-ku, Sapporo, Japan*

**Abstract.** It is important to correctly understand the road surface conditions, so that tactical decisions on the delivery of winter services can be made. Recent advances in sensing technologies have put non-invasive surface state sensors into practical use. These non-invasive sensors are able to remotely measure road surface conditions from the side of the road or from winter service vehicles. Although the sensors' abilities have been tested under various conditions, no studies are known to have addressed the reliability of the sensors on different pavement types. This study aims to test the performance of such sensors on different pavement types. The test was conducted at a test track that is paved with dense-graded asphalt, porous asphalt and stone mastic asphalt. As the non-invasive sensor, we used the Vaisala remote surface state sensor (DSC-111), which optically measures the layer thickness of water/snow/ice on the road and gives an estimation of grip level. In this study, wet and thin-ice surfaces were artificially created on the test track, and the grip levels obtained by the DSC-111 were compared with the friction values obtained by a continuous friction tester. The layer thickness values obtained by the DSC-111 were compared with those measured with a NASA water-film depth gauge.

## 1 Introduction

It is important to correctly understand the road surface conditions, so that tactical decisions on the delivery of winter services can be made and appropriate winter maintenance can be implemented. Among the most widely used tools for monitoring winter road surface conditions are road weather information systems (RWIS) [1], which are networks of weather monitoring sensors along roads. At these stations, valuable road weather data such as road surface temperature, air temperature, wind velocity and snow accumulation are collected and provided via Internet to maintenance staff in order to support decision-making [2]. However, the amount of information provided by the RWIS is still limited. Technically, data are collected only at specific locations where sensors are installed [3]. Besides, in most cases, we need to install sensors in the road.

Another approach to determining the state of the road surface involves measuring the road surface friction. This method has been used in the field by a number of road agencies, and it is widely adopted by airport authorities [4]. Various friction-measuring devices have been developed and tested by road agencies and researchers [5]. Friction has mainly been measured directly, by determining the frictional force produced from contact between the tire and the road surface. Since this method requires contact between a tire and the road surface, the measurement results are influenced by the type of vehicle and tire; what is more, the direct method cannot measure friction when the vehicle is stationary.

Recent advances in sensing technologies have put non-invasive surface state sensors into practical use. These non-invasive sensors are able to remotely measure road surface conditions from the side of the road or from winter service vehicles, and to provide cost and operational savings by eliminating the need to install anything in the road or to add any measuring mechanisms to the host vehicle.

Although the sensors' ability to provide reliable data has been tested and reported under various conditions (e.g., [6 - 14]), no studies are known to have addressed the reliability of the sensors on different pavement types. This study aims to test the performance of such sensors on different pavement types.

## 2 Study method

### 2.1 The devices compared in the study

In this study, a continuous friction tester (CFT) and the Vaisala remote surface state sensor (DSC-111) were tested. The CFT calculates friction by measuring the axial force created by a measuring wheel installed at a 1- to 2-degree skew from the direction of travel. A friction value computed in this way is referred to as a Halliday friction number (HFN). The HFN scale was established by the device's designer, and it usually ranges from 0 to 100. The smaller the HFN value is, the more slippery the road surface is.

The DSC-111 optically measures the thickness of water/snow/ice on the road surface and gives an estimated grip level on a scale of 0.0 to 1.0. A test vehicle equipped with the CFT and the DSC-111 was used to compare the measurement results (Figure 1).



**Figure 1.** Test vehicle equipped with the CFT and the DSC-111

[a] Corresponding author: takahashi-n24k@ceri.go.jp

## 2.2 Experiment site

The test was conducted at a test track of our institute. The test track is 2,700 m in circumference, and its 1,200-meter straightaway, which is paved with dense-graded asphalt (DGA), porous asphalt (PA) and stone mastic asphalt (SMA), was used.

## 2.3 Test conditions

On the straightway of the test track, wet and thin-ice surfaces were artificially created, in addition to the dry surface (Figure 2). The length of each road surface condition was set to be 100 meters (Figure 3).

The wet surfaces were created by applying water to the dry surface with a road sprinkler. The thickness of the water layer was set to be from 0.5 to 1.0 mm on the DGA.

The water thickness was measured with a NASA water-film depth gauge (Figure 4). The thin-ice surface was created by sprinkling water when the air temperature was below zero (thickness: 0.5 to 1.0 mm on the DGA).

Table 1 shows the test conditions. The test was conducted for 3 days. On the first day of the experiment, calibration of the DSC-111 (so-called "dry signals") was conducted on the DGA. On the second day, dry signals were conducted on the SMA, and then, dry signals were conducted on the PA on the final day of the test. Unfortunately, on the first day of the test, there was a passing shower after calibration. Therefore, we were unable to obtain data for dry surfaces in the case where dry signals were conducted on the DGA.



**Figure 2**. Road surface conditions used for the test.
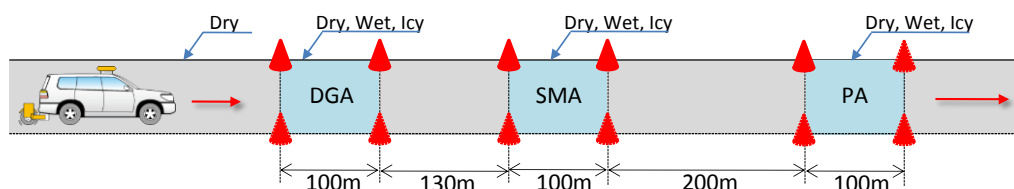


**Figure 3.** Test track layout.



**Figure 4**. Creation of the wet surfaces (left) and measurement of water thickness with the NASA water-film depth gauge (right).

**Table 1.** Test conditions.

| Date | 21-Jan-15 | 26-Jan-15 | 28-Jan-15 |
|---|---|---|---|
| Weather | Clear | Clear | Clear |
| Time | 14:50 ~ 18:51 | 14:01 ~ 20:02 | 14:01 ~ 18:03 |
| Air Temp. (℃) | -4.4 ~ 4.1 | 1.3 ~ 9.3 | -6.3 ~ 1.9 |
| Surface Temp. (℃) | -4.2 ~ 5.9 | -1.3 ~ 9.0 | -6.4 ~ 7.0 |
| Dry signals | DGA | SMA | PA |
| Surface conditions | Wet / Icy | Dry / Wet / Icy | Dry / Wet / Icy |
| Driving speed (km/h) | 20 | 20 | 20 |

A test vehicle equipped with both devices ran on these surfaces at 20 km/h to compare the HFN values obtained from the CFT with the grip levels determined by the DSC-111. Takahashi et al. reported that the data obtained by the DSC-111 are influenced by the driving speed of the host vehicle, especially on the wet and compacted-snow surfaces [14].

It is assumed that the water and snow kicked up by the test vehicle's tires might have influenced the evaluation of water and snow layer thickness. Therefore, the driving speed of the host vehicle was set to be 20 km/h to minimize the influence of driving speed.

## 3 Test Results

Figure 5 shows an example of measurement results on the wet and icy surfaces. In Figure 5, dry signals were carried out on the section paved with DGA. Although DSC-111 locally detected the ice layer on the section paved with DGA and the section paved with PA, and gave low grip levels on the wet surface, both the HFN and the grip level showed high values on the wet surfaces.

As shown in Figure 5, lags were found in the decrease in the grip level and the detection of the water, snow and ice layer relative to HFN values determined by the CFT. Takahashi et al. [14] conducted a time lag analysis. The study found that the time lag between measurement and output ranges from 4 to 10 seconds and that the time lag is unaffected by the driving speed of the host vehicle.

### 3.1 Measurement results for dry surfaces

Figure 6 (a) shows HFN values and the grip levels for the dry surface in the case where calibration of the DSC111 was conducted on the SMA, and Figure 6 (b) shows those in the case where dry signals were conducted on the PA.
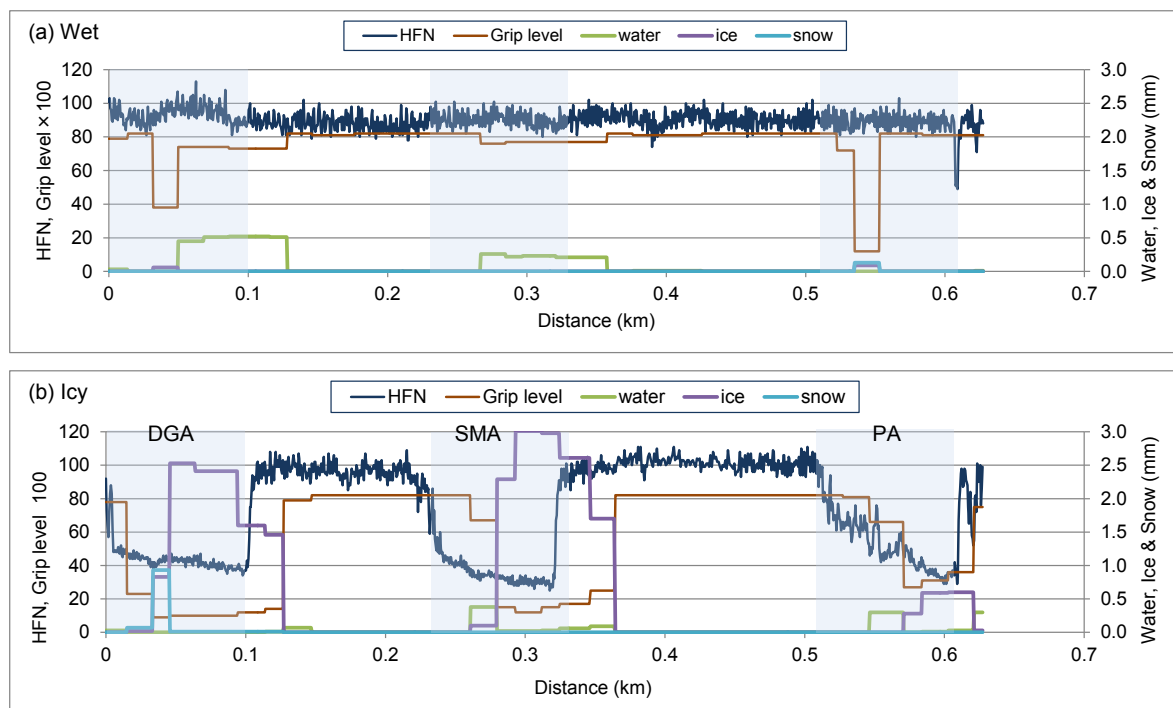


**Figure 5**. Example of measurement results. (a) wet, (b) icy
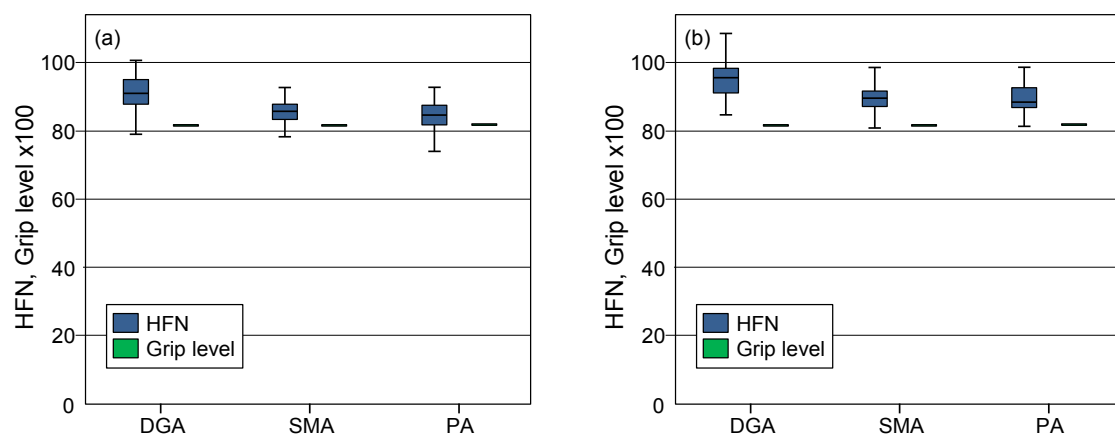


**Figure 6**. Measurement results for dry surfaces.

Since the time lag between the measurements and outputs had a maximum value of 10 sec., the figures were made by excluding the data of the first 10 sec. to eliminate the influence of the time lags.

As shown in the figure, the HFN showed high values on the dry surface, and the HFN for the DGA showed higher values than those for SMA and PA. It is considered that the rough surface of the SMA and the PA reduces friction-generating contact between the pavement and the tire. The grip levels also showed high values. Measurement results for the dry surface were not influenced by the pavement type on which dry signals were conducted. In contrast to the HFN values, the grip levels are consistent regardless of pavement type.

On the dry surfaces, the DSC-111 detected no water, snow or ice.

## 3.2 Measurement results for wet surfaces

Figure 7 shows the measurement results for the wet surface in the case where dry signals were conducted on the DGA. Figure 7 (a) represents the HFN and the grip level, and Figure 7 (b) represents the thickness of water, snow and ice layers detected by the DSC-111.

The HFN values for the wet surface were high, and they showed the same tendency as those for the dry surface.

The grip levels for the SMA were higher than those for the DGA, and the grip levels for the PA represented even higher values than those for the SMA. The results can be attributed to the thickness of water obtained by the DSC-111.

As shown in Figure 7 (b), the water layer on SMA is thinner than that on DGA. It is considered that the rough surface of the SMA traps some of the water. The water layer on the PA showed an even smaller value than that on the SMA. It is considered that the rough and drainable surface of the PA reduces the amount of water on the pavement surface.

Figure 8 shows the measurement results for the wet surface in the case where dry signals were conducted on the SMA. Although the DSC-111 locally detected snow on the DGA and gave a low grip level, the grip levels and the thickness of water, snow and ice in the case where dry signals were conducted on the SMA were generally high and showed the same tendency as those when dry signals were conducted on the DGA.

Figure 9 shows the measurement results for the wet surface in the case where dry signals were conducted on the PA. The grip levels and the thickness of water, snow and ice in the case where dry signals were conducted on the PA showed the same tendency as those when dry signals were conducted on the DGA and on the SMA.
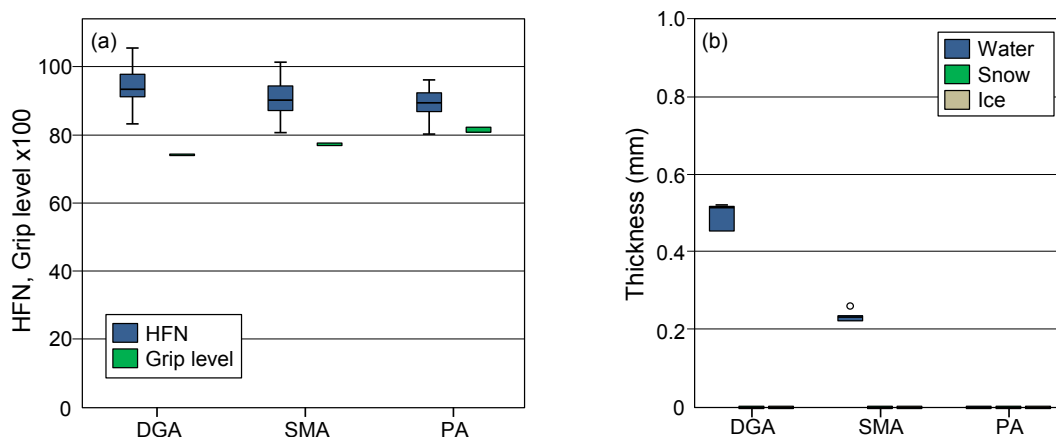


**Figure 7**. Measurement results for wet surfaces (dry signals: DGA).
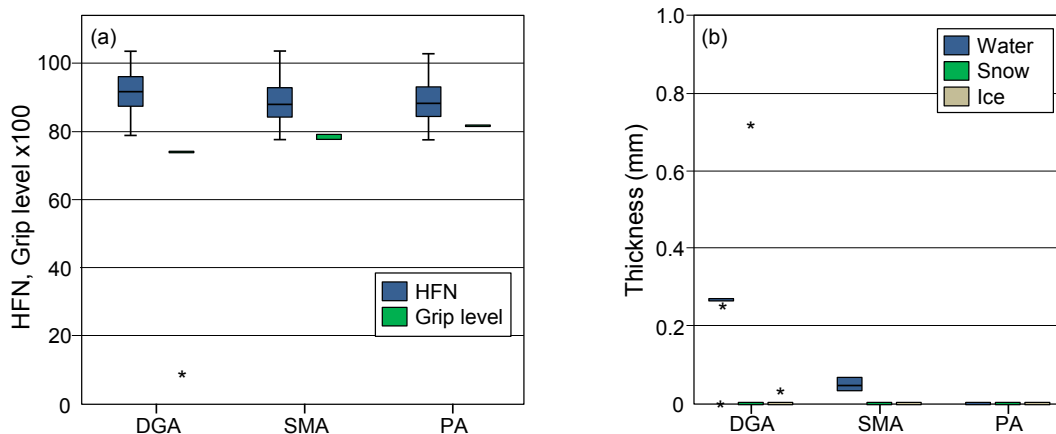


**Figure 8**. Measurement results for wet surfaces (dry signals: SMA).
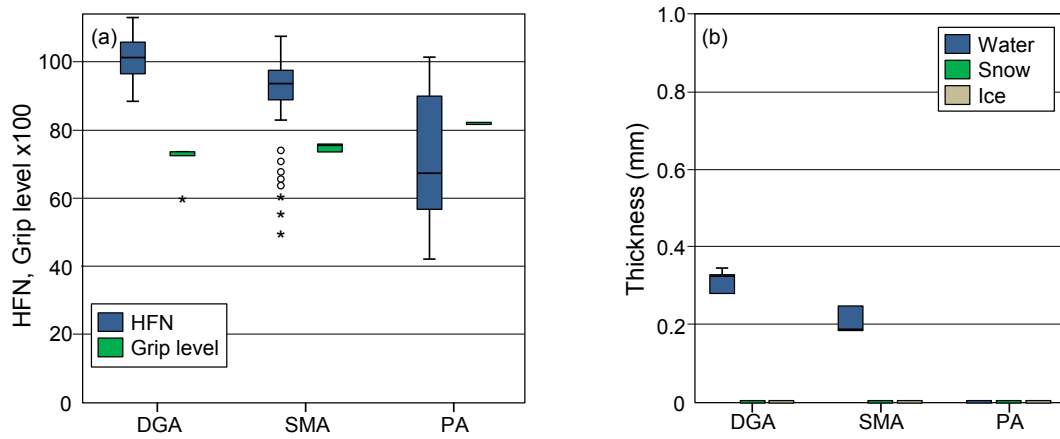
**Figure 9**. Measurement results for wet surfaces (dry signals: PA).

## 3.3 Measurement results for icy surfaces

Figure 10 shows the measurement results for the icy surface in the case where dry signals were conducted on the DGA.

As shown in the Figure 10 (a), both the HFN and the grip level showed low values on the icy surface. The grip levels for the PA showed higher values than those for the DGA and the SMA. The result was attributed to the ice layer thickness on the PA, which was thinner than that on SMA and DGA. The well-draining surface of the PA was thought to reduce the amount of water on the pavement surface.

On the other hand, the thickness of the ice layer on the SMA obtained by the DSC-111 was greater than the actual value. It is considered that the DSC-111 might have detected the ice within the voids in the SMA.

Figure 11 shows the measurement results for the icy surface in the case where dry signals were conducted on the SMA. Although the HFN values showed the same tendency as those when dry signals were conducted on the DGA, the grip levels showed high values relative to those when dry signals were conducted on the DGA (Figure 11 (a)).
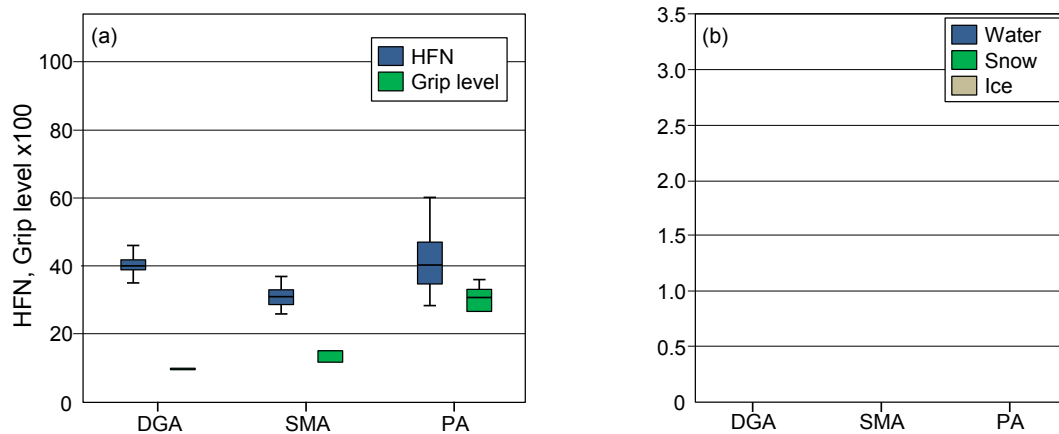


**Figure 10**. Measurement results for icy surfaces (dry signals: DGA).
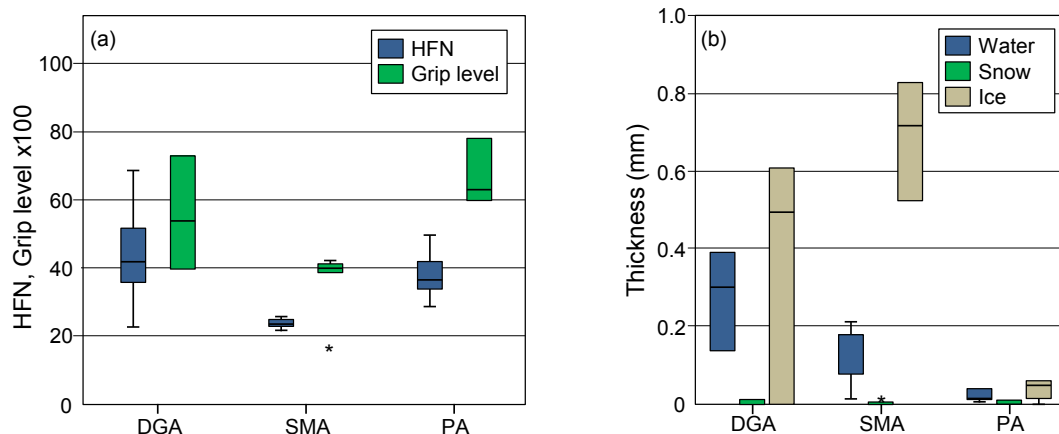


**Figure 11**. Measurement results for icy surfaces (dry signals: SMA).

As shown in Figure 11 (b), the DSC-111 detected not only ice but also water. It is considered that the water did not totally freeze under the condition of the lowest surface temperature of -1.3 degrees Celsius. Therefore, the DSC-111 might have detected both water and ice on the DGA and the SMA, and might have detected small amounts of water and ice on the PA because of its well-draining surface. And the water on the pavement surface might influence the estimation of the grip level.

Figure 12 shows the measurement results for the icy surface in the case where dry signals were conducted on the PA. Both the grip levels and the thickness of water, snow, and ice in the case where dry signals were conducted on the PA showed the same tendency as those when dry signals were conducted on the DGA.

### 3.4 Influence of pavement types on which dry signals were conducted

Figure 13 summarizes the results of measurement for each surface. In these figures, the vertical axis represents average grip levels for each pavement type. For both dry and wet surfaces, the grip levels are consistent. The dry signals were found to have little influence on the measurement results, regardless of the pavement type on which dry signals were conducted.

For the icy surfaces, the grip levels for each pavement type were high when dry signals were conducted on the SMA, relative to those when dry signals were conducted on DGA and on PA.

The cause is unclear, but relatively high surface temperature is considered to be the cause. It is considered that the water did not totally freeze under the condition of the lowest surface temperature of -1.3 degrees Celsius and that the water on the pavement surface influenced the estimation of the grip levels.



**Figure 12**. Measurement results for icy surfaces (dry signals: PA).
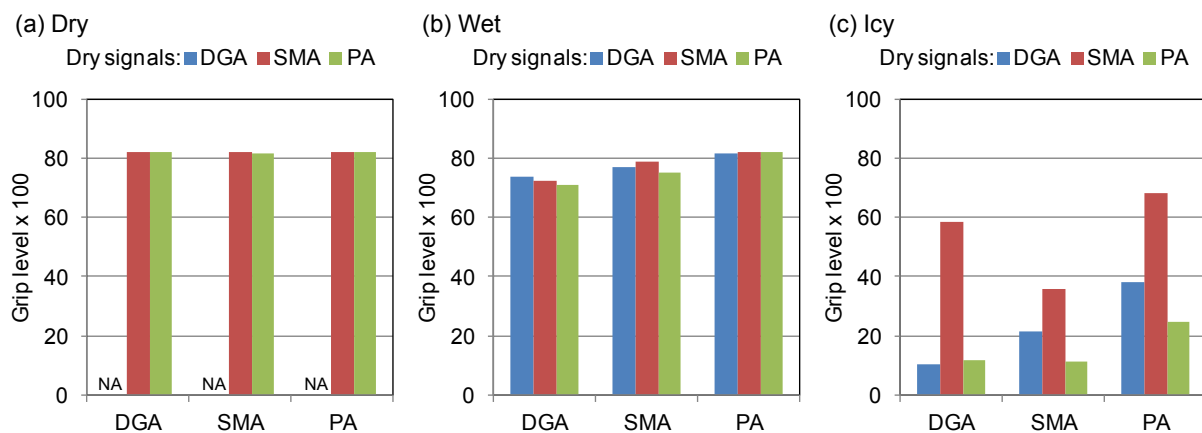


**Figure 13**. Average grip levels for each pavement type.

## 4 Conclusions

The study results are summarized here.

(1) Grip levels are generally consistent for each surface and correspond to the friction values obtained by the CFT. The precision is good enough to discriminate between the different surfaces.

(2) The thickness of the ice layer on the SMA obtained by the DSC-111 was occasionally greater than the actual value. The cause of this is unclear, but it seems that the DSC-111 might have detected the ice within the voids in the SMA.

(3) The pavement type on which calibration of the DSC-111 was conducted has little influence on the measurement results, except on the icy surface when dry signals were conducted on the SMA. It is assumed that the water did not totally freeze under the condition of the lowest surface temperature of -1.3 degrees Celsius and that the amount of water and ice influenced the estimation of the grip level.

## Acknowledgements

## References

1. PIARC Technical Committee B5 Winter Service, *SNOW AND ICE DATABOOK 2010* (2010)

2. K. Toivonen and J. Kantonen, *Web-based Distribution of Road Weather Information to Winter Road Maintenance Contractors in a Multiple Contractor Environment*, 11th International Road Weather Conference (2002)

3. C.K. Strong and X. Shi, *Integrating Weather into Transportation Operations: A Utah Department of Transportation Case Study*, Transportation Research Board, E-C **126**, pp 318-333 (2008)

4. I.L. Al-Qadi, A. Loulizi, G. Flintsch, D.S. Roosevelt, R. Decker, J.C. Wambold, and W. Nixon, *Feasibility of Using Friction Indicators to Improve Winter Maintenance Operations and Mobility*, NCHRP Web Document **53** (Project 6-14) (2002)

5. Transportation Association of Canada, *Winter Maintenance Performance Measurements Using Friction Testing* (2009)

6. F. Feng, L. Fu and M. Perchanok, *Evaluation of Two New Vaisala Sensors for Road Surface Conditions Monitoring*, University of Waterloo and Ontario Ministry of Transportation (2007)

7. T. Haavasoja, V. Haavisto, P. Nylander, Y. pilli-Sihvola and K. Toivonen, New approach to road weather : Measuring slipperness, 13th International Road Weather Conference (2006)

8. F. Feng, L. Fu and M.S. Perchanok, *Evaluation of two new Vaisala sensor for road surface conditions monitoring*, University of Waterloo and Ontario Ministry of Transportation (2007),

9. P. Bridge, Noninvasive road weather sensors, Transportation Research Board, E-C **126**, pp.407-415 (2008)

10. P. Jonsson, Road status sensors a comparison of active and passive sensors, 16th ITS World Congress (2009)

11. L. Ewan, A. Al-Kaisy and D. Veneziano, *Remote sensing of weather and road surface conditions : Is Technology Mature for Reliable Intelligent Transport System Applications?*, Transportation Research Record, No. **2329**, pp. 8-16 (2013)

12. D. Jensen, B. Koeberiein, E. Bala and P. Bridge, Ensuring and quantifying ITS return on investment through the development of winter maintenance performance measures, 20th ITS World Congress (2013)

13. T. Vaa, Remote sensing of road surface conditions and ITS applications, 20th ITS World Congress (2013)

14. N. Takahashi, M. Kiriishi and R. Tokunaga, *Cmparative study of friction measurement devices,* 14th International Road Weather Conference (2014)

# Poster session

# The protection of roads from blizzards

Tatiana Samodurova[a], Olga Gladysheva, Jurij Baklanov and Konstantin Panferov

*Voronezh State University of Architecture and Civil Engineering, Russia*

**Abstract.** The problems of snow protection designing of roads from blizzards snow were studied. The classification of snow protection was given. The type of snow protection depends on the blizzards parameters: blizzards intensity and duration, snow transfer volume and snowbring volume to the road. The mathematical models to determine the blizzards parameters for problem solving of protecting and cleaning the roads from snow were proposed. The meteorological data are used for calculations. The method of statistical processing was given. The study proposes to calculate the snowbring volume to the road for the winter period and for the single blizzard to design of snow protection. It is also recommended to take into account the losses of snow volume from evaporation and melting during thaw. The modeling results were verified by experiments on separate road sections. The comparison of modeling results with special snow surveys showed a high resemblance. The calculation results are presented in a series of road climatic maps. The realization of the study results by using GIS technology was proposed.

## 1 Introduction

Snowdrifts often form on the roads of Russia after blizzards in winter. Snowdrifts reduce the vehicle speed, worsening traffic conditions. Traffic interruptions occur during the intense and prolonged blizzards. In order to conduct effective snow-related maintenance of roads, it is necessary to know the estimated blizzards parameters (blizzards intensity and duration, volumes of snow drifting and snow accumulation on the roads)

The presented paper is focused on the systematic approach to the definition of estimated blizzards parameters, using the meteorological data necessary for the determination of estimated blizzards parameters. Mathematical models for the calculation and statistical processing of modeling results are carried out. Calculation results are presented in the form of climatic road maps, the practical work maps is possible with the use of GIS technology.

## 2 The variants of snow protection

Snowdrifts form on the roads after snowfalls and blizzards. Snowdrifts after snowfalls often have a height of 5-10 cm, rarely 15 cm, and even more rarely up to 35 cm. Snowdrifts after blizzards may have a greater height more than 1 meter. The amount of snowdrifts depends on the snow accumulation volume.

All measures to ensure the absence of drifts on the roads during a blizzard are based on the forecast of the possible snow accumulation volumes to the road sections in the winter or in a single blizzard and possible snow deposits volume at the end of winter or a blizzard.

The defense of roads from snowdrifts is done using permanent or temporary snow protection. The snow protective belts and fences are permanent snow protection. The snow boards, snow trenches and shafts are temporary snow protection.

The snow protection is divided on the basis of the windsnow flow impact:

- The snow protection with the accumulation effect. In this case the snow protection works on the principle of the detention of snow on the side of the road,
- The snow protection with the blown out effect. In this case the snow protection increases the speed of the windsnow flow and helps to transfer the snow across the road,
- The snow protection that completely insulates the road from snow.
- The snow protection with the accumulation effect are more common on the roads.
- To make a decision about what type of snow protection to use it is necessary to define:
- The estimated snow accumulation volume to the left side and right side of road in the winter,
- The estimated snow accumulation volume at the snow protection at the end of winter,
- The estimated parameters of blizzard: the snow accumulation volume and duration,
- The snow drifts volume after estimated snowfall.

## 3 The estimated blizzards parameters and models for calculation

### 3.1. The estimated blizzards parameters

The main blizzard parameters were determined using the study results conducted by the authors and other researchers. Their characteristics are given in Table 1 [1-5]. The parameters in the table describe blizzards in the region of an auto road. The observation data from meteorological stations is needed to determine the parameters.

Data selection from the tables performed under the following constraints that correspond to the physical processes of snow drifting during a blizzard: atmospheric phenomena – snow, sleet, all types of blizzards; wind speed – more than 5 m/s; air temperature – below $0^0$ C.

The wind direction in the calculation is taken by 16 rhumbs.

[a] Corresponding author: samodurova@vgasu.vrn.ru

**Table 1.** The estimated blizzards parameters

| Parameter name | Parameter physical characteristic and effect for winter road maintenance |
|---|---|
| Blizzard duration | Time of an actual snowfall and snowdrift (choice of snow plowing technology; number of cycles for snow plowing (work of snowplows)) |
| Wind speed | Determines the snowdrift intensity (intensity of snow accumulation on the road; time between cycles of snow removal) |
| Wind direction | Determines the snowdrift direction (defining the road sections with possible snow drifts) |
| Intensity of snowdrift | Amount of a snowdrift per unit time per unit area during a blizzard which is perpendicular to the wind snow flow stream (intensity of snow accumulation on the road; time between cycles of snow removal) |
| Volume of snowdrift | Amount of a snowdrift through the front unit length which is perpendicular to the wind direction at the time of a blizzard (amount of snow removal) |
| Snow accumulation volume for the winter period | Snow amount which is brought to one side of the road during the entire winter period (amount of snow which need to be kept away by using the snow protective structures) |
| Snow accumulation volume for a single blizzard | Snow amount which is brought to one side of the road during a single blizzard (number of cycles for snow plowing (work of snowplows); amount of cleaned snow) |
| Estimated snow accumulation volume | Snow accumulation volume with the exceeding probability obtained as a result of the statistical processing of snow accumulation volumes data(selecting the type of snow; protection (permanent or temporary)) |

Data selection is made no less than for 15 years of observation. The meteorological data is used to conduct the special calculations.

## 3.2 The models for calculation of snow accumulation volumes

For the detection of snow accumulation volumes the method of the summarized snow transfer suggested by D.M. Melnik is used [6]. The method takes into consideration the intensity of snow transfer, which depends on the wind speed and the time of a snowdrift with the given intensity.

The volume of snow transfer in winter period ($W_t$) is calculated by the formula:

$$W_t = \frac{t}{m} \sum_{i=1,(V>5)}^{m} C \cdot V_i^3 = I_c \cdot t, \qquad (1)$$

where $t$ is the summary duration of blizzards for winter period, hour; $m$ is the number of measurements of the wind speed during blizzards (at speeds over 5 m/sec); $C$ is an empiric factor which is equal to 0,00046, when the

average density of the fresh brought snow is 0,17 m³/m; $V_i$ is the wind speed during blizzards, m/sec; $I_c$ is the average intensity of blizzards during the entire winter period (m³/m hour).

Collecting the data provided by the meteorological stations, the winds with the speed less than 5 m/sec are not taken into consideration, because their energy is not sufficient for snow transfer.

The dependency between the average intensity of horizontal snow drifting and the wind speed at the weathercock height is expressed by the following formula:

$$I = C \cdot V^3, \qquad (2)$$

where $I$ is the intensity of horizontal snow transfer, m³/m h; $C$ is the proportionality factor which depends on density the snow; $V$ is the wind speed at the weathercock height, m/sec.

The volume of the snow accumulation on an auto road at the end of the winter period from one direction ($W_{sb}$) is calculated according to the formula:

$$W_{sb} = W_t \cdot \sin(\alpha_r - \alpha_i), \qquad (3)$$

where $\alpha_r$ is the direction of the auto road, degree ; $\alpha_i$ is the direction of the wind, degree.

The volume of the snow accumulation at one side of the auto road in winter ($W_b$ ) is calculated according to the formula:

$$W_b = \sum_{i=1}^{7} W_{sb,i} \cdot \sin(\alpha_\partial - \alpha_i), \qquad (4)$$

where $W_b$ is the amount of snow brought to one side of the road (m³/m); $W_{sb,i}$ is the snow drifting volume by one compass point (m³/m); $\alpha_i$ is the azimuth of compass points, degree; $\alpha_r$ is road azimuth, degree.

For each road direction the number of compass points in which the snowdrift is calculated equals 7. Counting the volume of snow transfer, winds blowing at an angle less than 30° are not taken into consideration. Figure 1 gives the scheme of calculating of directions from which the snow is brought to one side of the auto road directed northward. The zone of each direction (at 16 compass points) is determined by the sector with the arc of 22,5°.

## 3.3 The models for calculation of estimated blizzards parameters

To estimate the blizzards parameters the statistical analysis of the modeling results is carried out. The method of Federal Service for Hydrometeorology and Environmental is used for statistical processing [7]. Based on the calculation results the descending series of parameters are compiled.

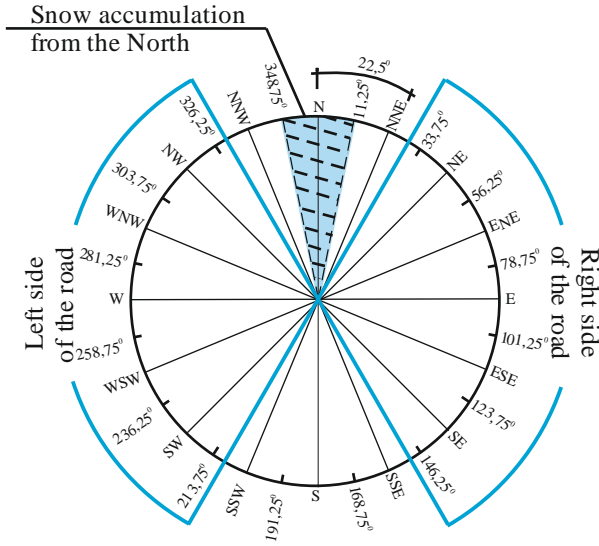For each series unit the empirical probability of exceeding is calculated:

**Figure 1.** Scheme of the calculation of snowdrift on the road directed northward.

$$p_э = \frac{m}{n+1} \cdot 100\%, \qquad (5)$$

where $m$ is the serial number of series unit; $n$ is the length of series (number of observation years).

The three-parameter gamma-distribution is taken for smoothing of empirical data and extrapolation of calculated parameters [7].

The integral curve characterizes the probability of exceeding the existing values of parameter and represents the integral of binomial distribution curve of continuous random variables:

$$P(x) = \frac{\beta^{\alpha}}{\Gamma(\alpha)} \int_{x_0}^{\infty} \bar{x}^{\alpha-1} \cdot e^{-\beta \cdot x} \cdot dx, \qquad (6)$$

where $\Gamma(\alpha)$ is the gamma function or Euler integral of the second kind:

$$\Gamma(\alpha) = \int_{0}^{\infty} z^{\alpha-1} \cdot e^{-z} \cdot dz, \qquad (7)$$

where $\bar{x}$ is an average long-term value of the parameter of estimated blizzard:

$$\bar{x} = \sum_{i=1}^{n} x_i / n, \qquad (8)$$

where $x_i$ is the parameter value for the $i$ year.

where $\alpha$ and $\beta$ are parameters of the law which are expressed by means of central moments:

$$\alpha = \frac{4m_2^3}{m_3^2}, \quad \beta = \frac{2m_2}{m_3}, \qquad (9)$$

where $m_2$, $m_3$ are the second and the third moments of the distribution curve:

$$m_2 = C_v^2, \quad m_3 = C_s \cdot C_v^3, \qquad (10)$$

where $C_v$ is the variation coefficient, $C_s$ is the asymmetry coefficient.

Statistical processing resulted in acquisition of the parameters of estimated blizzard were obtained, i.e. the snow accumulation volume on a section of an auto road , the blizzard duration with a different probability of exceeding, and the snow accumulation volume during the winter period.

## 3.4 The models for calculation of coefficient of snow losses from melting and evaporation

The winter seasons in Russia are characterized by the alternation of the air temperatures over zero degrees, thus the snow volume near roads depends on the air temperature change.

For the account of snow volume change it is proposed to calculate the "Coefficient of snow losses from melting and evaporation". The definition of this parameter is done according to the data observation of the snow cover characteristics, i.e. the snow height and density.

A snow mass per 1 m$^2$ ($Q$) is calculated by the formula:

$$Q = h \cdot \delta, \qquad (11)$$

where $h$ is snow cover height, m; $\delta$ is the snow cover density, g/m$^3$.

Reduction of the snow mass in the time period between blizzards:

$$P_i = Q_{max} - Q_{min}, \qquad (12)$$

where $P_i$ is the decrease of the snow mass, g/m$^2$; $Q_{max}$ is the maximum of the snow mass per unit area (g/m$^2$) ; $Q_{min}$ is the minimum of the snow mass per unit area (g/m$^2$).

The total reduction of the snow mass during the winter period is equal to the sum:

$$P = \sum_{i=1}^{m} P_i, \qquad (13)$$

where $n$ is the number of periods between blizzards during the winter period.

The coefficient of snow losses from melting and evaporation for the entire winter is calculated by the formula:

$$K_P = \frac{P}{Q_{max}}. \qquad (14)$$

The average long-term value of the coefficient is determined for practical calculations.

The volume of snow accumulations for the entire winter, considering the decrease of the snow mass, is calculated by the formula:

$$Q = W_{sb} \cdot \left(1 - K_P\right) \cdot \frac{\delta_s}{\delta_{av}}, \qquad (15)$$

where $\delta_s$ is average density of new snow, $\delta_s$=0,17 g/cm³; $\delta_{av}$ is average density of the snow cover (g/cm³).

The average annual snow density can be found, using the meteorological station data about the density changes during the winter, by the formula:

$$\delta_{av} = \frac{\sum\limits_{i=1}^{k} \delta_i}{T_s}, \qquad (16)$$

where $\delta_i$ is the density of snow accumulation in one test (g/m³) ; $k$ is the number of density estimations during the entire winter; $T_s$ is the number of observation years.

The proposed models allow to calculate the blizzards parameters which are essential parameters for snow protection maintenance and design on the roads of Russia.

The computer program «Blizzards» was specially developed for that kind of calculations [8]. The initial data and the calculation results are stored in the databases with specific structures. This allows using the data in other calculations and receiving the reports of various forms.

# 4 The experimental verification of the models

The experimental verification of the models has been done for the three seasoned road sections. During the experimental work adequateness of the models was tested according to the snow volume measurements.

The snow survey methodology provides the determination of the actual snow volume on the embankments subgrade according to the snow cover height and snow length parameters on the basis of their geometric parameters [9]. Tachometry has been conducted to determine the embankments geometrical parameters at selected seasoned road sections. Determined marks: subgrade verge, the bottom cuvette and land marks in field at a distance of 15-20 m from the cuvette embankment. In winter, with the leveling rods, the snowdrift height in the typical points of the land cross-sections and in the points of snowdrift shape and height change were measured, snow shafts was measured on the verge. Simultaneously, the snow density detection in snow accumulation zones was done using the cutting ring.

The cross sections on experimental open roadways and snow accumulation profiles were used for the calculation of the actual snow volume by their geometric shapes [9].

Snowdrift measurements were performed after the intense blizzard or in the late winter. If the snowdrift measurements were made in late winter with taking into account the determining of the snowdrift volume, the snow losses from melting and evaporation during thaws affected the changes in snowdrift density.

The convergence of the calculated and actual data on snowdrift volume is about 88% in average [9]. Therefore, we can conclude about the possibility of applying the model for solving tasks of winter road maintenance.

# 5 The road maps with blizzards parameters

The calculation results for one selected territory in Russia are shown in Figure 2.
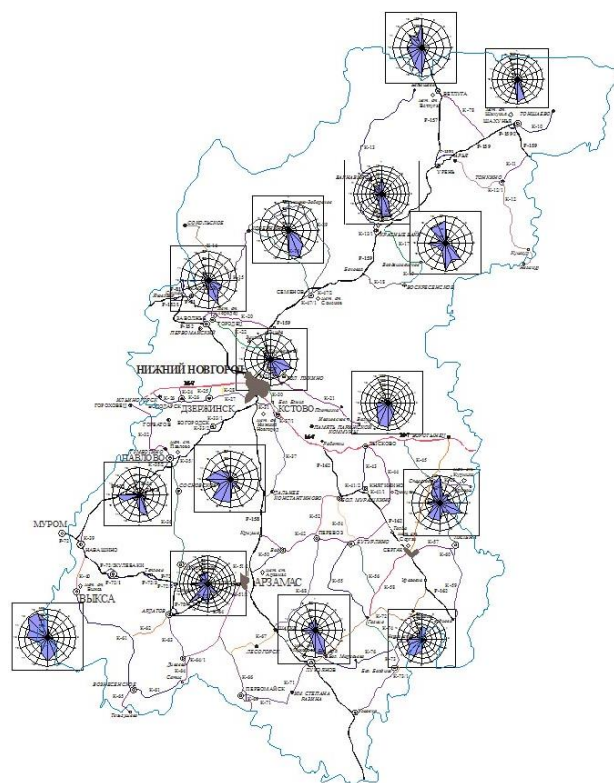


**Figure 2.** Distribution of snow drifting volumes to 16 directions for Nizhny Novgorod region.

Diagrams of the snow transfer volumes according to 16 rhumbs were placed in the locations of the State Meteorological Stations. The analysis of the diagrams shows a significant change of blizzards parameters within a single region. Therefore, for solving the practical problems the most convenient way of submitting the calculations results are in the form of maps form with isolines representing the estimated blizzards parameters. The calculation of isolines and drawing them on the map was automated by using the methods of creation of the digital terrain models. To calculate the program complex "CREDO Roads" from joint venture "Credo-Dialogue" was used.

Models are created in the following sequence:
– Bitmapped substrate is created in the program TRANSFORM, i.e. a map of the auto roads network and location of the weather observation points (e.g. State Meteorological Observation Network),

− Bitmapped substrate is exported to the program "CREDO Roads" to digitize.

The locations of meteorological stations served as control points for the digitizing maps. Numerical values of climatic parameters are given in control points. The layers are created for the construction of climatic models.

The model of one climatic parameter is constructed in each layer. This allows to observe simultaneously the change in the parameters distribution on the given territory and application of the additional data on the generated model.

The closed contour is created to build the model. Three-dimensional surface and its two-dimensional image in the lines interpolation (isolines) form are constructed inside of the contour. Isolines represent the equal parametrical values in the different points of the terrain (in the first approximation). Isolines increment can vary for different layers. Its value depends on the variability of climatic factors, accuracy of its calculation, and given tasks.

The program "CREDO Roads" allows to build 2D models in the form of cuts (sections) along road axis and to display any parameter distribution on the road as a line graph. The map fragment with the estimated snow accumulating volume for roads towards the north (left), to the south (right) is shown in Figure 3.
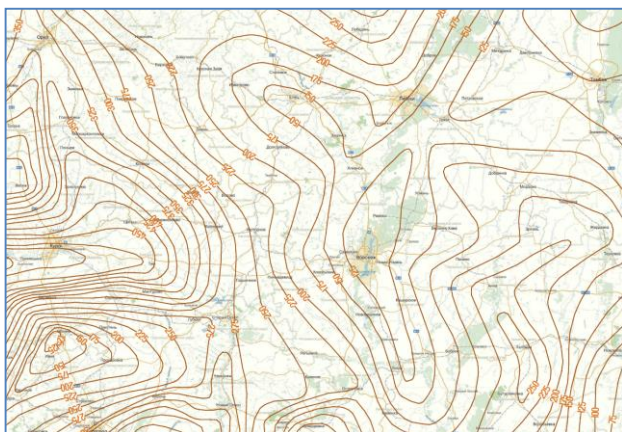


**Figure 3.** The distribution map of estimated snow accumulation volumes for roads towards the north (left) to the south (right)

The information on the map allows to reveal the prevailing direction of snow transfer and to estimate the possibility of snow drifts formation in separate road sections with the given road direction.

The maps with the blizzard parameters can be used to solve the following problems: detection of road sites with possible snow drifts; designing different variants of snow protection (forest belts, fences, etc.); planning snow removal (snow plowing); calculation of resources (equipment, anti-icing materials) for winter road maintenance.

The method of creation of digital terrain models and displaying of the information on maps makes possible the use of the results in the form of GIS technology. The calculations results in the program «CREDO Roads» can be exported into a GIS system. The calculation results in the program «CREDO Roads» after their export into a GIS system and automatic conversion of the calculation results allow to display the data in the Earth surface coordinates and put them together with the data from roads.

# 6 Conclusion

The estimated blizzards parameters influencing the road reliability and traffic safety during the winter period were determined using the system approach basis. The meteorological data necessary for calculating of estimated blizzards parameters was determined. The mathematical models for the calculation and statistical processing of the modeling results were presented. The results are presented in the form of maps which can be used in special GIS projects for the winter road maintenance.

The permanent snow protection should be designed on the estimated snow deposits volume at the end of winter or the estimated blizzard with a snow accumulation volume greater than the snow deposits volume at the end of winter. The snow drifts volume after snowfall must be taken into account in the calculations. It is also recommended to take into account the losses of snow volume from evaporation and melting during thaw.

The temporary snow protection should be designed for the estimated blizzard because after work of temporary snow protection it needs recovery.

# References

[1] O.V. Gladysheva, Estimation amount of snow deposit on the road, *14th International road Weather Conference*, Prague, Czech Republic, 19 (2008)

[2] T.V. Samodurova, O.V. Gladysheva, Determination amount of snow deposit on the road, *H. Ed. In. Pr. Construction*, **8**, 94 (2003)

[3] O.V. Gladysheva, Considering the dynamics of snow accumulation on the roads, *H. Ed. In. Pr. Construction*, **7**, 77 (2006)

[4] A.K. Djunin, *Road winter maintenance*, Publishing house «Transport», Moscow, Russia, (1966)

[5] R.D. Tabler, Controlling blowing and drifting snow with snow fences and road design, *Tabler and associates*, *Niwot, Colorao*, (2003)

[6] D.M. Melnik, About laws of snow transport and their use in snow-drift control, *Technics of railways*, 11 (1952)

[7] A.V.Rozhdestvensky, A.I. Chebotarev, *Statistical methods in hydrology*, Gidrometeoizdat, Moscow, (1974).

[8] T.V. Samodurova, O.V. Gladysheva, Blizzards: OFAP № 2063, № gos reg. 50200200397, *Comp. Teach. Pr. and In.*, **3**, 10 (2003)

[9] T.V. Samodurova, O.V. Gladysheva, N.Y. Alimova, S.M. Shiryayeva, Verification the adequacy of models to estimate of snow deposits on the roads, *Scientific Bulletin of the Voronezh State University of Architecture and Civil Engineering, Construction and architecture*, **1**, 66 (2013)

# Influence of sunshine hours in fine weather on the rate of wintry accidents

Akira Saida[1,a] , Masayuki Hirasawa[1], Naoto Takahashi[1] and Tateki Ishida[1]

[1] Civil Engineering Research Institute for Cold Region, Public Works Research Institute, National Research and Development Agency, Japan

**Abstract.** This study examined the relationship between sunshine hours, which are considered to greatly affect road surface conditions in winter, and the rate of wintry accidents on a national highway in Hokkaido. As a result, mostly in mountainous areas, a negative correlation was found between sunshine hours and the rate of wintry accidents. Also shown was the trend that, at sections with short sunshine hours, the rate of wintry (i.e., accidents per hundred million vehicle kilometers on a given road section) greatly increases if other danger factors such as sharp bends exist.

## 1 Background of the study

The basic plan in traffic safety of Japanese Government sets the goal to realize the world's safest road traffic. Its objective is to decrease the number of annual fatalities who are killed within 24 hours after traffic accident below 2,500 by 2018, compared to the 4,113 fatalities in 2014. Further actions are necessary as the pace of decreasing traffic accidents has been slower.

Snowy cold regions account for 60% of Japan's land area. These regions see many traffic accidents that stem from weather conditions peculiar to winter (hereinafter: "wintry accidents"). Typical examples include skidding accidents on snow-covered or icy roads and run-off-the-road accidents involving snowstorm-induced poor visibility. Approximately 80% of wintry accidents are skidding accidents, occurring when the road becomes very slippery[1]. Therefore, in taking measures against wintry accidents, it is highly useful to clarify how traffic accidents are influenced by sunshine hours and the intensity of solar radiation, both of which greatly affect the road surface conditions.

To this end, this study aimed to analyze the relationship between the distribution of sunshine hours on a route and the situations where wintry accidents occur on the route by using digital topography data and data on the injury/fatal accidents.

## 2 Literature review

There are many studies on the influence of weather conditions on traffic accidents. Such studies include Kojima and Takubo[2], which surveyed the number of accidents on the National Highway 13 in Akita Prefecture to indicate that the number of injury accidents decrease in winter while the property-damage-only accidents increase. Also, Hirasawa and Asano[1] reviewed how temperature variation affect the occurrence of accidents in Hokkaido and found that the accidents occur the most frequently when the daily mean temperature drops to approximately -4°C. Other studies similarly explore the influence of winter weather conditions on road traffic, showing that the number of accidents are likely to increase by adverse weather in winter.

However, there are few studies or analyses made to reveal the influence of sunshine hours and the intensity of solar radiation on traffic accidents, though these factors are considered to have a significant impact on road surface conditions. One of the few studies includes Iwasaki and Katahira[3] which examined the relationship between sunshine hours measured at Fukushima Local Meteorological Observatory and the number of traffic accidents occurring in the jurisdiction of Fukushima Police Station. Sunshine hours vary by topography and structures alongside the road. This may lead to the view that a location with shorter sunshine hours raises the risk in accidents. Unfortunately, there are no studies on how sunshine hours cause impact on traffic accidents by taking into account the topography and structures alongside the road.

## 3 Study method

For this study, we surveyed sunshine hours on sunny days in winter ("sunshine hours"), and compared the data to the rate of wintry accidents. The study details are shown in the following sections.

### 3.1 Estimation on Sunshine Hours

#### 3.1.1 Estimating the Location of the Sun

The location of the sun is expressed by azimuth $\theta$ and sun's altitude $\alpha$. $\theta$ is expressed between 0 (indicating due north) and 360 degree in a clockwise direction. $\alpha$ is an angle-off between the accident location-sun segment and horizon plane. It is 90 degree when the sun stays at the zenith, while it is 0 degree when the sun stays on the horizon.

$\theta$ and $\alpha$ are expressed by the following equations:

$$\cos\alpha = \sin\delta\sin\phi + \cos\delta\cos\phi\cos t \qquad (1)$$

$$\tan\theta = \frac{-\cos\delta\sin t}{\sin\delta\sin\phi - \cos\delta\sin\phi\cos t} \qquad (2)$$

[a] Corresponding author: saida-a@ceri.go.jp

where $\delta$: declination of the sun, $\phi$: the latitude of the location subject to sunshine hours calculation, $t$: the hour angle of the sun on the location where sunshine hours are estimated.

$\delta$ is expressed by the following equation:

$$\sin \delta = \sin \lambda_s \cos e \qquad (3)$$

where $\lambda_s$: the longitude of the sun and $e$: ecliptic angle of tilt. $\lambda_s$ is given by the equation proposed by Nagasawa[4].

$$
\begin{aligned}
\lambda_s &= 280.4603 + 360.007697T \\
&+ (1.9146 - 0.00005T) \\
&\times \sin(357.538 + 359.991T) \\
&+ 0.0200\sin(355.05 + 719.981T) \\
&+ 0.0048\sin(234.95 + 19.341T) \\
&+ 0.0020\sin(247.10 + 329.640T) \\
&+ 0.0018\sin(297.80 + 4452.670T) \\
&+ 0.0018\sin(251.30 + 0.200T) \\
&+ 0.0015\sin(343.20 + 450.37T) \\
&+ 0.0013\sin(81.40 + 225.18T) \\
&+ 0.0008\sin(132.50 + 659.29T) \\
&+ 0.0007\sin(153.30 + 90.38T) \\
&+ 0.0007\sin(206.80 + 30.35T) \\
&+ 0.0006\sin(29.80 + 337.18T) \\
&+ 0.0005\sin(207.40 + 1.50T) \\
&+ 0.0005\sin(291.20 + 22.81T) \\
&+ 0.0004\sin(234.90 + 315.56T)
\end{aligned} \qquad (4)
$$

where $T$: time variable.

When the elapsed time since the noon January 1, 2000 is referred to as $K$, $T$ is given by the following equation:

$$T = K / 365.25 \qquad (5)$$

$t$ is given by the following equation:



Triangular element   Solar ray

sunshine

shade   Calculation point

Sunlight interruption by triangular elements

**Figure 1.** Method for determining sunlight shielding

$$t = \Theta - \beta \qquad (6)$$

where $\Theta$: sidereal time, and $\beta$: right ascension of the sun.
$\beta$ is expressed by the following equation:

$$\tan \beta = \tan \lambda_s \cos e \qquad (7)$$

Near the surface of the ground, $\alpha$ is likely to be greater than the values estimated by equations (1) - (7). In consideration of its retraction through the air, the altitude of the sun, $\alpha'$, is given by the following equation:

$$\alpha' = \alpha + r \qquad (8)$$

$$r = \frac{0.0167}{\tan(\alpha + 8.6/(\alpha + 4.4))} \qquad (9)$$

### 3.1.2 Determination of Sunlight Shielding

Sunlight shielding at locations where the sunshine hours are estimated ("the locations") is determined by using the digital terrain data. Figure 1 shows the method of sunlight shielding determination. In this study, the topography around the locations as well as the shapes of structures are expressed as a set of triangular elements. Sunlight shielding is determined by looking at whether the segments which connects the sun and the locations are crossed with any triangular elements. If crossing is recognized, it is determined that the sunlight shielding occurs. This method is referred to in detail in References [5] and [6].

### 3.1.3 Computation of Sunshine Hour Distribution on the Route

By using the method mentioned in *3.1.2*, the sunshine hour distribution of each location of the route was estimated through a 24-hour observation of hourly sunlight shielding. The locations were set every 10 minutes along the observed section. From the obtained results, the average sunshine hours were estimated every 1 km across the section.

## 3.2 Calculation of the Rate of Wintry Accidents

The Hokkaido Prefectural Police categorizes traffic accidents occurred under wintry weather or road conditions and resulted in injury or death as "wintry accidents", and adds this category to its traffic accident record slip. In this study, we calculated the rate of such wintry accidents by using the data obtained at the observed route. The rate of wintry accidents is given by the following equation:

$$R_j = \frac{10^8 f_j}{365.25 P L_j Q} \qquad (10)$$
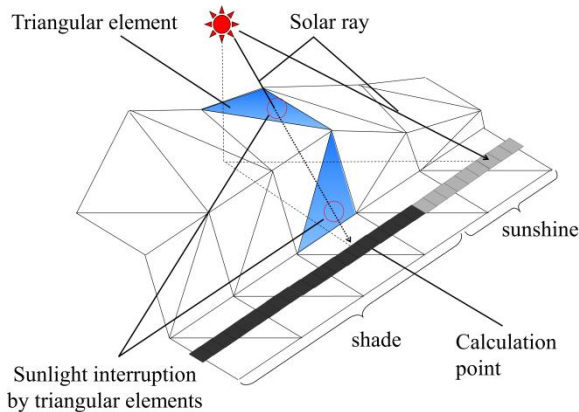
where $R_j$: the rate of wintry accidents at Section $j$ (case/hundred million vehicle-km), $f_j$: the number of wintry accident cases at Section $j$ (case), $P$: analysis period (year), $L_j$: distance of Section $j$ (km), $Q$: annual average traffic (vehicle/day).

## 4 Verification Conditions

This study computed the distribution of sunshine hours in fine weather in wintertime. The subject section was National Highway 230 between KP1.0 in Sapporo City and KP60.0 in Kimobetsu Town, Hokkaido prefecture (Figure 2). As the road condition varied by section, KP1.0 - KP18.0 were categorized as the urban section and KP18.0 - KP60.0 as the mountainous section, for both of which the relation between sunshine hours and the rate of wintry accidents was examined. In estimating sunshine hours, the digital altitude data from the base map information of the Geospatial Information Authority of Japan (spatial resolution of 10m) was used as topography data, and a digital housing map issued by Zenrin Co., Ltd. was used for data of building shapes.

In calculating the rate of wintry accidents, the data of 20-year traffic accident record slips between January 1, 1993 and December 31 2012 was used as the data of wintry accident locations, and the road traffic census data 2005 was used as the traffic volume data.

Additionally, the relation between air temperature and the rate of wintry accidents was investigated, in that the air temperature is considered as one of the factors for accidents. For the air temperature distribution data, the measurements of KP 1.0 - 45.0 at 3:00, 4:00, 8:00 and 10:00 on weekdays from December 2012 to February 2013.

## 5 Results and Discussion

Figure 3 shows the average sunshine hours in winter (wave line), average air temperatures (dashed line) and the rate of wintry accidents on the subject route (solid line).



**Figure 2.** Map of the subject route
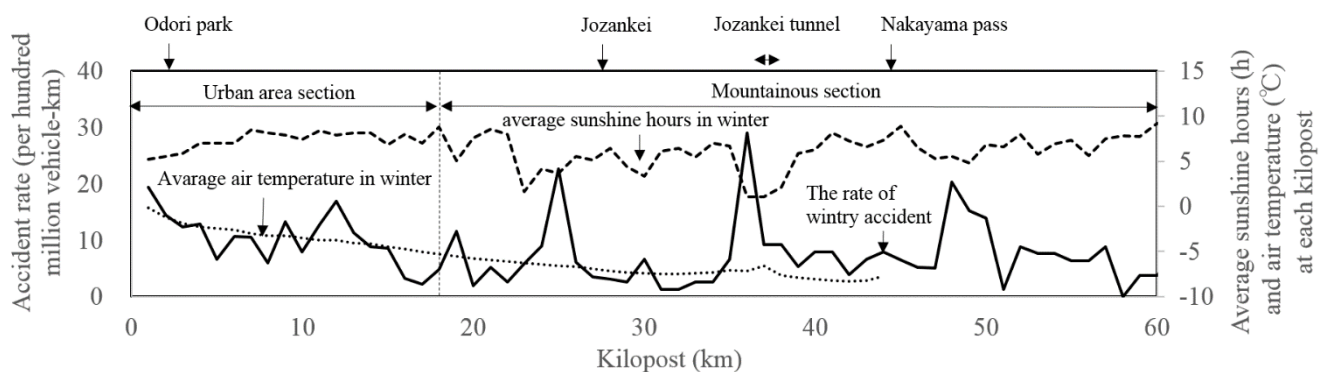


**Figure 3.** Sunshine hours and distribution of the rate of wintry accidents of the subject route
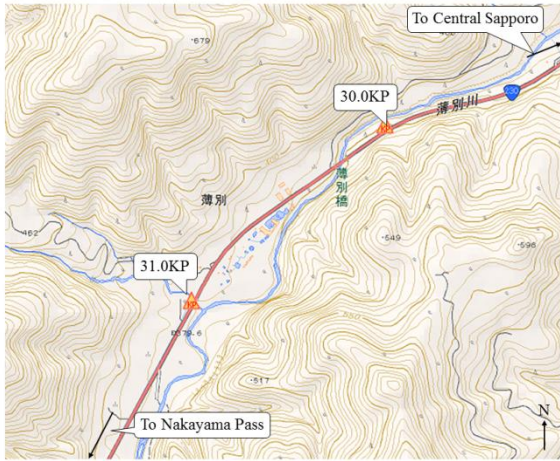
**Figure 4.** Alignment of road and topography around KP30.0, National Highway 230
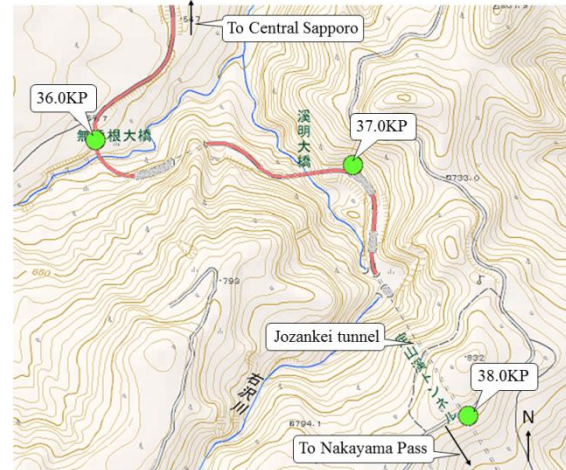


**Figure 5.** Alignment of road and topography around KP36.0, National Highway 230
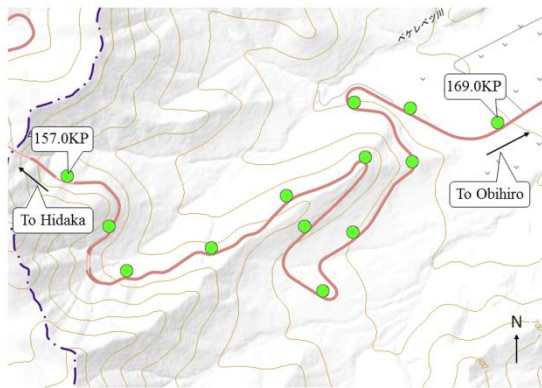


**Figure 6.** Alignment of road and topography around KP157.0, National Highway 274
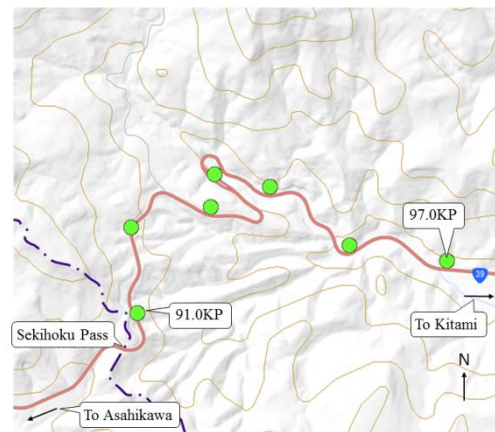


**Figure 7.** Alignment of road and topography around KP91.0, National Highway 39

Sunshine hours significantly vary by section: average sunshine hours at mountainous sections, at KP23.0 - KP24.0 and KP36.0 - KP38.0, were shorter than 2 hours because those sections were faced with mountain on the south of the road. In urban sections, KP1.0 - KP4.0 also recorded shorter sunshine hours than neighboring sections, because surrounding structures were higher at KP1.0 - KP4.0 than in others, causing sunlight shielding. Air temperature became lower as the altitude rose, and it was the lowest at KP45.0.

The rate of wintry accidents was considerably high at KP36.0 - KP37.0; the rate increased threefold compared to other sections. The rate was also likely to increase at KP25.0 - KP26.0 and KP49.0 - KP51.0.

Any significant relation between air temperature and the rate of wintry accidents was not recognized in mountainous sections (correlation coefficient: 0.08, p = 0.581). With regards to the relation between sunshine hours and the rate of wintry accidents in mountainous sections, the sections with shorter sunshine hours more likely caused wintry accidents. This indicates a negative correlation between sunshine hours and the rate of wintry accidents (correlation coefficient: 0.45, p = 0.002).

With regards to the relation between sunshine hours and the rate of wintry accidents in urban sections, it is suggested that a closer verification is necessary by including more urban routes/roads in further studies, as the studied distance was too short to verify the hypothesis.

It is noted that there were several sections, such as KP30.0 - KP31.0, with shorter sunshine hours and the rate of wintry accidents. This may suggest that wintry accidents may be subject to other factors than sunshine hours. We then focused on the alignment of road, which is considered as another accident factor, to additionally verify the relation between the road alignment and the rate of wintry accidents.

Comparing the road alignment of KP30.0 - KP31.0 to that of KP36.0 - KP38.0, it was found that KP30.0 - KP31.0 was a straight lane (Figure 4) and KP36.0 - KP38.0 consisted of several 150-km radius curves (Figure 5). In the straight lines, sections with shorter sunshine hours caused fewer wintry traffic accidents. Similarly as KP36.0 - KP38.0 of the subject route, National Highway 274's KP157.0 - KP169.0 (Figure 6; East of Nissho Pass, Shimizu-cho, Hokkaido Prefecture) and National Highway 39's KP91.0 - KP97.0 (Figure 7;

East of Sekihoku Pass, Kitami City, Hokkaido Prefecture) consist of curved lines and long sunshine hours. With regards to the relation between sunshine hours and the rate of wintry accidents, the rate of wintry accidents were 3.7 cases/billion vehicle-km for the former section and 6.6 cases/billion vehicle-km for the latter section. Both figures were smaller than that for KP36.0 - KP38.0 of National Highway 230. From this, it was suggested that curved line sections with longer sunshine hours may cause fewer wintry traffic accidents.

In summary, the occurrence of wintry accidents may be influenced by sunshine hours, as well as by other factors such as the alignment of road. A combination of these factors may likely cause a soaring rate of wintry accidents.

# 6 Conclusion

This study aimed to clarify the influence of sunshine hours on the rate of wintry accidents. Towards this goal, we measured sunshine hours of KP1.0 - KP60.0 of National Highway 230 in fine weather of mid winter, and compared the measurements to the rate of wintry accidents across the sections. The findings are as follows:

1. Sunshine hours at National Highway 230 greatly vary by section. Sunshine hours are likely to be short at sections facing mountains on the south of the road and the center of urban area.

2. For mountainous sections, a negative correlation was identified between sunshine hours and the rate of wintry accidents. For urban sections, however, no specific relationship, such as found in the data for mountainous sections, was identified between sunshine hours and the rate of wintry accidents, due to the insufficient amount of data.

3. The rate of wintry accidents is influenced not only by sunshine hours but by the horizontal alignment of the road. The sections with several risk factors (such as sharp curves and short sunshine hours) are likely to greatly increase the wintry accident rate.

Detailed examinations of the relationship between sunshine hours and situations in which accidents occurred in urban areas in winter will be conducted, with the addition of data on property damage accidents to the data on injurious/fatal traffic accidents.

# References

[1] Masayuki Hirasawa and Motoki Asano: Characteristic of Traffic Accidents in Hokkaido During Last Decade, *Monthly Report of Civil Engineering Research Institute of Hokkaido*, **Vol. 576**, pp. 13-21 (2001)

[2] Yukio Kojima and Nobuaki Takubo: Influence of weather factors on safe driving of motor vehicles. 3. Snowfall and snow- or ice-covered pavement, *Research on traffic safety and regulation, Reports of the National Research Institute of Police Science*, **Vol. 30**, No. 1, pp. 115-132 (1989)

[3] Shoichi Iwasaki and Kiyoaki Katahira: Correlational analyses between meteorological factors and traffic accidents, *Ergonomics*, **Vol. 30**, pp. 384-385 (1994)

[4] Ko Nagasawa: Computations of Sunrise and Sunset, Chijin Shokan Co., Ltd. (1999)

[5] Akira Saida, Akihiro Fujimoto and Teruyuki Fukuhara: Forecasting Model of Road Surface Temperature along a Road Network by Heat Balance Method, *Journal of Civil Engineering E1 (Pavement Engineering)*, **Vol. 69**, No. 1, pp. 1-11 (2013)

[6] Akira Saida, Teruyuki Fukuhara, Akihiro Fujimoto, Masayuki Hirasawa, and Tateki Ishida, A calculation method for the shady area of road surfaces in wide areas using data from a digital housing map, *Proceedings of the Cold Region Technology Conference*, **vol. 31**, (2015)

# Roof snow slide-off experiments using membrane deformation

Hiroaki Terasaki[1, a] and Teruyuki Fukuhara[1]

[1]University of Fukui, faculty of engineering, 910-8507 Bunkyo 3-9-1, Fukui-city, Fukui prefecture, Japan.

**Abstract.** This paper describes the snow sliding performance of a membrane roof snow removal system (MRSRS), which was applied to three different types of pitched roofs. Slide-off experiments were conducted in Katsuyama city, Fukui Prefecture, Japan in 2012 and 2013. The experimental equipment consists of a snow slide membrane (SSM), an inflation/deflation blower. The SSM is made from PVC resin sheet, and is swelled or shrunk due to air flow induced by the blower. Video-cameras recorded the crack propagation of roof snow and subsequent sliding down of snow blocks from the roof due to the deformation of the SSM. It was found that the MRSRS showed a satisfactory snow sliding performance for most experimental cases. The time required for cleaning snow from a roof was about 15 minutes at the maximum for snow depths varying from 0.1 to 0.65m.

## 1 Introduction

Every year in Japan, many peopled have been killed or injured while removing snow from rooftops. Especially, 152 people were killed in roof snow related accidents in 2006 [1]. In 2012, 131 people were killed or injured due to a heavy snowfall and 76% of them were caused by roof snow removal related accidents. 67% of them were elderly persons over the age of 65 [2]. This statistical percentage has never been changed in recent years and may reflect a social background such as declining birth rate and aging population. Heating systems using a heat tape/cable or a boiler are an effective solution [3, 4], but are very expensive in its energy use (electric power or fuel oil). For example, about 300-800 US$ is fuel expense for roof snow removal over the winter period in a part of heavy snow regions in Japan, although it depends on the snowfall conditions. In 2014 many houses, carports and greenhouses were damaged by snow load on rooftops in Kanto area [5, 6], which is near the border between snowy and non-snowy regions.

Fig. 1 shows the collapse of a cooperative pack house for packing vegetables and fruits due to excessive roof snow load in Koufu city, Yamanashi prefecture. Fig. 2 shows the collapse of strawberry greenhouses due to excessive snow accumulation in the gutters in Komoro city, Nagano prefecture. Renewing houses and equipment had a significant economic burden on farmers. Once heavy snowfall would occur in non-snowy regions, people removing roof snow would be exposed to more serious hazards associated with house or roof collapses due to snow loads falling down from a roof and an avalanche of snow falling off a roof.

In order to reduce the snow removal works and expense, we have been developing a new roof snow removal system with a membrane structure (membrane roof snow removal system; MRSRS) [7, 8]. The MRSRS can clear snow without going on a roof and does not require large-capacity electricity (thermal energy) such as consumed by a heat tape/cable system or a hydronic roof heating system. The snowfall from the roof by the MRSRS can be enhanced by the membrane deformation, i.e. swell or shrink of the soft membrane due to air flow by means of an air blower with an inflation/deflation feature (an inflation/ deflation blower). The MRSRS can terminate the roof snow removal within a reasonable amount of time after the start of the snow removal operation. Thus people below a roof can be protected from an unexpected sliding snow hazard.

This paper shows the snow removal performance of the MRSRS through field experiments conducted in Katsuyama city, Fukui prefecture, Japan from 2012 to 2014.



**Fig. 1** Collapse of packhouse and equipment for packing



**Fig. 2** Collapse of greenhouse due to excess snow load

---

[a] Corresponding author: terasaki@u-fukui.ac.jp
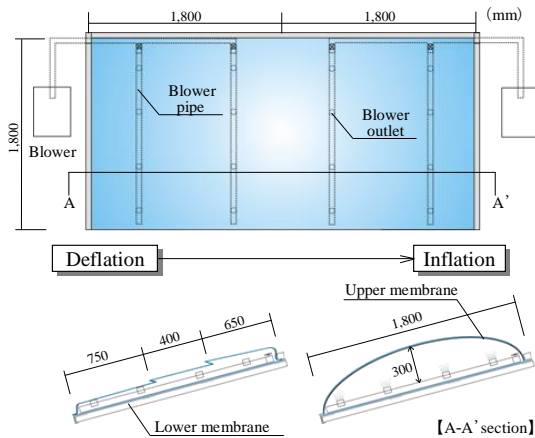
**Fig. 3** SSM for the first test
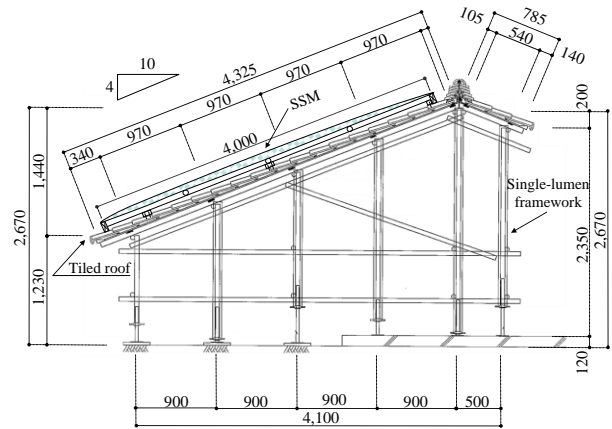


**Fig. 4** SSM on a dummy roof for the second test



a) SSM indtalling procedure
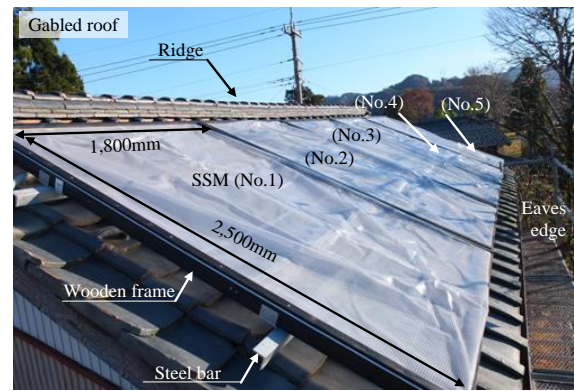


b) Overview of SSM

**Fig. 5** MRSRS for the third test

## 2 Snow sliding experiments

The slide-off performance of roof snow using the MRSRS was evaluated with data from three demonstration tests in Katsuyama city, Fukui prefecture, Japan. The annual maximum depth of snow cover in Katsuyama city ranged 0.4 to 2.1m in the period of 2000-2010 [9]. The first, second and third tests were carried out from January 31 to February 18, 2012, from December 25, 2012 to February 18, 2013, and from December 25, 2012 to February 18, 2013, respectively. The experimental equipment consists of a PVC resin membrane (hereafter referred to as 'snow slide membrane (SSM)'), an inflation/deflation blower (550W/100V) in the marketplace and a one-third pitched roof. The roof structure was changed for each demonstration test to design a wooden frame structure for mounting the SSM. The dynamic deformation of the SSM using the air blower can help improve sliding performance of the roof snow on the SSM.

In the first test (2012) one SSM (1.8m by 3.6 m) was mounted on a 3:10 pitched dummy wooden roof (1.8m by 3.6m) as shown in Fig. 3. The maximum height of the inflated SSM, 'rise' was 0.3m. The SSM was shortened approximately 0.1m in the horizontal (parallel to the ridge) and vertical (perpendicular to the ridge) directions, respectively to fix the SSM to the margin of the roof.

Therefore, the SSM can not be inflated at the edge of the roof.

In the second test (2013), two sets of the membrane (1.8m by 4.0m) were fixed onto the surface of a dummy roof with clay tiles as shown in Fig. 4. The second test was conducted to develop a more practical MRSRS by utilizing the results of the first test.

In the third test (2013) the latest MRSRS was applied to the roof of 2-story barn shown in Fig. 5. Five sets of the membrane (2.5m by 1.8m) were fixed onto the surface of a roof with clay tiles of a residential house. The SSM was mounted on the wooden frame combined with wooden roof boards under the roof tiles. The family members controlled the MRSRS according to their convenience. Actually they operated the inflation/deflation blower to supply air into or suck air from the SSM, observing the amount of snow remaining on the roof. The deformation of the SSM was generated due to the inflation-induced swelling at first and then turned to the deflation-induced shrinking. This inflation/deflation cycle was repeated until the snow removal was terminated.

Three video-cameras were used to measure an elapsed time to finish the snow removal as well as to observe the crack propagation of roof snow and subsequent sliding down of snow blocks from the roof. Other measurement items in the field tests were snow
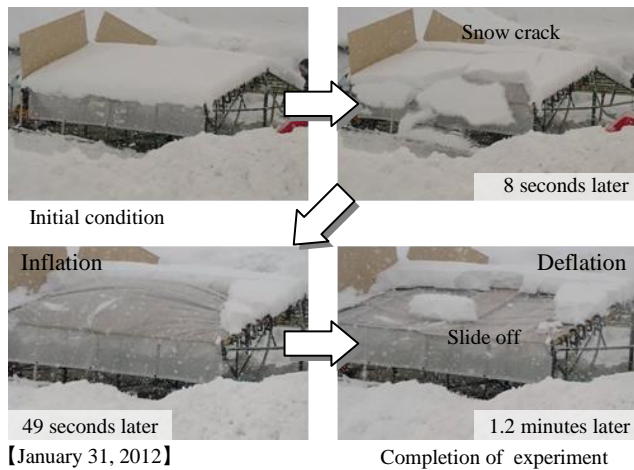
**Fig. 6** Snow slide-off motion in the first test (1/31)
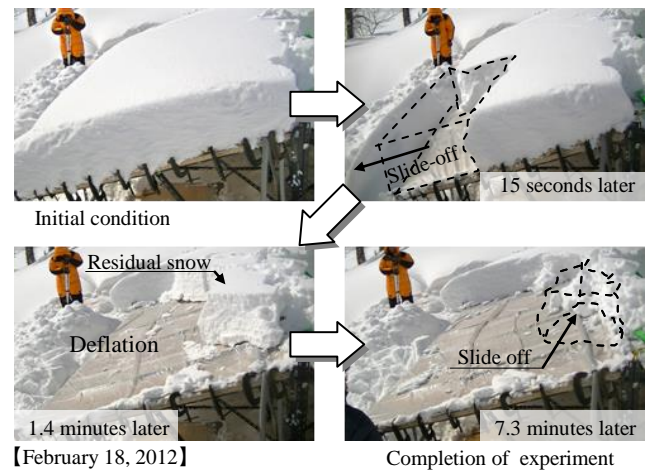


**Fig. 7** Snow slide-off motion in the first test (2/18)

**Table 1** Overview of the first test result

| Date (2012) | Whether condition | Air temp. (℃) | Snow temp. (℃) | Water content (%) | Snow depth (mm) | Snow density (kg/m³) | Roof snow load (kg) | Sliding velocity (m/s) | Snow removal time (min) | Volume ratio of snow removal (%) |
|---|---|---|---|---|---|---|---|---|---|---|
| 1/31 | Snow | +0.5 | +0.1 | 10.88 | 332 | 59.8 | 129 | 0.4 | 2.6 | 72 |
| 2/4 | Cloudy | -1.0 | -0.3 | 5.28 | 476 | 80.9 | 250 | 1.3 | 14.8 | 74 |
| 2/9 | Cloudy | -2.8 | -1.8 | 5.57 | 467 | 130.5 | 395 | 1.4 | 15.4 | 79 |
| 2/18 | Sunny | -2.8 | +0.4 | 6.61 | 649 | 104.2 | 438 | 0.5 | 7.3 | 99 |

density, snow depth, volumetric water content, snow and atmospheric temperatures on the SSM.

# 3 Experimental results and discussions

Fig. 6 shows the crack propagation of roof snow and the sliding down off of the roof in the first test, which was conducted on January 31, 2012. The snow depth and the bulk snow density were 0.33m and 59.8kg/m³, respectively, and the snow weight per unit roof area was 19.8kg/m². The atmospheric temperature was 0.5°C during the experiment. The snow sliding off of the roof occurred 8 seconds later from the beginning of the inflation (swell of the SSM) operation and 73% of the snow volume fell down onto the ground surface below the roof 49 seconds later. Thus the inflation operation ended and turned to the deflation one (shrink of the SSM). 69 seconds later a snow block sled down from the central part of the roof, then the experiment was terminated. It was confirmed that about 72% of the roof snow fell down onto the ground by three set of the inflation/deflation operation.

Fig. 7 shows the crack propagation of roof snow and the sliding down off of the roof in the first test, which was conducted on February 18, 2012. The snow depth and the bulk snow density were 0.65m and 104.2kg/m³, respectively. The snow weight per unit roof area was 67.6kg/m² and was 3.6 times heavier than that of Fig. 6. The atmospheric temperature was -2.8°C during the experiment. About 15.4% of the snow sliding off of the roof started from the left eaves of the roof 15 seconds later from the beginning of the inflation operation. Subsequently the snow sliding lasted intermittently, but snow blocks kept staying on the middle upper and right edge of the roof when 84 seconds have passed. About 67.9% of the snow volume fell down onto the ground surface by the first inflation/deflation cycle. Finally, almost 100% of the snow removal was terminated 7.3 minutes later, which was in the 6th inflation/deflation cycle. Four experiments were carried out in the first test, and average snow weight per unit area was 47kg/m². The velocity of snow blocks sliding down from the roof was varied 0.4 to 1.4m/s. The roof snow removal was satisfactory for every experiment and the time required to terminate the snow removal was in the range of 2 to 15 minutes (See Table 1).
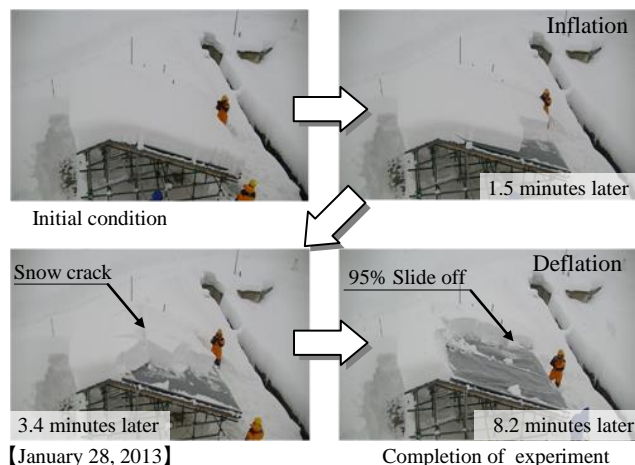
**Fig. 8** Crack propagation of roof snow in the second test



**Fig. 9** Snow sliding-off in the third test

Fig. 8 shows the crack propagation of roof snow and the sliding down off of the roof in the second test, which was conducted on January 18, 2013. The snow depth and the bulk snow density were 0.46m and 285.9kg/m$^3$, respectively. The snow weight per unit roof area was 131.7kg/m$^2$ (Total snow weight on the SSM was 947kg), which was 6.7 times heavier than that of Fig. 6. The atmospheric temperature was 0.1°C during the experiment. The snow sliding off of the roof started from the right eaves of the roof 1.5 minutes later from the beginning of the inflation operation. A large crack appeared in a direction parallel to the ridge of the roof about 3.4 minutes later. Finally, when about 95% of the snow volume fell down onto the ground surface 8.2 minutes later, the snow removal operation was stopped. Six experiments were carried out in the second test without any trouble. The time required to terminate the snow removal ranged 0.5 to 8 minutes.

Fig. 9 shows the snow sliding down off of the roof in the third test, which was conducted on January 12, 2014. The maximum snow depth was 0.065m because of a light snow fall. The atmospheric temperature was 0.2°C during the experiment. The snow sliding off of the roof started suddenly about 20 seconds later from the beginning of the inflation operation. Finally, the snow removal was terminated within one minute. Unfortunately, only a few experiments in this winter were carried out in the third test because of a light snow fall.

## 4 Conclusions

In order to reduce roof-snow removal related accidents, we have been developing a new roof snow removal system with a membrane structure (membrane roof snow removal system; MRSRS). The slide-off performance of the MRSRS is demonstrated by the membrane deformation, i.e. swell or shrink of the soft membrane using an air blower, so that the snow removal can be carried out without going on a roof.

We conducted field snow removal tests using the MRSRS mounted on three kinds of sloped roofs for two winter seasons (from 2011 to 2014) and surveyed the slide-off conditions for a range of snow depths, 0.2 to 0.65m and atmospheric temperatures, -3.0 to 0.2°C. It was found that the MRSRS showed a satisfactory snow slide-off performance, especially when snow is frozen hard. Conversely, the MRSRS did not go as smoothly as expected when roof snow was very fluffy. The time required for cleaning snow from a roof in 2013 and 2014 was about 15 minutes at the maximum.
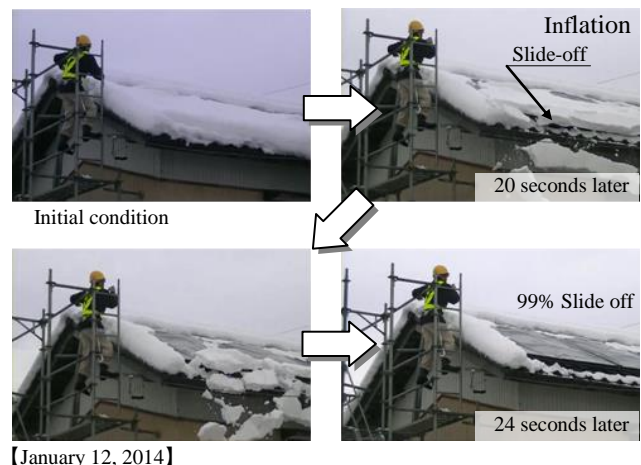
Further field experiments will be conducted to improve the snow-removal performance of the MRSRS technically and economically.

## Acknowledgments

## References

1. A. Sato, Journal of JSNDS, **25-1**, 71-81 (2006)
2. Cabinet Office, Government of Japan, (http://www.bousai.go.jp/setsugai/index.html), (2015/10/31 reference)
3. S. Kamimura, T. Umemura, Journal of JSSE, **12-3**, 212-21719 (1996)
4. T. Yamaguchi, Y. Habu, Journal of JSSE, **13-1**, 13-19 (1997)
5. D. Fukazawa, Journal of JSSE, **30-2**, 114-118 (2014)
6. T. Takahashi, Summaries of technical papers of Annual Meeting AIJ(B. Structures I), 95-96 (2014)
7. H. Terasaki, A. Fujimoto, T. Fukuhara, Summaries of JSSI & JSSE joint conference, 257 (2013)
8. H. Terasaki, A. Fujimoto, T. Fukuhara, Summaries of JSSI & JSSE joint conference, 270 (2014)
9. Katsuyama city office, (http://www.city.katsuyama.fukui.jp/docs/uploads/data/3658_data_lib_data_110328105242.pdf), (2015/10/31 reference)

# Accuracy of snow depth measurements on roods measured with photogrammetry

Takahiro Chiba[1,a] and Thomas K. Thiis[2]

[1]Department of Architecture, Faculty of Engineering, Hokkaido University of Science, Sapporo, Japan
[2]Department of Mathematical Science and Technology, Norwegian University of Life Science, Ås, Norway

**Abstract.** In this study, we conducted the photogrammetry using digital images for measuring snow depth on roofs. Two kinds of photo recording platform were considered in this study. Remotely Piloted Aircraft System (RPAS) and hand-held camera. To be able to validate the photogrammetry method, the snow depth distribution on the roofs were simultaneously measured with a snow sonde. The accuracy of the snow depth estimated by photogrammetry was examined by comparison with estimated value and measured value. As the results, the accuracy of estimated snow depth was affected by size of 3D mesh generated using digital images.

## 1 Introduction

The relationship between projective geometry and photogrammetry was first developed by Sturms and Hauck in Germany in 1883 [1]. Use of recently developed software to generate 3D mesh of objects using digital images is now relatively easy. 3D mesh for large areas can be obtained using images taken by aerial shot. Photogrammetry using digital images is being applied in research fields such as sediment disaster and glacier observation [1, 2] Sakurai et al (1998, 2000) measured the snow depth on roofs in discreet points using photogrammetry and helicopter and estimated the accuracy to be 30 - 40 mm [3, 4]. Yan et al (2008) has measured snow distribution on model building reproduced wind tunnel test based on the photogrammetry [5]. However, photogrammetry has not yet been used to measure the continuous snow distribution on full scale buildings

In this study, we tested photogrammetric measurements of snow distribution on four buildings with different roof shapes. The accuracy of the measurements is compared to snow sonde measurements and the accuracy of the photogrammetric measurements is estimated

## 2 Measuring methods

Table 1 shows a summary of the buildings for the photogrammetry in this study. The buildings all have different size, height, and roof shape. The roof shapes were three kinds of roof shape such as arched roof, frat roof, and pitched roof. The usefulness of No.1, No.2, No.3 and No.4 is sport arena, 4 story schoolhouse, garage and cabin respectively. In this study, to examine the accuracy of photogrammetric depth of roof snow, we measured the depth using snow sonde. The maximum depth dmax, No.1 was 0.30 m (3/2/2015), No.2 was 0.04 m (6/12/2014) and 0.09 m (11/1/2015), No.3 was 0.08 m (10/1/2015), and No.4 was 0.90 m (4/3/2015).

In this study, 3D mesh of surface of roof snow was generated using the software PhotoScan from Agisoft. The photogrammetric depth of roof snow was measured based on the 3D mesh. To obtain the suitable mesh, it is

**Table 1.** Buildings in the survey.

| Buildings | Summary |
|---|---|
|  | 【No.1 Arched roof】<br>・Site: Oslo, Norway<br>・Size: 86 × 120m<br>・Height: 28m (Radius: 62m)<br>・Use: Football stadium<br>・Date: 3/2/2015 ($d_{max} = 0.30$m) |
|  | 【No.2 Flat roof】<br>・Site: Ås, Norway<br>・Size: 11.7 × 31.5m<br>・Height: 15m（Ph: 0.5m）<br>・Use: School building<br>・Date: 6/12/2014 ($d_{max} = 0.04$m)<br>　　　 11/1/2015 ($d_{max} = 0.09$m) |
|  | 【No.3 Pitched roof Ⅰ】<br>・Site: Ås, Norway<br>・Size: 6.8 × 22.3m<br>・Height: 2.0m (Slope: 24.5°)<br>・Use: Garage<br>・Date: 10/1/2015 ($d_{max} = 0.08$m) |
|  | 【No.4 Pitched roof Ⅱ】<br>・Site: Gålå, Norway<br>・Size: 6.0 × 9.0m<br>・Height: 2.5m (Slope: 28.0°)<br>・Use: Cabin<br>・Date: 4/3/2015 ($d_{max} = 0.90$m) |

**Table 2.** Photo recording methods used in each case

| No. | Shooting method | Camera | Number of images | Shooting distance (Mean value) |
|---|---|---|---|---|
| 1 | RPAS | Canon IXUS (16M pixel) | 250 | 45m |
| 2 | Hand-held | Pentax Q (12M pixel) | 25 | 5m |
| 3 | Hand-held | Pentax Q (12M pixel) | 60 | 7m<br>15m |
| 4 | RPAS | Canon IXUS (16M pixel) | 245 | 15m |
| | Hand-held | Pentax Q (12M pixel) | 89 | 7.5m |

necessary to use photographs which have more than 60% overlap in each other. Also size of the mesh become small

---

**Figure 1.** Photographing the arched roof (No.1).
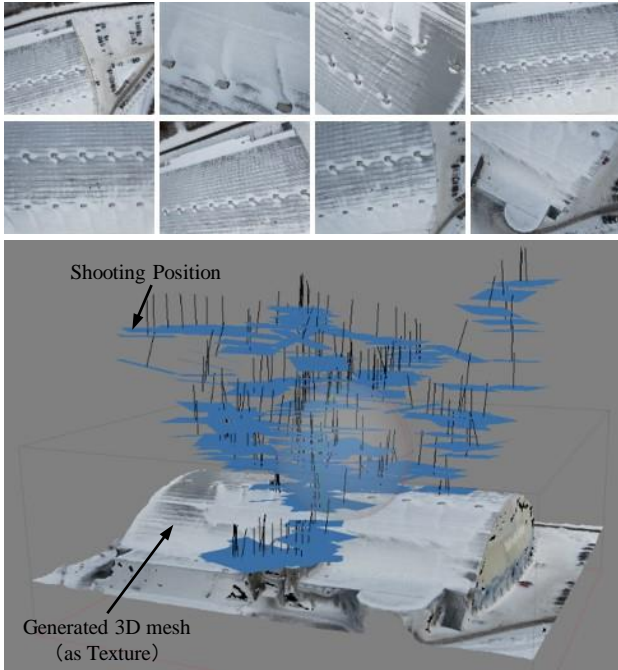


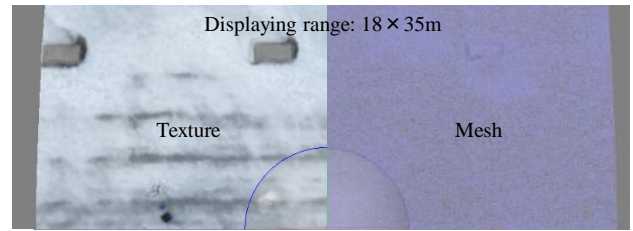**Figure 2.** 3D model and position of images used in No.1.
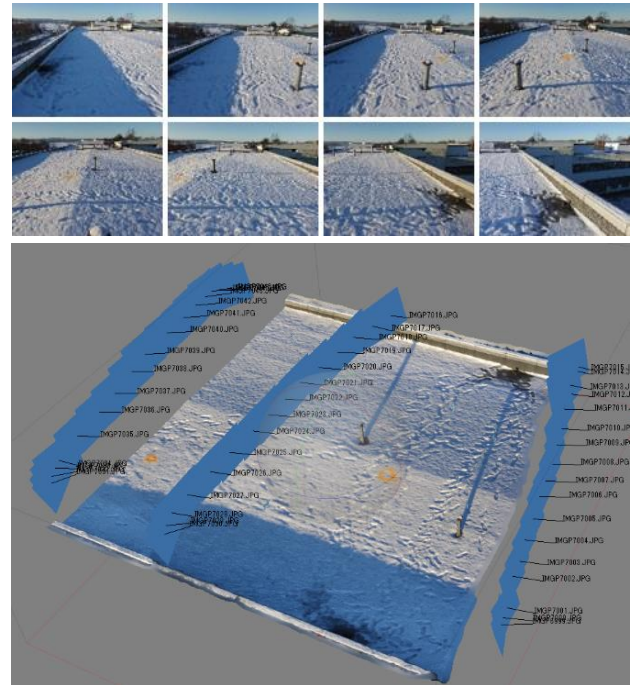


**Figure 3.** Summary of obtained mesh size



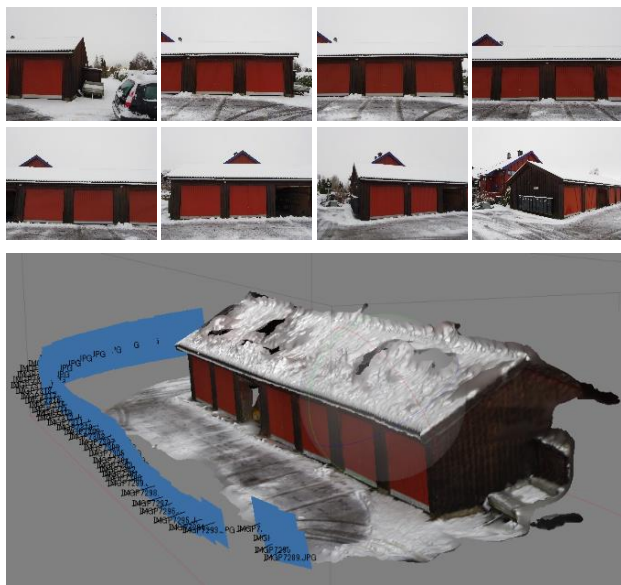**Figure 4.** 3D model and position of images used in No.2 (6/12/2014).
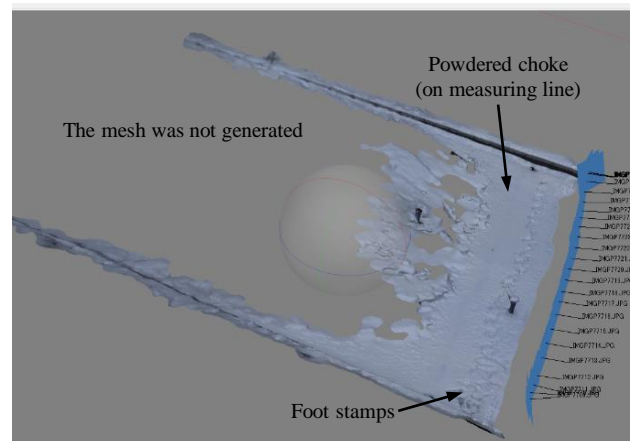


**Figure 5.** 3D model and position of images used in No.2 (11/1/2015).

with the pixel's number increases. Therefore, Accuracy of the 3D mesh is affected by photograph's number and the shooting distance. Table 2 shows photo methods, property of digital cameras, and shooting distance. Two kinds of photo recording platforms were used in this study. Remotely Piloted Aircraft System (RPAS) and hand-held camera. We used digital camera Canon IXUS (16M pixel) in RPAS and Pentax Q (12M pixel) in hand-held. Approximately 250 photographs were taken in RPAS. The shooting distance increased with building size increase. For hand-held camera, Number of photograph was less compared to RPAS, and also shooting distance was short.

## 3 Results

### 3.1 Conditions of generated 3D mesh

Figure 1 shows the use of the RPAS in case No.1 (Arched roof). The camera used with the RPAS was a standard Canon IXUS camera that was attached to the RPAS and programmed to take 20 pictures every minute. Figure 2 shows the shooting position of each picture and the 3D photogrammetrically surveyed model of the building. 250 images were taken in the investigation, and approximately 30% of the pictures were discarded due to bad quality. Figure 3 shows a detail of the 3D mesh. In the area which could be displayed as suitable texture, detailed mesh was sufficiently generated.

Figure 4 and Figure 5 shows quality of photographs and conditions of 3D mesh in case of No.2 (Flat roof). The conditions of 3D mesh were different in two kinds of weather such as sunny and cloudy. For sunny weather,

< Cloudy weather >

**Figure 6.** 3D model and position of images used in No.3.



< Sunny weather >
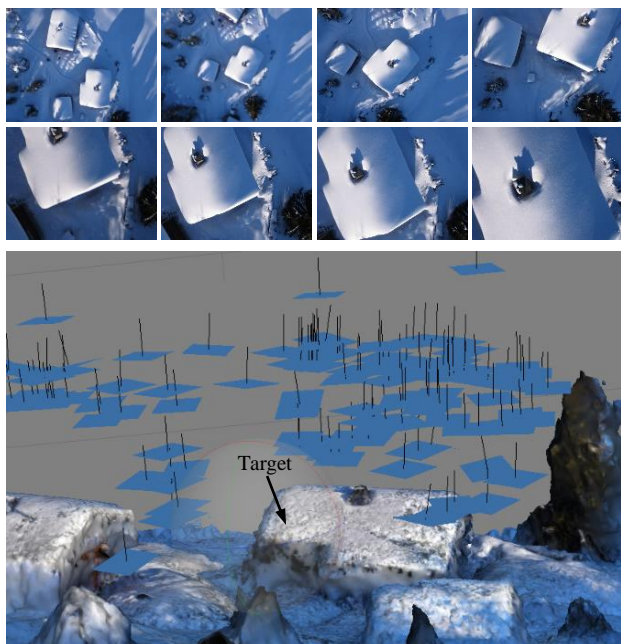


< RPAS >
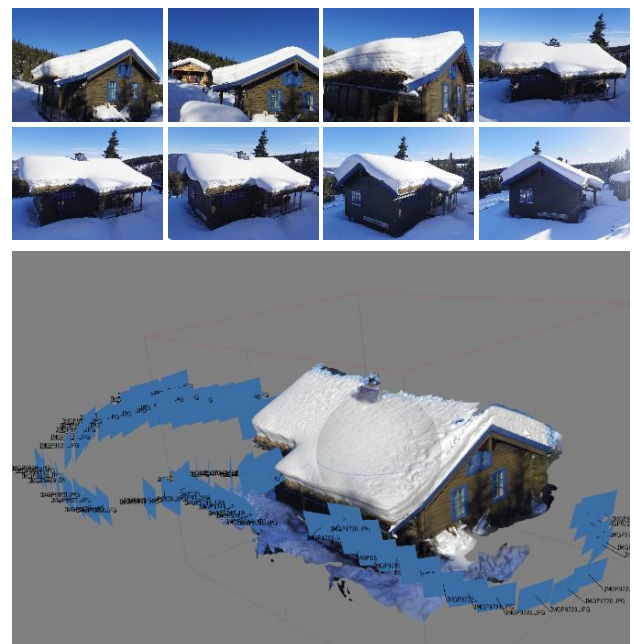
**Figure 7.** 3D model and position of images used in No.4.



< Hand-held camera >

pattern of snow surface could be taken clearly. Also the detailed 3D mesh was sufficiently generated. However, for cloudy weather, it was difficult to recognize the pattern of snow surface from the photographs. The generated 3D mesh was the area which was sprinkled the powdered blue choke, and which was placed some foot stamps. Figure 6 shows conditions of generated 3D mesh in No.3 (Pitched roof Ⅰ). The 3D mesh was similar to the conditions of No.2. According to these results, the quality of 3D mesh of snow surface was affected by the weather conditions of when were taken photographs. It is desirable that the shooting condition of snow surface is sunny, which is easy to recognize the pattern. Figure 7 shows conditions of generated 3D mesh in No.4 (Pitched roof Ⅱ). For the sunny weather, the pattern of snow surface could be taken

in both RPAS and hand-held camera. However, the quality of 3D mesh obtained from RPAS was not good compared to hand-held camera. This is that unfocussed photographs caused by flight shooting was included in the 3D mesh analysis.

## 3.2 Comparison with photogrammetric depth and sonde measurements

Figure 8 shows comparison with photogrammetric depth and sonde measurements in No.1 (Arched roof), and distribution of the error which was calculated by photogrammetric depth minus sonde measurements. In upper side of the roof, the photogrammetric depth was similar to the sonde measurements. For lower side of the

< No.1 Arched roof >



< No.2 Flat roof >
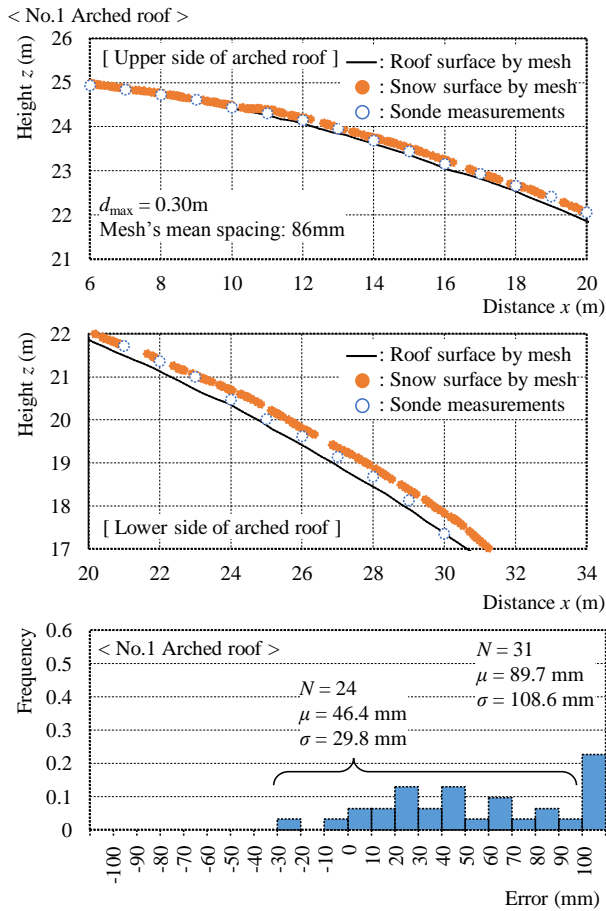


**Figure 8.** Comparison with photogrammetric depth and sonde measurements, and distribution of the error (No.1).
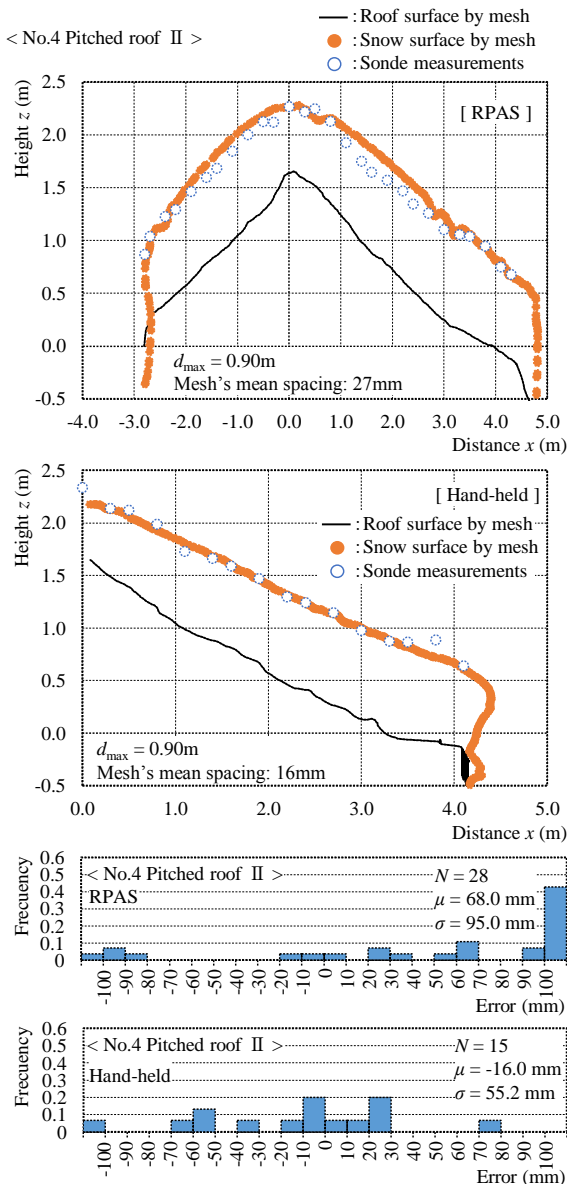
roof, the error between the photogrammetric depth and sonde measurements was large. The distribution of the error in the upper side had normal distribution. However, the error of the lower side was more than 100 mm. The error of the lower side might be affected by some unfocussed photographs and long shooting distance. Figure 9 shows the error and the distribution in No2 (Flat roof). The mean error between the photogrammetric depth and sonde measurements was 1 to 3 mm. To be taken by hand-held camera, also to be short shooting distance, the error was very small. In addition, the error in case of sunny weather was small compared to cloudy weather. Figure 10 shows the error and the distribution in No3 (Pitched roof Ⅰ). The error between photogrammetric depth and sonde measurements increased with shooting distance increase. Figure 11 shows the error and the distribution in No4 (Pitched roof Ⅱ). The error was large compared to the case of stated above. Also the distribution was not normal distribution. The roofing of this building has been constructed in traditional method in Norway, which has some planting. The tip of the snow sonde using in this investigation was deeper than the roof surface.

### 3.3 Relationship between shooting distance and accuracy of photogrammetric depth

The size of 3D mesh depended on number of pixel in the digital photographs. Therefore, the photogrammetric depth might be affected by the shooting distance. Figure 12
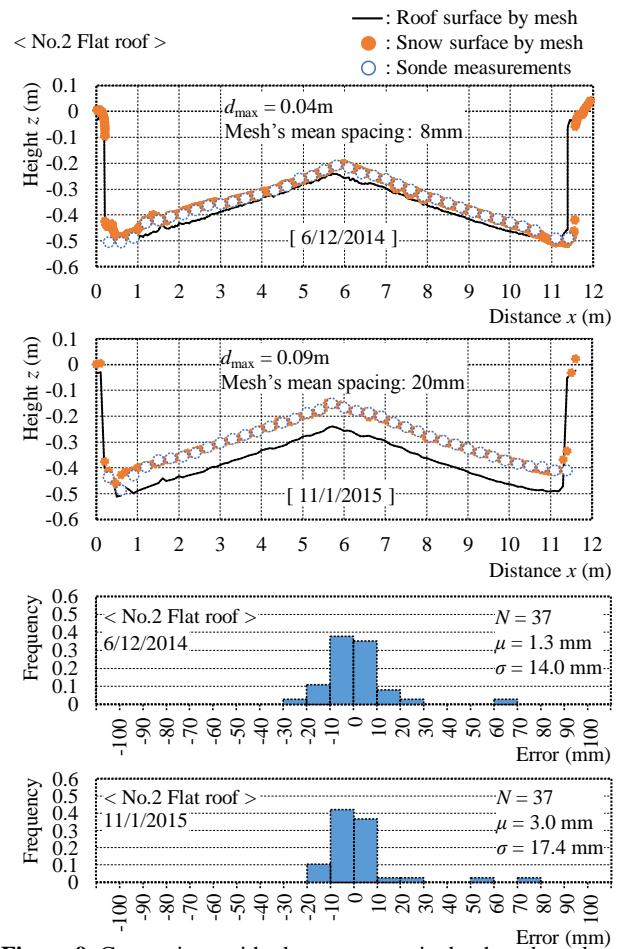
**Figure 9.** Comparison with photogrammetric depth and sonde measurements, and distribution of the error (No.2).

< No.3 Pitched roof Ⅰ >
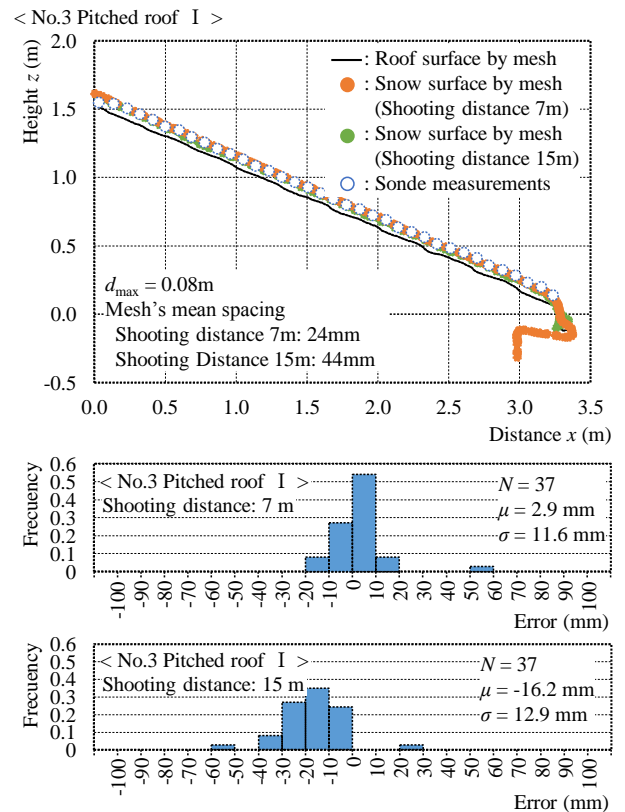


**Figure 10.** Comparison with photogrammetric depth and sonde measurements, and distribution of the error (No.3).

**Figure 11.** Comparison with photogrammetric depth and sonde measurements, and distribution of the error (No.4).

shows relationship between shooting distance and mesh's mean spacing. The mean spacing increased with shooting distance increase in each shooting method. In this study, the accuracy of the photogrammetric depth was defined as $|\mu| + \sigma$ ($\mu$: mean error, $\sigma$: standard deviation of the error) [5]. Figure 13 shows relationship between shooting distance and $|\mu| + \sigma$. The accuracy of the photogrammetric depth was similar to the mean spacing in except lower side roof of No.1 and No.4. Therefore, the accuracy of the photogrammetric depth can be estimated using mean spacing of the 3D mesh.

## 4. Conclusions

In this study, we conducted shooting of digital photographs by RPAS and hand-held camera, and then examined accuracy of photogrammetric snow depth on roofs. As the results, it was found that accuracy of the photogrammetric depth depended with mean spacing generated 3D mesh.
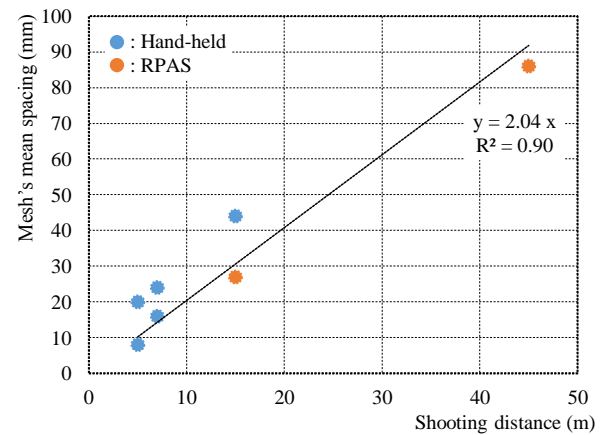


**Figure 12.** Relationship between shooting distance and mesh's mean spacing.
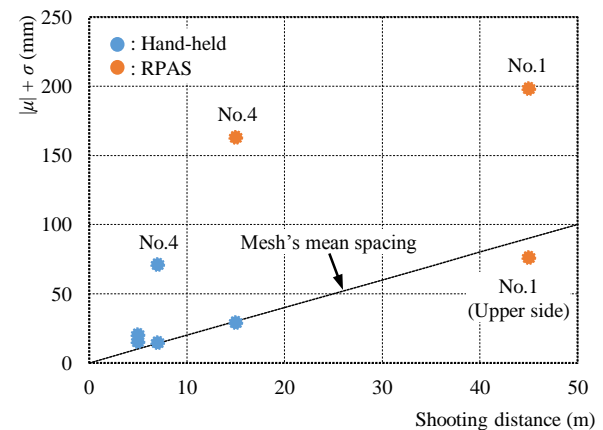


**Figure 13.** Relationship between shooting distance and accuracy of photogrammetric depth.

## References

1. Doyle, F.: The Historical Development of Analytical Photogrammetry, Photogrammetric Engineering, 30(2), pp.259-265 (1964)
2. Uchiyama, S., Inoue, H., Suzuki, H.: Approached for Reconstructing a Three-dimensional Model by SfM to Utilize and Apply this Model for Research on Natural Disaster, Research Report of Earth Science and Disaster Prevention, No.81, pp.37-60 (2014)
3. E. Bernard, J.M. Friedt, F. Tolle, et al.: Monitoring seasonal snow dynamics using ground based high resolution photography, ISPRS Journal of Photogrammetry and Remote Sensing, 75, pp.92-100 (2013)
4. Sakurai, S., Joh, O., Shibata, T.: Survey of Roof Snow Depth by Aerial Photogrammetry, Proceedings of the Second International Conference on Snow Engineering, pp.93-103 (1993)
5. Sakurai, S., Joh, O., Shibata, T.: Aerial photogrammetry of roof snow depths using three different aircraft, Proceedings of the Fourth International Conference on Snow Engineering, pp.81-87 (2000)
6. Yan, K. and Cheng, T.: Close Shot Photogrammetry for Measuring Wind-Drifted Snow Distribution on Stepped Flat Roofs, 2008 ISECS International Colloquium on Computing Communications, Control, and Management, pp.332-335 (2008)

# A new ring-shaped wind tunnel facility to study wind-packing of snow

Christian G. Sommer[1,2,a], Michael Lehning[1,2] and Charles Fierz[1]

[1]WSL Institute for Snow and Avalanche Research SLF, Davos, Switzerland
[2]CRYOS, School of Architecture, Civil and Environmental Engineering, EPFL, Lausanne, Switzerland

**Abstract.** A new wind tunnel was designed and built at SLF. The facility is ring-shaped to simulate an infinite fetch. This is important for experiments where the observed processes have a slow time scale (minutes to hours). The wind tunnel was developed to study the formation of wind-packed snow. The facility is equipped with sensors to monitor environmental parameters such as wind speed, air temperature and air humidity. A SnowMicroPen and an industrial camera allow to measure properties of the snow surface. The facility is flexible and mobile having outer dimensions of 2.3x1.3x0.5 m. Airflow is created by a model aircraft propeller and the wind speed reaches values of up to 10 m/s. First experiments show that saltation is needed for wind crust formation.

## 1 Introduction

An open-circuit linear wind tunnel already exists at SLF and has, for example, been used to measure the saltation threshold of snow [1]. For slow processes like the formation of a wind slab/crust, the fetch of this wind tunnel is too short because drifting particles leave the facility in less than a second. A ring-shaped wind tunnel mimics an infinite fetch and is therefore better suited to study the formation of wind-packed snow. Wind-packing is the process through which a hard surface layer is formed due to wind action [2].

Ring-shaped wind tunnels have been built before. At the University of Heidelberg such facilities have been in operation since 1980 and are used to study air-sea gas transfer under different water surface conditions [3].

The primary goal of our new wind tunnel is to study the formation of wind slabs but care was taken to design a flexible and mobile facility. For example, it could also be used to study the evolution of saltating particles or for experiments in the field.

## 2 First prototype and experiments

To gain a basic understanding of the flow in a curved duct and how drifting snow behaves in such a situation, a prototype wind tunnel was built and used for preliminary experiments. These tests also provided valuable insight as to how such a facility is best operated.

### 2.1 Design

The prototype had an outer diameter of about 1.3 m. The channel was 18 cm wide and 50 cm high (Figure 1). A model-aircraft propeller created the airflow. The correct propeller was chosen based on the Cordier Diagram [4] after estimating the pressure drop and the volume flow in the tunnel. The propeller rotated at up to 12000 rpm and was driven by an electric motor. Wind speeds of up to 12 m/s could be reached. The covers of the wind tunnel were removable and a section was made of transparent Plexiglas. The prototype was equipped with a wind speed

sensor and an instrument to measure air temperature and humidity.
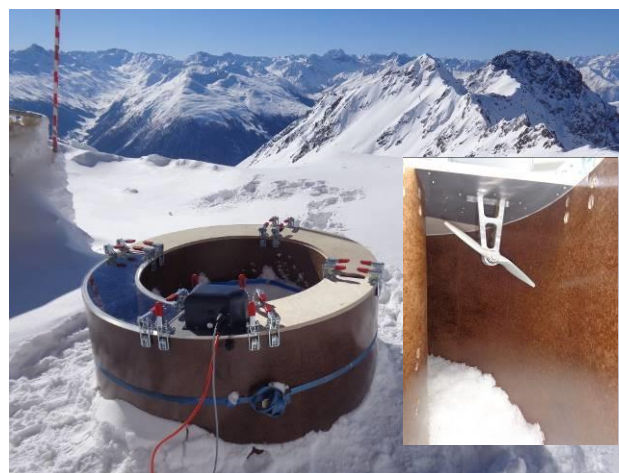


**Figure 1.** The prototype wind tunnel deployed in the field. The outer diameter is about 1.3 m. The channel width is 18 cm. The insert shows the propeller.

### 2.2 Operation

The prototype wind tunnel was open at the bottom and could therefore simply be placed on the snow surface by two people. To collect fresh snow, the covers were removed and the wind tunnel was left open during a snowfall. Unfortunately, the resulting snow surface in the channel was usually not flat and appeared to have been influenced by wind. Placing the wind tunnel on the snow surface was also problematic as the rings tended to settle considerably, especially in sunny weather.

### 2.3 Results

Measurements of air temperature and humidity revealed considerable variations of these variables depending on whether the covers were closed or partly open.

During operation, the snow did not accumulate at the outer wall as might have been expected. However, surface features formed rapidly (Figure 2a).

---

[a] Corresponding author: sommer@slf.ch

Large snow accumulations behind the propeller (Figure 2b) revealed the poor quality of the flow in the tunnel. Because of the centrifugal effects, a boundary layer with a logarithmic profile cannot be achieved but the flow quality should be improved nevertheless (see below).
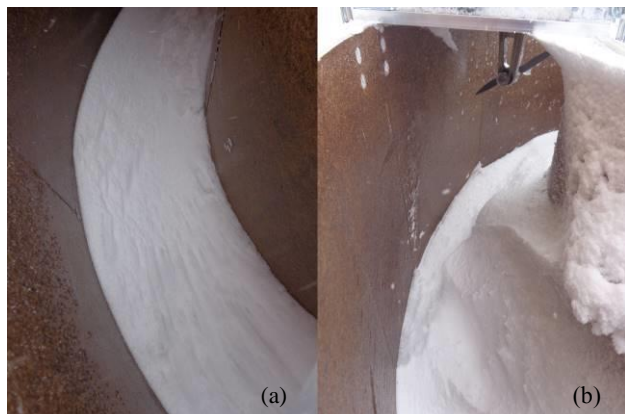


**Figure 2.** (a): The snow surface in the channel showing surface features. (b): Snow accumulations on the inner wall downstream of the propeller.

## 3 Redesign of the wind tunnel

To increase the flow quality a honeycomb and two one-metre long straight sections were added to the tunnel (Figure 3). The straight sections also provide additional space for measurements. The covers feature four circular holes, which can be left open or closed. This allows a basic control over air temperature and humidity. When closed, both variables tend to increase. Opening the holes leads to the entrainment and mixing with surrounding air, which is generally drier and colder.



**Figure 3.** The redesigned wind tunnel.

The new wind tunnel features an automatic data acquisition system based on LabVIEW to measure parameters such as wind speed, air temperature and humidity at three locations as well as snow temperature and snow surface temperature. LabVIEW is also used to control an industrial camera. This camera will detect

drifting snow and allow to perform near-infrared (NIR) photography [5]. Additional measurements include the snow height (millimetre scale) and the snow hardness (using a SnowMicroPen [6]).

The wind tunnel now includes an aluminium structure that allows the tunnel to be lifted by a crane. The new facility is operated as follows: Fresh snow is collected on wooden trays outside the building, the snow-filled trays are then brought inside on a cart and the wind tunnel is lowered onto this snow surface. This ensures that the snow surface is flat and that the wind tunnel is in a stable position. The same procedure to collect snow is used in the straight wind tunnel facility [1].

## 4 Results

During the winter 2016, experiments were performed to test which processes are important for the formation of wind-packed snow. Based on literature, it appears that the air humidity has to be high and that the main process is fragmentation of snow particles in the saltation layer followed by sintering [2, 7]. Therefore, experiments with and without drifting snow were carried out. Thus far in our experiments, we never observed a relative humidity below about 80% even with the holes opened.

The experiments showed that no hardening occurs if there is no saltation. If there is drifting snow, the hardening is closely correlated with areas of deposited snow. Erosion without hardening and deposition appear to alternate in a random fashion in space and time. For the moment these processes can only be analysed qualitatively.
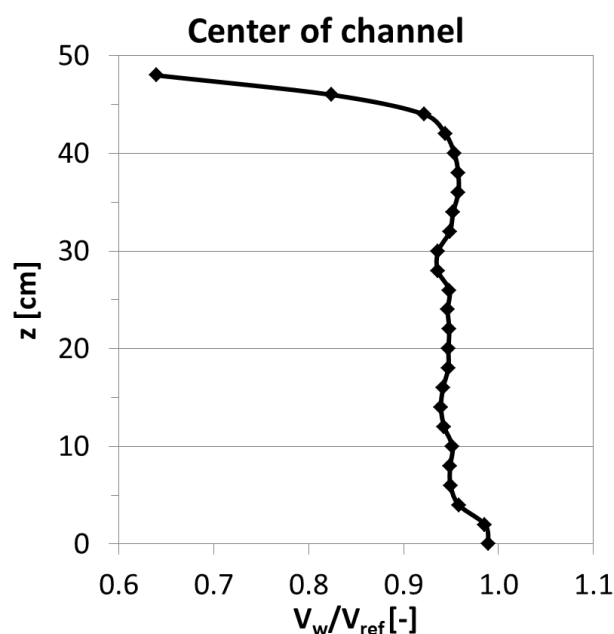


**Figure 4.** Relative velocity profile at the center of the channel in the main test section.

The flow quality turned out to be improved by the addition of the straight sections. The flow is still chaotic behind the propeller but can now settle sufficiently until

it reaches the test section. The honeycomb only covered the top half of the channel to limit contact with flying snow particles. Unfortunately, many particles still reached the honeycomb, so that it had to be removed due to clogging. The flow in the test section could, however, be further improved by moving the propeller to the rightmost position in Figure 3. This made the saltation intensity more uniform across the width of the channel.

Figure 4 shows a velocity profile in the main test section. As mentioned before, there is no logarithmic profile at the surface. The wind speed is almost constant over much of the channel height. The reference wind speed $V_{ref}$ used to normalized the profile is the wind speed measured in the usual position of the MiniAir wind speed probe.

## 5 Outlook

For next winter we would like to introduce a system to better control the temperatures in the wind tunnel while the air humidity is now less a concern, because there is no hardening without saltation even if the humidity is high. At low air humidity, hardening would be even less likely. Moreover, with saltation, the air close to the surface is almost saturated in any case.

In addition, a system to measure quantitatively erosion and deposition appears necessary. A possibility would be to use a Microsoft Kinect, which is a low-cost 3D scanner. Otherwise, the wind tunnel and its operation will remain largely the same.

## References

1. A. Clifton, J. Rüedi, M. Lehning, J. Glaciol., **52**, 585-596 (2006)
2. G. Seligman, *Snow structure and ski fields*, (1936)
3. B. Jähne, *Zur Parametrisierung des Gas-austauschs mit Hilfe von Laborexperimenten* (1980)
4. O. Cordier, BWK Zeitschrift, **5**, 337-340 (1954)
5. M. Matzl, M. Schneebeli, J. Glaciol., **52**, 558-564 (2006)
6. M. Schneebeli, J.B. Johnson, Ann. Glaciol., 26, 107-111 (1998)
7. V. Kotlyakov, *The Snow Cover of the Antarctic and its Role in the Present Day Glaciation of the Continent* (1966)

# The use of sheet piles as measures against rapid mass flows

Árni Jónsson[1a], Guðmundur Heiðreksson[2], Torfi B. Jóhannsson[3], Magnús Steinarsson[3]

[1] *Norwegian Geotechnical Institute (NGI), Sognsveien 72, 0806 Oslo, Norway*
[2] *Icelandic Road and Coastal Administration (IRCA)Borgartúni 5-7, 105 Reykjavík, Iceland*
[3] *MogT Engineering, Akralind 1, 201 Kópavogur, Iceland*

**Abstract.** Steel sheet piles have been used for mitigation against small snow avalanches and rock falls for over twenty years in Iceland in areas with limited space for other types of mitigation measures at road sides. Those approx. 3 m high structures have proved to be useful and have resulted in fewer road closures. Little is known about the forces that avalanche or rock falls exert to these structures and it hampers further development. For this reason, the Icelandic Road and Coastal Administration (IRCA) and the Norwegian Geotechnical Institute (NGI) decided to instrument one such wall in north Iceland.

## 1 Introduction

Narrow fjords with steep mountainsides are a challenge for road safety in Iceland, Norway and many other mountainous countries. Conventional mitigation measures in the run-out zone, like dams, are usually not applicable due to limited space. Supporting structures in the starting zone are in many cases too expensive in relation to the traffic volume of the road. Therefore space-saving structures are needed.

While steel sheet piles are well known as a wall material in piers and in excavations in loose and unstable soil, there are virtually no reports on their use in mitigation against rapid mass movements. However, for over twenty years steel sheet piles have been protecting road sections in Iceland against small snow avalanches and rock falls. These typically 3 m high structures have proved to be useful and have resulted in fewer road closures even though the snow cloud and part of the dense part can overtop the wall. Larger/higher structures to stop larger avalanches are feasible.

Little is known about the forces that avalanches or rock falls exert on the steel sheet piles and how the latter react to these loads. Yet good control over this is necessary for ensuring the functioning of the walls and optimizing their design also with respect to cost. For this reason, the Icelandic Road and Coastal Administration (IRCA) and the Norwegian Geotechnical Institute (NGI) decided to instrument one such wall in northern Iceland.

## 2 The test site

The first installations of steel sheet piles were alongside the road in Óshlíð just outside of Ísafjörður in Iceland. The experience from these steel sheet pile walls was positive and therefore protection of other road sections was considered. The road section between the villages Dalvik and Ólafsfjörður in northern Iceland is known for high avalanche activity, especially along the section just outside the abandoned farm at Sauðanes [1]. IRCA installed three steel sheet pile sections in three known avalanche paths, each of about 50 m in length. Avalanches usually fall several times per winter in these paths. Even though they are rather small, they are nevertheless big enough to throw cars off the road.



**Figure 1**. Installation of the steel sheet piles in 2011. Photo: IRCA

The steel sheet pile wall measures about 3 m above the ground and approximately 1.5 m in the ground see Figure **1**. It is built of Z profiles, which gives approx. 40 cm depth of the form in flow direction. Due to the thin layer of loose material at the site, it was necessary to excavate a trench, fill it with compacted gravel, and drive the sheet piles into it.

In order to have sufficient storage capacity for snow avalanches and to dissipate part of the kinetic energy of both rocks and snow avalanches, the foot of the slope was removed to a distance of about 16 m from the wall. It is, however, necessary to clear this area from avalanche debris after each event because subsequent avalanches would otherwise easily overflow the wall.

## 3 Instrumentation

The instrumentation consists of five strain gauges that are located on the middle sheet of the wall at 231, 144, 67, −10 and −87 cm from the ground surface, Figure 2. Two further strain gauges are located on the fifth sheets to the north and the south from the central one, respectively, at a depth of −10 cm from the ground surface. The signals

---

[a] Corresponding author: arni.jonsson@ngi.no

from these seven sensors are sampled at 270s-1 and stored in Campbell CR 5000 data logger that is placed on the outs side of the wall and can be accessed remotely. The battery is sufficient for two months of continuous unattended operation and 100W solar panel is also as a reserve power. The data is sent through a 3G router to the base in Kópavogur Iceland.



**Figure 2**. Installation of monitoring instruments in January 2015. Photo: MogT.

The strain gauges were installed in January 2015. Due to an unusual winter 2014/2015 no avalanche has hit the wall (which is unusual for this location in a normal winter). Therefore, no results can be presented yet, but we expect to obtain measurements during the winter 2015/2016.

## 4 Conclusions

Sheet pile walls can provide adequate and cost-effective protection against rock fall and small snow avalanches. They are particularly valuable in locations close to the foot of slopes where there is little space available. The ongoing measurement campaign on a road in northern Iceland will help to optimize their design and to put the dimensioning of such structures on a secure footing.

## References

1. ORION Consulting. (2007). ÓLAFSFJARÐAR-VEGUR (82), DALVÍK – ÓLAFSFJÖRÐUR. Greinargerð um snjóflóð, snjóflóðahættu og tillögur um varnaraðgerðir. (e: Report on snow avalanches, snow avalanche danger and proposed mitigation measures).

# In flight wet snow particles characterisation

Philippe Delpech[1,a], Guy Febvre[2], Christophe Gourbeyre[2], Dominique Lenoir[1] and Fabrice De Oliveira[1]

[1]Centre Scientifique et Technique du Bâtiment (CSTB), CAPE Department, 11 rue Henri-Picherit 44300 Nantes, France
[2]Laboratoire de Météorologie physique, UMR 6016, université Blaise Pascal, CNRS,  63178 Aubière, France

**Abstract.** Wet snow is composed of water particles, in transient state between liquid and solid state. Snow characteristics as the Liquid Water Ratio (LWR) of in-flight snow particles is valuable information along ambient temperature, wind velocity and mass flux to ensure the reproducibility of the snow tests undertaken in climatic wind tunnel, as well as the analysis of the phenomena of snow accumulations and accretions to test structures. The paper discusses the potentiality of optical measurement systems to assess the snow LWR. The design of a thermal measurement system based on the hot wire probe concept is presented. The mechanical and thermal parts are described. The analyses of the early experimental results are tackled, as the prospects of optimization.

## 1 Introduction

Ice accretions due to driving wet snow events are common atmospheric icing phenomena and concern several fields of engineering, i.e. civil engineering, transport, energy production, etc…. Precipitation particles which generate wet snow accretion are characterized by a mixed phase. The water/solid ratio of water particles can be evaluated according the liquid water ratio: *LWR*. This dimensionless parameter represents the ratio of the liquid mass of the particle to the total mass of the particle: $LWR = \frac{m_l}{m_p}$.

Climatic wind tunnel testing with artificial snow making capacity belongs to the usual methods of evaluation of constraints applied to structures due to regular and wet snow events.



**Figure 1.** Snow test in a climatic wind tunnel

Moreover, wind tunnel experiments support the development of numerical models to be used to assess the risks of large scale snow and ice accretion on building or vehicle elements. This requires that experimental conditions leading to a specific snow accumulation are accurately identified including measurement and control of freezing precipitations that are produced in the climatic chamber.

Previous works have shown the primary effect of the LWR of snow on the snow accretion mass and volume [1]. The experimental approach was based on the assessment of wet snow accretion formation on simple geometric shapes. Cylinders were placed in the snow particle flow produced in the climatic wind tunnel. If all other parameters are kept constant, the ambient temperature setting (from -10°C to -2°C) allows to modify the thermodynamic state of the snow particle at time of impact. It is then possible to assess the effect of the liquid water ratio on the accretions and perform a parametric study.

A numerical model for two-phase flows simulation was developed in parallel. The study has been setup mainly to identify the most important parameters that drive the accretion phenomenon. In the particular wind tunnel conditions, the results obtained with -10°C and -2°C experimental tests provided the limiting cases as being the conditions were the accretion was either very thin and could not be weighted or too humid and could no longer be considered as actual snow.

With the three intermediate ambient temperatures, 6°C, -5°C, -4°C, one could observe the evolution of the accretion sizes to the structures (Figure 2).
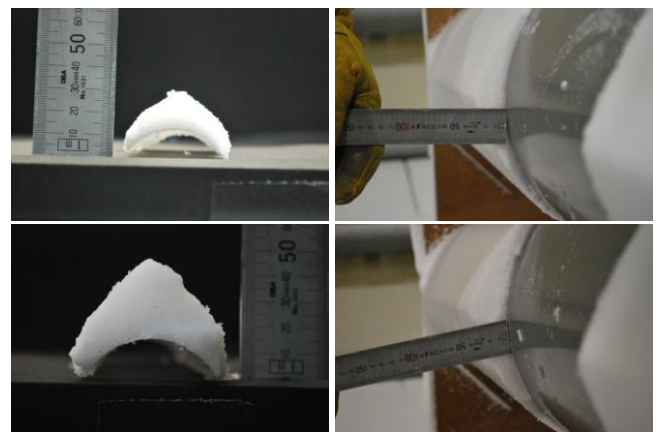


**Figure 2**: Examples of wet-snow accretion (ambient temperature -6°C top and -4°C bottom)

Qualitatively, one could observe how the augmentation of temperature induces accretions more humid and dense on the cylinders.

Evaluation of the parameters, which govern wet snow accretion, leads to the possibility to undertake a

---

[a] Corresponding author: philippe.delpech@cstb.fr

numerical study to characterize the different accretions by using a so called "stick-function" for wet snow particles. Such a modelling requires to assess experimentally the sticking capacity of snow and the associated LWR at the impact time.

There are several techniques available to measure liquid mass fraction of snow deposited on the ground. They are based on electric permittivity measurements or melting calorimetry [2]. Measurement pieces of equipment are readily available and commonly operated in the field in avalanche engineering to assess stability of snow cover.

On the other hand, there are few means of measuring in real time the LWR of inflight snow particles. The objective of this article is to present the methods tested in the climatic chamber of CSTB either based on optical and thermal measurement systems.

## 2 Experimental Setup and test conditions

The experimental test conditions used for the snow particle measurements are inspired from a configuration commonly implemented for snow icing experiments in the CSTB climatic wind tunnel.

The snow is produced by one snow cannon placed on the central axis of the test section at 7.30m from the wind tunnel nozzle. The measurements area is located 10m downstream of the snow canon (Figure 3). The snow cannon has been setup in a counter-current configuration to enhance the spatial uniformity of particle concentration in the air flow. This configuration also ensures that particles are carried out to the test structure in equilibrium with the air flow.
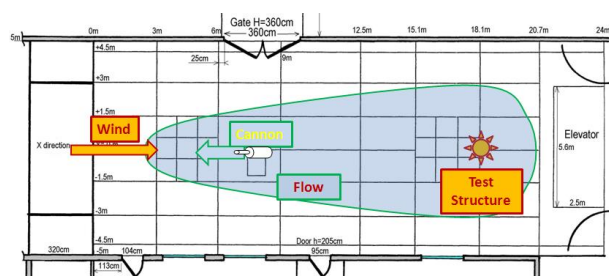


**Figure 3.** Experimental setup for the wet snow icing tests

The snow used during the tests is produced by one high-pressure snow cannon (model Y10 York). This cannon produces snow by mixing water and air at high pressure (from 6 to 10bar), after the mixing the flow is expulsed by an orifice at high speed (80 to 100m/s). The snow cannon injects in the air flow particles of water which temperature is close to 0°C. The particles begin to freeze as soon as they enter in contact with the cold air stream.



**Figure 4.** Positioning of snow cannon against the flow in the wind tunnel

The distribution of water droplets produced by the snow cannon has been characterized in several previous studies with the help of different instruments (Malvern Spraytec, Aerometrics PDPA). The measurements have revealed a medium particle size close to 250µm as shown in (Figure 5).
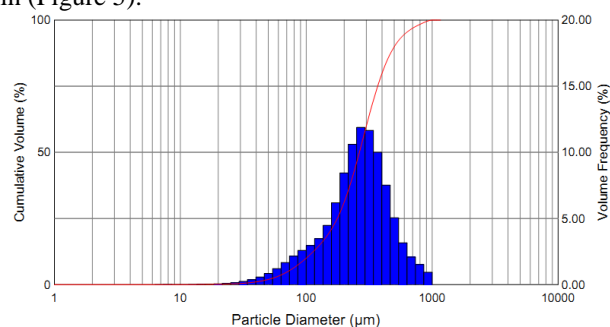


**Figure 5.** Particles diameter distribution (Malvern Spraytec)

The measurements were made for ambient temperatures between -10 ° C and + 5 ° C. The wind speed was varied between 10m/s and 20m/s. The settings of the snow cannon have been also adjusted to test several air / water ratios.

## 3 Optical measurement systems

The in situ means traditionally used to characterize cloud particles are of two types, the imagers (2DC, 2DS, CPI ...) or laser particle size analyzers based on the principles of light scattering by a particle (FSSP, CDP, …).

The imager type probes are well suited to the discrimination of solid and liquid phases of natural icing particles since the morphology parameter identifies the type of particles without doubts especially for larger ones.

### 3.1 2DS probe measurements

The 2DS is an imager whose operating principle is based on the recording signal from an array of photodiodes illuminated by a collimated laser. The path of a particle in the laser beam disturbs the lighting of the photodiodes. The sampling rate of the photodiode array being controlled by the velocity of the particle, that is to say the speed of the air flow passing through the sampling volume, the two-dimensional image of the particle is reconstituted with pixel resolution of 10 microns [3].

Discrimination of water and ice is essentially based on the shape of particles, assuming a spherical shape corresponds to the liquid phase [4]. Indeed vapor diffusion and / or coalescence crystal growth processes usually lead to non-spherical geometries, although some cases of spherical crystals or deformed water drops situations have been reported which animates the specialized scientific community. Hence, according the analysis of the images, discrimination water/ice can be made, based on the assumption that the phase ice leads to an aspect ratio of the particles different than 1.



**Figure 6.** Particle imaging probes 2DS (left) and FSSP (right)

Initial measurements were made at positive temperature with the 2DS probe in order to get a reference data sample of liquid droplets. Measurements in freezing conditions were then in varying ambient temperature, wind velocity and location in the wind tunnel test section.



**Figure 7.** Snow test with the particle imaging probes 2DS

Computerized post-treatment enables processing of the images captured by the 2DS one by one with artifacts elimination algorithm. A filtering function from a standard aspect ratio is used as a mean to discriminate water from ice. Characteristic parameters are extracted from the particle morphology.
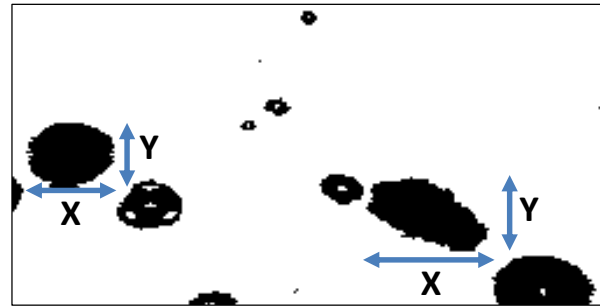


**Figure 8.** 2DS sample image and definition of characteristic length in terms of number of shaded pixels.

The aspect ratio parameter $\alpha$ is defined as the X/Y ratio. Filtering is based on a user defined value of this ratio from 1 to infinity. It is commonly accepted by the operators of 2DS that the water / ice discrimination corresponds to the limiting value $\alpha = 2$.

In the experimental conditions of the wind tunnel, the assumption is that the ice phase is due to the freezing of droplets. The vapor diffusion growth process (Wegener-Bergeron-Findeisen) leading to dendritic shapes require longer periods than the wind tunnel flight time that it is the order of the second. The deformation of the droplets, if any, during freezing will be minimal.

Hence, the differentiation criterion suggested by the 2DS manufacturer should be revalued. For this it is necessary to assess the parameter $\alpha$ as a filtering parameter. This was done by counting the number of drops detected by the 2DS according the value of $\alpha$.

Measurements made at positive temperature, for which water droplets produced by the snow cannons remain liquid during their trajectory, allow assessing the sensitivity of the parameter $\alpha$ to image artifacts or to deformation of the drops during flight.

After eliminating image artifacts, 55000 different particle images were processed. For each image the X/Y ratio was calculated. It was then possible to count the number of particles with respect to the parameter $\alpha$. This count is normalized by the total amount of particles.

For the icing experiments the same approach was followed regarding the sensitivity analysis of the $\alpha$ parameter at different stages of freezing along their trajectory. The normalized counting of the number of particles as a function of aspect ratio was plotted for freezing and non-freezing conditions.
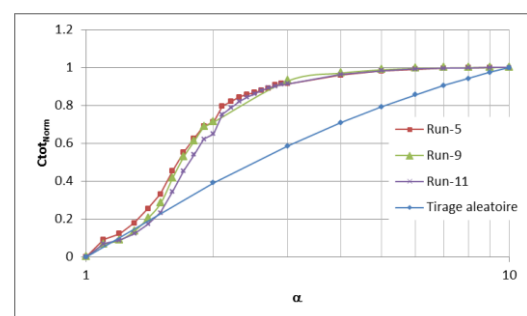


**Figure 9**: Evolution of the number of freezing droplets with respect to the aspect ratio during 3 experiments at positive (Run 5) and negative temperature (Run 9 and 11) according the 2DS probe measurements.

Filtering based on the value of α does not highlight significant differences between the run. It is therefore not possible with this criterion to identify possible morphological evolution of the particles depending on the icing conditions. We can conclude that the 2DS probe cannot identify the morphological differences between a drop of water and particles sampled at a lower temperature. According the 2DS probe, the spherical particle geometry seems maintained regardless of temperature.

Nevertheless, careful examination of the images provided by the 2D-S could indicate some dependence of the surface condition of the particles depending on the temperature. The development of a specific analysis tool of the roughness of the contour of the particle images, could, if appropriate, quantify this observation.

It seems that the 2D-S instrumentation will not distinguish any phase difference within a snow particle.

## 3.2 CPI probe measurements

The CPI (Cloud Particle Imager) probe is an optical instrument that allows high-resolution imaging of cloud particles [8]. It allows the observation and digital recording (CCD camera, 1M pixels) image of the particles (from 20 to 2300 microns) with remarkable precision (pixel resolution of 2.3 microns). It uses an electro-optic system that allows real-time sampling of a maximum volume of 1L/s at 200m/s at a rate of 40 frames per second.

The CPI probe produces images by freezing the motion of the particles using a 25ns pulsed, high power laser diode. A particle detection system (PDS), made of two laser beams, defines the focal plane, identifies candidate cloud particles and triggers the imaging system (Figure 10).
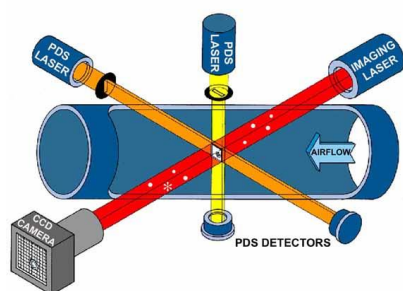


**Figure 10.** Schematic drawing of the internal electro-optical configuration of the CPI (from SPEC, Inc).

What makes the CPI probe particularly interesting for the observation of natural could particles is that, in addition to discrimination of the thermodynamic phase of the particles, the information delivered allows for the shape recognition of particles as well as the quantitative observation of their surface state (degree of icing for example).
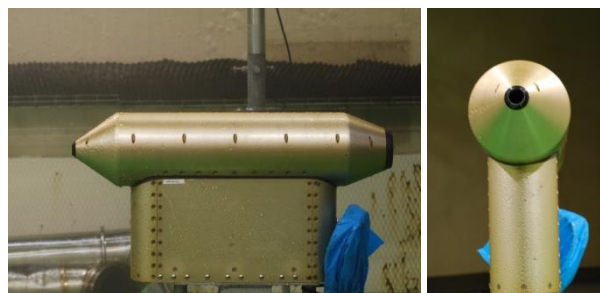


**Figure 11.** The CPI Particle imaging probe (side and front view)

As in the case of measurements with the 2DS probe, several ambient condition configurations were tested. The reference case was provided by measurements in positive temperature conditions. In this case, the particles produced by the snow gun remained liquid. Further measurements in freezing and intermediate thermal conditions were performed.



**Figure 12.** Setting of the CPI Particle imaging probe

The images produced by the CPI probe at positive temperature (+10°C) are characteristic of liquid droplets. They show spherical shapes including a bright spot at their center due to light diffraction. Let us precise that for all the CPI images, the dark and bright areas have been inverted to enhance the visual contrast detection.
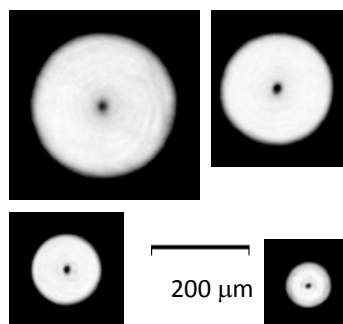


**Figure 13.** Sample of snow particle images obtained by the CPI probe for ambient temperature of + 10°C.

Conversely, the images of particles obtained at low temperature (-15°C) still show the Fresnel spot in the particle center but with heterogeneous shapes which are characteristics of ice crystals.
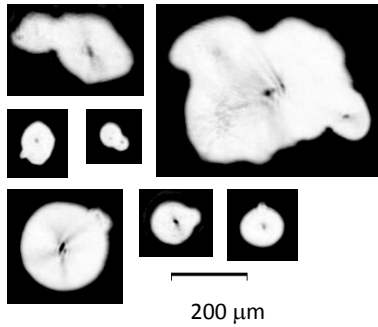
**Figure 14.** Sample of snow particle images obtained by the CPI probe for ambient temperature of -15°C.

Images obtained for the intermediate temperatures of -3°C and - 5°C have mixed populations particles which generally exhibit less deformed contours compared to observed shapes at -15°C.
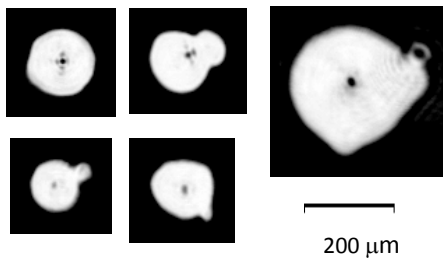


**Figure 15.** Sample of snow particle images obtained by the CPI probe for ambient temperature of -5°C.

Using the CPI images, a phase criterion based on a geometric aspect ratio seems being usable to discriminate the particle phase. Hence, defining a coefficient of sphericity as the aspect ratio of particles (i.e. coefficient ratio close to 1 meaning a round particle), one can sort the number of particles according the coefficient of sphericity for different ambient temperature. One can observe that the number of round particles decrease with the temperature. At +10 °C more than 75% of particles are spherical while at -15°C, about 25% of particles can be considered spherical.
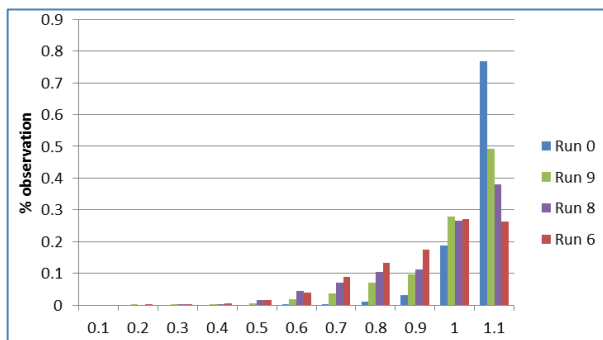


**Figure 16.** Coefficient of sphericity of particles at different ambient temperature (Run 0: +10°C, Run 9: -3°C, Run 8: -5°C, Run 6: -15°C).

# 4 The hot wire snow probe

The hot wire snow probe is derived from an airborne in-cloud icing probes, embarked on meteorological aircraft, and known as the Nevzorov sensor [5, 6, 7]. It consists of two separate sensor elements, with convex and concave windward face, placed in an airflow carrying freezing particles. The convex sensor mainly collects the liquid particles, while the concave sensor collects all of the particles (solid and liquid).

## 4.1 Working principle of the snow probe

The working principle of the probe is similar to aforementioned airborne cloud particle measurement probe.

It is made of two heated elements with a convex (or circular) and a concave element facing the wind. The geometry of these sensors is such that the solid particles, carried by the air flow, break or bounce in contact with the convex surface. Hence the circular probe only collects liquid particles. The semi-circular probe has a concave geometry that allows collecting all of incoming particles.
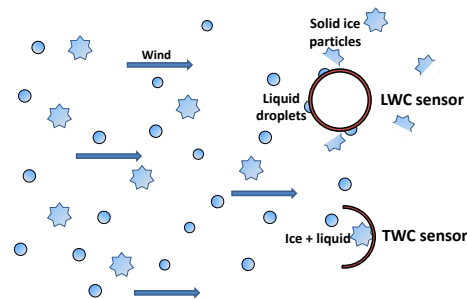


**Figure 17.** Working principle of the Liquid and Total Water sensors of the hot wire snow probe

Both elements are heated at elevated temperature (150 °C) to allow the melting and evaporation of the collected snow particles. The power needed to maintain the temperature of each element to a stabilized value is measured. From the coupled heat balance of each probe element one can deduce the liquid and solid water content present in the airflow.

## 4.2 The Probe Design

Prototype version of the sensors are in the form of a copper wire coil surrounding a cylindrical hollow support made of refractory material, with a length of about 60mm and 10mm in diameter. The wire diameter is chosen to be sufficiently fine so as to obtain uniform heat dissipation throughout the winding. The support is suspended by fine wires in a circular frame. This arrangement aims to reduce the probe contact surface with its support.
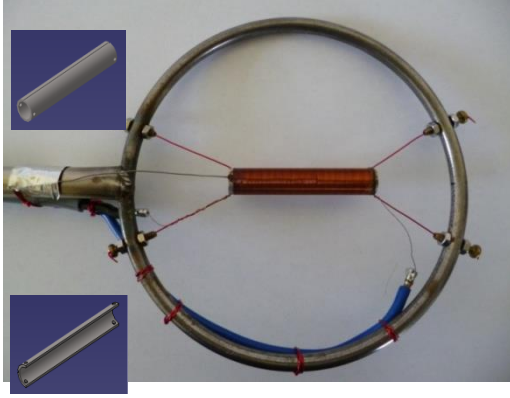
**Figure 18.** Prototype of the hot wire snow probe.

Given the amplitude of variation of the operating conditions of the hot-wire probe, a robust control system CRONE (Non Integer Order Robust Control) was implemented to ensure the stability of the regulation regarding the uncertainties of the process [9].

## 4.3 Thermal balance

Let us assume C (kg/m³) is the water concentration in the air flow and x.C (kg/m³) concentration of solid water phase, x being the solid fraction of water.

The power required to maintain both the O (liquid water sensor) and U (total water sensor) probes at the set temperature Tp can be divided into four contributions:

**Pdry**, power dissipated by convection: This is actually the power dissipated to the air flow,

**Pmelt**, latent heat of melting ice,

**Pwater**, sensible heat to raise the temperature of the water to the vaporization temperature,

**Pvap**, latent heat of vaporization of water,

Let Po be the power required to maintain the O probe at constant temperature:

$$Po = Pdry + Pwater + Pvap \qquad (1)$$

Let Pu be the power needed to maintain the U probe at constant temperature:

$$Pu = Pdry + Pmelt + Pwater + Pvap \qquad (2)$$

Detailing each equation one obtains a system of two equations with two unknowns, C(kg/m³) the water particle concentration and x.C (kg / m3) the concentration of solid water, x being the solid fraction of water.

The resolution of the equation system leads to:

$$x.C = \frac{\left(\frac{Pu-Pu\_dry}{v*Au} - \frac{Po-Po\_dry}{v*Ao}\right)}{Lf+Lv+Cpwater*100} \qquad (3)$$

$$C = \frac{\frac{Pu-Pu\_dry}{v*Au} - Lf*x.C}{Lv+Cpwater*100} \qquad (4)$$

One obtains the values of total and solid fraction concentration of water in the air flow from the measured power dissipated by the U and O probes.

## 4.4 Preliminary results

Measurements made with a preliminary design of the probe have shown promising results. Several experiments were made at -10°C. Examples of measured dissipated power are:

Po_dry= 27,4W,          Pu_dry= 40,7W,
Po= 40,6W,               Pu= 101,8W

The powers dissipated by the TW and LW sensors are used to calculate the snow particle concentration C= 4.2g/m³, and the fraction of solid water x=50%.

In parallel, a mesh collector was used to measure the snow particle concentration of 4.9 g/m³

The assessed total snow concentration and LWR are realistic.
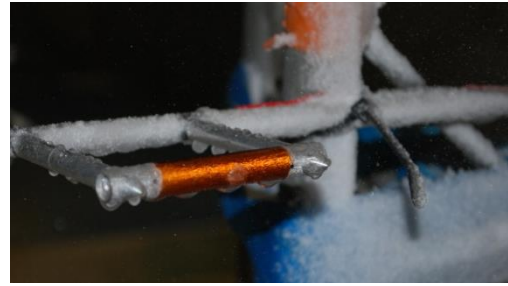


**Figure 19.** Early version of the LW hot wire snow probe.

## 5 Comments and perspectives

Measurements made with the 2DS probe to analyze the icing particles from snow cannons show that there is no morphological difference between liquid and solid phase particles produced in the climatic wind tunnel. The spherical particle geometry seems preserved whatever the temperature and the state of solidification.

In the analysis there is nothing to disambiguate the phase of negative temperature particles, that is to say, the fact of being in the presence of supercooled drops or frozen drops.

The measurements made with the CPI probe were more instructive. In particular, they confirmed the deformation of frozen particles with respect to liquid ones. The comparison of different situations in positive and negative temperature show that a criterion based on the sphericity coefficient can be used to post- process the images provided by the CPI. However, the method is far from being fully operational, since a truly quantitative information on the solid fraction of a complete population of particles requires statistical identification of the number of particle and as well as their volume associated with the sphericity coefficient. Such development has not been undertaken to date.

In parallel, the development of the hot wire probe should continue to provide a robust measurement tool that would monitor in real time the snow flow conditions produced in the wind tunnel. Measurements made with a preliminary design of the probe have shown promising results. The powers dissipated by the TW and LW sensors were used to calculate the snow particle

concentration which was close to that measured with a mesh collector.

Further experiments are planned with the improved probe design to confirm the relevance of this approach and establish the correspondence with actual snow mass accumulated on simple shapes.

Adaptation of the probe for measurements onboard of road or rail vehicle could be further developed.

## References

1. Vigano A. Experimental and Numerical modelling of wet snow accretion on structures. PhD thesis, France, (2012)
2. Boyne, H.S., Fisk, D.J., A laboratory comparison of field technique for measurement of the liquid fraction of snow. CRREL Spec. Rep 90.3 (1990)
3. Lawson, R. Paul, Darren O'Connor, Patrick Zmarzly, Kim Weaver, Brad Baker, Qixu Mo, et Haflidi Jonsson, The 2D-S (Stereo) Probe: Design and Preliminary Tests of a New Airborne, High-Speed, High-Resolution Particle Imaging Probe. *Journal of Atmospheric and Oceanic Technology,* 23, no 11 (novembre 2006): 1462-1477, (2006)
4. Baumgardner, D., J.L. Brenguier, A. Bucholtz, H. Coe, P. DeMott, T.J. Garrett, J.F. Gayet, Airborne instruments to measure atmospheric aerosol particles, clouds and radiation: A cook's tour of mature and emerging technology. *Atmospheric Research, 102*, no 1-2 (octobre 2011): 10-29, (2011)
5. Merceret F.J., Schricker T.L., A New Hot-Wire Liquid Cloud Water Meter, *J. Appl. Met.*, 14, 319-326 (1975)
6. King W.D., Parkin D.A., and Handsworth R.J., A hot-wire liquid water device having fully calculable response characteristics, *J. Appl. Met.*, 17, 1809-1813 (1978)
7. Korolev, A.V., Strapp J.W., Isaac G.A., Nevzorov A.N., The Nevzorov Airborne Hot-Wire LWC–TWC Probe Principle of Operation and Performance Characteristics, *J. Atm. Oce. Met.*, 15, 1495-1510. (1998)
8. Lawson R. P., Baker B.A., Schmitt C.G., and Jensen T.L., An overview of microphysical propoerties of Artic clouds observed in May andJuly 1998 during FIRE.ACE. *J. Geophys. Res.*, 106, 14989-15014, (2001)
9. Oustaloup A. (1991), « La commande CRONE », Editions Hermès, Paris

# CR 1-1-3/2012 - the snow loads code in Romania

Alexandru Aldea[1,a], Sorin Demetriu[1], Dan Lungu[1], Cristian Neagu[1], Radu Vacareanu[1] and Cristian Arion[1]

[1]Technical University of Civil Engineering Bucharest, Bd. Lacul Tei nr.122-124, Bucharest 020396 Romania

**Abstract.** The paper presents the most recent Romanian code for snow loads, CR 1-1-3/2012, enforced since October 2013. The code is harmonised with the Eurocode EN 1991-1-3 in what concerns the general approach and the snow loads on roofs. The paper focuses on the zonation of the snow load on the ground, using data recorded during the time interval 1930-2005 at 122 meteorological stations. The Gumbel probability distribution for maxima was used for computing characteristic values of snow load on the ground with an annual probability of exceedance of 0.02 (i.e., mean return period of 50 years). The zonation map is developed at ground level and is valid up to an altitude of 1000 m. The code provides relationships for establishing snow loads on the ground at altitudes between 1000 m and 1500 m. CR 1-1-3/2012 does not consider zones with exceptional snow loads on the ground. However, the paper includes considerations on several cases where the criteria for exceptional snow loads are fulfilled.

## 1 Introduction

### 1.1 Romania's winters

Located in Eastern Europe (between 43.55º and 48.28º North latitude and 20.25º and 29.83º East longitude), Romania is a country with a transition temperate-continental climate [1].

The exiled Roman poet Ovid (Publius Ovidius Naso, 43 BC – AD 17/18) left probably the oldest (AD 8-12) mentions on the hard winters on the Romanian Black Sea Coast in his work Tristia (i.e. "Sorrows") and Epistulae ex Ponto (i.e. "Letters from the Black Sea") [2]:

*"And when dark winter shows its icy face,*
*and the earth is white with marbled frost, [...]*
*Snow falls, and, once fallen, no rain or sunlight melts it,*
*since the north wind, freezing, makes it permanent.*
*So another fall comes before the first has melted,*
*and in many parts it lingers there two years. [...]*
*Shall I speak of solid rivers, frozen by cold,*
*and water dug out brittle from the pools?*
*The Danube itself, no narrower than lotus-bearing Nile,*
*mingling with deep water through many mouths,*
*congeals, the winds hardening its dark flow,*
*and winds its way to the sea below the ice:*
*Feet cross now, where boats went before, [...]*
*I've seen the vast waters frozen with ice,*
*a slippery shell gripping the unmoving deep.*
*Seeing was not enough: I walked the frozen sea, [...]*
*The ships stand locked in frozen marble,*
*and no oar can cut the solid wave."*
*"I'm here, abandoned, on the furthest shores of the world,*
*where the buried earth carries perpetual snowfall.[...]*
*here winter makes the sea a pathway for walkers,[..] [2].*

If in mountain region first snows appear even in August and September, in general the snowy winter comes for most of the territory in November and last until March-April. Based on data from the time interval 1961-2000, the average annual number of days with snow falls varies between ~20 (lowlands and plains), ~30 days (hills and plateau) to ~100 days (top of mountains) [3]. The average annual number of days with snow layer on the ground varies between less than 20 days on the Black Sea shore and over 200 days on high mountain tops. As an example, in Tables 1 and 2 are presented data [3] [4] from several meteorological stations in Romania, whose locations are shown in Figure 1 (design snow load data for the same stations are presented in Chapter 2).

**Table 1.** Examples of snow data [3] [4] at meteorological stations in Romania: (i) station altitude, (ii) average annual number of days with snow layer (1926-1955) (iii) average annual number of days with snow layer (1961-2000), (iv) maximum annual number of days with snow layer (1961-2000)

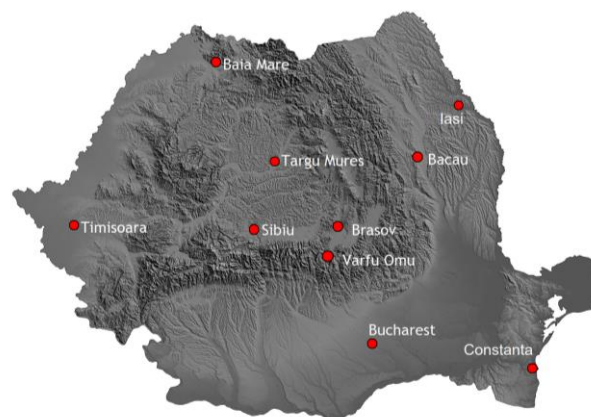| Station | (i) [m] | (ii) 1926-1955 | (iii) 1961-2000 | (iv) |
|---|---|---|---|---|
| Constanţa | 13 | 24 | 15 | 44 |
| Bucharest | 90 | 53 | 48 | 93 |
| Vârful Omu | 2504 | 219* | 220 | 280 |
| Târgu Mureş | 308 | 57 | 62 | 92 |
| Braşov | 534 | 71 | 73 | 102 |
| Sibiu | 443 | 54 | 58 | 102 |
| Iaşi | 102 | 57 | 65 | 115 |
| Bacău | 184 | | 64 | 115 |
| Baia Mare | 216 | | 63 | 98 |
| Timişoara | 86 | 30 | 29 | 63 |

* data from 1941-1955



**Figure 1.** Location in Romania of the meteorological stations from Tables 1÷4

[a] Corresponding author: aldea@utcb.ro

In Figure 2 are exemplified histograms of the monthly average number of days with snow layer (1926-1955) for several meteorological stations from those indicated in Table 1 (data from [4]).
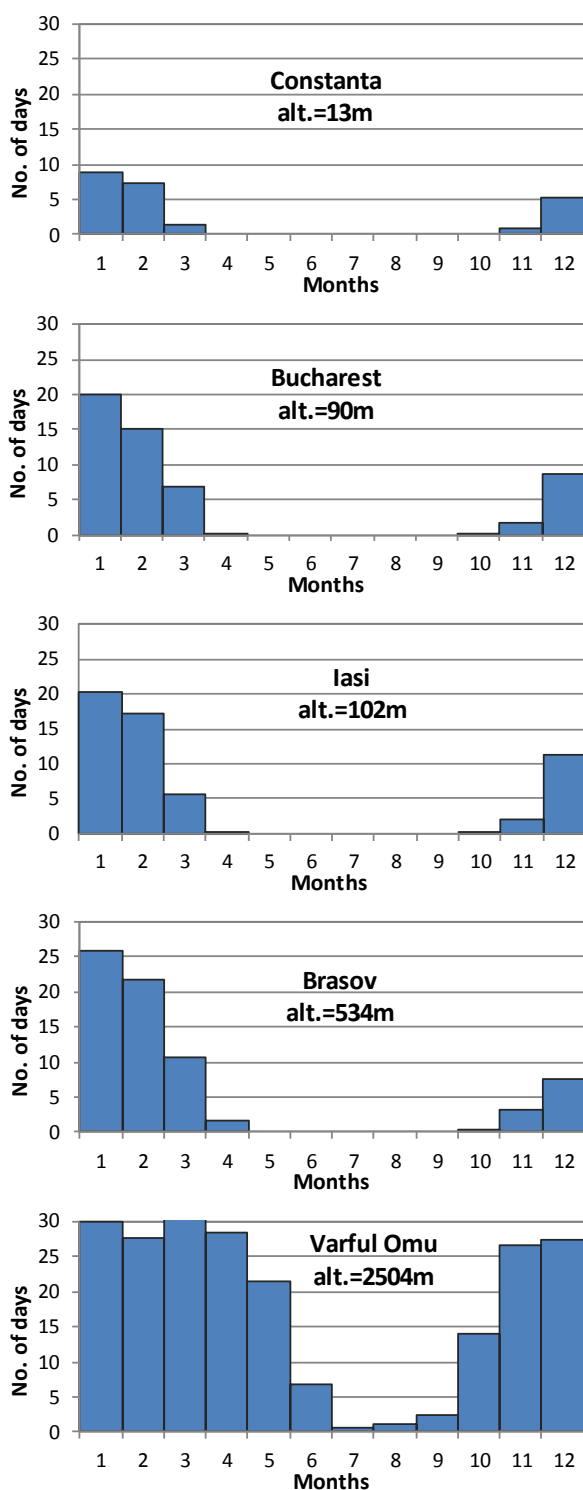


**Figure 2.** Examples of histograms of the monthly average number of days with snow layer (1926-1955) for meteorological stations in Romania

In Table 2 are indicated values of the maximum annual snow depths [3] [4] at several meteorological stations in Romania.

| Station | Alt. $A$ [m] | $h_{max}$ 1926-1955 [m] | $h_{max}$ 1961-2000 [m] |
|---|---|---|---|
| Constanţa | 13 | 0.54 | 0.46 |
| Bucharest | 90 | 1.06 | 0.80 |
| Vârful Omu* | 2504 | 3.70 | 2.92 |
| Târgu Mureş | 308 | 0.75 | 0.48 |
| Braşov | 534 | 0.66 | 0.44 |
| Sibiu | 443 | 0.65 | 0.60 |
| Iaşi | 102 | 0.64 | 0.66 |
| Bacău | 184 | | 0.65 |
| Baia Mare | 216 | | 0.82 |
| Timişoara | 86 | 0.6 | 0.43 |

* data from 1941-1955

An exceptionally hard winter with heavy snow falls and blizzards was experienced in 1953-1954, when in the southern and eastern Romania the snow layer depth over passed 1 m at 20 meteorological stations (a maximum of 1.73 m was observed), and the snowdrifts reached 4÷6 m height due to strong winds reaching 125 km/h [4]. In Figure 3 is presented an image from Bucharest [5] during the 1954 winter. Almost every winter significant snowdrifts occur in south-eastern Romania (Figure 4).



**Figure 3.** Tramway in Bucharest during 1954 winter [5]



**Figure 4.** Snow drift in south-eastern Romania (January 2014 [6])

## 1.2 Meteorological observations

The first meteorological observations were made on Romanian territory starting with 19th century (in 14 major cities), and the National Meteorological Institute of Romania was established in 1884, Romania being one of the founding countries of the International Meteorological Organization [1]. The meteorological network quickly developed: 1887 - 30 stations, 1899 - 50 stations, 1906 - 66 stations [3], 2013 – 258 stations [1].

Nowadays the meteorological observations are performed by the National Meteorological Administration [1], with 71% of stations in lowlands, 12% in hilly areas, 4% on the sea shore and 13% in mountains. Some stations are located on mountain's top, like Ceahlău Toaca – 1897 m and Călimani – 2021 m, the highest station being Vârful Omu, located at 2504 m.

The Romanian meteorological network is integrated in the permanent world survey within the Region VI – Europe of the World Meteorological Organization.

## 1.3 Snow load codes

In Romania snow loads were considered in design since 1950, the code being revised in 1956, 1974, 1978 and 1992 [7].

The 1992 code consisted of 12 pages: 4 pages indicate the snow load on the ground (map and table with main localities), 5 pages the snow load on the roof, 1 page the partial safety factors and 2 pages the snow loads principles. The characteristic snow load on the ground was defined with 10 years mean return period. The territory was divided in 4 areas A÷D plus the mountain area E for which a table for snow load on the ground was recommended (with altitude dependent values from 700m to 2500m). In Figure 5 is presented the zonation map of the snow load on the ground (in kN/m²) from the 1992 snow load code. The E zones contours are not shown in Figure 5, they were highly irregular, identifying the borders of the regions with altitudes higher than 700 m.
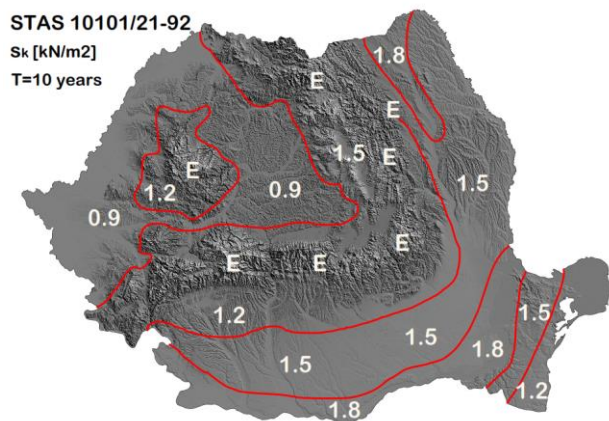


**Figure 5.** Zonation of snow load on the ground in the 1992 code

As Romania became a candidate state for joining European Union, in 2005 was issued the CR 1-1-3/2005 snow loads code, enforced from 2006. The provisions were following the Eurocode EN 1991-1-3

recommendations. A major change was the definition of the characteristic snow load on the ground with 50 years means return period. The lognormal probability distribution was used for computing the characteristic values of snow load on the ground [8] [9]. In Figure 6 is presented the zonation map of the snow load on the ground (in kN/m²) from the 2005 code.
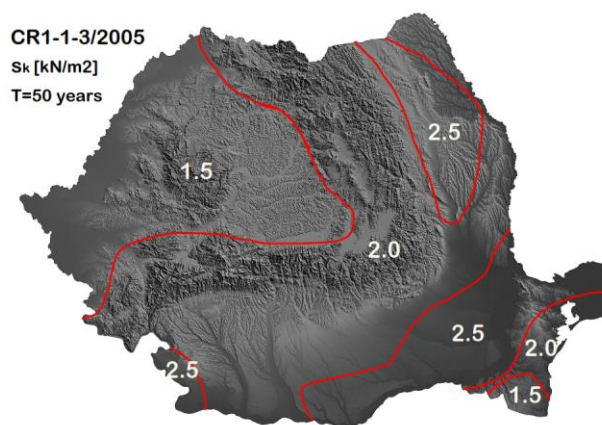


**Figure 6.** Zonation of snow load on the ground in the 2005 code

An updated edition of the Romanian snow loads code, CR 1-1-3/2012 [10] was enforced in 2013. This code is harmonised with the Eurocode EN 1991-1-3 [11] in what concerns the general approach and the snow loads on roofs.

# 2 The 2012 snow loads code for design

## 2.1 Snow load on the ground

The setting of the snow load on the ground in the recent Romanian code CR 1-1-3/2012 [10] was done using data from 122 meteorological stations [12].

The snow data (annual maxima) was available from the period 1930-2005, with different time intervals for different stations. In case of three recently installed meteorological stations the number of available annual maxima was 10÷13 (they were included in the data set in order to ensure a reasonable geographical coverage of stations); the largest number of data at a station was from 74 years with snow, and the average number of data was 48, a number that can be considered as reasonable for establishing values with a mean return period of 50 years.

The coefficient of variation of the maximum annual ground snow load in Romania varies between 0.35 and 1.38, with an average value of 0.59). The frequency histogram of the coefficient of variation is shown in Figure 7. In Figure 8 is presented the coefficient of variation as function of the altitude. The range of coefficients of variation and the tendency to decrease with altitude are similar to those from European countries [13], and one may notice that this tendency is slightly slower than in the case of Germany for example.

The skewness of the maximum annual ground snow load was found to vary in between 0.22 and 4.14, with an average value of 1.38. The skewness frequency histogram is shown in Figure 9.
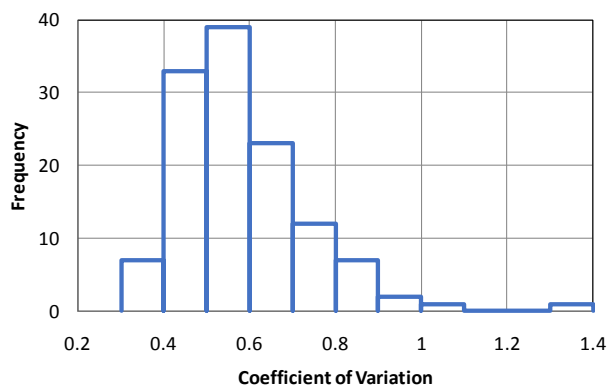
**Figure 7.** Histogram of the coefficient of variation of observed annual maximum snow loads on the ground at 122 meteorological stations in Romania
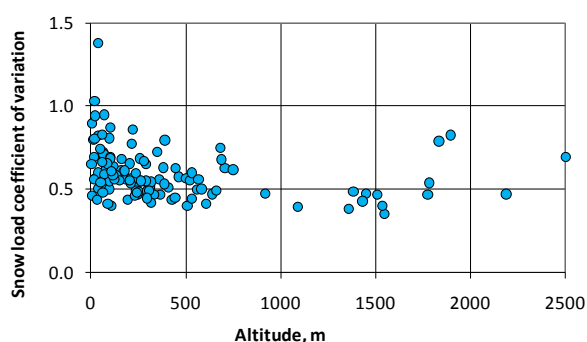


**Figure 8.** Coefficient of variation of observed annual maximum snow loads on the ground at 122 meteorological stations versus altitude in Romania

The largest values of the coefficient of variation were observed at low altitudes, but some large values also came out at altitudes higher than 1700 m.
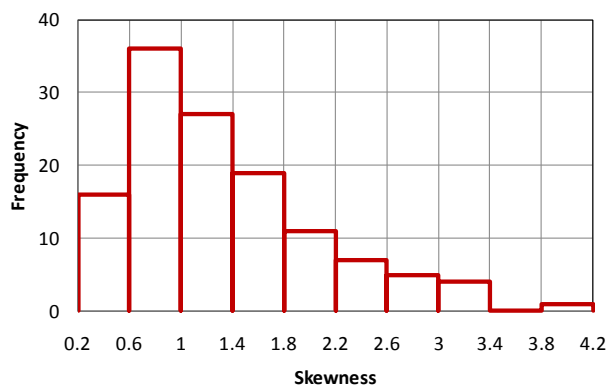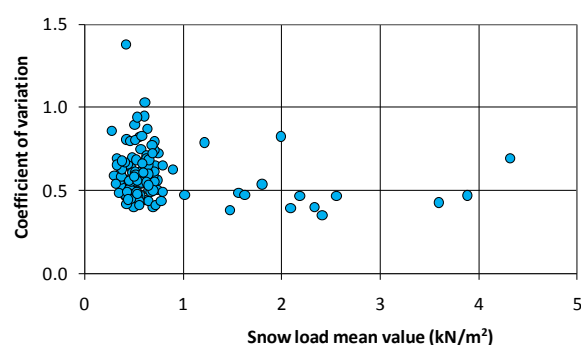


**Figure 9.** Histogram of the skewness of observed annual maximum snow loads on the ground at 122 meteorological stations in Romania

In Figure 10 is presented the variation of the mean value of the annual maximum snow load on the ground with altitude. In Figures 11 and 12 are shown the standard deviation and the coefficient of variation versus the mean value of the annual maximum snow load on the ground. Again the tendencies are similar to those from other European countries [13].
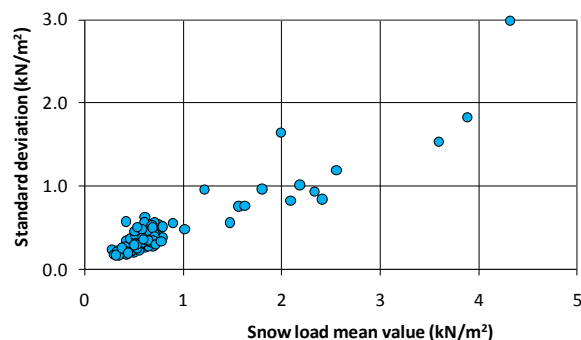


**Figure 10.** Standard deviation versus mean value of observed annual maximum snow loads on the ground at 122 meteorological stations in Romania
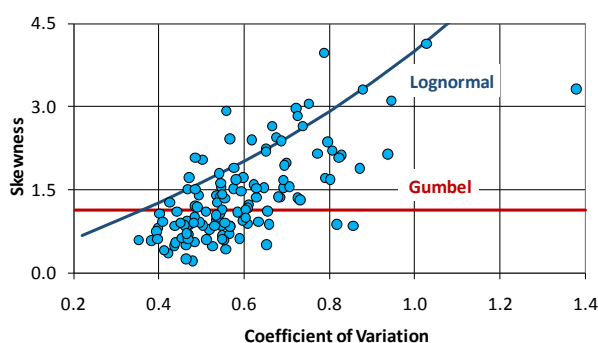


**Figure 11.** Coefficient of variation versus mean value of observed annual maximum snow loads on the ground at 122 meteorological stations in Romania

In Table 3 are exemplified annual maximum snow load on the ground data and statistics at the meteorological stations from Table 1 and Figure 1.

**Table 3.** Examples of data and statistics of annual maximum snow load on the ground meteorological stations in Romania: station altitude, number of years with snow data, coefficient of variation (COV), and skewness

| Station | Alt. [m] | No. yrs. | COV | Skew. |
|---|---|---|---|---|
| Constanţa | 13 | 45 | 0.79 | 1.71 |
| Bucharest | 90 | 69 | 0.54 | 1.40 |
| Vârful Omu | 2504 | 65 | 0.69 | 1.68 |
| Târgu Mureş | 308 | 60 | 0.49 | 1.19 |
| Braşov | 534 | 67 | 0.44 | 0.85 |
| Sibiu | 443 | 64 | 0.45 | 0.91 |
| Iaşi | 102 | 61 | 0.69 | 1.94 |
| Bacău | 184 | 58 | 0.57 | 0.70 |
| Baia Mare | 216 | 60 | 0.54 | 0.95 |
| Timişoara | 86 | 48 | 0.68 | 1.37 |

The Gumbel probability distribution for maxima was used for computing characteristic values of snow load on the ground with an annual probability of exceedance of 2% (i.e., mean return period of 50 years). Whenever conversions from snow depth to snow load were done, the snow weight density was considered to be 2 kN/m³.

Gumbel distribution is recommended by the Eurocode [11] and was found appropriate for modelling snow loads on the ground in several countries around the world [13, 14, 15, 16, 17]. In Figure 12 is presented the skewness versus the coefficient of variation for the annual maximum snow load on the ground in Romania. The plot suggests that in future detailed analysis of data at each station are necessary, and that probably a mixed solution like the one in case of Germany [13] may apply. Moreover, "For future research it is recommended that to solve this problem it will be necessary to work together with meteorological people taking into account local climatic conditions" [13, Annex 3].



**Figure 12.** Skewness versus coefficient of variation of observed annual maximum snow loads on the ground at 122 meteorological stations in Romania

In Table 4 are exemplified annual maximum snow load on the ground data and statistics together with the characteristic values of snow load on the ground (computed with 2% annual probability of exceedance in Gumbel distribution for maxima).

The Romania zonation map of snow load on the ground has areas of constant values according to the set of values recommended by ISO 4355 [18]: 1.5, 2.0 and 2.5 kN/m². The corresponding code values of the snow load on the ground for the selected stations in Table 1 and Figure 1 are also given in Table 4.

**Table 4.** Examples of data and statistics of annual maximum snow load on the ground meteorological stations in Romania: maximum snow load, mean annual maximum snow load, characteristic value, and code snow load $s_k$

| Station | Max. load [kN/m²] | Mean load [kN/m²] | Charact. load [kN/m²] | $s_k$ [kN/m²] |
|---|---|---|---|---|
| Constanţa | 1.7 | 0.5 | 1.4 | 1.5 |
| Bucharest | 2.0 | 0.7 | 1.6 | 2.0 |
| Vârful Omu | 14.9 | 4.3 | 12.1 | - |
| Târgu Mureş | 1.1 | 0.4 | 1.0 | 1.5 |
| Braşov | 1.4 | 0.6 | 1.3 | 2.0 |
| Sibiu | 1.1 | 0.5 | 1.0 | 1.5 |
| Iaşi | 2.5 | 0.6 | 1.8 | 2.5 |
| Bacău | 1.7 | 0.7 | 1.8 | 2.5 |
| Baia Mare | 1.7 | 0.6 | 1.5 | 2.0 |
| Timişoara | 1.2 | 0.4 | 1.0 | 1.5 |

The Romania's zonation map is for snow load on the ground (and not at sea level) and is valid for altitudes lower or equal to 1000 m, Figure 13.
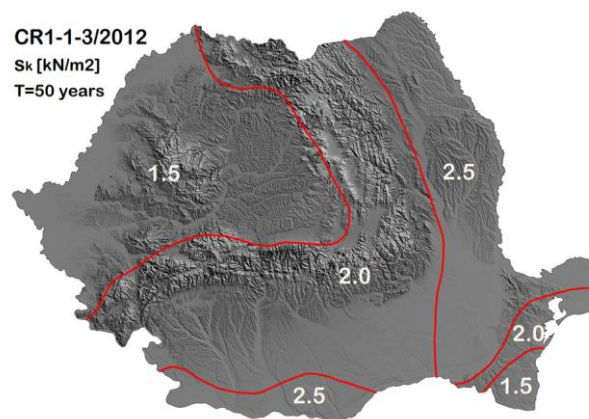


**Figure 13.** Zonation of the snow load on the ground in Romania, for altitudes ≤ *1000 m* [10]

The central and western part of Romania (somehow protected by Carpathian Mountains) and the south-eastern corner on Black Sea coast shows the lowest snow load, while the north-east and south-west parts, exposed to strong winter winds have the highest snow loads.

For altitudes *1000 m < A ≤ 1500 m*, the code snow load on the ground is given by following relations, equations (1) and (2).

For areas with $s_k (A≤1000 m)=2.0 kN/m²$:

$$s_k (1000 m<A≤1500 m) = 2.0 + 0.00691 (A-1000) \quad (1)$$

for areas with $s_k (A≤1000 m)=1.5 kN/ m²$:

$$s_k (1000 m<A≤1500 m) = 1.5 + 0,00752 (A-1000) \quad (2)$$

where $s_k (A≤1000 m)$ values are those from Figure 13. In Table 5 are given examples of snow loads on the ground at different altitudes, from the application of equations (1) and (2).

**Table 5.** Examples of snow loads on the ground at different altitudes between 1000 m and 1500 m

| Altitude A [m] | $s_k$ (1000 m < A ≤ 1500 m), kN/m² | |
|---|---|---|
| | Zone where | |
| | $s_k$ (A≤1000 m)= 1.5 kN/m² | $s_k$ (A≤1000 m)= 2.0 kN/m² |
| 1000 | 1.5 | 2.0 |
| 1100 | 2.3 | 2.7 |
| 1200 | 3.0 | 3.4 |
| 1300 | 3.8 | 4.1 |
| 1400 | 4.5 | 4.8 |
| 1500 | 5.3 | 5.5 |

The exceptional snow load on the ground, as indicated in [13], can be identified through the ratio of the maximum observed load to the characteristic snow load determined without that value. If the ratio is greater than 1.5, the conditions of exceptional snow load are fulfilled. In Romania such case appeared at several stations. For example, at Sulina, a city on the extreme eastern Black

Sea border, at an altitude of 3 m, the ratio was 1.54; at Giurgiu, in southern Romania on Danube river, at an altitude of 24 m, the ratio was 1.82. Also in mountain area, at Fundata, at an altitude of 1384 m, the ratio was 1.61. As mentioned in [14], it is difficult to draw exceptional loads maps, and in Romania also, future studies are necessary, involving up-to-date data and the cooperation of meteorology specialists. In CR 1-1-3/2012 there are no areas with exceptional snow loads.

## 2.2 Snow load on the roof

The snow load on the roof is established in the Romanian code CR 1-1-3/2012 in the same way as in the Eurocode, with the same loading patterns and shape coefficients.

However, a supplementary factor is considered in the Romanian code: the importance-exposure factor for snow loads $\gamma_{Is}$.

The importance-exposure building categories are defined in the Romanian code CR-0/2012 „Basis of constructions design" [19] based on the human and economic consequences that may be induced by a major natural and/or anthropic hazard and on the role and importance in post-disaster activities.

There are four importance-exposure categories with the following simplified description:
− category I – essential/vital for society and for post-disaster intervention (for example: emergency hospitals, medical emergency facilities, police stations, firefighter stations, communication centers, essential buildings for public administration, water storage constructions, constructions containing hazardous materials, etc.);
− category II – with high danger for humans in case of damage (for example: hospitals with over 100 beds, education facilities with over 250 persons capacity, residential, commercial, offices with over 300 persons capacity, museums and cultural heritage buildings, stadiums, etc.);
− category III – current buildings and constructions (all except those from categories I, II and IV), and
− category IV – of less importance, with low danger for humans in case of damage (for example: temporary constructions, agriculture facilities, storage facilities, etc.

For the categories III and IV the importance-exposure factor for snow loads $\gamma_{Is}=1$, for the category II $\gamma_{Is}=1,1$, and for the category I $\gamma_{Is}=1,15$. The values of the importance-exposure factor roughly correspond to an increase of the mean return period of snow load on the ground from 50 years to 100 years (considering the Gumbel distribution for maxima).

Other codes also have a similar factor. For example, in the International Building Code [20], ASCE-7 [21], New York City Building code [22], etc. are defined structural occupancy categories (category order is reversed compared to Romania) that have an associated importance snow factor $Is$ with values: for category I – $Is=0.8$, II – $Is=1$, III – $Is=1.1$ and IV – $Is=1.2$.

The 2005 Canadian National Building Code [23] defines importance categories with associated importance

snow factors: importance category Low - $Is=0.8$, Normal – $Is=1$, High – $Is=1.15$ and Post disaster – $Is=1.25$.

The code CR 1-1-3/2012 was accompanied by comments and examples, published as an informative annex.

Following the French example [24], a snow load application/guide volume was published by the Technical University of Civil Engineering Bucharest [25].

## 3 Final considerations

Proper consideration of snow loads in the design of new buildings and in the evaluation of existing buildings will reduce the chances of accidents that, unfortunately, continue to appear from time to time.

For example, in Romania, due to snow load, in 2012 in Cluj [26] and Iasi [27] the metallic roof structure at entrance of shopping areas collapsed, Figures 14 and 15, and in Suceava [28], Cavnic [29], Podgoria [30] and Focsani [31] wooden roofs collapsed, Figures 16, 17, 18 and 19.



**Figure 14.** Collapse of a new metallic roof structure in Cluj [26]



**Figure 15.** Collapse of a new metallic roof structure in Iasi [27]



**Figure 16.** Collapse of an old wooden roof in Suceava [28]

**Figure 17.** Collapse of a wooden roof structure in Cavnic [29]



**Figure 18.** Collapse of a wooden roof structure in Podgoria [30]



**Figure 19.** Collapse of a wooden roof structure in Focsani [31]

The recent snow load code of Romania (2012) is harmonised with the Eurocode EN 1991-1-3. It adopted the same 2% annual probability of exceedance, and the characteristic snow load (obtained from Gumbel distribution) on the ground is defined at the ground level, and not at the Sea level.

The strong winter winds from south-west and north-east are correlated with the areas of highest characteristic snow load on the ground (2.5 kN/m$^2$), while inside the Carpathian arch and on the south-eastern Black Sea shore the load is lower (1.5 kN/m$^2$).

At present, an update of the zonation map is expected, for considering the observed snow data from the last 10 years, for performing a detailed analysis on the type of probability distribution to be considered and on the exceptional snow loads. Also, there is a need for details of snow loading for solar panels (on ground and on roofs) and other special cases.

## References

1. National Meteorological Agency (in Romanian) http://www.meteoromania.ro
2. Ovid, *Tristia* and *Epistulae ex Ponto* (AD 8-12) Book TIII.X:1-40 Winter in Tomis, and Book TIII.X:41-78 Barbarian Incursions, http://www.poetryintranslation.com/PITBR/Latin/ translation by Kline, A.S., accessed – April 2016
3. *Romania's climate*, by National Meteorological Administration, Romanian Academy Publishing house, 365p., in Romanian (2008)
4. O. Bogdan, A.F. Marinica, I. Marinica. Comparative climatic characteristics between the winter of 2011–2012 and the winter of 1953–1954 in the south of Romania, Rev. Roum. Géogr./Romanian Journal of Geography, 57, (1), p. 9–24 (2013)
5. http://www.otopeni.net/?p=916
6. http://adevarul.ro/locale/buzau/
7. STAS 10101/21-78 and 92. *Actions in construction. Snow loads* (in Romanian), National Institute of Standardization (1978 and 1992)
8. D. Lungu, S. Demetriu, A. Aldea. Basic Code parameters for Environmental Actions in Romania harmonised with EC1, Proceedings *7th International Conference on Applications of Statistics and Probability in Civil Engineering, Reliability and Risk Analysis*, ICASP-7, Paris, Vol. 2, p. 881-887, A.A. Balkema, Rotterdam (1995)
9. D. Lungu, A. Aldea, S. Demetriu. Probabilistic wind and snow hazards assessment for Romania, Proceedings of the *1st International Scientific-Technical Conference – Technical Meteorology of the Carpathians*, Ukraine, p.35-43 (1998)
10. *CR 1-1-3/2012 – Design code. Evaluation of snow loads on constructions*, Ministry of Regional Development and Tourism, Romania, 36p. (2013)
11. European Standard EN 1991-1-3, Eurocode 1, 2002, 2006. Basis of design and actions on structures, Part 1-3: Snow loads. CEN/TC250
12. D. Lungu, S. Demetriu, A. Aldea, C. Arion, R. Vacareanu. Statistics of the Maximum Annual Snow Load in Romania. Proceedings *6th International Symposium on Environmental Effects on Buildings and People: Actions, Influences, Interactions, Discomfort*, EEBP VI, Book of keynote lectures and extended abstracts / eds. A. Flaga, T. Lipecki. - Cracow: Polish Association for Wind Engineering, CD-ROM, 8p. (2010)
13. L. Sanpaolesi. Scientific Support Activity In The Field Of Structural Stability Of Civil Engineering Works - Snow Loads, Final Report, Commission Of The European Communities, DGIII - D3, Contract n° 500269/1996, 55p. + Annexes 1-5, 75p. (1998)
14. L. Sanpaolesi. Snow loads on roofs in Europe: research and standardization. *Proceedings of Snow Engineering International Conference*, Hjort-Hansen, Holand, Loset and Norem (eds.), Balkema, p.3-10 (2000)
15. S. Sakurai, O. Joh. Statistical analysis of annual extreme ground snow depths for structural design, J. of Struct. Constr. Engngr., AIJ, nr.436, 11p. (1992)

16. S. Sakurai, O. Joh, T. Shibata. Statistical analysis of annual extreme ground snow loads for structural design, J. of Struct. Constr. Engngr., AIJ, nr.437, 10p. (1992)
17. V. Otstavnov. Elaboration of draft map for snow loads in Russia, Research Report 16-13-135/96, CNIISK, Moscow (1996)
18. *ISO DIS 4355. Bases for design of structures. Determination of snow loads on roofs* (1992-2013)
19. *CR-0/2012. Basis of constructions design.* Ministry of Regional Development and Tourism, Romania, 32p. (2012)
20. *International Building Code,* International Building Council, USA, 684p. (2003)
21. *ASCE/SEI 7-10. Minimum design loads for buildings and other structures.* American Society of Civil Engineers, USA, 658p. (2010)
22. *New York City Building Code* 2008, with 2011 Supplement, http://publicecodes.cyberregs.com/st/ny/ (2008)
23. R. Riffel. 2005 National Building Code. Wind and Snow Importance Factors, Canadian Society for Civil Engineering Annual Conference, http://www.ucalgary.ca/en/civil/csce_calgary/2004/riffellcodecommittee (2004)
24. *Actions de la neige sur les bâtiments. D'après l'Eurocode 1, Calcul des charges de neige sur les toitures*, 71p, CSTB (2010)
25. A. Aldea, C. Neagu, C. Arion. *Guide for snow loads according to CR 1-1-3/2012*, Ed. Conspress of Technical University of Civil Engineering Bucharest, 77p., (2013)
26. http://www.stiridecluj.ro/
27. http://adevarul.ro/
28. http://www.romaniatv.net/
29. http://maramedia.ro
30. http://www.jurnaluldebuzau.ro/
31. http://www.monitorulvn.ro/

# Authors index